T-ray Biosensing

by

Samuel Peter Mickan

B.E. (Electrical & Electronic, First Class Honours),
The University of Adelaide, Australia, 1997

B.A. (European Studies),
The University of Adelaide, Australia, 2002

Thesis submitted for the degree of

Doctor of Philosophy

in

The School of Electrical & Electronic Engineering,
The Faculty of Engineering, Computer and Mathematical Sciences
The University of Adelaide, Australia

December, 2003

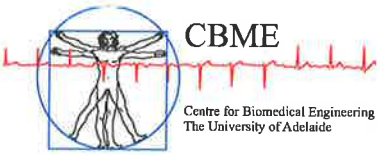

to my family

Contents

Abstract

This Thesis focusses on the area of biosensing with terahertz radiation, or T-rays. Terahertz (THz) refers to electromagnetic radiation in the 0.1 THz to 10 THz frequency range, where 1 THz = 10^{12} Hz.

The work described in this document contributes three major advances to research on T-ray biosensing: (i) the development of a novel technique for T-ray protein spectroscopy, using organic solvents to study water binding to biomolecules; (ii) the application of double-modulation to T-ray Differential Time-Domain Spectroscopy (DTDS), enabling the characterisation of thin dielectrics and sensing of thin biomolecular films; and (iii) the exploration of near-field T-ray generation using a tightly-focussed laser beam.

In this Thesis, the basics and previous work in T-ray instrumentation and sensing techniques are reviewed, explained and developed, covering generation and detection of T-rays, pulsed T-ray systems, previous studies in T-ray sensing, and T-ray imaging.

Novel protein spectroscopy experiments in organic solvents are described, demonstrating the first observations of free water molecules binding to protein with T-rays.

Double-modulated DTDS is used for the first time to characterise thin samples in the GHz–THz range, and a novel technique of T-ray bioaffinity sensing is shown to compete with commercial biosensors.

Liquid DTDS is presented as a method to improve the sensitivity of liquid spectroscopy using double-modulated DTDS. Preliminary experiments indicate the potential of this technique for achieving higher levels of sensitivity to liquids. This will lead to improved protein spectroscopy and measurements in biological systems.

One of the major limitations of T-ray systems in imaging applications is the wavelength-dependent Rayleigh limit of resolution, which can be surpassed using near-field techniques. A novel implementation uses highly focussed optical light to generate near-field T-rays. Studies of near-field T-ray generation point the way to a new source for T-ray microscopy, potentially producing unprecedented resolution and sensitivity. Combined with a DTDS biosensor, near-field resolution opens up possible applications in non-invasive probing of high-density biochips.

The significance of applying T-rays to biosensing arises from the enormous complexity of biological problems, the potential market for novel biochemical instrumentation, the noninvasive nature of T-rays, and the potential benefit to mankind. The contributions in T-ray biosensing presented in this Thesis are important steps towards the understanding of protein structure and function, the development of next-generation high-speed electronic materials, and the eventual clinical applications of T-rays.

Conventions used in this Thesis

The following conventions have been adopted in this Thesis:

1. **Definitions.** The T-ray band is defined in this Thesis to span from 0.1 to 10 THz (THz = 10^{12} Hz). This is an emerging definition in the literature. The T-ray band overlaps a little with the millimetre wave band (at lower T-ray frequencies) and the far-infrared band (at higher T-ray frequencies).

2. **Notation.** The acronyms and symbols used in this Thesis are defined in the Glossary on p. 349. Standard abbreviations are used for the order of magnitude: T, tera-, 10^{12}; G, giga-, 10^{9}; M, mega-, 10^{6}; k, kilo-, 10^{3}; m, milli-, 10^{-3}; μ, micro-, 10^{-6}; n, nano-, 10^{-9}; p, pico-, 10^{-12}; f, femto-, 10^{-15}.

3. **Units.** All T-ray electric field amplitude data in this Thesis is expressed in *arbitrary units* (A.U.). This means that the amplitude of the T-ray electric field has been normalised to a peak measurement, or to another reference measurement on the same system, depending on the experiment.

4. **Spelling.** Australian English spelling conventions have been used, as defined in the Macquarie English Dictionary (A. Delbridge (Ed.), Macquarie Library, North Ryde, NSW, Australia, 2001).

5. **Formatting.** This document was compiled using LaTeX2e.

6. **Mathematics.** MATLAB code was written using MATLAB Version 6.1 (Release 12.1) – manufacturer: the MathWorks Inc., Natick, MA, USA; URL: `http://www.mathworks.com`.

7. **Referencing.** The Harvard style has been adopted for referencing.

8. **Diagram colours.** The following colour scheme is approximately followed in the diagrams:

   - Blue: T-ray beams (T-rays are invisible to the naked eye).

- Red: laser beams (the majority of laser beams appearing in the diagrams are from infrared lasers, which appear a dull red colour in the laboratory).
- Yellow: motion stages and samples (motion stages represent moving equipment, and samples can represent a wide variety of substances).
- Orange: electro-optic and semiconductor crystals (these are typically T-ray sources and detectors).
- Black/white: equipment, including optical components such as lenses and beam splitters.

9. **URLs.** Universal Resource Locators are provided in the Thesis for finding information on the world wide web using the hypertext transfer protocol (HTTP). The information at the locations listed was current on 30 October 2003.

Statement of Originality

This work contains no material that has been accepted for the award of any other degree or diploma in any university or other tertiary institution and, to the best of my knowledge and belief, contains no material previously published or written by another person, except where due reference has been made in the text.

I give consent to this copy of the Thesis, when deposited in the University Library, being available for loan and photocopying.

29 April 2004

Date

Acknowledgments

I would like to sincerely thank my supervisors, Associate Prof. Derek Abbott (Director of the Centre for Biomedical Engineering; the School of Electrical & Electronic Engineering at the University of Adelaide) and Prof. Jesper Munch (Chair of Experimental Physics, and Head of Department of Physics at the University of Adelaide). Under a Fulbright fellowship, I spent two years in the United States, collaborating with Prof. Xi-Cheng Zhang (Director of the Center for Terahertz Research in the Department of Physics, Applied Physics and Astronomy, and Department of Electrical, Computer and System Engineering at Rensselaer Polytechnic Institute), whom I sincerely thank for his unparalleled hospitality and guidance.

I would like to thank the following engineers and scientists at the University of Adelaide, Rensselaer Polytechnic Institute and the New York Department of Health's Wadsworth Center (Albany NY, USA), from whom I have learnt so much: Associate Prof. Bruce Davis, Prof. Jonathon Dordick, Bradley Ferguson, Dr. Gregory Harmer (currently at Sensor Research and Development Corporation, Orono ME, USA), Alex Hemming, Dr. Kwang-Su Lee, Dr. Moo-Yeal Lee, Haibo Lui, Dr. Abdellah Menikh, Tao Yuan, Shaohong Wang, and Dr. Jing-Zhou Xu. I would also like to acknowledge Chris Kona and Regina Shvartsman, undergraduates at Rensselaer, for experimental assistance, Dr. Justin Coombs and Dr. Peter Mickan for proof reading.

For personal financial support I would like to thank the Australian Fulbright Commission (Canberra ACT, Australia), the George Murray Scholarship Fund, the Barbara Crase Bursary Fund (AFUW), Clough Engineering Ltd. (Perth WA, Australia), and the Australian Commonwealth Department of Education, Science and Training (Canberra ACT, Australia). My research has been funded through the US National Science Foundation, the US Army Research Office and the Australian Research Council.

Lastly, I would like to acknowledge the priceless support of my friends and family.

Sam Mickan. December 2003.

Members of Prof. X.-C. Zhang's Terahertz Group at Rensselaer Polytechnic Institute in June 2002.

Members of A/Prof. Derek Abbott's Biomedical Engineering Group at the University of Adelaide in October 2000.

Publications

MICKAN-S. P. AND ZHANG-X.-C. (2003b). T-ray sensing and imaging, *International Journal of High Speed Electronics and Systems*, **13**(2), pp. 601–676; also reprinted as a book chapter in:

MICKAN-S. P. AND ZHANG-X.-C. (2003a). T-ray sensing and imaging, *in* D. Woolard, M. S. Shur and W. Leorop (eds.), *Terahertz Sensing Technology: Electronic Devices & Advanced Technology*, Selected Topics in Electronics and Systems, Word Scientific Publishing Company, Chapter 8, pp. 251–326.

MICKAN-S. P., SHVARTSMAN-R., ABBOTT-D., MUNCH-J. AND ZHANG-X.-C. (2003a). Noise reduction in dual-thickness laser-based T-ray material characterization, *in* D. Abbott (ed.), *Proceedings of SPIE - Fluctuations and Noise in Photonics and Quantum Optics*, Vol. **5111**, Washington, DC, U.S.A., pp. 198–213.

MICKAN-S. P., XU-J., YUAN-T., MUNCH-J., ABBOTT-D. AND ZHANG-X.-C. (2003b). The limits of time-domain THz spectral resolution, *in* C. Jagadish (ed.), *Proceedings of SPIE - Photonics: Design, Technology, and Packaging*, Vol. **5277**, Perth, Australia, (accepted 2003-09).

CHAN-C. A., **MICKAN-S. P.**, WILLIAMS-G. AND ABBOTT-D. (2003). Terahertz calculations for the Australian synchrotron, *in* C. Jagadish (ed.), *Proceedings of SPIE - Photonics: Design, Technology, and Packaging*, Vol. **5277**, Perth, Australia, (accepted 2003-09).

MENIKH-A., **MICKAN-S. P.** AND ZHANG-X.-C. (2002). Detection of biospecific interactions using amplified differential time domain spectroscopy signal, *US Patent & Trademark Office*, No. **60/382,761**.

MICKAN-S. P., LEE-K. S., LU-T.-M., MUNCH-J., ABBOTT-D. AND ZHANG-X.-C. (2002d). Double modulated differential THz-TDS for thin film dielectric characterization, *Microelectronics Journal* (Elsevier), **33**(12), pp. 1033–1042.

MICKAN-S. P., MENIKH-A., LIU-H., MANNELLA-C. A., MACCOLL-R., ABBOTT-D., MUNCH-J. AND ZHANG-X.-C. (2002e). Label-free bioaffinity detection using terahertz technology, *Physics in Medicine and Biology*, **47**(21), pp. 3789–3796.

MICKAN-S. P., MENIKH-A., MUNCH-J., ABBOTT-D. AND ZHANG-X.-C. (2002f). Amplification and modelling of bioaffinity detection with terahertz spectroscopy, *in* D. Nicolau (ed.), *Proceedings of SPIE - Biomedical Applications of Micro- and Nanoengineering*, Vol. **4937**, Melbourne, Australia, pp. 334–342.

MICKAN-S. P, ABBOTT-D, MUNCH-J AND ZHANG-X. C (2002a). Noise reduction in terahertz thin film measurements using a double modulated differential technique, *Fluctuation and Noise Letters*, **2**(1), pp. 13–29.

MICKAN-S. P., DORDICK-J. S., MUNCH-J., ABBOTT-D. AND ZHANG-X.-C. (2002b). Pulsed THz protein spectroscopy in organic solvents, *Conference on Lasers and Electro-Optics '02*, IEEE LEOS & OSA, Long Beach, CA, U.S.A., p. 640.

MICKAN-S. P., DORDICK-J. S., MUNCH-J., ABBOTT-D. AND ZHANG-X.-C. (2002c). Terahertz spectroscopy of bound water in nano suspensions, *in* D. Nicolau (ed.), *Proceedings of SPIE - Biomedical Applications of Micro- and Nanoengineering*, Vol. **4937**, Melbourne, Australia, pp. 49–61.

YUAN-T, **MICKAN-S. P.**, XU-J.-Z., ABBOTT-D. AND ZHANG-X.-C. (2002). Towards an apertureless electro-optic T-ray microscope, *Proceedings of the Conference on Lasers and Electro-Optics '02*, IEEE LEOS & OSA, Long Beach, CA, U.S.A., pp. 637–638.

MICKAN-S. P., LEE-K.-S., DORDICK-J. S., MUNCH-J., ABBOTT-D. AND ZHANG-X.-C. (2001a). Highly sensitive terahertz spectroscopy of thin protein films for biochip applications, *in* J. M. Chamberlain and M. A. Smith (chairs), *First International Conference on Biomedical Imaging & Sensing Applications of Terahertz Technology*, Leeds, UK, internal conference booklet. (**Invited talk**).

MICKAN-S. P., LEE-K.-S., LU-T.-M., BARNAT-E., MUNCH-J., ABBOTT-D. AND ZHANG-X.-C. (2001b). Thin film characterization using terahertz differential time-domain spectroscopy and double modulation, *in* N. W. Bergmann (ed.), *Proceedings of SPIE - Electronics and Structures for MEMS II*, Vol. **4591**, Adelaide, Australia, pp. 197–209.

FERGUSON-B., **MICKAN-S. P.**, HUBBARD-S., PAVLIDIS-D. AND ABBOTT-D. (2001). Investigation of gallium nitride T-ray transmission characteristics, *in* N. W. Bergmann (ed.), *Proceedings of SPIE - Electronics and Structures for MEMS II*, Vol. **4591**, Adelaide, Australia, pp. 210–220.

MICKAN-S. P. AND ABBOTT-D. (2003). A diagnostic apparatus using Terahertz radiation, *US Patent & Trademark Office*. No. **10/016,489** (August 12). Also issued as an Australian patent:

MICKAN-S. P. AND ABBOTT-D. (2000). A T-ray diagnostic apparatus, *IP Australia*. No. **PR2139** (December 15).

MICKAN-S. P., ABBOTT-D., MUNCH-J., ZHANG-X.-C. AND VAN DOORN-T. (2000b). Analysis of system trade-offs for terahertz imaging, *Microelectronics Journal* (Elsevier), **31**(7), pp. 503–514.

MICKAN-S. P., ABBOTT-D., MUNCH-J. AND ZHANG-X. C. (2000a). Chemical sensing in the submillimeter wave regime, *Proceedings of SPIE - Smart Structures and Devices 2000*, Vol. **4235**, Melbourne, Australia, pp. 434–442.

PERKINS-M. L., HILL-S. J., **MICKAN-S. P.**, ABBOTT-D., MUNCH-J. AND VAN DOORN-T. (2000). Review of tradeoffs for quenched avalanche photodiode sensors for imaging turbid media, *Microelectronics Journal* (Elsevier), **31**(7), pp. 605–610.

MICKAN-S. P., ABBOTT-D., MUNCH-J., ZHANG-X. C. AND VAN DOORN-T. (1999). Analysis of system trade-offs for terahertz imaging, *Proceedings of the SPIE - Electronics and Structures for MEMS*, Vol. **3891**, Gold Coast, QLD, Australia, pp. 226–237.

HILL-S. J., PERKINS-M. L., **MICKAN-S. P.**, ABBOTT-D., MUNCH-J. AND VAN DOORN-T. (1999). Tradeoffs for quenched avalanche photodiode (QAPD) sensors for imaging turbid media, *Proceedings of SPIE - Electronics and Structures for MEMS*, Vol. **3891**, Gold Coast, QLD, Australia, pp. 218–225.

List of Figures

List of Tables

Chapter 1

Introduction and Motivation

THIS Chapter introduces T-ray biosensing and outlines the motivation for the work in this Thesis. The structure of the Thesis and the contents of the separate Chapters are outlined, and the original contributions are highlighted.

1.1 Biosensing with T-rays

T-rays are a form of electromagnetic radiation, lying between millimetre waves and infrared radiation on the electromagnetic spectrum, as shown in Fig. 1.1. T-ray radiation interacts in a unique way with matter, relating to rotational and vibration modes in gas, inter-domain movement in large biomolecules, and resonances in crystals. T-rays have been used to identify water levels in living tissue, to measure the real-time 'dressing' of electrons in semiconductors, to detect malignant skin cancer and to detect Anthrax-like spores in envelopes. A newly-accessible region of the electromagnetic spectrum will provide new technologies, including the area addressed in this Thesis: T-ray Biosensing.

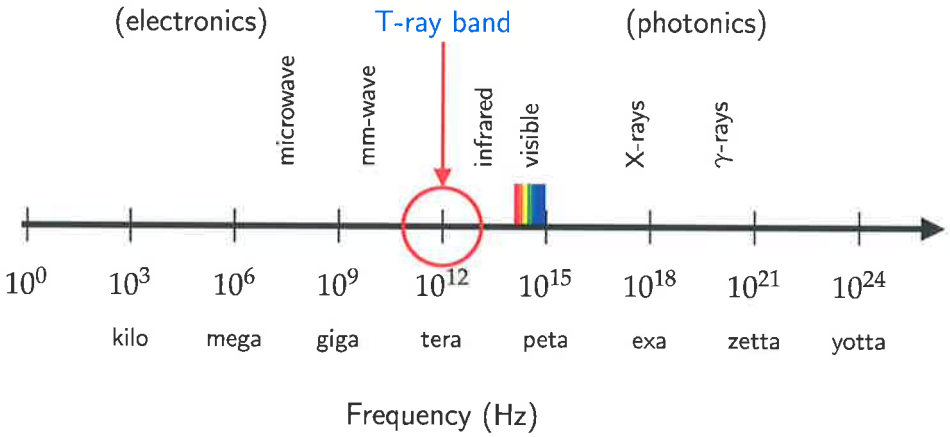

Figure 1.1. Electromagnetic spectrum. A representation of the electromagnetic spectrum, showing the T-ray band between the well-developed fields of millimetre waves (mm-waves) and the infrared. The T-ray band lies between 0.1 and 10 terahertz (THz).

The T-ray band has been described as the *THz Gap*, due to the lack of convenient and highly sensitive instruments for generating and detecting T-ray, or terahertz (THz), radiation prior to the 1990s.

In the early to mid-1990s, however, the T-ray region become more accessible due to ultra-sensitive pulsed sources and detectors based on pulsed laser excitation, which generate and detect free-space T-ray radiation (Nuss, 1996). Two broad classes of T-ray generation and detection relying on ultrafast laser pulses have been developed. The first, using Photoconductive Antennas (PCAs), was developed at Bell Labs and the IBM Watson Research Center and is now available in a commercial product from Picometrix Inc, MI (Rudd et al., 2000b). The second, using the nonlinear effects of Optical Rectification (OR) and Electro-Optic Sampling (EOS), first observed by Auston (Hu et al., 1990) and Zhang (Wu and Zhang, 1995), is presently marketed by Zomega

Technology Corp, NY (Li et al., 1999b). Large-scale stand-alone imaging systems became available in 2002 from TeraView Ltd. (2002) and Nikon Corp. (2002). As the THz Gap is filled, T-rays are being used for an increasing range of sensing and imaging applications.

Ultrafast T-ray spectrometers are well suited to complement existing chemical sensing and analysis tools, such as Fourier Transform Infrared (FTIR) spectroscopy and Nuclear Magnetic Resonance (NMR) spectroscopy. Pulsed T-ray radiation consists of ultrashort pulses, each with a bandwidth spanning the range from approximately 0.1 to 10 THz, covering the THz Gap.

The electric field of a typical T-ray pulse is shown in Fig. 1.2. The vertical axis shows the magnitude of the pulse, which is proportional to the T-ray electric field, and the horizontal axis shows the time-delay between the optical generation and detection pulses. The short time-duration of the T-ray pulse means that high signal-to-noise ratios are achievable with gated detection techniques, which detect the high peak power of the T-ray pulse instead of the low average power (see Sec. 3.3): pulsed T-ray systems have demonstrated signal-to-noise ratios (SNRs) of over 10,000:1 using Lock-In Amplifier detection (van Exter and Grischkowsky, 1990b), with only small pulse energies.

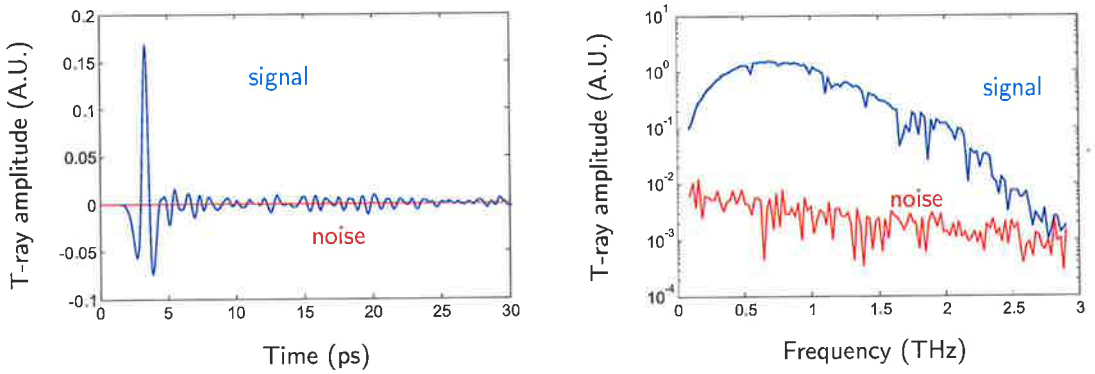

(a) Time-domain T-ray electric field pulse

(b) Frequency-domain spectrum of the T-ray pulse

Figure 1.2. An example of a sampled T-ray waveform and its spectrum. Subfigure 1.2(a) shows an example of a T-ray pulse. The X axis shows the ps duration of the pulse. The Y axis shows the electric field amplitude of the broadband signal. Subfigure 1.2(b) shows the frequency-domain spectrum of pulse lying in the THz band. The pulse was measured experimentally on a typical T-ray spectrometer, described further in Ch. 3. The blue T-ray pulse is compared to the noise of the T-ray system in red, showing the high dynamic range of the T-ray spectrometer.

Having very low average power, these T-ray techniques are particularly attractive for biomedical applications, where they are currently considered harmless (see Sec. 4.3.4). T-ray biosensing is one application growing from the development of the T-ray band. This Thesis reviews the background literature on T-ray biosensing and imaging, and describes original research in protein sensing, thin-film sensing, biosensing, T-ray microscopy.

1.2 Thesis overview

Chapter 1 introduces T-ray biosensing, while Ch. 2 reviews the literature on T-ray generation and detection. Chapter 3 reviews the design and operation of ultrafast T-ray generation and detection, which is the technique used for the work in this Thesis. Chapter 4 describes applications of T-rays in sensing, including details of methods used for material parameter extraction, and a range of the samples that have been studied with T-rays.

Novel contributions to protein sensing are presented in Ch. 5, including experimental design and results. A specific sensing method, T-ray Differential Time-Domain Spectroscopy (DTDS), and its application to thin film characterisation is described in Ch. 6. Chapter 7 shows how DTDS can be applied to bioaffinity sensing by detecting thin biomolecular films. Chapter 8 uses DTDS, combined with novel sample holder and signal processing techniques, to increase the sensitivity of T-ray liquid spectroscopy.

The final section of research concentrates on the spatial limitations of T-rays. T-ray imaging is reviewed in Ch. 9, followed by novel research on high resolution T-ray microscopy in Ch. 10.

Chapter 11 concludes the Thesis with a summary of its outcomes and conclusions, and recommendations for extending T-ray biosensing in future work.

Appendix A shows how the spectral resolution of ultrafast T-ray spectroscopy measurements is limited by the *dynamic range* (signal-to-noise ratio between the T-ray signal and the laser beam noise) of a T-ray system. Appendix B describes the standard experimental procedures for operating a T-ray spectrometer. Appendix C lists the materials used in experiments and their parameters, and Appendix D presents some of the algorithms used for data analysis. These algorithms are also found in the attached CD-ROM, `SPM_PhD_Thesis/MATLAB_Algorithms`.

The basic structural interconnections of the main Chapters are shown in Fig. 1.3. This flow chart shows which Chapters contain original experimental work, and how they are linked. The Thesis progresses along this chart from top to bottom and left to right.

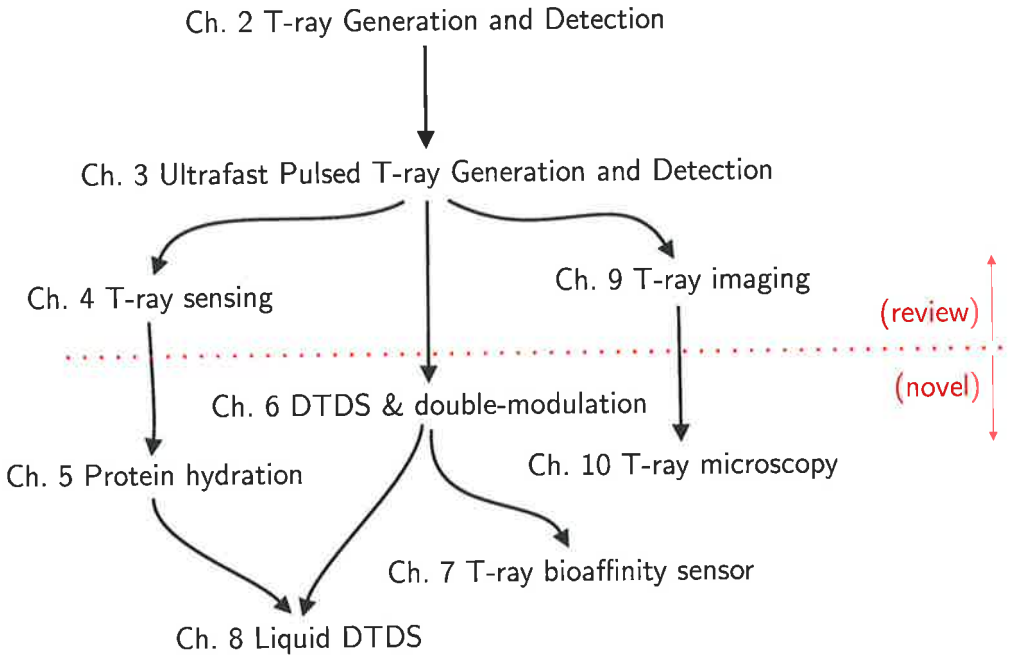

Figure 1.3. Thesis structural flow chart. This flow chart indicates how the Chapters in the Thesis fit together. Starting with the literature review, Chapters above the dotted line survey existing work. The original contributions are found in the Chapters below the dotted line. The review Chapters summarise the state of the art and provide the foundation for the experimental Chapters.

1.3 Original contributions

The original contributions in this Thesis made to T-ray science lie both in system design and T-ray applications. The originality and breadth of these contributions is evidenced by the list of publications on page xxiii.

The work in this Thesis was the first to study directly the T-ray response of protein in a non-aqueous environment, which is important for studying enzyme conformation in biochip manufacture (Ch. 5). Studies were carried out on the protein Subtilisin Carlsberg (SC) in the organic solvent 1,4-dioxane. The samples were prepared in collaboration with Prof. J. Dordick's group in the Department of Chemical Engineering at Rensselaer Polytechnic Institute.

Following from the initial demonstration of DTDS by scientists at Rensselaer (USA) and Aachen (Germany), this Thesis shows improved DTDS with double-modulation for material characterisation. In this Thesis, double-modulated DTDS is demonstrated experimentally, modelled theoretically, and is shown to improve the signal-to-noise ratio of T-ray sensing (Ch. 6).

In collaboration with Dr. A. Menikh in the Department of Physics at Rensselaer, double-modulated DTDS was used for bioaffinity sensing. T-ray spectroscopy was used for the first time to measure the binding of thin biomolecular layers, relying on the high sensitivity of double-modulated DTDS (Ch. 7).

For competitive biochip applications, the resolution of T-ray imaging needs to be pushed beyond the Rayleigh limit. To this end, in collaboration with Tao Yuan at Rensselaer, a novel high-resolution T-ray generation technique was demonstrated. The near-field technique relied on creating a sub-THz-wavelength sized T-ray by focussing an optical light beam into a very small volume (Ch. 10).

Following the observation of bound water on protein in dioxane, interest developed in higher accuracy measurements. Preliminary experiments were conducted and a system designed to apply double-modulated DTDS to liquid samples. This novel technique offered a far greater sensitivity than pre-existing liquid transmission systems. The prototype system demonstrated the potential of liquid double-modulated DTDS, especially for sensing highly-absorbing liquids, as found in biological samples (Ch. 8).

The original contributions of this Thesis, including those in collaboration with others, offer benefits to T-ray bioscience, to the technology of T-ray spectrometers, and to potential applications of T-rays in biomedicine.

Chapter 2

T-ray Generation and Detection

THIS Chapter introduces T-rays, describes techniques and systems for generating T-ray radiation, and reviews recent research in these areas. The terahertz technologies outlined in this Chapter provide a background to the experimental work on biomaterials later in the Thesis, which relies on ultrafast pulsed systems. Ultrafast pulsed T-ray generation and detection are described in detail in Ch. 3.

2.1 Introduction

Terahertz (THz) radiation, or T-rays, can be generated and detected by systems with a range of output powers, sensitivities, bandwidths and technological implementations.

The purpose of this Chapter is to broadly review T-ray systems. The experiments in this Thesis on T-ray biosensing have been conducted on systems that rely specifically on ultrafast pulsed generation and detection of T-rays. Ultrafast pulsed T-ray systems are reviewed in more detail in Ch. 3 as background to the T-ray experiments in later Chapters.

2.2 The T-ray band

As shown in Fig. 1.1, the T-ray band lies at the boundary between electronics and photonics, approximately 0.1 to 10 THz. T-rays overlap with high-frequency millimetre-waves (mm-waves) and the long wavelengths of the far-infrared (FIR), but have unique properties. T-rays have a diffraction-limited spatial resolution of approximately 0.3 mm at 1 THz, which is better than mm-waves, and T-ray Rayleigh scattering is less than for IR light due to its λ^{-4} dependence. The approximate bandwidth of typical pulsed T-ray spectrometers spans from 0.1 THz to 10 THz, although the power is often higher in the 0.3 THz to 3 THz range (Siegel, 2002). Alternative expressions of where T-rays are located in the electromagnetic spectrum are summarised in Table 2.1.

Table 2.1. T-ray band definitions. Comparison of different parameters used to describe where the T-ray frequencies, from 0.1 to 10 THz, lie on the electromagnetic spectrum.

Wavenumber	Wavelength	Frequency	Photon energy	Blackbody temp.
1 cm^{-1}	10 mm	30 GHz	120 μeV	1.4 K
3 cm^{-1}	3 mm	0.1 THz	410 μeV	4.8 K
10 cm^{-1}	1 mm	300 GHz	1.2 meV	14 K
33 cm^{-1}	300 μm	1 THz	4.1 meV	48 K
100 cm^{-1}	100 μm	3 THz	12 meV	140 K
200 cm^{-1}	50 μm	6 THz	25 meV	290 K
330 cm^{-1}	30 μm	10 THz	41 meV	480 K
670 cm^{-1}	15 μm	20 THz	83 meV	960 K

Research interest in T-rays stems from the T-ray frequency response of materials, ranging from semiconductors to human tissue. Broadly speaking, T-rays are transmitted

by dry, non-conducting materials (such as cloth or plastic), and absorbed by damp or conducting materials (such as water or metal). Polar molecules interact strongly with T-rays. Water molecules absorb T-rays very strongly, on the one hand limiting penetration of the radiation into moist substances, and on the other making it readily detectable even in very low concentrations.

Most molecules have dense and distinctive absorption spectra at T-ray frequencies, which has led to much interest in T-ray spectroscopy (van Exter et al., 1989b; Duvillaret et al., 1996; Gallot and Grischkowsky, 1999; Li et al., 1999a). Using T-ray transmission or reflection spectroscopy, samples ranging from gases to solids can be completely characterised at T-ray frequencies. The density of molecular twisting and bending modes in the T-ray band provides a wealth of information about the composition and state of samples (Wiltse, 1984).

T-ray photons have energy quanta corresponding to many discrete energy levels in matter. In molecules, vibrational states are typically separated by energy transitions of approximately 0.1 eV and rotational states are separated by approximately 0.001 eV. Multi-atomic molecules have many vibrational and rotational modes, resulting in a very large number of T-ray transitions for large molecules (Svanberg, 1991). In larger systems, the relative vibration of sub-domains in a molecule and the vibration of hydrogen bonds between molecules interact with T-ray photons. In condensed matter systems, typical T-ray energies can excite polaritons, phonons and plasmons in semiconductors, and energy gaps in superconductors (Möller and Roschild, 1971; Sherwood, 1972).

2.3 Terahertz radiation (T-rays)

T-ray radiation has historically been difficult to generate and detect (Coleman, 2000). Thermal sources have weak emission at long wavelengths and gas vapour lasers are cumbersome (Lax, 1976). Bolometric detectors only operate under vacuum conditions at liquid-helium temperatures (Dereniak and Boreman, 1996), and although Fourier Transform Infrared (FTIR) spectroscopy offers spectroscopic information down to approximately 1 THz, lower frequencies are difficult to access (Genzel et al., 1998; Han et al., 2001).

The simplest T-ray sources and detectors are thermal in nature: hot emitters, such as globars, and cooled detectors as used in far-infrared FTIR spectroscopy systems. The

third and fourth most common T-ray sources have arisen from opposite sides of the T-ray spectral band; electronic sources are based on microwave-style resonators and circuits, whereas nonlinear optical sources rely on laser technology. Three classes of T-ray laser have been introduced in the last thirty years and remain in various stages of development: Free-Electron Lasers (FELs), gas-vapour lasers and semiconductor lasers, including Quantum Cascade Lasers (QCLs). Ultrafast T-ray generation and detection uses the ultra-broadband nature of femtosecond (fs) optical laser pulses to reach the T-ray region of the spectrum.

The following Sections review current research on T-ray sources and detectors. Ultrafast generation and detection, used in the experiments in this Thesis, is described in Ch. 3.

2.4 Thermal sources

Fourier Transform Infrared (FTIR) spectroscopy is a powerful and well-developed technique for studying resonances from the visible to the mid-infrared. FTIR relies on incoherent thermal sources and detectors for T-ray frequency measurements. Despite the low power and poor sensitivity of thermal sources and detectors in the T-ray band, FTIR is used widely and extensively in material and biological studies (Globus et al., 2002).

T-ray FTIR spectroscopy relies on T-ray radiation generated by a mercury arc lamp, or SiC rod (globar), directed into two arms of an optical interferometer. The T-ray frequencies are split off using filters designed for T-ray frequencies. The sample to be studied is placed in one arm of the interferometer, and a characteristic interference pattern, influenced by the T-ray properties of the sample, is measured by scanning the length of one arm of the interferometer. The actual spectral response of the sample can be calculated from the interferogram using Fourier theory and the numerical Fast Fourier Transform (FFT), with consideration of zero-padding, apodization and aliasing (Genzel et al., 1998).

With regard to speed, frequency resolution and reliance on the FFT, FTIR is comparable to T-ray spectroscopy, to be introduced in Ch. 3. The main advantage of FTIR spectroscopy is its sensitivity spanning many frequencies, from the far-infrared (FIR) up to the visible, whereas T-ray spectrometers are more sensitive below 3 THz (Han et al., 2001).

2.5 Photonic sources

The primary difficulty in developing a T-ray laser is finding a cheap and convenient gain medium that can be pumped efficiently, with high gain and high output power.

2.5.1 Free-electron laser, linear accelerator and synchrotron sources

The gain medium of a Free-Electron Laser (FEL) is an oscillating beam of electron bunches, modulated by a spatially-periodic magnetic 'wiggler' field. The emitted radiation can be tuned by changing the frequency of the wiggler and can in principle reach from mm to X-ray wavelengths. The FEL is the highest-power source of T-ray radiation available, producing a pulsed beam of coherent, diffraction-limited T-ray radiation with an efficiency potentially close to unity (Saldin et al., 2000).

Despite requiring large dedicated installations, FELs are used for studying T-ray radiation and its interaction with, for example, condensed matter and biological materials (Schwettman, 1993), and current research aims to produce more compact FEL systems (Gallerano et al., 1999). A new source of T-rays was first demonstrated in 2002 using a linear accelerator (linac) – T-rays were emitted by electron bunches accelerating around a curve – up to 50 W of average T-ray power was generated at a 75 MHz pulse rate (Carr et al., 2002). Synchrotron radiation has also been proposed as a source of T-rays, which can be enhanced by narrowing the electron bunches using Thompson scattering (Chan et al., 2003).

2.5.2 Gas-vapour lasers

Simple molecules such as water have many rotational and vibrational resonances within the T-ray region. These molecules can be used as a laser gain medium if efficiently pumped into a long-lived excited state. The first obstacle in creating a T-ray source is finding a suitable radiative transition, since rotational and vibrational energy levels of large molecules are difficult to use in a laser (Lax, 1976). A number of solutions have been found, including methanol and Hydrogen Cyanide (HCN) vapour, pumped either optically or electronically. Methanol lasers, for example, are designed around optically exciting the rocking and asymmetric deformation modes of methanol with a CO_2 laser (Telles et al., 1998). HCN lasers are the most popular gas-vapour lasers, with CW (continuous-wave) or pulsed lasing possible at T-ray frequencies. HCN lasers require

large cavities (2 m or more), large voltages and currents (kV with up to 100s of amps), and active temperature stabilisation (Ghoranneviss et al., 1998).

The gas-vapour laser is a commercially-available source of T-ray radiation (model: SIFIR-50; manufacturer: Coherent Inc, Santa Clara, CA, USA; URL: `http://www.cohr.com`). Although not continuously tunable, gas-vapour lasers have been shown to operate at over 2000 discrete wavelengths from 26 to 254 μm, with power levels ranging from μW to 10 mW (Jackson et al., 2001), and have been used to characterise many materials at T-ray frequencies, including liquids, bulk semiconductors, thin-film semiconductors and thin film superconductors (Bean and Perkowitz, 1979). Gas-vapour lasers have recently been reviewed by Blake et al. (1991) and current developments continue to reduce their size and increase their tunability.

2.5.3 Semiconductor lasers

The requirement for small, cheap and tunable solid-state T-ray sources has led to two main approaches in developing a T-ray semiconductor laser: (i) p-Germanium (Ge) lasers, and (ii) semiconductor heterostructure lasers (Quantum Cascade Lasers). Other solid-state T-ray lasers are proposed using narrow bandgap lead salts, intersubband quantum fountain oscillations (Gauthier-Lafaye et al., 1999) and impurity centres in Silicon (Shastin et al., 2002; Pavlov et al., 2002).

The Ge laser operates through the electrical excitation of hot holes in p-doped Ge. The laser cavity is created by polishing the surfaces of the Ge crystal since Ge has a high T-ray refractive index, n=4.0 (Gornik et al., 1991). Ge lasers doped with beryllium have exhibited up to 5% duty cycles, with up to 1 W of output power, continuously-tunable from 1 to 4 THz. With advances in crystal slab design and cooling, Bründemann et al. expect to achieve continuous-wave (CW) lasing in the near future (Bründermann et al., 1998; Bründermann et al., 1999; Bründermann et al., 2000). Current devices operate at 20–30 K, with 10–20 W of refrigeration, although the challenges of implementing the necessary high electric and magnetic fields have contributed to a decline in Ge laser research since the mid-1980s. A commercial p-Ge laser was first available in 2002 (manufacturer: Zaubertek, Orlando, FL, USA; URL: `http://www.zaubertek.com`, Peale et al. (2002)).

T-ray radiation emission from quantum heterostructures in semiconductors is based on intersubband transitions (Gornik and Kersting, 2001). The first T-ray Quantum

Cascade Laser (QCL) was recently reported by Kohler et al., using a quantum cascade gain medium (Faist et al., 1994), after many groups had demonstrated T-ray emission from quantum structures. These devices are pumped with low voltages and milliamp currents, and generate narrow band radiation between 1 and 5 THz from intersubband transitions and resonant tunnelling processes (Rochat et al., 1998; Blaser et al., 2000; Dhillon et al., 2001). Quantum gain media are currently operational only at low temperatures (≈4.2 K) and suffer from fast depopulation of the excited states (Xu et al., 1997), although room-temperature emission is predicted from 4-level asymmetric quantum well structures (Harrison and Kelsall, 1997; Kinsler et al., 1999). Quantum cascade structures have been used to generate T-rays in a nonlinear mixer configuration (Gagliardi et al., 2002). T-ray frequency QCL research has been reviewed by Tredicucci et al. (2001).

2.6 Nonlinear optical processes

Nonlinear optical materials with an appreciable electro-optic (EO), or $\chi^{(2)}$, nonlinear optical coefficient provide a medium for generation of radiation at the beat frequency between two pump sources (Franken et al., 1961; Bjorkholm, 1966). For pump sources with wavelengths offset by T-ray frequencies, the EO material can act as a source of T-rays (Shen, 1984). Difference Frequency Generation (DFG), or three-wave mixing, was an early source of T-rays, but was hampered by low conversion efficiencies and phase matching requirements (Zernike, Jr. and Berman, 1965; Zernike, 1969; Aggarwal et al., 1974; Shen, 1976; Morris and Shen, 1977). DFG was revisited in 1990 as a T-ray source using the patented organic crystal DAST (4-dimethylamino-*N*-methyl-4-stilbazolium-tosylate), designed to have a very high nonlinear electro-optic (EO) coefficient and low dielectric constant at T-ray frequencies (Nakanishi, 1990). DAST has been used to mix quasi-CW pulses from a tunable dual-wavelength Ti:sapphire laser to generate 32-ns T-ray pulses with over 2 μW of T-ray power (Kawase et al., 1999). A more compact and lower power source has been demonstrated using a Nd:YAG pump and dual wavelengths generated in a Periodically-Poled Lithium Niobate (PPLN) Optical Parametric Oscillator (OPO); the T-ray output wavelength is tuned from 120 to 160 μm using temperature control of the PPLN crystal (Kawase et al., 2000). T-ray beat frequencies are now available from dual-frequency laser diodes (Barry et al., 1998) and injection-locked semiconductor lasers (Chattopadhyay and Bhattacharya, 2002). DFG is closely related to Optical Rectification (OR), described in Sec. 3.2.2, where pulsed

T-rays are generated as the difference frequencies between Fourier components of the pulse (Shen, 1984).

A nonlinear optical crystal can also be used to generate T-ray radiation via a parametric effect. In Optical Parametric Generation (OPG), a near-infrared (NIR) pump beam generates a second NIR *idler* beam in a nonlinear crystal, and T-ray radiation is generated from the beating of the pump and the idler (Shen, 1984). If the nonlinear crystal is placed in a cavity for the idler beam, feedback amplifies the idler beam, creating an Optical Parametric Oscillator (OPO). OPG was used to generate T-ray radiation in the early 1970s, using a Nd:YAG pump beam, polariton scattering in $LiNbO_3$ to generate the Stokes (down-shifted) idler, and angular rotation of the parametric oscillator cavity to tune the T-ray output wavelength (Yarborough et al., 1969; Johnson et al., 1971; Piestrup et al., 1975). Since the mid-1990's, Kawase et al. have made a number of improvements to what they call the *T-ray Parametric Oscillator* (TPO) by decreasing system size, enhancing wavelength selectivity and increasing the output power by several orders of magnitude. A grating coupler on the $LiTaO_3$ crystal was used to improve the coupling of the T-ray radiation into free space (Kawase et al., 1997), and a prism coupler was used to remove the dependence of the T-ray output direction on the angle of the parametric cavity (and thus the output wavelength) (Kawase et al., 1997). Rapid wavelength tuning was achieved by scanning the angle of the pump beam with a fast mirror (Imai and Kawase, 2001). The TPO has also been implemented in a ring cavity configuration (Minamide et al., 2001) and in cryogenically-cooled crystals, which improves the T-ray output power by over 100 times and reduces the gain threshold (Shikata et al., 1999). More recently, *T-ray Parametric Generation* (TPG), with an injection seeded idler beam, has been experimentally shown to be superior to TPO (Kawase et al., 2001). TPG shows a reduced line width ($\Delta\nu/\nu \approx 10^{-4}$) and a peak T-ray power of over 100 mW for 3.4-ns pulses. TPG has also been demonstrated in a compact form, admittedly with limited tunability (from 1.2 to 2.4 THz) and 30 μW power (Sato et al., 2001).

Nonlinear optical methods of generating T-ray radiation are attractive for their simplicity, availability of solid-state pump sources, linewidth and tunability. Although more cumbersome than proposed electrically-pumped solid-state sources, discussed in Sec. 2.5.3 above, DFG and OPG systems are significantly smaller than free-electron and gas-vapour lasers.

2.7 Photomixing in biased semiconductors

In a manner similar to Difference Frequency Generation (DFG), biased semiconductors with very short carrier lifetimes and high carrier mobility can be used to convert a T-ray beat frequency between two optical beams into T-ray radiation.

Brown et al. (1993a) initially developed GHz and T-ray photomixers, or optical-heterodyne converters, using electrodes and antennas deposited on low-temperature-grown Gallium Arsenide (LT-GaAs). LT-GaAs is characterised by sub-ps electron-hole recombination rates, a high carrier mobility ($\mu \approx 200$ cm^2/V-s) and a high breakdown field ($> 4\times10^5$ V/cm). The photomixer was an array of interdigitated electrodes with micron spacing, connected either to a stripline, for GHz generation, or a spiral antenna for free-space radiation of T-ray frequency radiation (Brown et al., 1993b; Brown et al., 1994; Brown et al., 1995). Initially limited to 200 GHz, the bandwidth was increased to above 5 THz of coherent, tunable T-ray radiation (McIntosh et al., 1995), and demonstrated for use in a spectrometer (Pine et al., 1996; Verghese et al., 1998). The biased photomixer is very similar to a photo-conductive antenna (Sec. 3.2.1), which is used with pulsed optical excitation (Goyette et al., 1995). Photomixing of fiber-coupled beams has been demonstrated with dipole (Matsuura et al., 1997), log-spiral and slot antennas at different temperatures (Verghese et al., 1997), and analysed with theoretical modelling (Duffy et al., 2001).

A number of optical sources have been used to generate the two pump beams for mixing, including two fiber-coupled Ti:sapphire lasers (Brown et al., 1993a), two Distributed Bragg Reflector (DBR) laser diodes (Chen et al., 1997), two longitudinal modes in laser diodes (Hidaka et al., 1997), microchip lasers (for mm-waves) (Hyodo et al., 1996) and iodine lasers (up to 14 GHz) (Nicholson et al., 1998). The advantage of using two modes in a single laser diode is the compact nature of the source, and a very narrow spectral linewidth (Gu et al., 1998). Other dual-mode lasers have been used to generate THz-frequency amplitude beats, for example a Ti:sapphire ring cavity, a Ti:sapphire α-cavity (Siebe et al., 1999) and a laser diode array with a bandwidth reaching 7 THz (Wang and Pan, 1995). A novel method of tuning the T-ray beat frequency is to use two linearly chirped pulses, and control the phase difference between them at the photomixer with, for example, a Michelson interferometer (Weling and Auston, 1996). Biased photoconductors are also very important in generating T-ray pulses from ultrashort optical pump pulses, as discussed in Sec. 3.2.1 below.

Recently, a continuous-wave (CW) photomixing system was used for scanning imaging (Kleine-Ostmann et al., 2001), analogous to T-ray imaging systems, described in Ch. 9. With CW T-ray power output levels of approximately 1 mW (Brown et al., 1995), photomixing systems are useful in applications requiring excellent tunability, small system size and narrow linewidth.

2.8 Ultrafast sources

Picosecond-duration pulses of T-rays can be generated using the very broad bandwidth of femtosecond laser pulses, commonly with nonlinear crystals (optical rectification) or fast photo-generated current transients in semiconductors (photo-conductive switches). These and other ultrafast-based generation techniques are described in detail in Ch. 3. Ultrafast systems were used for the experiments described in this Thesis.

2.9 Electronic sources

The frequency of electronic sources has increased steadily for many years, from MHz to the GHz frequencies. State-of-the-art electronic sources are currently limited to frequencies in the hundreds of GHz and sub-mW powers (Eisele et al., 2000). A number of promising sources include Gunn diodes (Alekseev et al., 2001; Alekseev and Pavlidis, 2000), heterojunction bipolar transistors (HBTs) (Mohammadi et al., 2000; Pavlidis, 1999), high electron mobility transistor (HEMT) mixers (Kwon and Pavlidis, 1995), PIN diodes (Pavlidis et al., 1997) and Schottky diodes (Kyushik et al., 1994).

High-speed electronic devices are suited to low-power CW operation, although a non-contact system based on complex impedance bridges (Sridhar et al., 1985) has been used to characterise accurately the dielectric constant of thin films between 30 GHz and 1 THz (Reedijk et al., 2000).

Nonlinear Transmission Lines (NLTLs) have been used to generate electronically-tunable sub-ps transients (van der Weide et al., 1991), which can drive antennas (van der Weide, 1994) to generate T-ray radiation (van der Weide and Keilmann, 1998). NLTL T-ray sources have demonstrated very narrow linewidths in room-temperature spectroscopy applications (Bostak et al., 1994; van der Weide et al., 2000).

Backward Wave Oscillators (BWOs) are electrically-driven microwave generators that can generate CW radiation from mm-waves up to 2 THz (Kozlov and Volkov, 1998).

BWOs are large table-top devices, requiring powerful magnetic fields and water cooling, but provide up to 300 mW of polarised, narrowband ($\Delta\nu/\nu \approx 10^{-5}$), tunable T-ray radiation (Dressel, 2001). Each BWO is tunable within approximately ±30% of its central value, therefore a number of devices are required for full frequency coverage. BWOs have been used in T-ray spectroscopy of gases (Klaus et al., 1997; Takano et al., 1998; Morino et al., 2000), thin film superconductors (Pimenov et al., 2000), and biomolecules (Woolard et al., 1999).

Electronic T-ray generation techniques are primarily of interest for their simplicity and integratability with other electronic systems. The BWO provides a high quality source of T-rays at power levels between electronic and large laser systems.

2.10 Detection

T-ray radiation can be detected using thermal, optical or electronic effects. Detecting T-ray signals is difficult because blackbody radiation at room temperature is strong at T-ray frequencies, as shown in Table 2.1. The most common T-ray detectors are thermal detectors, for example the helium-cooled bolometer, which is desensitised to ambient temperature and registers only the heating effect of the T-ray radiation (Dereniak and Boreman, 1996). The bolometer is an incoherent detector, registering only incident power, which is appropriate for CW detection, but limits the information available in broadband systems. In FTIR, the bolometer is combined with an interferometer to resolve the different frequency components of the broadband source (Genzel et al., 1998; Han et al., 2001).

In an analogous manner to nonlinear optical mixing and photomixing in biased semiconductors, T-ray radiation can be coherently detected using homodyne mixing in nonlinear crystals (Nahata et al., 1999) and photoconductive switches (Weling and Auston, 1996; Verghese et al., 1998). For CW detection with T-ray local oscillators, electronic detectors have been developed based on cooled photodetectors (Katterloher et al., 1995), electron plasmas in semiconductors (Dyakonov and Shur, 1997; Yngvesson, 2000), semiconductor superlattices (Klappenberger et al., 2001), mesoscopic quantum devices (Orellana and Claro, 1999), resonant Quantum Well Infrared Photodetectors (QWIPs) (Gadir et al., 2002) and high-electron-mobility transistors (HEMTs) (Shur et al., 1999). Purely electronic systems incorporate symmetrical sources and detectors (van der Weide and Keilmann, 1998; Reedijk et al., 2000).

Two-dimensional detection, or imaging, is used in T-ray astronomy, as reviewed by Siegel (2002). CW T-ray imaging has been demonstrated with QWIP arrays (Dupont et al., 2002) and in laboratory conditions using photomixing (Siebert et al., 2002).

Both imaging and spectroscopy have been demonstrated with ultrafast pulsed detection of T-rays, using the high sensitivity of gated detection. Ultrafast laser-based T-ray detection is reviewed in detail in Ch. 3.

2.11 Chapter summary

The preceding Sections have broadly introduced the properties of the T-ray band and described T-ray detection and generation, putting the pulsed T-ray experiments in this Thesis into context. The T-ray band has been studied for many years, primarily using very far-infrared (FIR) Fourier Transform Infrared (FTIR) spectrometers, Backward Wave Oscillators (BWOs) and T-ray lasers, all of which are commercially available, despite their individual drawbacks. In the future, the most promising T-ray sources seem to be: (i) Quantum Cascade Lasers (QCLs), for their small size and tunability, (ii) high frequency electronic sources, for their integration into existing electronic technology, and (iii) pulsed T-rays based on ultrafast laser sources (Ch. 3).

The pulsed nature of ultrafast T-ray systems provides high signal-to-noise ratios, broad bandwidth and low average power, making them ideal tools to study biological and medical materials. The following Chapter introduces and reviews pulsed T-ray spectrometers, and later Chapters apply this instrument to make real measurements on a wide variety of biosamples, from protein hydration to thin biomolecular films.

Chapter 3

Ultrafast Pulsed T-ray Generation and Detection

ULTRAFAST pulsed T-ray systems were first demonstrated in 1988, are now configured with a number of alternative sources, detectors and layouts. Ultrafast pulsed generation and detection is a subset of T-ray generation and detection reviewed in the last Chapter, and is the technique used for T-ray experiments described in this Thesis. An ultrafast T-ray system (or T-ray spectrometer) uses ultrafast laser pulses to generate short pulses of T-ray radiation, which are then detected using time-gated detectors. The average generated power is very low, but gated detection is sufficiently sensitive so the signal-to-noise ratio of ultrafast spectrometers is higher than other T-ray systems.

This Chapter examines the advantages and disadvantages of various methods for generating and detecting T-rays, and how T-rays interact with components of a T-ray system. It is important to understand the limitations and capabilities of T-ray spectrometers, as these limitations and capabilities define the possible applications of T-ray biosensing.

3.1 Introduction

The development of T-ray technology using ultrafast optical lasers provides a highly-sensitive means for accessing the T-ray frequency regime. Pulsed T-ray spectrometers are based on ultrafast pulsed generation and detection using mode-locked lasers. Mode-locked Ti:sapphire ultrafast lasers became commonly available in the 1980s, triggering increased research into ultrafast sources and detectors of T-ray radiation (Haus, 2000). Pulsed T-ray spectrometers use picosecond pulses of T-ray radiations and are thus inherently broadband systems. Pulsed T-ray spectroscopy is frequently called Terahertz Time-Domain Spectroscopy (THz-TDS) since the measurements are made using time-domain pulses. Spectroscopic information is then determined via a numerical Fourier transform. The broadband nature of T-rays means they are able to probe a wide region of the electromagnetic spectrum, depending on the actual system, from DC to the mid-infrared (>30 THz). The cost and size of T-ray spectrometers is dominated by the cost and size of the ultrafast laser, a technology that continues to become more convenient, compact, reliable and economical. T-ray spectrometers are now commercially available as entire systems, assisting the increase in applications of T-ray spectroscopy to sensing, imaging and biosensing, as discussed in future Chapters.

The two most common methods of generating and detecting pulsed T-rays are: (i) using micro-scale, Photoconductive Antennas (PCAs), and (ii) using electro-optic (EO) crystals. PCAs have high power and a limited bandwidth, while EO systems have lower power and a higher bandwidth. The reasons for these differences are explained in Secs. 3.2 and 3.3 below.

Historically, pulsed T-ray techniques were initially developed for waveguide and circuit characterisation (Auston and Nuss, 1988; Valdmanis et al., 1982; Valdmanis et al., 1983; Frankel et al., 1992), until free-space T-ray Time-Domain Spectroscopy (TDS) grew from the development of both PCAs and EO crystals as sources and detectors (Auston et al., 1984a; Auston and Cheung, 1985; DeFonzo and Lutz, 1987; DeFonzo et al., 1987; Smith et al., 1988; Fattinger and Grischkowsky, 1988; Hu et al., 1990; Wu and Zhang, 1995). The first complete T-ray spectrometers were used for spectroscopy of bulk dielectrics at T-ray frequencies (van Exter et al., 1989a; Pastol et al., 1989c; Grischkowsky et al., 1990). Pulsed T-rays can be generated from other physical processes, including quantum oscillations in semiconductor heterostructures and superconductive effects, as listed in Sec. 3.2.4. These alternative processes are not efficient sources

of T-ray power, but the generated T-rays can be used to study the physical processes themselves.

Continuous-wave (CW) T-ray detection, as described in Ch. 2, is compatible with pulsed generation, but does not benefit from the high signal-to-noise ratio (SNR) of gated detection. Gated detection, a feature of ultrafast laser systems, is explained in Sec. 3.3. The other elements of a T-ray spectrometer, apart from the emitter and detector, are discussed in Sec. 3.4. This Section discusses how T-rays propagate in free space and through T-ray optical components, such as lenses and filters. This leads to a discussion of T-ray spectrometers configured to generate and detect T-rays with the same element, that is, using one PCA or EO crystal as a T-ray transceiver.

The main purpose of this Chapter is to review the T-ray literature on systems and technologies as a background to T-ray sensing and imaging in Chs. 4 and 9 respectively. The background in this Chapter explains the tradeoffs between the alternate systems used for generation and detection, and why certain configurations were chosen for the experiments in this Thesis.

The T-ray spectrometers used for experiments in this Thesis, and their specific configurations for experiments, are described in detail in the experimental Chapters: Ch. 5, 6, 7, 8 and 10. The experimental systems used T-rays generated by Optical Rectification (OR) (see Sec. 3.2.2), or by fast currents in semiconductors (see Sec. 3.2.4). The T-rays were detected by Electro-Optic Sampling (EOS) (see Sec. 3.3.2). The specifications of the optical hardware used in T-ray spectrometers are described in Appendix B.

3.2 Generation

T-ray generation from nonlinear optical effects is developed in a text by Shen (1984), and early T-ray spectroscopy is well covered by Auston (1988) and Auston and Nuss (1988). Gornik and Kersting (2001) present a recent review of pulsed T-ray sources.

3.2.1 Photoconductive antennas

A Photoconductive Antenna (PCA) has two important features: an antenna structure and a photoconductive substrate. During T-ray generation, photocarriers are generated in the photoconductive substrate by an ultrafast laser pulse. The photocarriers

are swept by an applied DC electric field, creating an ultrafast current transient in the substrate, which drives the current in the antenna. The antenna structure is designed to radiate sub-mm-wavelength electromagnetic waves into free space. A PCA can be designed with different substrates and different actual antenna designs, which in turn influence the possible T-ray bandwidth and output power. When an ultrafast optical pulse is absorbed by an appropriate substrate, carriers are generated and swept apart by the DC bias field, which creates the current transient to drive the antenna. The substrate must be able to have a sufficiently fast carrier recombination time and high carrier mobility to support an ultrafast transient. A sub-ps transient will generate a free-space pulse with a duration of a few ps. A ps-duration pulse, by Fourier theory, has a bandwidth in the order of 1 THz.

A simple schematic of a PCA is shown in Fig. 3.1, accompanied by a graph that shows the dependance of generated T-ray power on the applied bias field.

Historically, the first PCA was demonstrated by Mourou et al. (1981) at microwave frequencies, although the PCA sources used in T-ray spectrometers were developed primarily by Lucent Technologies and IBM in 1988 and 1989 (Fattinger and Grischkowsky, 1988; Fattinger and Grischkowsky, 1989; van Exter et al., 1989a; van Exter et al., 1989b). Other groups were involved in developing sources and detectors at about the same time, as reviewed by Smith et al. (1988). A schematic of the first T-ray spectrometer, based on PCAs, is shown in Fig. 3.2. The basic elements of a PCA, that is: (i) the antenna geometry, (ii) the photoconductive switch, (iii) the electric bias and (iv) the optical pulse, have been subsequently varied in many ways to study and improve the following characteristics of the generated radiation: (i) the power, (ii) the bandwidth, (iii) the radiation pattern, and (iv) the pulse characteristics.

The high SNR of T-ray spectrometers is due to high peak power and sensitive detection (Sec. 3.3). The average T-ray power in a focused beam has increased from nW to μW levels (Ralph and Grischkowsky, 1992; Cai et al., 1997), with current systems achieving 30–40 μW of average T-ray power (Andrews et al., 2001; Zhao et al., 2002a). The availability of high power, high repetition rate femtosecond laser sources has enabled PCAs to be driven into saturation (Budiarto et al., 1996; Park et al., 1999b), and photoconductive substrates with high breakdown voltages permit large bias fields (Yoneda et al., 2001). As shown in Fig. 3.1(b), emitted T-ray power scales with both the DC bias across the emitter and the power in the optical beam.

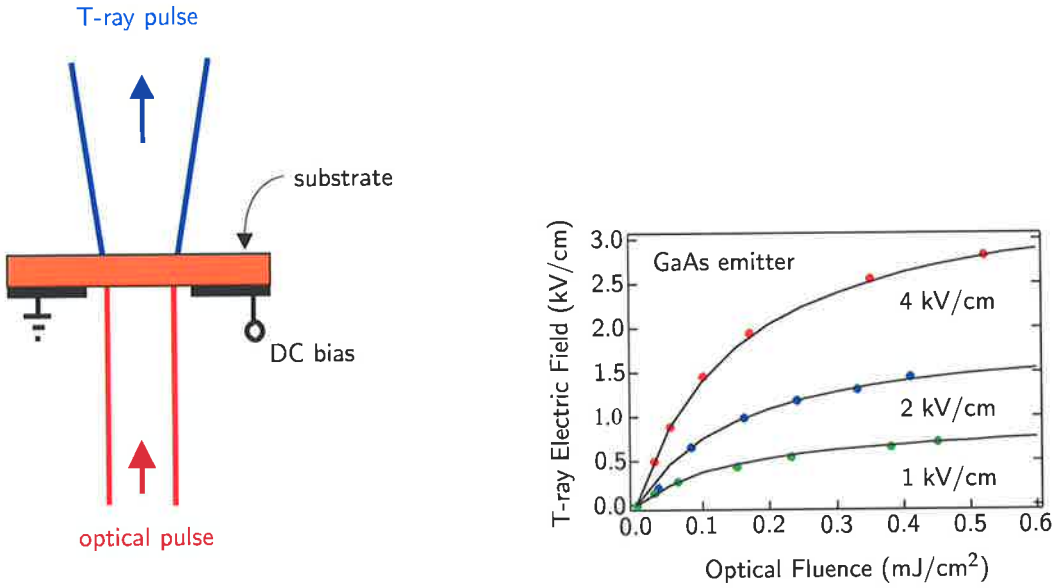

(a) PCA emitter

(b) PCA output power dependence on optical pump power

Figure 3.1. PCA emitter and output characteristic. A schematic PCA emitter is shown in Subfig. 3.1(a). This is a DC biased dipole antenna. Subfig. 3.1(b) shows how the emitted T-ray electric field draws both on the power in the optical pump pulse and the DC bias field applied to the PCA electrodes. The curves are plotted with DC bias field as a parameter. The T-ray output saturates for high levels of optical fluence due to limited doping levels. The DC bias is limited by breakdown in the photoconductive switch, thus limited the output power of the T-ray emitter.

The efficiency of a PCA depends on the photoconductive substrate and the coupling efficiency of the antenna. A photoconductive switch material should have a high breakdown voltage, a low optical refractive index, low bandgap, low carrier lifetime, high optical absorption and high carrier mobility (Benicewicz and Taylor, 1993; Benicewicz et al., 1994; Tani et al., 1997). The polarisation of the normally-incident optical pulse is perpendicular to the bias electrodes (Huggard et al., 1998). High power PCAs were demonstrated initially on implanted Silicon-on-sapphire (SOS) and low-temperature-grown GaAs (LT-GaAs) (Warren et al., 1991), and since with semi-insulating Gallium Arsenide (SI-GaAs) (Zhao et al., 2002a; Budiarto et al., 1996), ion-implanted GaAs and InGaAs (Andrews et al., 2001). T-ray emission has also been observed with air as the photoconductive switch (Löffler et al., 2000). Antenna design and coupling influences the efficiency, bandwidth and radiation pattern of T-ray emission (Nahata and

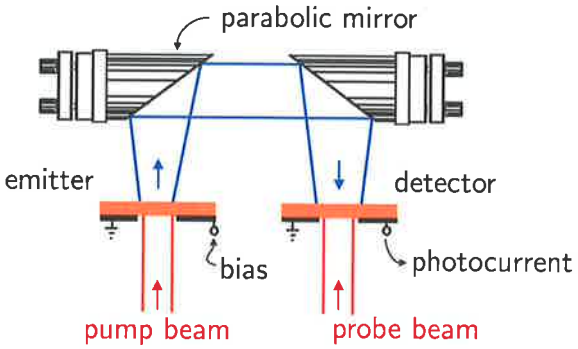

Figure 3.2. Elementary T-ray beam system with PCA emitter and detector. A T-ray beam is generated and detected using two PCAs (Fattinger and Grischkowsky, 1988). The ultrafast probe beam pulse shorts the biased electrodes and the resulting current transient is coupled into free space. Gold or Al-coated parabolic mirrors collimate and focus the T-rays onto a second PCA. The PCA detector, described in Sec. 3.3.1, is gated by the probe pulse; when the PCA is conducting, a current can be measured across the electrodes that is directly proportional to the amplitude of the T-ray electric field.

Heinz, 1996; Cai et al., 1997). Many antenna geometries have been explored (Dykaar et al., 1991; Arjavalingam et al., 1991; Gitin et al., 1994; Pfeider et al., 1994; Brener et al., 1996; Cai et al., 1997; Nuss and Orenstein, 1998; Feng and Winful, 1998; Liu et al., 1998), however high power T-rays are still generated with coplanar striplines and large aperture emitters (Zhao et al., 2002a; Andrews et al., 2001). A large aperture PCA is a dipole antenna with lines placed a distance of approximately 1 mm to 1 cm apart, as opposed to striplines lithographically deposited tens of microns apart.

After output power, a broad bandwidth is the second most desirable characteristic of a T-ray source, which relies on a short T-ray pulse duration. PCAs in GaAs typically have a useful bandwidth extending from less than 100 GHz to 2 THz (Grischkowsky et al., 1990), which can be extended to 4 THz by injecting carriers close to the band edge (Katzenellenbogen and Grischkowsky, 1991; Nuss and Orenstein, 1998). Bandwidths up to 6 THz (Zhao et al., 2002a) have been reported for PCAs, but pulse duration continues to be limited by carrier mobility, leading to interest in Optical Rectification (OR) emitters, discussed in Sec. 3.2.2 below. The exact emission bandwidth can be controlled by shaping the optical pulse, either to tune the output frequency or increase the overall output power (Liu et al., 1996; Weling and Auston, 1996; Weling and Heinz, 1999; Park et al., 1999a).

The radiation pattern of a PCA is important for designing beam-steering optics and imaging systems. Generally, T-ray radiation is coupled out from the antenna and collimated into a beam with a hemispherical lens (Fattinger and Grischkowsky, 1989; van Exter et al., 1989b; Jepsen and Keiding, 1995; Chung et al., 2000; Rudd and Mittleman, 2002). The radiation pattern for the common dipole antenna is essentially dipolar, with a weak quadrupole component perpendicular to the bias field (Rudd et al., 2000a), weak elliptical polarisation (Rudd et al., 2001) and propagates as a Gaussian into the far-field (Gürtler et al., 2000) with high frequency components concentrated in the centre of the beam (Jiang and Zhang, 1999a; Jiang and Zhang, 1999b). Near-field effects are important for understanding screening of the bias field, pulse propagation and applications in near-field imaging, and are described in Ch. 10.

Recently, PCA emitters have been integrated into commercial optical fiber-coupled T-ray systems, for their convenience and high power (Rudd et al., 2000b). Miniature PCAs have been demonstrated on optical fibers for potential endoscopic applications (Lai et al., 1998). PCAs have also been incorporated directly into ultrafast laser cavities to produce up to 7 μW of pulsed T-ray power (Darmo et al., 2002).

3.2.2 Optical Rectification

Optical Rectification (OR) is a nonlinear optical effect that can generate T-ray pulses with very large bandwidth from ultrafast optical pulses (Bonvalet and Joffre, 1998). OR is a second-order effect that occurs in materials with a non-zero electro-optic EO, or $\chi^{(2)}$, coefficient, and is referred to as the inverse EO, or Pockel's effect (Saleh and Teich, 1991; Yariv, 1991; Shen, 1984). The power and bandwidth of T-rays generated by OR are determined by the driving optical pulse, the nonlinear EO coefficient of the crystal, the crystal damage threshold, the output coupling constraints and the visible-to-THz phase matching (Rice et al., 1994; Khurgin, 1994). OR emitters produce T-rays with a lower power and broader bandwidth than PCA emitters.

Historically, OR was first observed in 1962, with a high intensity 100-ns laser pulse causing a DC polarisation in certain crystals (Bass et al., 1962). With the development of ps and fs laser systems, faster polarisation transients were induced, with bandwidths reaching to T-ray frequencies (Yajima and Takeuchi, 1971; Yang et al., 1971; Morris and

Shen, 1971; Auston et al., 1972; Bagasaryan et al., 1983). An ultrafast 'shock wave' propagating through a nonlinear medium was observed to generate T-ray Čerenkov radiation, but was confined to the medium due to Total Internal Reflection (TIR) (Auston, 1983; Auston et al., 1984b; Kleinman and Auston, 1984). The T-ray shock wave was caused by the optical pulse, the source of T-rays through OR, moving more rapidly through the crystal than the emitted T-ray radiation due to the crystal's high T-ray refractive index. After the development of the PCA for free-space T-ray generation, the Čerenkov radiation was coupled out of $LiTaO_3$ into T-ray beams (Hu et al., 1990).

Unlike a PCA, the T-ray power generated by OR is due only to the incident laser power (Carrig et al., 1995). The maximum optical power is limited by available ultrafast laser sources and by damage to the medium (Sun et al., 2000). With the development of high-power solid-state mode-locked lasers, sub-100-fs pulse trains can be generated at tens of MHz repetition rates and up to 2 W of average power. The generation efficiency depends on the magnitude of the $\chi^{(2)}$ coefficient, T-ray absorption in the material and phase matching between the optical and T-ray pulses (Wu and Zhang, 1996a; Nahata et al., 1996a). The magnitude of the $\chi^{(2)}$ coefficient varies with the crystal cut and orientation (Yariv, 1989; Xu et al., 1992; Zhang et al., 1992a; Chen et al., 2001).

The most popular EO material is ZnTe (Zinc Telluride), because of its physical durability and excellent phase matching (Rice et al., 1994). Although the organic crystal DAST has a very large EO coefficient (Yakymyshyn et al., 1991; Zhang et al., 1992c), it is hygroscopic, and therefore difficult to use experimentally. With a broadly focused optical pump beam, to avoid damaging the medium, and a ZnTe crystal, nW T-ray average power can be generated by OR. Saturation of OR due to second harmonic generation of the pump beam at high optical fluence has been studied in ZnTe (Sun et al., 2000), $LiTaO_3$, $LiNbO_3$ and DAST (Carrig et al., 1995).

OR owes its intrinsically broad bandwidth to the Pockel's effect, which can operate on a sub-fs time scale (Saleh and Teich, 1991). The actual bandwidth depends on the duration of the optical pump pulse. With ultrashort optical pulses, down to 15 fs in duration, T-ray pulses have been generated with spectra extending to the mid-infrared, above 40 THz or 7 μm (Bonvalet et al., 1995; Han and Zhang, 2001).

OR effects have been observed in air (Cook and Hochstrasser, 2000), in biased quantum wells (QWs) (Citrin, 1997), Periodically-Poled $LiNbO_3$ (PPLN), in poled polymers (Nahata et al., 1995), in polymer thin films (Sinyukov and Hayden, 2002), in superconducting thin films (Siders et al., 2000), and from beating in coupled quantum wells

(Luo et al., 1993). T-rays generated from OR in PPLN can be tuned by the polling period, the temperature or the crystal orientation (Weiss et al., 2001; Lee et al., 2000c; Lee et al., 2000b; Lee et al., 2001b). Typically, OR is driven by ultrafast pulses from a solid-state Ti:sapphire mode-locked laser, although 1.55-μm light has been used in optical fiber-based systems (Li et al., 2000).

Figure 3.3 illustrates an ultrafast optical laser pulse generating a T-ray pulse in a nonlinear EO crystal. The optical pulse, with a time-bandwidth product $\Delta\tau\Delta\omega$ close to unity, generates a polarisation transient in the EO crystal, $\mathbf{p}(t)$, which acts as a source of electromagnetic radiation, $E_{\mathrm{THz}}(t)$. The speed of the EO effect is sub-fs, so the duration of the polarisation transient depends on the duration of the optical pump pulse. The bandwidth of the emitted pulse is determined by the transient nature of the polarisation transient – for a fs optical pulse, the bandwidth of the electromagnetic pulse can extend to over 40 THz.

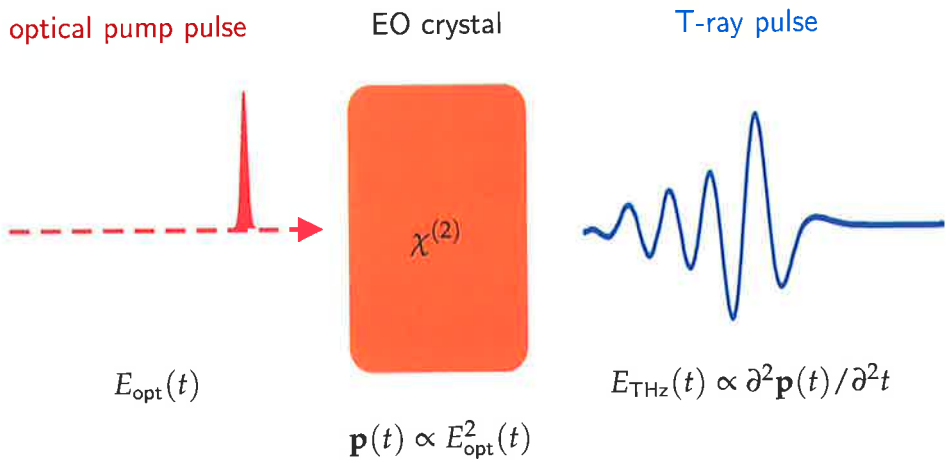

Figure 3.3. Optical Rectification. Optical Rectification (OR) is a second-order nonlinear effect, whereby an ultrafast electric field pulse is rectified in a $\chi^{(2)}$ medium, in this case an EO crystal. The ultrafast pump pulse induces a transient polarisation, $\mathbf{p}(t)$, which in turn emits a T-ray-bandwidth pulse. The time evolution of the T-ray pulse is given by the second time derivative of the polarisation transient, $E_{\mathrm{THz}}(t) \propto \partial^2 P(t)/\partial^2 t$ (Zhang et al., 1992a; Rice et al., 1994).

Optical Rectification was used as a source of nearfield T-ray radiation in the microscopy experiments described in Ch. 10. The nearfield OR system, described in Sec. 10.2, produced nearfield T-rays from a tightly-focussed optical beam.

3.2.3 Pulsed photomixing

Pulsed photomixing in biased semiconductors uses similar physical devices to T-ray generation in PCAs (Sec. 3.2.1), continuous-wave (CW) photomixing (Sec. 2.7) and CW nonlinear DFG (Sec. 2.6). Photomixing enables generation of tunable CW T-ray radiation, which is valuable for high-resolution spectroscopy applications, but does not provide simultaneous access to the broad frequency range of T-ray pulses, thus limiting the available spectral information.

T-rays are generated by mixing two ultrafast laser pulses in a PCA. An ultrafast laser is used to generate optical pulses, each of which is split into two pulses. The pulses are split in an interferometer, which can control the relative phase of the pulses. The phase difference between the pulses determines the output T-ray pulse shape (Ralph and Grischkowsky, 1992; Weling et al., 1994; Joffre et al., 1996). Shaping of the optical near-infrared (NIR) pump pulse enables T-ray pulse shaping generated from nonlinear optical mixing effects (Kawase et al., 1999; Eickemeyer et al., 2000; Sohn et al., 2002). Mixing pulses with an equal frequency chirp creates a difference frequency that depends on the phase delay of the two pulses in the arms of the interferometer. Chirped pulse mixing therefore generates relatively narrowband, frequency-tunable T-rays (Veitas and Danielius, 1999; Belabas et al., 2001). Photomixing has been observed in quantum well structures using resonant excitation of plasmons (Ryzhii et al., 2002).

3.2.4 Photoexcited semiconductors and superconductors

T-ray emission has been observed from unbiased semiconductors due to OR, photocarriers accelerated in the semiconductor surface field, coherent polarisation oscillations (Luryi, 1991), coherent phonons (Dekorsky et al., 1995; Garrett et al., 1996; Merlin, 1997; Han et al., 1999), coherent plasmon oscillations (Kersting et al., 1997; Kersting et al., 1998a), coherently controlled photocurrents (Côté et al., 1999), transitions in coupled quantum wells (Pötz, 1996), intersubband transitions in quantum wells (Kersting et al., 1998b), coherent charge oscillations in quantum wells (Bonvalet et al., 1996), Rabi oscillations (Harel et al., 1999), Stark wave packets (Schafer and Krause, 1997), coherent Bloch oscillations in superlattices (Roskos et al., 1992; Waschke et al., 1993; Chansungsan et al., 1994; Dekorsky et al., 1994; Victor et al., 1994), photo-Dember fields (Sarukura et al., 1998b; Gu et al., 2002) and superluminal ionisation

fronts (Hashimshony et al., 2001b). Of these physical effects, the most common sources of T-ray pulses are OR and photocarrier acceleration due to their relatively high power.

T-ray emission has been observed in high-T_c superconductors due to ultrafast modulation of the superconductivity (Tominari et al., 2002).

T-ray emission from unbiased semiconductor surfaces excited with ultrafast optical pulses was first observed by Zhang et al. (Zhang et al., 1990b; Zhang et al., 1990a). Figure 3.4 shows a schematic of T-ray generation from an unbiased semiconductor surface and the intrinsic bias field at the surface. The radiated T-ray field is proportional to the optical pump power and is due to a combination of OR (Chuang et al., 1992; Zhang et al., 1992a), bulk DFG (Saeta et al., 1993) and photocarrier acceleration in the surface field of the semiconductor (You et al., 1994; Han et al., 2000b).

T-ray emission from semiconductor surfaces is influenced by the magnetic field surrounding the emitter, which can be used to switch or enhance the generation efficiency (Ohtake et al., 1998; Ono et al., 2000; McLaughlin et al., 2000; Ono et al., 2001; Corchia et al., 2001). T-ray emission from an unbiased GaAs wafer in a switchable magnetic field is shown in Fig. 3.5, indicating enhancement and phase reversal of the generated T-ray pulse (Zhang et al., 1993a; Zhang et al., 1993b). This enhancement has been explained by considering the alignment of the induced radiating dipoles and Total Internal Reflection (TIR) at the semiconductor-air interface (Shan et al., 2001; Johnston et al., 2002).

As in pulsed photomixing, optical pulse shaping and magnetic field control enables both enhancements and spectral control of the emitted T-rays (Sarukura et al., 1998a; Izumida et al., 1999). T-ray emission from semiconductor heterostructures has been coherently controlled by shaping the optical pump pulse (Brener et al., 1994).

Photoexcited semiconductors were used as T-ray sources in the experiments in this Thesis. The experimental system is described in Sec. 5.2.2 and the output characteristics are shown in Sec. 5.3.1.

3.3 Detection

Although continuous-wave (CW) techniques can be used for T-ray detection, as described in Ch. 2, the high signal-to-noise ratio (SNR) of T-ray spectrometers is due to time-gated detection (pump-probe) techniques. Gated detection relies on an optically

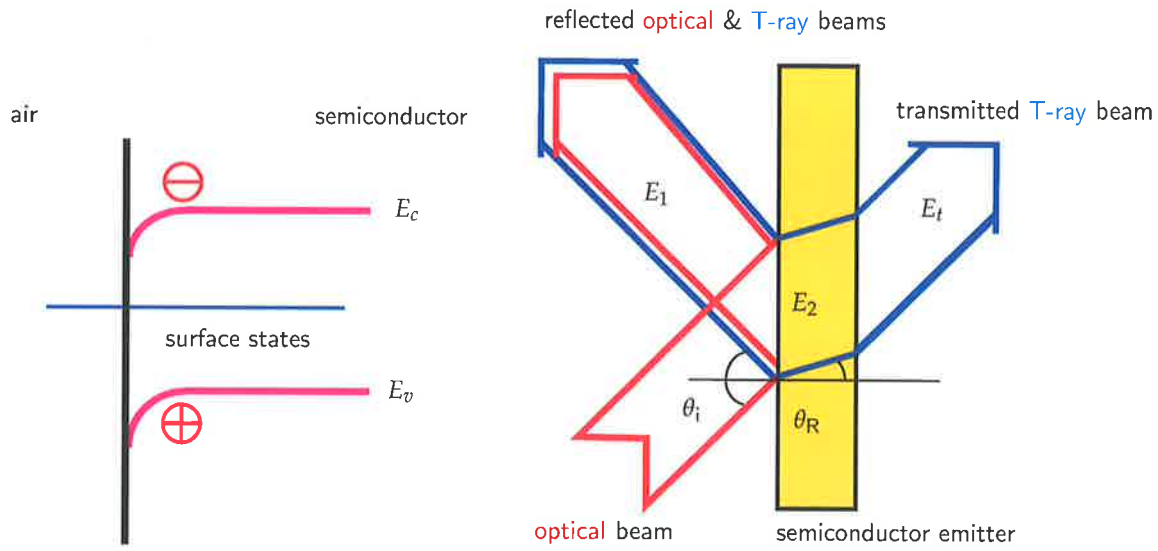

(a) Surface bias field in a bare semiconductor

(b) T-ray Surface Current Generation (SCG)

Figure 3.4. Semiconductor surface currents. The intrinsic bias at a semiconductor surface is shown in Subfig. 3.4(a) – E_c is the conduction band and E_v is the valence band in the semiconductor. This bias field sweeps ultrafast photo-generated carriers, and for high-mobility semiconductors, the resulting current transient acts as a source of T-rays. Subfigure 3.4(b) shows T-ray generation from a semiconductor surface either in transmission or reflection. The optical pump beam, incident at angle θ_i to the semiconductor surface, generates T-rays, which are partially transmitted through semiconductor, and partially reflected back (collinearly with the reflected pump beam). The angle of incidence θ_i is set at Brewster's angle to improve coupling of the optical and T-ray beams at the air-semiconductor interface. The semiconductors used, for example, LT-GaAs, are opaque to the optical beam.

switched detector, and part of the pulse split from a mode-locked laser, as illustrated in Fig. 3.6.

Gated detection systems acquire a time-domain response by scanning the time delay of the detector across the generated waveform. For T-ray generation, the detector operates on a fs time scale, which is faster by at least two orders of magnitude than the ps duration of the T-ray pulse that is being sampled. The time delay of the detection pulse relative to the generated waveform is achieved with a variable path length, represented by the delay stage in Fig. 3.6. The total length of the delay stage movement determines the duration of the sampled pulse. The speed at which the waveform is

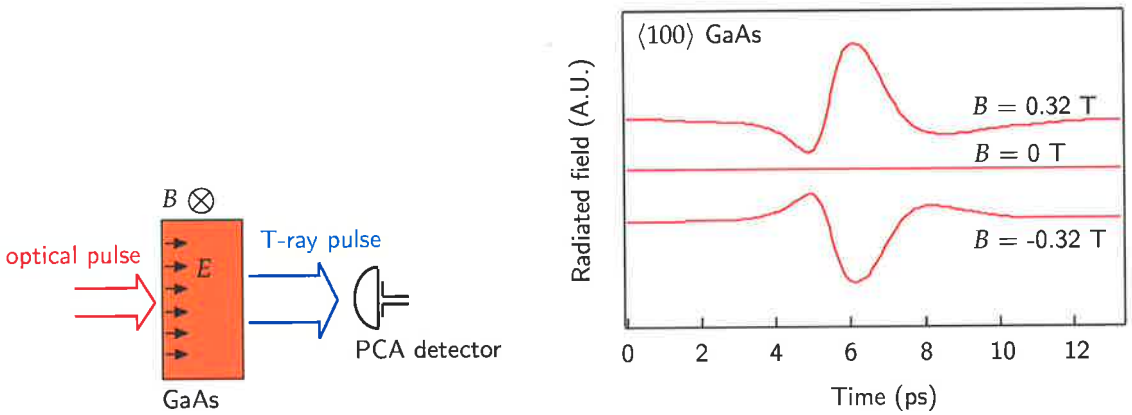

(a) Emission schematic (b) Dependence on applied magnetic field

Figure 3.5. T-ray generation from an unbiased semiconductor in a magnetic field. The intrinsic bias field, E, is shown parallel to the page (that is, normal to front face of the semiconductor surface). The T-rays generated from an unbiased semiconductor are enhanced by the application of a DC magnetic field, B, shown normal to the page. The enhancement can be seen in Subfig. 3.5(b). This effect is discussed in Sec. 3.2.4. (After Zhang et al. (1993a).)

acquired is limited by the desired SNR. A faster scan leaves less time for the signal at each point to be averaged with, for example, a Lock-In Amplifier (LIAs), thus increasing the noise level. In T-ray spectroscopy and imaging, there is a fundamental tradeoff between signal acquisition time and SNR.

The two major methods of T-ray detection, as with generation, use Photoconductive Antennas (PCAs) or electro-optic (EO) crystals.

3.3.1 Photoconductive sampling

Photoconductive sampling was developed in conjunction with PCA emitters (see Sec. 3.2.1). For T-ray detection, an unbiased PCA is placed in the T-ray beam path and gated with an optical probe pulse. A PCA in detection configuration is shown in Fig. 3.8. The gating pulse allows current to flow in the PCA, which is connected to an ammeter. The T-ray electric field biases the PCA, and the current is therefore proportional to the T-ray field. The optical probe pulse has a far shorter duration than the T-ray pulse, so the T-ray waveform is sampled in time by changing the time delay of the two optical pulses (Valdmanis et al., 1983; Auston and Smith, 1983). The detected T-ray

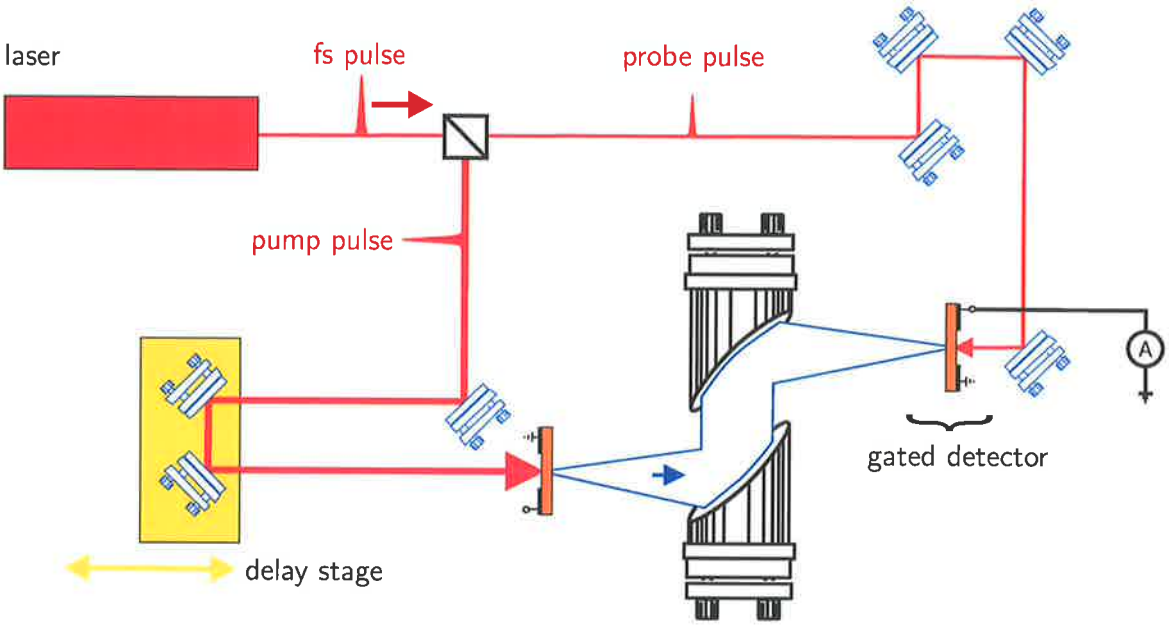

Figure 3.6. Schematic functional diagram of gated detection. This T-ray generation and detection schematic is an example of a pump–probe experiment. The pump beam initiates a T-ray pulse, which is detected by a gated detector. The gated detector is activated by the probe pulse. The time delay is varied with a delay stage. Thus the time evolution of the pulse can be sequentially sampled. The extra distance in the probe pulse path is required so that the optical path lengths of the pump and probe pulses are identical – the probe beam must gate the detector at the same time as the T-ray pulse arrives at the detector. In this example, PCAs are depicted as the T-ray emitter and detector. (Note that this bare bones schematic only shows the system components that are relevant to gated detection. Typical auxiliary elements in a T-ray spectrometer, such as the optical chopper, are not essential to gated detection.)

signal is a convolution of the incident T-ray waveform and the response of the PCA (Bromage et al., 1999; Duvillaret et al., 2001). In spectroscopy experiments, the detector and emitter responses are accounted for by deconvolution, or signal normalisation with a reference pulse, as discussed in Sec. 4.2.

Initially fabricated on LT-GaAs, PCA detectors achieved a maximum bandwidth of ≈2 THz (Smith et al., 1988; Fattinger and Grischkowsky, 1989). Recent experiments with ultrafast gating pulses of 15-fs duration have extended the detection bandwidth to 40 THz (Kono et al., 2000; Kono et al., 2001). LT-GaAs PCAs can be gated with 1.55-μm wavelength light through a two-photon absorption process (Tani et al., 2000b).

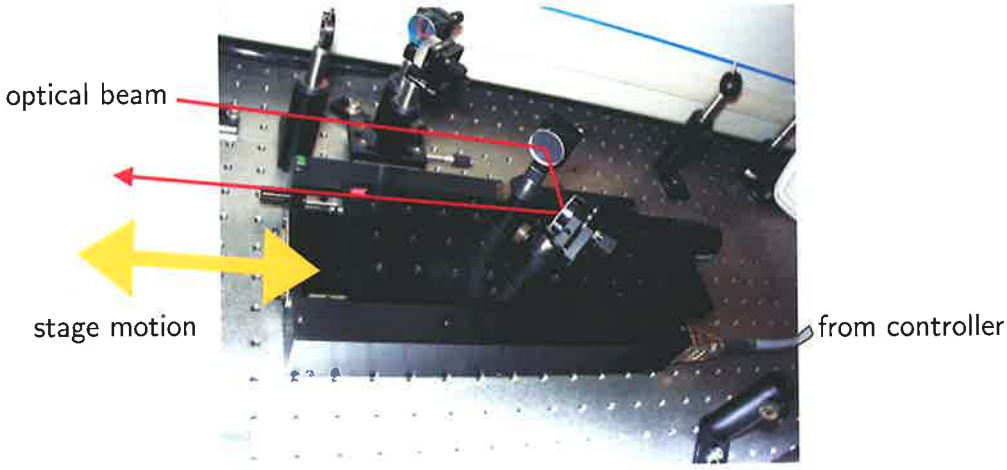

Figure 3.7. Pump-probe delay stage. The delay stage pictured here is the essential element in pump-probe experiments, of which T-ray spectroscopy is one example. The stage is used to sweep the ultrafast probe pulses over the temporal profile of the free-space T-ray pulse, thereby sampling the entire T-ray waveform. The stage motion is coordinated with the detection electronics via a computer and General Purpose Interface Bus (GPIB)) interface.

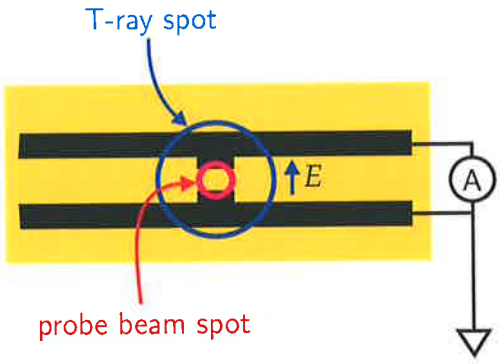

Figure 3.8. Sketch of a PCA used for photoconductive sampling. This sketch shows a photoconductive dipole antenna (looking face on) used for T-ray detection. The large T-ray spot (shown as a blue circle) biases the electrodes with a free-space electric field. The probe spot is focussed into the biassed region of the antenna substrate. The fs-duration probe switches the electrodes with transient photocarriers, allowing a current to flow, which is detected by an ammeter. The current flow is proportional to the applied T-ray field.

3.3.2 Electro-Optic Sampling

Electro-Optic Sampling (EOS) is a broadband T-ray sampling technique. EOS is more complex to implement and align than T-ray detection using a PCA – this can be seen by comparing Figs. 3.8 and 3.9 – however EOS demonstrates a broader detection bandwidth and greater sensitivity.

In EOS, as in photoconductive sampling, the detector is gated by a time-delayed probe pulse. The detector is an EO crystal, placed between crossed polarisers, and the optical and T-ray beams propagate collinearly through it, shown in Fig. 3.9. The incident T-ray pulse modulates the birefringence of the crystal, through Pockel's effect (Yariv, 1989; Saleh and Teich, 1991; Shen, 1984). The induced birefringence in the crystal is proportional to the electric field strength of the T-ray pulse, and causes a rotation of the polarisation of the optical pulse. The crossed polarisers (linear polarisers aligned with their axis perpendicular to each other) effect an amplitude modulation of the optical pulse, which is proportional to the polarisation modulation and thus the T-ray field strength. The linearity of EOS for detecting a freely propagating T-ray electric field is demonstrated in Fig. 3.10(a).

Initially used in the characterisation of high-speed electronic circuits (Auston and Glass, 1972; Valdmanis et al., 1982; Valdmanis et al., 1983; Valdmanis and Mourou, 1986; Wiesenfeld, 1990), EOS was first used for free-space T-ray detection in 1995 by Wu and Zhang (Wu and Zhang, 1995). Although more difficult to align experimentally than PCA detectors (Wu et al., 1996b; Cai et al., 1998; Park et al., 1998; Park et al., 1999a; Chen et al., 2001; Planken et al., 2001), EOS soon demonstrated a wide bandwidth and high sensitivity (Wu and Zhang, 1996b; Wu and Zhang, 1996a; Uhd Jepsen et al., 1996; Nahata et al., 1996a; Nahata et al., 1996b; Wu and Zhang, 1997b). The sensitivity of EOS depends on the EO $\chi^{(2)}$ nonlinear coefficient of the detection crystal, which must be transparent to the probe beam, and the quality of phase matching between the T-ray and optical pulses (Park et al., 1999a).

The central trade-off for EOS is the thickness of the crystal. A thicker crystal provides a longer interaction length for the coupled pulses, hence a larger signal. However, since perfect phase matching between the optical and T-ray pulses is not possible, a thinner crystal with less dispersion provides a broader detection bandwidth (Cho et al., 1998). Figure 3.11 shows T-ray waveforms detected with an EO crystal, indicating the increased bandwidth but reduced signal amplitude for a thinner detector. Using sub-100-μm-thick crystals, mid-infrared pulses are detectable (Han and

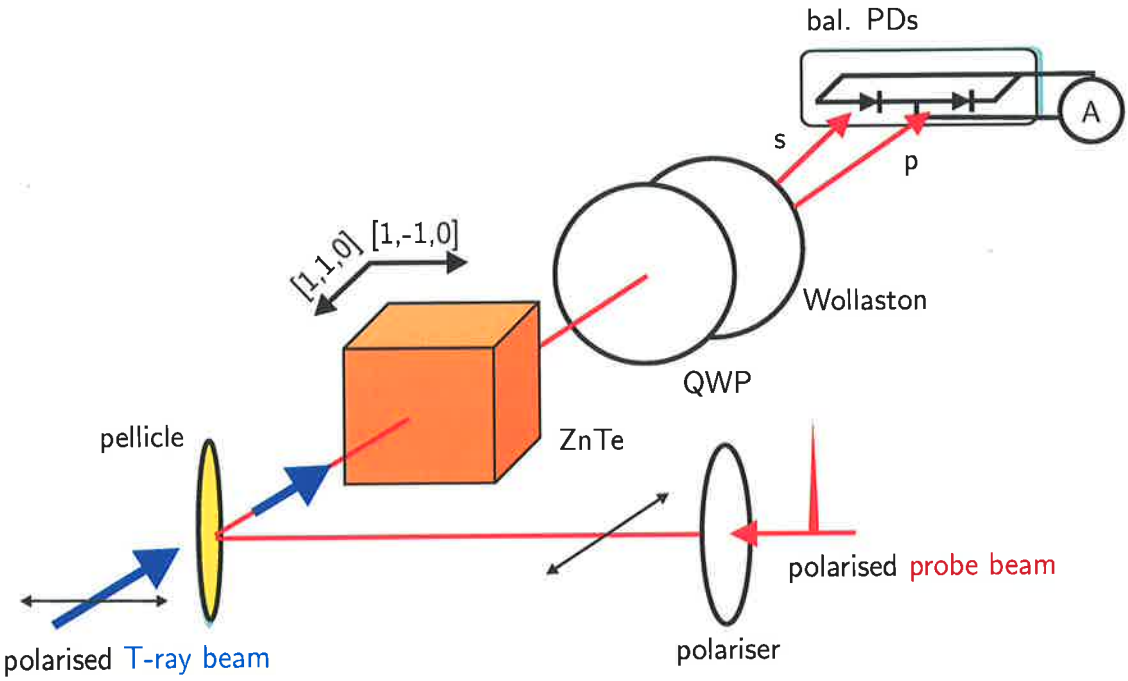

Figure 3.9. Sketch of an Electro-Optic Sampling setup. The Electro-Optic Sampling (EOS) scheme is more complex than PCA detection, but has better sensitivity and a broader bandwidth. The polarised T-ray electric field induces a birefringence in the detector, depending on the $\chi^{(2)}$ coefficient of the specific crystallographic orientation of the crystal (Chen et al., 2001). A pellicle beam-splitter directs the pump and probe beam collinearly through the EO detector. The polarisation of the probe beam is rotated by the birefringent medium, which is converted to an intensity modulation using an analyser. The analyser is a polarising beam splitter or second polariser rotated 90° from the first polariser. This is a typical crossed-polariser detection method (Saleh and Teich, 1991; Yariv, 1991). The analyser, in this diagram a Wollaston beam splitter, directs the two polarisations to balanced photodiodes. A quarter-wave plate (QWP) is rotated to balance the difference current to zero for zero T-ray field, accounting for residue birefringence in the EO crystal.

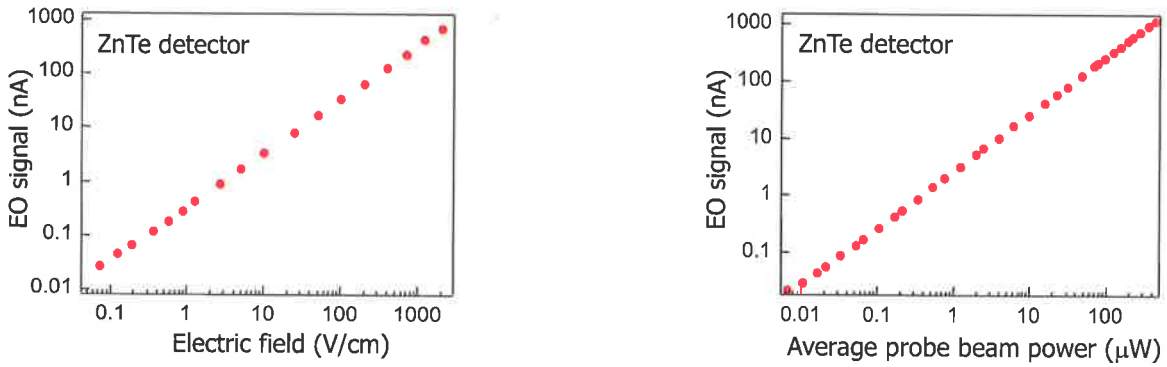

(a) To electric field

(b) To probe beam power

Figure 3.10. Measured linearity of ZnTe EOS. These results demonstrate the linearity of ZnTe as a T-ray sensor, to both the probe beam power and the T-ray electric field. The linearity is (<2%) for over more than 5 orders of magnitude. (After Wu et al. (1996c).)

Zhang, 1998a; Leitenstorter, 2001; Leitenstorfer et al., 1999). The most popular crystal used for T-ray EOS is ZnTe due to its high EO coefficient, low group velocity mismatch between T-ray pulses and optical probe pulses, and good mechanical properties (Gallot et al., 1999). GaP (Gallium Phosphide) (Wu and Zhang, 1997a), GaAs (Vossebrger et al., 1998), multilayered EO polymer films (Sinyukov and Hayden, 2002), poled polymers (Cao et al., 2002) and DAST are among alternative materials used for EOS (Han et al., 2000d; Han et al., 2000c; Walther et al., 2000b).

A primary advantage of EOS is its extension to 2D, 3D and single-shot imaging, as discussed in Sec. 9.4 (Jiang and Zhang, 1998a; Jiang and Zhang, 1998c; Jiang and Zhang, 1999b; Weling et al., 1999; Shan et al., 2000; Ferguson et al., 2001b). With a larger EO crystal and an expanded optical beam, the intensity modulation across the transverse T-ray beam can be imaged with a CCD camera(Wu et al., 1996c; Wu et al., 1996a).

The EOS equipment used in the experiments in this Thesis is described in Sec. 5.2.2, which includes diagrams and photographs of the apparatus.

3.3.3 Single-shot EO detection

Single-shot detection is fundamentally different to normal gated detection in that the entire T-ray waveform is measured by each probe beam pulse, and then detected spatially. The ps time duration of the T-ray pulse is transferred to the spatial domain using non-collinear propagation of the T-ray and probe beams in an EO crystal (Weling

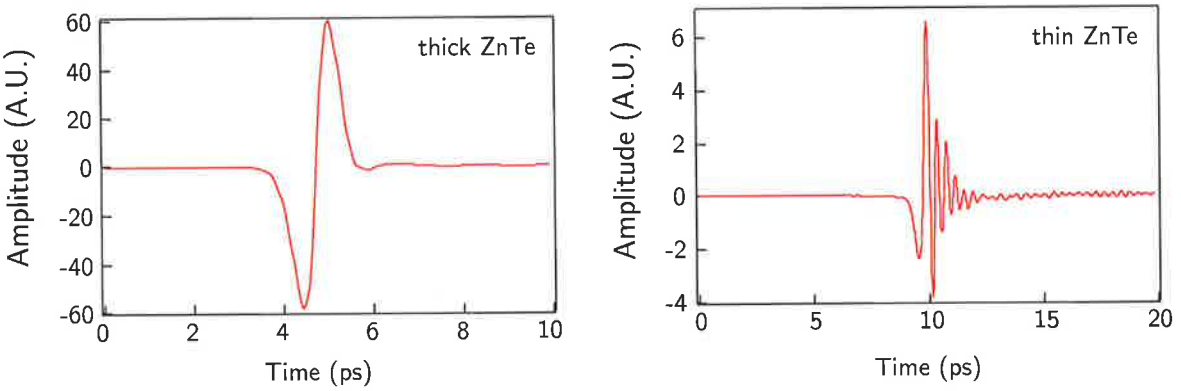

(a) Typical T-ray pulse (2-mm-thick EO detector)

(b) Ultra-broadband T-ray pulse (100-μm-thick EO detector)

Figure 3.11. Measured broadband T-ray pulses. Crystal thickness determines signal sensitivity and bandwidth in EOS. The two Subfigures show a T-ray pulse sampled with two ZnTe detectors. Typically a 2-mm-thick ZnTe crystal provides a high signal, but a bandwidth limited to under 10 THz. ZnTe is a good EO sensor because of phase matching between the T-ray and optical pulses. Ultra-broadband phase matching is, however, not possible, so a thinner crystal detects higher frequencies. Using a 10-μm-thick crystal, frequencies up to 70 THz have been measured (Leitenstorfer et al., 1999). (After Han and Zhang (1998b).)

et al., 1999) or collinear propagation of a chirped probe beam. In chirped probe detection, the spatial distribution of the T-ray pulse along the propagation axis in the EO crystal is mapped onto the different wavelengths of a chirped probe pulse, and then separated with an optical grating (Jiang and Zhang, 1998a) or streak camera (Jiang et al., 1999). A schematic of chirped pulse detection is shown in Fig. 3.12. Chirped pulse detection can be designed with automatic background cancelling with dual photodetector arrays (Jiang and Zhang, 1998c), or extended to 1D imaging with a CCD. Single-shot detection has been used for electron bunch measurements in FELs (Wilke et al., 2002) and rapid imaging applications (see Sec. 9.4).

3.3.4 Magneto-optic detection

Magneto-optic detection is analogous to EOS in that the transient magnetic component of a propagating free-space T-ray pulse can be detected using crossed polarisers and a

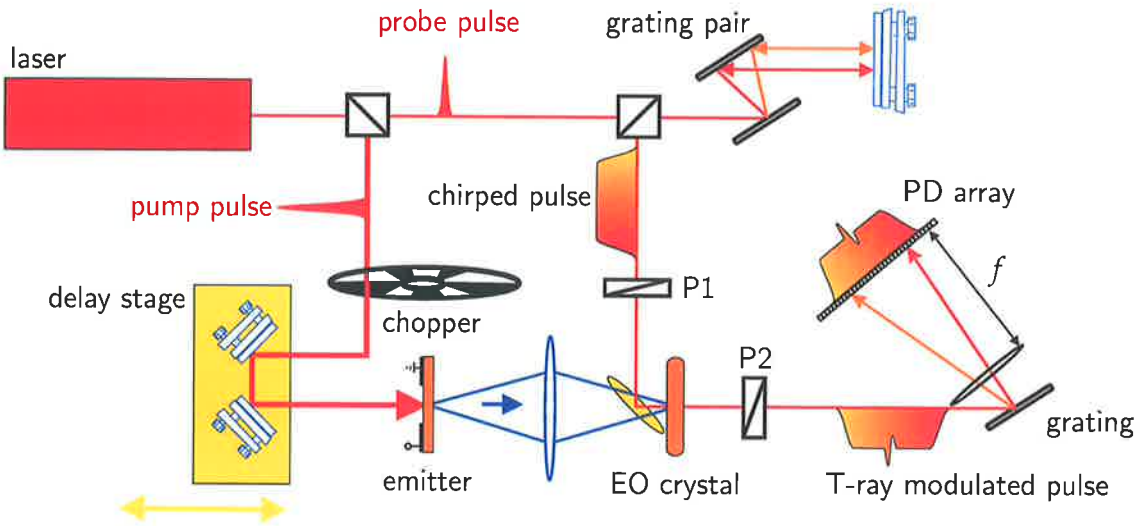

Figure 3.12. Single-shot detection. This schematic shows the chirped pulse single-shot T-ray pulse detection technique. The single-shot spectrometer is similar to a typical T-ray detection system, using OR and EOS, except the probe pulse is stretched to a ps duration with a grating pair. The polarisers 'P1' and 'P2' are used for crossed polarisation detection (see Sec. 3.3.2). When the T-ray and probe pulses propagate collinearly through the EO detector, they both have approximately the same duration, thus different wavelengths in the spread probe pulse experience different levels of intensity modulation. As the pulse is chirped, these different levels are separated with a spectral grating, and detected with a linear photodiode (PD) array. A lens with focal length f focuses the pulse onto the array. Apart from a background measurement of the unmodulated chirped pulse required to extract the T-ray waveform, the technique can measure the entire T-ray waveform in a single shot. The T-ray wavefront is focused from emitter to detector in this scheme with a polyethylene lens, which has a very low dielectric constant for T-rays. The purpose of this particular configuration is to study the propagating wave shape; for material measurements, a sample can be placed between two polyethylene lenses (2-f spacing) in the T-ray beam path. For single-shot imaging, discussed in Sec. 9.4, the T-ray beam is spatially expanded in 1D and the PD array is replaced with a CCD. (After Jiang and Zhang (1998a).)

magneto-optic crystal (Riordan et al., 1997). The T-ray magnetic field is detected using the Faraday effect in an optical medium (Saleh and Teich, 1991).

3.3.5 Lock-in detection

A feature of PCA and EO detection is the large DC background in the probe compared to the modulation due to the T-ray field. A common method used to observe a T-ray signal is to AC modulate the free-space T-ray beam at a certain frequency, indicated by the chopper in Fig. 3.6, then electronically filter out any signals not at this modulation frequency. Laser noise is greater at lower frequencies – due to its $1/f$ characteristic (von der Linde, 1986) – so a higher modulation frequency leads to less noise. The maximum desirable modulation frequency is approximately 3.5 MHz, where the noise floor is set by instrumentation and photon noise (Chwalek and Dykaar, 1990).

The signal detected in a T-ray system is a current from the photodiodes that are monitoring the probe beam. The probe beam power depends partially on incident T-ray power, but the T-rays are only one source of probe beam modulation: laser noise is also measured by the T-ray system. Lock-in detection enables the signal from T-rays to be distinguished from the noise by modulating the T-rays at a certain pre-defined frequency f_{mod}. The chopper is required to modulate the T-ray signal at the modulation frequency, that is in the pump beam path. The lock-in detector (Lock-In Amplifier) then looks for the AC modulated part of the measured signal specifically at f_{mod}.

The Lock-In Amplifier used in the experiments in this Thesis is described in more technical detail in Appendix B.

3.4 T-ray propagation

This Section describes how T-rays propagate through T-ray lenses, T-ray filters, and free space. This leads to a discussion of T-ray spectrometers configured to generate and detect T-rays with the same element, that is, using one PCA or EO crystal as a T-ray transceiver.

3.4.1 Propagation and filters

With the development of free-space T-ray emitters and detectors, interest increased in the propagation of T-ray-band pulses in a vacuum and through quasi-optical elements. T-ray systems use quasi-optical collimation and focusing elements, including gold-coated off-axis parabolic mirrors (van Exter et al., 1989a), Silicon hyperhemispherical lenses (Mittleman et al., 1996; Rudd and Mittleman, 2002), anti-reflection coatings (Kawase and Hiromoto, 1998), variable phase polarisation compensators (Cumming and Blaikie, 1999), reflective gratings, Teflon prisms (White et al., 1995), and transmissive optics fabricated from Silicon or polyethylene (Ruffin et al., 1999).

T-ray spatial filters are fabricated using metal, which has a very high absorption at T-ray frequencies (Arjavalingam et al., 1992), including high-pass filters with metal slits (Bromage et al., 1997; Lee et al., 2001a), apertures (You and Bucksbaum, 1997; Bromage et al., 1998), band-pass filters (MacDonald et al., 2000), low pass filters of glass beads in polyethylene (Sato et al., 1989), filter cascades (Winnewisser et al., 1999) and dichoric filters (Winnewisser et al., 1998; Winnewisser et al., 2000).

Fresnel lenses have been modelled and constructed from Silicon to allow frequency-dependant focusing of the broadband T-ray beams (Wang et al., 2002). A Silicon binary lens for T-ray wavelengths is pictured in Fig. 3.13(a) and the sharp T-ray focus is shown in Fig. 3.13(b).

T-ray beam propagation has been studied in scattering media (Pearce and Mittleman, 2001) and simulated with finite-difference time-domain techniques (Beard and Schmuttenmaer, 2001). T-rays have been used to study single cycle pulse propagation (Kaplan, 1998), the Gouy phase shift at a focus (Hunsche et al., 1999) and T-ray whispering-gallery modes in cylinders (Zhang and Grischkowsky, 2002). The study of T-rays propagating through air and optical elements has been greatly enhanced by techniques for imaging the T-ray emission patterns and beam profiles using either scanned PCAs (Sec. 9.2) or EO detection (Ch. 10).

Dynamic T-ray filters have been demonstrated using free carrier generation in a semiconductor to block, or reflect, the T-ray pulse. This transient mirror can be used to slice up very short duration sections of a T-ray pulse (Cole et al., 2001), or reflect a sub-wavelength diameter cross-section of the beam for near-field studies (see Ch. 10).

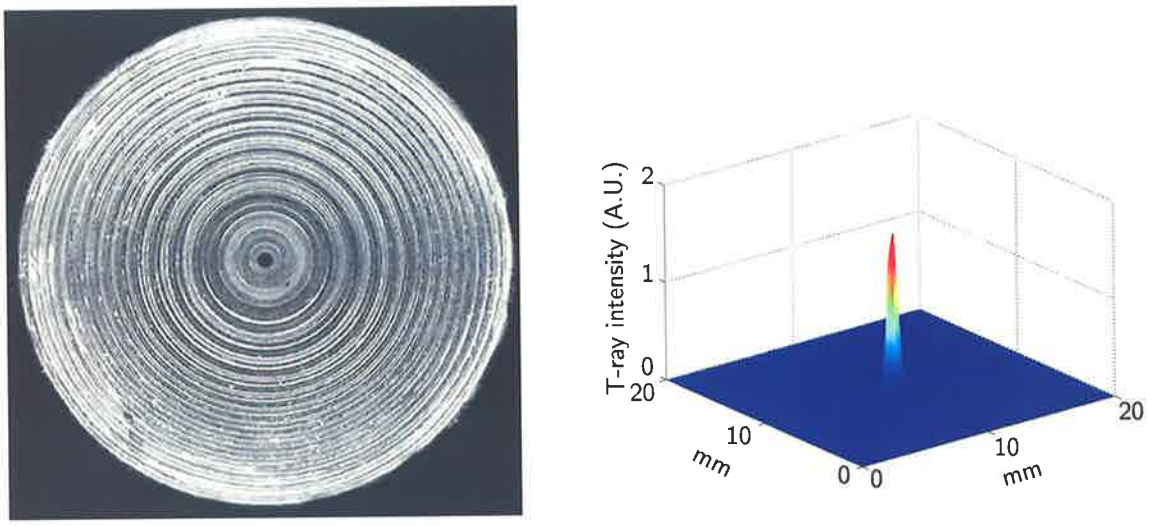

(a) Eight level silicon Fresnel lens (b) Focused T-ray electric field

Figure 3.13. Silicon Fresnel lens. A Fresnel lens constructed from high-resistivity Silicon demonstrates sharp focusing of the terahertz beam. This is comparable to a conventional refractive T-ray lens. (After Wang et al. (2002)).

3.4.2 Transmission and reflection

T-ray spectrometers can be used either in transmission or in reflection (Khazan et al., 2001). The T-ray pulses are detected after transmission through a sample, or reflection from its surface. The mode used depends on the type of sample being studied. For samples with very high absorption, no transmitted signal is detectable. However, normalising the system response is more difficult with a reflective system, because a reference pulse must be taken without the sample present, and it is difficult to maintain exactly the same free-space path length between the emitter and detector. Alternative geometries used for T-ray spectroscopy and analysis techniques are discussed in Sec. 4.2.

3.4.3 Transceivers

In an extension of the standard T-ray reflection system, the roles of emitter and detector can be combined into one device, either a PCA or an EO crystal (Tani et al., 2000a; Chen et al., 2000a; Chen et al., 2001; Chen and Zhang, 2000). In a T-ray transceiver, the pump and probe pulses travel collinearly with opposite polarisation and an adjustable time-delay to reflect off a sample, as shown in the schematic in Fig. 3.14. The EO transceiver

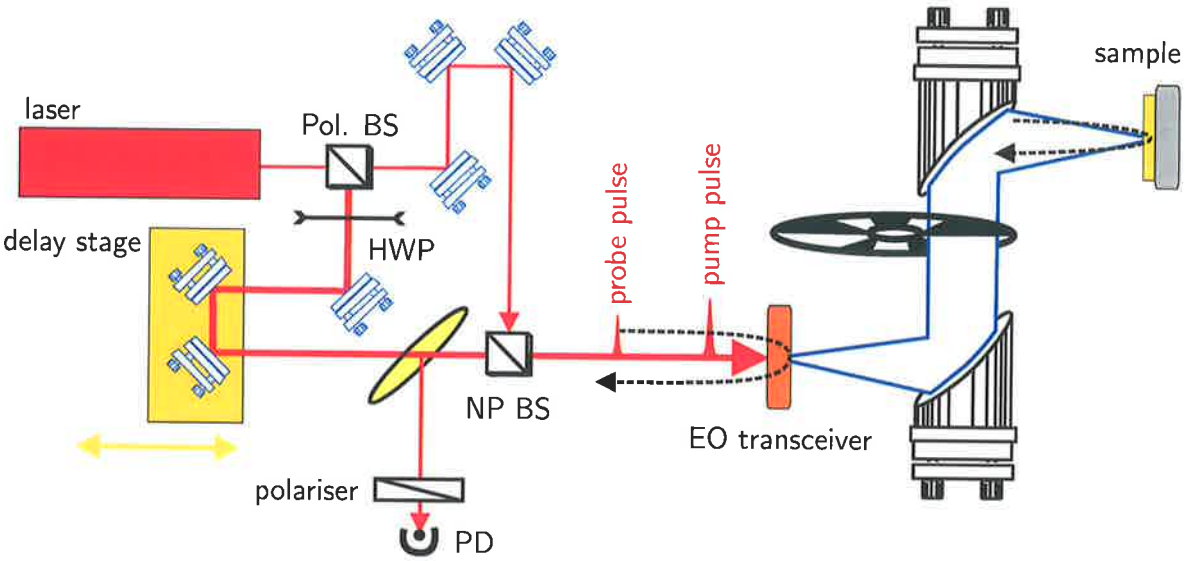

Figure 3.14. Free-space EO transceiver. A free-space electro-optic (EO) transceiver combines Optical Rectification (OR) and Electro-Optic Sampling (EOS) in the same EO crystal. As shown in this schematic, the optical laser pulses are split into pump and probe pulses with a polarising beam splitter (Pol. BS), then recombined with a non-polarising beam splitter ('NP BS') and directed collinearly into the EO transceiver. The pump pulse generates T-rays, which are focused onto a sample and reflected back into the transceiver (as indicated by the blue U-shaped arrow). The probe pulse has an orthogonal polarisation to the pump pulse and arrives at the EO transceiver after the pump pulse (the exact delay is controlled by the delay stage). The probe pulse is reflected off the far face of the EO transceiver (as indicated by the black U-shaped arrow), after which it travels from right to left through the transceiver at the same time as the returning T-ray pulse. The returning probe pulse detects the reflected T-ray pulse by EOS and is then passed though an analysing polariser into a photodetector (PD). The half-wave plate (HWP) is used to rotate the polarisation of the pump beam to the optimal polarisation for the orientation of the EO crystal and the probe polarisation. A PCA transceiver has a similar geometry, except the reflected T-ray pulse is detected as a gated current in the PCA (Tani et al., 2000a). (After Chen et al. (2001).)

extends into free space the concepts of early spectroscopy with T-rays confined to a single crystal by Total Internal Reflection (TIR) – see Sec. 4.2.3.

3.4.4 Waveguides

T-ray propagation in waveguides is related to microwave technology in the same way that focusing and filtering in free space are related to optical techniques (Grischkowsky, 2000). Waveguide propagation is relevant in studying near-field T-ray devices (Gallot et al., 2000; Wynne et al., 2000; Filin et al., 2001; Reiten et al., 2001a; Mitrofanov et al., 2001a), T-ray interconnects (Hadjiloucas et al., 2003; Mendis and Grischkowsky, 2001; Digby et al., 2000; Mendis and Grischkowsky, 2000; Jamison et al., 2000; Kazemi et al., 1999; Collins et al., 1999), T-ray cavities (Zhang et al., 2001b) and integrated T-ray resonators (Nagel et al., 2002b).

3.5 Chapter summary

Pulsed T-ray systems have been reviewed in this Chapter, and the important elements of T-ray generation, propagation and detection have been described. The background in this Chapter underpins the design and operation of the T-ray experiments described in Chs. 5, 6, 7, 8 and 10.

The application of this T-ray spectrometer to biosensing is introduced in the following Chapter with a review of the field of T-ray sensing.

Chapter 4

T-ray Sensing and Spectroscopy

ONE of the first applications of T-rays was as an ultrasensitive gas transmission spectrometer. T-ray spectroscopy has now evolved to cover experiments in fields from clinical biology to solid-state physics. This Chapter is divided into two main Sections: (i) descriptions of the various geometries used for material characterisation in a T-ray spectrometer, and (ii) a review of the materials that have been studied.

Our experimental work on T-ray sensing of protein hydration is presented in greater detail in Ch. 5, and bio-affinity sensing is described in Chs. 6 and 7.

4.1 Introduction

T-ray sensing involves applying T-ray techniques to the study of materials by monitoring transmitted or reflected radiation. The T-ray spectrum is populated by energy transitions of 0.4 to 40 meV, which correspond to different rotational and torsional states of a whole molecule (Chantry, 1971). For larger molecules, the far-infrared (FIR) has fewer transitions than the near-infrared (NIR), which can be very densely populated. The T-ray band also corresponds to energy transitions in superconductors, plasma states, lattice vibrations and other resonances in crystals (Houghton and Smith, 1966).

Pulsed T-ray spectroscopy is a coherent technique, in which both the amplitude and phase of the T-ray pulse are measured. Coherent detection enables direct calculation of absorption and refraction profiles without using the Kramers-Kronig relations (Jackson, 1998). T-ray spectrometers provide a high SNR (Signal-to-Noise Ratio) and a broad bandwidth, making them attractive to sensitive spectroscopic studies in the T-ray band.

Pulsed T-ray spectroscopy builds upon a rich history of sub-mm and FIR spectroscopy, as described in Ch. 2

The main purpose of this Chapter is to describe: (i) the published methods used in pulsed T-ray sensing, and (ii) the materials that have been studied with T-ray systems. This forms a background to the novel experiments in T-ray sensing in Chs. 5 and 7.

4.2 T-ray time-domain spectroscopy

Time-domain spectroscopy (TDS) is a long-established method in the study of electronic circuits. T-ray TDS uses free-space T-ray radiation to study dielectrics. T-ray TDS is markedly different from optical spectroscopic techniques that rely primarily on incoherent detectors. Any sample can be characterised by a complex dielectric constant $\tilde{\epsilon}$, which describes the attenuation and delay of transmitted radiation at a given frequency ω, where $\omega = 2\pi f$, and f is the frequency of the T-ray radiation in Hz. In free space, the wavelength and frequency of the radiation are related by $c_0 = f\lambda$, where c_0 is the speed of light in a vacuum. A coherent detector is able to determine the delay, or phase relationship, between incident radiation with and without a sample present, and thus directly measure both the real and imaginary parts of $\tilde{\epsilon}$. With an incoherent detector, however, additional processing is required to estimate the phase

delay caused by a material, using the Kramers-Kronig relations, integrals that relate the real and imaginary parts of the complex dielectric constant (Born and Wolf, 1997).

T-ray spectroscopy is a coherent detection method, and therefore measures the complex dielectric constant of the material, $\tilde{\epsilon} = \epsilon' - j\epsilon''$, or equivalently the complex index of refraction of the material $\tilde{n} = n - j\kappa$, where $(\tilde{n})^2 = \tilde{\epsilon}$. The dielectric constant is typically referred to in the field of high-speed electronics and the refractive index in T-ray optics. The power absorption coefficient, α, is related to κ through $\alpha = 2\omega\kappa/c_0$.

In this Thesis, the frequency-dependent quantities, $\tilde{n}$ and $\tilde{\epsilon}$, are written without ω (that is, $\tilde{\epsilon}(\omega) = \tilde{\epsilon}$) for purposes of brevity. A frequency-dependent spectrum is always assumed.

Estimating these material properties from T-ray Time-Domain Spectroscopy (TDS) measurements requires calculations that depend on the system configuration. Essentially, an expression is derived for the expected delay and attenuation of the pulse due to passing through or reflecting from the material of interest. This expression is in terms of the complex material properties and the thickness of the sample(s), and can be written as a product of factors in the frequency domain.

The interaction between a sample and the incident T-ray radiation can be expressed as a transfer function $\tilde{H}$,

$$\tilde{S}_{\text{final}} = \tilde{H} \cdot \tilde{S}_{\text{incident}}, \tag{4.1}$$

where $\tilde{S}_{\text{incident}}$ and $\tilde{S}_{\text{final}}$ are the complex spectral components of the incident and final T-ray pulses, both of which are frequency-dependent, that is $\tilde{S} = \tilde{S}(\omega)$. The transfer function $\tilde{H}$ is a product of reflection (r), propagation (p) and transmission (t) coefficients, which in turn depend on the geometry of the system. The specific geometries are described later in this section.

The notations for transmission, reflection and propagation coefficients at the interfaces of a dielectric slab are sketched in Fig. 4.1.

The reflection and transmission at each material interface depend on $\tilde{\epsilon}$ (or equivalently $\tilde{n}$) of the adjacent dielectrics, and the polarisation of the incident light, as shown in Fig. 4.2.

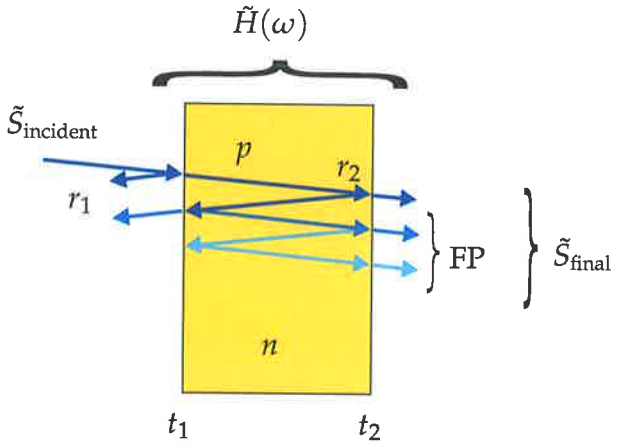

Figure 4.1. Multi-reflections and transmission through a dielectric slab. This Figure shows a dielectric slab of complex refractive index $\tilde{n}$, with an incident plane wave of electromagnetic radiation, represented by the single spectral component $\tilde{S}_{\text{incident}}$. Each spectral component represents a different frequency component of the plane wave (or equivalently, a different wavelength). The plane wave undergoes reflections r at the interfaces of the dielectric (first and second interfaces have coefficients r_1 and r_2), and propagates through p. Multi-reflections cause interference patterns in the final output wave, represented by the Fabry-Pérot factor, FP. The various coefficients are multiplied together to give a transfer function $\tilde{H}$ for the dielectric slab.

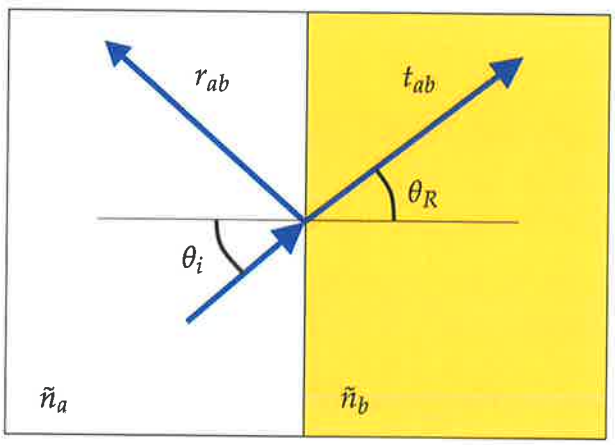

Figure 4.2. Fresnel coefficients. This diagram shows the notation for the reflection and transmission coefficients at a dielectric interface (Born and Wolf, 1997; Saleh and Teich, 1991).

For TE (transverse electric) polarisation, the complex frequency-dependent coefficients of transmission $t(\omega)$ and reflection $r(\omega)$ are

$$r^s_{ab}(\omega) = \frac{\tilde{n}_a \cos\theta_i - \tilde{n}_b \cos\theta_R}{\tilde{n}_a \cos\theta_i + \tilde{n}_b \cos\theta_R}, \tag{4.2}$$

$$t^s_{ab}(\omega) = 1 + r^s_{ab}, \tag{4.3}$$

For TM (transverse magnetic) polarisation, the complex frequency-dependent coefficients are

$$r^p_{ab}(\omega) = \frac{\tilde{n}_b \cos\theta_i - \tilde{n}_a \cos\theta_R}{\tilde{n}_b \cos\theta_i + \tilde{n}_a \cos\theta_R}, \tag{4.4}$$

$$t^p_{ab}(\omega) = \frac{\tilde{n}_a}{\tilde{n}_b}(1 + r^p_{ab}), \tag{4.5}$$

where $\tilde{n}_a$ and $\tilde{n}_b$ are the complex refractive indices of the homogeneous materials before and after the interface, θ_i is the incident angle and θ_R is the refracted angle. With knowledge of the refractive indices $\tilde{n}_a$ and $\tilde{n}_b$, θ_R can be determined from θ_i and Snell's Law, $\tilde{n}_a \sin\theta_i = \tilde{n}_b \sin\theta_R$. For a sample oriented normal to the radiation path, $\theta_i = 90°$, the propagation equations simplify to (Duvillaret et al., 1996)

$$t_{ab} = t_{ab}(\omega) = \frac{2\tilde{n}_a}{(\tilde{n}_a + \tilde{n}_b)}, \tag{4.6}$$

$$r_{ab} = r_{ab}(\omega) = \frac{\tilde{n}_a - \tilde{n}_b}{\tilde{n}_a + \tilde{n}_b}. \tag{4.7}$$

Radiation propagating a distance d through a linear medium, $\tilde{n}_a$, is delayed and attenuated according to the factor

$$p = p(\omega) = e^{-j\tilde{n}_a \omega d / c_0}, \tag{4.8}$$

where ω is the angular frequency in rads/s, and c_0 is the speed of light in a vacuum in m/s.

A sum of reflections between two plane parallel interfaces (*etalon* or Fabry-Pérot reflections), as shown in Fig. 4.1, can be represented by a FP factor,

$$\mathrm{FP} = \sum_{k=0}^{\infty} \left\{ r_2 \cdot p^2 \cdot r_2 \right\}^k, \tag{4.9}$$

where r_2 is the reflection coefficient for a plane wave reflecting internally from an interface, p is the coefficient for propagating through the slab, and k is the number of reflections, which depends on the time duration of the measured waveform and the delay caused by propagation between the interfaces.

For a very large number of multi-reflections, $k \to \infty$, the Fabry-Pérot factor (FP) can be approximated by

$$\mathrm{FP} = \frac{1}{1 - \left(\frac{\tilde{n}_2 - \tilde{n}_1}{\tilde{n}_2 + \tilde{n}_1}\right)\left(\frac{\tilde{n}_2 - \tilde{n}_3}{\tilde{n}_2 + \tilde{n}_3}\right) \cdot e^{-j2\tilde{n}_2 \omega d_2 / c_0}}. \tag{4.10}$$

The Fabry-Pérot factor introduces frequency-domain interference fringes into transmitted or reflected radiation from thin samples, and is unavoidable in very thin samples.

Typically in T-ray TDS experiments, it is simplest to measure two time-domain pulses, a reference y_r and a sample pulse y_s. The characteristic response of the entire system, which depends on many factors including the emitter and detector, is cancelled out by normalising the sample pulse with the reference pulse in the frequency domain. This is *deconvolution*. The complex frequency spectra $\tilde{S}_r$ and $\tilde{S}_s$ are calculated using numerical Fourier transforms from the time-domain waveforms sampled in the experiment,

$$\tilde{S}_r = \mathcal{FT}(y_r), \tag{4.11}$$

$$\tilde{S}_s = \mathcal{FT}(y_s). \tag{4.12}$$

The effect of the sample on the propagating pulses can be modelled using Eqs. (4.6)–(4.10), which provide a theoretical expression relating $\tilde{S}_r$ and $\tilde{S}_s$ to the material properties $\tilde{\epsilon}$. The material properties are then estimated by comparing the model to the measured spectra. Depending on the complexity of the model expression, it may be possible to solve it analytically, otherwise an iterative curve-fitting procedure is used.

The method described in this Section is used for most T-ray TDS measurements, with the model expressions for $\tilde{S}_r$ and $\tilde{S}_s$ varying with sample geometry. The geometries are described in the following sections. The expression of interest is the ratio of the complex sample spectrum to the complex reference spectrum, $\tilde{T} = \tilde{S}_s / \tilde{S}_r$, which enables the responses (transfer functions) of all invariant system components (for example, the emitter, detector, free-space propagation and mirror surfaces) to be cancelled out. This ratio is the deconvolved sample response.

4.2.1 Transmission geometry

The simplest and most common geometry for free-space T-ray TDS is transmission through an orthogonally-positioned slab of homogeneous material, characterised by $\tilde{n}_s$ (Fig. 4.1). The transmission geometry described here was used for experiments described in Chs. 6 and 7. This slab may be free-standing in air, or either deposited on or

implanted into a substrate or holder. The model for the normalised sample spectrum depends on each individual experiment, but three main classes can be discerned: (i) thick samples, (ii) thin samples, and (iii) dual-thickness samples.

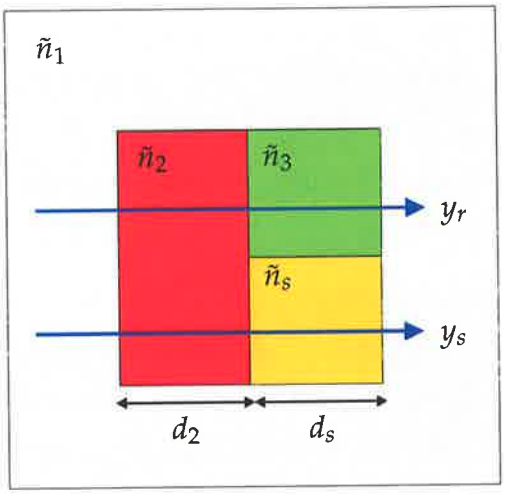

Figure 4.3. T-ray transmission notation for a single-thickness sample. This schematic shows the notation for modelling T-ray propagation through a sample slab, mounted on a substrate. The sample to be studied, with refractive index $\tilde{n}_s$, is attached to a substrate material with refractive index $\tilde{n}_2$, and both are immersed in a medium of refractive index $\tilde{n}_1$. The green area, $\tilde{n}_3$, typically has a refractive index equal to $\tilde{n}_1$ or to $\tilde{n}_2$, depending how the sample is prepared: if the sample is implanted into the substrate, $\tilde{n}_3 = \tilde{n}_2$. If the sample is deposited onto the substrate, then $\tilde{n}_3 = \tilde{n}_1$. In single-thickness measurements, the reference pulse y_r passes through the substrate then the green area. The spectral components of the waveforms are determined by FFT, $\tilde{S}_s = \mathcal{FT}(y_s)$ and $\tilde{S}_r = \mathcal{FT}(y_r)$. Single-thickness samples are used for experiments in Chs. 6 and 7.

A thick sample is a slab that causes sufficient delay so that the transmitted pulse can be measured without any overlap with the first Fabry-Pérot (FP) reflection. The exact requirements for the delay will depend on the desired total scan length (see Sec. 4.2.9). A diagram of a thick sample and the reference and sample paths is shown in Fig. 4.3. Note that the substrate material both before and after the sample must also be sufficiently thick to avoid any FP reflections in the measured pulses. Thin substrates are discussed below with thin samples.

In the thick sample geometry, the experimentally-measured spectral components of the reference and sample pulses can be modelled by

$$\tilde{S}_r = A(\omega) \cdot t_{12} \cdot p_2 \cdot t_{23}, \tag{4.13}$$

$$\tilde{S}_s = A(\omega) \cdot t_{1s} \cdot p_s \cdot t_{s3}, \tag{4.14}$$

where $A(\omega)$ is a factor representing all other system responses that remain constant between the sample and reference measurements. Using Eqs. (4.6) and (4.8), the ratio of transmission spectra can be entirely determined in terms of refractive indices and the sample thickness,

$$\frac{\tilde{S}_s}{\tilde{S}_r} = \frac{\tilde{n}_s(\tilde{n}_1+\tilde{n}_2)(\tilde{n}_2+\tilde{n}_3)}{\tilde{n}_2(\tilde{n}_1+\tilde{n}_s)(\tilde{n}_s+\tilde{n}_3)} \cdot e^{-j(\tilde{n}_s-\tilde{n}_2)\omega d/c_0}. \tag{4.15}$$

This set of equations can be solved for the real and imaginary parts of $\tilde{n}_s$ using iterative techniques (Duvillaret et al., 1996).

For the common case where the sample $\tilde{n}_s$ is placed in a vacuum or air, $\tilde{n}_1 = \tilde{n}_2 = \tilde{n}_3 = 1.0$, a simplified expression can be determined for the transmitted pulse (and any time-separated FP pulses) (Duvillaret et al., 1999). For a sample with very low T-ray absorption, that is $\kappa_s \ll n_s$, analytic expressions for n_s and κ_s can be written in terms of the magnitude ρ and phase ϕ of the transmission ratio T,

$$\tilde{T}_{\text{trans}} = \frac{\tilde{S}_s}{\tilde{S}_r} = \rho_{\text{trans}} \cdot e^{-j\phi_{\text{trans}}}, \tag{4.16}$$

$$n_s = \phi_{\text{trans}} \cdot \frac{c_0}{\omega d} + 1, \tag{4.17}$$

$$\kappa_s = \ln\left(\frac{4n_s}{\rho_{\text{trans}} \cdot (n_s+1)^2}\right) \cdot \frac{c_0}{\omega d}. \tag{4.18}$$

A thin sample is one where a number of Fabry-Pérot reflections overlap in the measured pulse train. Theoretically, this geometry can be modelled by using Eq. (4.15) multiplied by a FP factor from Eq. (4.9) or Eq. (4.10), and then solved iteratively. The samples used for the thin film spectroscopy experiments in Ch. 6 and biofilm experiments in Ch. 7 caused many FP reflections, and the transmission was modelled using iterative techniques.

4.2.2 Dual-sample geometry

A simpler transmission geometry is constructed of two thicknesses of the same material, as shown in Fig. 4.4. A dual-thickness measurement greatly simplifies modelling, and was used for spectroscopic measurements in the experiments described in Chs. 5 and 8. The reference pulse y_r passes through the sample material, but the thickness is less than the sample used for y_s.

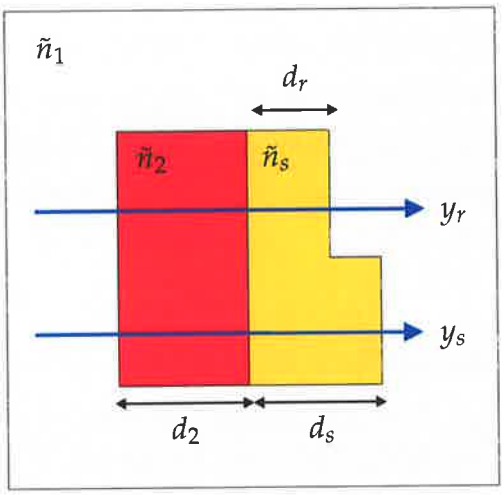

Figure 4.4. T-ray transmission notation for dual-thickness sample. This Figure shows the notation for modelling T-ray propagation through a sample slab of two different thicknesses. The sample to be studied, with refractive index $\tilde{n}_s$, is attached to a substrate material with refractive index $\tilde{n}_2$, and both are immersed in a medium of refractive index $\tilde{n}_1$. In dual-thickness measurements, the reference pulse travels through a reduced thickness of the sample – this ensures that the reflections at the dielectric interfaces are identical, and the only difference between sample and reference will be due to the thickness change of the sample. In dual-thickness measurements, the difference in thickness between d_s and d_r is denoted d in this Thesis. The spectral components of the waveforms are determined by FFT, $\tilde{S}_s = \mathcal{FT}(y_s)$ and $\tilde{S}_r = \mathcal{FT}(y_r)$. Dual-thickness samples are used for experiments in Chs. 5 and 8.

The advantage of dual-thickness measurements is that both reference and sample pulses pass through the same interfaces, so for a thick sample, the transmission is

$$\tilde{T}_{\text{dual}} = \frac{\tilde{S}_s}{\tilde{S}_r} = \frac{p_s}{p_r}. \tag{4.19}$$

The spectral components of an electric field after propagating through a sample $\tilde{n}_2$, of thickness d_2, can be expressed as (Sec. 4.2.1)

$$\tilde{S} = A(\omega) \cdot t_{12} \cdot p_2 \cdot t_{21} \cdot \text{FP}, \tag{4.20}$$

$$= A(\omega) \frac{2\tilde{n}_1}{\tilde{n}_1 + \tilde{n}_2} e^{-j\tilde{n}_2 \omega d_2 / c_0} \frac{2\tilde{n}_2}{\tilde{n}_2 + \tilde{n}_1} \text{FP}, \tag{4.21}$$

where FP accounts for Fabry-Pérot reflections in the sample, and $A(\omega)$ accounts for the incident T-ray field, invariant for sample or reference, and losses of the system between the sample and the T-ray emitter and detector. $A(\omega)$ is constant for any sample.

For two samples of the same material, identical except for thickness, the transmission spectrum of the pure material can be obtained by taking the ratio of the two spectra: for a sufficiently thick sample there are no FP reflections, so FP = 1, and all the interface effects cancel out, leaving only the propagation effects, which are simple to model. The transmission ratio for dual-thickness spectroscopy with thick samples is expressed as

$$\tilde{T}_{\text{dual}} = \tilde{S}_s / \tilde{S}_r = \frac{e^{-j\tilde{n}_2 \omega d_s / c_0}}{e^{-j\tilde{n}_2 \omega d_r / c_0} e^{-j\tilde{n}_1 \omega (d_s - d_r)/c_0}}, \tag{4.22}$$

where $\tilde{n}_1$ is the material that replaces the space taken up by the extra thickness of the thick sample, typically air, d_r is the thickness of the sample for the reference pulse, and d_s is the thickness of the sample for the sample pulse (see Fig. 4.4).

Equation (4.22) simplifies to

$$\tilde{T}_{\text{dual}} = \exp(-j\omega / c_0 d(\tilde{n}_2 - 1)), \tag{4.23}$$

where $d = d_s - d_r$ and $\tilde{n}_1 = 1$. Since $\tilde{T}$ is complex vector with a value for each T-ray-frequency component, $\tilde{T}_{\text{dual}} = \rho_{\text{dual}} e^{j\phi_{\text{dual}}}$, and $\tilde{n} = n - j\kappa$,

$$\rho_{\text{dual}} = \exp(-\omega d \kappa / c_0), \tag{4.24}$$

and

$$\phi_{\text{dual}} = \omega \Delta d (n_2 - 1)/c_0. \tag{4.25}$$

The material parameters can then be extracted by rearranging the above equations (Arjavalingam et al., 1990),

$$n = \frac{-\phi_{\text{dual}}\, c_0}{\omega d} + 1, \tag{4.26}$$

$$\kappa = -\ln(\rho_{\text{dual}}) \frac{c_0}{\omega d}. \tag{4.27}$$

The accuracy of these estimates can be calculated from the partial derivatives of Eqs. 4.26 and 4.27, using multiple measurements to obtain the experimental fluctuation of the transmission ratio. This method was used to estimate the experimental accuracy in our protein studies in Ch. 5.

For thin dual-thickness samples, where multiple FP reflections are present, the expression for the normalised transmission is more complex and must be solved iteratively.

One of the major sources of error in material parameter estimation is the measurement of the thickness d (Duvillaret et al., 1999). To increase the accuracy of measuring d and

integrate it with T-ray spectroscopy, a scheme has been proposed using a train of time-separated FP pulses from a sufficiently thick sample to simultaneously estimate $\tilde{n}_s$ and d (Duvillaret et al., 1999; Dorney et al., 2001a). The effect of errors in d can be reduced by increasing d relative to the error Δd. This idea is fully explained in Ch. 8, where a novel system for high accuracy T-ray liquid spectroscopy is described.

4.2.3 Reflection geometry

Reflection spectroscopy is useful for large or highly-absorbing samples where transmission is inappropriate, for example polar liquids, human tissue, or surface characterisation. As with transmission spectroscopy, the structure of the sample plays a role in the analysis and accuracy of the parameter estimations – different models are used for straight reflections, Total Internal Reflection (TIR), and tomographic first-surface spectroscopy.

The first pulsed T-ray spectroscopy measurements were performed in reflection, with the T-rays confined by Total Internal Reflection (TIR) to an EO crystal that acted as both emitter and detector. T-ray spectroscopy could only be performed on the EO crystal itself (Cheung and Auston, 1986), or on materials placed in direct contact with the EO crystal, into which the radiated pulses were coupled by Attenuated Total Internal Reflection (Auston and Cheung, 1985). Fig. 4.5 shows the geometry of TIR T-ray Time-Domain Spectroscopy (TDS). The basic elements of a T-ray spectrometer are present: a pump pulse to generate the T-ray radiation and a time-delayed probe pulse to sample the T-ray pulses, either with a sample or without.

The geometry of first surface T-ray spectroscopy is the same as the TIR geometry in Fig. 4.5, except the initial medium is typically air or vacuum. The measured spectral components of the reference and sample pulses are given by

$$\tilde{S}_r = A(\omega) \cdot r_{12}, \tag{4.28}$$

$$\tilde{S}_s = A(\omega) \cdot r_{2s}, \tag{4.29}$$

where r, the reflection coefficient, is found from the Fresnel equations above, and $A(\omega)$ represents the common factors between reference and sample. The reference interface is created with a material of known $\tilde{n}$. It is critical that the reference and sample path lengths are identical, which means the sample interface must be placed at the same position as the reference interface. This geometry allows the deconvolved spectrum

(a) TIR reference (b) TIR sample

Figure 4.5. Total Internal Reflection (TIR) geometry. In this Figure, T-rays are generated in the EO material and detected by a probe pulse after interacting with a reference or sample by frustrated TIR. An optical beam in the crystal generates T-rays ('E_{THz}'), which propagate in the EO crystal and are reflected from the surface boundary with the reference or sample material. The reflected T-rays ('E_r' & 'E_s') then have characteristics which depend on the characteristics ($\tilde{\epsilon}$) of the reference and sample respectively (Auston and Cheung, 1985).

$\tilde{S}_s/\tilde{S}_r$, which is calculated from the measured data, to be modelled in terms of the reflectivity of the reference r_{12},

$$\frac{r_{1s}}{r_{12}} = \tilde{T}_{\text{refl}} = \frac{\tilde{S}_s}{\tilde{S}_r}, \tag{4.30}$$

where r_{12} can be calculated from Eq. (4.4), or Eq. (4.2), depending on the T-ray polarisation, since $\tilde{n}_1$, $\tilde{n}_2$ and the incident angle θ_i are known. Once r_{12} is known, Eq. (4.30) can be rearranged to estimate r_{1s}. The dielectric constant of the sample, $\tilde{\epsilon}_s = \tilde{n}_s^2$, is estimated by re-arranging Eq. (4.4) (or Eq. (4.2)) (Auston and Cheung, 1985),

$$\tilde{\epsilon}_s = \left[\sin^2\theta_i + \cos^2\theta_i \left(\frac{1-r}{1+r}\right)^2\right]\tilde{\epsilon}_1. \tag{4.31}$$

For reflection spectroscopy at or near normal incidence, which includes T-ray transceiver applications (Sec. 3.4.3), the above expressions simplify by setting $\theta_i \approx 90°$.

A major experimental problem in reflection geometry is the accurate positioning of the reference mirror. This problem can be overcome by using another reflection geometry, such as a Total Internal Reflection (TIR) geometry, a goniometric geometry, ellipsometry, interferometry or Differential Time-Domain Spectroscopy.

For measurements using Total Internal Reflection (TIR), the position of the interface is set by the edge of the TIR prism. The difficulty is in knowing accurately the refractive indices of the prism and the reference material (Auston and Cheung, 1985). One

method to avoid making a separate reference measurement is to use the pulse reflected from the top of a TIR prism, as shown in Fig. 4.6 (Rønne et al., 1997).

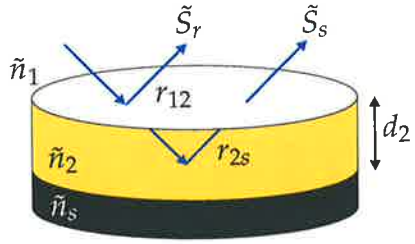

Figure 4.6. TIR prism and reflection. Infrared spectroscopy using a first surface reflection as the reference pulse (Sec. 4.2.3).

In a TIR geometry, the reference pulse is detected from the air-Silicon window interface, and the sample pulse comes from the Silicon window-sample interface. The spectral reflection ratio of sample to reference can be written

$$\tilde{T}_{\text{refl}} = \frac{\tilde{S}_s}{\tilde{S}_r} \tag{4.32}$$

$$= \frac{t_{12} \cdot r_{2s} \cdot t_{21}}{r_{12}} \cdot e^{-j2\tilde{n}_2 d_2 \omega / c_0}, \tag{4.33}$$

for a deconvolved sample response $\tilde{T}_{\text{refl}} = \rho_{\text{refl}} e^{-j\phi_{\text{refl}}}$. The equations can then be solved iteratively.

If $n_1 \gg \kappa_1$ and $n_2 \gg \kappa_2$, which holds for a Silicon TIR prism in air, the sample properties can be estimated by

$$n_s = \frac{n_2(1-\rho_{\text{refl}}^2)}{1+\rho_{\text{refl}}^2+2\rho_{\text{refl}}\cos\phi_{\text{refl}}}, \tag{4.34}$$

$$\kappa_s = \frac{2n_2\rho_{\text{refl}}\sin\phi}{1+\rho_{\text{refl}}^2+2\rho_{\text{refl}}\cos\phi_{\text{refl}}}. \tag{4.35}$$

For samples with internal surface reflections, for example multiple quantum wells, the expression for reflection is complicated by FP factors and must be solved iteratively (Cheung and Auston, 1986).

An integrated method for determining the thickness d of a thin surface layer, analysed in reflection, is to observe frequencies where destructive interference occurs. This technique relies on the broadband nature of the T-ray pulse, requiring a bandwidth of 12 THz to measure films of 1-μm thickness (Hashimshony et al., 2001a).

4.2.4 Differential Time-Domain Spectroscopy

The differential geometry involves rapidly switching a sample in and out of the beam, simultaneously sampling both the sample and reference pulses. This can greatly improve the SNR of T-ray sensing. Differential Time-Domain Spectroscopy (DTDS) is described in Ch. 6 and implementations of double-modulated DTDS are found in Chs. 7 and 8.

4.2.5 Goniometric geometry

Measuring reflectance as a function of incident angle, specifically near Brewster's angle, involves a reflection geometry where the angle of incidence is variable. These measurements require rotation of the sample by an angle θ and the detector by 2θ in a goniometer. With a series of measurements, the amplitude and phase shift of the T-ray pulse can be observed around Brewster's angle, specifically the 180° phase shift for p-polarised radiation (Li et al., 1999a; Ming et al., 2001).

The refractive index of a thin film $\tilde{n}_s$ on a substrate can be estimated by measuring the reflectance at different angles and comparing it to a model based on Drude and Fresnel equations. The Drude equation predicts the complex reflectance $\tilde{r}_D$ from a thin film,

$$\tilde{r}_D = \frac{r_{1s} + r_{s2} p_s}{1 + r_{1s} r_{s2} p_s}, \tag{4.36}$$

where r and p are given by Eqs. (4.7) and (4.8). The values of d, $\tilde{n}_2$, $\tilde{n}_1$, the wavelength λ and θ_1 are known for each measurement, so the reflectance can be modelled using estimates for $\tilde{n}_s$, and compared to experimental measurements.

For two angles of θ_1 (θ_{1A} & θ_{1B}), the T-ray spectra are $\tilde{S}_A = A(\omega)\,\tilde{r}_{DA}$ and $\tilde{S}_B = A(\omega)\,\tilde{r}_{DB}$, where $A(\omega)$ is a product of the transfer functions of the system which remain constant as the angle is varied. Thus the ratio of reflectances is given by

$$\frac{\tilde{r}_{DB}}{\tilde{r}_{DA}} = \frac{\tilde{S}_B}{\tilde{S}_A}. \tag{4.37}$$

The value of $\tilde{n}_s$ that fits the model can be estimated by iteratively fitting the experimental reflectance ratio to the modelled reflectance ratio, using Eq. (4.36). Specifically, when measurements are made close to Brewster's angle, the large variation in phase enables more reliable estimates of $\tilde{n}_s$ than normal reflection or transmission measurements (Ming et al., 2001).

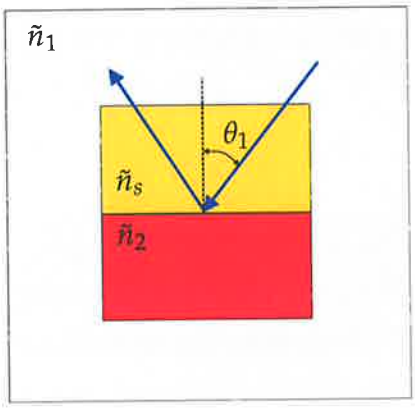

Figure 4.7. Sample in goniometric geometry. This diagram shows how a sample, typically a thin film, is aligned in goniometric geometry. The angle θ_1 is changed by rotating the sample (by angle θ_1), and rotating the T-ray detector by double that angle ($2\theta_1$).

The advantage of goniometric over normal reflection geometry is that it enables resolution of sub-wavelength-thickness films without a need to model the FP reflections. The main disadvantages are the rotating experimental apparatus and the iterative modelling.

4.2.6 Ellipsometry

Normal optical ellipsometry is a technique that can measure the dielectric properties at the surface of a sample by reflecting circularly-polarised beams of light. The polarisation of the reflected beam will change depending on the dielectric properties of the sample. For a given angle of incidence, the reflection coefficients for the orthogonal linear polarisation components of the beam (s- and p-) may not be equal. If they differ, the polarisation of the reflected beam can be measured to estimate the dielectric properties of the sample. A specific example of this occurs at Brewster's angle, when the reflected beam becomes linearly polarised (Azzam and Bashara, 1977).

T-ray ellipsometry is a technique used to estimate a sample's dielectric constant by measuring two reflected pulses with s- and p-polarised T-rays (Nagashima and Hangyo, 2001). The s-polarisation is perpendicular to the plane of the incident and reflected beams, from the German word for perpendicular, *senkrecht*. The p-polarisation is parallel to the beams' plane, from the German *parallel*. This method is the same as used in normal optical ellipsometry. The advantages of this technique over simple reflection

spectroscopy is that there is no need to position a reference mirror, and the equipment is simpler than for goniometric measurements.

4.2.7 Interferometry

Another method to increase the sensitivity of T-ray spectrometers to thin films, along with DTDS, goniometry and ellipsometry, is interferometry. T-ray interferometric techniques typically induce a 180° phase shift (a Gouy phase shift) between two arms of an interferometer, and detect phase changes introduced by a thin sample into one arm. The Gouy shift inverts one of the pulses, so that they interfere destructively. This cannot be achieved by simply increasing the delay in one arm, as in continuous-wave (CW) interferometry, because the pulses would not arrive at the detector at the same time. An example of a T-ray interferometer is shown in Fig. 4.8.

The signal at the detector in a T-ray interferometer is the sum of the pulses in the two arms, $y = y_1 + y_2$. For a system with identical pulses in both arms, differing only by a (small) phase difference ϕ,

$$\tilde{S}_1 = A(\omega), \tag{4.38}$$

$$\tilde{S}_r = A(\omega)(1 - e^{j\phi}), \tag{4.39}$$

$$\tilde{S}_s = A(\omega)(1 - t_{1s}p_s t_{s2}e^{j\phi}), \tag{4.40}$$

where $\tilde{S}_1$ is the spectral response of Arm 1 of the interferometer when Arm 2 is blocked, and t and p are the transmission and propagation coefficients for the sample placed in Arm 2 of the interferometer. The phase difference ϕ can be calculated by normalising the reference spectrum to the spectrum in Arm 1 alone

$$\frac{\tilde{S}_r}{\tilde{S}_1} = 1 - e^{j\phi}. \tag{4.41}$$

Typically, interferometric precision is required for samples with very low refractive index, so the transmission coefficients can be approximated $t \approx 1$. For very thin samples, where $k_0(n_s - 1)d \ll 1$, the sample spectrum can be normalised to the spectrum measured by arm 1 alone, giving an approximate expression for the sample's properties (Krishnamurthy et al., 2001),

$$\frac{\tilde{S}_s}{\tilde{S}_1} = \rho e^{-j\phi} \tag{4.42}$$

$$\approx k_0\kappa d + jk_0(n-1)d + j\phi. \tag{4.43}$$

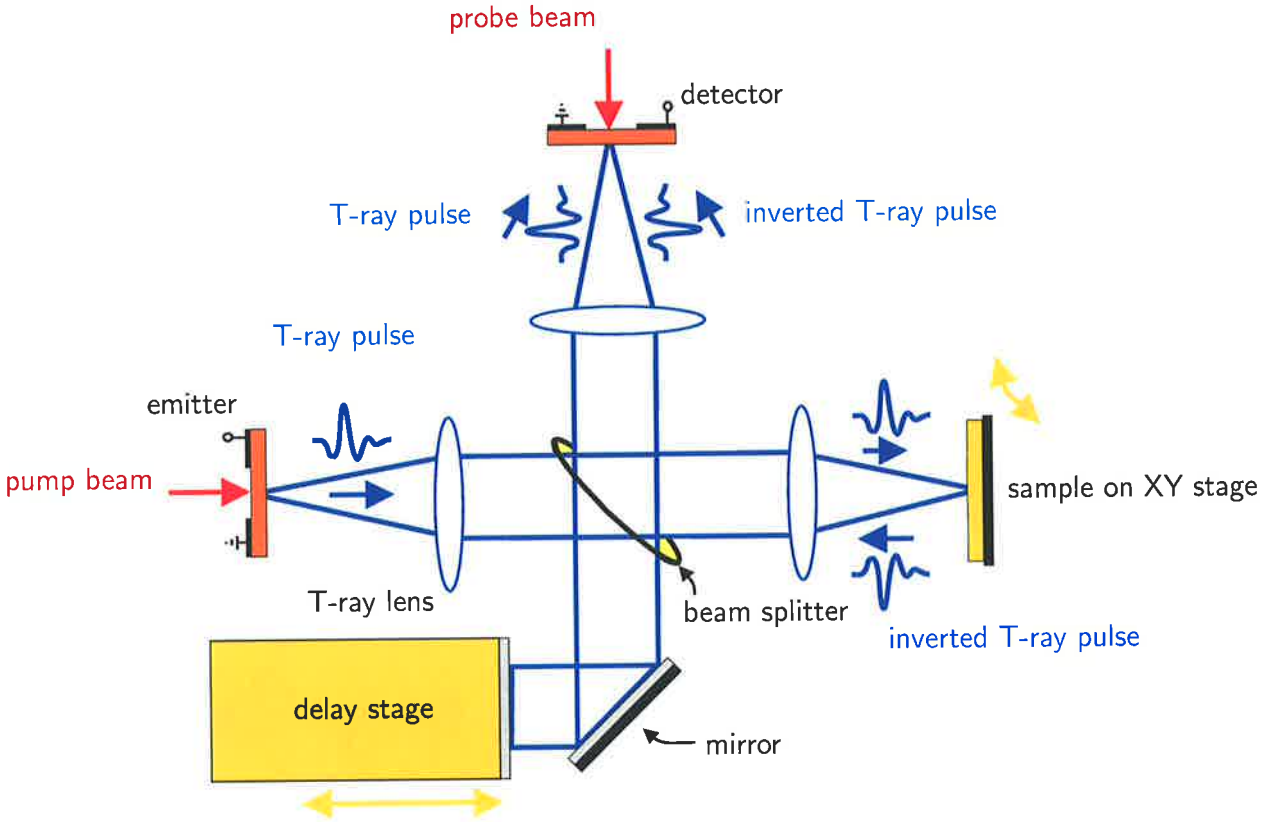

Figure 4.8. T-ray interferometry. This Figure shows the T-ray interferometer of Johnson et al. (2001a) and Johnson et al. (2001b). The interferometer operates by detecting the interference between a T-ray pulse reflected from the sample and a pulse reflected from the fixed mirror on the delay stage. The pulse reflected from the sample is inverted by the Gouy phase shift – the inversion of a pulse at a focus. The two pulses interfere destructively at the detector when there is no sample present. Very thin samples bring about a discernible signal by causing slight phase changes in the inverted T-ray pulse. A similar system has been published by Krishnamurthy et al. (2001), who achieved pulse inversion using total-internal reflection inside a 45° cut quartz prism.

Enhanced depth and spatial resolution have been achieved with T-rays focused to a point on a reflective sample in one arm of an interferometer, where the Gouy phase shift (the inversion of a pulse at a focus) occurs on the sample (Johnson et al., 2001a; Johnson et al., 2001b). The peak amplitude showed a 20% change for a 12.5-μm-thick air gap in Teflon. Other interferometers have been constructed using Silicon prisms as reflectors, where the 180° phase shift was induced by a fixed end reflection from one of the faces (Krishnamurthy et al., 2001), and using counter-propagating Optical

Rectification (OR) to generate T-ray pulses with an opposing sign (Grebenev et al., 2001).

4.2.8 Waveguide resonators

An important new demonstration of T-ray spectroscopy is in micro-stripline resonators (Nagel et al., 2002b). In this geometry, T-rays propagate along a micro-stripline rather than through free space, returning to the original experiments with T-ray radiation in circuits (Wiesenfeld, 1990). The presence of a different dielectric in the resonator cavity causes a frequency-dependent amplitude in the transmitted T-ray pulses.

Currently, this geometry has only demonstrated qualitative estimates of the sample dielectric, although it is potentially a method for measuring $\tilde{n}_s$ of extremely small sample sizes $\approx 250 \times 50\ \mu\text{m}^2$ (Nagel et al., 2002b; Nagel et al., 2002a).

4.2.9 Numerical Fourier spectra

Pulsed T-ray spectroscopy has limitations placed on its frequency resolution by the duration of time-domain measurements, which is fundamentally limited by the *dynamic range* (the ratio of the T-ray signal to the probe beam noise) of the T-ray spectrometer. The fundamental limit on the frequency resolution of T-ray spectrometers is described in Appendix A in full.

The duration of a T-ray measurement, $\mathcal{T} = n\Delta t$, where n is the number of data points and Δt is the duration between each sample. This duration is limited by two experimental considerations: (i) the scan length of the delay stage or pulse reflections in the system (longer scans, free of pulse reflections, are required for high frequency resolution), and (ii) the dynamic range of the spectrometer (Appendix A). This limitation is best understood in terms of Fourier theory.

The Fast Fourier Transform (FFT) algorithm is used for spectroscopic analysis in time-domain spectroscopy. A number of points need to be made regarding the relationship between the sampled time-domain waveform data and the frequency (FFT) spectrum in any given measurement. These issues are typical of systems using numerical Fourier transforms, including well-established Fourier Transform spectroscopy (Griffiths, 1975).

Of primary concern in spectroscopy are the frequency range and resolution of measurements. From basic Fourier considerations, the time between data points, Δt, determines the maximum frequency observable in a spectrum $f_{max} = 1/(2\Delta t)$. However, when a time-domain signal is represented as discrete data points, high-frequency signals above f_{max} can be *aliased* to frequencies below f_{max}, thus it is important to ensure that there are no signals present above the f_{max} set by Δt. For T-rays, this upper signal cut-off is typically determined by the emission or detection bandwidth of between 5 and 10 THz.

The frequency resolution, $\Delta f = 1/(\mathcal{T})$, is determined by the total duration of the sampled data $\mathcal{T}$. Spectral resolution can be improved by artificially adding zeros to the time-domain data. Although this provides smoother spectra, if the time duration is more than doubled, no new information is actually present. The extra points that appear in the spectra are just sinusoidal interpolations (estimates of where the intervening points might lie).

Reflected pulses due to Fabry-Pérot (FP) reflections can arise in the sample, the emitter and the detector. When an electro-optic (EO) crystal is used, the FP reflections can be removed by bonding a refractive index-matched material to the crystal itself, thereby increasing its thickness. For example, the $\langle 110 \rangle$ ZnTe emitter or sensor can be bonded to a $\langle 100 \rangle$ ZnTe crystal, which has a null transverse EO coefficient (Wu and Zhang, 1996a). Removing FP reflections in the EO crystal enables longer time-domain samples to be measured, increasing $\mathcal{T}$, and thus increasing the spectral resolution.

The fundamental limit on the maximum duration is given by the dynamic range of the T-ray spectrometer, that is the ratio between the T-ray waveform peak and the probe beam noise. Probe beam noise can be measured by blocking the T-ray pulse and is independent of the T-ray amplitude. While the T-ray power varies along the duration of a time scan, with most power contained in the pulse peak (see Fig. 1.2(a)), probe beam noise power is invariant over the duration of the measurement, so as a longer sample duration is used, there is an increase in the measured noise power without adding further T-ray power. Essentially, longer scans reduce the signal-to-noise ratio of the measurements as the affect of probe beam noise accumulates. The limit to spectral resolution due to a spectrometer's dynamic range is detailed fully in Appendix A.

One of the advantages of T-ray spectroscopy over other T-ray optical techniques is the acquisition of phase information (time delay). Unfortunately, the phase spectrum from the FFT output needs to be *unwrapped* before it is useful. The FFT algorithm calculates

the phase at any given frequency only to within 2π of the previous phase value, so to calculate a whole phase spectrum, which will cover a range greater than 2π, the phase spectrum needs to be unwrapped. Common unwrapping algorithms can distort the unwrapped phase due to noise at low frequencies. One method to overcome this is to take phase information only at frequencies where the SNR is high, then artificially extrapolate back to DC (Duvillaret et al., 1996).

For high accuracy T-ray spectroscopy, CW techniques, reviewed in Ch. 2, provide a far higher frequency resolution. These do not, however, provide simultaneous access to the broad bandwidth of pulsed T-ray spectroscopy. Fourier Transform-based spectroscopy is very accurate if applied with consideration of the points in this Section and Appendix A.

4.3 Materials studied with T-rays

The following Sections review T-ray spectroscopy of gases, vapours, liquids, solids and bio-materials. Applications of T-ray spectroscopy include measuring picosecond liquid dynamics, characterising solids for upper GHz performance in electronics, and detecting the binding state of DNA. The limitations of T-ray spectroscopy for certain applications are also indicated: for example, (i) the high absorption due to water in bio-samples, (ii) severe broadening of spectral lines in condensed matter, and (iii) difficulties in modelling terahertz-frequency behaviour of molecules.

4.3.1 Gases and vapours

The first application of a T-ray spectrometer was on water vapour in the air, measuring the frequencies and strengths of absorption due to rotational water molecule transitions (van Exter et al., 1989b). Gas and vapour transmission experiments have typically used PCA emitters and detectors with an enclosed metal gas sample cell with thick ($>$ 10-mm) high resistivity ($\approx$ 10-kΩ/cm) Silicon windows. The T-ray windows are designed to minimise T-ray attenuation and avoid multiple Fabry-Pérot reflections inside the windows. The length of the sample cell is chosen depending on the strength of the absorption at the pressures of interest. The entire T-ray cell must be dried or evacuated to remove absorption from residue polar molecules, such as water, in the beam path.

T-ray gas spectrometers can accurately measure absorption lines and collision broadening for molecules that have a permanent dipole moment, as demonstrated with H_2O (van Exter et al., 1989b), SO_2 (Pine et al., 1996), methyl halides (Harde et al., 1997a), ammonia (Harde et al., 2001; Jacobsen et al., 1996) and CH (Cheville and Grischkowsky, 1995a). T-ray measurements allow absorption, dispersion and line shape data to support theoretical models of these molecules (Pine et al., 1996; Harde et al., 1997a; Harde et al., 2001). Although T-rays have low average power, gated detection is blind to incoherent thermal emission from hot objects, and T-rays can therefore be used for spectroscopy of samples with a large average background T-ray radiation, such as flames. In a flame, gases with no permanent dipole moments, such as N_2, O_2 and CO_2, show no T-ray absorption, whereas the concentrations of H_2O, CH and NH_3 can be estimated from the T-ray spectra (Cheville and Grischkowsky, 1995a). T-ray spectra of flames can be used to study the higher rotational absorption states of hot water molecules (Cheville and Grischkowsky, 1998).

Gas identification in a mixture, and classification using a linear predictive coding algorithm, has been demonstrated from the T-ray power spectra of NH_3 and H_2O (Jacobsen et al., 1996; Mittleman et al., 1998). An accurate gas filter correlation (GFC) system for detecting specific gas species has been demonstrated for H_2S (Mouret et al., 1999). The H_2S GFC system used a calibrated sample cell in one arm of an interferometer and the unidentified gas mixture in the other, and was implemented using a pulsed photomixer emitter. A detection sensitivity of 30 ppm of H_2S was achieved using GFC.

An important characteristic of polar gases and vapours at room temperatures and atmospheric pressures is line broadening. The broadened absorption lines from most gases overlap, making identification difficult (van Exter et al., 1989b; Jacobsen et al., 1996; Mouret et al., 1999). To avoid line broadening, the sample cell (or the calibration cell in GFC) must be held at a reduced pressure. Collision-broadened rotational lines in gases studied with T-rays has been reviewed by Harde et al. (1997b).

Vapours have been shown to re-emit T-ray pulses after excitation with a primary T-ray pulse, for example, N_2O (Harde and Grischlowsky, 1991) and methyl chloride (Harde et al., 1994). These experiments have been used to characterise rotational and vibrational constants, and to study line shape broadening, which shows excellent agreement with linear dispersion theory.

4.3.2 Liquids

T-rays are unique in their ability to sensitively measure the characteristic relaxation times of permanent or induced molecular dipole moments in liquids. Keiding et al. have studied T-ray spectra of liquid water as a function of temperature, and modelled the spectra using a Debye relaxation model and numerical simulation (Thrane et al., 1995; Rønne et al., 1997). These experiments are performed using a reflective TIR method, described in Sec. 4.2.3 above. The temperature dependence of liquid water has also been compared to deuterated water D_2O (Rønne and Keiding, 1998). An alternative model of the T-ray response of liquid water, describing molecular plasma oscillations in an ice-like crystalline lattice, has been proposed from transmission data (Libon et al., 1999).

Liquid water shows a very high T-ray absorption, greater than 200 cm^{-1} at 1 THz, whereas non-polar liquids have coefficients around 100$\times$ smaller – for example, benzene, carbon tetra-chloride and cyclohexane (Pedersen and Keiding, 1992). Keiding et al. have studied the temperature dependence of the solvents benzene and toluene, observing rotational and librational bands (Rønne et al., 2000). Kindt and Schmuttenmaer (1996) have studied numerous liquids of varying polarity with a dual-thickness sample cell, based on a polyethylene bag held between two movable Silicon or polyethylene windows, including water, methanol, 1-propanol and liquid ammonia. A number of optical-pump and T-ray-probe studies have explored the response of solvents and dyes to photoexcitation (Beard et al., 2000b), and linked these results to finite difference time-domain models (Beard and Schmuttenmaer, 2001). The solvation dynamics of polar and non-polar liquids, including acetonitrile and water (Venables and Schmuttenmaer, 1998), acetone, acetonitrile and methanol (Venables et al., 2000) and water (Venables and Schmuttenmaer, 2000a), have been related to molecular dynamics simulations to explore the relationship of decreasing T-ray absorption with increasing liquid structure (Venables and Schmuttenmaer, 2000b). The solvation dynamics of lithium salts in water, methanol and propylene carbonate have been explained with Debye relaxation models (Asaki et al., 2002).

Mittleman et al. have measured and modelled the T-ray response of inverse surfactant micelles of water in heptane compared to bulk water (Mittleman et al., 1997a). The reduced dielectric constant of the micelles is attributed to confinement effects on the water molecules.

The primary difficulties in liquid T-ray spectroscopy are: (i) the high absorption in polar solvents, and (ii) modelling the results. The issue of high solvent absorption is addressed in this Thesis, in Chs. 5 and 8, in two ways: (i) examining biomolecules in a non-polar solvent, and (ii) ultrasensitive DTDS.

4.3.3 Solids

Spectroscopy of crystalline solids with T-ray spectroscopy is well-developed for two reasons: (i) its simplicity in the physics laboratory, and (ii) its importance to the semiconductor industry. The earliest studies using pulsed T-ray spectroscopy were on $LiTaO_3$, generating and detecting the T-ray radiation inside the same crystal (Cheung and Auston, 1986). The importance of EO materials in OR and EOS has led to further studies, characterising the complex dielectric of ZnTe (Gallot et al., 1999), GaAs (Cho et al., 2000), $LiTaO_3$ and organic crystals (Ma and Zhang, 1993), and the temperature-dependent power absorption spectrum of two-phonon processes in ZnTe and CdTe (Schall et al., 2000).

Table 4.1. T-ray dielectric constants of solids. Dielectric constants of select solids at 1 THz, as measured using T-ray TDS. n_o refers to the *ordinary* refractive index and n_e refers to the *extraordinary* refractive index for birefringent materials. High-resistivity (10-kΩ-cm) Silicon demonstrates the lowest dispersion, with n almost constant across the spectrum from 0.2 to 2 THz. The accuracy of the first six measurements is better than 0.0004. These results are sourced from three publications, [A] Grischkowsky et al. (1990), [B] Zhang et al. (2001a) and [C] Katzenellenbogen and Grischkowsky (1992).

Solid	Refractive index	Absorption coefficient	Ref.
sapphire	$n_o = 3.070$, $n_e = 3.415$	$\alpha \approx 1$ cm^{-1}	[A]
crystalline quartz	$n_o = 2.108$, $n_e = 2.156$	$\alpha = 0.1$ cm^{-1}	
fused silica	$n = 1.952$	$\alpha = 1.5$ cm^{-1}	
intrinsic Ge	$n = 4.002$	$\alpha = 0.5$ cm^{-1}	
high-$\mathcal{R}$ GaAs	$n = 3.595$	$\alpha = 0.5$ cm^{-1}	
high-$\mathcal{R}$ Si	$n = 3.418$	$\alpha < 0.05$ cm^{-1}	
ice (H_2O)	n = 1.793	$\alpha = 8.6$ cm^{-1}	[B]
0.19-Ω-cm N-GaAs	n $\approx$ 2.97	α= 320 cm^{-1}	[C]
0.36-Ω-cm P-GaAs	n $\approx$ 3.44	α= 270 cm^{-1}	

Historically, early free-space T-ray systems were used for spectroscopy of common homogeneous solids. Arjavalingham et al. measured the complex dielectric constants,

and their polarisation and angular dependence, of fused silica, sapphire and plexiglass slabs up to 130 GHz with ps optical pump pulses (Pastol et al., 1989c; Pastol et al., 1989b; Pastol et al., 1989a; Arjavalingham et al., 1989; Arjavalingam et al., 1990). Wire grid polarisers were used to control the T-ray polarisation. Grischkowsky et al. extended these measurements to 2 THz, studying common solids, as summarised in Table 4.1, and modelled the conductivity of doped Si with an extension of the Drude dielectric model to include energy-dependent carrier relaxations (van Exter and Grischkowsky, 1990a).

For the semiconductor industry, T-ray spectroscopy is an attractive non-contact, non-destructive and rapid technique for semiconductor wafer characterisation in a variety of geometries. Transmission measurements, described above, are limited to samples with low absorption. Doped n-GaAs, doped n-Si and bulk GaAs wafers have been characterised in reflection, with an Al mirror providing the reference pulse, and modelled using Drude theory to determine carrier density and mobility (Jeon and Grischkowsky, 1998; Cho et al., 2000). The dielectric properties of 600 to 15 μm films of highly doped semiconductors have been measured in reflection, where the thickness is measured by observing frequency of destructive interference in the T-ray spectrum (Hashimshony et al., 2001a). T-ray ellipsometry has been demonstrated on doped Si wafers to estimate $\tilde{\epsilon}$ (Nagashima and Hangyo, 2001), and the Hall effect has been used to estimate the full conductivity tensor of n-GaAs, implemented with a 1.3-T magnetic field and dual detectors for the two emitted polarisations (Mittleman et al., 1996; Mittleman et al., 1997a).

As potential substrates for superconductive circuits, MgO has been measured with a low T-ray transmission loss, unlike YSZ (yttrium stabilised zirconia) and $LaAlO_3$ (Grischkowsky and Keiding, 1990). T-rays can be used to observe static and dynamic characteristics of superconducting films themselves (Tonouchi et al., 2000; Kiwa and Tonouchi, 2001).

Of relevance to the development of T-ray (THz-speed) integrated circuits are goniometric measurements of FLARE, TiO_x and PZT thin films (Ming et al., 2001), and parylene-N films (Lee et al., 2000a). Novel photoresists have been characterised for T-ray-speed integrated circuits (Collins et al., 1998).

Non-contact characterisation, and modelling with localisation-modified Drude theory, is particularly valuable for conducting polymers, such as polypyrrole and poly-3-methylthiophene (Jeon et al., 2000; Jeon et al., 2001), and single-walled carbon nanotube films (Jeon et al., 2002). Organic thin polymer films were first characterised by T-rays in 1992 (Ree et al., 1992). Microwave ceramics for telecommunications have recently been analysed in transmission (Kamba et al., 2001) and corrosion layers beneath opaque paints analysed in reflection (Geltner et al., 2002).

The optical pulse driven nature of T-rays lends itself to the study of photoexcited carrier dynamics in semiconductors. Optical-pump and T-ray-probe experiments have the advantage of ultrafast resolution and a probe in the T-ray band (Greene et al., 1991). The T-ray reflectivity of photoexcited GaAs can be measured by T-ray reflection (Schall and Jepsen, 2000). The time-dependent conductivity of GaAs-AlGaAs quantum wells (Groeneveld and Grischkowsky, 1994), bulk GaAs and epitaxial LT-GaAs have been studied under 800-nm and 400-nm light, and modelled using a modified Drude model (Beard et al., 2000a; Beard et al., 2001). Two-colour EOS, with time-delayed collinear pulses transmitted through a GaAs sample, has been used to study T-ray generation from surface field dynamics (Han et al., 2000b). Using ultrafast optical excitation pulses, T-rays have been used to observe photocarrier generation and the subsequent screening processes in semiconductors (Jepsen et al., 2001; Leitenstorter, 2001; Huber et al., 2001). Optical-pump and T-ray-probe experiments have also enabled a form of near-field imaging with a dynamic aperture, as described in Ch. 9, and the creation of transient mirrors for T-ray pulse slicing (Cole et al., 2001).

4.3.4 Biological materials

Biomolecules, such as proteins and nucleic acids, have broad T-ray features arising from a multitude of dense rotational, vibrational, inter-domain and hydrogen bond energy transitions (Hayward and Go, 1995; Roitberg et al., 1995). The complex spectra of biomolecules can be understood through molecular dynamics simulations (Walther et al., 2000a; Walther et al., 2002).

The applications of T-rays to experiments in biosensing and spectroscopy of biological samples are addressed in the experimental chapters, Ch. 5, Ch. 7 and Ch. 8.

Larger, more complex structures have been studied phenomenologically, with an emphasis on contrast rather than full spectroscopic information. This is typically the case

for sensor applications, or in imaging of tissues (see Ch. 9). One example is the image of a drying leaf (Hu and Nuss, 1995), which has been studied spectroscopically with CW techniques in the 100 to 500-GHz range (Hadjiloucas et al., 1999). Two reviews of T-ray studies in biomedicine have been written by Chamberlain et al. (Smye et al., 2001; Fitzgerald et al., 2002b). T-ray biosensing, using contrast derived from a combination of sample properties, including thickness, absorption, scattering and phase delay, has been used to detect the binding of lipids to proteins with a sensitivity of 1 ng/mm^2, described experimentally in Ch. 7. The push to clinical applications of T-rays (see Ch. 9) has led to studies of potential damage caused by T-rays (Walker et al., 2002; Matei and Dressel, 2002; Veryret, 2002).

4.4 Radar and ranging sensing

As free-space pulses of radiation, T-rays have been used for scaled-down versions of radar applications, such as distance and thickness measurements, measuring the radar profiles of scaled-down objects, such as 1/200th-sized model planes and tanks (Cheville and Grischkowsky, 1995b; Mittleman et al., 1999), or to characterising micromachined components (Pellemans et al., 2000).

The interpretation of reflected pulses necessitates the modelling of single-cycle electromagnetic pulse interactions with dielectric objects (Cheville et al., 1997; Cheville et al., 1988). Measuring T-ray pulse delay through a sample enables the T-ray refractive index profile of a flame to be estimated (Mittleman et al., 1996) and the number of pages in a book to be counted, as demonstrated in Fig. 4.9. This work has been applied to studying the T-ray time delay caused by dollar bills, whereby cash can be counted by its thickness, as seen in Fig. 4.10.

T-ray scattering from objects has been extended to imaging research, including quasi-optical imaging (O'Hara and Grischkowsky, 2001), synthetic aperture imaging (McClatchey et al., 2001) and T-ray propagation around a cylinder (McGowan et al., 2000; Reiten et al., 2001b). These topics are further discussed in Ch. 9.

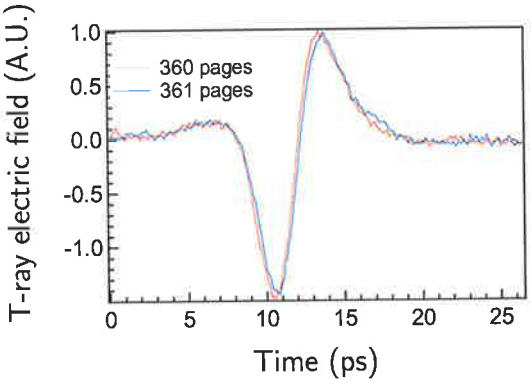

Figure 4.9. Measured pulse delay from one page in a book. Each page of paper in the T-ray beam path delays the arrival time of the pulse by about 200 fs. The number of pages in a book can be counted by measuring the phase delay of T-ray pulses in transmission. The resolution shown here is better than 1 in 400 (after Chen et al. (1998)).

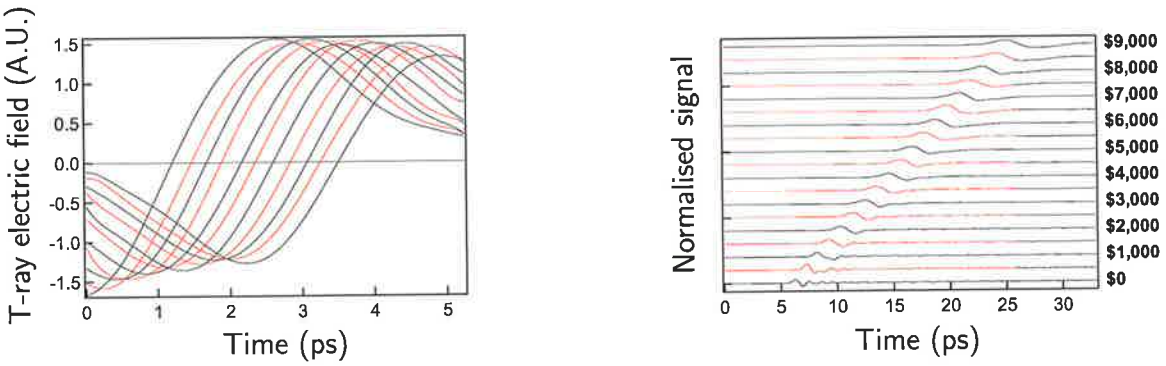

(a) Time waveforms

(b) Normalised waveforms

Figure 4.10. Experimentally counting US dollar bills with T-rays. In a similar application to Fig. 4.9, the time delay of T-ray pulses in transmission have been used to count stacks of paper currency. Subfig. 4.10(a) shows an expanded part of the time-domain waveform. Subfig. 4.10(b) shows both the time delay and pulse spreading as T-ray pulses are transmitted through thicker stacks of paper currency (after Chen et al. (1998)).

4.5 Terahertz-induced activity

Despite their low average power, T-rays can be used for coherent manipulation of states in atoms, for spectroscopy and for quantum information processing. Rydberg wave packets have been created, probed and ionised using ultrashort T-ray pulses (Jones et al., 1993; Jones, 1996; Raman et al., 1996; Krause et al., 1997). T-ray pulses have similarly been used to excite Rabi oscillations in donor impurities in GaAs (Cole et al., 2001). Theoretical modelling suggests that narrowband T-rays could be used for tuning the resonance of semiconductor microcavities, and pulsed T-rays may be used to control coherent mode oscillations (Citrin, 1999).

4.6 Chapter summary

Ultrafast pulsed T-ray spectrometers are being used for an increasing number of applications, from solid-state physics to functional biology. It is due to these applications in biology that understanding how T-ray radiation interacts with biological materials has become important. The T-ray measurements and analysis of protein hydration in the next Chapter show how T-rays can be used to sense the hydration state of a protein, for example.

A result of the development of wider T-ray applications is the development of a wider array of T-ray spectrometer configurations for measuring specific samples or effects. The novel modulated liquid measurement technique described in Ch. 8 is an example of a spectrometer specifically designed for sensitive liquid measurements. The work on protein hydration sensing presented in the following Chapter was carried out with a simple dual-thickness transmission geometry.

Chapter 5

T-ray Protein Sensing

T-RAY spectroscopy can provide information on the large-scale formation of biomolecules, for example, proteins. Molecular hydration, or bound water, is a critical parameter that can be used to measure catalytic activity of enzymes, and T-ray system measurements are very sensitive to water (see Sec. 2.2). Measuring hydration is a step towards more informative biomolecular spectroscopy. The study of enzyme molecules using T-ray spectroscopy has the potential to reveal enzyme activity in real time without the use of labelling.

This Chapter introduces experimental measurements of the T-ray response of micron-sized particles of protein and their level of molecular hydration. These measurements show T-rays can be used to monitor enzymes' catalytic activity non-invasively through the measurement of hydration.

5.1 Introduction

The conformation and hydration of an organic macro-molecule is a critical parameter for determining its catalytic activity (Partridge et al., 1998). The T-ray band contains a range of conformationally-dependent vibrational and rotational resonances (Brucherseifer et al., 2000a; Nagel et al., 2002a; Nagel et al., 2002b). Standard techniques used for monitoring the hydration of a protein require a small sample of the material, for example in Karl Fischer titration (Scholz, 1984). The volume of water is measured through its reaction with a hydration-sensitive chemical standard.

The objective of the experiments described in this Chapter was to measure the molecular hydration non-invasively. A non-invasive probe does not affect the enzyme mixture and would allow hydration to be monitored continuously during a chemical reaction.

The experimental T-ray absorption spectra of the suspended enzymes show a combination of two effects: (i) the amount of free water in solution, and (ii) the absorption spectrum of the hydrated enzyme.

5.1.1 Motivation

There were two primary motivations for the experiments described in this Chapter. The first was to demonstrate a real-time, non-invasive and label-free method of monitoring the activity of enzymes in low-water environments. The second was to study the T-ray response of these proteins with a view to increase our understanding of how biological macro-molecules interact with terahertz radiation. Probing protein hydration and conformation in a low-water environment would be useful for non-invasively monitoring enzymes attached to chips in micro-fluidic technologies.

Catalytic activity of enzymes is dependant on protein conformation and hydration. Conformation-dependant absorption changes have been observed in some biomolecules using terahertz spectroscopy, which suggests T-rays may be useful in more general observations of enzyme activity (Walther et al., 2000a). In micro-fluidic and biosensor experiments, for example, enzymatic proteins are routinely attached to the surfaces of the chip. The activity of these deposited proteins is very difficult to determine using existing spectroscopic methods. However if T-rays are to be used to determine the activity of proteins on surfaces, a good understanding of the T-ray spectra of proteins and how the influence of hydration must be developed.

5.1.2 Previous studies

Biological systems are overwhelmingly water-based, but the high absorption of water makes it difficult to conduct experimental studies of proteins in their native environment. Previous biomolecule studies have used dried pellets and thin film samples (Brucherseifer et al., 2000a; Markelz et al., 2000). This contrasts with the samples explored in this Chapter, where the target biomolecules of Subtilisin Carlsberg (SC) are suspended in a dry liquid environment.

In the experiments in this Chapter, SC molecules were held in suspension in an organic solvent during measurements. An organic solvent was used in place of water so controllable levels of hydration could be investigated. The solvent had to have good water miscibility and low T-ray absorption. The selection process is described in Sec. 5.2.1.

The biomolecules of SC in our suspensions have many randomly-oriented dipoles, which largely cancel out, and as the protein cannot rotate at T-ray frequencies, only atomic and electrical polarisation play a part, resulting in an expected dielectric constant for the protein far less than water (Pethig and Kell, 1987, p. 944). The molecules do, however, retain some polarity so their absorption is slightly higher than the organic solvent used for suspending the protein (see Sec. 5.3.3).

The T-ray absorption of biological macro-molecules has been measured (Markelz et al., 2000) to be of the order of $\alpha \approx 60$ cm^{-1}. These previous studies have allowed careful control of pressure, temperature and humidity, but it is difficult to conduct real-time chemical reactions using solids. An explanation of the fine structure of the spectra cannot be achieved before the samples are studied over a broader frequency band, and with a wide variation in temperature and concentration (Walther et al., 2000b), so only the broad, dielectric-constant-like absorption spectra are of interest in this Chapter.

Water binding to ionic salts have been studied with T-rays, but not to biomolecular samples (Asaki et al., 2002).

Protein molecules operate natively in water-rich environments, and the binding of water molecules to the protein surface is a critical process in understanding activity and interaction of protein systems. The hydration shell of a protein molecule has been described as a tightly-bound layer of low-mobility water molecules, surrounded in turn by free water molecules in the liquid matrix (Nandi and Bagchi, 1997). The two types of water, free water and bound water, exhibit different dielectric constants. Free water interacts with incident radiation similarly to bulk water, having a very high relative

dielectric constant ($\epsilon_r \approx 80$). The dipole of bound water is hindered in its motion and has a far lower dielectric constant. The measurements of the water-protein mixture, suspended in an organic solvent, can be explained by the model of bound and free water.

Protein activity studies have been conducted in a range of organic solvents, showing a dependance on solvent dielectric constant, temperature, ionic salts and hydration (Ru et al., 2001).

The T-ray spectra of organic solvents have been characterised by various groups, including Pedersen and Keiding (1992) and Mickan et al. (2002a). Mixtures of dioxane and water have been studied with microwave spectroscopy, and characterised with Debye models (Critchfield et al., 1953; Crossley and Smith, 1969; Clemett et al., 1964; Mashimo et al., 1992). The absorption spectra of organic solvent mixtures in the range 0.2 – 1.1 THz at room temperature are not expected to show any specific resonance absorption lines, as are found in gas vapour samples (van Exter et al., 1989b). Typically, liquid samples do not show specific absorption lines at T-ray frequencies because the rotational and translational bands are so closely spaced and the overall absorption is so high (Birch et al., 1985).

5.1.3 Objective summary

The objective in this Chapter was to use T-ray transmission spectroscopy to measure the change in T-ray spectra of enzymes when mixed with water in an organic solvent. The organic solvent needed to have a low T-ray absorption, to improve measurement accuracy, and be highly water miscible, so the level of hydration in the mixture could be carefully controlled: an ideal solvent for this purpose was 1,4-dioxane. A dry solvent was prepared using molecular sieves to remove 99.997% of water from the solvent. The hydration of the enzymes was controlled by controlling the volume of water mixed into the otherwise dry solvent and protein mixture.

5.2 Experiments

This Section describes the preparation of the organic solvent mixtures, the T-ray spectrometer and the data analysis.

The samples were prepared with off-the-shelf chemical and biological materials. The T-ray spectroscopy was conducted with a custom-built T-ray spectrometer, based on Surface Current Generation (SCG) and Electro-Optic Sampling (EOS), both described in Sec. 5.2.2. The spectroscopic responses of the samples were analysed in terms of their complex refractive index, $\tilde{n} = n - jk$, extracted with a knowledge of the transmission spectrum and the sample thickness (see Sec. 4.2.2).

5.2.1 Sample preparation

Pure water, the native environment for biomolecules, has a very high absorption at T-ray frequencies, with an absorption coefficient of $\alpha = 100$–$200\ \mathrm{cm}^{-1}$ between 0.1 and 1.0 THz (Thrane et al., 1995). The high absorption of an aqueous environment makes it difficult to observe small changes in protein hydration. In these experiments, anhydrous organic solvents were used to suspend the protein molecules, enabling highly accurate control of the hydration level. Depending on concentration levels, the protein forms micro-sized clumps, suspended in the solvent, and water binds to the protein depending on the available hydration.

The samples under investigation were all organic solvent mixtures with different levels of hydration, either with or without suspended enzyme. The experiments were designed to firstly measure the T-ray response of the organic solvent alone. From these measurements, 1,4-dioxane was chosen as the solvent for further experiments. The remaining mixtures were based on dioxane, firstly to measure the effect of increased hydration, and secondly to measure the response of the enzyme to hydration.

The organic solvents used for absorption measurements are listed in Table 5.1. These solvent samples were provided from bulk supplies (the Department of Chemical Engineering at Rensselaer Polytechnic Institute). The solvents were stored over molecular sieves to maintain a low water concentration. A molecular sieve is a microporous material that can selectively chemically or physically absorb molecules, in this case water molecules. Table 5.1 also indicates the dielectric constant and T-ray absorption of the solvents, obtained from previous work. The dielectric constant can indicate whether a solvent exhibits high T-ray absorption. Polar molecules have high dielectric constants and high T-ray absorption.

For T-ray spectroscopy, a solvent is required that has a very low T-ray absorption, thus a solvent that is largely non-polar. 1,4-dioxane is a non-polar solvent with high water

Table 5.1. Index and solubility of organic solvents and water. This Table shows the physical constants of some liquids relevant to T-ray spectroscopy in the literature. Column 1 lists some of the solvents of interest, including pure water. Column 2 lists the optical refractive index of each solvent, measured at visible wavelengths, and column 3 lists the dielectric constant, measured at radio frequencies. Column 4 shows the miscibility of the solvent in water – those solvents with 100% water miscibility are marked 'miscible'. This data is available from solvent supplies (manufacturer: Burdick & Jackson; URL: `http://www.bandj.com`).

Solvent	$n_{optical}$	dielectric constant	[w/w]% H_2O
iso-octane	1.3914	1.94	0.006
n-hexane	1.3749	1.88	0.01
toluene	1.4969	2.38	0.03
dioxane	1.3330	2.22	miscible
tert-amyl-alcohol	1.4	2.22	miscible
acetonitrile	1.5	2.22	miscible
water	1.3914	80.1	miscible

miscibility. A 1,4-dioxane molecule is charge symmetric (see Fig. 5.1), and therefore has a small electrical dipole, but the two oxygen groups enable the integration of water molecules into the dioxane matrix. Dioxane (supplier: Aldrich, 99.8% anhydrous, CAS No. 123-91-1, lot no. 29630-9) was stored over Fisher 3-Å molecular sieves for >24 hrs to maintain low hydration. The volume of dioxane used in the experiments was 10 mL (Table 5.2).

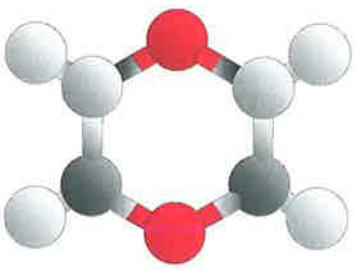

Figure 5.1. 1,4-dioxane molecule, $C_4H_8O_2$. The symmetric nature of the dioxane molecule is visible in this sketch, which causes its weak permanent dipole moment. The red spheres represent oxygen groups, which readily form hydrogen bonds with water, giving it a very high water miscibility, unlike other non-polar liquids.

Deionised, doubly-distilled water was obtained from a purification system (manufacturer: Millipore, model: *RiOs*) and mixed into the solvents using a pipette. Twenty μL of distilled water was mixed into 10 mL of dioxane to hydrate the solvent (Table 5.2).

Although there are many biologically important and easily-available enzymes used to study activity, the protein Subtilisin Carlsberg (SC) was used, as it is known to demonstrate changes in activity for small changes in molecular hydration and because the water shell bound to SC has been previously documented by Pal et al. (2002). SC was purchased from Sigma (CAS No. 9014-01-1, lot no. 91K1107) and used without further purification. The SC was buffered in doubly-distilled water and freeze dried for >24 hrs, then immediately suspended in dioxane. Twenty mg was added to 10 mL of dioxane (Table 5.2). SC has a tendency to settle out of suspension in dioxane, so all mixtures were thoroughly mixed directly prior to spectroscopic measurement with a sonicator (model: *Vortex*). The sonicator vibrated the sample at a frequency of about 10 Hz for over one minute.

To observe the measure the amount of water bound to the protein, the mixture of dioxane and SC and water was centrifuged. Centrifuging removed the suspended SC, and thus the water molecules bound to the SC, leaving only free water in the mixture. The amount of remaining free water is variable, depending on the binding affinity for SC to water, so the volume of water is indicated as variable ('var.') in Table 5.2.

Table 5.2. Partial volumes of experimental mixtures. The dioxane and free water mix was prepared by removing the suspended protein, Subtilisin Carlsberg (SC), from the dioxane and SC and water mix, which removes the water that has become bound to the protein. The 'var.' for dioxane and free water indicates that the volume of water remaining in the mixture is variable, and depends on the water binding affinity of the SC. Volume measurements are accurate to 5% using pipettes.

Mixture	Dioxane	Water	SC
dioxane	10 mL	-	-
dioxane & water	10 mL	20 μL	-
dioxane & SC	10 mL	-	20 mg
dioxane & SC & water	10 mL	20 μL	20 mg
dioxane & free water	10 mL	var.	-

5.2.2 T-ray spectrometer

The T-ray spectrometer used in these experiments is sketched in Fig. 5.2. In this system, T-rays are generated from an unbiased semiconductor, in this case GaAs, as described in Sec. 3.2.4. Gated detection with a ZnTe crystal is described in Sec. 3.3.2. Section 5.2.3 below describes how the raw data from T-ray spectroscopy of the thick and thin samples are analysed.

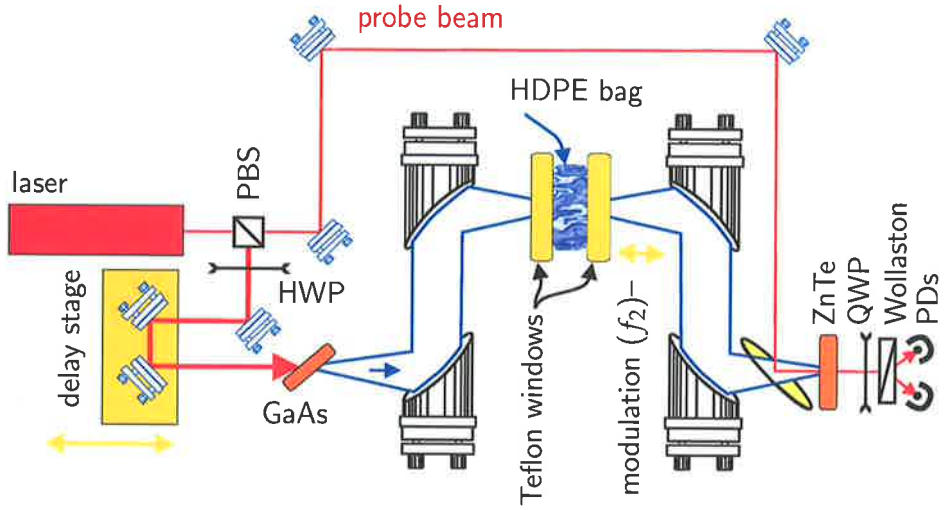

Figure 5.2. T-ray liquid spectrometer. T-ray spectrometer configured for dual-thickness liquid spectroscopy. The Ti:sapphire mode-locked (ML) laser generates a train of 100-fs pulses at 82 MHz. Each pulse is split into a pump beam and a probe beam with a Polarising beam splitter ('PBS'). The pump beam generates T-ray pulses when incident at Brewster's angle on the GaAs wafer, positioned at the focal point of a gold-coated parabolic reflector. Parabolic reflectors collimate the T-rays, focus it into the sample holder, then collect the transmitted radiation and direct it into a ⟨110⟩ ZnTe T-ray detector. The probe beam detects the T-ray electric field in the ZnTe, and is in turn recorded with crossed polarisers and balanced photodetectors. (The functions of the common optical components in a T-ray spectrometer, included in this diagram, are described in Ch. 3, and their specifications are found in Appendix C.) The thickness of the sample is modulated with two Teflon windows, one of which was mounted on manual translation stage. The mixture was held in a sealed, thin-walled, high-density polyethylene (HDPE) bag, which does not react with or dissolve in dioxane.

The T-ray free path section of the T-ray spectrometer was enclosed in a sealed, air-tight box to block air movement which would disturb the pellicle beam splitter. This box is pictured in Fig. 5.3. The experiments were conducted at room temperature, held by air conditioning to about 20°C, and at a relative humidity of approximately 40%. The humidity can be decreased by purging the experimental chamber with dry nitrogen or

by using an enclosed T-ray spectrometer (Mickan et al., 2000a). Although not done in the experiments in this Chapter, purging with dry nitrogen reduces water absorption lines. Water absorption lines are visible in the experimental spectra in Sec. 5.3.1 below.

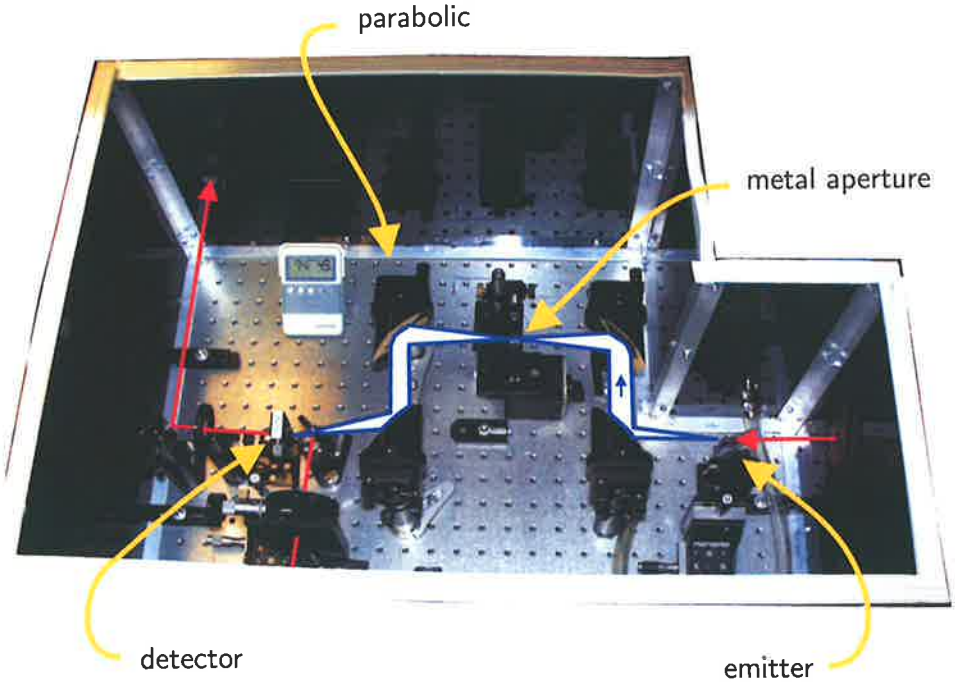

Figure 5.3. Spectrometer in box. This Figure shows the T-ray path of the spectrometer used for protein hydration spectroscopy. This photograph shows a mirror image of the layout sketched in the schematic Fig. 5.2. An aperture is shown at the focus of the T-ray beam. The aperture was used to define the transverse extent of the sample, thus avoiding the possibility of any T-rays diffracting around the sample into the detector crystal. The box had thin quartz windows for the optical beam (red) to enter and leave the experimental chamber, and could be sealed with a lid, thus enabling partial evacuation of water vapour with a dry air purge. The main optical components of a T-ray spectrometer visible in this photo: (i) the GaAs emitter, (ii) the gold-coated parabolic mirrors, and (iii) the EO detector. A temperature and humidity sensor was placed in the box to monitor environmental conditions.

In the experiments in this Thesis, T-rays were generated using a photoexcited semiconductor, LT-GaAs, pictured in Fig. 5.4. The GaAs wafer was mounted on a glass slide at Brewster's angle with respect to the optical beam, which has a horizontal polarisation. Experimentally, the optimal angle is set by carefully rotating the emitter to achieve a maximum T-ray signal. The T-rays generated at the surface of the GaAs pass through

the bulk of the GaAs with little attenuation, while the optical beam is blocked. Surface current generation is described in detail in Sec. 3.2.4.

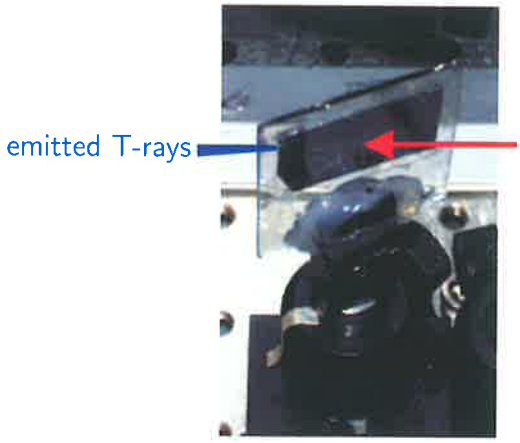

Figure 5.4. GaAs surface current emitter. This photograph shows the T-ray emitter used to generate T-rays for the measurements in this Thesis. A beam of ultrafast optical pulses incident on an unbiased semiconductor surface generates T-rays from a number of nonlinear phenomena, described in Sec. 3.2.4).

The EOS configuration used for the experiments in this Thesis is shown in Fig. 5.5. The crossed polarisers and balanced photodiodes are described in detail in Appendix B. In EOS, the critical interaction is between the T-ray pulse and optical pulse propagating collinearly through the crystal, which is aligned to present the optimal EO coefficient (<110> orientation). EOS is described in detail in Sec. 3.3.2.

The fluid sample to be studied was contained in a sealed high-density polyethylene sample bag with a wall thickness $\approx$60 μm, pictured in Fig. 5.6(b), and held in a variable path-length liquid sample holder, based on a design by Kindt and Schmuttenmaer (1996) and pictured in Fig. 5.6(a). The overall thickness of the sample was controlled by two 10-mm-thick Teflon windows, placed parallel to each other and perpendicular to the beam path. Teflon was chosen for its low T-ray absorption, low T-ray refractive index, low cost and machinability.

All spectroscopic measurements require the sampling of two waveforms, a sample waveform y_s and a reference waveform y_r. The sample waveform is radiation that has passed though a thick sample, thickness d_s, and the reference waveform is from a thin sample, d_r, shown in Fig. 5.7. The sample thickness was varied by a manual stage, which translated one of the windows of the sample holder along the axis of the beam path (see Fig. 5.6(a)).

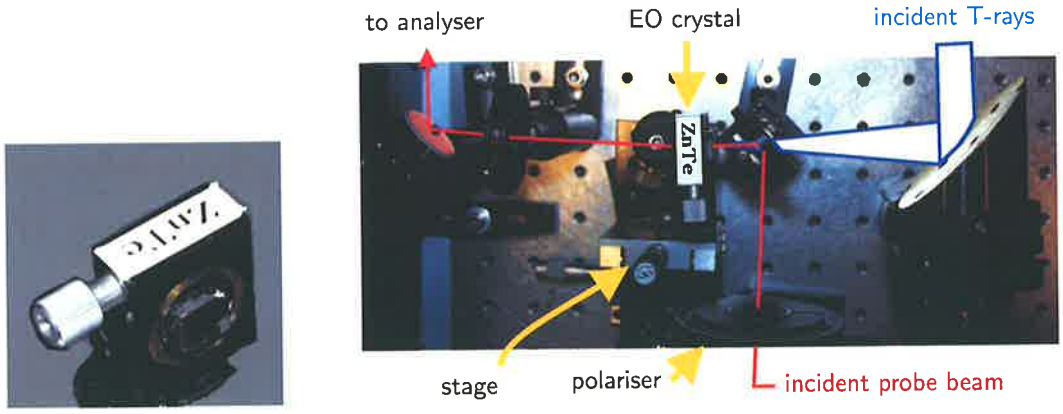

(a) ⟨110⟩ ZnTe crystal

(b) EOS layout

Figure 5.5. Electro-Optic Sampling. These pictures show the experimental layout of T-ray Electro-Optic Sampling (EOS) used in the experiments in this Thesis. EOS is the most sensitive, broadband technique of gated T-ray detection. The T-ray beam is focussed into the detection crystal using a gold-coated parabolic mirror. A pellicle directs the optical probe beam to travel collinearly with the T-rays through the crystal. The T-ray electric field rotates the polarisation of the probe beam. ZnTe is commonly used for EOS since the T-ray and optical pulses traverse it with similar velocities. The crystal is mounted in a rotating stage as the orientation of the EO crystal is critical to the sensitivity of the detection.

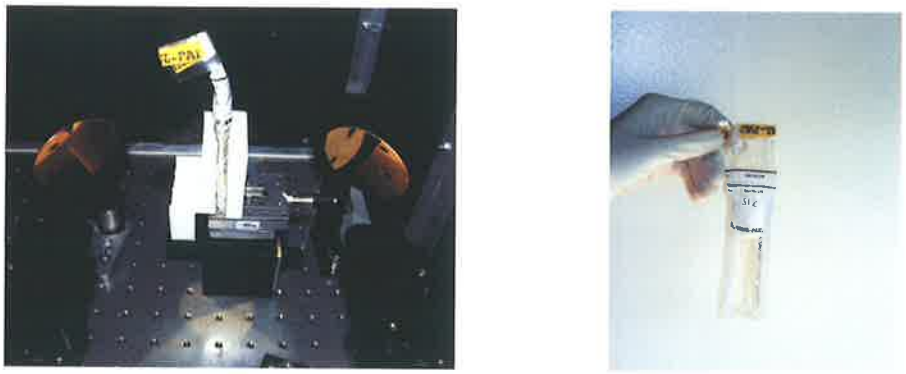

(a) Variable-thickness sample holder (b) Sample in HDPE bag

Figure 5.6. Photograph of a liquid sample holder for T-ray spectroscopy. The variable-length holder is shown at the focal point of the focusing and collection optics. The thickness of the Teflon windows is >10-mm to avoid any Fabry-Pérot (FP) reflections within our timing window. The thickness of the sample was modulated from a minimum of 3-mm, chosen to avoid FP reflections, to a maximum of 7-mm, the maximum possible with this liquid volume that ensures a complete coverage of the transverse T-ray beam path. A large thickness change was desirable to minimise the uncertainly in our parameter estimations (see low-noise liquid spectroscopy in Ch. 8).

5.2.3 Fluid parameter estimation

The T-ray pulse was modelled as a spectrum of Fourier components, propagating as a plane wave through the sample. Figure 5.7 shows the propagation of radiation through the sample, of complex refractive index $\tilde{n}_2$, and across two interfaces between the sample and the surrounding medium (air), $\tilde{n}_1 \approx 1.0$. The simple equations used for estimating the material parameters are derived from the equations for Fresnel transmission and reflection at interfaces (Sec. 4.2.1),

$$n = \frac{-\phi\, c_0}{\omega d} + 1, \tag{5.1}$$

$$\kappa = -\ln(\rho)\frac{c_0}{\omega d}. \tag{5.2}$$

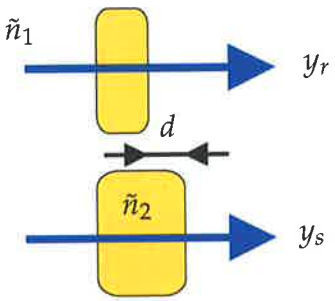

Figure 5.7. Dual-thickness parameter estimation geometry. Waveforms y_s and y_r are measured having respectively passed through the thick (sample) and thin (reference) samples. The spectral components of the waveforms are determined by FFT, $\tilde{S}_s = \mathcal{FT}(y_s)$ and $\tilde{S}_r = \mathcal{FT}(y_r)$. The difference in thickness between the two measurements is denoted d.

These calculations provide a value for the T-ray refractive index n and extinction coefficient κ of the mixture. The values of $\tilde{S}_s$ and $\tilde{S}_r$ were measured by taking the Fourier transform of the transmitted time-domain T-ray pulses, y_s and y_r respectively. The uncertainty in the preliminary measurements was estimated from the standard deviation of repeated measurements of y_s and y_r.

5.3 Results

The following Section describes the T-ray spectroscopy results. The basic bandwidth and SNR of the spectrometer was tested first, then a number of solvents were characterised with T-rays. Dioxane was subsequently chosen for the protein mixture experiments, which included pure solvent characterisation and a measurement of protein hydration. The T-ray absorption spectra of hydrated and anhydrous protein mixtures were measured with an objective of detecting a clear change in T-ray absorption.

5.3.1 Measurement bandwidth

The frequency range of our measurements was determined to be approximately 0.2–1.1 THz – this range had sufficient SNR for accurate measurements. The bandwidth of our measurements can be judged from Fig. 5.8, which shows the spectrum of a sample waveform y_s having passed through an anhydrous dioxane sample in the liquid holder described above (see Fig. 5.6). The sample spectrum $\tilde{S}_s$ is compared to the spectral noise, or uncertainty $\Delta|\tilde{S}_s|$, and the ratio is plotted as a measure of SNR. The mixtures were therefore studied in the range 0.2–1.1 THz, indicated by the two vertical orange lines in Fig. 5.8.

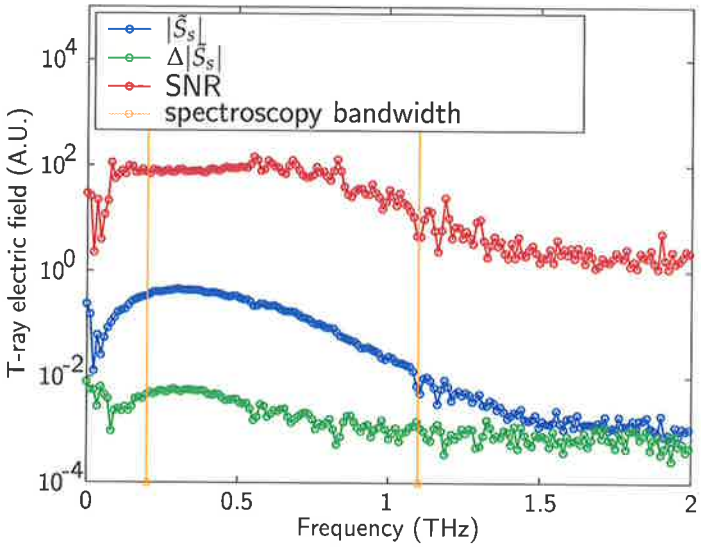

Figure 5.8. Bandwidth for protein spectroscopy. These data show the measured spectral components of the mean of six sample T-ray waveforms, $\tilde{S}_s$, through pure dioxane. The blue plot ('$|\tilde{S}_s|$') is the amplitude of the FFT of the sample waveform. The green plot ('$\Delta|\tilde{S}_s|$') is the standard deviation over six waveforms. The red plot shows the signal-to-noise ratio, $\Delta|\tilde{S}_s|/|\tilde{S}_s|$. These curves demonstrate a good SNR for our spectrometer from 0.1 to 1.1 THz, and show absorption lines due to atmospheric water (at 0.56, 0.75 and 1.1 THz), as discussed in van Exter et al. (1989b). The region between the two vertical orange lines is the frequency range chosen to display the spectroscopy results in this Chapter – experiments performed using larger and smaller frequency ranges indicated that this range provided the most dependable results.

Visible in the sample spectrum in Fig. 5.8 are absorption lines due to atmospheric water vapour – these lines are present in both the sample and reference spectra, and are normalised out in the parameter estimation (see Eq. (4.22) in Ch. 4). The sample spectrum in a dual-thickness measurement is the transmitted spectrum through the thicker

sample. The both the sample and reference spectra had water vapour absorption lines (only the reference spectrum is shown in Fig. 5.8). The absorption lines increase the uncertainty of measurements at those specific frequencies.

5.3.2 Organic solvent comparison

The T-ray absorption of a number of organic solvents was measured to select a solvent with low T-ray absorption and high water miscibility. The data in Table 5.3 indicate that non-polar solvents have a very low T-ray absorption, but most also have a very low water miscibility. Dioxane stands out as a non-polar solvent with extremely high water miscibility.

Table 5.3. Table of organic solvents. Measured T-ray refractive index n and extinction coefficient κ of organic solvents used in studying protein suspensions. The measurement accuracy of n and κ is better than ± 0.005. These measurements were made with a standard transmission T-ray spectrometer, with the sample held between two Teflon windows in a HDPE bag, described in Sec. 5.2.2 above. The solvents were taken from bulk supplies and stored over molecular sieves to remove any water. Column 1 names the solvents and column 2 indicates at what frequency the T-ray parameters have been measured. The parameters were measured over a range from approximately 0.1 to 2.2 THz. Columns 3 and 4 show the measured values of the parameters, and column 5 compares the measured parameters to the known optical refractive index for each solvent. The solvents with highest water miscibility, and therefore molecular polarity, exhibit the highest T-ray absorption (κ), with the exception of 1,4-dioxane.

Solvent	Freq (THz)	n	κ	$n_{optical}$	[w/w]% H_2O
iso-octane	0.2	1.421	0.003	1.3914	0.006
	2	1.415	0.003		
n-hexane	0.2	1.408	0.008	1.3749	0.01
	2	1.404	0.002		
toluene	0.2	1.555	0.015	1.4969	0.03
	2	1.540	0.008		
dioxane	0.2	1.47	0.008	1.3330	miscible
	2	1.4	0.005		
water	0.2	2.7	7.5	1.3914	miscible
	2	2.1	2.3		

Although dioxane was chosen for subsequent hydration experiments, described below, other organic solvents also showed spectral shifts due to hydration. Figure 5.9 shows

an increased absorption spectrum for hydrated toluene over anhydrous toluene. The increased average refractive index of the mixture is due to water's high T-ray refractive index.

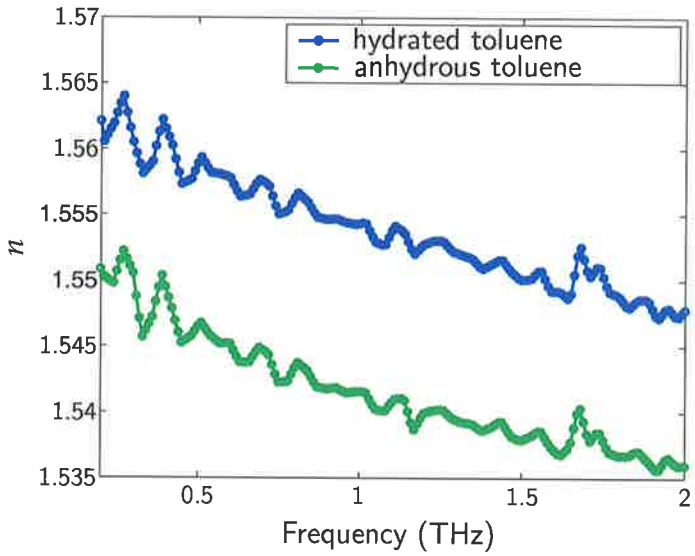

Figure 5.9. Measured T-ray dielectric constant of toluene. This graph shows the T-ray refractive index of an organic solvent that was initially considered for protein suspensions, but then rejected in favour of dioxane. These measurements were taken in transmission using a dual-thickness geometry. The T-ray spectrometer used Surface Current Generation (SCG) and Electro-Optic Sampling. The spectra compare the T-ray refractive indices of hydrated and anhydrous toluene, showing a measure of dispersion and a marked refractive index shift upon the addition of water.

5.3.3 Dioxane

The estimation of the absorption spectrum of anhydrous dioxane is shown in Fig. 5.10. As discussed in the introduction, dioxane demonstrated a low absorption in the T-ray range, far less than polar liquids, for example water, and only slightly greater than highly non-polar liquids, including toluene and hexane.

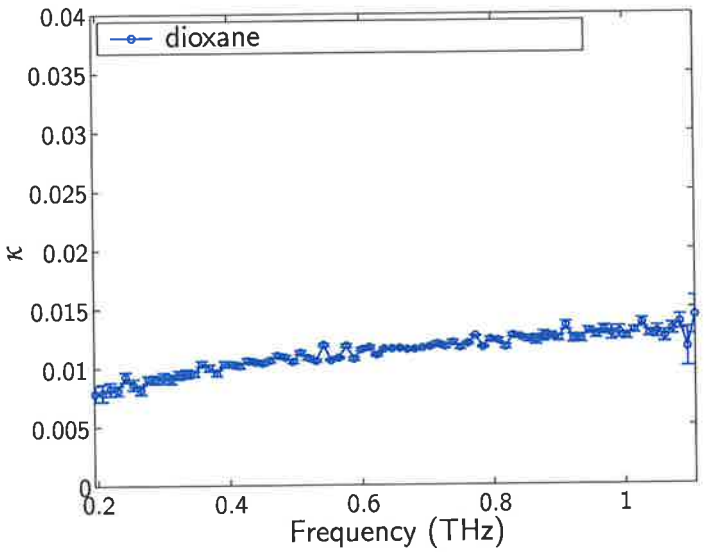

Figure 5.10. Measured T-ray absorption spectrum of dioxane. The absorption spectrum of dioxane was measured using dual-sample T-ray spectroscopy, described in Sec. 5.2. The bandwidth is limited to the region of maximum SNR. The error bars on the plot indicate the standard deviation over six separate samples.

5.3.4 Dioxane and water

The addition of 2 μL/mL of pure water to the dioxane greatly increased the absorption of the mixture. The absorption of dioxane and water is shown in Fig. 5.11, and is clearly greater than pure dioxane. The increase is caused by the addition of polar molecules to the essentially non-polar dioxane matrix.

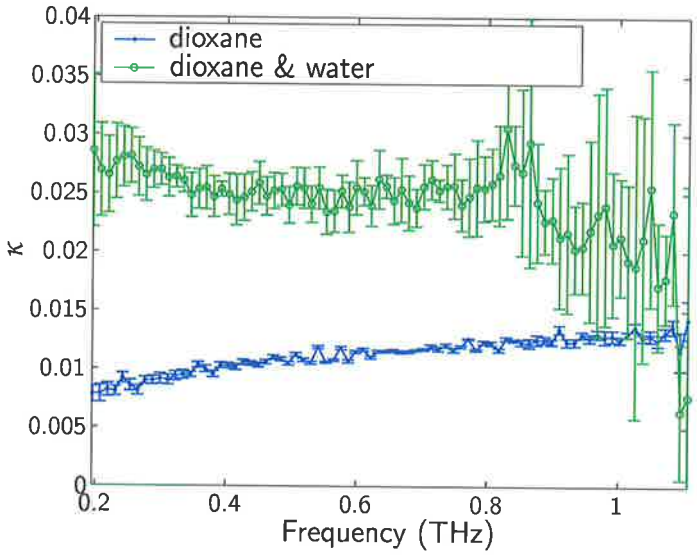

Figure 5.11. Measured T-ray absorption spectrum of dioxane & water. The absorption spectrum of dioxane and 2 μL/mL of water was measured using dual-sample T-ray spectroscopy, described in Sec. 5.2. The bandwidth is limited to the region of maximum SNR. The error bars on the plot indicate the standard deviation over six separate samples.

Dioxane and water dispersion

Although dioxane and water do not mix as ideal liquids, that is, there are interactions between the two types of liquid molecules, the ideal-mixing model can provide a guide as to the accuracy of the experimental results described above.

The dioxane-water mixture can be compared to a mix of ideal liquids, where the mixture absorption would be given by the relation

$$\kappa_{\text{dioxane \& water (ideal)}} = v_w\, \kappa_{\text{water}} + v_d\, \kappa_{\text{dioxane}}, \tag{5.3}$$

where v_w and v_d are respectively the partial volume fractions of water and dioxane (Venables et al., 2000). The experimentally-measured absorption of dioxane and water, 'dioxane & 2 μL water – exp.' in Fig. 5.12, is compared to the predicted absorption of an ideal mixture of 2 μL/mL of water in dioxane, 'dioxane & 2 μL water – model'.

The ideal mixture model demonstrates an increased absorption, but not as large as the measured absorption. This quantitative mismatch is probably caused by the non-ideal mixing of water and dioxane; the addition of water to dioxane requires the use of extra relaxation terms in a Debye model of the mixture even at microwave frequencies (Clemett et al., 1964; Crossley and Smith, 1969).

Despite the quantitative mismatch, it is interesting to note that the measured spectral curve of dioxane & water has a negative slope, whereas the curve of pure dioxane has a positive slope. The measured data can be matched by an ideal model, using an artificially high water concentration, 15 μL/mL, which fits both the absolute measured absorption and the slope of the curve ('dioxane & 15 μL water – model'). This match indicates that a more advanced water-dioxane mixing model could be found to fit the T-ray spectra, which needs to consider an increased role of water than models for water and dioxane at lower frequencies.

The water spectrum used to estimate the ideal liquid absorption in Fig. 5.12 was calculated from the double Debye model of pure water published by Rønne et al. (1997), based on their experimental T-ray data, and later experimentally corroborated by Koch et al. (1999). The T-ray absorption of a dioxane mixture including water must be compared to the absorption of a dioxane mixture with SC to eventually quantify the interaction between the biomolecules and the water.

For 2 mg/mL of SC in dioxane, the absorption of dioxane, water and SC can be modelled as an ideal mixture if $\alpha_{SC} < 200$ cm^{-1}. Although the ideal model is not wholly accurate, it indicates a probable maximum absorption for SC at T-ray frequencies.

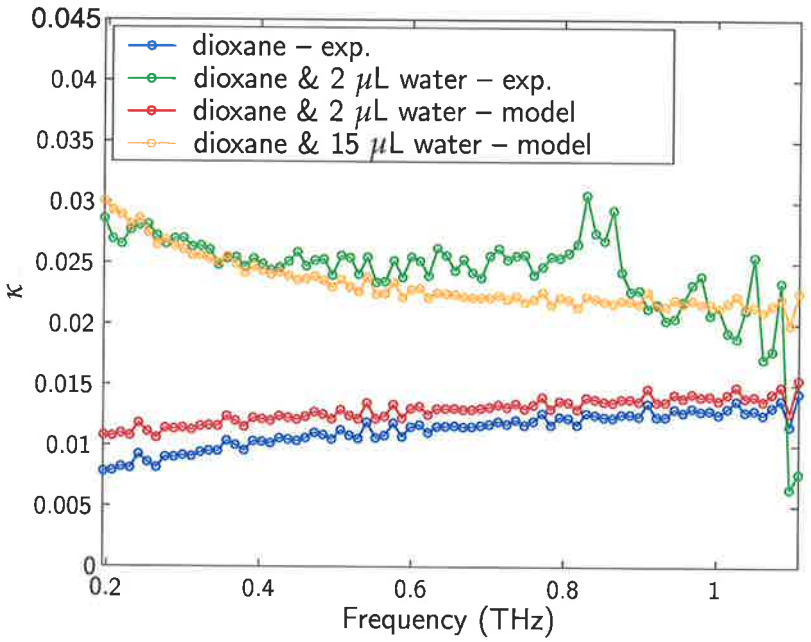

Figure 5.12. Modelled absorption spectra for dioxane and water. The measured absorption of dioxane and water is compared to the calculated absorption spectrum of hydrated dioxane, assuming ideal liquids (mixing by volume fraction), for two added water volumes. For the experimental value, 2 μL/mL of water in dioxane, a slight increase in absorption is visible. This is, however, less than the experimentally-observed increase in absorption (dioxane and water) since the ideal-mixing model is not complete for this mixture (shown in microwave experiments). The trend towards higher absorption, however, is clear. This trend can be further explored by artificially increasing the volume fraction of water in our model, to give the plot for dioxane plus 15 μL/mL water. This artificial plot shows that the changed slope of absorption from dioxane to dioxane and water could be attributed to the water curve. Water was estimated from the Debye model of Rønne et al. (1997). This analysis suggests that models for water-dioxane mixtures at T-ray frequencies need to consider an increased role of water than models at lower frequencies.

5.3.5 Dioxane and Subtilisin Carlsberg

The T-ray absorption spectrum of the dioxane-SC mixture is shown in Fig. 5.13, indicating only a slight increase in absorption over the anhydrous dioxane. These measurements indicate two important results: (i) that the dielectric constant of the lyophilised protein is greater than anhydrous dioxane, and (ii) that the increased absorption of 2 mg/mL of SC in dioxane is slight (less than 10%). As discussed in Sec. 5.1.2 above, only a slight increase is expected because proteins typically have a low T-ray absorption.

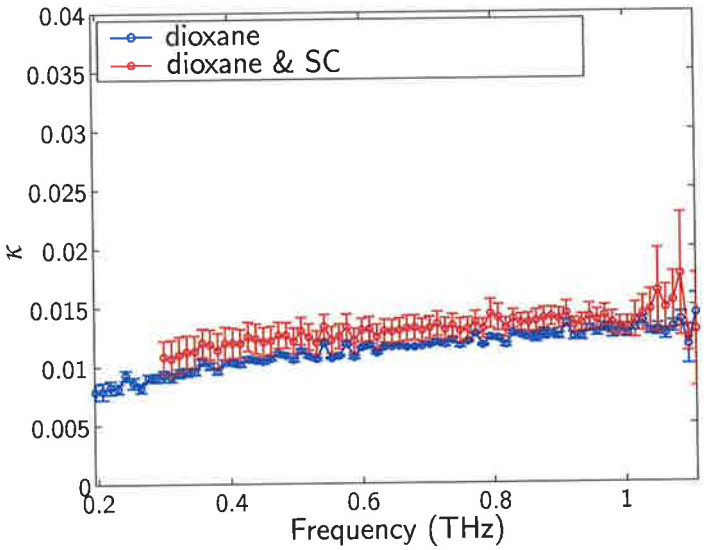

Figure 5.13. Measured T-ray absorption spectrum of dioxane & Subtilisin Carlsberg. The absorption spectrum of dioxane and 2 mg/mL of Subtilisin Carlsberg was measured using dual-sample T-ray spectroscopy, described in Sec. 5.2. The bandwidth is limited to the region of maximum SNR. The error bars on the plot indicate the standard deviation over six separate samples.

The spectra from the first three mixtures in Table 5.2 are compared in Fig. 5.14. This demonstrates that: (i) the T-ray absorption spectrum of 2 mg/mL SC in dioxane has a small but discernable increase over the spectrum of pure dioxane, and (ii) the spectrum of 2 μL/mL water in dioxane has a large increase over the spectrum of pure dioxane.

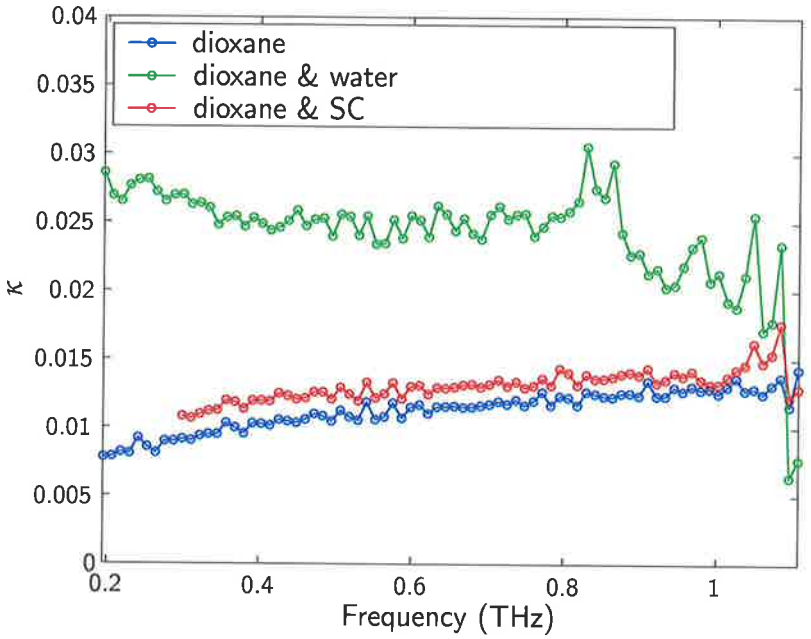

Figure 5.14. Comparing the first three mixtures in Table 5.2. This plot shows the measured absorption spectra of the first three mixtures from Table 5.2, measured using dual-sample T-ray spectroscopy, described in Sec. 5.2. The bandwidth is limited to the region of maximum SNR. The broad features are of interest, since characterisation of small-scale features at T-ray frequencies is difficult. The mixture of dioxane and SC shows a very slight increase in absorption over pure dioxane. Hydrated dioxane shows a marked increase in absorption, due to the increased polarity caused by adding strongly polar water molecules.

5.3.6 Dioxane and water and SC

The absorption spectrum of a mixture of pure dioxane, 2 μL/mL water and 2 mg/mL SC is shown in Fig. 5.15, and compared to the absorption spectra of (i) dioxane and 2 μL/mL water, and (ii) dioxane and 2 mg/mL SC. Dioxane and water and SC has a clear increase in absorption over dioxane and SC due to the addition of water. There is, however, a decrease compared to dioxane and water, indicating that some of the water present has a lower dielectric constant when interacting with the SC molecules.

These results show that the addition of SC to a mixture of dioxane and water lowers the dielectric constant of the mixture. Without the consideration of water binding to the lyophilised SC molecules, the addition of a small volume fraction of SC should make no difference to the absorption spectrum of the mixture. For 2 mg/mL of SC in 2 μL/mL water in dioxane, the volume fraction of SC was 0.2%. The observed decrease cannot be due to volume displacement effects alone because the volume of SC (0.2%) is small compared to the observed shift in absorption ($\sim$25% in Fig. 5.15).

It seems there is a clear difference between mixture with anhydrous and hydrated dioxane. However, there are two contributions to the mixture's spectral response: (i) the hydrated protein, and (ii) free water molecules not attached to the protein. The percentage of the free water present in the mixture of dioxane and water that is subsequently bound to the introduced SC molecules in the mixture of dioxane, water and SC can be estimated from previous measurements of the hydration shell of SC (Pal et al., 2002). It is estimated that there are 500 bound water molecules per SC, approximately 400 of which are removed by lyophilisation. From molar calculations, the number of SC molecules present in dioxane and SC equals 75 nMol/mL, which corresponds to approximately 30 μMol/mL of water being bound to the added lyophilised SC. The concentration of water in the mixture of dioxane and water $\approx$ 110 μMol/mL, predicting a decrease in the free water increment of approximately 27%. The water increment over pure dioxane in Fig. 5.13 is decreased by about 30%–40% with the addition of SC, depending on frequency. These results can be explained by assuming that a measurable portion of the free water molecules responsible for the absorption of dioxane and water are bound to the SC in the mixture of dioxane and water and SC.

To estimate the water actually attached to the protein, the effect of free water was measured separately by removing the protein in the final absorption measurement.

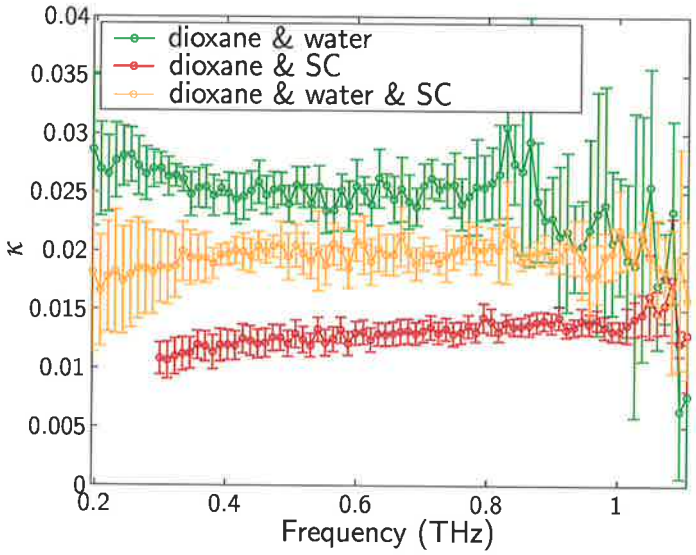

Figure 5.15. Measured absorption of dioxane, water and SC. The graph shows absorption spectrum of dioxane and water and SC, compared to the absorption spectra of (i) dioxane and 2 μL/mL water, and (ii) dioxane and 2 mg/mL SC, measured using dual-sample T-ray spectroscopy (described in Sec. 5.2). The bandwidth is limited to the region of maximum SNR. The bandwidth of the 'dioxane & SC' measurement is slightly less than the bandwidth of the other two curves as the data were measured under slightly different experimental conditions. The error bars on the plots indicate the standard deviation over six separate samples. The errors increased for samples that had undergone further steps due in part to sample contamination. These errors can be reduced as the measurements become routinised.

5.3.7 Dioxane and free water

The addition of protein to the dehydrated and hydrated solvents showed a shift in the complex T-ray refractive index of each mixture, and this shift depended on the fraction of free water present in the mixture.

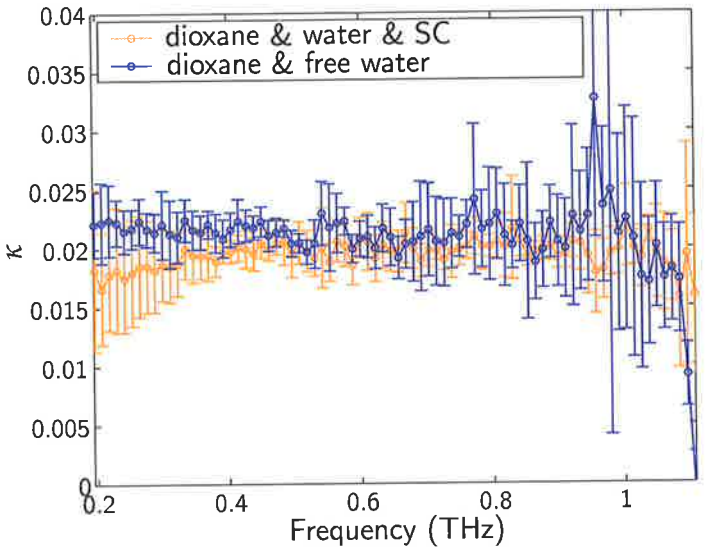

Figure 5.16. Measured absorption of dioxane & free water. This Figure compares the measured absorption spectra of mixtures of dioxane and free water to dioxane and water and SC. The data were measured using the T-ray spectrometer as described in Sec. 5.2. The bandwidth is limited to the region of maximum SNR. The error bars on the plots indicate the standard deviation over six separate samples.

Physically removing the protein tested the assumption of free water binding to the SC in the mixture of dioxane and water and SC. The SC was filtered out with a centrifuge, leaving only the liquid phase, that is the supernatant. Bound water was removed with the protein. The refractive index of the supernatant showed how much of the water present in the hydrated solvent was attached to the SC molecules. The absorption spectrum of dioxane and free water is compared to the spectrum of dioxane and water and SC in Fig. 5.16.

The absorption of dioxane and free water was almost identical to the absorption of dioxane and water and dioxane, and discernably less than dioxane and water. The SC molecules have interacted irreversibly with the mixture, and acted to reduce the overall absorption spectrum. This can be well explained by the bound water model. The slight increase in absorption from the mixture of dioxane and water and SC to the

dioxane and free water mixture may be due to the slight increase in volume fraction of the free water as the protein and bound water is removed.

5.4 Conclusion

The estimated volume fractions of the five mixtures are presented in Table 5.4. The estimates for free and bound water in the last mixtures (dioxane and water and SC, and dioxane and free water) are calculated assuming 500 bound water molecules per SC (see Sec. 5.3.6).

Table 5.4. Estimated volume fractions of experimental mixtures. This Table offers an explanation for the measured absorption spectra of the mixtures by showing the percentage volume fractions of dioxane, water and SC in each of the measured mixtures. Pure dioxane has low T-ray absorption, so mixing dioxane with water will increase the absorption. Mixing dioxane with SC increases the absorption only slightly, but when water and SC are mixed in the dioxane, the absorption is less than the sum of the individual absorptions. In fact, the absorption of a hydrated dioxane mixture is *reduced* by adding SC. This decrease can be modelled by assuming a certain volume fraction of the added free water binds to the lyophilised SC, and thus has a reduced T-ray absorption. The estimate volume fraction of bound water was calculated from Table 5.2 an assumption of 500 water molecules being bound to each SC molecule (Pal et al., 2002). The mixtures in this Table correspond to the measured spectra in this Chapter: 1-mL anhydrous dioxane, 2-μL pure water and 2-mg lyophilised SC.

Mixture	Dioxane	Water		SC	Total
		Free	Bound		
dioxane	100.0%	–	–	–	100.0%
dioxane & water	99.8%	0.2%	–	–	100.0%
dioxane & SC	99.8%	–	–	0.2%	100.0%
dioxane & water & SC	99.6%	0.1%	0.1%	0.2%	100.0%
dioxane & free water	99.9%	0.1%	–	–	100.0%

Pure dioxane, with a largely non-polar liquid matrix, shows a relatively low T-ray absorption of approximately $\kappa = 0.01$ (at 0.5 THz). Adding even a small fraction of water to the mixture, 0.2% by volume, increases this to $\kappa = 0.025$ (at 0.5 THz) due to the non polar nature of water molecules, which have many rotational modes at T-ray frequencies.

Adding a 0.2% volume fraction of a freeze-dried protein, SC, to the mixture had only a small influence on the absorption because most dipoles cancel out in a large biomolecule. However, when pure water (0.2% by volume) and SC (0.2% by volume) were both added, a portion of the water became bound to the free-dried SC – this bound water has a reduced ability to freely rotate at T-ray frequencies, and therefore has a lower absorption than the free water. In the mixture of dioxane, water and SC, only 0.1% by volume of the added water remained free, so the overall T-ray absorption of the mixture was lower than that of just dioxane and water. The idea of water binding to SC was confirmed by centrifuging out the SC, which made only a small difference to the absorption of the mixture – the bound water made only a small contribution to the T-ray absorption.

The experiments in this Chapter demonstrate that T-ray transmission spectroscopy can sense the absorption spectra of large biomolecules, and measure a change in their hydration levels, using a bandwidth of 0.2 to 1.2 THz. Molecular hydration can indicate the state and activity of a biomolecule. Furthermore, the dioxane environment provides a way to study biomolecules in T-ray transmission, where hydration and temperature can be carefully controlled and real-time chemical reactions can conceivably be carried out.

5.4.1 Future work

Numerical modelling is the best way to understand the interaction of liquids and biomolecules at a molecular level (Venables and Schmuttenmaer, 2000b; Walther et al., 2002; Hayward and Go, 1995). Future work will lead to more quantitative measurements of solvents and protein absorption in the T-ray band. T-rays can non-invasively estimate the activity of enzymatic proteins, used for example in micro-flow reactors, by measuring water content with high sensitivity.

Future work should also increase the bandwidth of the experimental system, by using for example thinner EO detection crystals (see Sec. 3.3.2). The temperature of the samples could also be decreased to reduce the population of upper-level resonances in the solids – this may lead to specific resonances becoming visible.

5.5 Chapter summary

This Chapter has described T-ray absorption experiments on protein suspensions in organic solvents. The high water miscibility of the non-polar solvent dioxane was used to conduct hydration measurements on the protein Subtilisin Carlsberg (SC). The bandwidth of the T-ray spectrometer provided access to the under-explored T-ray region of the electromagnetic spectrum, a region where water is high and research indicates the possibility of conformation-dependant biomolecular resonances. The T-ray dielectric constants of free water and water bound to the suspended protein have been indirectly observed in the organic solvent mixtures.

One promising method to decrease the uncertainly in these liquid measurements is a *differential* sampling technique for liquids in the T-ray spectrometer. Differential Time-Domain Spectroscopy (DTDS) is introduced in Ch. 6 and demonstrated by firstly using solid dielectric films. Differential sampling is applied to biomolecular films in Ch. 7 and finally liquids in Ch. 8.

Chapter 6

Differential Time-Domain Spectroscopy

CHARACTERISING the properties of thin films in the GHz to THz range is critical for the development of new THz-speed technologies in integrated circuitry and photonics. T-ray Differential Time-Domain Spectroscopy (DTDS) is a novel technique that detects phase changes of less than 0.6 fs and absorption changes corresponding to several molecular monolayers. This Chapter shows how DTDS can be combined with double-modulation in the pump-probe system to improve sensitivity by an order of magnitude. The technique is experimentally verified by characterising 1-μm-thick samples of Silicon Dioxide on Silicon.

6.1 Introduction

This Chapter considers the problem of thin film characterisation with T-rays and proposes a solution using double-modulated DTDS, first described by Mickan et al. (2002c). Using a detailed noise analysis of DTDS, this Chapter shows, theoretically and experimentally, the benefits of using DTDS with double-modulation. For material characterisation, double-modulated DTDS potentially provides an improvement in T-ray signal-to-noise ratio (SNR) of over 100 times. Double-modulated DTDS is used to characterise a thin Silicon Dioxide test film in this Chapter, and to study biomolecular films and liquids in Chs. 7 and 8.

The novel contributions of this Chapter are: (i) a noise analysis of DTDS, (ii) double modulation applied to DTDS, (iii) an experimental demonstration of T-ray DTDS, and (iv) the demonstration of an algorithm to estimate material properties of thin films using DTDS.

6.1.1 Motivation

Thin film characterisation is a fundamental problem in optics and electronics. T-ray spectroscopy provides a new non-destructive method for probing thin films at speeds higher than network analysers and wavelengths longer than optical sources. Table 6.1 lists the techniques used for thin film characterisation, showing a gap of easy-to-use technologies in the T-ray frequency band.

Table 6.1. Thin film characterisation techniques. This Table lists methods used for thin film characterisation from DC to the mid-IR, comparing them to T-ray techniques.

Technique	Freq. range	Comments
Ellipsometry	20 THz–800 THz	optical technique (Ulman, 1995)
FTIR	5 THz–80 THz	for bulk and sheets (Han et al., 2001)
T-rays	0.1 THz–10 THz	ultrafast pulsed T-rays (see Ch. 4)
Resonator	35 GHz–144 GHz	for sheets
Vector Network Analyser	50 MHz–100 GHz	requires electrode patterning
RF Impedance Analyser	1 MHz–1 GHz	for circuits
LCR Meter	10 Hz–1 MHz	for circuits
C-V technique	DC and low freq.	can require Hg probe contacts (Schroder, 1990)

Thin film characterisation is important for the semiconductor industry as it pushes for smaller and faster devices. Materials with a high dielectric constant are required for improved insulation to stop tunnelling between layers, and materials with a low dielectric are needed for interconnects with reduced capacitance (Green et al., 2001). As feature sizes approach 100 nm and chip frequencies climb into the upper GHz range, it becomes increasingly important to have a convenient method of characterising the T-ray properties of thin dielectric films (Kingon et al., 2000). Thin film dielectric materials are being explored for many applications. Interest in plastic-based electronics is spurring the development of organic–inorganic hybrid materials and organic transistors on plastic (Kagan et al., 1999; Dimitrakopoulos et al., 1999). Single crystal optoelectronic devices are being developed for Micro-Opto-Electro-Mechanical Systems (MOEMS) and thin film transistors (Meyer zu Heringdorf et al., 2001). T-ray systems are non-contact, non-destructive and highly sensitive. T-rays penetrate optically opaque materials that cannot be characterised using optical methods, and can be used in transmission, reflection and tomographic experiments (Brucherseifer et al., 2001).

The complex dielectric constant of a sample is related to its optical properties by the relation $\tilde{\epsilon} = (\tilde{n})^2$, where, for extinction coefficient κ and refractive index n, $\tilde{n} = n - j\kappa$. The phase shift caused by a dielectric sample in the T-ray radiation path is proportional to $(\tilde{n} - 1)d/\lambda$, where $\tilde{n}$ is the complex refractive index of the medium, d is the sample thickness and λ is the T-ray wavelength (Lu et al., 1997). For small $\tilde{n}$ and d, this phase change is difficult to detect.

6.1.2 Previous studies

The spectroscopy of bulk dielectrics at T-ray frequencies was part of the early work in the field (Pastol et al., 1989c; Grischkowsky et al., 1990). Now there is a need for a non-contact, room temperature technique to characterise thin films at T-ray frequencies for THz-speed electronics. Current methods of dielectric thin film characterisation show a gap in information from 0.144 to 5 THz (Li et al., 1999a). This gap is covered by the typical operating bandwidth of T-ray systems. Thin film analysis is limited by system sensitivity; the thickness of a thin film, being microns or less, is far less than the T-ray wavelength. A number of approaches have been used to increase system sensitivity, including DTDS, angle-dependant spectroscopy, interferometry and planar waveguides.

T-rays have been used to characterise a wide variety of thin film materials. T-rays can be used to observe static and dynamic characteristics of superconducting films, dielectrics in waveguides and DNA thin films (Tonouchi et al., 2000; Grischkowsky, 2000; Gallot et al., 2000; Brucherseifer et al., 2000a). Organic thin polymer films were first characterised by T-rays in 1992 (Ree et al., 1992). A reliable algorithm for estimating the T-ray characteristics of thin film dielectrics was proposed in 1996 (Duvillaret et al., 1996). This method uses a model based on simple Fresnel equations and an iterative fit algorithm. Near-Brewster angle (goniometric) phase shift reflection has been used to determine the refractive index of 3.27-μm-thick polymer films (see Sec. 4.2.5). An incorporation of this technique into tomography has been suggested by angle-dependant T-ray tomography of thin films for fuel cell applications (Brucherseifer et al., 2001).

Thin film T-ray spectroscopy has been demonstrated with a number of techniques, as described in Sec. 4.2 above – goniometric spectroscopy, ellipsometry, interferometry and waveguide approaches have been used to analyse thin samples with T-rays. Using planar waveguides and a T-ray resonator, Bolivar et al. have demonstrated a highly sensitive device for probing the binding state of DNA (Nagel et al., 2002b). This thin film micro-stripline approach can be extended to two-dimensional gene chips for high speed DNA analysis. The T-ray waveguide and resonator structure is sensitive to single-base mismatches in a 1.1 femtomol volume of 0.52 g/L DNA-in-water. Although highly sensitive and integrable, this technique is not ideal for non-contact characterisation of thin dielectric films.

6.1.3 Objective summary

The central contribution of this Chapter is the analysis and implementation of DTDS with double-modulation to improve T-ray thin film measurements. The techniques described in Sec. 4.2.5 to Sec. 4.2.8 have achieved spectroscopy and imaging of dielectrics of micron thickness, however the challenge remains to extend T-ray frequency characterisation to thinner films and lower dielectric constants. The problem of detecting the small signal from absorption, reflection and delay in a thin film will be solved using double-modulated DTDS.

6.2 Theory

6.2.1 DTDS

The DTDS technique was first called *differential* because the DTDS signal is a first order derivative of the reference signal with respect to time; a very small optical delay, Δt, is achieved when the thin film moves into the beam path. The small change in amplitude of the transmitted signal, Δy_r (due to the thin film moving into and out of the T-ray beam path), is measured as a function of time delay steps, $n\Delta t$, where $n\Delta t = t$ (the time duration of the measurement). As the small optical delay, Δt, is the same for all points along the T-ray waveform, y_r, the DTDS technique is approximately measuring the slope of the reference waveform, dy_r/dt. DTDS has been used to determine the refractive index of a 1.8-μm-thick parylene-N film (Jiang et al., 2000). This first work dithered the sample at 16 Hz, and developed an analytical expression for the refractive index of the film, as given in Eq. (6.1). An improvement on this work was to increase the dither frequency to 66 Hz and thereby reduce the noise in the detected T-rays (Lee et al., 2000a).

DTDS measures a signal that comes purely from the difference caused by a thin film deposited on half of a sample holder; the other half is used as a reference (Jiang et al., 2000; Brucherseifer et al., 2000b). DTDS measures only the difference between the two halves every 100 ms or less, thereby cancelling out noise from slow fluctuations in the laser power. The magnitude of this modulation is detected using a Lock-In Amplifier (LIA) synchronised to the frequency of the modulated sample. The sample is a substrate half-covered with the film and half bare, as shown in Fig. 6.1.

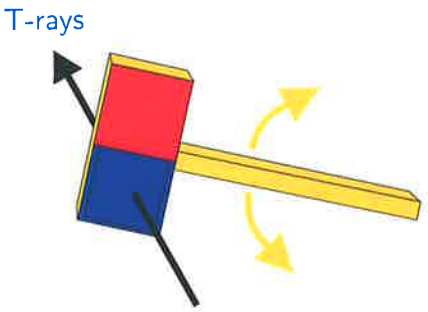

Figure 6.1. Sketch of the DTDS sample holder. This sketch shoes the dithered sample used in DTDS. The device is a slide attached to a mechanical arm, which is dithered at a constant frequency as shown by the gold arrows in the diagram. A thin film of interest half covers the slide. The device is switched in the T-ray beam path between the sample film (shown in blue) and the substrate (shown in red).

For a thin film with thickness d and $n_s \gg \kappa_s$, deposited (so $n_2 = n_1$) on a substrate n_3, shown schematically in Fig. 6.2, where $n_1 \gg \kappa_1$, $n_2 \gg \kappa_2$ and $n_3 \gg \kappa_3$, an analytic expression for the refractive index of the film can be derived (Jiang et al., 2000):

$$n_s = \sqrt{(1 + \frac{c_0}{\omega d}\left|\frac{\tilde{S}_d}{\tilde{S}_r}\right|)(n_1 + n_3) - n_1 n_3}, \tag{6.1}$$

where $\tilde{S}_d = \mathcal{FT}(y_d)$, and $\tilde{S}_r = \mathcal{FT}(y_r)$ (where $\mathcal{FT}(y_a)$ is the Fourier Transform of y_a).

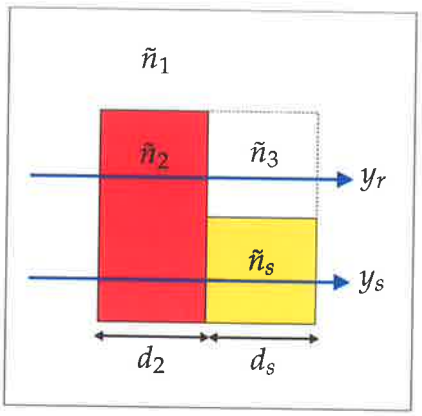

Figure 6.2. Thin film schematic. The thin film in this diagram, characterised by the complex refractive index $\tilde{n}_s$, is supported by a substrate, $\tilde{n}_2$. The surrounding medium, commonly air, has the complex refractive index $\tilde{n}_1$. $\tilde{n}_3$ is the complex refractive index of the medium that replaces the volume of the thin film, indicated by the dotted lines – in these experiments this is air, although if the thin layer is created by implantation of the substrate, $\tilde{n}_3$ may equal $\tilde{n}_2$. The reference pulse, y_r, passes through the substrate, and the sample pulse, y_s, passes through the substrate and the film. The spectral components of the waveforms are determined by FFT, $\tilde{S}_s = \mathcal{FT}(y_s)$ and $\tilde{S}_r = \mathcal{FT}(y_r)$. d_s is the thickness of the thin film, which was measured in the experiments in this Chapter using Atomic Force Microscopy (AFM). The film thickness, d_s, is not measured directly by the T-ray spectrometer.

For a typical T-ray spectrometer, the major source of noise is the pump laser, which is very sensitive to slow fluctuations in temperature. These nonlinear fluctuations can cause larger changes in the detected T-ray signal than the thin film sample itself. The advantage of differential spectroscopy is that the signal transmitted through the film is compared to the signal through the substrate at each point of the delay stage, thus normalising the laser-based fluctuations.

DTDS takes advantage of the $1/f$ noise characteristic by making measurements at a higher frequency, therefore at a lower noise level. The differential waveform is equivalent to the difference between the reference and sample waveforms, $y_d = y_r - y_s$. The

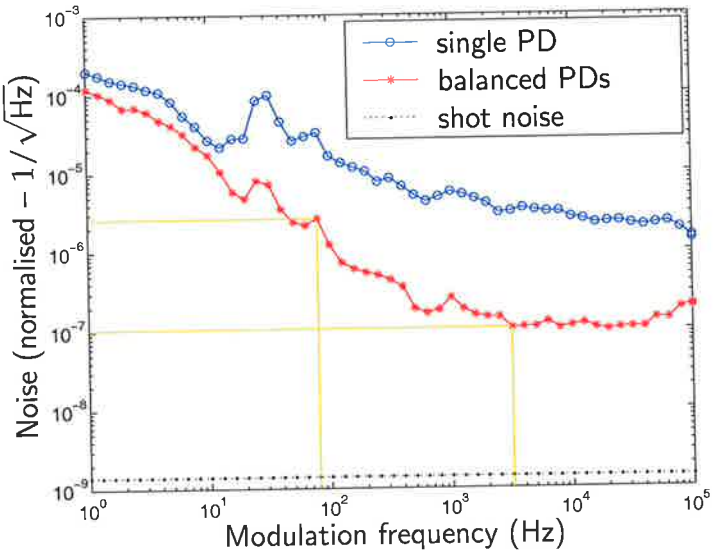

Figure 6.3. Measured noise spectrum of a T-ray system. This graph shows the measured noise spectrum of a T-ray system as a function of modulation frequency. The measurement frequency in this measurement was scanned by a Lock-In Amplifier (LIA). The noise spectrum shows a $1/f$ noise characteristic typical of ultrafast laser-driven experiments (von der Linde, 1986; Haus and Mecozzi, 1993; Son et al., 1992; Poppe et al., 1998). The benefit of double-modulation is highlighted by the two yellow lines at 100 Hz and 3 kHz – the noise level at 3 kHz and above is more than an order of magnitude lower than the noise at 100 Hz and below. The shot noise limit is determined by the detector current and is shown as a dotted line on the graph. The noise spectrum was measured using either a single photodiode ('single PD'), or a current difference circuit ('balanced PDs'), with biased PDs and a 50-Ω load impedance. The noise output of the LIA was measured with a settling time of 60 times the time constant to allow spurious transients to settle out. The noise level was normalised to the LIA filter bandwidth, thus normalising for different LIA time constants. In these measurements a time constant of 100 ms was used.

material parameters can be estimated by measuring y_r and y_d, calculating y_s, and using the transmission equations for thin samples in Sec. 4.2.1.

6.2.2 Noise analysis

DTDS is able to measure very subtle variations in phase and absorption. In a normal T-ray TDS experiment, this difference is determined from the ratio of two complex spectra, $\tilde{S}_s/\tilde{S}_r$, where the complex spectral components $\tilde{S}$ are the Fourier Transforms

of the time domain waveforms measured in the experiment (see Fig. 6.2). Each waveform is measured in a separate scan of the pump beam delay stage, resulting in a delay between scans of ten minutes or more for sensitive scans. In DTDS, the signal transmitted through the film is compared to the signal through the substrate at each point of the delay stage. In effect, the differential waveform is equivalent to the difference between the reference and sample waveforms, $y_d = y_r - y_s$. The benefit of using DTDS over normal TDS for characterising thin films can be estimated using a simple analysis of measurement error in the amplitude spectrum, that is errors arising from $\Delta|\tilde{S}| = \Delta S$.

The quantity of interest in dielectric characterisation experiments is the deconvolved system response, or the transmission spectrum (see Sec. 4.2.1),

$$\tilde{T}_{\text{exper}} = \frac{\tilde{S}_s}{\tilde{S}_r}. \tag{6.2}$$

The *amplitude* of the transmission spectrum,

$$|\tilde{T}_{\text{exper}}| = T_{\text{exper}} = \frac{S_s}{S_r}, \tag{6.3}$$

where S_s and S_r are the amplitudes of the spectral components of the film (sample) and reference waveforms, $S_s = |\tilde{S}_s|$ and $S_r = |\tilde{S}_r|$, and $T = |\tilde{T}|$. For nominally uncorrelated measurement errors of the amplitude spectra ΔS_s and ΔS_r, the relative error in the amplitude transmission spectrum can thus be approximated by

$$\left(\frac{\Delta T}{T}\right)^2_{\text{TDS}} \approx \left(\frac{\Delta S_s}{S_s}\right)^2 + \left(\frac{\Delta S_r}{S_r}\right)^2. \tag{6.4}$$

For a thin film sample, the relative errors in the reference and sample spectra are largely equal, so the relative error in the amplitude transmission spectrum of a thin film measured with normal T-ray TDS can be approximated by

$$\left|\frac{\Delta T}{T}\right|_{\text{TDS}} \approx \sqrt{2}\left|\frac{\Delta S_r}{S_r}\right|. \tag{6.5}$$

In DTDS, the complex transmission spectrum is calculated from

$$\tilde{T}_{\text{exper}} = 1 - \frac{\tilde{S}_d}{\tilde{S}_r}, \tag{6.6}$$

where $\tilde{S}_d$ is the complex differential spectrum. Hence

$$\left(\frac{\Delta T}{T}\right)^2_{\text{DTDS}} \approx \left[\left(\frac{\Delta S_d}{S_d}\right)^2 + \left(\frac{\Delta S_r}{S_r}\right)^2\right]\left(\frac{S_d}{S_s}\right)^2, \tag{6.7}$$

where $S_s = S_r - S_d$. Equation (6.7) shows that using DTDS instead of normal TDS reduces the relative error in the amplitude transmission spectrum by a factor of S_d/S_s, so long as

$$\Delta S_d/S_d \approx \Delta S_s/S_s. \tag{6.8}$$

These results are summarised in Table 6.2.

Table 6.2. Error estimation equations. Comparison of equations for estimating the experimental error in measured transmission coefficients in T-ray TDS and DTDS. DTDS has an inherently lower noise level than TDS by a factor of approximately $|\tilde{S}_d|/|\tilde{S}_r|$, the ratio of the differential and reference spectra. For thin films, where the sample and reference spectra are substantially similar, the ratio $|\tilde{S}_d|/|\tilde{S}_r|$ is far less than unity, so noise in DTDS is less than in TDS.

	Measured	$\lvert\Delta T/T\rvert$
TDS	$\frac{\lvert\Delta S_r\rvert}{\lvert S_r\rvert}$	$\sqrt{2}\left\lvert\frac{\Delta S_r}{S_r}\right\rvert$
DTDS	$\frac{\lvert\Delta S_d\rvert}{\lvert S_d\rvert}$	$\sqrt{2}\left\lvert\frac{\Delta S_r}{S_r}\right\rvert\left\lvert\frac{S_d}{S_r}\right\rvert$

Equation (6.8) is valid for a system dominated by noise in the T-ray generation arm of the pump-probe system. DTDS is most beneficial for very thin films, where the transmission spectrum of the differential signal S_d is much smaller than the spectra of the film or the reference. The T-ray phase change induced by a dielectric sample is proportional to its thickness. The improvement in SNR due to DTDS is shown experimentally in Sec. 6.4 by measuring the reference and differential spectra of a thin film sample.

6.2.3 Double-modulation

In standard DTDS, the samples cannot be physically switched at very high frequencies, which removes the benefit of high frequency modulation with an optical chopper and Lock-In Amplifier (LIA, described in Sec. B.7). The maximum demonstrated sample dithering frequency, using a galvanometric shaker, had been 66 Hz (Lee et al., 2000a). Double-modulation combines the benefits of high-frequency modulation and DTDS to provide a reduced noise over both normal DTDS and high-frequency-modulated T-ray TDS.

Double-modulation is a technique similar to encoding information on a carrier wave in telecommunications. The signal, already modulated at a lower frequency f_2 by the thin

film sample, is additionally modulated at a higher frequency f_1 by an optical chopper. The frequency f_1, equivalent to the carrier frequency, is then removed in the detection system through demodulation. The advantage of double-modulation is that the noise level is less at the higher modulation frequency, as shown in Fig. 6.3.

In most laser-driven T-ray systems, the main source of noise is the mode-locked Ti:sapphire laser, which has a $1/f$ noise characteristic. Noise can thus be reduced by modulating the pump beam at some audio or radio frequency f_2 with a mechanical chopper, or an acousto- or electro-optic (EO) device. An optical chopper is shown in the schematic experimental layout in Fig. 6.4. Once converted to an electronic signal with a photodetector of appropriate bandwidth, the depth of the modulation is detected with a LIA. The LIA then passes the signal through a very narrow band filter to reject any variations not at the modulation frequency. Single frequency modulation is diagrammatically described in Fig. 6.5. The frequency of f_2 in single modulation is limited by, for example, how rapidly a sample can be mechanically modulated in and out of the T-ray beam. The important quantity is the shaded area under the noise curve, which indicates the amount of noise appearing at the output of the LIA.

Ideally an experiment should be modulated at as high a frequency as possible. For mode-locked lasers, $1/f$ signal fluctuations dominate at frequencies below 3 MHz, where the shot noise limit is reached (Andor et al., 1984). As discussed in Sec. 6.3, a galvanometric scanner has been used as the second modulator, and it is impossible to shake the thin film sample above audio frequencies because of mechanical inertia. Galvanometric scanners do not have sufficient travel at frequencies above 100 Hz when a sample is attached, and at modulation frequencies below 100 Hz, the $1/f$ noise levels are very high, greatly reducing the sensitivity of DTDS.

Double-modulation enables the use of an high carrier frequency, which sets the noise level, and an arbitrarily low shaker frequency. Galvanometer operation at a frequency less than 20 Hz, where $1/f$ noise is very high, eliminates heating problems and enables a larger shaking amplitude. The process of double modulation and demodulation is shown in Fig. 6.6. The narrow detection bandwidth of LIA2 at f_2 rejects any harmonics caused by double-modulation, and the advantage of double-modulated DTDS is that the noise found at the output of the second LIA is far less than in the single LIA setup.

Various embodiments of double-modulated DTDS can be designed, for example the embodiment in Fig. 6.4. In another embodiment, the two LIAs could be replaced with

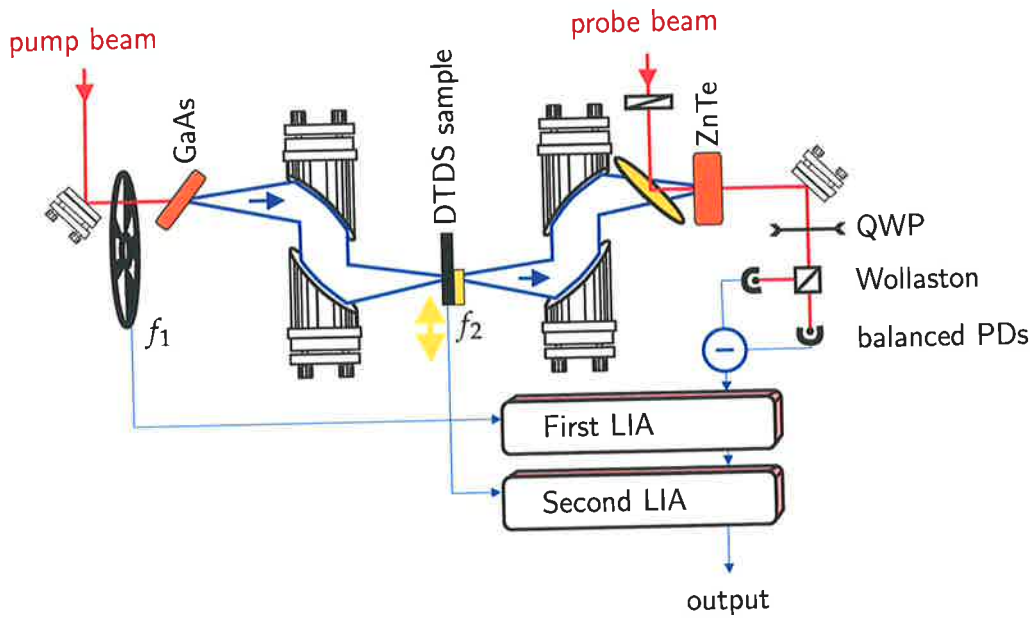

Figure 6.4. DTDS system schematic with dual LIAs. This diagram shows the embodiment of the double-modulated DTDS scheme that was used for the experiments in this Chapter. The pump and probe beams come from an ultrafast laser, and two Lock-In Amplifiers (LIAs), with a shaker (at f_2) and an optical chopper (at f_1), implement the double-modulation scheme. The functions of the other system components (the GaAs emitter, the gold-plated parabolics, the ZnTe detector, the quarter-wave plate 'QWP', the Wollaston polariser and the balanced photodiodes 'PDs') are explained in Ch. 3. The DTDS output signal depends on the differences between the films on opposite ends of the slide (Mickan et al., 2002d).

a high speed analogue-to-digital converter and a digital signal processor. Double-modulation can also be achieved using a LIA driven by a synthesised frequency $f_1 + f_2$, unless the sum frequency is at radio frequencies (RF). In that case, it is advantageous to have the second LIA operating at audio frequencies (AF) because an AF LIA has better signal-to-noise ratio than a RF LIA (Frolov and Vardeny, 1998).

To quantify the improvement in SNR due to double-modulation, both the decrease in noise level and the decrease in signal level it causes must be considered. Modulating the signal with a second modulator decreases its amplitude by half; each modulator blocks 50% of the pump beam. If, however, the reduction in noise is better than 50%, then double-modulation results in an improved SNR. The improvement in SNR can be seen in Fig. 6.3, showing the noise spectrum of the T-ray system. If the modulation frequency is set to 3 kHz or higher, the noise level drops by an order of magnitude

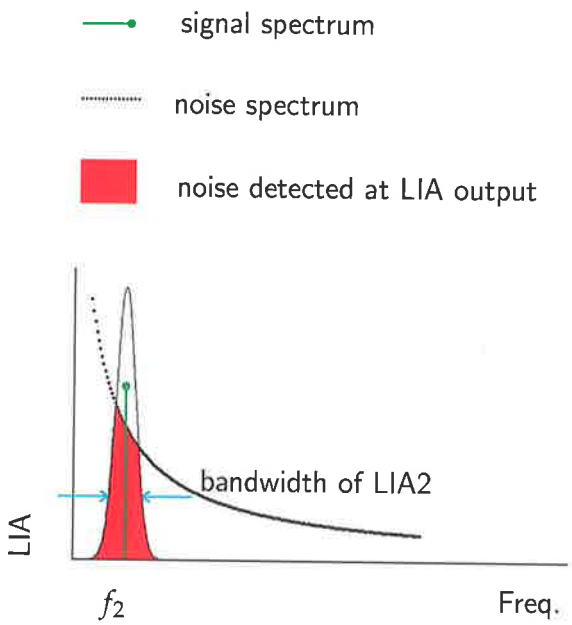

Figure 6.5. Explanation of single LIA modulation. This graph shows the output spectrum of an experiment with a single Lock-In Amplifier (LIA). The signal is modulated at a frequency f_2 by, for example, a galvanometric shaker. Although the signal is chopped by a square wave, the LIA detects the fundamental sine wave, so it is considered as a single frequency spike. The LIA has a certain bandwidth, set by its time constant, and the noise at the LIA output is determined by the noise power within that bandwidth, which corresponds to the shaded region in Fig. 6.5.

compared to a modulation frequency of 100 Hz or lower. This is the improvement expected for a system dominated by $1/f$ noise.

6.3 Experiments

The objectives of the experiments in this Chapter were to: (i) confirm the accuracy of DTDS, that is $y_d = y_r - y_s$, (ii) compare the noise performance of DTDS and double-modulated DTDS, and (iii) characterise a thin film sample using double-modulated DTDS.

The embodiment of double-modulated DTDS shown in Fig. 6.4 is the setup used for the experiments in this Section. The pump beam is first modulated at f_1 by the mechanical chopper and then modulated at f_2 by the dithered thin film sample. The double-modulated T-ray signal is converted to a polarisation modulation of the probe

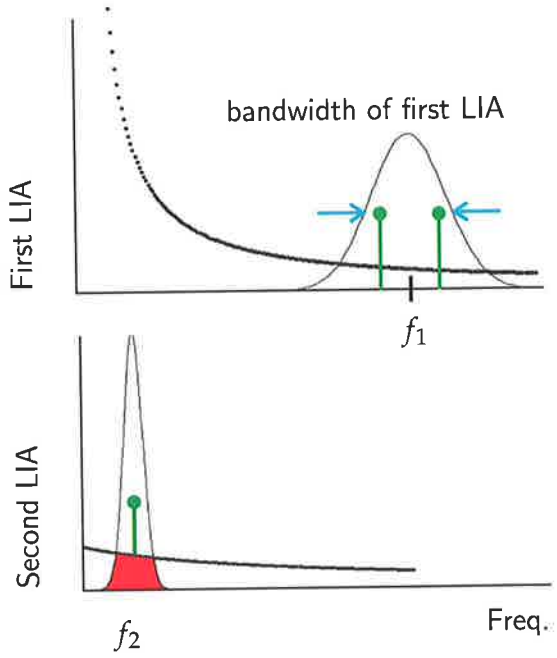

Figure 6.6. Explanation of double-modulation. These graphs outline the operation of double-modulation. In double-modulation, the signals at the input to the first LIA are found at the sum and difference of the modulation frequencies, $f_1 + f_2$ and $f_1 - f_2$. The first LIA acts as a frequency mixer and demodulates the f_1 frequency, so that at the input of the second LIA, the signal is modulated at f_2. One important point is that the bandwidth of the first LIA has to be set sufficiently wide to allow the signal to pass through at a frequency $\pm f_2$ from the centre frequency (Hemenway et al., 1987; Zhang et al., 1999).

beam using Electro-Optic Sampling (EOS, see Sec. 3.3.2). Balanced photodiodes (PDs) detect the polarisation modulation of the probe beam, and the first LIA, acting as a mixer, demodulates the chopper f_1. The second LIA detects the thin film signal at f_2 and provides a complex output representing the DTDS waveform at a given pump-probe delay. The delay is scanned to sample the entire T-ray waveform.

6.3.1 Equipment

In the experimental system shown in Fig. 6.4, the ultrafast Ti:sapphire oscillator (model: Tsunami; manufacturer: Spectra-Physics, Mountain View, CA, USA; URL: `http://www.spectra-physics.com`) was multi-line pumped by a large frame argon-ion laser (model: BeamLoc; manufacturer: Spectra-Physics, Mountain View, CA, USA; URL:

http://www.spectra-physics.com), and produced 1.7 W average power of 100-fs pulses at an 82-MHz repetition rate. The pump beam power was about 800 mW after passing through a mechanical chopping wheel, which modulated the beam at f_1. T-rays were generated by ultrafast current transients in a thin GaAs wafer mounted at Brewster's angle to the optical beam. The T-rays were collimated and focused with off-axis gold-coated parabolic mirrors, and detected with a collinear geometry in a 2-mm-thick <110>-oriented ZnTe crystal. The probe beam power was approximately 100 mW and there was 1 mA of current in each of the balanced photodiodes (PDs). The polarisation rotation of the probe beam was detected by a Wollaston analyser and balanced PDs, and a quarter-wave plate (QWP) was used to compensate for the intrinsic birefringence of the ZnTe, which is the standard setup for Electro-Optic Sampling (EOS, see Sec. 3.3.2).

The difference current from the PDs, proportional to the T-ray electric field, was demodulated by two LIAs, as described in Sec. 6.2.3. The first LIA had a time constant of 300 μs, which corresponded to a 260-Hz filter bandwidth, and the second LIA had a time constant of 100 ms, corresponding to a bandwidth of approximately 0.78 Hz. The bandwidth of the first LIA must be large enough to allow the modulated signal (at frequency $f_1 + f_2$) to pass though. The bandwidth of the second LIA must be as narrow as possible to block unnecessary noise at the output. The function of the LIA is explained in Sec. B.7.

The first LIA is pictured in Fig. 6.7, showing the connections to the current pre-amplifier, the chopper driver (f_1) and the second LIA. The settings on the first LIA are almost typical for a T-ray TDS experiment. The voltage input amplifier was selected for the voltage signal from the pre-amplifier, and the amplifier settings were set to 'float' and 'AC' as the input signal was floating and has no DC component. The gain of the LIA was chosen to be 1 V/V so the first LIA did not introduce an unnecessary voltage gain factor, which would have to be accounted for in the signal strength measured at the second LIA. Both notch line filters in the LIAs were selected to remove signals at 50 and 100 Hz. During experiments, the reference frequency was set to 'external', and the displayed frequency was f_1 = 2 kHz. The Channel 1 output amplifier of the LIA was set to 'X', that is, to be in phase with the reference frequency, and the phase was set using the 'auto-phase' function when the delay stage was at the peak of the T-ray pulse. Setting the LIA phase at the T-ray peak correctly displayed the T-ray waveform on the 'X'-channel (Channel 1). The time constant, which determined the bandwidth

of the first LIA's low-pass filter, was set sufficiently short to allow the f_2-modulated side-band to pass. For f_2 = 10 Hz, a 300-μs time constant provided a 260-Hz filter bandwidth, quite sufficient for the 10-Hz signal.

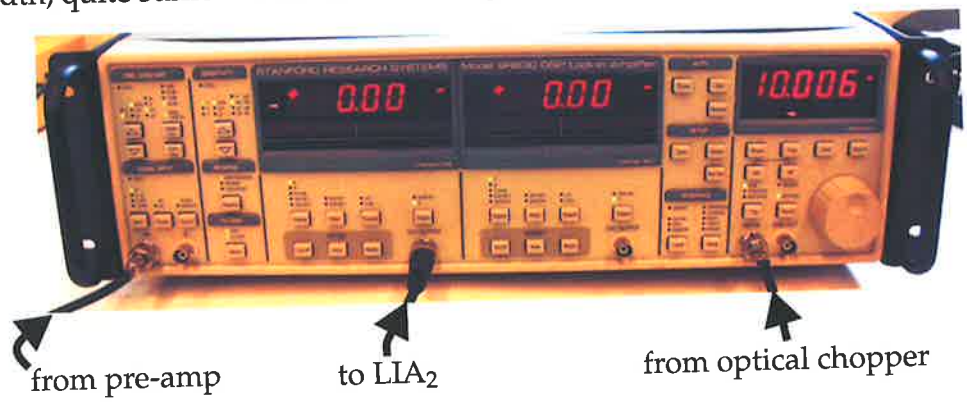

Figure 6.7. Lock-In Amplifier (LIA) photograph. This picture shows the front panel of a Stanford Research Systems LIA used in the double-modulation detection scheme. The signal from balanced photodiodes is amplified by a current amplifier, then input to the LIA for demodulation and low-pass filtering. The settings on the LIA are set manually using the front panel or using General Purpose Interface Bus (GPIB) commands from the computer. A more detailed description of this LIA, the SR830 DSP, is given in Sec. B.7.

The thin film sample was held in a galvanometric shaker (manufacturer: Cambridge Technology, Cambridge, MA, USA; URL: `http://www.camtech.com`), operating at f_2 and pictured in Fig. 6.8. The shaker itself was mounted in a large aluminium heat sink to keep its operating temperature below 50°C. The heat sink was close to but did not occlude the T-ray beam – this was determined experimentally by comparing waveforms transmitted both with and without the heat sink in place. The diameter of the T-ray spot on the sample was less than 2 mm, measured with a large-diameter metal iris diaphragm.

The galvanometer was driven by a sinusoidal waveform f_2 from a function generator, shown in Fig. 6.9. The amplitude of the waveform was set to drive the sample slide at approximately 1 cm peak-to-peak. The galvanometer driver, a single axis board level mirror positioning system (manufacturer: Cambridge Technology, model: 678xxx), was mounted in a box with power supply, shown in Fig. 6.10.

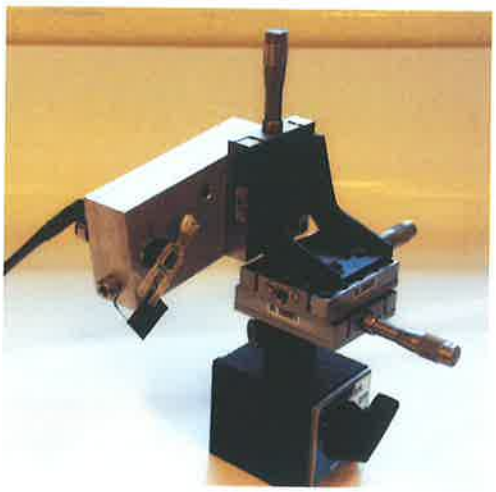

Figure 6.8. Photograph of a galvanometer holder and sample for DTDS. This picture shows a Cambridge Technology galvanometer mounted in an aluminium heat sink, with a substrate sample attached. The motion of the sample is shown in Fig. 6.1. The heat sink is held in an XYZ positioning stage for positioning the sample at the focal point of the T-ray beam. The stage is held in place with a magnetic base.

Figure 6.9. Photograph of a function generator used for double-modulated DTDS experiments. A Stanford Research Systems DS340 function generator was set to generate a sinusoidal 8.0 V peak-peak amplitude, which drove the DTDS galvanometer at 1 cm peak-to-peak.

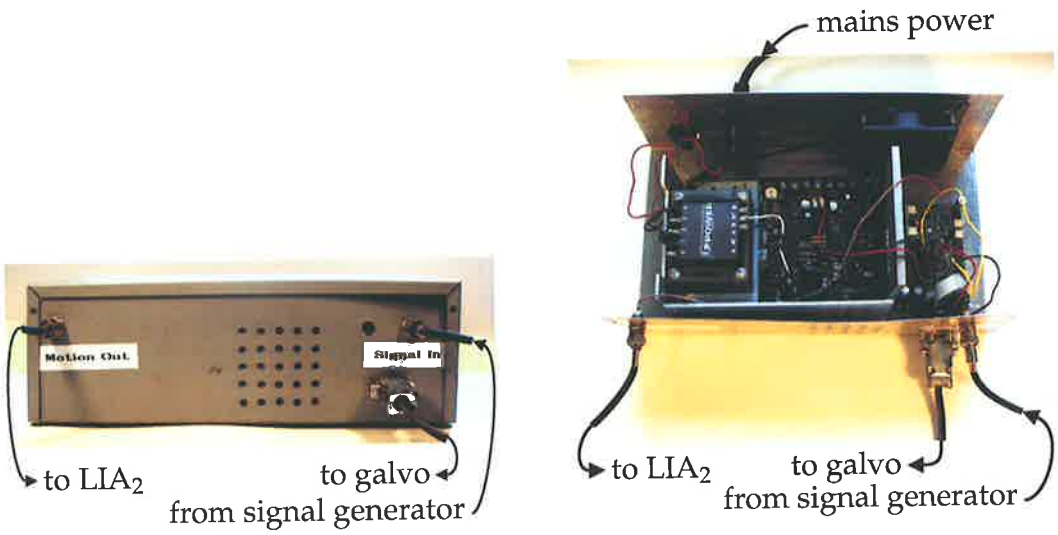

(a) Exterior (b) Interior

Figure 6.10. Photograph of the galvanometer driver electronics. These photographs depict the commercial driver board used to power the galvanometer. The board was housed in a home-made box with a home-built power supply.

6.3.2 Sample

The thin film sample used in these experiments was a rectangle of amorphous glass, half-covered with a 180-μm-thick layer of black electrical tape. A relatively thick film was used to demonstrate the reduction of noise in DTDS compared to TDS; if a film was too thin, no results were observed in TDS. The glass slide was approximately 30-mm high, 13-mm wide and 1-mm thick. A sample this size ensured the T-ray beam passed wholly and exclusively through either the sample or the substrate as it oscillated. The sample was driven sinusoidally at $f_2 = 5$ Hz – a low frequency allowed the galvanometer to operate with a large amplitude without over-heating.

Various thin films have been characterised in this system, including 0.934-μm-thick SiO_2 on Silicon. The SiO_2 thin films in this experiment were prepared by etching half of the SiO_2 deposited on the Si wafer with hydrofluoric acid, Hydrogen Fluoride (HF). The samples were characterised under normal indoor conditions, with approximately 25°C and 35% humidity. The parameter estimation was performed as described in Sec. 6.3.3.

6.3.3 Parameter estimation algorithm

Material parameters in T-ray TDS must be estimated from the time-domain data using methods similar to Fourier Transform spectroscopy (Marshall and Verdun, 1990). In essence, a pulse that has been transmitted through or reflected from the sample contains absorption and phase delay information about the sample. The effect on the pulse caused only by the sample is determined by deconvolving the sample pulse with a reference pulse (Ferguson and Abbott, 2000),

$$\tilde{T}_{\text{exper}} = \tilde{S}_s / \tilde{S}_r. \tag{6.9}$$

The deconvolved signal is compared to a model based on Fresnel equations to determine its frequency-dependent complex refractive index, $\tilde{n} = n - j\kappa$, where n and κ are the refractive index and extinction coefficients of the sample material (see Sec. 4.2).

The complex transmission spectrum of normal T-ray TDS can be modelled as (Duvillaret et al., 1996):

$$\tilde{T}_{\text{model}} = \frac{2\tilde{n}_2(\tilde{n}_1 + \tilde{n}_3)}{(\tilde{n}_2 + \tilde{n}_1)(\tilde{n}_2 + \tilde{n}_3)} \cdot \exp\left[-i(\tilde{n}_2 - \tilde{n}_s)\frac{\omega L}{c_0}\right] \cdot \text{FP}, \tag{6.10}$$

where ω is the angular frequency, c_0 is speed of light in a vacuum, FP is the frequency-dependent contribution of Fabry-Pérot reflections in the thin film, and the film thickness d_s and complex refractive indices, $\tilde{n}_1$, $\tilde{n}_2$ & $\tilde{n}_3$, are defined in Fig. 6.2.

The complex refractive index of the sample can be estimated using this model either by iterative approximation or, in some situations, analytically. If the sample is sufficiently thick so no Fabry-Pérot reflections are present, or if the successive reflections can be isolated from each other, then analytic expressions for n and κ can be found approximately (see Sec. 4.2.1). For thin film samples, however, Fabry-Pérot reflections overlap in the primary T-ray pulse, and an iterative technique must be used.

The thin films studied with double-modulated DTDS in these experiments generated many FP reflections. An iterative approximation technique was used to solve $\tilde{T}_{\text{model}} = \tilde{T}_{\text{exper}} = \tilde{S}_s / \tilde{S}_r$, represented by the flow chart in Fig. 6.11. The iterative parameter estimation algorithm was implemented for normal T-ray TDS. Essentially, a guess was made of the material parameters, and from information on the physical structure of the sample (for example, layer thickness), the algorithm made an estimate of the transmission ratio, $\tilde{T}_{\text{model}}$. This model was compared to the measured transmission ratio, $\tilde{T}_{\text{exper}}$, and any error in the model demonstrated the direction for another estimate of the material parameters (in Fig. 6.11 this is $\tilde{n}_2$). The algorithm typically converged in fewer than 100 estimates. The code for this algorithm is found in Appendix D.

For the DTDS measurements in this Chapter, the sample waveform was calculated from $y_s = y_r - y_d$ because y_d was measured instead of y_d (to achieve a better noise performance). It turns out that y_s can be calculated from $y_r \pm y_d$, depending on the phase of the time-domain pulses, which depended in turn on the phase setting of the LIA. An error in the sign of y_d leads to non-physical estimates of the refractive index and can be corrected. The advantage of using the substitution $y_s = y_r - y_d$ rather than separately deriving the model equation $\tilde{T}_{\text{model}}$ for DTDS was that the accuracy of the algorithm can be tested with normal TDS data before applying it to DTDS data.

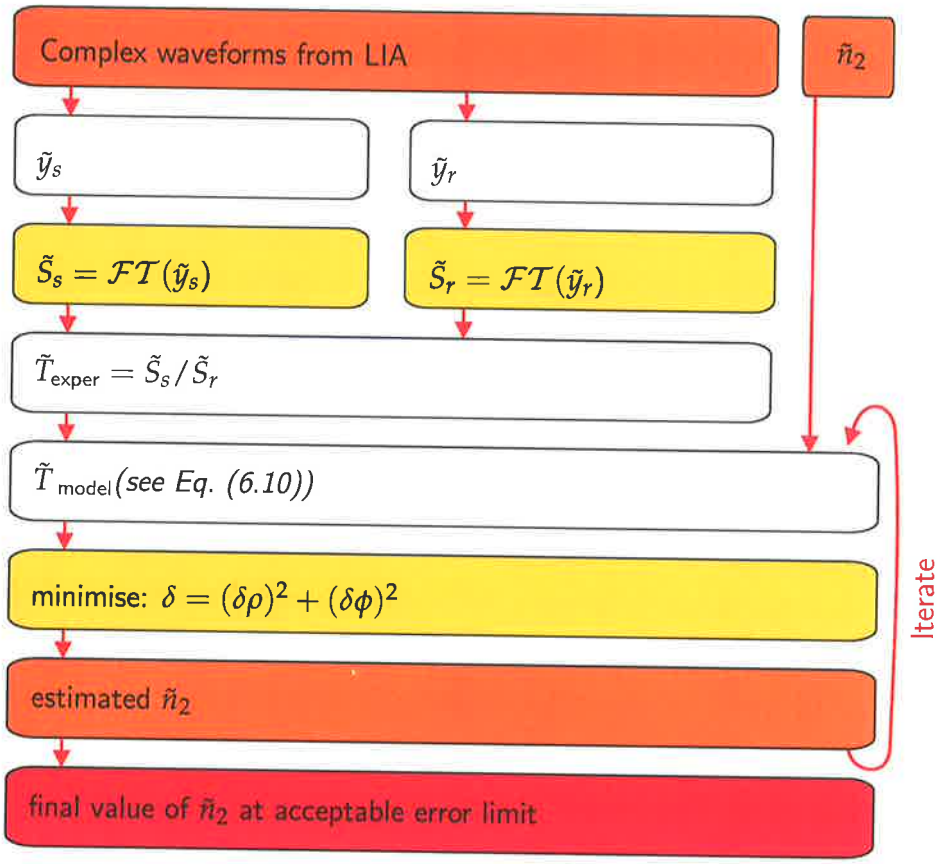

Figure 6.11. Algorithm for iterative parameter estimation. This flow chart shows the algorithm used to iteratively estimate the material parameters n and κ from Eq. (6.10), as described in Sec. 6.3.3 – this algorithm is based on Duvillaret et al. (1996). The complex waveforms $\tilde{y}_s$ and $\tilde{y}_r$ are obtained from the experiment, where the real and imaginary values are the X and Y outputs of the LIA. An estimate of $\tilde{n}_2$ is provided as seed for the search algorithm, which operates to minimise the error metric δ, where $\delta\rho = \log|\tilde{T}_{\text{model}}| - \log|\tilde{T}_{\text{exper}}|$, and $\delta\phi = \arg(\tilde{T}_{\text{model}}) - \arg(\tilde{T}_{\text{exper}})$. The re-estimation step is performed with MATLAB's `fminsearch` function, which minimises a function of several variables, using the simplex search algorithm of Lagarias et al. (1998). This algorithm takes approximately 0.6 seconds to estimate the complex refractive index $\tilde{y}_s$ for each frequency of interest, given 1024 data points in the FFTs and a 1.5-GHz Pentium 4 processor. The MATLAB code is found in Appendix D.

Testing

To confirm that the data processing algorithm was correct, two tests were performed: (i) the standard DTDS algorithm was used to characterise a simple test subject, and (ii) the model was compared to the experimental values once the complex refractive index had been estimated.

Figure 6.12(a) shows the refractive index of a test sample calculated using a standard dual-thickness geometry (see Sec. 4.2.2). The test sample is bulk polyethylene. Figure 6.12(b) shows the refractive index of one of the polyethylene samples calculated using the iterative algorithm depicted in Fig. 6.11. This test confirmed that the parameter estimation algorithm was correct.

To confirm that this model gives transmission data matching the experimental data for the estimated values of $\tilde{n}_2$, the experimental transmission spectrum and the modelled transmission spectrum were plotted in Fig. 6.13. The circles from the modelled transmission spectrum $\tilde{T}_{\text{model}}$ and the crosses from the experimental data $\tilde{T}_{\text{exper}}$ show a one-to-one correspondence.

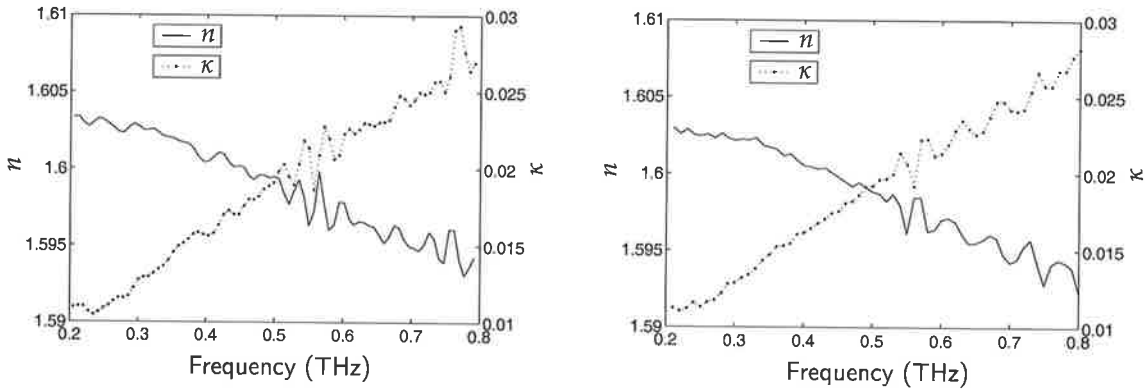

(a) Dual-thickness sample

(b) Iterative algorithm

Figure 6.12. Measured confirmation of parameter extraction algorithms. These measured results were generated in a test of the iterative parameter estimation algorithm in Fig. 6.11. Both Subfigures show the T-ray material parameters of a block of plastic (polyethylene), estimated with different techniques: standard dual-thickness spectroscopy versus the iterative algorithm. The parameters in Subfig. 6.12(a) were estimated using dual sample spectroscopy. In dual-thickness spectroscopy, two samples of the same material are used for a highly accurate measurement, as described in Sec. 4.2.2. The samples have different thicknesses, both sufficiently large to avoid Fabry-Pérot reflections. In this case, the two samples were polyethylene blocks of thicknesses 11.4 mm and 4.73 mm. The T-ray waveform transmitted through the thin sample is used as the reference, so all Fresnel transmission coefficients at the interfaces are automatically accounted for. The advantage of dual sample spectroscopy is that simple and exact analytical expressions to estimate $\tilde{n}_2$ can be easily derived. The parameters in Subfig. 6.12(b) were estimated using the iterative approximation algorithm. The correspondence between the results in Subfigs. 6.12(a) and 6.12(b) confirms the accuracy of the iterative algorithm.

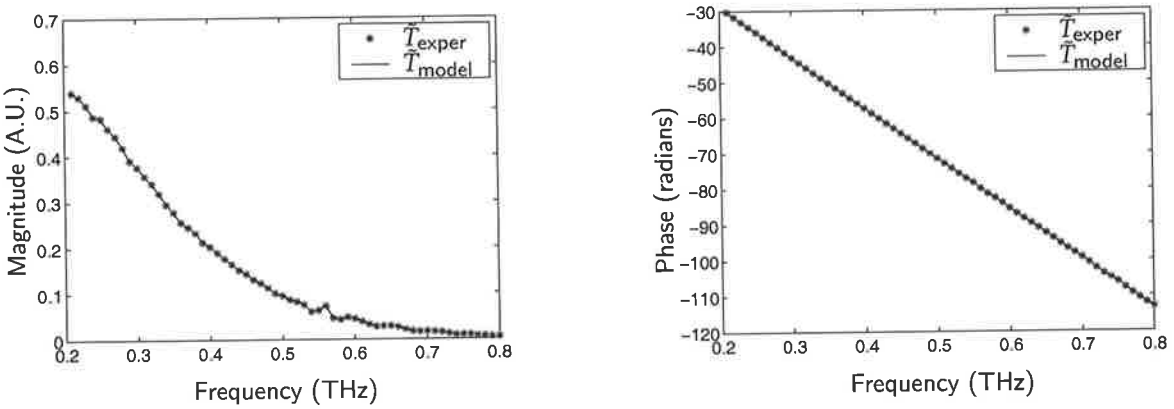

(a) Experiment & model: magnitude

(b) Experiment & model: phase

Figure 6.13. Comparison of modelling and experimental results. Plot of modelled and experimental transmission spectra. These plots confirm that the estimated refractive index and extinction coefficient values do correctly model the transmission spectrum of the experiment. These data are from an 11.4-mm-thick block of polyethylene plastic and the algorithm depicted in Fig. 6.11.

6.4 Results

The improvement of double-modulated DTDS over normal DTDS was demonstrated by: (i) measuring the experimental noise levels, and (ii) measuring the optical parameters of a sample film that was too thin for normal TDS to detect.

6.4.1 Measured noise

The raw time-domain data from a double-modulated DTDS experiment are shown in Fig. 6.14(a). The differential signal is far smaller than the other waveforms, and is 90° out of phase with the reference waveform. The amplitude spectra of the reference and differential waveforms are plotted in Fig. 6.14(b). The band of high SNR from 0.2 to 2 THz in the reference pulse was typical for the 100-fs laser T-ray system. The strong absorption lines were due to water vapour in the air (van Exter et al., 1989b). This was experimentally verified in our system by partially purging the T-ray beam path, shown in the air-tight box in Fig. 5.3, with dry air. The water lines are removed in the deconvolution process, but still result in a lower SNR at affected frequencies. The differential signal has a reduced bandwidth due to the decreased SNR, although the approximate shape is the same as the reference spectrum.

The noise level in these measurements was estimated through repeated measurements. Each experiment was repeated four times over a day to estimate the uncertainty. The experimental errors for TDS and DTDS are summarised in Table 6.3. As described in the caption of Table 6.3, the observed noise was less than expected because the noise in each waveform is correlated to some extent. The noise values for DTDS are larger than TDS only because double-modulation halves the signal, and noise is introduced by the galvanometer – at higher frequencies, where double-modulated DTDS is used, the noise due to DTDS drops proportional to the modulation frequency. The results of this experiment demonstrate the accuracy of the DTDS technique, and confirm the estimates of noise reduction from thin film samples.

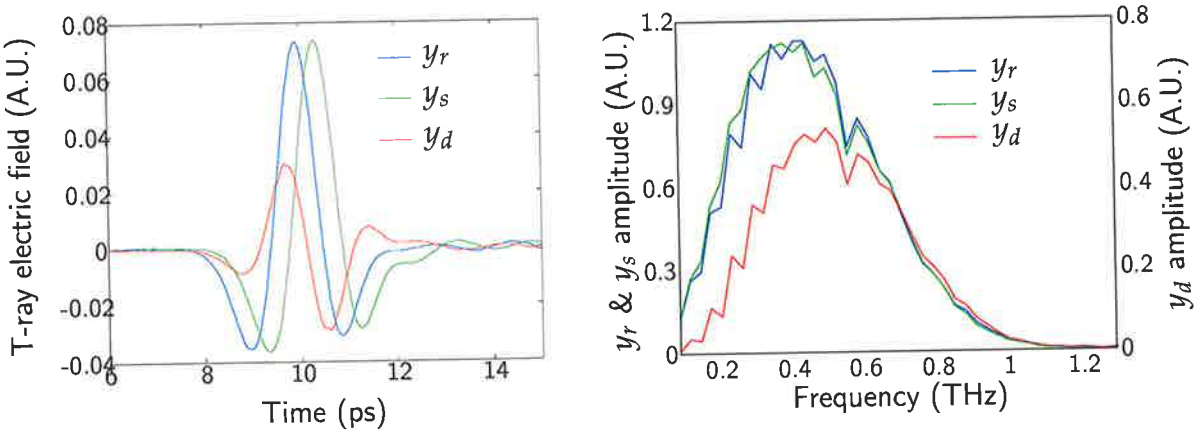

(a) Free space T-ray waveforms

(b) T-ray transmission spectra

Figure 6.14. Measured DTDS waveforms and spectra. These two graphs compare the differential pulse to the reference and sample pulses in both the time and frequency domain. The reference pulse y_r has the largest amplitude. The sample pulse y_s has a reduced amplitude and phase shift, which is characteristic of the material being studied. The differential pulse is the difference $y_d = y_r - y_s$. The differential pulse also approximates the slope of y_r, as discussed at the start of Sec. 6.2.1. These measurements were taken with a LIA time constant of 100 ms, at room temperature. The bandwidth of the reference pulse is typical for a T-ray system, driven as it is by T-ray generation from a GaAs surface using 100-fs optical pulses. The absorption lines in all three spectra, at 0.56, 0.75 and 1.1 THz, were caused by water vapour in the air (van Exter et al., 1989b).

Table 6.3. Calculated and measured errors for TDS vs. DTDS (without double-modulation). This Table shows calculated and observed measurement fluctuations for the 0.5-THz frequency component of the reference, differential and transmission spectra. The fluctuation level at 0.5 THz was chosen because it is close to the peak of the frequency spectrum (see Fig. 6.14(b)). The measured errors were determined from the spread of four repeated measurements under identical conditions. The raw error in DTDS is much larger than for TDS for two main reasons: firstly, this data was taken with double-modulation, so the signal level is half that in TDS. Secondly, there is noise inherent in the galvanometer system, which contributes to measurement fluctuations. The calculated $|\Delta T/T|$ were estimated using the equation in Table 6.2 for TDS and from Eq. (6.7) for DTDS. Equation (6.7) must be used because, in this experiment, the condition expressed in Eq. (6.8) does not hold. The observed $|\Delta T/T|$ were determined from four numerical calculations of the transmission amplitude at 0.5 THz. The observed values are both less than the expected values. This probably arises from the assumption of uncorrelated noise in successive measurements. The measurement-to-measurement fluctuations for the reference, sample and differential waveforms is correlated to some extent, so there is an element of noise cancellation in the deconvolution calculation that determines $\tilde{T}$.

	Measured	Calculated $\lvert\Delta T/T\rvert$	Observed $\lvert\Delta T/T\rvert$
TDS	$\left\lvert\frac{\Delta S_r}{S_r}\right\rvert = 1.0\%$	1.4%	1.0%
DTDS	$\left\lvert\frac{\Delta S_d}{S_d}\right\rvert = 4.6\%$	2.4%	1.4%

Figure 6.15 shows the noise spectrum of the T-ray system, and demonstrates the benefits of using double-modulated DTDS (d-DTDS) over 'normal' DTDS. Normal DTDS has a noise level of $0.5/\sqrt{\text{Hz}}$ at the maximum frequency of the galvanometer. Double-modulated DTDS had a noise level of $0.02/\sqrt{\text{Hz}}$ at the maximum frequency of the chopper – using an optical chopper with double-modulation showed a order of magnitude improvement in the noise performance of a thin film measurement. This could be further improved by modulating f_1 at even higher frequencies, up to 3 MHz, using an acousto-optic or electro-optic modulator.

The spectrum in Fig. 6.15 was measured using a Lock-In Amplifier (LIA) at values of frequency from 2 Hz to 2 kHz. The galvanometer was used to measure noise from 2 to 10 Hz and an optical chopper was used for 10 Hz to 2 kHz. Each set of measurements was repeated, giving upper and lower bounds of error in the measurements. For these values the delay stage shown in Fig. 6.4 was set at the pulse peak, and each noise value was measured using the Lock-In Amplifier (LIA), resulting in root-mean-squared noise value found at the peak of the T-ray signal pulse. The measured noise value from the LIA was normalised to the actual value of the T-ray peak, to account for very slow laser fluctuations, and to the bandwidth of the LIA low-pass filter – this value can be considered an *inverse* signal-to-noise ratio. There is a clear discrepancy between the noise level of the chopper modulation and the galvanometer modulation. This noise increase is due to the physical instabilities in the galvanometer and slight fluctuations in its modulation frequency. This problem could be reduced by engineering a better shaker and drive circuitry.

The measured noise spectrum in Fig. 6.15 has a $1/f$ trend, which is typical of laser noise spectra (von der Linde, 1986). System noise measured under chopper modulation corresponds well to this relationship, until it is driven at higher frequencies, above 500 Hz. The optical chopper used in this experiment has an operational limit of 6 kHz, and at the higher operating frequencies starts to introduce additional noise into the system. This could be avoided by using a modulator designed for higher frequency operation, such as an acousto-optic modulator, allowing noise reduction to the shot noise floor (Andor et al., 1984).

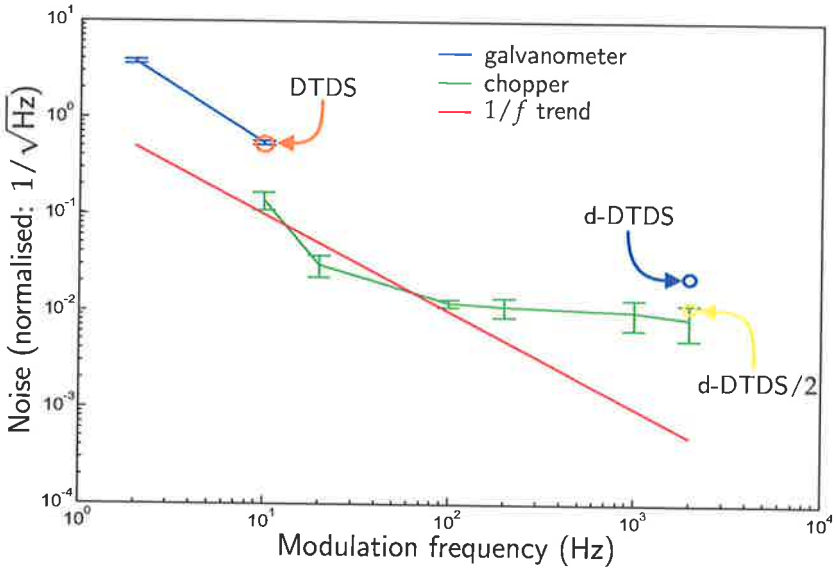

Figure 6.15. Measured noise spectrum. This plot shows the experimental noise density spectrum of the T-ray system as a function of increasing modulation frequency. The noise reduction due to double-modulation is the difference in noise between the low and high modulation frequencies. The noise spectrum measured with the galvanometer and the optical chopper are compared to a theoretical $1/f$ trend, which is typical of experiments dominated by laser noise. The measured noise spectra are normalised to the signal strength – in effect this is a plot of the inverse signal-to-noise ratio. Error bars indicate the repeatability of the measurements. Both modulators show noise spectra that follow a $1/f$ trend, although the noise level with galvanometer modulation is larger, due to mechanical instabilities and jitter in the shaking frequency. The measured noise level of the normal (one LIA) DTDS experiments in this Chapter, which used only a 10 Hz galvanometer, is shown as a single point marked 'DTDS'. The noise level is shown as a single point because at that modulation frequency, the normalised noise density is constant. The noise level lies on the noise spectrum of the galvanometer, as expected. The measured noise level of the double-modulated DTDS experiments in this Chapter, in which a 2-kHz chopper was used in addition to the galvanometer, is shown as a point marked 'd-DTDS'. The 'd-DTDS' point is greater than the measured chopper noise at a 2-kHz modulation frequency because the SNR is halved in double modulation, basically because inserting the chopper cuts away 50% of the power. The point 'd-DTDS/2' indicates half the noise value of 'd-DTDS'. The 'd-DTDS/2' point is shown to demonstrate that, had the signal level not been halved by the dual modulators (and thus the noise-to-signal ratio doubled), the experimental noise would fit within the error bounds of the chopper noise spectrum.

6.4.2 Example thin film characterisation

Figure 6.16 shows the estimated optical parameters of a SiO_2 thin film from 600 GHz to 1.6 THz. The experimental values, indicated by crosses, are compared to the predicted values in the literature (Palik, 1985). Although there is some variation in the estimated parameters due to noise, they correspond to the predicted value of refractive index and extinction coefficient within ± 0.2. The error in refractive index is $\pm 10\%$. The κ value was identified to within the bounds 0.0 to 0.4, which is an accuracy comparable to measurements of very low absorption values in the literature. These results confirm that the experimental technique and modelling is able to estimate the optical parameters of thin films with usable accuracy.

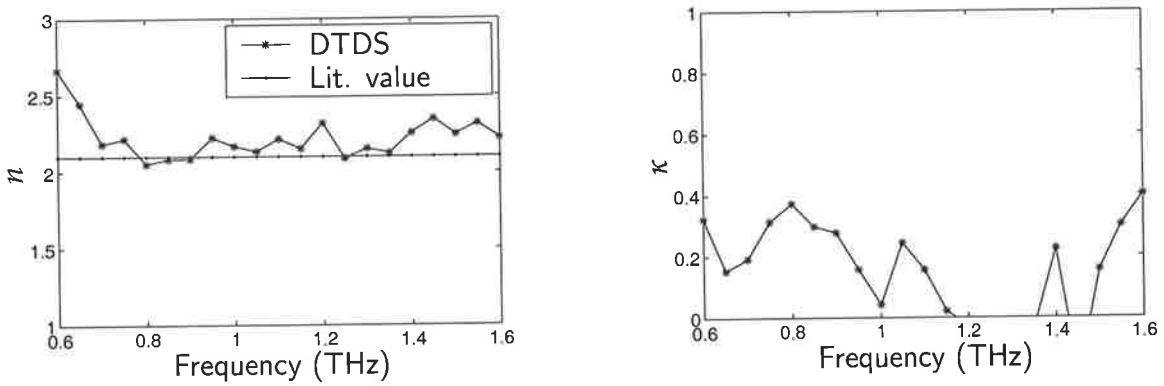

(a) Refractive index

(b) Extinction coefficient

Figure 6.16. Measured optical parameters of SiO_2. These graphs show the estimated optical parameters of SiO_2 thin film. The refractive index n is comparable to values for SiO_2 given in the literature ($n = 2.1$) (Palik, 1985). The literature value for the extinction coefficient has been omitted because there is some disagreement on its value at this frequency. The bandwidth of these measurements is limited primarily by the limited bandwidth of the differential signal, whose spectrum is shown in Fig. 6.14(b). The error in the estimates of n and κ is about ± 0.2 – the zero values for κ are due to measurement uncertainty.

6.5 Conclusion

The experimental results in this Chapter demonstrate three main points. Firstly, DTDS has a better noise performance than TDS for thin film characterisation, by a factor of $|\tilde{S}_d|/|\tilde{S}_s|$, which increases for thinner sample films, and is therefore ideal for thin film characterisation (Table 6.3). Secondary, double-modulation enables noise reduction by at least an order of magnitude, which can be further improved by modulating at even higher frequencies (Fig. 6.15). Lastly, double-modulated DTDS was used to characterise the parameters of an actual thin film sample (Fig. 6.16).

6.5.1 Future work

There are a number of system improvements and potential applications that remain to be explored in double-modulated DTDS. It is expected that the noise of the system can be further reduced by using a modulation frequency higher than 3 kHz, coupled with a radio-frequency LIA.

This simple technique will enable thin films to be characterised in the GHz-THz range for fast integrated circuit technology, and for novel work in T-ray biosensors. Novel T-ray biosensors are described in Ch. 7.

6.6 Chapter summary

The work in this Chapter demonstrated for the first time: (i) the application of double-modulation to improve the SNR of DTDS of thin films (by over an order of magnitude), (ii) a mathematical quantification of the improvement, and (iii) an experimental implementation of the double-modulated DTDS system.

The following Chapter details the application of double-modulated DTDS to characterising thin biomolecular films for lab-on-a-chip applications. It is valuable to be able to non-invasively probe the hydration, conformation and activity of protein films used, for example, as enzyme catalysts layered on inorganic substrates. DTDS is an ideal technique for such research.

Double-modulated DTDS was first applied to liquid samples in the experiments described in Ch. 8.

Chapter 7

T-ray Biosensing

T-RAY biosensing is a new field in T-ray science. This Chapter presents a new bioaffinity sensor based on double-modulated DTDS, able to sensitively detect the presence of ultra-thin bound biomolecular layers. There has been no previous demonstration of bioaffinity detection using the unique properties of T-rays.

Biosensor technology is used in bioscience, health care, food monitoring and hazardous substance detection. The biosensor described in this Chapter is simple, non-invasive, inexpensive and does not require hardware modification in a typical T-ray spectrometer.

7.1 Introduction

A typical biosensor detects the presence of biomolecules that deposit to certain sites on a pre-prepared sensor chip – the importance of biosensing to health care and is described in Sec. 7.1.1. In this Chapter, a novel biosensor is demonstrated, based on T-ray Differential Time-Domain Spectroscopy (DTDS), thus benefiting from the sensitivity of the technique to thin biomolecular layers. The T-ray biosensor was tested experimentally, as described in Secs. 7.2 and 7.3, and the results were modelled by considering transmission of the T-ray radiation at the thin film interfaces, in Sec. 7.5.

7.1.1 Motivation

There is a need for non-invasive biosensor technology in health care, food monitoring and hazardous substance detection. 'Biosensor' is a broad term for technologies that detect the presence of biomolecules, for example the presence of glucose in an aqueous mixture. The Freedonia Group, an industrial research firm, predicts that the $2.3 billion US chemical sensor industry will grow at a rate of 8.6% per annum until 2007 – this growth is predicted to be primarily in the areas of optical sensors and biosensors, and specifically in the large medical diagnostic segment (Group, 2002). The T-ray biosensor described in this Chapter has the potential to enter this market in a niche for non-invasive detection based on T-ray material properties.

7.1.2 Previous studies

Optical detection techniques of biomolecules have been used for more than a decade in the analytical laboratory, since they provide a possible means of detecting biomolecules.

The most successful optical biosensor in the market place is Surface Plasmon Resonance, SPR, (Kalsson and Stahlberg, 1995; Song and Swanson, 1999). A SPR system monitors the binding of molecules to a sensor by probing refractive index changes of the target layer relying on the principle of *bioaffinity*, that is the affinity between two biomolecules. Bioaffinity can be used in a biosensor by attaching a layer of sensor molecules, or *analytes*, to a sensor slide, as shown in Fig. 7.1. The biosensor slide is used by exposing it to a mixture of unknown molecules, to test if any target molecules, or *ligands*, are present. SPR detects this new layer by probing the refractive index change

with an optical laser beam – a change in refractive index results in a change in the intensity of light reflected off the film at some angle, given by the experiment. SPR relies on the refractive index change at optical wavelengths, as determined by the laser. Certain biomolecules, however, do not show contrast at optical wavelengths. Some such molecules could be sensed using T-rays.

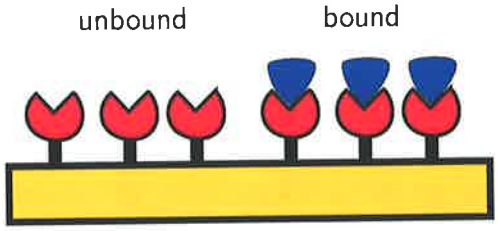

Figure 7.1. Model of ligand-analyte binding. This sketch shows a slide with chemically attached sensor molecules, for example Avidin. The sensor molecules have a strong binding affinity for a target molecule, for example Biotin, which creates a second layer of material when it binds to the sensors. Other molecules that do not bind to the sensor will be washed away and not form an extra layer. The ligand is chosen to have a high binding affinity and high specificity (that is, it will not bind to non-target molecules) for the analyte.

The most useful techniques for monitoring on-off binding at T-ray frequencies have been Attenuated Total Internal Reflection Fourier Transform Infrared (ATR-FTIR) spectroscopy and Raman spectroscopy (Deckert et al., 1998; Regan et al., 1996). Unfortunately, the complications associated with cryogenic detectors in FTIR, and Rayleigh lines in Raman spectroscopy are among the anomalies that hamper FTIR and Raman spectroscopy from being widely used.

A new detection method based on T-rays operating on the same principle as SPR has been proposed, and used successfully to detect minute amounts of label-free DNA molecules (Menikh et al., 2002). This approach uses integrated T-ray waveguides, incorporating resonant T-ray structures, and has achieved femtomole (fm) sensitivity to label-free DNA hybridisation using T-rays (Nagel et al., 2002b; Nagel et al., 2002a). This approach opens up new avenues for label-free detection. However, the integrated waveguides require application-dependent hardware modifications, delicate sample handling procedures, and the interconnection of a large number of resonators for simultaneous detection. The free-space T-ray biosensor proposed in this Chapter would use a standard T-ray spectrometer.

The current state-of-the-art in biosensor technology is the microbalance, which has achieved femtogram (fg) mass detection (Lavrik and Datskos, 2003). Driven at MHz

frequencies with a diode laser, the tiny cantilevers (tiny slivers of Silicon as small as 2 μm long and 50 nm thick) are exposed to an atmosphere of small particles or molecules. Depending on how the cantilever is coated, some of the particles will be absorbed onto the surface of the cantilever, altering its resonance frequency in a measurable way. In a recent test, the vapour used was an acidic substance, which was absorbed with a mass change that was noticeable at the 5 fg level. Other subject particles, such as DNA, proteins, cells, or trace amounts of various chemical contaminants, should be detectable by this process. The experiment was carried out at room temperature, pressure and humidity (Lavrik and Datskos, 2003). The sensitivity of the quartz microbalance represents the goal to achieve with the proposed T-ray biosensor. The T-ray biosensor will not require expensive cantilever sample slides, and samples can be probed without physical contact, making the process rapid and easy to automate.

7.1.3 Objective summary

This Chapter describes the development of a new biosensor technique that can achieve high sensitivity using an unmodified T-ray spectrometer. The objective is to detect the presence of molecules that bind to a biosensor slide, relying on the altered T-ray transmission characteristics of the detected layer. The experiments use a double-modulated DTDS technique, described in Ch. 6, to measure the T-ray response of carefully prepared biomolecular samples. The origin of the T-ray signals is modelled using a simple understanding of dielectric layers. Although other techniques exist, such as SPR, for detecting thin films, there is no well-developed technique that relies on the T-ray characteristics of the films.

The proposed T-ray biosensor is, like SPR, a bioaffinity detector. A common bioaffinity pair is Biotin and Avidin. Biotin is a water-soluble lipid, and is commonly referred to as *vitamin H* – a member of the B-complex group of vitamins. Avidin is a protein that occurs in raw egg white and is remarkable for its high binding affinity for Biotin, as discussed in Sec. 7.2.1. T-ray DTDS is known to detect the presence of thin films, for example SiO_2 in Ch. 6. In this Chapter, T-ray DTDS is used to detect the presence of thin bound biomolecular layers.

7.2 Preliminary experiments

Preliminary experiments were used to test the sensitivity of the T-ray DTDS spectrometer to thin layers of bound biomolecules. T-ray signals were observed for Biotin molecules bound to an Avidin sensor, Avidin molecules bound to a Biotin sensor, bead-enhanced Avidin bound to Biotin, and the explosive trinitrotoluene (TNT) bound to TNT antibodies.

Avidin and Biotin together constitute a pair of biomolecules commonly used in demonstrations of bioaffinity, due to their high binding affinity. Bead-enhanced Avidin target molecules, sketched in Fig. 7.11, create a much thicker molecular layer than Avidin target molecules alone. Avidin is enhanced by binding to large, μm-sized Agarose beads. Agarose is an inert substance, extracted from Agar, that is easy to *derivitise*, or attach to other biomolecules. The Agarose beads attached to the Avidin amplify the target layer thickness, potentially increasing the biosensor's signal.

Trinitrotoluene is a common explosive and a hazardous substance that is important to detect in security situations. TNT is therefore an important target molecule. A sensor molecule is available, the TNT antibody (Bromberg and Mathies, 2003). This antibody has a very strong affinity for TNT molecules, and can be attached to biochips in a similar way to Biotin (Bowen et al., 2003). A TNT biosensor slide is demonstrated in Sec. 7.2.3, with TNT molecules binding to their antibodies.

7.2.1 Sample preparation

The protein Avidin was chosen to test the T-ray biosensor due to its high binding affinity to the lipid Biotin and its usefulness in other applications. Avidin comprises four identical subunits, each of which binds one Biotin molecule – see Fig. 7.2. The binding affinity between Avidin and Biotin is so high ($K_a = 10^{15}$ mol^{-1}) that the formation of this complex can be regarded as nearly irreversible, on a scale comparable to a covalent bonding (Green, 1975). The high binding affinity of this system has found many applications, for example in affinity chromatography, in attaching antibodies to solid surfaces, precipitating liposomes, or targeting cells with liposomes (Cuatrecasas and Wilchek, 1968; Wilchek and Bayer, 1988). Importantly, it has been shown that Biotin can be adsorbed to a hydrophobic surface without losing its specificity towards Avidin, leading to the possibility of studying ligand-analyte interactions on supported lipid membranes.

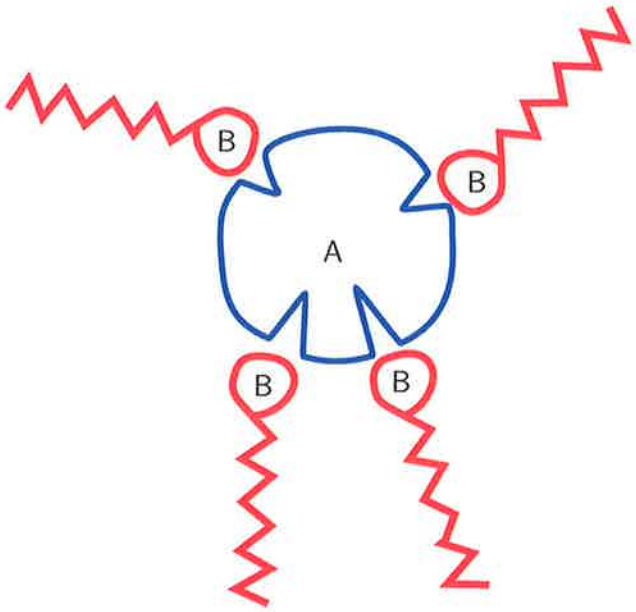

Figure 7.2. Sketch of Biotin and Avidin molecules. This sketch shows sketches of the molecules Biotin (marked 'B') and Avidin (marked 'A'). The essential characteristics of Biotin are the polar head and long non-polar tail. Avidin, a protein, has four binding sites for Biotin. Biotin-Avidin binding is sketched in Fig. 7.11. The molecules are not to scale.

The biosensor samples were prepared on quartz slides. Quartz is largely transparent to T-rays and biosensor molecules can be chemically attached to its surface. A photograph of a typical quartz slide used in our experiments is shown in Fig. 7.3. Two films of unusually high thickness have been deposited on the slide to make the bound and unbound areas clearly visible.

Prior to deposition of the Avidin film, the quartz slides were cleaned with 50% hot nitric acid, and rinsed several times with doubly-distilled water. To attach the biosensor molecules to the slide, the quartz substrate was derivitised by placing it in a 5% solution of 3-mercaptopropyltrimethoxysilane in toluene for 1 hour. An organic cross linker, succinimide ester, was dissolved in 3-millimolar (mM) dimethylformide, and the silanized substrate was treated with the cross linker for another 1 hour, washed thoroughly in phosphate buffered salt (PBS) solution and dried under vacuum.

To coat the first slides with a layer of Avidin sensor molecules, a small volume of 200-ml solution of 0.2-mg/ml Avidin in sodium phosphate buffer (pH 7.4) was applied to each quartz slide and allowed to incubate for about 30 minutes. After washing and drying under nitrogen, half of the biosensor slide was exposed to 15 ng of Biotin dissolved

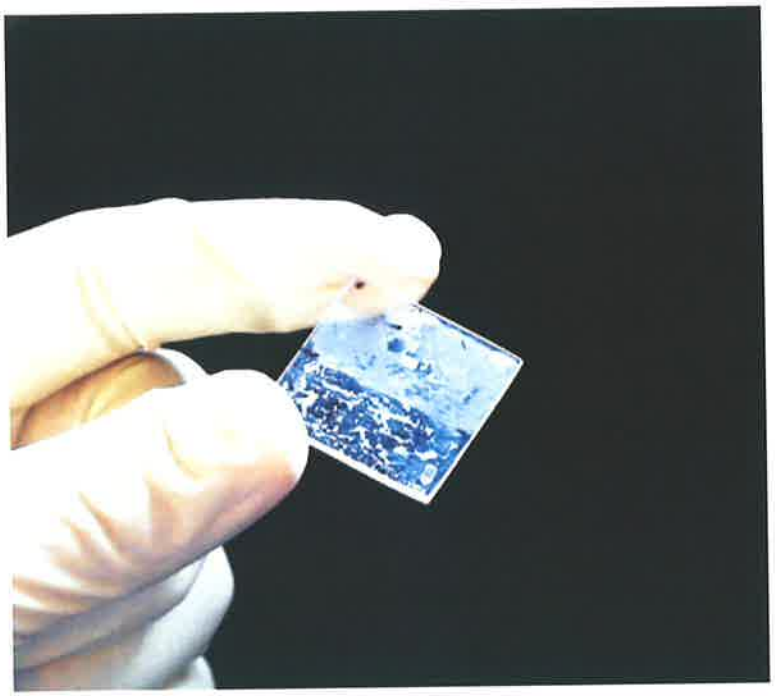

Figure 7.3. Photograph of biosensor slide. Showing a layer of TNT antibody bound to TNT on a 1-inch-square quartz slide. A very thick layer of antibodies has been deposited to make it visible. The entire film was coated with antibodies and the upper right-hand half was exposed to target molecules. A thick layer of molecules was deposited by evaporation to show the film in this photograph. A dark point in the top corner was used to orient the sample, after preparation, in the T-ray spectrometer.

in a mixture of (2:1), and then washed with pure chloroform/methanol to remove any unbound Biotin. The reference sample was not exposed to the Biotin solution. A sketch of the prepared slide is shown in Fig. 7.4.

In the case of TNT the quartz slide was derivatised as described above and then 0.5-mg of anti-TNT antibody was allowed to interact with the quartz slide surface. As with Biotin, half of the biosensor slide was exposed to TNT in solution, and then washed with a mixture of chloroform/methanol (2:1) to remove any unbound target molecules.

7.2.2 T-ray spectrometer

The double-modulated DTDS system used in this work has been described in Ch. 6, and is schematically represented in Fig. 7.5. The femtosecond laser source generated 150-fs pulses at 86 MHz and 1.5 W of average power. A beam splitter separated the

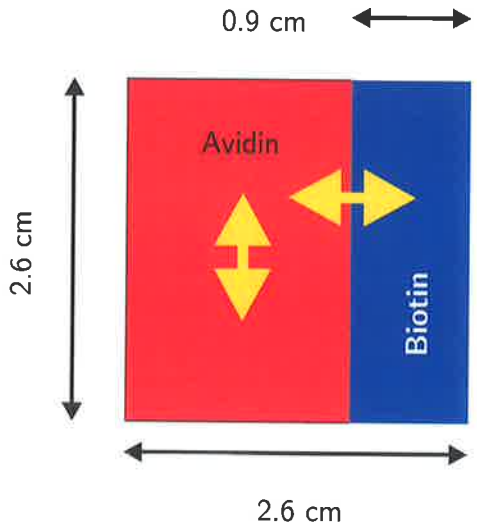

Figure 7.4. Sketch of Biotin-Avidin slide. Sample slide for preliminary experiments, showing approximate dimensions in cm. The yellow double-headed arrows approximately indicate the scan range of the T-ray beam across the sample, which was about 10 mm peak-to-peak. The two cases indicated are *Avidin* for a test of the signal that occurs due to surface inhomogeneities, and *Biotin* for a test of bioaffinity sensing. These cases correspond to the waveforms in Fig. 7.6.

laser beam into pump and probe pulses. The probe pulse illuminated an unbiased GaAs semiconductor emitter wafer to generate T-rays, which were collimated and focused onto an Electro-Optic Sampling (EOS) crystal with parabolic mirrors. A pellicle after the second parabolic mirror allowed the reference beam to travel collinearly with the T-ray wave through the electro-optic (EO) crystal ⟨110⟩ ZnTe. A quarter-wave plate (QWP), a Wollaston polarising beam splitter and a pair of balanced photodiodes comprise the crossed-polariser detector (described in Sec. 3.3.2). The quartz slide was mounted on a galvanometer and dithered in the T-ray beam at 10 Hz over a peak-to-peak distance of about 10 mm.

The detection electronics were implemented using two Lock-In Amplifiers (LIAs, manufacturer: Stanford Research Systems, model: SR830 DSP). The time constant on the LIAs used at 2 kHz was 100-ms, which determined the detectors' noise bandwidth and thus the system SNR – see Sec. B.7 for a description of LIA operation.

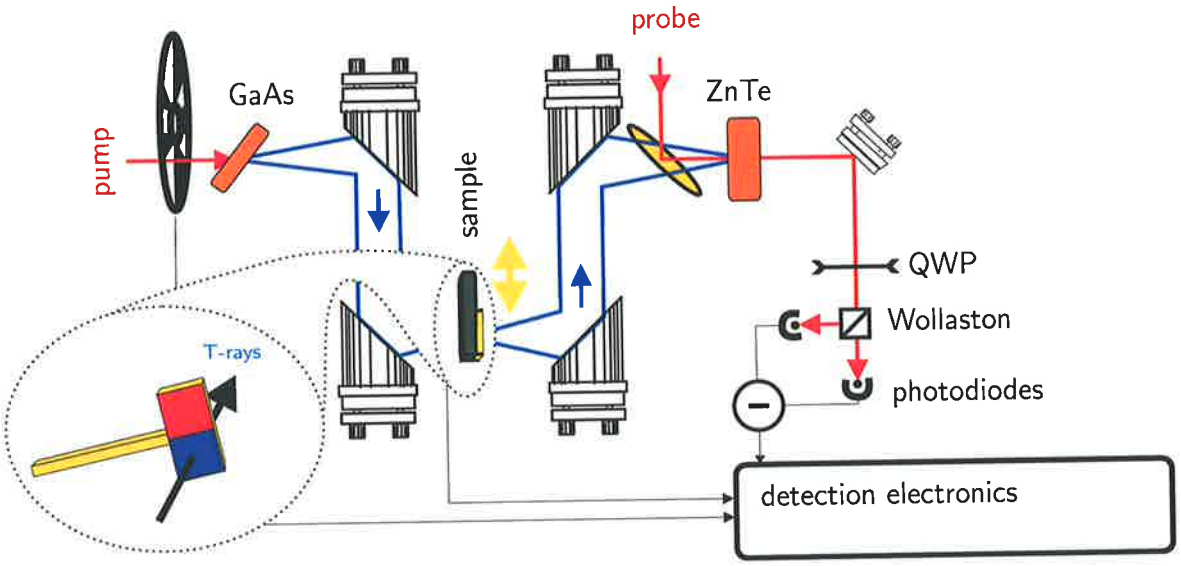

Figure 7.5. DTDS spectrometer schematic. This schematic shows the terahertz biosensor system, with an unbiased GaAs crystal T-ray emitter, and a ⟨110⟩ ZnTe crystal detector. The sample was dithered in and out of the T-ray beam by a galvanometer at a frequency of 10 Hz. The T-ray beam was apertured to have a 2-mm diameter, which corresponded to approximately 90% transmission of T-ray power through the aperture. The travel distance of the sample slide was approximately 10 mm peak-to-peak, driven by a sinusoidal wave input. The detection electronics demodulated the 10-Hz sample modulation and suppressed background noise (phase-sensitive detection). A detailed functional implementation of this system is described in Ch. 6, especially Fig. 6.4, including those parts of the diagram obscured by the blow-up view of the sample.

7.2.3 Preliminary results

The preliminary experiments tested the sensitivity of T-ray DTDS to biomolecular layers of Biotin, Avidin and TNT.

The first samples tested were of target Biotin molecules bound to an Avidin-coated sensor slide (see Fig. 7.4). The result of this test was the T-ray DTDS waveform measured through the sample and labelled 'Biotin-Avidin' in Fig. 7.6. The time-domain waveforms are sufficient to distinguish between the bound and unbound states of the biosensor. To estimate the accuracy of the result, and test that the signal was coming from the bound layer of target molecules alone, a DTDS signal was measured from the slide where no Biotin was present, labelled 'pure Avidin' in Fig. 7.6 and corresponding to the vertical yellow arrow in Fig. 7.4. The waveforms shown in Fig. 7.6 indicate that

the DTDS signal caused by the presence of a thin layer of target molecules is larger than the signal from the sensor with no target molecules present. This indicates the potential utility of a T-ray-based biosensor.

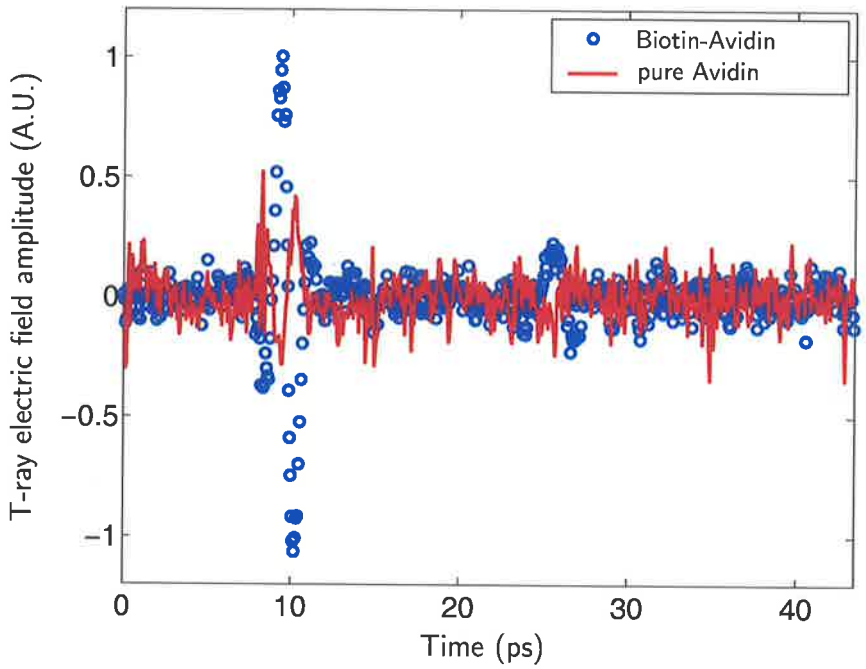

Figure 7.6. Preliminary results showing bioaffinity detection with a T-ray spectrometer. Two time-domain scans are made, one to test for the presence of an Avidin layer ('Biotin-Avidin') and one to confirm that the measurements are due solely to the Avidin layer ('pure Avidin'). The DTDS waveform caused by dithering across the Biotin-Avidin boundary (see Fig. 7.4) is shown in blue circles. This signal is greater than 2× the noise level due to surface inhomogeneities in the film, shown in red. The concentration of the Avidin layer is less than 15 ng/cm^2. These waveforms were detected with a LIA time constant of 300 ms and each scan took 15 mins. The spot size of the T-ray beam on the sample is 5 mm, limited by a metal iris placed in the beam path less than 5 mm from the sample (99% of signal transmitted). The SNR is 10. The secondary pulse is due to a Fabry-Pérot reflection of the T-ray pulse inside the quartz slide.

The noise signal ('pure Avidin') in Fig. 7.6 is larger than the background noise of the T-ray DTDS system. To test whether it was due to inhomogeneities in the prepared surface of the biosensor slide, the surface was imaged using an Atomic Force Microscope (AFM). A scan of the slide surface is pictured in Fig. 7.7, where the roughness in the surface is visible.

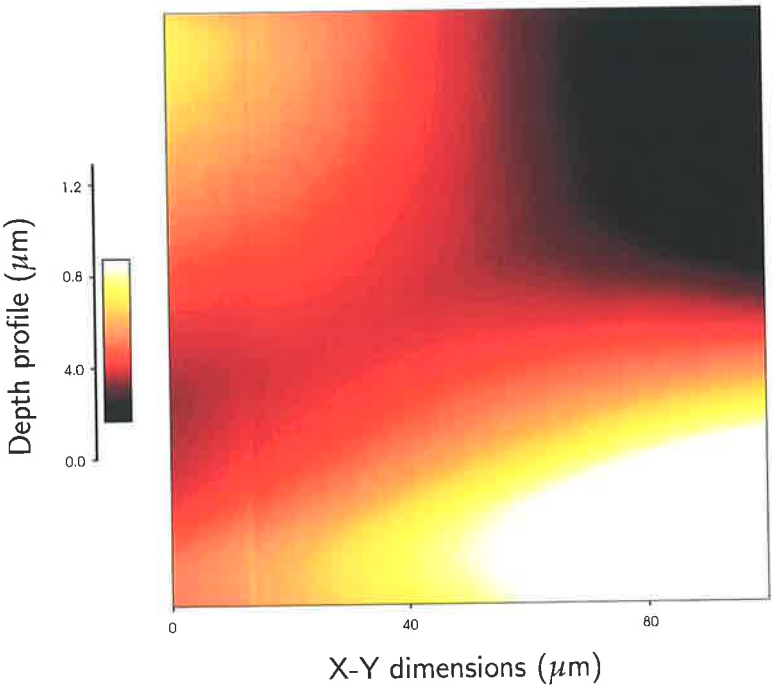

Figure 7.7. Measured physical structure of Biotin on Avidin. An Atomic Force Microscope (AFM) scan of the Biotin surface gives an indication of the roughness of the biosensor film. Surface inhomogeneities are the main contributing factor to the spurious signals labelled as pure Biotin in the waveform graphs. The roughness is approximately ± 0.3 μm, or 5% of the target molecule layer.

The surface roughness of the prepared slide is compared to the thickness of the target molecule layer in Fig. 7.8. The thickness of the target layer is greater than the roughness of the surface, thereby generating a differential T-ray signal. However two other factors also contribute to the biosensor signal: (i) the increased thickness is constant, whereas the roughness is averaged out over the area of the T-ray beam, and (ii) the T-ray radiation is modulated not only by the thickness of the layers, but by reflections at the boundary between Avidin and Biotin molecules. The reflection at the interface between the layers is shown in models to be the main contributing factor in the amplitude of the T-ray DTDS signal (see Sec. 7.5).

In a second set of preliminary experiments, the T-ray bioaffinity detector was extended to antigen-antibody affinity detection using TNT and a TNT antibody. The waveform in Fig. 7.9 shows a signal from a 10-ng/cm^2 TNT target layer compared to the noise from sensing a pure antibody layer. Figure 7.10 shows the same signal smoothed using

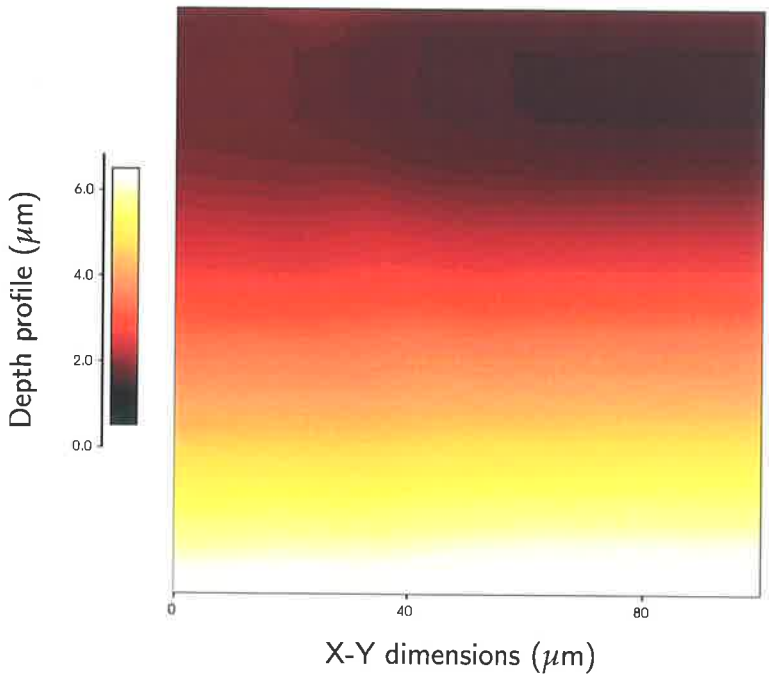

Figure 7.8. Measured boundary between Biotin and Avidin. This Figure shows an Atomic Force Microscope (AFM)i scan at the edge of our target layer of Biotin captured with an Avidin sensor. The step size indicates a layer thickness of 6 μm. The thin layer of target molecules, with a different T-ray dielectric constant (or refractive index) to the underlying sensor layer attenuates and delays the transmitted T-rays. The biosensor operates on this principle as discussed in Sec. 7.5.

a bandpass filter to cut out the background noise, thereby showing the biosensor signal more clearly.

The preliminary results in Sec. 7.2.3 show the potential of the T-ray biosensor for detecting the difference between thin biomolecular films with and without a bound layer of target molecules. The examples shown are protein-lipid binding (Biotin-Avidin), enhanced Avidin binding to Biotin (enhanced with Agarose beads), and antigen-antibody binding (with TNT). The preliminary experiments do not, however, fully quantify the sensitivity and selectivity of the biosensor, so a set of highly repeatable experiments using enhanced Avidin are presented in the following Section. The demonstrated potential for T-ray bioaffinity sensing remains to be fully explored.

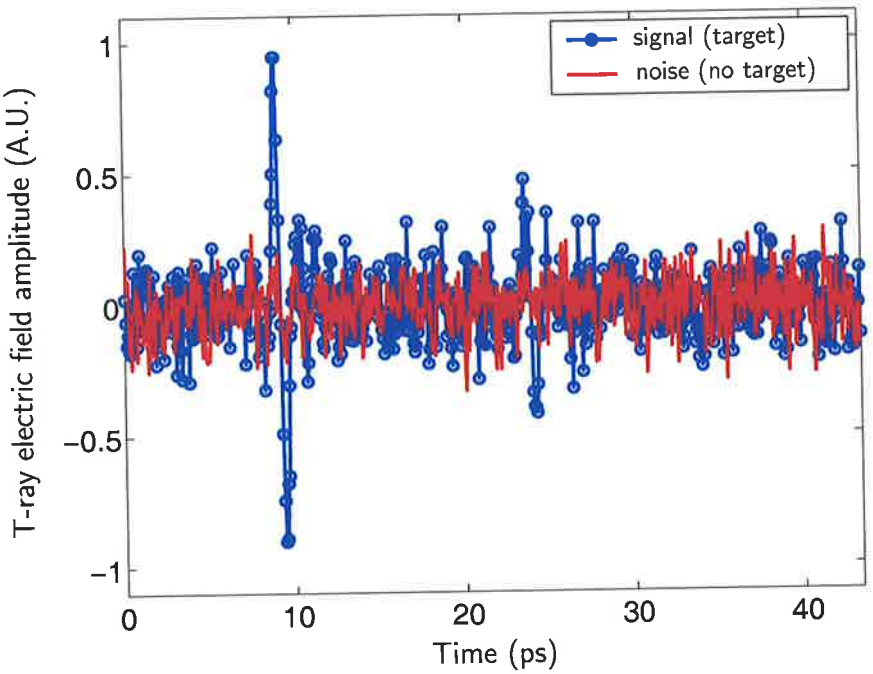

Figure 7.9. Preliminary measured results from an example of antibody-antigen binding using a TNT-antibody to detect TNT. The measured DTDS waveform from a TNT layer, shown in blue, is greater than twice the amplitude of the system noise, shown in red. The beam was apertured to 3 mm diameter (95% of signal) and the SNR was 2. The LIA time constant was 100 ms, each scan took 4.5 mins. The secondary pulse, which is more visible in Fig. 7.10, is due to a Fabry-Pérot reflection of the T-ray pulse inside the quartz slide.

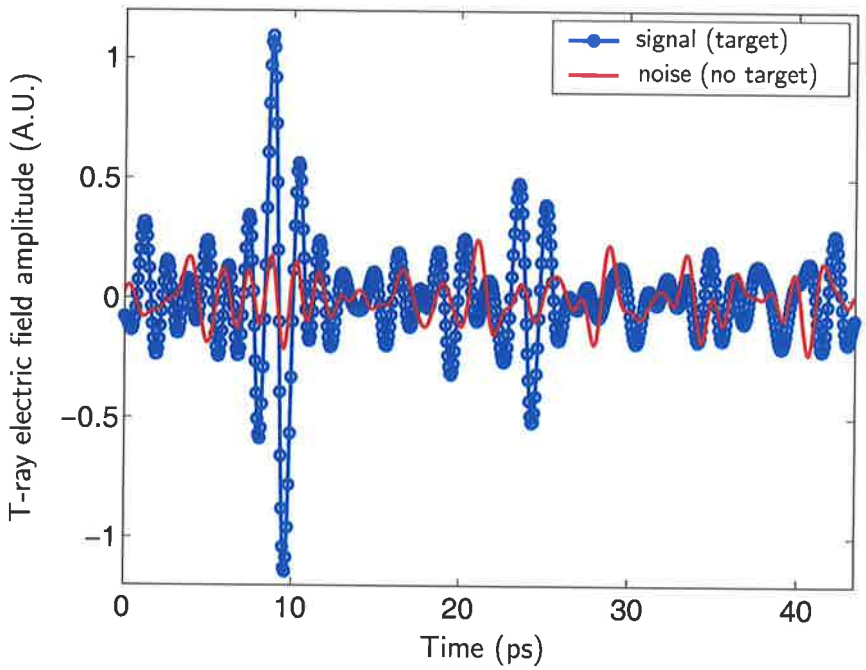

Figure 7.10. Preliminary measured results from TNT antibody-antigen binding – smoothed waveforms. This plot shows the same data as in Fig. 7.9 after smoothing. The SNR was increased by digitally smoothing the waveforms in Fig. 7.10 to block frequencies where the T-ray spectrum is very low – the waveform was bandpass filtered between 0.2 and 0.8 THz, where the signal is strongest. The secondary pulse is due to a Fabry-Pérot reflection of the T-ray pulse inside the quartz slide.

7.3 Experiments

The preliminary results indicated the potential for a T-ray-based bioaffinity sensor. The next step was to amplify the T-ray signal by attaching Agarose beads to Avidin and use Avidin as the target molecule. The presence of μm-sized Agarose beads in the target layer increased the DTDS signal of the T-ray biosensor.

7.3.1 Sample preparation

The process of sample slide preparation for bead-enhanced Avidin detection is shown in Fig. 7.11. The following chemicals were used in the preparation as obtained without further purification (supplier: Sigma, St. Louis, MO, USA; URL: `http:www.sigma-aldrich.com`): octadecanol, Bovine Serum Albumin, Biotin, and Agarose beads, with an average diameter of 40 μm, conjugated to Avidin. The quartz microscope slides (25×25 mm, supplier: Electron Microscopy Sciences, Washington, PA, USA; URL: `http://www.emsdiasum.com`), were tested for thickness homogeneity before use in a separate DTDS experiment – a null signal $y_d = 0$ indicated that the slide was homogeneous. The reagents were high-performance liquid chromatography (HPLC) grade, and aqueous solutions were prepared in double-distilled deionised water.

Prior to deposition, the quartz slides were cleaned in 50% hot nitric acid for an hour, and then rinsed thoroughly in double distilled water. The quartz slides were then subjected to 1 mg/ml octadecanol solution for half an hour. The approach used to immobilise a hydrophobic substrate on a hydrophilic surface relies on systematically controlling the interfacial region of the biosensor chip using a process widely referred to as molecular self-assembly. The spontaneous organisation of the Biotin lipid into the octadecanol self-assembled bilayers guarantees a certain level of stability to the octadecanol-Biotin complexes. After drying and washing with double distilled water, the sample was dipped in 0.5 mg/ml Biotin dissolved in chloroform/methanol (5:1), and allowed to incubate for 45 minutes. Immersion in a solution of Biotin resulted in an increase in thickness of 5 nm/cm^2, caused by the Biotin interaction with octadecanol through hydrophobic interaction. The Biotin was the sensor layer on the biochip. Lastly, to eliminate the effect of non-specific interactions, the quartz slides were further incubated in 1% Bovine Serum Albumin (BSA), then dried and washed several times with a phosphate buffer solution. The BSA solution interacted with any exposed areas of the quartz slide, filling in any holes left by the Biotin layer. Filling the holes with

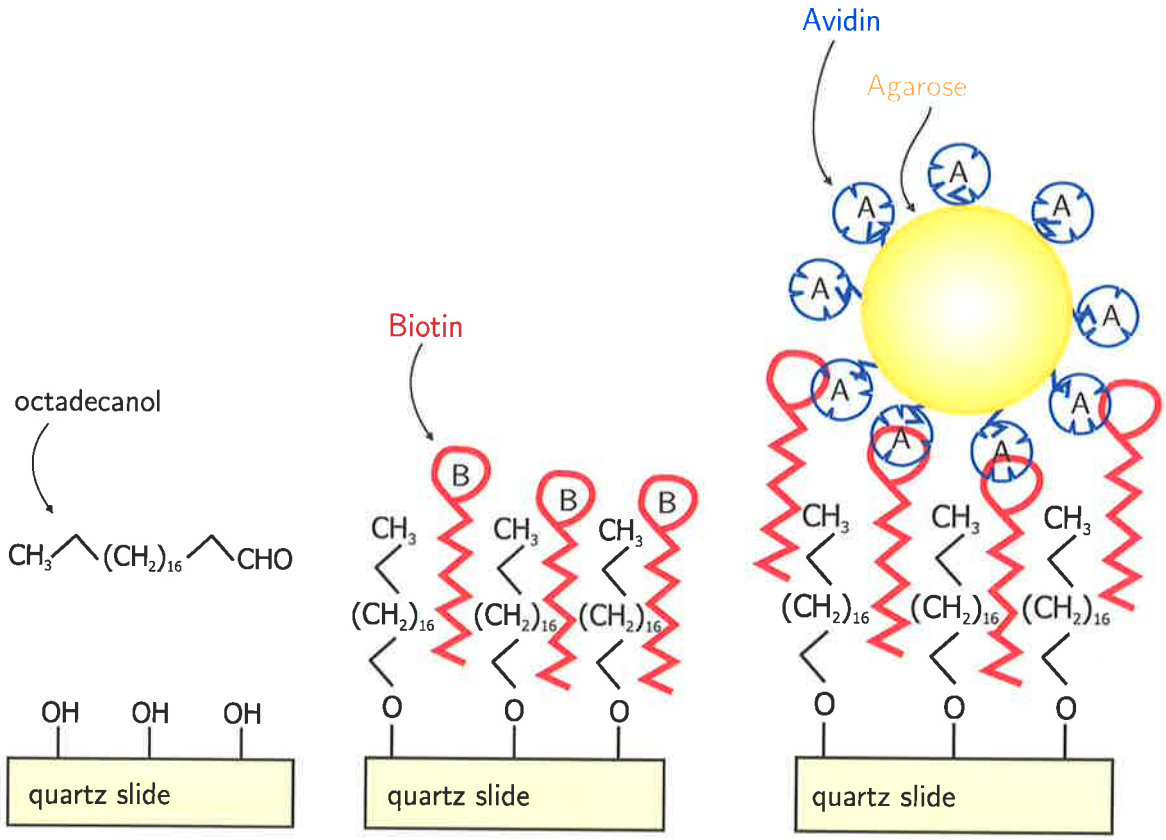

(a) Clean sensor slide, & octadecanol

(b) Biotin attached with octadecanol

(c) Avidin on an Agarose bead, linking to Biotin

Figure 7.11. Diagrams of biosensor derivitisation, preparation and target detection. This sketch shows the steps involved in the preparation and application of a Biotin-Avidin bioaffinity slide. The first step in preparing a slide was cleaning the quartz, leaving a surface of hydroxyl (OH) groups. The quartz crystal surface was then modified by self-assembly of the octadecanol molecule, which created a dense array of hydrophobic strands aligned perpendicularly to the surface. The hydrophobic tails of the Biotin molecules, red in the diagram, then fitted into the hydrophobic octadecanol matrix. The Biotin was anchored to the surface and only the charged heads of the Biotin molecules were exposed. The detection step is shown in Subfig. 7.11(c), where Avidin molecules bound to the Biotin layer. In the experiment shown here, the Avidin molecules were attached to a large Agarose bead, thus the bound target layer had a thickness greater than a layer of bound Avidin molecules.

BSA removed the possibility that any target molecules would bind non-specifically to the slide – if the holes had remained, molecules may have bound to the slide by interacting with the quartz rather than the Biotin detector layer, thus generating spurious signals.

After biosensor preparation, the target molecules were applied to one side of the biosensor slide. Either 10.3 ng of Avidin in 200 μl double-distilled water, or Avidin conjugated to Agarose beads, was spread on 1 cm^{-2} of the sensor surface and allowed to incubate for half an hour. After drying, the sample was washed with double-distilled water to remove unbound molecules. The only remaining molecules formed a thin layer of tightly-bound Avidin, or the Avidin conjugate (a layer of Avidin or a layer of bead-enhanced Avidin).

7.3.2 T-ray spectrometer

The T-ray spectrometer was configured in the same way as for the preliminary experiments, as described in Sec. 7.2.2.

7.4 Results

By conjugating Agarose particles to Avidin, rather than Avidin alone, the T-ray difference signal between Biotin and the Biotin-Avidin complex increased sharply. The two time-domain T-ray waveforms measured from the Avidin target and the amplified Avidin target were both larger than the signal from surface inhomogeneities and a non-specifically bound protein (in this case digalactosyldiacyl glycerol). The waveforms are shown in Fig. 7.12. Less than 10.3 ng/cm^2 of Avidin was detected on the quartz surface, indicating the potential capability of this newly developed method to detect DNA hybridisation and antigen-antibody interactions.

Compared to the similar Biotin-Avidin experiment without Agarose beads, an eight-fold enhancement in signal amplitude due to the beads is observed. The signal enhancement is due to the increased refractive index of Agarose particles, causing increased T-ray reflection at the Biotin-Avidin interface. This model is explored in Sec. 7.5. The repeatability of the waveforms shown in Fig. 7.12 is tested by measuring the DTDS signal at different lateral positions on each biosensor slide. The signal variation with position is $< 10\%$.

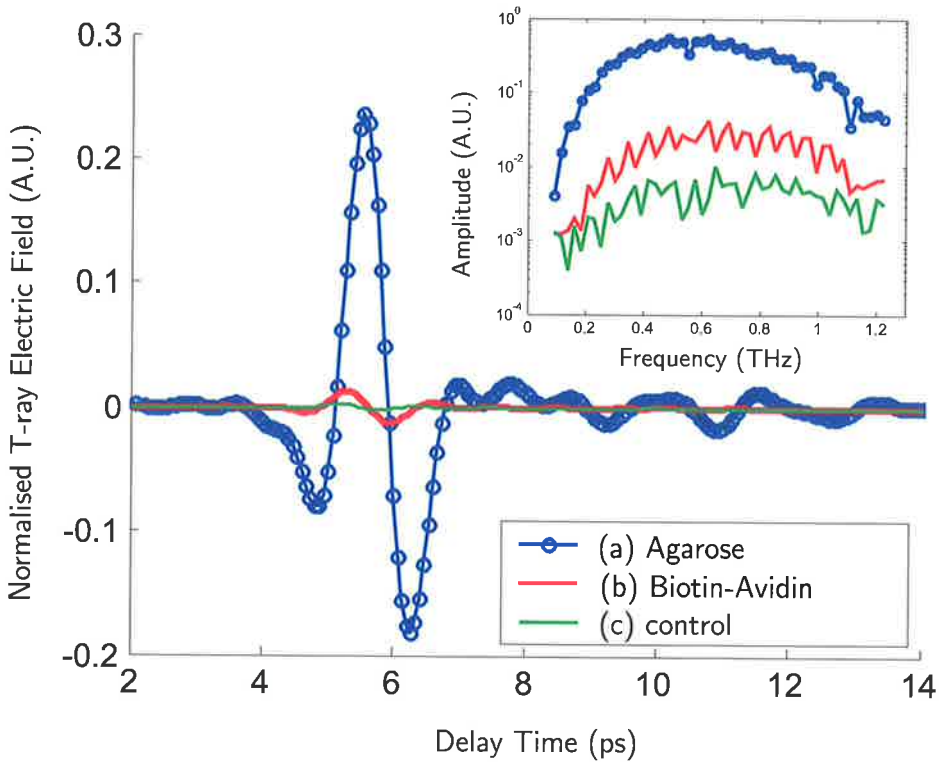

Figure 7.12. Measured biosensor waveforms for Biotin detection of Avidin, enhanced Avidin and a control. The three time-domain T-ray pulses in this graph were obtained by measuring the difference signal between (a) Biotin and Biotin-Avidin conjugated Agarose, (b) Biotin and Biotin-Avidin complexes without beads, and (c) Biotin and Biotin-DGDG (control sample). These time-domain pulses have been smoothed numerically using a 0.1–1 THz band-pass filter. The spectrometer signal-to-noise ratio in these measurements was greater than 10^2. The inset shows the waveforms in the Fourier domain (FFT). The intensity of the signal due to inhomogeneities and non-specific binding is less than the Agarose and Biotin-Avidin signals. The waveforms have been normalised to the peak of the T-ray reference waveform, y_r.

In order to test for the non-specific interaction of Biotin towards Avidin, and avoid false positive results, a control sample was prepared. When a quartz crystal bearing Biotin was incubated with a suspension of Digalactosyldiacyl Glycerol (DGDG), instead of Avidin-tagged Agarose, the T-ray differential signal dropped by an order of magnitude, indicating that the previously observed T-ray signal was solely due to Biotin-Agarose conjugated Avidin. The small T-ray signal that did result from the Biotin-DGDG interaction was presumably due to surface inhomogeneity. Selectivity is not

quantified here, but other studies have shown that the specificity of Biotin towards DGDG is far less than towards Avidin.

7.5 Modelling

A model of the biosensor system was critical for system development and understanding the system's limitations. For the work in this Chapter, the experimental results were simulated by modelling the biosensor slide as a series of homogeneous dielectric layers. The model construction is shown in Fig. 7.5. The T-ray radiation propagates through the layers, represented in Fig. 7.5 by the Fourier components of the sample and reference waveforms, $\tilde{S}_s$ and $\tilde{S}_r$, where $\tilde{S}_s = \mathcal{FT}(y_s)$ and $\tilde{S}_r = \mathcal{FT}(y_r)$. Expressions for $\tilde{S}_s$ and $\tilde{S}_r$ in terms of the incident T-rays and the dielectric layers are developed in Sec. 7.5.1.

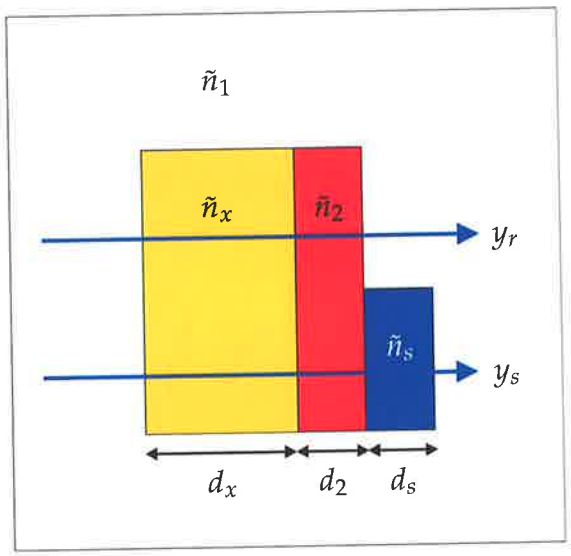

Figure 7.13. Notation used in DTDS simulation. n_x is the quartz substrate, n_2 is the thin sensor layer (Biotin) and n_s is the thin target layer (Avidin and conjugate Avidin). The surrounding medium, n_1, is air. The transmitted spectral components of the waveforms are determined by FFT, $\tilde{S}_s = \mathcal{FT}(y_s)$ and $\tilde{S}_r = \mathcal{FT}(y_r)$.

The actual measured double-modulated DTDS signal, as in Fig. 7.12, is represented by the half difference between $\tilde{S}_s$ and $\tilde{S}_r$, as discussed in Ch. 6. The biosensor is therefore modelled by the inverse Fourier transform of the difference between the reference and sample spectra. A simulated difference waveform is based on estimated material properties and the reference waveform y_r, which is measured using normal T-ray TDS (as opposed to double-modulated DTDS). The material properties are estimated to obtain a close fit to the experimental results. Section 7.5.2 shows that the simulated DTDS pulses fit very closely to the experimental results, thus validating the model.

7.5.1 Propagation and transmission

The propagation of a plane electro-magnetic wave through the dielectric layers shown in Fig. 7.5 can be modelled using Fresnel equations, as described in Sec. 4.2. The transmission coefficient for a plane wave at normal incidence to a plane interface of two materials, passing from the dielectric of complex refractive index $\tilde{n}_a$ to that of $\tilde{n}_b$, is given by

$$t_{ab} = \frac{2\tilde{n}_a}{\tilde{n}_a + \tilde{n}_b}. \tag{7.1}$$

Similarly, the reflection coefficient is given by

$$r_{ab} = \frac{\tilde{n}_a - \tilde{n}_b}{\tilde{n}_a + \tilde{n}_b}. \tag{7.2}$$

The propagation coefficient for a dielectric of thickness d,

$$p_a = \exp(-j2\pi\tilde{n}_a d/\lambda), \tag{7.3}$$

$$= \exp(-j2\pi n_a d/\lambda) \cdot \exp(-\alpha_a d/2), \tag{7.4}$$

where λ is the wavelength of the radiation (in m), n_a is the real part of the complex refractive index and α_a is the absorption coefficient (in m^{-1}) of material a.

For thin layers, the transmission is modified by a Fabry-Pérot factor, FP, due to interference of multi-reflections within each layer (see Sec. 4.2). The FP factor for a dielectric $\tilde{n}_b$, found between two dielectrics $\tilde{n}_a$ and $\tilde{n}_c$, is given by

$$\mathrm{FP}_{abc} \approx \frac{1}{1 - \left(\frac{\tilde{n}_b - \tilde{n}_a}{\tilde{n}_b + \tilde{n}_a}\right)\left(\frac{\tilde{n}_b - \tilde{n}_c}{\tilde{n}_b + \tilde{n}_c}\right) \cdot e^{-j2\tilde{n}_b d_b/\lambda}}. \tag{7.5}$$

DTDS measures time-domain pulses, thus the number of multi-reflections detected from each dielectric layer depends on the measurement duration and the thickness of each layer. For the biosensor experiments in this Thesis (see Fig. 7.5), the quartz layer was thick enough so that no FP reflections were recorded. The Biotin and Avidin layers were sufficiently thin, $d \approx 1\ \mu$m, that influence from multi-reflections was small, although in the model calculations used, full FP expressions were included.

The spectral components of the signal and reference waveforms can be expressed in terms of a common term, $A(\omega)$, which represents common elements in the wave propagation, and the coefficients listed above (see also Fig. 7.5):

$$\tilde{S}_r = A(\omega)\, p_2\, \mathrm{FP}_{x21}\, t_{21}, \tag{7.6}$$

$$\tilde{S}_s = A(\omega)\, t_{2s}\, p_s\, \mathrm{FP}_{x2s}\, t_{s1}\, \mathrm{FP}_{2s1}. \tag{7.7}$$

$A(\omega)$ represents effects in the system, including the characteristics of the emitter and detector, that are common to both the sample and detector. These effects are cancelled out in DTDS measurements.

7.5.2 DTDS modelling

In DTDS, the spectral components $\tilde{S}$ of the differential waveform are measured with high sensitivity by rapidly switching between the sample and reference,

$$\begin{aligned} y_d &= (y_s - y_r)/2, \\ \tilde{S}_d &= (\tilde{S}_s - \tilde{S}_r)/2. \end{aligned} \tag{7.8}$$

The factor of a half comes from the double-modulation detection scheme, as explained in Ch. 6.

To model the measured system, it was necessary to estimate the material parameters shown in Fig. 7.5. In the experiments, the T-ray frequency parameters for air, $\tilde{n}_1$, and the substrate, $\tilde{n}_x$, were known from literature and past experiments. For air, $\tilde{n} = 1 - j0.0$ and for quartz (Grischkowsky et al., 1990), $\tilde{n} = 2.1081 - j0.00032$. The remaining parameters relate to the sensor layer (Biotin) and the target layer (Avidin or conjugated Avidin).

The differential waveform is modelled by substituting the expressions for $\tilde{S}_s$ and $\tilde{S}_r$, Eqs. (7.7) and (7.6), into the difference Eq. (7.8). The simulated waveform, as shown in Fig. 7.14, is determined with an inverse Fourier transform.

$$\tilde{S}_d = \tilde{S}_r \left(\frac{t_{2s} p_s t_{s1} \mathrm{FP}_{x2s} \mathrm{FP}_{2s1}}{t_{21} p_1 \mathrm{FP}_{x21}} - 1 \right), \tag{7.9}$$

$$y_{d\ \mathrm{simulated}} = \mathcal{FT}^{-1}(\tilde{S}_d). \tag{7.10}$$

The T-ray refractive index of a thin Biotin layer was estimated using standard DTDS of the Biotin deposited on half a quartz slide, the other half of which was blank. The thickness of the Biotin film was measured using Atomic Force Microscopy (see Fig. 7.8), and found to be approximately 5 μm. The refractive index of the Biotin film was then estimated by fitting a differential waveform, y_d, to the experimental data. $\tilde{n}_2$ was estimated to be approximately equal to air, $\tilde{n}_{\mathrm{Biotin}} \approx 1.001 - j0.001$. This is reasonable for a primarily non-polar molecule such as Biotin; non-polar materials have a low T-ray absorption due to their lack of dipole moment.

The refractive index of the target layer is the main free parameter for fitting the simulated waveform to the measured waveform. For the simulated fits shown in Fig. 7.14, the refractive index of Avidin was taken to be approximately $\tilde{n}_s = 1.1 - j0.0005$, and of the conjugated Avidin and Agarose, $\tilde{n}_s = 3 - j0.4$. The conjugated Avidin layer is expected to have a far greater thickness than the Avidin alone, and the simulation of conjugated Avidin fits with a layer thickness of $d_s = 50$ μm, which is far greater than the estimated thickness of the Avidin layer alone, $d_s = 5$ μm.

The simulated DTDS waveforms approximate the experimental data well, as seen in Fig. 7.14.

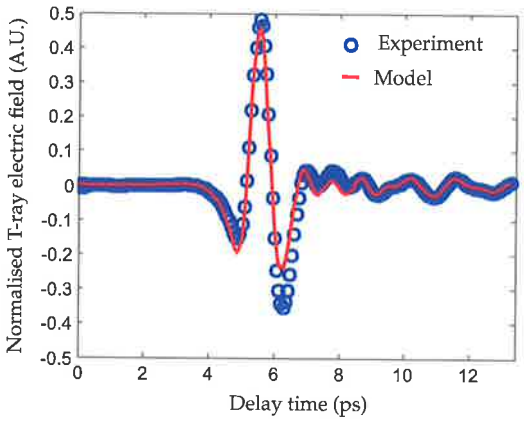

(a) Estimated parameters of the target layer (Avidin conjugated to Agarose beads): $d_s = 50$ μm, $\tilde{n}_s = 3 - j0.4$.

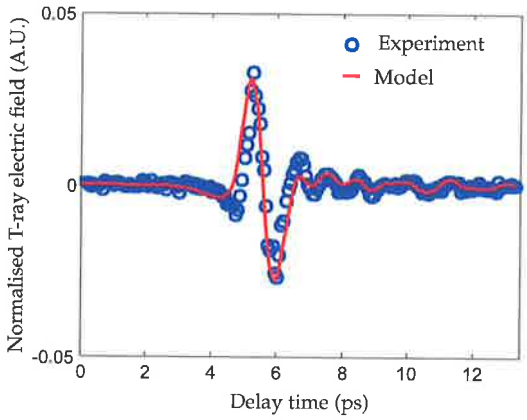

(b) Estimated parameters of the target layer (Avidin): $d_s = 5$ μm, $\tilde{n}_s = 1.1 - j0.0005$.

Figure 7.14. Experimental and simulated biosensor waveforms. Simulated fits to the data shown in Fig. 7.12. The measured waveforms are normalised in amplitude to the peak of the T-ray reference pulse, y_r. The model waveforms are simulated using Eqs. (7.9) and (7.10) parameters in the simulation are the air, the quartz and the Biotin layer. For the surrounding air, $n_1 = 1.0$ and $\kappa_1 = 0$. For the quartz substrate, $d_x = 1$ mm, $n_x = 2.1081$ and $\kappa_x = 0.00032$. For the Biotin sensor layer, $d_2 = 5$ μm, $n_2 = 1.0001$ and $\kappa_2 = 0.001$.

The estimated parameters for layer thickness and dielectric constant are reasonable for Avidin and conjugated Avidin, where a higher T-ray absorption and refractive index are expected for more polar molecules. It should be noted, however, that these simulations are intended primarily as a tool for understanding the mechanism of the biosensor's sensitivity, not for directly determining material properties. There is some mismatch between the experiments and modelled results (see Fig. 7.14), which is due to inaccuracies in the parameter estimations, inhomogeneities in the deposited films, and

the assumption of a single refractive index value across the entire T-ray band, that is, a zero dispersion approximation. Nevertheless, the basic similarity in phase and amplitude indicates that the experimental signal is probably due to T-ray transmission and reflection at the boundaries of the Biotin and Avidin dielectric layers. This indicates that further signal enhancements will be possible using greater dielectric mismatches. The noise from inhomogeneities can be reduced by using more laborious biofilm deposition techniques, such as spin-coating or Langmuir-Blodgett troughs.

7.6 Conclusion

T-ray DTDS has been applied to thin layers of biomolecules for use as a T-ray biosensor. The experimental results and simple models indicate that the T-ray spectrometer is highly sensitive to thin layers of target molecules and can clearly differentiate between target and control samples, even for samples prepared by hand.

Bioaffinity sensing was demonstrated experimentally and modelled for thin films of (i) the protein Avidin, (ii) the lipid Biotin and (iii) TNT. The best results were obtained from amplified Avidin: by conjugating Agarose particles to Avidin and detecting them with a Biotin-coated quartz surface, a clear T-ray difference signal between the Biotin sensor and the Biotin-Avidin complex was detected. The protein Avidin and lipid Biotin are noted for their very high binding affinity, and the ease with which they can be attached to residues with importance in many applications (see Sec. 7.6.1).

7.6.1 Future work

The inherently high affinity of the Biotin-Avidin pair makes the T-ray biosensor highly attractive as an analytical device for a wide variety of biochemical studies. Owing to the technical difficulties encountered in the preparation of protein markers, the Biotin-Avidin system has proved of particularly broad application; almost any biologically active molecule can be tagged with Biotin or Avidin with only minimal effect on biological activity. Therefore using Biotin-Avidin technology together with high-refractive index beads, the DTDS biosensor may be able to play a pivotal role in detecting trace amounts of biological materials.

A concentration of 10.3 ng/cm^2 Avidin on the quartz surface was detected, a level comparable with other thin film measurement techniques such as ellipsometry and reflectometry, indicating that the T-ray biosensor has the potential to compete in detecting DNA hybridisation and antigen-antibody interactions.

Antibody-antigen technology may also benefit from this new amplified T-ray detection method. Since antibodies can be produced for almost all classes of substances, for example, proteins, polysaccharides, nucleic acids, more complex particles such as pollens, infectious agents, viruses and prokaryotic (simple) and eukaryotic (complex) cells, it is expected that the enhanced DTDS system should be able to detect minute amount of a wide range of biomolecules. Further enhancement may be possible by conjugating target molecules to gold or carbon micro-spheres.

The quality of the sensor slides used in this Chapter was limited by their preparation – surface inhomogeneities made a large contribution to experimental noise. In the future, more uniform sensor preparation techniques could be used to coat the quartz slide, such as spin coating, or the Langmuir-Blodgett (LB) technique. Spin coating uses a rapidly rotating disk to coat evenly a thin layer of biomolecules onto a sensor slide. The LB technique uses a mono-molecular layer of biomolecules floating in a liquid-filled trough float – the sensor slide is pulled through the floating layer on the surface of the liquid, and is coated with a single homogeneous layer of molecules (Atkins, 2002).

For high-volume analysis, sample and reference films can be deposited into a biochip array containing many samples. For very small sample sizes, less than 1-mm in diameter, T-ray near-field techniques will be required to create a tightly-focused beam. Near-field T-ray technology, and methods of near-field T-ray generation, are described in Ch. 10. A large array of samples, all modulated for DTDS, and addressed with near-field T-ray pulses, is sketched in Fig. 7.15 – such a system would be necessary for high-density T-ray biosensing applications.

7.7 Chapter summary

This Chapter has described an application of T-ray technology in the field of biosensing. Using the highly-sensitive technique of double-modulated DTDS, a standard T-ray spectrometer was used to detect the binding of target molecules to pre-prepared sensor molecules, that is, detect bioaffinity. The molecules used as ligands (targets)

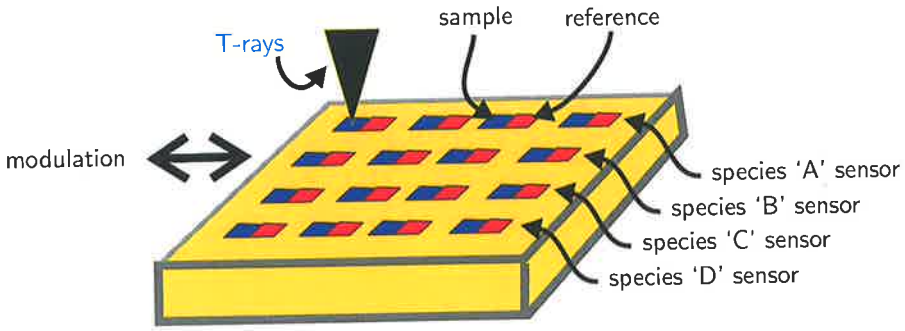

Figure 7.15. Concept diagram of a high-resolution T-ray biosensor array. This concept diagram shows an array of sample and reference films being probed by near-field T-ray DTDS. Each sample dot is prepared to bind to a given molecular species: for example, the four dots on the far right could be prepared to detect the four species 'A' to 'D' (the array pictured here would detect target binding to 16 separate species). When a mixture of unknown components is washed over the slide, any species that matches a sample dot will bind to the sample. DTDS will then detect the extra layer of bound molecules, and thereby determine what species are present in the mixture.

and analytes (sensors) to confirm the technique experimentally included: (i) the egg-white protein Avidin and the vitamin Biotin, (ii) Biotin and Avidin attached to Agarose beads (enhanced Avidin), and (iii) the explosive TNT and its antibody. The use of other ligand-analyte pairs can extend this technique into a broad range of applications.

Experimentally a sensitivity of ng/cm^2 was achieved, which approaches the sensitivity of other non-contact bioaffinity sensing technologies, such as Surface Plasmon Resonance (SPR). In future work, this can be improved through better film preparation techniques, such as the Langmuir-Blodgett technique.

Although other well-developed techniques exist for detecting layers of thin biomolecules, this Chapter has demonstrated the first free-space biosensor that relies on the T-ray properties of the biomolecules. The sensitivity of the T-ray biosensor is comparable to other methods, and will be primarily useful in detecting biolayers that do not have distinguishing characteristics at other wavelengths. Some examples of this might be detecting similar proteins that have differing conformations.

Double-modulated DTDS (d-DTDS) was used to characterise thin layers of material in Ch. 6, and to detect thin biomolecular layers in this Chapter. In the following Chapter, d-DTDS is extended for the first time to characterising liquid samples.

Chapter 8

Liquid Differential Time-Domain Spectroscopy

LIQUID transmission T-ray studies at T-ray frequencies are valuable for understanding solvation dynamics of salts, exploring long-range structure in mixtures and probing biomolecules in suspension. These studies are, however, limited in accuracy by the inherent fluctuations of the T-ray spectrometer. One way to reduce this measurement uncertainty is to use double-modulated DTDS, which is applied here for the first time to liquids.

In this Chapter the uncertainty in double-modulated DTDS measurements of liquid samples is shown to be dependent on: (i) the noise of the T-ray spectrometer, and (ii) the thickness change of the liquid sample. It turns out that for many important liquids with high T-ray absorption, such as water, the measurement uncertainty can be greatly decreased using a dynamically-modulated liquid sample, in T-ray Differential Time-Domain Spectroscopy (DTDS). Preliminary experiments with a novel sample holder, based on an audio speaker, supported these calculations, and *amplitude and mean detection* was used to measure the two waveforms of double-modulated DTDS simultaneously, potentially decreasing the noise by over two orders of magnitude.

8.1 Introduction

Characterising materials in liquid form is a valuable role for T-ray spectroscopy, and much research has been done in this area. T-ray material studies in pure liquids have measured the characteristic relaxation times of permanent or induced molecular dipole moments, as described in Sec. 4.3.2. Liquid studies are also important, however, in studying real life systems, especially in biology, and T-ray bioscience is an area of rapid development (see Sec. 4.3.4).

In T-ray studies of liquids and liquid mixtures, the main limitations on accuracy are the fluctuations in T-ray pulse amplitude arising from laser noise. Liquid spectroscopy is best carried out with dual-thickness measurements, using a thick sample and a thin sample of the liquid. This Chapter proposes making dual-thickness measurements at higher modulation frequencies by rapidly swapping between the thick and thin samples, that is, a novel technique of liquid DTDS. Liquid DTDS combines the benefits of: (i) accurate parameter estimation due to dual-thickness measurements (see Sec. 4.2.2), and (ii) reduced noise from double-modulated DTDS (see Ch. 6).

In this Chapter, liquid DTDS is proposed, modelled and tested. Noise analysis in Sec. 8.2 shows the potential for improving the accuracy of T-ray measurements of liquids, especially for biologically important high-dielectric constant mixtures containing water. Experiments in Sec. 8.3 with a prototype sample modulation system based on an audio speaker are used to demonstrate the feasibility of liquid DTDS. The results in Sec. 8.4 show liquid DTDS provides the same information as traditional T-ray TDS, but has the potential for far lower noise, when used for example with a high-accuracy modulation device, such as a piezoelectric translator.

8.1.1 Motivation

The accuracy of estimating the T-ray frequency parameters of fluid samples in dual-thickness T-ray spectroscopy is limited by fluctuations in the T-ray pulses, caused by laser fluctuations, and by the accuracy of the thickness measurements (Mickan et al., 2002a; Mickan et al., 2002b). Noise in the T-ray beam is caused primarily by laser fluctuations, which are known to have a $1/f$ characteristic, that is, the fluctuation amplitude is greater at lower frequencies (von der Linde, 1986).

A measured graph of T-ray spectrometer noise is shown in Fig. 8.1, where the $1/f$ trend is visible. Normally the two measurements required for material characterisation are

measured over a period of minutes. The length of time required depends on the signal-to-noise ratio (SNR) of the system. By taking the reference and sample measurements, required in T-ray spectroscopy, at a higher speed, the fluctuation in laser power between measurements is reduced. Rapid sample modulation, dubbed T-ray Differential Time-Domain Spectroscopy (DTDS), has previously been used on solid thin films (see Ch. 6) and biosensor slides (see Ch. 7), but not on liquid or gas samples.

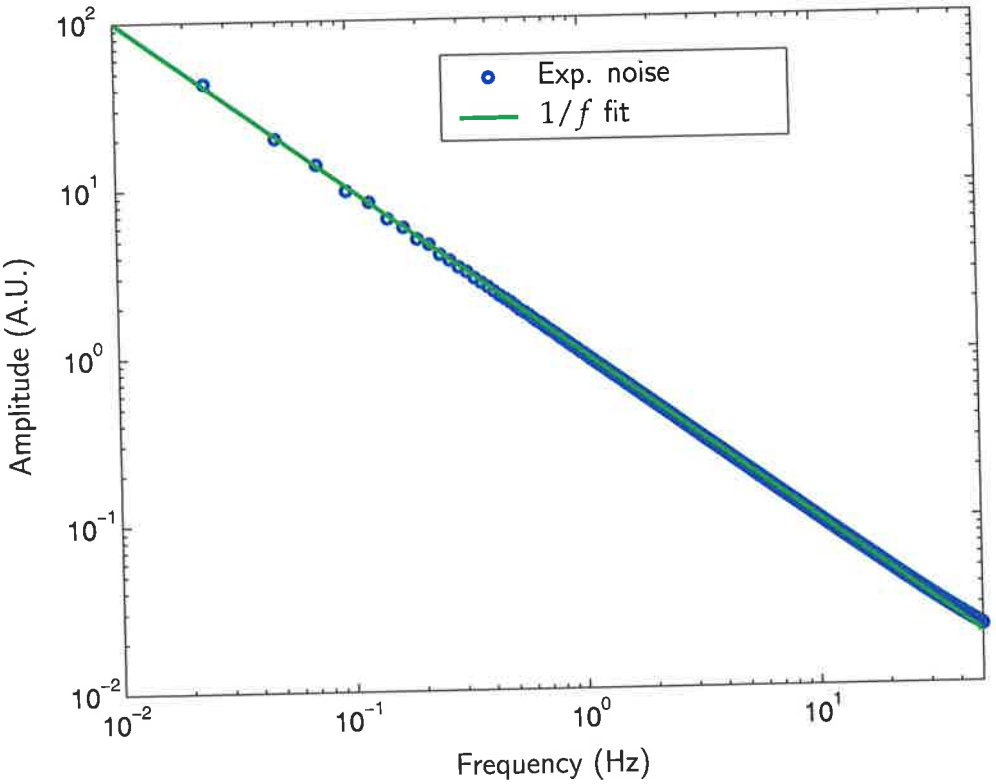

Figure 8.1. Experimental T-ray noise spectrum. This measured plot shows the $1/f$ trend of laser-based T-ray noise. The experimental spectrum, shown as blue circles, was calculated using a numerical FFT from a set of time-domain measurements of the peak of the T-ray pulse, partially shown in Fig. 8.2. The experimental spectrum fits very closely to a $1/f$ relationship, shown as a green line, over the available measurement frequency range. The 8,192 time-domain samples were taken with a time spacing of approximately 5 ms, giving a sample time of 41 s and a measurement frequency range of approximately 0.024 to 100 Hz. Using liquid DTDS instead of normal T-ray TDS would decrease the drift time from approximately 5 mins to 0.05 s (0.003 Hz to 50 Hz), theoretically decreasing the noise caused by laser fluctuations by up to 4 orders of magnitude.

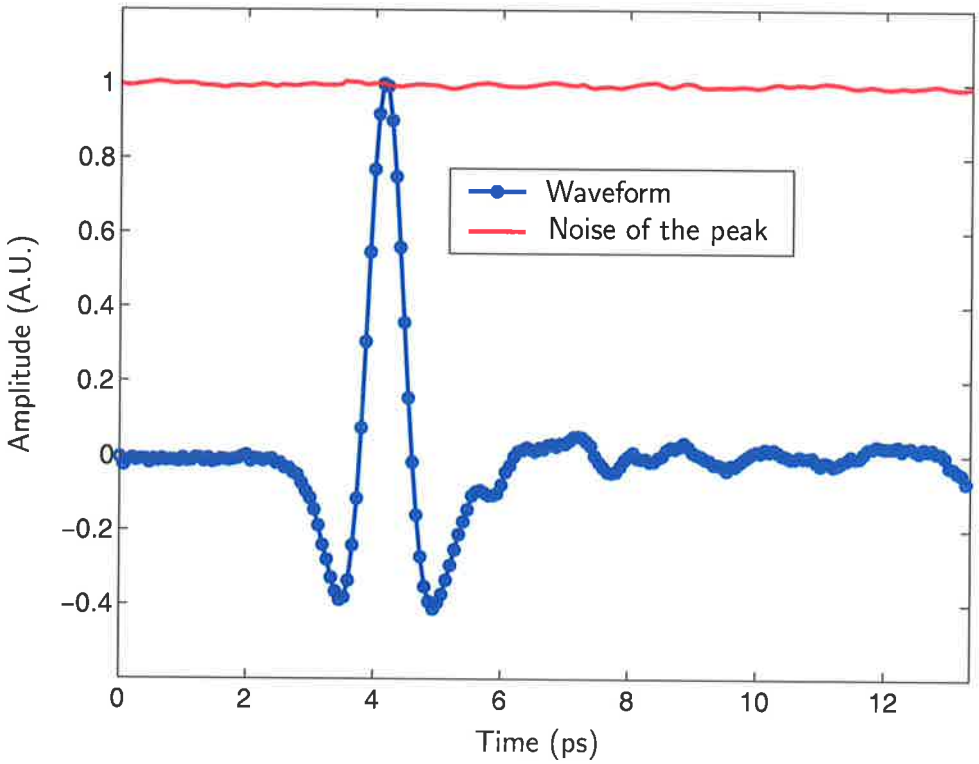

Figure 8.2. Measured T-ray waveform, and peak fluctuations (noise). This graph shows in blue a T-ray waveform measured over about 5 minutes with the T-ray spectrometer used for the experiments in this Chapter (Sec. 8.3). The peak of this waveform fluctuated over time, as shown by the red plot in this Figure, giving an estimation of the noise, or inaccuracy, in the waveform measurement. This peak fluctuation represents the main source of noise in T-ray measurements not limited by absorption. The fluctuation has a spectral distribution shown in Fig. 8.1. Each of the plots comprises 201 points. The measurements were made with a LIA time constant of 100-ms. T-ray waveform acquisition is described in Ch. 3.

8.1.2 Previous studies

The experiments in this Chapter use a dual-thickness geometry, where the sample and reference waveforms are measured through thick and thin versions of the sample respectively (see Sec. 4.2.2). Dual-thickness geometry systems have been used by Kindt and Schmuttenmaer (1996) and Mickan et al. (2002b).

The typical accuracy of measured parameters is to two decimal places, or worse than 0.1% (Zoidis et al., 1996; Rønne et al., 1997; Rønne et al., 2000; Venables et al., 2000;

Asaki et al., 2002). The work in this Chapter attempts to improve the accuracy of these measurements by two orders of magnitude.

8.1.3 Objective summary

This Chapter uses double-modulated DTDS to reduce the noise in fluid parameter estimation. In a typical T-ray transmission spectrometer with a SNR of 100:1, each time-domain measurement takes approximately 5 mins, and noise is dominated by laser fluctuations ($1/f$). Using a DTDS technique and simultaneous dual waveform acquisition (amplitude and mean detection), the time between measuring the sample and reference waveforms can be reduced to a time determined by the speed of the modulator. Therefore only one delay scan is required to sample both T-ray waveforms, and the time delay between each sample and reference measurement is the inverse of the modulation frequency. For a 10-Hz modulation speed, the increase in effective modulation frequency is 3000 times, and the corresponding decrease in the amplitude of $1/f$ noise is 3000 times.

8.2 Noise reduction theory

For liquid spectroscopy using a dual sample geometry, the accuracy of parameter estimation depends on fluctuation of the T-ray spectrometer and the accuracy of the thickness change. This Section quantifies the benefits of double-modulated DTDS for characterising two classes of liquids: those with a low T-ray absorption and those with a high T-ray absorption, for example, water. The aim is to measure material parameters with an accuracy better than 10^{-4}.

8.2.1 Dual-sample theory

The T-ray pulse is modelled as a spectrum of Fourier components, propagating as a plane wave through the sample as discussed in Sec. 4.2.1. Figure 8.2.1 shows the propagation of radiation through the sample, of complex refractive index $\tilde{n}_2$, and across two interfaces between the sample and the surrounding medium (air), $\tilde{n}_1 \approx 1.0$. The simple equations used for estimating the material parameters are derived from the equations for Fresnel transmission and reflection at interfaces.

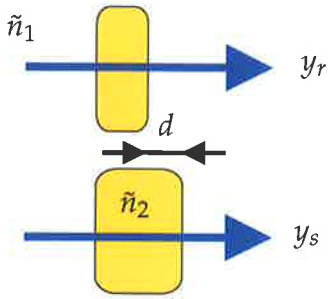

Figure 8.3. Diagram of the dual-thickness parameter estimation geometry. Waveforms y_s and y_r are measured having respectively passed through the thick (sample) and thin (reference) samples. The spectral components of the waveforms are determined by FFT, $\tilde{S}_s = \mathcal{FT}(y_s)$ and $\tilde{S}_r = \mathcal{FT}(y_r)$. The difference in thickness between the two measurements is denoted d.

The ratio of the transmission spectra $\tilde{S}$ can be entirely determined in terms of refractive indices and the sample thickness, as shown in Sec. 4.2.1,

$$\tilde{T} = \tilde{S}_{\text{sample}} / \tilde{S}_{\text{reference}} = \frac{e^{-j\tilde{n}_2\omega d_{\text{thick}}/c_0}}{e^{-j\tilde{n}_2\omega d_{\text{thin}}/c_0} e^{-j\tilde{n}_1\omega(d_{\text{thick}}-d_{\text{thin}})/c_0}}, \tag{8.1}$$

where $\tilde{n}_1$ is the material that replaces the space taken up by the extra thickness of the thick sample, typically air.

Equation (8.1) simplifies to

$$\tilde{T} = \exp(-j\omega/c_0 d(\tilde{n}_2 - 1)), \tag{8.2}$$

where $d = d_{\text{thick}} - d_{\text{thin}}$ and $\tilde{n}_1 = 1$. Since $\tilde{T}$ is complex, $\tilde{T} = \rho e^{j\phi}$, and $\tilde{n} = n - j\kappa$,

$$\rho = \exp(-\omega d\kappa/c_0), \quad \phi = \omega d(n_2 - 1)/c_0. \tag{8.3}$$

The material parameters can then be extracted by rearranging the above equations (Arjavalingam et al., 1990),

$$n = \frac{-\phi\, c_0}{\omega d} + 1, \quad \kappa = -\ln(\rho)\frac{c_0}{\omega d}. \tag{8.4}$$

where the complex refractive index $\tilde{n} = n - j\kappa$, d is the thickness change of the sample, c_0 is the speed of light in a vacuum.

These calculations provide a value for the T-ray refractive index and extinction of the mixture. The values of $\tilde{S}_s$ and $\tilde{S}_r$ were measured by taking the Fourier transform of the transmitted time-domain T-ray pulses, y_s and y_r respectively. The accuracy of Eq. (8.4) depends only on the noise of the T-ray spectrometer, ϕ and ρ, and of the accuracy of d.

8.2.2 Uncertainty

The influence of errors arising from the thickness measurement, δd, and from T-ray spectrometer noise, $\delta\rho$ & $\delta\phi$, can be estimated using the partial derivatives

$$\delta n = \frac{\partial n}{\partial d}\,\delta d + \frac{\partial n}{\partial \phi}\,\delta\phi, \tag{8.5}$$

$$= \delta n_d + \delta n_\phi, \tag{8.6}$$

and

$$\delta\kappa = \frac{\partial \kappa}{\partial d}\delta d + \frac{\partial \kappa}{\partial \rho}\delta\rho, \tag{8.7}$$

$$= \delta\kappa_d + \delta\kappa_\rho. \tag{8.8}$$

So

$$\delta n = \frac{\phi\, c_0}{\omega}\,\frac{1}{d^2}\,\delta d, \quad \delta\kappa = \frac{\ln(\rho)\, c_0}{\omega}\,\frac{1}{d^2}\,\delta d,$$

and

$$\delta n = -\frac{c_0}{\omega d}\,\delta\phi, \quad \delta\kappa = -\frac{c_0}{\omega d}\,\frac{\delta\rho}{\rho}.$$

The errors introduced by the T-ray noise can be written as:

$\delta\rho_r$: error in magnitude of $\tilde{S}_r$ (reference spectra),

$\delta\phi_r$: error in phase of $\tilde{S}_r$ (reference spectra),

$\delta\rho_s$: error in magnitude of $\tilde{S}_s$ (sample spectra),

$\delta\phi_s$: error in phase of $\tilde{S}_s$ (sample spectra).

The T-ray noise comes from two main sources: (i) the T-ray emitter and T-ray detector (T-ray noise), and (ii) the probe beam (optical noise). The noise in the emitter dominates and is multiplicative, that is, proportional to the signal strength. The noise in the probe beam is additive, that is, independent of signal strength, and only dominates when the signal strength is low.

T-ray noise is multiplicative and probe beam noise is additive. T-ray noise arises from fluctuations in the power and alignment of the pump laser beam – as the alignment and power change, the intensity of the generated T-rays and the efficiency of the T-ray detector both fluctuate. In experiments, it turns out that amplitude of the T-ray fluctuations is proportional to the measured T-ray amplitude; this can be understood by

considering that at peak T-ray powers, the alignment is critical and is easy to disturb. For zero T-ray power, when the T-ray beam is completely blocked, there is no T-ray noise – in this case, the noise is due to fluctuations in the probe beam. Probe beam noise is independent of the T-ray power and depends on the characteristics of the laser itself. These two sources of noise both contribute to errors in T-ray measurements, but each source tends to dominate in different situations.

For experiments dominated by multiplicative noise, that is, noise due to fluctuations in the T-ray signal (pump beam) rather than noise in the detection system (probe beam) (Duvillaret et al., 2000), the phase error is approximately equal in both the sample and reference spectra,

$$\delta\phi_s \approx \delta\phi_r.$$

From $\phi = \phi_s - \phi_r$ and Eq. (8.2.2), $\delta\phi \approx 2\delta\phi_r$.

For uncorrelated amplitude noise in both the sample and reference, the combined effect of noise in both sample and reference can be estimated from

$$\frac{\langle\delta\rho^2\rangle}{\rho^2} = \frac{\langle\delta\rho_r^2\rangle}{\rho_r^2} + \frac{\langle\delta\rho_s^2\rangle}{\rho_s^2}. \tag{8.9}$$

For multiplicative noise, the relative amplitude error is similarly approximately equal in both the sample and reference spectra, giving

$$\frac{\delta\rho}{\rho} \approx \sqrt{2}\frac{\delta\rho_r}{\rho_r}, \tag{8.10}$$

$$\delta\rho = \frac{\sqrt{2}\exp(\frac{-\omega d\kappa}{c_0})}{\rho_r}\delta\rho_r. \tag{8.11}$$

Using Eq. (8.3), and the principle that uncorrelated errors must be added in quadrature,

$$\langle\delta n^2\rangle = \langle\delta n_d^2\rangle + \langle\delta n_\phi^2\rangle, \quad \langle\delta\kappa^2\rangle = \langle\delta\kappa_d^2\rangle + \langle\delta\kappa_\rho^2\rangle, \tag{8.12}$$

expressions for the uncertainty in measurements due to phase, amplitude and thickness uncertainties are obtained:

$$\delta n = \frac{n-1}{d}\sqrt{(\frac{2\,c_0\,\delta\phi_r}{\omega(n-1)})^2 + (\delta d)^2}, \tag{8.13}$$

$$\delta\kappa = \frac{\kappa}{d}\sqrt{(\frac{\sqrt{2}\,c_0}{\omega\kappa}\cdot\frac{\delta\rho_r}{\rho_r})^2 + (\delta d)^2}. \tag{8.14}$$

The uncertainty in the estimation of refractive index and extinction coefficient can be predicted from the inherent noise in the T-ray spectrometer, T_r, and the accuracy of the thickness modulator measuring d.

To study the influence of these uncertainties, four cases are important:

1. δd dominant in a low-κ sample (for example, a non-polar solvent);
2. $\delta\rho$ and $\delta\phi$ dominant in a very thick low-κ sample;
3. δd dominant in a high-κ sample (for example, water);
4. $\delta\rho$ and $\delta\phi$ dominant in a high-κ sample.

δd dominant in low-κ

For noise dominated by errors in d, Eqs. (8.13) and (8.14) can be simplified by ignoring the first term in the square root, giving

$$\delta n = (n-1)\frac{\delta d}{d}, \quad \delta\kappa = \kappa\frac{\delta d}{d}. \tag{8.15}$$

Equation (8.15) indicates that noise can be reduced by using a large thickness change d compared to the thickness measurement error δd. The value of δd is limited by the resolution of the actuator controlling the sample thickness.

The measurement of thickness change d can be extremely accurate, better than 1:10^4, using closed-loop feedback control of the mechanism used for changing the sample thickness. An accuracy of $\frac{\delta d}{d} < 10^{-4}$ can be achieved by using, for example, a 5-mm distance change between thicknesses and 0.4-μm stage resolution, or a 30-μm piezoelectric stage with 1-nm resolution. An accuracy of 10^{-4} would constitute an improvement of 100 times over most T-ray liquid characterisation results. Such high-accuracy mechanical modulators are commercially available.

As the noise due to δd can be reduced to less than 10^{-4}, the dominant source of noise is typically spectrometer noise, $\delta\rho$ & $\delta\phi$.

$\delta\rho$ and $\delta\phi$ dominant in low-κ

For T-dominated errors, Eqs. (8.13) and (8.14) can be simplified by ignoring the small second term in the square root, giving

$$\delta n = \frac{2\,c_0\,\delta\phi_r}{\omega\,d}, \quad \delta\kappa = \frac{\sqrt{2}\,c_0}{\omega\,d}\cdot\frac{\delta\rho_r}{\rho_r}.$$

These equations can be understood by substituting approximate values from a typical T-ray spectrometer measurement. A typical measurement could have, for example, $\omega = 6.3 \times 10^{12}$ rad/s at a frequency of 1 THz, and $\rho_r = 0.655$, $\delta\rho_r = 0.015$ and $\delta\phi_r = 0.025$ rad for a scan of the organic solvent 1,4-dioxane, using the liquid T-ray spectrometer from Sec. 8.3. In this measurement, the LIA time constant was 100 ms, giving a scan duration of approximately 5 mins. Using the numbers in this example,

$$\delta n \approx \frac{5 \cdot 10^{-6}}{d}, \quad \delta\kappa \approx \frac{3 \cdot 10^{-6}}{d}. \tag{8.16}$$

From Eq. (8.16) it can be seen that an accuracy of 10^{-4} is achievable at this noise level (100-ms LIA time constant and 5 min scan) by using an approximate thickness change of $d > 10$ mm. This large thickness change is possible with large volumes of liquid with a low T-ray absorption. If, however, the T-ray absorption of the liquid is not very low, a 50-mm-thick sample will attenuate the T-rays too greatly to be detected. For high-κ samples, for example water, the initial noise in the T-ray signal must be reduced to compensate for the necessity of a small thickness change.

δd dominant in high-κ

For high-κ samples, the uncertainty caused by δd is governed by the same equations as for low-κ samples, Eq. (8.2.2). For a highly-absorbing liquid, however, it is not possible to use a 5-mm distance change. The sample modulation must be less than 100 μm and be measured with a very high accuracy, using for example a piezoelectric translator.

$\delta\rho$ and $\delta\phi$ dominant in high-κ

For high-κ samples, $\tilde{S}_s$, is greatly attenuated, and $\delta\rho$ is dominated by additive noise.

Thus

$$\delta\kappa = \frac{\sqrt{2}\, c_0}{\omega\, d} \cdot \frac{\delta\rho_s}{\exp\left(\frac{-\omega d\kappa}{c_0}\right)}, \tag{8.17}$$

$$\approx \frac{1.3 \cdot 10^{-4}}{d}\, \delta\rho_s\, \frac{1}{\rho}. \tag{8.18}$$

From Eq. (8.18), the error is proportional to $1/\rho$.

The influence of increasing the modulation thickness, d, on the accuracy of our estimations when using two different example liquids, dioxane ($\kappa_{\text{dioxane}} = 0.013$) and water

($\kappa_{water} = 0.478$). The graph in Fig. 8.4 shows that the error in κ decreases with increasing thickness, from the first term in Eq. (8.18), until a maximum thickness is reached, beyond which the error begins to increase again, due to attenuation of the T-ray signal in the sample, shown as the second term in Eq. (8.18). The thickness d that corresponds to a minimum error depends on the T-ray extinction coefficient of the liquid sample (κ).

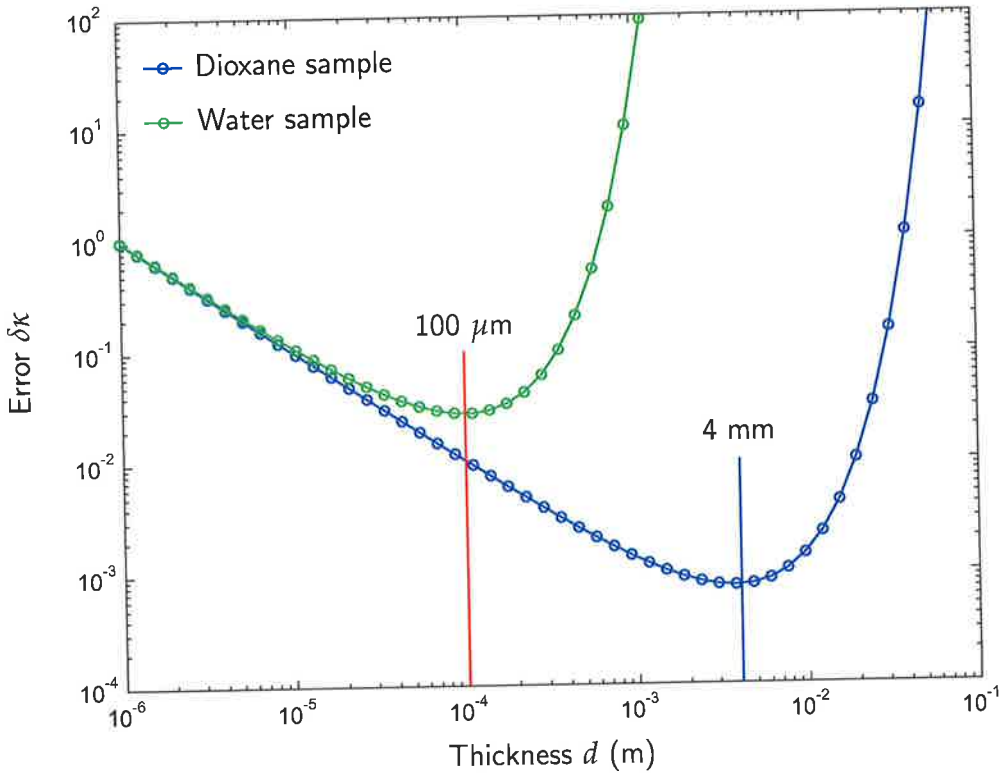

Figure 8.4. Calculated error (in κ) as a function of sample thickness. This plot shows the relationship of measurement error $\delta\kappa$ to the thickness change of the sample d in dual-thickness T-ray material characterisation (see diagram in Fig. 8.2.1). The two liquids represented in the graph are dioxane, $\kappa = 0.013$, and water, $\kappa = 0.478$. For the typical noise in a T-ray spectrometer, for example $\delta\rho_s = 0.015$ (error in real part of measured sample spectrum $\tilde{S}_s$), the error in the estimation of κ depends on the thickness change of the sample. The error decreases for thicker samples, from Eq. (8.17), but for highly-absorbing liquids, such as water, the increased thickness attenuates the T-ray signal to a large degree. The vertical lines show the approximate thickness change desirable for minimum error. For dioxane (low κ), a thicker sample is desirable, approximately 4 mm. For water (high κ), the thickness change is much less, approximately 100 μm.

Figure 8.4 shows that a thickness change of even 1 mm generates a very high error in a high-κ liquid, thus limiting experiments to sub-mm modulation.

Conclusion

From the foregoing analysis of uncertainty, the best modulation system for liquid spectroscopy can be seen to depend on the properties of the liquid. For a low-κ liquid, a high accuracy can be achieved by using a very large thickness change up to $d = 10$ mm. For a high-κ liquid, only a small thickness change is possible, and the errors must be reduced in two ways: (i) the thickness change must be accurate, for example, by using a piezoelectric translator, and (ii) the inherent noise in the T-ray signal must be reduced, by using for example high-frequency sample modulation in double-modulated DTDS.

For dioxane measurements, an accuracy of approximately 10^{-4} is desirable, thus from Eq. (8.16), a thickness change of approximately 10 mm is required, with a resolution of 1 μm. Since dioxane has low absorption, this is possible.

For water measurements, a thickness of 1 cm is unusable since the T-ray absorption is too high. A thickness change of approximately 100 μm and a resolution of 10 nm is required, using for example a piezoelectric actuator.

8.3 Experiment

This Section describes an initial experimental verification of the accuracy of liquid DTDS and discusses its limitations.

The experimental implementation of liquid DTDS involved three main elements: (i) a standard T-ray transmission spectrometer, (ii) a sample holder for modulating the liquid sample at a modulation frequency f_2, and (iii) electronic signal processing to extract the sample and reference waveforms, y_s and y_r. The spectrometer used in these experiments was the same system used in standard liquid transmission spectroscopy (see Secs. 4.2.1 and 5.2.2), and is shown schematically in Fig. 8.5.

The sample holder was required to provide a rapid transition between a thick and thin sample, corresponding to y_s and y_r in dual-thickness spectroscopy. In the prototype system this was implemented using one large fixed Teflon window and one moving window mounted on an audio speaker, as shown in Fig. 8.6. The speaker was driven by a square wave to switch rapidly between the thick and thin positions. The signal processing consisted of two parts: the standard DTDS double de-modulation to extract

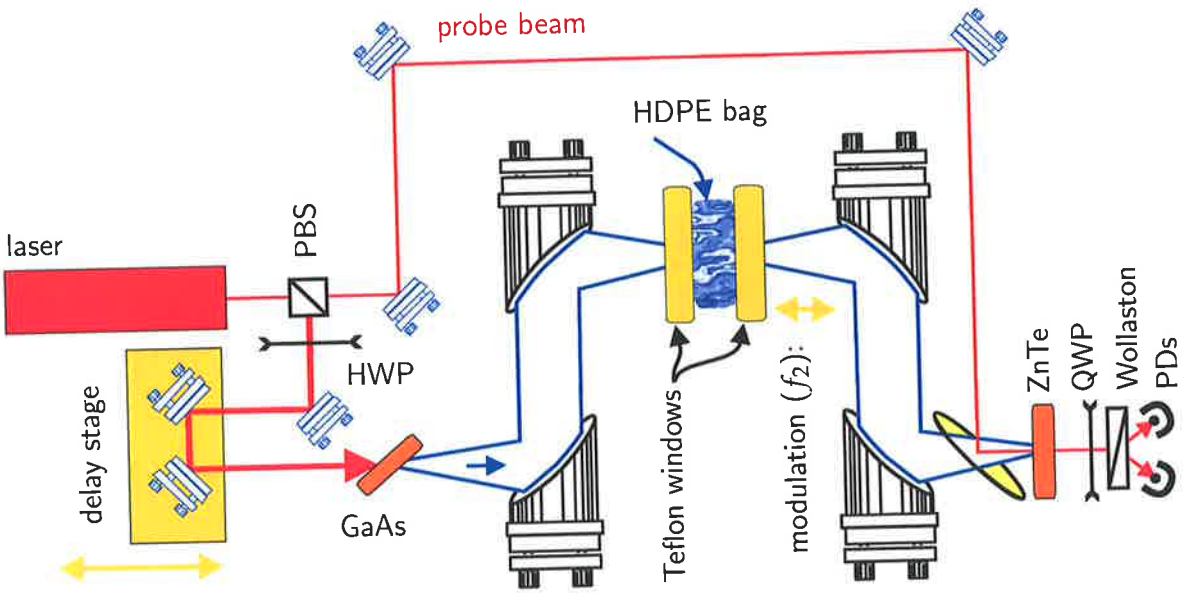

Figure 8.5. Liquid DTDS spectrometer schematic. This schematic depicts a standard T-ray spectrometer configured for characterising a liquid sample, described in Sec. 5.2.2. In liquid DTDS the thickness of the sample was modulated dynamically at a frequency f_2, and the electronic demodulation is similar to thin film double-modulation DTDS. The Ti:sapphire mode-locked laser generated a train of 100-fs pulses at 82 MHz. Each pulse was split into a pump beam and a probe beam with a polarising beam splitter (PBS). The pump beam generated T-ray pulses when incident at Brewster's angle on the GaAs wafer – a half-wave plate (HWP) was used to optimise the polarisation of the pump beam for maximum T-ray power, and the delay stage changed the relative time-delay of the T-ray pulse and probe beam in the ZnTe T-ray detector. The GaAs emitter was positioned at the focal point of a gold-coated parabolic mirror, which collimated the T-rays. Three other mirrors focused the T-rays into the sample holder, then collected the transmitted radiation and directed it into a ⟨110⟩ ZnTe T-ray detector. The probe beam detected the T-ray electric field in the ZnTe through polarisation rotation, which was recorded with a Wollaston polarising beam splitter and balanced photodetectors (PDs). A quarter-wave plate (QWP) was used to balance the photodiodes to have equal current when no T-ray pulse was present. The thickness of the sample was modulated with two Teflon windows, one of which was mounted on a translation stage. The mixture was held in a sealed, thin-walled, high-density polyethylene (HDPE) bag, which did not react with the liquid samples used. Teflon and HDPE are transparent to T-rays (see Appendix C).

the difference waveform $y_d = y_s - y_r$, and a second part to measure the mean waveform $y_m = y_s + y_r$ (see Ch. 6). *Amplitude and mean detection* is described in Sec. 8.3.1 below.

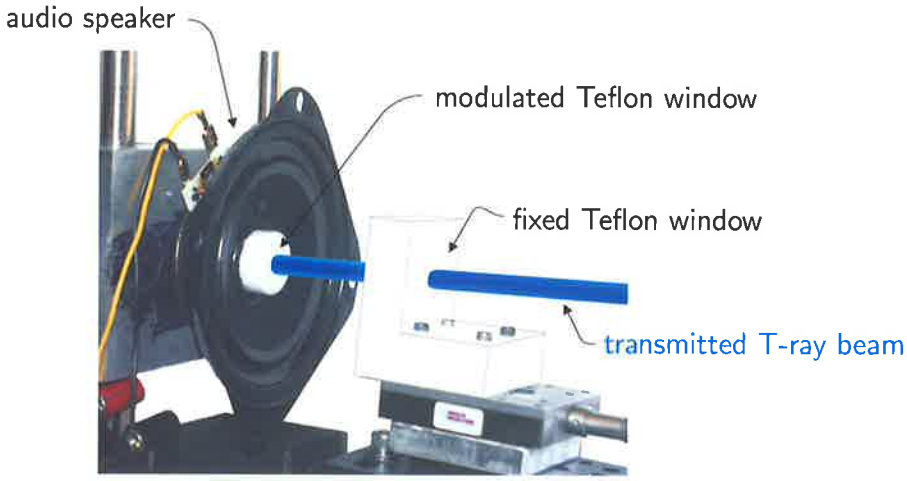

Figure 8.6. Photograph of the prototype liquid sample holder. This photograph shows the two Teflon windows of the sample liquid DTDS holder, one fixed to a stage and the other modulated by an audio speaker. One window was fixed to the optical table via a manual translation stage, which was set to the starting thickness of the sample to be modulated. The second window was mounted in an audio speaker, which was driven by a square wave of frequency f_2 from a signal generator (manufacturer: Stanford Research Systems, model: DS340). The thickness change must be a square wave because the models assume only two thicknesses are present: thick and thin. The modulated window travelled axially along the T-ray beam propagation direction, providing the required thickness modulation d. The amplitude of the modulation was set by the amplitude of the square wave current driving the speaker. The speaker was a 4"-diameter mid-range speaker with 8-Ω DC coil resistance (supplier: Radio Shack) and had a hole drilled through its permanent magnet to allow transmission of the T-ray beam. The hole in the speaker was over 5 mm in diameter, which was sufficiently large to prevent any clipping of the T-ray beam on the speaker housing, as confirmed experimentally. The path of the T-ray beam is marked in blue for clarity.

The two Teflon windows, mounted perpendicular to the T-ray beam axis, were thicker than 10 mm to avoid Fabry-Pérot reflections in the recorded waveform. Teflon is a good material for T-ray windows because of its low refractive index and low absorption (see Appendix C). The actual liquid samples are held in an high-density polyethylene (HDPE) bag, a material that does not dissolve in the solvent. HDPE has a low T-ray refractive index and low T-ray absorption (see Appendix C). With an average wall

thickness less than 0.1-mm thick, less than the majority of T-ray wavelengths, and a very low refractive index mismatch between Teflon and HDPE, etalon effects from the plastic bag walls were negligible. Experimentally, no multi-reflections were observed in the measured pulses.

For a liquid in the HDPE bag undergoing rapid movement, when the Teflon walls move apart, it is important that no bubbles form in the liquid itself due to the drop in pressure. The process by which bubbles form spontaneously in a liquid is generally called cavitation. Cavitation occurs on a liquid if the local pressure drops below the vapour pressure of the liquid (Lohse, 2003). Each bag was at least 50% filled with air, thus any increase in volume between the Teflon plates was compensated for by a decrease in air pressure, rather than a change in the pressure of the liquid by any large amount. No bubbles formed, and sufficient liquid was in the bag, so gaps were being filled by liquid pulled into the increasing volume.

The sample liquids used in the experiments were mixtures of the low-κ organic solvent 1,4-dioxane, similar to those used in Ch. 5. Most experiments were conducted using pure, anhydrous dioxane. The only experiments that used other mixtures were the uncertainty comparisons in Sec. 8.4.2. The dioxane (supplier: Aldrich, CAS No. 123-91-1, lot no. 29630-9) was 99.8% anhydrous and stored over Fisher 3-Å molecular sieves for over 24 hrs to maintain low hydration, as in Sec. 5.2.1. To hydrate the dioxane, deionised double distilled water was obtained from a purification system (manufacturer: Millipore, model: *RiOs*) and mixed into the solvents using a pipette. The third mixture used the protein Subtilisin Carlsberg (SC), (supplier: Sigma, CAS No. 9014-01-1, lot no. 91K1107) without further purification. The SC was buffered in doubly-distilled water and freeze dried for over 24 hrs, then immediately suspended in dioxane.

8.3.1 Amplitude and mean detection

Amplitude and mean detection is an electronic technique that enables the simultaneous measurement of both the sample and reference waveforms, y_s and y_r, when a sample is modulated in the T-ray beam. Amplitude and mean detection can be used in any double-modulated DTDS experiment and is implemented as part of the signal detection electronics. In amplitude and mean detection, instead of discarding 50% of the y_d waveform as in double-modulated DTDS (see Sec. 6.2.3), half the signal is used

to simultaneously measure y_r. The hardware requires no modification from double-modulated DTDS, and the time between measuring y_d and y_r is reduced from the order of minutes to the order of milliseconds. For measurements dominated by $1/f$ noise, a reduction in the scan-to-scan delay time increases the SNR, potentially by several orders of magnitude.

Conceptually, mean and amplitude detection can be implemented in stand-alone electronics, using for example a fast analog-to-digital converter ($\gg f_1$) and two stages of digital demodulation, synchronised with the movement of the delay stage. The diagram in Fig. 8.9 shows schematically how the double-modulated signal from the T-ray system is demodulated in two stages.

The double demodulation process can be understood in the time domain by looking at the square waveform detected by the photodiodes as the sample is modulated differentially. A model of the waveform current that would be detected by the photodiodes is shown in Fig. 8.7. The sketch includes indications of the relationships between the mean and amplitude waveforms (y_m and y_a respectively) and y_s and y_r, which are measured at the output of the first mixer (see Fig. 8.8).

The relationship in Fig. 8.7 shows that the sample and reference waveforms can be calculated from the amplitude and mean as follows:

$$y_s = y_m - y_a, \tag{8.19}$$

$$y_r = y_m + y_a. \tag{8.20}$$

The factors of 2 are missing in Eq. (8.19) and Eq. (8.20) because y_r and y_s are effectively halved by dithering the sample – double modulation causes a 50% reduction in the T-ray signal (see Sec. 6.2.3). The trade-off is a 50% reduction in the signal level for measuring y_r and y_s simultaneously.

The experiment can be realised with an anti-aliasing filter, a local oscillator referenced to f_1, a local oscillator referenced to f_2 and an integrator, as shown in Fig. 8.8.

In the experimental work in this Thesis, the system was implemented with three LIAs (Lock-In Amplifiers), as shown in Fig. 8.9. The same effect could be achieved digitally with a low-noise preamplifier, a fast analog-to-digital converter and a dedicated processor.

Figure 8.10 shows the results of an experimental test of mean and amplitude detection in the T-ray spectrometer. The mean and amplitude waveforms were measured

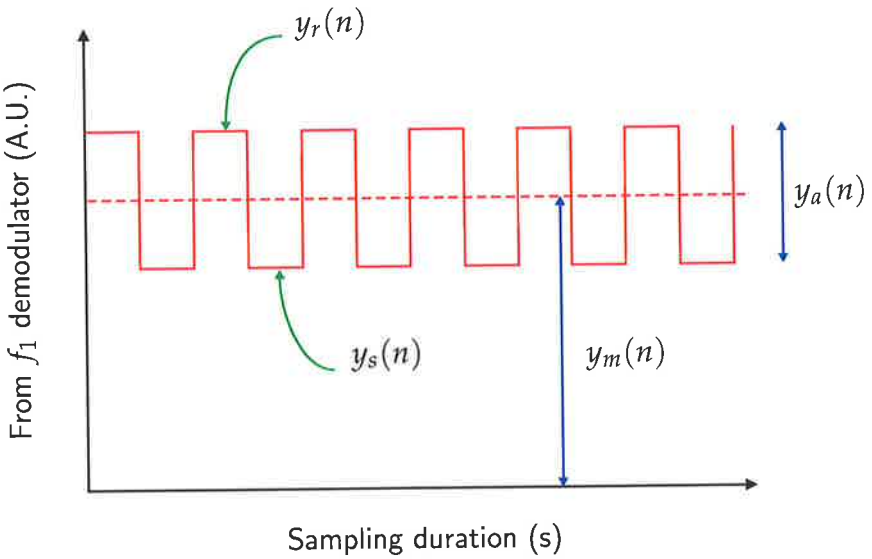

Figure 8.7. Modelled waveform at one delay point in amplitude and mean detection. This sketch models the output of the f_1 demodulator, shown in Fig. 8.9, being modulated by the sample modulation (for example, by repeatedly changing between two liquid sample thickness). This is the time-domain waveform seen for the nth step of the delay stage. The relationship between y_m, y_a, y_s and y_r can be seen in the diagram. Errors arising from amplitude and mean detection are caused by deviations of the observed signal from an ideal square wave, and this depends on the physical constraints of the system, as discussed in Sec. 8.2.2.

as shown in Fig. 8.9, that is, the outputs of the 2nd and 3rd LIAs respectively. The accuracy of the technique was confirmed by comparing the calculated waveforms, from y_r-calc $= y_m - y_a$ and y_s-calc $= y_m + y_a$ using amplitude and mean data, to two waveforms measured using normal T-ray TDS, y_r-exp and y_s-exp. The slight difference between y-calc and y-exp in Fig. 8.10 was due to the sample being modulated by an imperfect square wave. This was a mechanical error introduced by the prototype mechanical sample modulation arm, that is the galvanometer (see Fig. 6.8).

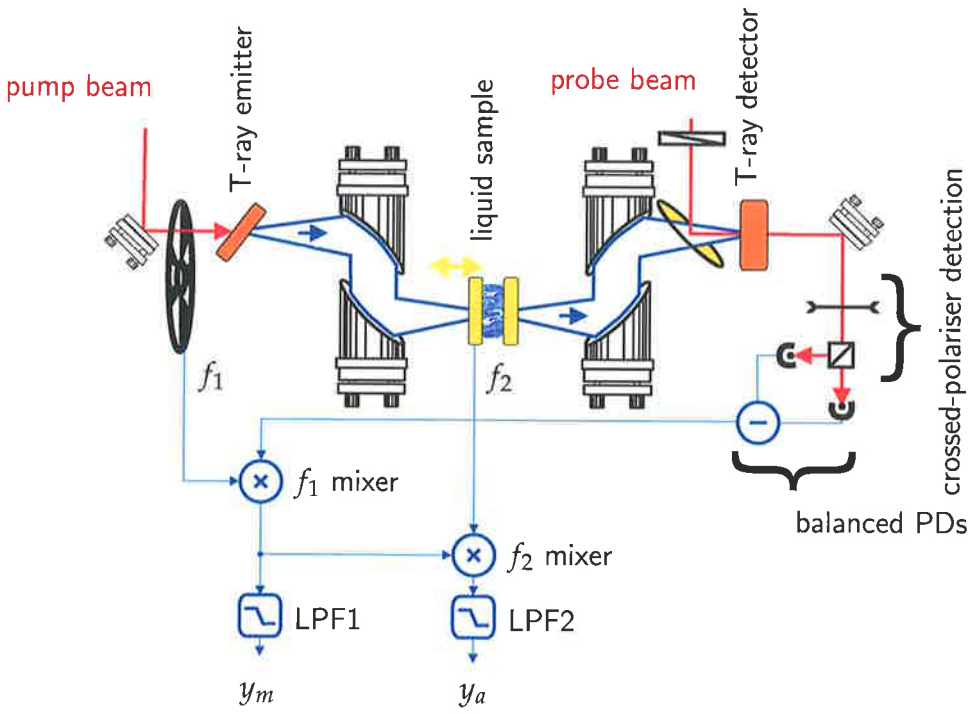

Figure 8.8. Liquid DTDS spectrometer schematic, configured for amplitude and mean detection. This schematic describes a T-ray spectrometer with a liquid DTDS sample holder. The standard spectrometer elements are described in Ch. 3. The experimental system is the same as described in Fig. 8.5, except this Figure also shows the electronics used in amplitude and mean detection (described in Sec. 8.3.1). The optical chopper wheel modulates the T-ray beam at frequency f_1 with an on-off square wave signal, then the sample holder imparts an additional modulation at frequency f_2. The T-ray signal is detected using the crossed polarisers and balanced photodiodes, then demodulated in two stages by mixing with electronic oscillators f_1 and f_2. The phase on these local oscillators is locked to the physical modulators. By low-pass filtering the outputs of the two mixers, the values of y_m and y_a can be measured at each delay stage point, as shown in the time-domain in Fig. 8.7.

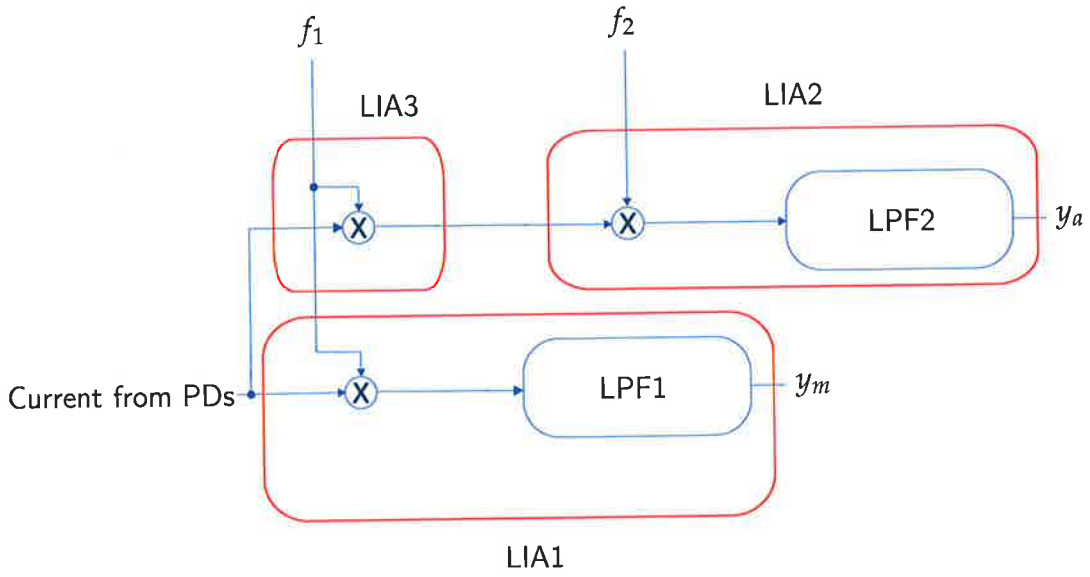

Figure 8.9. Data flow schematic of mean and amplitude detection. This block diagram shows the signal processing steps required to extract the y_m and y_a waveforms from the balanced photodiode current. The blocks are shown implemented with LIAs, as in the experimental Section of this Chapter, Sec. 8.4. The double-modulated signal from the balanced photodiodes (PDs) is demodulated in two stages. The first demodulation by the higher frequency f_1 is performed by the third LIA. The output of this first demodulator is shown as the square waveform in Fig. 8.7. The first LIA performs the same demodulation, then uses an in-built Low-Pass Filter (LPF), 'LPF1', to output the mean of the modulated waveform. The first LIA is part of the normal noise reduction of T-ray TDS: the mechanical chopper provides an AC signal that is detected by the first LIA, which smooths out any other modulation. The second demodulation by the low frequency f_2 in the second LIA is followed by a narrow band 'LPF2'. Experimentally, the bandwidth of the LPFs are determined by the time constants of the LIAs. The third LIA acts as the f_1 demodulator, with a short time constant (approximately 30 μs), and the second LIA acts as the f_2 demodulator with a long time constant (approximately 100 ms).

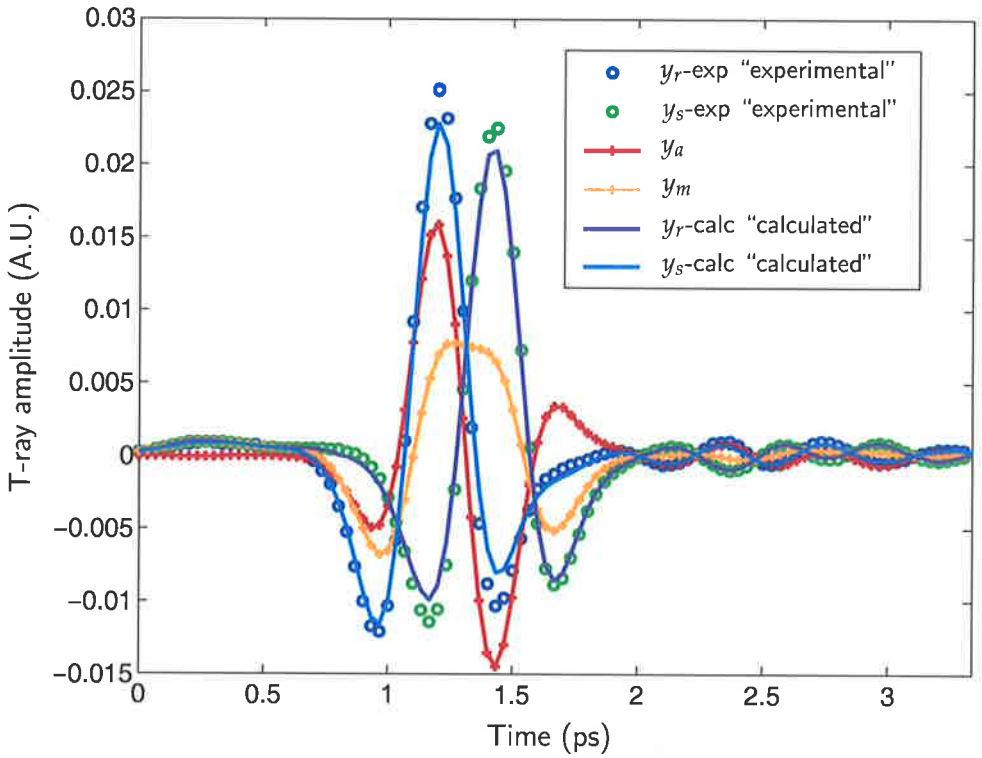

Figure 8.10. Measured waveforms from amplitude and mean detection. These waveforms are an example of single-scan DTDS. The waveforms y_m and y_a were measured with double-modulated DTDS, using the system shown in Fig. 8.9. The 'y-calc' waveforms were calculated from $y_r = y_m - y_a$ and $y_s = y_m + y_a$. 'y_r-exp' and 'y_s-exp' were measured using the same T-ray spectrometer and sample, but without modulating the sample and taking two separate sample and reference scans (normal T-ray TDS). The match between 'y-calc' and 'y-exp' is an experimental confirmation that amplitude and mean detection provides exactly the same information about a sample as normal T-ray TDS, but with a potentially far lower noise level.

8.4 Results

The results for a preliminary demonstration of liquid DTDS show that liquid spectroscopy is functional, and show the technique's limitations. The difference waveform y_d was shown experimentally to be equal to $y_r - y_s$, as required for the DTDS analysis. The accuracy of the measurements, which is critical to accurate sample characterisation, was shown to depend on the static linearity of the actuator (audio speaker), the dynamic non-linearities introduced at higher modulation frequencies and larger modulation amplitudes. The goal in a liquid DTDS system is to have as large a movement as possible at as high a frequency as possible. A large movement (thickness change d) increases the accuracy of the parameter estimation (see Sec. 8.2). A higher modulation frequency reduces $1/f$ noise in the final result – this is due to the nature of $1/f$ noise, where larger fluctuations occur over longer time scales than the short modulation period. The best possible modulation amplitude and frequency depends on the mechanical limitations of the sample holder, as seen in the following results.

8.4.1 Sample modulator calibration

The mechanical modulation system had to be experimentally calibrated to explore: (i) its accuracy, (ii) its possible modulation frequency range, and (iii) possible modulation amplitude range.

Linearity

For DC driving voltages, the audio speaker was found to have a displacement vs. voltage characteristic shown in Fig. 8.11. The displacement was essentially linear for a nominal driving voltage from -3.0 to +3.0 volts, with a slope of approximately 0.36. The error in displacement measurements $\delta d \approx 0.05$ mm. The displacement to displacement error ratio, $\delta d/d$ can dominate uncertainty in parameter estimation, and therefore must be minimised (Sec. 8.2). For accurate sample characterisation, linearity is required to create a mechanical square wave (see Fig. 8.7), and repeatability is required for high accuracy.

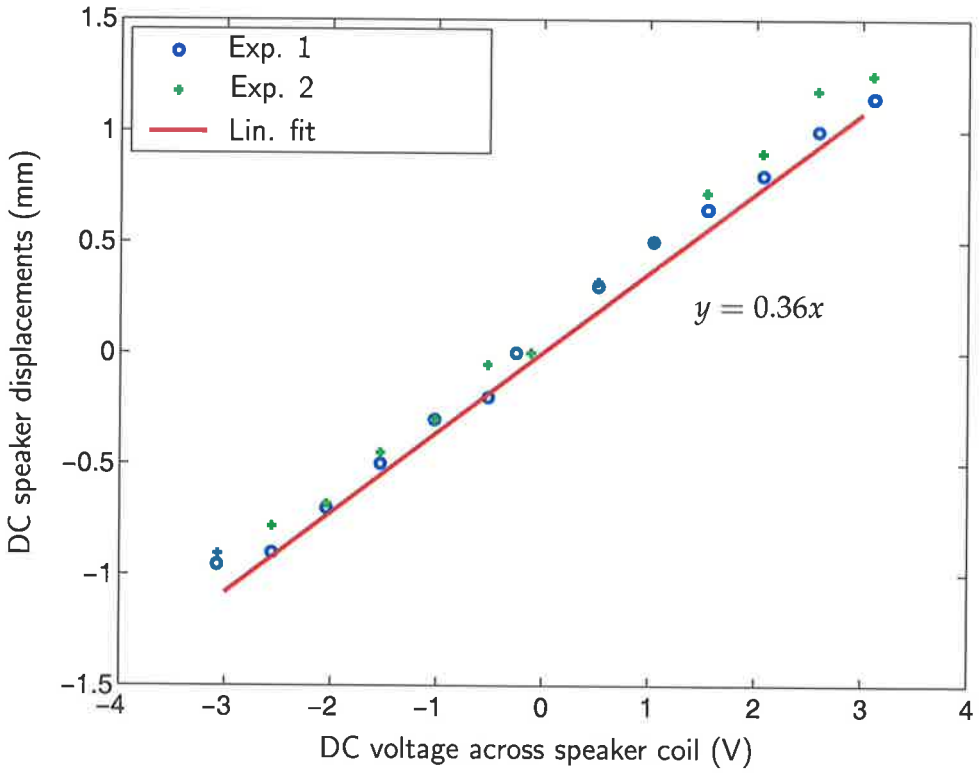

Figure 8.11. Calibration of DC linearity in the audio speaker. This plot demonstrates the DC linearity of the 4" mid-range audio speaker. This data was determined manually using a micron-resolution manual stage to measure the displacement at each different DC bias voltage. The two measured plots, green and blue, give an indication of the repeatability of the speaker's motion. The linear fit shows the speaker's displacement is almost linear to the driving voltage. This linear relationship was necessary for the experiments in this Chapter in estimating a value for the thickness modulation of the liquid sample d in dual-sample DTDS – the dynamic value of d was estimated from the driving voltage and this static linear relationship. This technique does not provide a wholly accurate measurement of d and contributed to errors in the prototype measurements.

Modulation frequency range

The DC characteristics of the audio speaker are less important than its AC, or dynamic, characteristics. The most important feature of the system's dynamic characteristics is that it accurately provides a square-wave motion, and therefore a y_d (and y_m) is accurately detected. This accuracy can be estimated by comparing a normal TDS difference measurement, $(y_r - y_s)/2$, to a DTDS measurement y_d. The accuracy is quantified by the spectral ratio of the two measurements over a certain frequency range where the T-ray signal is strong, for example 0.3 to 1.1 THz.

To determine the best modulation amplitude and frequency, measurements of y_s, y_r and y_d were taken with the T-ray spectrometer and a sample of anhydrous hexanes (approximately 10-mL in the HDPE bag).

Figure 8.12 shows the measured accuracy of the DTDS measurements for increasing modulation frequency. The modulation frequency was limited to a range of approximately $2< f_3 <10$. These measurements were all made at a modulation amplitude of 1 V AC. The 'ref' line indicates a ratio of 1.6, which is the ideal ratio between $(y_r - y_s)/2$ and y_d for a modulation system of perfect accuracy. Using double-modulation, this ideal amplitude would be

$$y_d = A \times (y_r - y_s) \tag{8.21}$$

where $A = 0.5 \times 0.6$. The factor of 0.5 arises from double-modulation, and the factor of 0.6 accounts for the LIA measuring only the fundamental sinusoidal component of the actual square wave (see Sec. B.7).

These results indicated a maximum possible modulation frequency of about 10 Hz for this hardware.

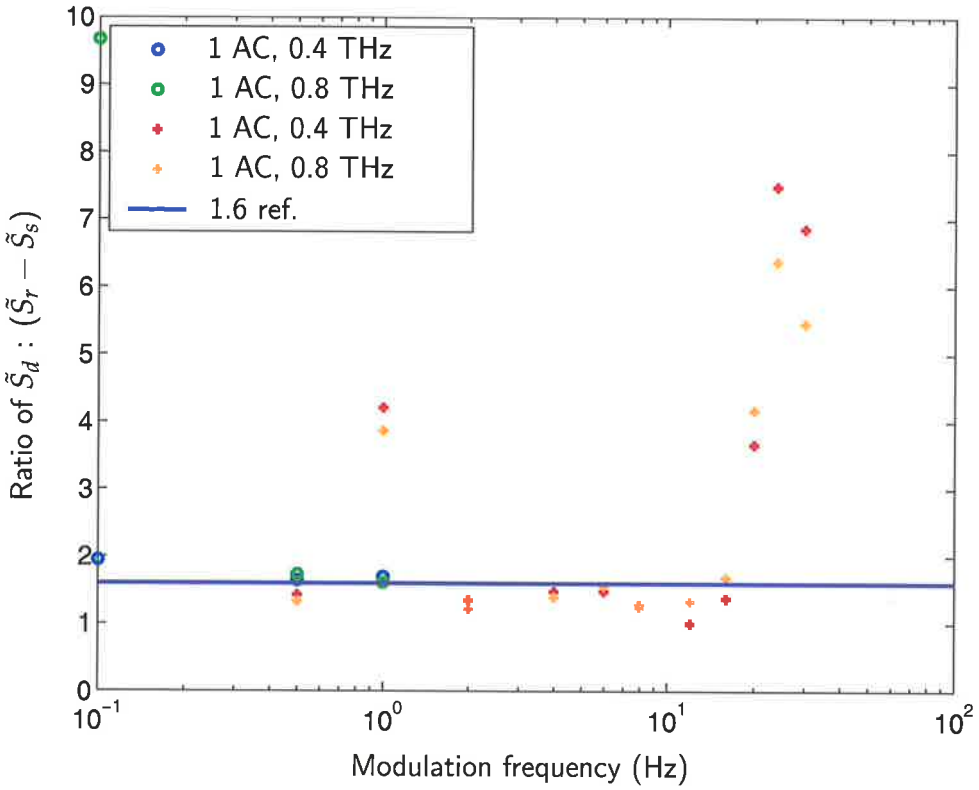

Figure 8.12. Calibration of optimal audio speaker modulation frequency. These data show how the accuracy of liquid DTDS decreases at high and low modulation frequencies. The accuracy was measured by calculating the ratio between the DTDS waveforms and the TDS waveforms from the same sample – The purple reference line indicates a ratio of 1.6, which is the ideal ratio of $\tilde{S}_d/(\tilde{S}_r - \tilde{S}_s)$ if the DTDS measurements were ideal (no errors due to the modulation mechanism). This plot indicates that the best accuracy is obtained at a modulation frequency of between 2 and 8 Hz. The inaccuracies at higher and lower modulation frequencies arise from mechanical instabilities in the audio speaker modulation system. At frequencies outside the range 2 to 8 Hz, the displacement of the speaker is no longer linearly proportional to the driving voltage, thus distorting the ideally square waveform used in DTDS (see Fig. 8.7). All the measurements for this Figure were made with a displacement amplitude of 1 V AC peak. The plots for 0.4 and 0.8 THz are spectral components extracted from the pulsed waveforms. The plots for different T-ray frequencies have similar responses to the modulation frequency. This data was measured with a sample of anhydrous hexanes, chosen for its low T-ray absorption.

Modulation distance range

The accuracy of double-modulated DTDS measurements at different amplitudes was measured using a test sample of hexanes and a 10-Hz modulation frequency. The displacement amplitude d was limited to about 2.2 mm. Figure 8.13 shows the highest accuracy of the double-modulated DTDS measurements occurs at a displacement of 1.6 mm.

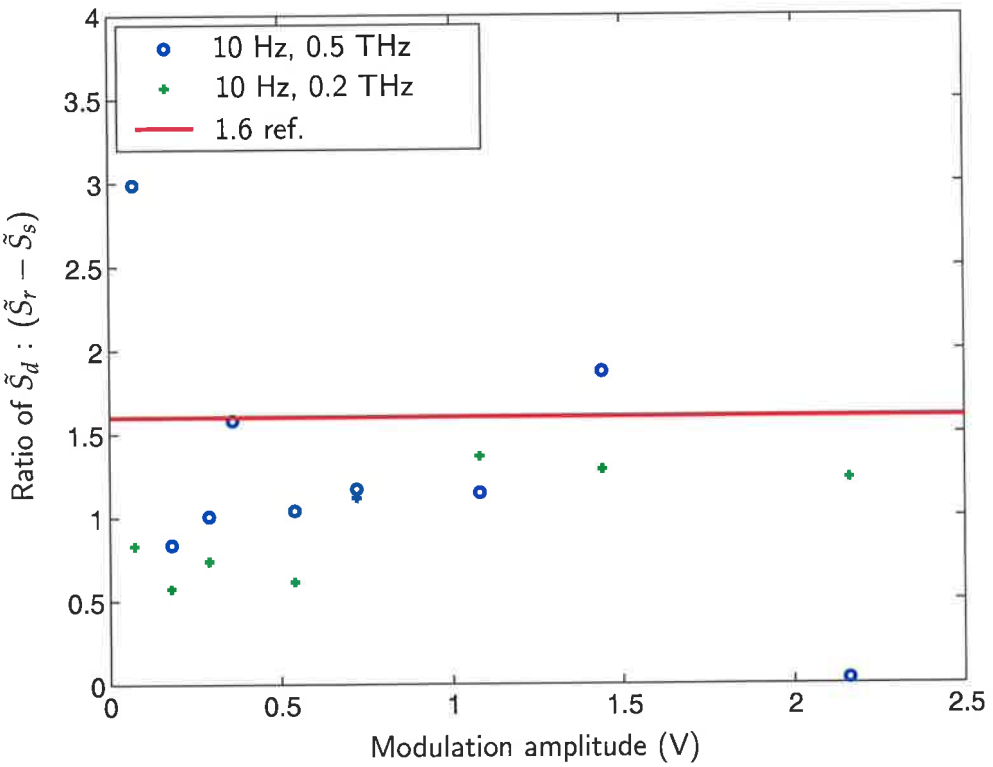

Figure 8.13. Calibration of optimal audio speaker modulation distance. This plot shows how the accuracy of liquid DTDS decreases at high and low modulation amplitudes. The same system and analysis were used as for the data in Fig. 8.12, except in this case the audio speaker limit of linearity for high and low modulation amplitude was explored. The 'ref' line indicates a ratio of 1.6, which is the ideal ratio of $\tilde{S}_d$:$(\tilde{S}_r - \tilde{S}_s)$ if the double-modulated DTDS measurements were ideal (no errors due to the modulation mechanism). The highest accuracy is achieved for a modulation amplitude of about 1 V AC (peak). From Fig. 8.11, this corresponds to an approximate displacement d of about 1.6 mm.

The most accurate measurements were taken at 10 Hz with a displacement of 1.6 mm. Figure 8.14 shows a direct comparison of the waveforms from double-modulated

DTDS (y_d) and normal TDS with these optimal settings. The large overlap of the waveforms experimentally verifies Eq. (8.21), and thus the assumptions behind amplitude and mean detection.

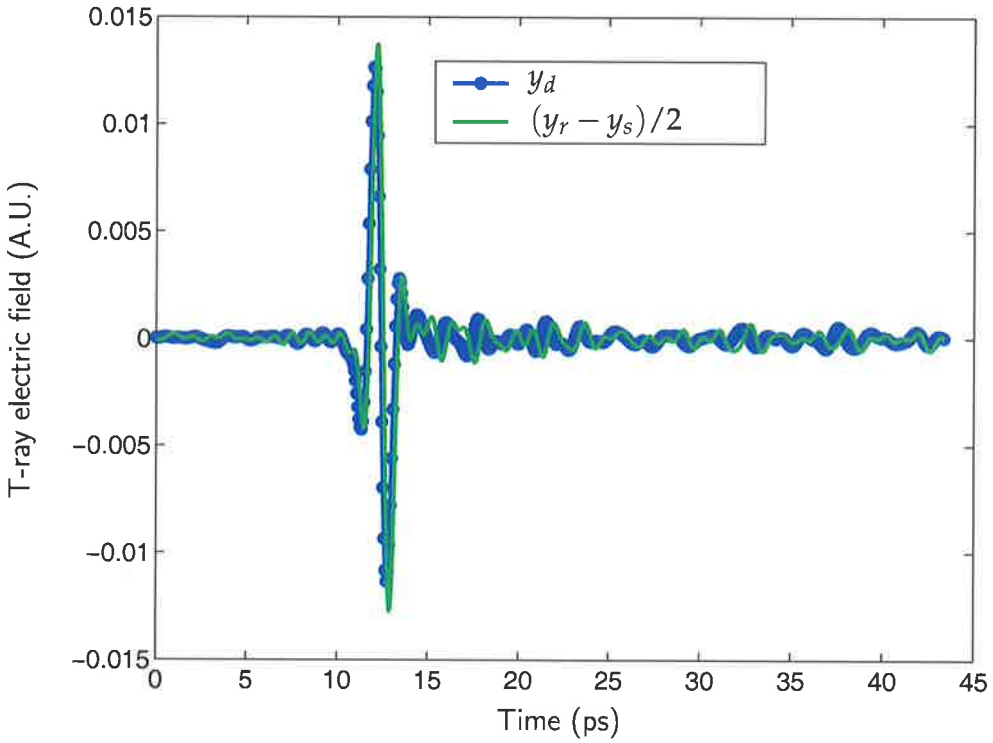

Figure 8.14. Measured comparison between TDS and DTDS. This graph compares the waveform from a liquid DTDS experiment, y_d, to the difference between two waveforms from normal TDS, $(y_r - y_s)/2$. Apart from changing the modulation of the sample, exactly the same experimental conditions were used. The waveforms have been smoothed with a bandpass filter for clarity. The filter was set at the T-ray frequencies with highest SNR for this experiment, which were 0.2 to 1.2 THz. The close match of the two waveforms demonstrates the accuracy of liquid DTDS in characterising a material – the same results are achievable as with T-ray TDS, with potentially far less noise.

The biggest problem with this system was the inaccuracy in the displacement measurements. The error due to δd is far greater than the error due to δT. For example, Table 8.1 shows approximate error levels for a typical spectroscopy measurements. The greatest source of error comes from inaccuracies in the measurement of d. The mechanical displacement accuracy can be greatly increased using a number of methods, including real-time external displacement measurement and closed-loop control. One method

of achieving a very low δd is to use a piezoelectric translation system, as discussed in Sec. 8.5.1.

Table 8.1. Measured error sources in liquid DTDS. This Table compares the errors arising from the T-ray spectrometer (due to $\delta\tilde{T}$) and the thickness measurement (due to δd) as they contribute to the overall material parameter uncertainty (δn and $\delta\kappa$). For the spectral component at 0.5 THz, for example, the noise in the T-ray spectrum was measured to be $\delta\rho = 0.020$ and $\delta\phi = 0.037$. The signal level was given by $\rho = 0.67$ and $\phi = 22.30$. The thickness change d was 1.6 mm. The thickness accuracy was either $\delta d = 5$ μm for the manual translation state in normal TDS, or $\delta d = 0.1$ mm for the audio speaker in double-modulated DTDS. These results come from actual measurements of anhydrous dioxane. The error estimates are calculated using the equations in Sec. 8.2.2. This Table shows that the effect of both sources is approximately the same for the manual stage, but the error due to δd is much greater for the double-modulated DTDS measurement. As discussed in Sec. 8.2.2, the error due to δd can be reduced even further for the manual stage by using a thicker sample change (increase d from 1.6 mm), then $\delta\tilde{T}$ dominates. The error in $\delta\tilde{T}$ can conceivably be reduced through double-modulated DTDS, but unfortunately in this prototype, the noise due to δd is so great, the overall noise is higher. This is addressed in Sec. 8.5.1 by proposing a new piezoelectric modulator.

Source	Parameter	Error	Modulation
due to $\delta\tilde{T}$	δn	0.0044	both TDS & DTDS
	$\delta\kappa$	0.0025	both TDS & DTDS
due to δd	δn	0.0042	TDS
		0.083	DTDS
	$\delta\kappa$	0.000075	TDS
		0.0015	DTDS

8.4.2 Experimental examples of uncertainty

To confirm the equations of Sec. 8.2.2, this Section describes the experimental repeatability and estimated uncertainty in actual dual-thickness experiments. Six T-ray TDS measurements of anhydrous dioxane were taken and the standard deviation was estimated using MATLAB. Then Eq. (8.16) was used to calculate the predicted uncertainty. The calculated uncertainty spectra for estimates of n and κ are shown in Figs. 8.15 and 8.16. The actual uncertainty in a series of measurements can be estimated from the standard deviation of a series of estimated values of n and κ. As shown in Figs. 8.16 and 8.15, the equations provide an accurate estimate or an over-estimation of the error. These results confirm the accuracy of the equations used above to quantify the sources of uncertainty.

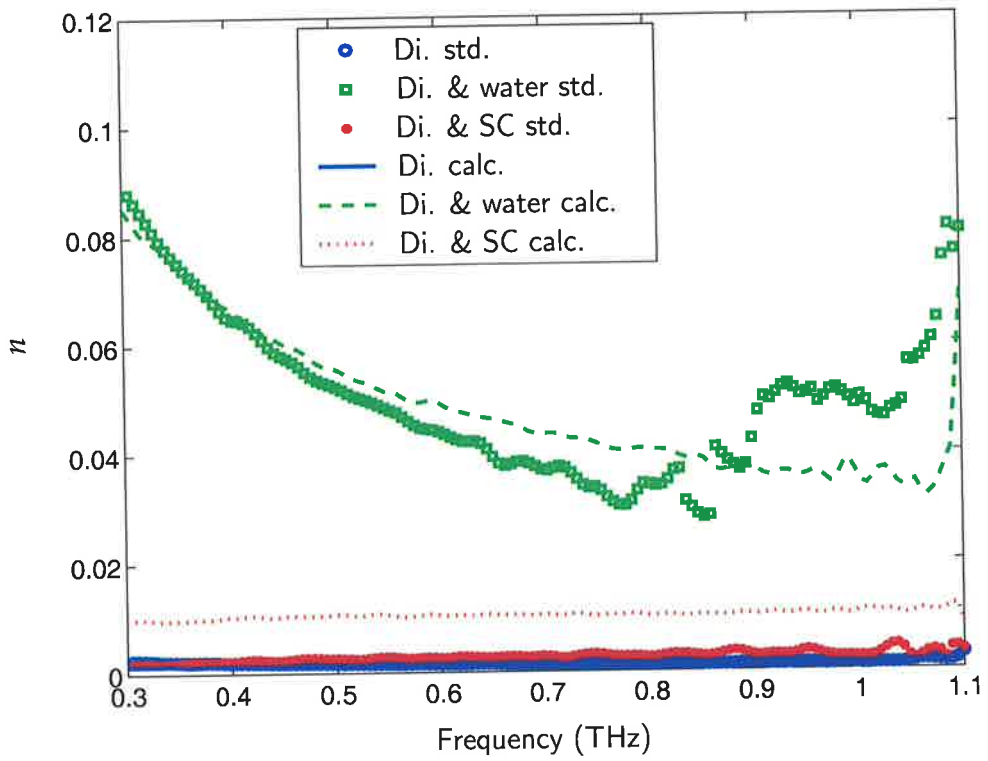

Figure 8.15. Theoretical vs. experimental uncertainties: refractive index n. This Figure compares: (i) the experimentally-determined standard deviation of six measurements, to (ii) the calculated standard deviation that would be expected from the uncertainty analysis in Sec. 8.2.2. The uncertainties, 'std.' are estimated with MATLAB's standard deviation function from six repeated experimental measurements. The dots, 'calc.' represent the standard deviation of the estimated values. The lines represent Eq. (8.16). The three examples are for mixtures of: anhydrous dioxane ('Di.'), dioxane & water ('Di. & water'), and dioxane & a protein suspension ('Di. & SC'). This Figure shows that, for the three liquids shown, the equations provide an accurate estimate or an over-estimation of the error, thus confirming the accuracy of the equations used to quantify the sources of uncertainty in Sec. 8.2.2.

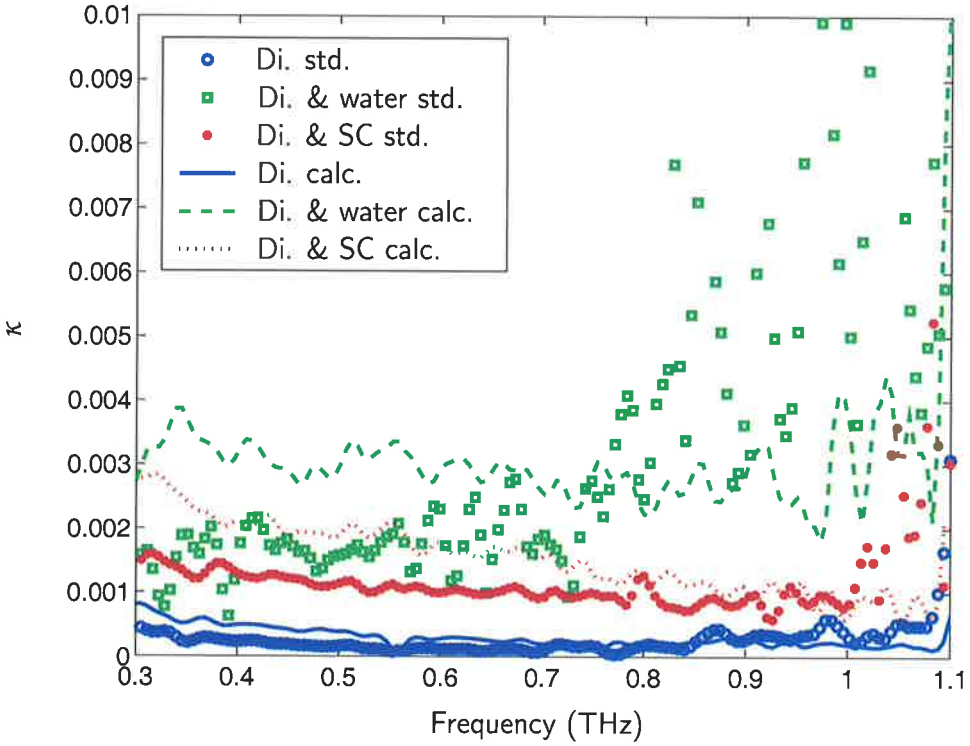

Figure 8.16. Theoretical vs. experimental uncertainties: extinction coefficient κ. As in Fig. 8.15, this Figure compares: (i) the experimentally-determined standard deviation of six measurements, to (ii) the calculated standard deviation that would be expected from the uncertainty analysis in Sec. 8.2.2. The uncertainties, 'std.' are estimated with MATLAB's standard deviation function from six repeated experimental measurements. The dots, 'calc.' represent the standard deviation of the estimated values. The lines represent Eq. (8.16). The three examples are for mixtures of: anhydrous dioxane ('Di.'), dioxane & water ('Di. & water'), and dioxane & a protein suspension ('Di. & SC'). This Figure shows that, for the three liquids shown, the equations provide an accurate estimate or an over-estimation of the error, thus confirming the accuracy of the equations used to quantify the sources of uncertainty in Sec. 8.2.2.

8.5 Conclusion

The results in this Chapter demonstrate a novel implementation of double-modulated DTDS for liquid spectroscopy. The prototype system confirmed a reduction in noise at an increased modulation frequency, and confirmed the accuracy of calculations to estimate the potential noise reduction achievable with this technique (Eq. (8.16)). Unfortunately the prototype system built introduced excessive mechanical noise at higher modulation frequencies and amplitudes.

8.5.1 Future work

In future work it is recommended that the sample holder system be implemented using a piezoelectric driven window. The advantage of a piezoelectric modulator over an audio speaker is the extreme accuracy of movement, with $\delta d/d$ better than 10^{-4}. A photograph of the proposed piezoelectric modulator is shown in Fig. 8.17.

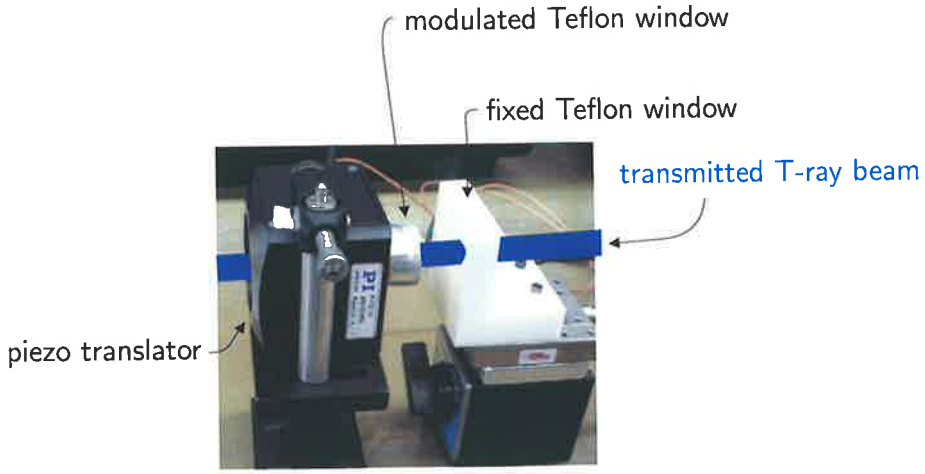

Figure 8.17. Piezoelectric sample modulator. The modulated Teflon window shown in this photograph is driven by a piezoelectric microscope objective positioner (manufacturer PI, Germany), instead of an audio speaker as in Fig. 8.6. The positioner has a travel of 350 μm, closed-loop resolution of 10 nm and a loaded resonant frequency of 100 Hz. It will be used to characterise highly-absorbing liquids. The mechanical noise will be far less than that of the audio speaker modulator. The path of the T-ray beam is marked in blue for clarity although it is not visible to the eye.

8.6 Chapter summary

The theoretical analysis in this Chapter, supported by preliminary experiments, indicates that rapid sample modulation can increase the accuracy of T-ray transmission spectroscopy of liquids by over 100 times. An increase in the accuracy of liquid parameter estimation by two or three orders of magnitude will be extremely valuable in many T-ray liquid experiments, including observing solvation processes and biomolecules in solution or suspension. The development of a piezoelectric-driven DTDS stage will enable highly-accurate measurements of highly-absorbing liquids, which is a step towards studying biological systems with T-rays.

T-ray systems are not only used for spectroscopy. One of the key developments of the last decade has been extending T-rays into two and three dimensions, creating images with T-rays. T-ray imaging is reviewed in the following Chapter.

Chapter 9

T-ray Imaging

THE ability to perform T-ray imaging demonstrates the value of T-ray applications in fields from ultrafast solid-state physics to clinical medicine. T-ray images are created when standard spectrometers are adapted for viewing samples in 2D or 3D, using raster scanning, Electro-Optic Sampling (EOS) and numerical image reconstruction techniques, including tomography. T-ray imaging is vitally important in biosensing of large-area biochips and in clinical applications of T-ray biosensing. Wider applications for T-ray imaging have been demonstrated in non-destructive industrial inspection and hazardous substance detection.

This Chapter reviews T-ray imaging techniques, technology and applications as background to the near-field imaging research in Ch. 10.

9.1 Introduction

T-ray techniques have been extended to two-dimensional imaging using a variety of scanning and CCD camera methods. These provide parallel processing for speed and image processing for visualisation. The first T-ray imaging systems used raster scanning of the sample to build up a 2D image, as discussed in Sec. 9.2. Using electro-optic (EO) detection, this has been extended capturing the T-ray image of the whole sample with a CCD camera. Using a 2D array of data speeds up the acquisition of information at the expense of losing signal power at each pixel. Simple contrast images in the T-ray domain can be developed using absorption information, delay information or a combination of the two. A T-ray image is shown in Fig. 9.1 of three digits on a plastic $100 note, showing the different T-ray transmission of the inks. Dry substances, such as paper and plastic, transmit T-rays with less than 1% attenuation. Further to a simple contrast image, it is possible to generate a two-dimensional array of waveforms at each pixel. Spectral analysis at each pixel can then provide molecular information about the sample across the field of view. Using a metric relevant to T-ray molecular classification, it is be possible to map samples in terms of their specific molecular composition, potentially valuable in chemistry, biology and medicine.

9.2 Scanning and synthetic aperture imaging

The first T-ray images were obtained by simply scanning a sample across the T-ray beam, and presenting neighbouring data points as pixels. The images were constructed of transmitted T-ray waveforms, with a number of contrast mechanisms available: total transmitted amplitude, peak delay at each pixel, and transmitted amplitude or delay of a given Fourier component. The technical advances that led to T-ray imaging were primarily methods of increasing the T-ray signal strength, coupled with faster acquisition speeds. The first demonstration of T-ray imaging had a 10–20 pixel-per-second waveform acquisition rate with a signal-to-noise ratio (SNR) of 100:1. This system relied on a 50-μm-gap SI-GaAs Photoconductive Antenna (PCA) emitter, a 5-μm-gap PCA detector, a 7.5-mm, 20-Hz scanning delay line for the gated detector, and a dedicated Digital Signal Processing (DSP) chip to sample, process and display the data (Hu and Nuss, 1995).

T-ray imaging based on detector scanning has been simplified by the availability of fiber-coupled PCA detectors, where the probe time delay and alignment remain fixed

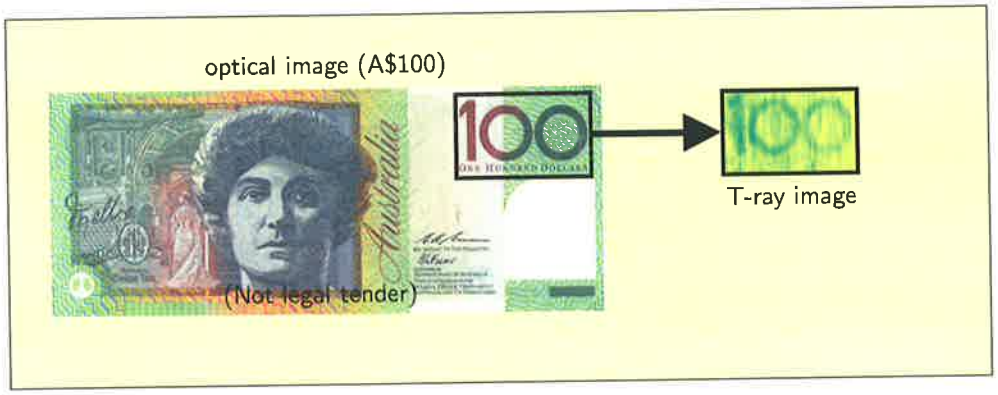

(a) Terahertz transmission image of a portion of an Australian $100 note. The T-ray absorption of the ink used to write the '100' is greater than that of the surrounding plastic, so the digits appear darker.

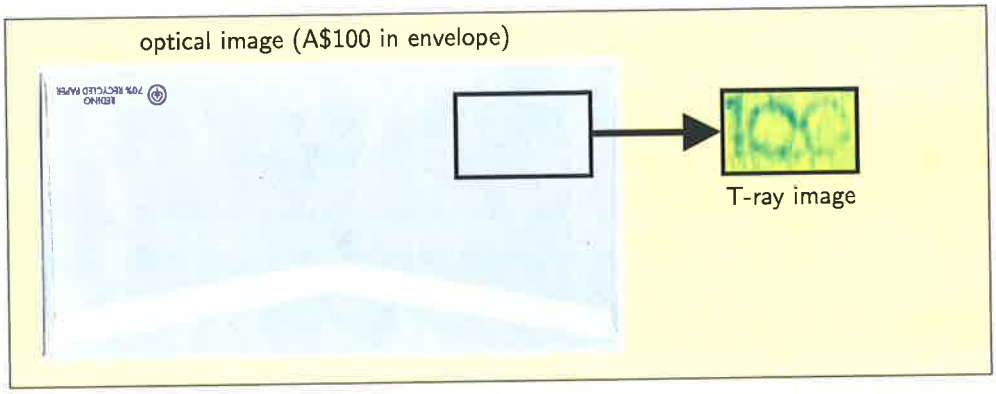

(b) Same note as in Subfig. 9.1(a), but this time the note is inside a paper envelope. The '100' still appears because paper has little effect on T-ray radiation.

Figure 9.1. Optical photograph and measured T-ray image of a plastic Australian $100 dollar note. This experimental data demonstrates that T-rays can be used to detect contrast in dry, non-polar samples, in this case due to the different T-ray spectroscopic differences in the inks used to print the currency. When the plastic note is placed in an envelope, the writing it no longer visible in the optical image. However, the T-ray image still shows the '100'. The dry paper envelope shows very low T-ray absorption (Mickan et al., 2000b). The envelope is oriented with the flap at the bottom, not in the T-ray path, otherwise the increased thickness of the flap would be visible in the T-ray image. The image was taken by raster scanning the note in a standard T-ray spectrometer.

by the fiber (Rudd et al., 2000b). A scanned PCA detector has been used to characterise the emission patterns from PCAs (Rudd et al., 2000a; Rudd et al., 2001; Rudd and Mittleman, 2002), and image the spatial reshaping of T-rays as they tunnel through a narrow air gap (Reiten et al., 2001c).

Reflection imaging requires reconstruction algorithms to estimate the shape and structure of the reflecting object. The reflected data can be acquired along a straight line, perpendicular to the emitter-sample normal, and the object shape can be reconstructed using Kirchhoff migration (Dorney et al., 2001b), or for data acquired over a hemisphere, the object profile can be calculated by numerical back-propagation (Ruffin et al., 2001). Enhanced depth resolution is achieved by scanning the sample in an interferometer, as described in Sec. 4.2.7 (Johnson et al., 2001a; Johnson et al., 2001b).

Synthetic aperture processing is used to reconstruct 3D T-ray images (McClatchey et al., 2001) and images with enhanced resolution (O'Hara and Grischkowsky, 2002).

9.3 PCA array imaging

It is preferable in an imaging system to have a 2D array of detectors, so the sample and detector remain stationary. Imaging array detectors are available for continuous-wave (CW) terahertz detection, from applications in mm and sub-mm astronomy (Uehara et al., 1992). Arrays of gated PCAs have been proposed but not yet developed (Mickan et al., 2000b; Abbott, 2000).

9.4 EOS CCD camera imaging

An effective method of 2D T-ray detection is to use an expanded probe beam in Electro-Optic Sampling (EOS), and detect the probe beam's polarisation rotation with a polariser and a CCD, as shown in Fig. 9.2. The advantage of using EOS is the increased bandwidth over PCAs and the simplicity of array imaging. The central trade-off remains between speed and SNR; for 2D imaging, the T-ray beam is expanded to encompass the entire object, which spreads out the available T-ray power over the number of pixels. The main advantage is that neither sample nor detector need be moved to acquire the entire image.

An advance of EOS imaging is the ability to use chirped optical probe pulses, as described above in Sec. 3.3.2. The advantage of chirped probe measurements is that the

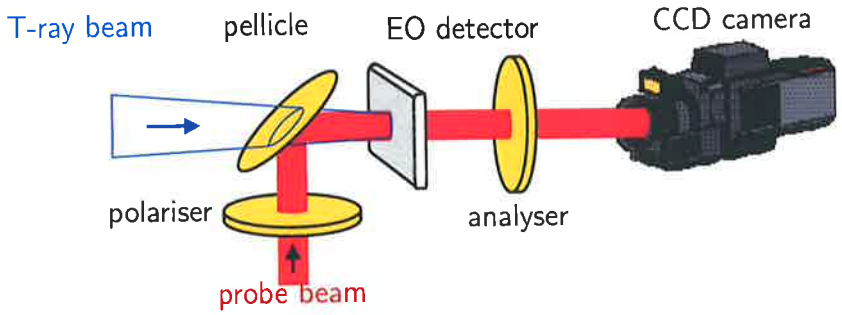

Figure 9.2. Diagram of CCD Electro-Optic Sampling. This schematic shows how Electro-Optic Sampling (EOS) can be implemented in 2D. As in normal EOS, described in Sec. 3.3.2, the T-ray beam is coincident with a polarised probe beam inside an EO crystal. Through the nonlinearity of the EO crystal, the electric field of the T-ray pulse rotates the polarisation of the probe beam. The extent of polarisation rotation is turned into an intensity modulation though an analyser (optical polariser oriented perpendicular to the first polariser). The intensity modulation of the probe beam is detected using a photodetector, or in the case of 2D EOS, an array of detectors. 2D EOS differs from point EOS in that both the probe beam and the T-ray beam are expanded onto the EO detector, and the transverse intensity modulation of the probe is detected by a CCD camera. The data is loaded directly to a computer for presenting a visual image. Three-dimensional data sets can be built up and analysed in XY slices, or with time on one axis. (After Wu et al. (1996c) and Wu et al. (1996a).)

entire T-ray waveform can be sampled with only one pulse, as schematically described in Fig. 3.12. Full waveforms can be acquired from 1D images with a CCD camera (Jiang and Zhang, 1998c). Two example waveforms are shown in Fig. 9.3, where a cross-sectional array of time-domain waveforms have been imaged simultaneously. This technique is close to the theoretical speed limit of T-ray imaging, although a reference measurement needs to be made to interpret the chirped waveform (Jiang and Zhang, 2000).

9.5 Tomography

When detected in reflection, the pulsed nature of T-rays enables analysis of a sample's internal structure, using tomographic reconstruction (Mittleman et al., 1996). T-ray tomography is an extension of T-ray ranging studies to more complex internal structures and 1D or 2D imaging. Tomography enables the visualisation of internal structure as different interfaces reflect pulses with varying delay and intensity. For example, a slice

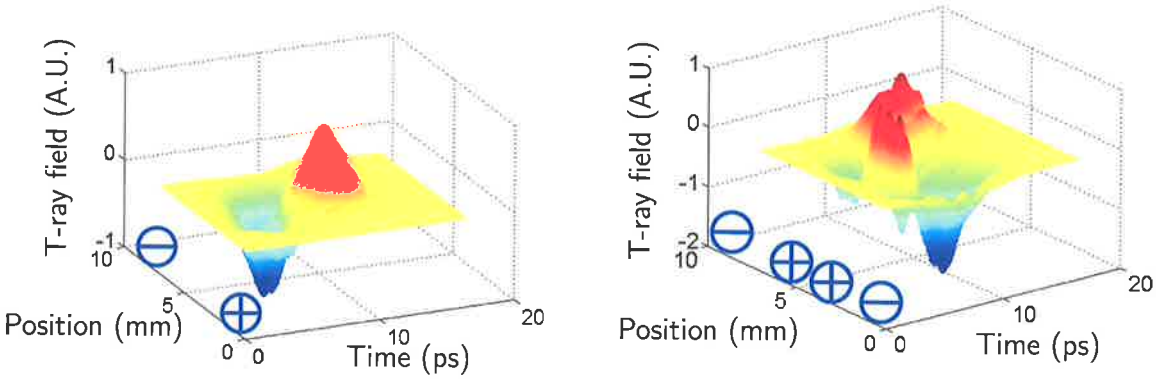

(a) Dipole field

(b) Quadrupole field

Figure 9.3. Measured images using single-shot 2D Electro-Optic Sampling. These examples of single-shot imaging show the spatial and temporal evolution of dipole and quadrupole T-ray fields (after Jiang and Zhang (1998b) and Jiang and Zhang (2000)). The EOS images show the emitted T-ray fields from dipole and quadrupole PCA emitters. The time evolution of the T-ray pulse is shown across the X dimension of the emitter, while the Y dimension shows a 1D spatial distribution of the field. The physical structure of the PCA emitters is represented by positive (+) and negative (-) voltage terminals on the plots. The dipole emitter has two terminals. The quadrupole emitter has four terminals.

of a floppy disc reveals layers of air, plastic and metal (Mittleman et al., 1997b). Information on the complex dielectric profile of a multilayered object can be estimated using Fresnel equations (Sec. 4.2) and an iterative algorithm (Mittleman et al., 1999). Using the frequency-dependent focal length of a Fresnel lens (see Fig. 3.13) enables images at different depths in a sample to be obtained using the different Fourier components of the broadband T-ray pulse (Wang et al., 2002; Ferguson et al., 2002c).

T-ray Computed Tomography (CT) and Diffraction Tomography are techniques for reconstructing an estimate of the internal structure of an object based on numerous transmission measurements (Ferguson et al., 2002b; Ferguson et al., 2002a). Fig. 9.4 shows a schematic T-ray CT spectroscopy system for imaging a small object, in this case a ping-pong ball.

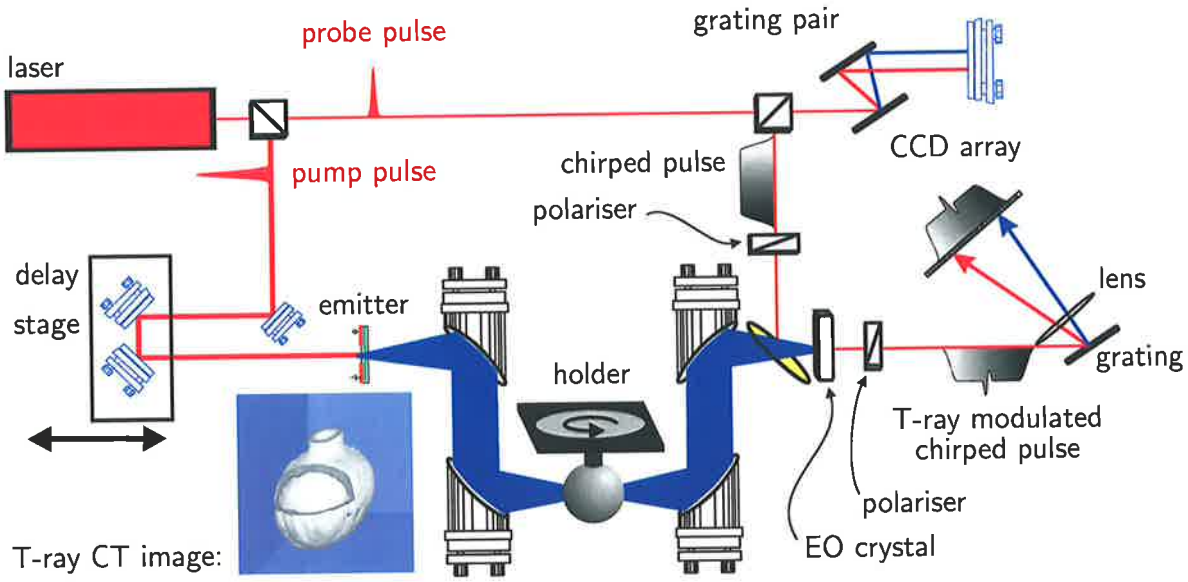

Figure 9.4. Schematic of T-ray Computed Tomography. This schematic layout of a T-ray CT experiment is based on a typical T-ray spectrometer layout, as described in Ch. 3 (after (Ferguson et al., 2001a)). The additions that allow single-shot imaging are: (i) the grating pair in the probe beam, (ii) the second grating and lens in the detector, and (iii) the CCD array detector. The second grating and CCD array can be replaced by an optical spectrometer. For a tomography measurement, the sample holder is scanned X–Y and rotated about its axis. To generate a CT image, it takes approximately 1 hour to scan 100×100 images at 18 projection angles, which is sufficient to reconstruct a 3D sectionable profile of the object using computed tomography algorithms. A T-ray CT profile is shown in the bottom left, with a quarter cut away to reveal the internal structure. The spatial resolution of T-ray CT is given by the angular rotation multiplied by the radius of rotation at the edge of target. For the plastic ball, the radius is approximately 2 cm, therefore the spatial resolution on the surface of the ball is 3.5 mm.

9.6 Speed

The trade-off of speed versus SNR is central to all T-ray spectrometers, particularly in imaging where large data sets have to be acquired in a realistic time, for example, while a person waits in a clinical setting. The speed of image acquisition can be estimated from the time taken to acquire a sufficiently long T-ray waveform at each pixel at a certain SNR. For example, the first scanning PCA imaging system demonstrated 25-ps-long scans acquired in 5 ms with a SNR of 100:1 (Hu and Nuss, 1995). In 2001, high-power PCA T-ray systems reported 35-ps-long scans acquired in 20 ms with a

SNR $\approx$ 3000:1 (Zhao et al., 2002a). The SNR increases proportionally to $\sqrt{t}$, where t is the time spent averaging data samples. For a SNR of 100:1, 2D EO imaging can be used to sample 20-ps T-ray waveforms, at 200 sample points, over a 288×384-pixel array in approximately 200 ms. Signal processing can be used to improve the SNR of T-ray images (Mittleman et al., 1996; Ferguson and Abbott, 2001b; Ferguson and Abbott, 2001a).

9.7 Dielectric imaging

Samples that have been studied in the search for applications of T-ray imaging include those where spectroscopic information is of interest, such as gas flames, and more complex samples, where contrast cannot be clearly linked to a single dielectric constant. Dielectric studies have been performed to image the carrier concentration and mobility in Silicon wafers (Herrmann et al., 2002), the Hall effect (Sec. 4.3.3), currency watermarks (Chen and Zhang, 1999) and thin ceramic oxide with tomography (Brucherseifer et al., 2001).

9.8 Classification algorithms

One of the advantages of T-ray imaging over incoherent imaging techniques, such as those using X-rays or visible light, is the coherent nature of the measurements. A full T-ray waveform can be acquired for each pixel and used to interpret the image spectroscopically. For 2D images, the intensity of each pixel can be linked to a number of spectroscopic parameters, including absorption or phase delay of a specific spectral component, peak absorption or peak delay. Images of flames have been false colour coded to indicate the magnitude of T-ray pulse delay in transmission (Mittleman et al., 1996). The magnitude of the pulse peak has been used to code images of currency (Mickan et al., 2000b; Ferguson and Abbott, 2000). More complex metrics can be developed to represent a combination of factors, specifically chosen to emphasise differences in spectra of different materials. This becomes a classification task, and the metrics can be algorithms trained from known data to be either one sample or another. The results of the application of a simple classification algorithm are shown in Fig. 9.5. Classification is a digital signal processing task, often using linear filters to generate the parameters of importance.

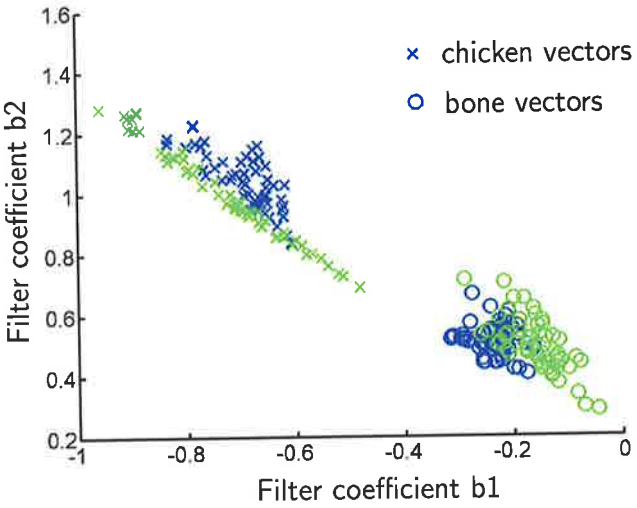

Figure 9.5. Classification results for measured bone and chicken spectra. This plot shows the effective classification of T-ray waveforms using coefficients $b1$ and $b2$ derived by fitting the data to one of two finite impulse response filters. The filters were developed with known training data. The fast algorithm clearly differentiates between bone and meat in this chart, depending only on the two coefficients (after Ferguson et al. (2001b)). The use of this classifier in imaging is shown in Fig. 9.6.

T-ray images coloured by classification metrics have been used for imaging the Hall effect in semiconductors (Mittleman et al., 1996), and biological tissues (Woodward et al., 2001; Ferguson et al., 2001b). An example of a classified T-ray image is shown in Fig. 9.6. The image is a two-dimensional map of the output from the classifier shown in Fig. 9.5.

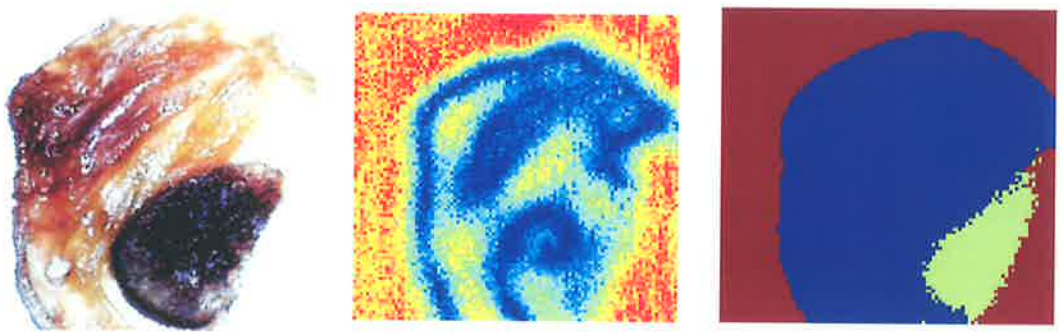

(a) Optical photograph (b) T-ray amplitude image (c) Classified T-ray image

Figure 9.6. Comparison of a classification image with a T-ray amplitude and an optical image for cooked meat and bone. These three images demonstrate the utility of a simple classification algorithm (classification is shown in Fig. 9.5). The optical image in Subfig. 9.6(a) shows a sample of cooked meat and bone. The image in Subfig. 9.6(b) is a plot of transmitted T-ray amplitude, and shows poor discrimination between the sample meat and bone. Using a classifier algorithm on T-ray data of the same sample, the background, meat and bone can be automatically and clearly differentiated, as shown in Subfig. 9.6(c). The classifier provides far clearer data than just using transmission amplitude information. This demonstrates that signal classification is successful in utilising the entire sample T-ray waveform to differentiate between two classes (after Ferguson et al. (2001b)).

9.9 Bio-imaging

The importance of T-rays in biomedicine has been demonstrated in human and plant tissue (Fitzgerald et al., 2002a; Woodward et al., 2001; Han et al., 2000a). An example of T-ray contrast in biological tissue is shown in Fig. 9.7. T-rays are valuable for their low power and non-ionising nature, meaning living tissue it not damaged.

Although some information on the T-ray response of biomaterials and tissues is clearly available, an understanding of the contrast mechanisms can only be achieved through more fundamental biosensing experiments, such as those described in previous Chapters. An understanding of T-ray contrast in bio-tissues will link real-time T-ray imaging with non-invasive, *in situ* T-ray biopsy. Bio-imaging is closely linked to T-ray biosensing in the field of array biochips, where samples are analysed in large numbers in parallel. Biochip arrays are used in studies of DNA and proteomics. For high-density arrays, as used for high-throughput applications, high resolution T-ray imaging is required. To achieve micron-scale resolution with T-ray radiation, for biosensing and biochip applications, it is necessary to use near-field techniques, as described in Ch. 10.

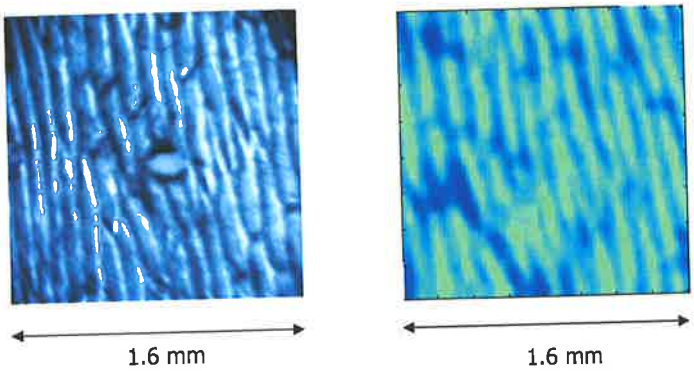

(a) Optical image (b) T-ray image

Figure 9.7. Comparison of an optical photograph and a T-ray transmission image of a slice of onion skin.. The T-ray image on the right shows cell-level resolution and contrast due to the biological structure. The resolution of the image is limited by the wavelength of the T-rays to the order of 100 μm. In this particular image, the resolution has been improved by filtering out the lower-frequency components of the T-ray pulses, which have a worse resolution of the order of 1 mm. The two images in this Figure are from the same onion sample, but at different areas on the surface. (After Han et al. (2000a))

9.10 Chapter summary

This Chapter has reviewed the advances in T-ray imaging from raster scanning to one-shot imaging. This discussion of T-ray imaging provides the background to the near-field T-ray experiments described in the following Chapter. Near-field techniques are needed for T-ray imaging with spatial resolution higher than the wavelength of the T-rays, which limits far-field T-ray image resolution to the order of 100 μm.

The following Chapter discusses experiments conducted on a sub-wavelength-sized T-ray source using Optical Rectification (OR).

Chapter 10

T-ray Microscopy

T-RAY microscopy is necessary for imaging samples with sub-100-μm resolution. At this resolution, cell-level functional medical imaging, for example, would be an important application for T-ray microscopy. To achieve this sub-wavelength (sub-λ) spatial resolution, near-field imaging techniques are required. In the past, mainly aperture-based techniques have been used to improve T-ray resolution, but this Chapter presents an all-optical technique through Optical Rectification (OR) in a sub-λ-sized volume. A tightly-focused optical beam generated T-rays in a 10-μm-sized spot, enabling imaging resolution below 100-μm in preliminary experiments. These experiments showed the value of using a thin EO crystal for near-field T-ray generation and revealed an unexpected enhancement in the T-ray electric field emitted from intense beams in very small volumes.

10.1 Introduction

Improving the spatial resolution of T-ray images is an important direction in T-ray research. For example, to be competitive with existing products, medical imaging and high-density biochip reading requires spatial resolution in the order of 10 μm. The concept of such a T-ray microscope is shown in Fig. 10.1.

Section 10.1.2 reviews a number of methods used to improve the resolution of T-ray images, all of which trade off sensitivity, resolution, bandwidth, emitter design and detector design. A novel approach is then presented in Sec. 10.1.3, utilising a sub-wavelength (sub-λ) sized source of T-rays created by focused optical light in an electro-optic (EO) crystal. Using Optical Rectification (OR) for generation and Electro-Optic Sampling (EOS) for detection this approach has a potentially higher sensitivity, bandwidth and resolution than standard aperture-based techniques.

The results in this Chapter indicate that generating T-rays from a sub-λ-sized volume in an EO crystal caused an unexpected enhancement in the efficiency of T-ray generation, making it an attractive component for a future T-ray microscope.

10.1.1 Motivation

The lateral resolution of far-field T-ray images is limited by the wavelength of the radiation, λ, to approximately $0.61\lambda/(n \sin\theta)$, where the refractive index of the focusing medium n is typically unity for air and θ is the half angle of the focal point (Saleh and Teich, 1991). T-ray pulses have wavelengths spanning from 3 mm to 100 μm (0.1–3 THz), limiting the average resolution at the T-ray peak to approximately 500 μm. In practice, by selecting only high-frequency components after numerical Fourier analysis, the resolution can be improved to approximately 100 μm (Mittleman et al., 1999). To study broadband T-ray pulses interacting with sub-λ-sized areas, however, near-field techniques are required.

Near-field techniques rely on an aperture, diameter a, placed in the optical near-field of the sample to be studied, with separation distance $L < a$, so the size of the interaction spot is defined by a and not the wavelength of the radiation (Fillard, 1996). A review of the development of T-ray near-field microscopy was prepared in 2002 by Rosner and van der Weide (Rosner and van der Weide, 2002).

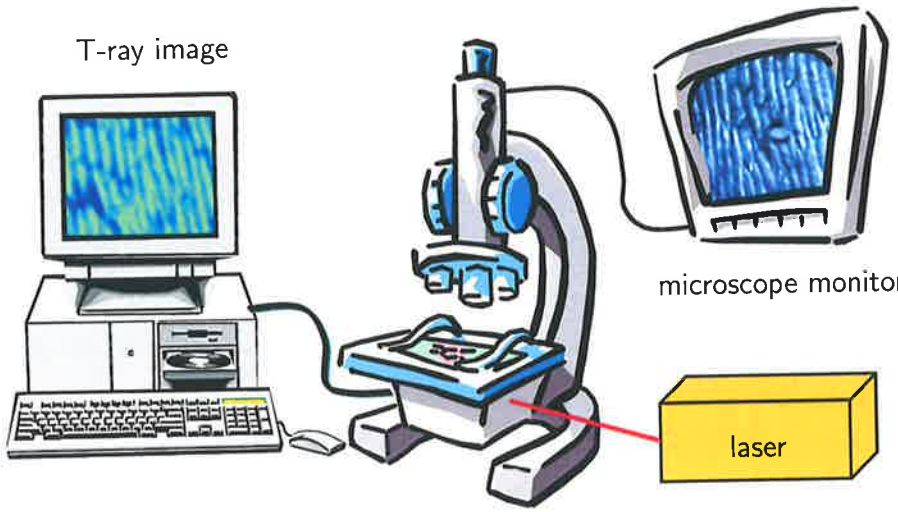

Figure 10.1. Functional concept diagram of a T-ray microscope. This diagram shows how high-resolution T-ray imaging could be combined with optical microscopy into a system for high resolution biosensing. The optical system, consisting of a reflection-mode optical microscope objective and a CCD monitor would show the optical image for sample alignment. The T-ray system, driven by an ultrafast laser, would simultaneously show the T-ray image on a computer. The T-ray system would also be in reflection mode, shown in Fig. 10.8. The sample images shown in this diagram are the optical and T-ray images of a slice of onion skin, imaged by Han et al. (2000a) (see Fig. 9.7) (Figure courtesy of Xi-Cheng Zhang, Physics, Rensselaer Polytechic Institute, NY USA).

10.1.2 Previous studies

An early evaluation of using tapered waveguides as apertures for T-ray light was carried out using continuous-wave (CW) T-rays from a gas-vapour laser (Keilmann, 1995), and the first reports of near-field T-ray imaging used an elliptical aperture at the end of a tapered metal tip, $a \approx 50$ μm by 80 μm (Hunsche et al., 1998b). T-rays were focused to a diffraction-limited spot with a parabolic mirror, the tapered tip was placed at the focal point and a sample was placed in the near-field of the aperture, that is, within a length less than a (Hunsche et al., 1998a). A resolution of approximately 50 μm was achieved. Two typical aperturing effects were observed: the transmitted T-ray electric field dropped by approximately 130 times, and T-ray frequencies below 0.5 THz were strongly attenuated. A similar resolution was achieved without an aperture, by holding the sample in the near-field of a Photoconductive Antenna (PCA) – in this case a virtual aperture existed due to the sub-λ dimensions of the spot where T-rays are generated (Brener et al., 1998).

To date, the highest resolution using near-field apertures, 7 μm, was achieved in 2001 using a collection-mode Photoconductive Antenna (PCA) detector, which had an approximate SNR of 10:1 (Mitrofanov et al., 2001b; Mitrofanov et al., 2000a). The detector had a 10-μm diameter aperture fabricated directly onto a 4-μm-thick PCA, so T-rays passed through the aperture and were detected by the PCA all in the near-field. The operation of the aperture was enhanced by having a high-refractive-index GaAs tip, $n_{\mathrm{GaAs}} = 3.6$, protruding through it. The tip refracted the T-rays, decreasing the wavelength of the radiation by a factor n_{GaAs} as it passed through the aperture (Mitrofanov et al., 2000b). The problems with apertured T-ray near-field imaging were temporal reshaping of the pulse and the finite thickness of the aperture itself, which caused a limitation on the bandwidth of the T-rays, as high frequencies were cut off in the waveguide-like structure of the aperture (Bromage et al., 1998; Mitrofanov et al., 2001c; Mitrofanov et al., 2001a). A finite thickness was required to limit T-ray tunnelling through the metal surrounding the aperture, but caused very high losses, proportional to the aperture diameter.

An alternative method of near-field T-ray imaging is to use a sub-λ-sized mirror induced by photocarriers in a semiconductor. Using a tightly focused optical pulse, a dynamic inverse aperture can be created to block a sub-μm cross-section of the T-ray beam (Chen et al., 2000b). A schematic of the dynamic aperture system is shown in Fig. 10.3. For a semiconductor placed at the focal point of a T-ray beam, and samples placed in the near-field of the aperture, a 40-μm resolution has been achieved with the dynamic aperture (Chen and Zhang, 2001), as shown in the images in Fig. 10.2. This technique requires the sample to be prepared in contact with an additional piece of semiconductor, rather than directly in contact with the emitter or detector, and the near-field interaction must be discerned against a high transmitted T-ray background around the inverse aperture using lock-in techniques.

Sub-λ T-ray spatial resolution, better than 10 μm, has also been achieved using solid metal tips (van der Valk and Planken, 2002), based on work using infrared radiation (Knoll and Keilmann, 1999; Hillenbrand et al., 2002). A sharp metal tip interacts with the evanescent wave of the T-rays near the surface of the sample, and only in a cross-sectional area as large as the tip diameter. By modulating the tip at a frequency f_{tip} and measuring the reflected T-rays with a Lock-In Amplifier also at f_{tip}, the interaction between the sample and a very small volume of T-ray radiation can be measured. This

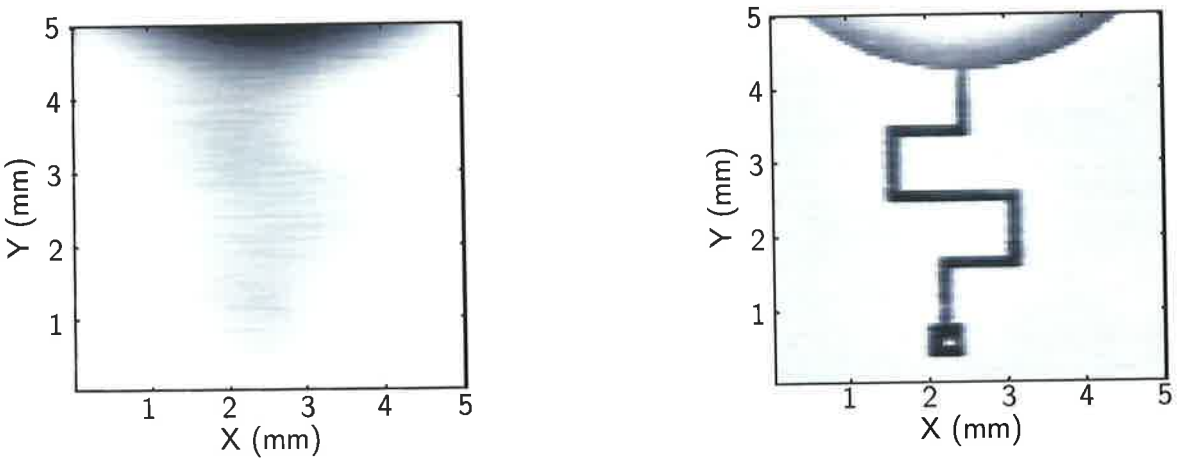

(a) Standard far-field T-ray image

(b) Dynamic aperture near-field T-ray image

Figure 10.2. Measured images from a dynamic T-ray aperture. These images demonstrate the improved spatial resolution achieved by near-field imaging with a dynamic aperture. The sample is a metal circuit deposited on a GaAs wafer. This technique has demonstrated resolution of better than 50 μm (after Chen et al. (2000b)).

technique has promise in high-resolution joint topographic and T-ray imaging, but sacrifices simplicity by introducing a near-field tip, and can only be used in transmission.

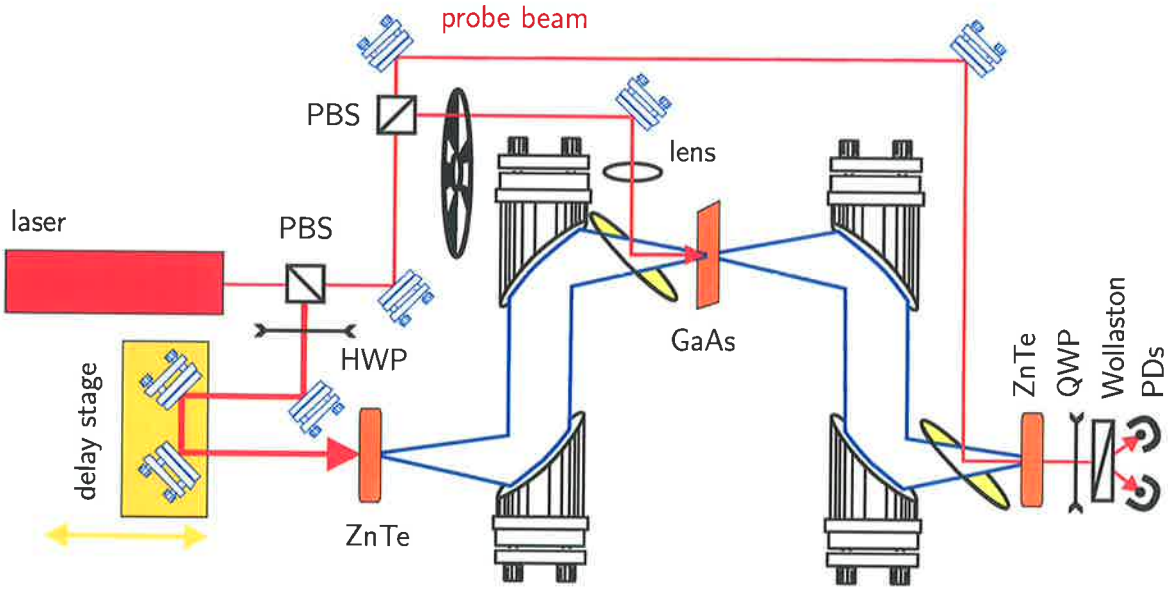

Figure 10.3. Near-field dynamic aperture schematic. As described in Ch. 10, a sub-λ-sized spot of T-rays can be blocked by the gated generation of photocarriers in a semiconductor. GaAs is normally transparent to T-rays, but the photocarriers act as a mirror screen. Samples are attached to the back (right-hand) side of the GaAs wafer to measure their T-ray transmission with high spatial resolution. The schematic is the same as a typical T-ray spectrometer based on OR and EOS in Zinc Telluride (ZnTe), except a gated beam for the sample is incorporated. Such a layout allows other optical-pump T-ray-probe experiments on ultrafast processes (Huber et al., 2001). The half-wave plate (HWP) and quarter-wave plate (QWP) are used to optimise the pump polarisation and balance the photodiodes (PDs). The polarising beam splitters (PBS) are used to divide the pump, probe and gating pulses from the same beam, and the lens is used to focus the optical beam to a sub-100 μm spot on the GaAs wafer. Missing from this diagram is a delay stage between the lens and the GaAs sample, which is used to control the relative timing of the T-ray and gating pulses incident on the GaAs wafer. (After Chen and Zhang (2001).

Near-field EO techniques

Electro-Optic Sampling (EOS) has been used to acquire T-ray images by placing an EO crystal in the near-field of a sample (collection mode), using a large area EO detector. A schematic of near-field collection mode EO imaging is shown in Fig. 10.4. This provides a method to measure the 3D T-ray beam profile directly by moving the detector crystal along the beam path, thereby generating images of T-ray wavefronts, shown in Figs. 10.5 and 10.6 (Jiang and Zhang, 1999a).

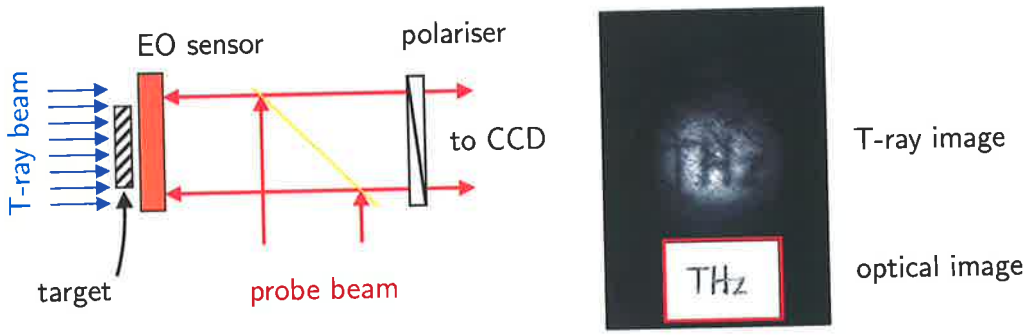

Figure 10.4. Schematic and measured image from collection mode near-field EO imaging. This Figure shows collection mode near-field EO imaging being performed by holding an EO sensor in the T-ray near-field of a sample, and measuring the T-ray electric field with a probe pulse reflected from the sample side of the crystal (after Jiang and Zhang (1999a)). This technique has a reduced signal because the internal reflection is small, but it provides sufficient resolution for the image of the letters 'THz'; the line width of the word is 0.5 mm and the image was taken in less than 1 s.

In a manner analogous to EOS, Optical Rectification (OR) can be used to generate T-ray in sub-λ-sized areas. To summarise the discussion of OR in Sec. 3.2.2: OR describes T-ray generation in a nonlinear optical crystal excited by an optical pulse. T-rays are generated from a transient polarisation, caused by an interaction between the optical pulse and the $\chi^{(2)}$ nonlinearity of the EO crystal. The strength of the generated polarisation is proportional to the square of the optical electric field, and therefore proportional to the optical intensity:

$$\mathbf{p} \propto |E_{\text{opt}}|^2, \tag{10.1}$$

$$\mathbf{p} \propto I. \tag{10.2}$$

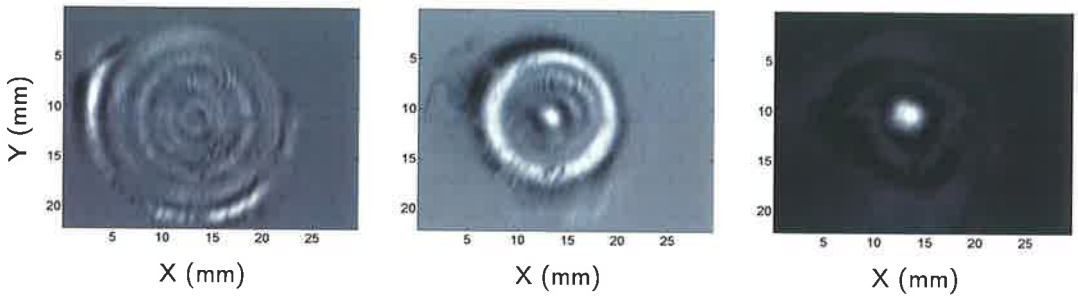

Figure 10.5. Transverse T-ray wavefront imaged with collection mode near-field EOS. The measurements were made in real-time and the time evolution of the wavefront can be directly observed: each image is a 2D slice across the T-ray beam at a different setting of the delay stage (that is, at a different temporal point on the waveform). The XY slices shown in this Figure can be collected to build up a 3D image of the T-ray pulse in space and time – from this 3D data set, XZ slices can be extracted, as shown in Fig. 10.6. The circular waves in these images are due to the curved nature of the wavefront and the brightness levels indicate the intensity of T-ray radiation. Slight defects in the images are caused by imperfections in the large detector crystal (2-mm-thick ZnTe). (After Jiang and Zhang (1999a).)

The total emitted T-ray electric field strength, as measured in EOS, is the integral over the area of polarisation, $\int_{\text{area}} \mathbf{p}$. This is proportional to the area integral of the optical intensity, which equals the optical power. Thus the detected T-ray electric field is proportional to the generating optical power.

T-ray power generated by OR is limited by the incident optical power, which is in turn limited by the damage threshold of the EO crystal (Carrig et al., 1995; Sun et al., 2000). Some damage thresholds of EO crystals are listed in Table 10.1. For T-ray microscopy, a thin generating crystal is required because the optical beam is only tightly focused for a short distance in space. An EO crystal that is significantly thicker than the Rayleigh range of the beam will generate T-rays in an area greater than the diameter of the optical focus, thereby reducing the resolution of the technique.

Table 10.1. Crystal damage threshold. This Table shows the crystal damage threshold for exposure to 800-nm light for the important EO crystal, ZnTe.

Crystal	Damage threshold (GW/cm^2)	Reference
ZnTe	200	Sun et al. (2000)

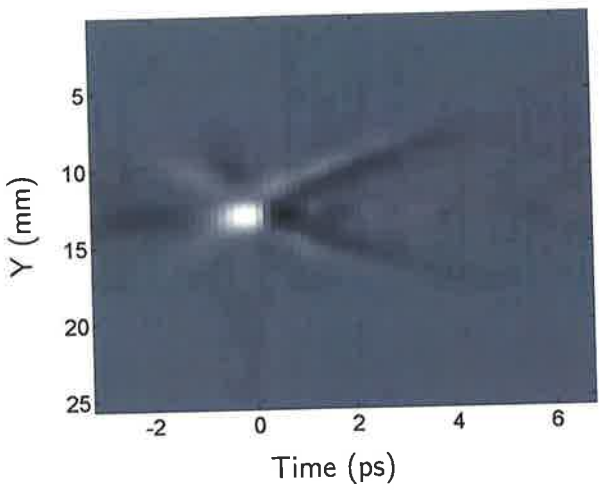

Figure 10.6. A 2D image of a T-ray pulse propagating through a focal point, sampled with collection mode near-field EOS. The focal point, where the high intensity T-rays are visible (bright colour), was formed by focusing the T-rays through a polyethylene lens. The phenomenon of a pulse flipping at its focus, the Gouy phase shift, is visible where the bright spot at the focus is followed directly by a dark spot. This XZ image was extracted from a 3D data set of a T-ray pulse propagating through space – the 3D data was collected from XY slices, some of which are shown in Fig. 10.5. (After Jiang and Zhang (1999a).)

Near-field EO generation was first attempted by Wynne and Jaroszynski (1999), who mounted a sample directly onto a EO crystal, generating T-rays in the near-field of the sample (Wynne and Jaroszynski, 1999). A resolution of 200 μm was demonstrated, but higher resolution was limited by two-photon absorption due to high intensity at the focal point (Sun et al., 2000). In this Thesis, experiments are carried out with very low optical excitation power. The importance of using a very small generating volume is demonstrated by using a thin EO crystal. An enhancement in generated T-ray power is observed when using a thin crystal.

10.1.3 Objective summary

In EO T-ray generation, as opposed to PCA generation, the volume of material for T-ray generation theoretically depends on the size of the exciting optical beam rather than the photo-conductive antenna structure. It would therefore be possible to create a sub-λ-sized source of T-ray radiation in the crystal by tightly focusing the exciting optical

beam. Such a source could form the basis of a T-ray microscope, either in transmission or reflection, as shown in Figs. 10.7 and 10.8.

The objective of the experiments in this Chapter was to demonstrate high-resolution T-ray imaging with a sub-λ-sized T-ray source, formed by tightly focussing an optical beam in an EO crystal.

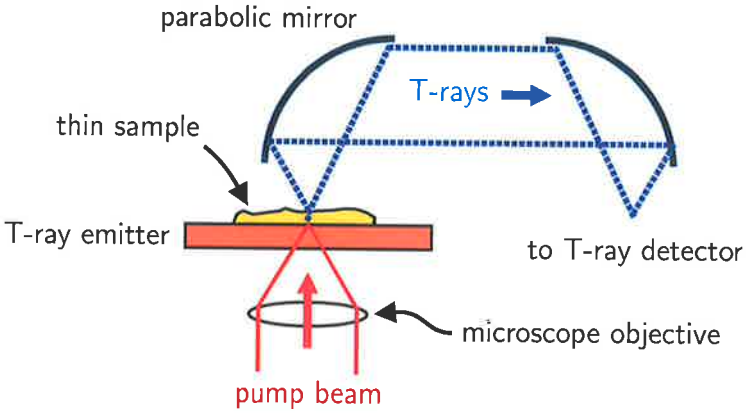

Figure 10.7. Concept diagram of a transmission T-ray microscope. This concept diagram explains the motivation behind the experiments in this Chapter. The novel step is to generate T-rays in a sub-λ-sized volume in the near-field of a sample, using OR. As in standard OR (Sec. 3.2.2), an optical pump beam generates T-rays in an EO crystal, which pass through a sample to be collected by parabolic mirrors, and then recorded. The important changes to a transmission system described in Ch. 3 is the objective lens, which focuses the pump beam to a micron-sized spot in the EO crystal, thus generating T-rays in a micron-sized area. The part of the sample in the near-field of the generated T-rays, that is within a few microns, is the only part of the sample that interacts with the T-rays, giving a micron spatial resolution (figure courtesy of Xi-Cheng Zhang, Physics, Rensselaer Polytechic Institute, NY USA).

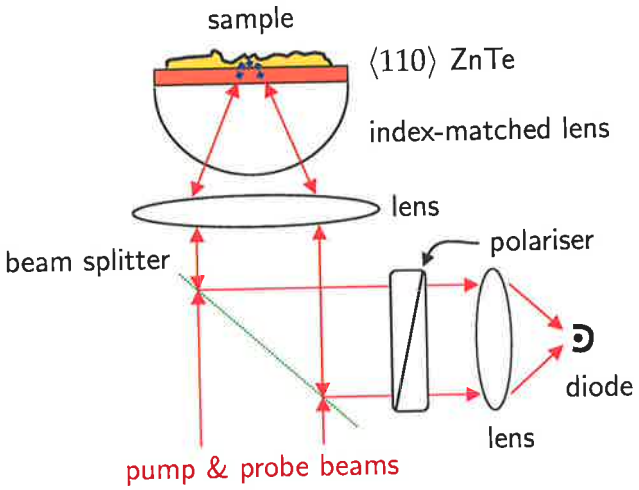

Figure 10.8. Concept diagram of a reflective T-ray microscope. This diagram explains, with Fig. 10.7 above, the motivation behind the experiments in this Chapter. This sketch shows how an EO transceiver, described in detail in Sec. 3.4.3, can be modified for near-field microscopy with the addition of an objective lens. A pump pulse from the red laser beam is focused into a sub-λ-sized spot in the EO crystal, which generates T-rays to interact with a tiny section of the sample. The T-ray pulse is reflected after interacting with the sample, and is detected by a second laser pulse, the probe pulse, travelling collinearly with the pump pulse, but delayed in time. The probe pulse is split from the pump pulse as it reflects back to the beam splitter, and the detected T-ray pulse is read out using a crossed-polariser detection scheme (Sec. 3.3.2) – the polariser shown passes only the polarisation component of the probe beam that has been rotated in the EO crystal as a consequence of the reflected T-rays pulse (figure courtesy of Xi-Cheng Zhang, Physics, Rensselaer Polytechic Institute, NY USA)

10.2 Experiments

In the experiments described in this Thesis, near-field EO T-ray generation was implemented using OR in an EO crystal and detected with EOS (Sec. 3.2.2 and Sec. 3.3.2), shown schematically in Fig. 10.9. The actual experimental setup is shown in Fig. 10.10 and a full optical layout is found in Appendix B. The laser system used was an ultrafast laser, with a pulse width of ≈100 fs and repetition rate of 76 MHz (model: Mira900; manufacturer: Coherent Inc, Santa Clara CA, USA; URL: `http://www.cohr.com`). The pump power was 10 mW after the acoustic optic modulator. The optical excitation beam was tightly focused with an optical objective lens into the EO crystal, where T-ray generation took place. The emitted T-rays were collected by a pair of gold-coated off-axis parabolic mirrors and refocused into a second crystal for EOS.

The two lenses used are a 20× lens with a Numerical Aperture (NA) of 0.4, and a 40× lens with NA = 0.65. For an optical wavelength of approximately 0.8 μm, as used in these experiments, the focused spot sizes and Rayleigh ranges are calculated to be 2.55 μm and 1.57 μm for NA = 0.4 and NA = 0.65 respectively. The actual spot sizes in air were measured after the optical beam had passed through the generating crystal, shown in Fig. 10.11. The measurement was made by monitoring the transmitted optical power while translating a razor blade across the optical beam. The beam waist was found by translating the objective lens along the beam in the z direction and measuring the diameter at each point. The measured values were found to be close to the calculated values, as shown in Table 10.2. The optical beam can be focused down to a spot size of 1.7 μm even after it passes a several hundred mm thick media plate of high refractive index ($n_{\mathrm{ZnTe}} \approx 2.9$).

Two crystal thicknesses were used to demonstrate that a small volume is required to achieve very tightly focused T-ray generation. Both crystals were ⟨110⟩ ZnTe, rotationally aligned for optimal T-ray generation efficiency. The crystal thicknesses were 250 and 16 μm. The thin crystal was much more fragile than the thick crystal under a focused ultrafast laser. A 16-μm-thick crystal lasts for less than half a minute before it is destroyed by a pump power of over 10 mW. The laser used has a 10-mW threshold power and gives a threshold intensity of 50 GW/cm^2. In short, the laser can be focused down to a spot size of 1.7 mm even after it passes a several-hundred-mm thick media plate of high refractive index ZnTe ($n_{\mathrm{ZnTe}} \approx 2.9$).

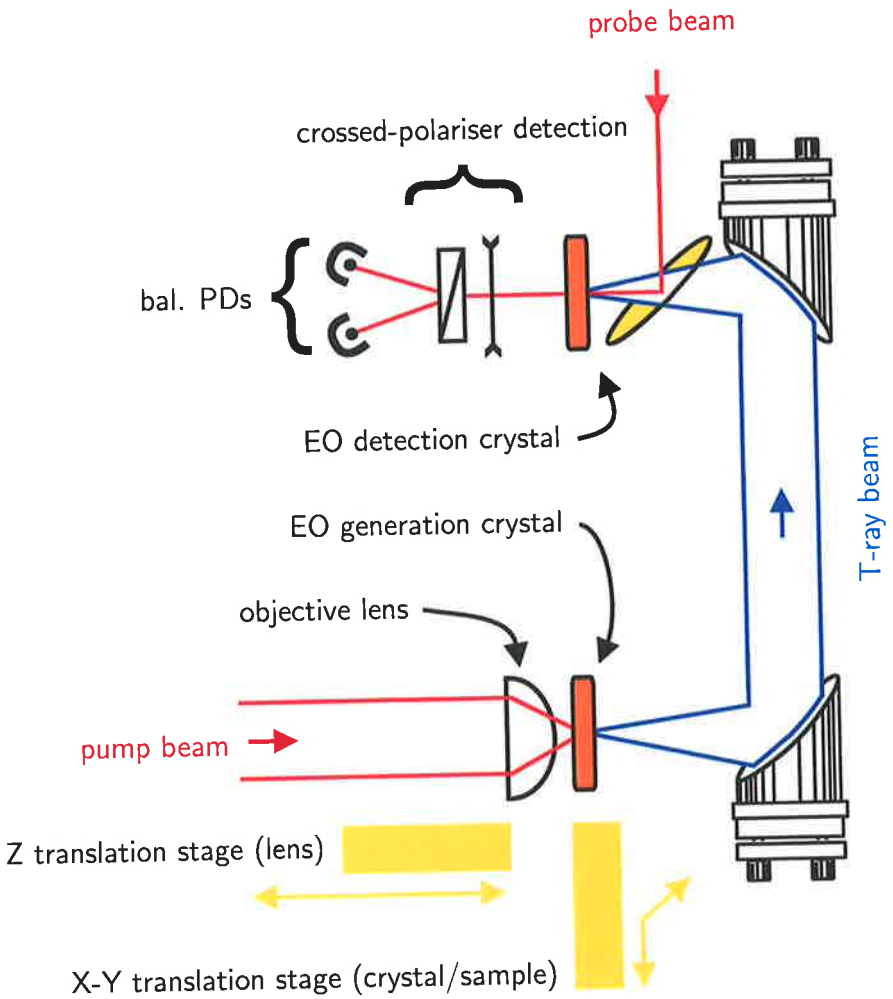

Figure 10.9. Electro-optic T-ray microscope schematic. This drawing shows the experimental layout for demonstrating T-ray microscopy. The system components common to normal T-ray spectrometers are described in Ch. 3. The pump beam from an ultrafast laser was focused into an EO crystal using an objective lens. The lens was mounted on a Z translation stage so the focus point of the pump beam could be translated through the generating crystal. The crystal was mounted on an X-Y translation stage so samples, which were in turn mounted on the crystal itself, could be translated across the beam to measure resolution. T-rays are generated through a process of Optical Rectification (OR), described in Sec. 3.2.2, re-focused into a detector crystal, and detected by Electro-Optic Sampling (EOS) (after Yuan et al. (2002)).

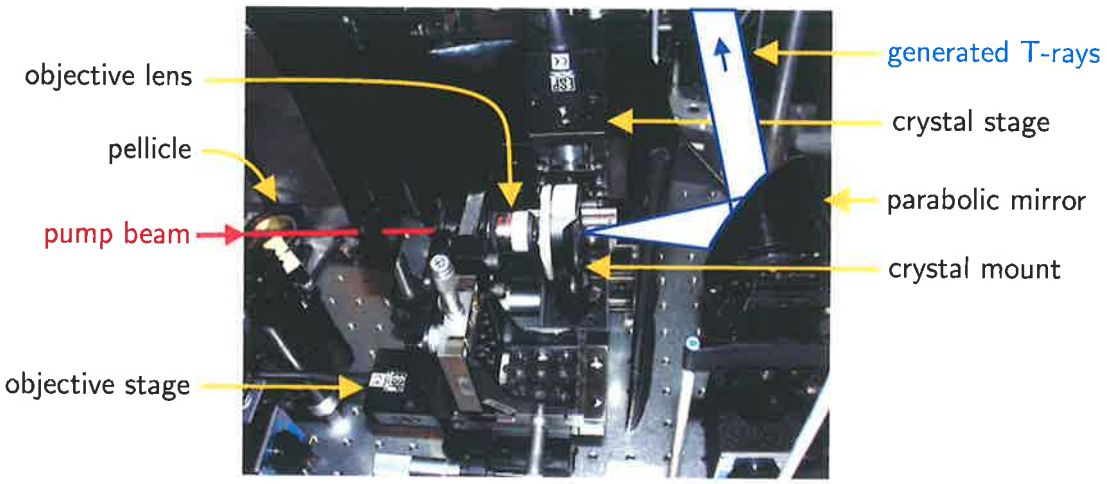

Figure 10.10. Photograph of the Electro-optic T-ray microscope. This photograph shows the experimental implementation of sub-λ-sized OR. The elements of Fig. 10.9 are shown on an optical table, with hole spacing of 1 inch. The OR crystal is mounted in a circular rotation mount so the optimal crystallographic orientation can be selected to optimise T-ray generation efficiency (Sec. 3.2.2).

Table 10.2. Measured focussed optical spot sizes. This Table lists the characteristics of the two objective lenses used to focus the optical pump beam into the OR crystal. The two lenses used were 20× and 40×, with Numerical Apertures (NAs) of 0.4 and 0.65 respectively. The calculated spot sizes of the optical beam (centre wavelength 800 nm) at the focal point, calculated assuming a Gaussian beam, compare closely to the measured spot sizes. The measurements are shown in Fig. 10.11. The Rayleigh ranges for these Gaussian beams are calculated, giving an estimate of the divergence of the generated radiation.

Lens	NA	800-nm spot size (μm)	measured spot size (90-10%) (μm)	Rayleigh range (μm)
20×	0.4	2.55	2.55	25.54
40×	0.65	1.57	1.7	9.68

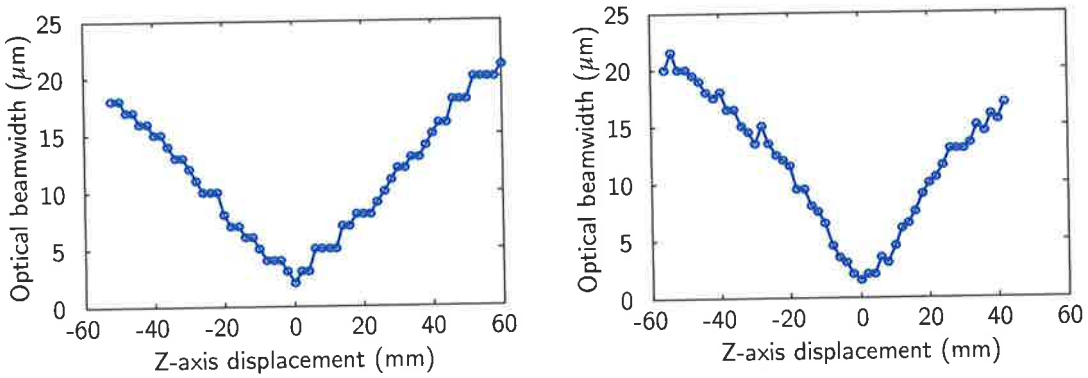

(a) 2.55 μm spot size for a 20× lens

(b) 1.7 μm spot size for a 40× lens

Figure 10.11. Measured focussed optical spot sizes. These plots show the measured optical spot size of focused optical beam using two objective lenses. The spot size was measured by scanning a sharp blade across the beam and estimating the distance over which the transmitted power dropped from 90% to 10% of the full, unobstructed optical power. These measurements indicate that the objective lenses used to generate sub-λ-sized T-rays were focussing as expected (Yuan et al., 2002).

10.3 Results

The lens-crystal distance for focussing the optical beam in the crystal is found by scanning the objective lens on the Z axis, and monitoring the output T-ray signal. This experiment is sketched in Fig. 10.12. It is necessary to measure the position of maximum focus in the crystal, as calculating and measuring the exact distance is prone to large errors. In this experiment, the objective lens was translated, leaving the EO crystal fixed, so it remained at the focal point of the first parabolic mirror (see Fig. 10.9).

The first EO crystal used to generate near-field T-rays was a 250 μm-thick sample of ZnTe. Figure 10.13 shows the T-ray peak signal from a 250 mm-thick ZnTe crystal versus the focus lens position. The T-ray signal was reduced when the focal spot was in the thick crystal – this was due to depletion of the optical beam through competing nonlinear processes in the crystal, specifically two-photon absorption.

If third-order processes played no role, there should be little change in the peak amplitude of the T-ray pulses as the z distance between the lens and EO crystal is changed. This can be understood by using the model of OR described in Sec. 3.2.2: the amplitude of the generated T-ray electric field, E_{THz}, is proportional to the second time derivative of the polarisation transient in the crystal $\frac{\partial^2 \mathbf{p}}{\partial t^2}$, which is in turn proportional

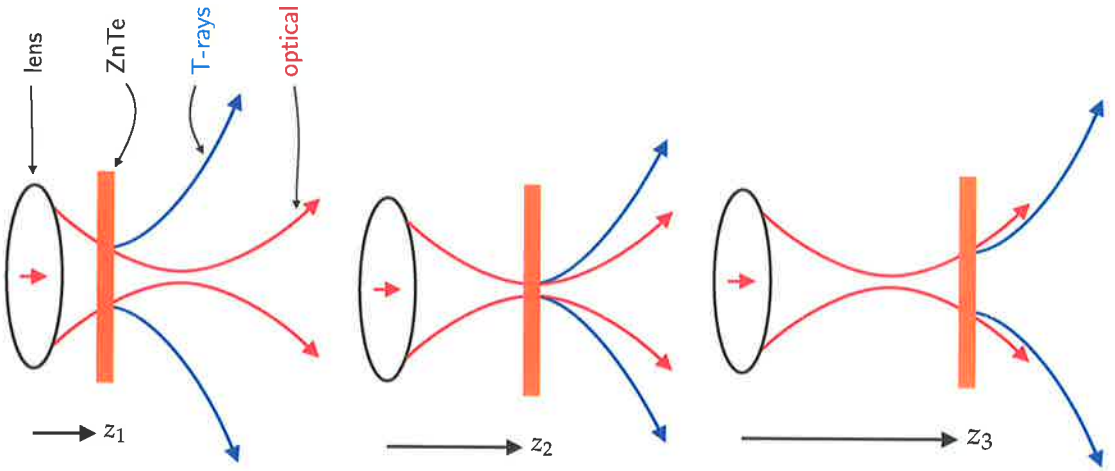

(a) Before the focal point (b) At focal point (c) After the focal point

Figure 10.12. Sketch of near-field EO generation with a focussed optical beam. These three sketches show the experimental positions used to generate T-rays from an EO crystal with a tightly focused optical beam. The objective lens focuses the optical pump beam, shown in red, to a tight focus at a given distance from the lens. T-rays are generated in the EO crystal, in this case ⟨110⟩ ZnTe, from the optical power. The size of the generated T-ray beam depends on the size of the optical beam when it intersects the EO crystal. To determine the distance where the EO crystal is at the focus of the optical beam, the Z distance is scanned and the output T-ray signal observed, as shown in Figs. 10.13 and 10.14. The three relative positions of the EO crystal and the objective lens, z_1, z_2 and z_3, correspond to the waveform measurements shown Fig. 10.15.

to the square of the optical electric field E_{opt}:

$$E_{\text{THz}} = \int_{\text{volume of OR}} \frac{\partial^2 \mathbf{p}}{\partial t^2},$$

$$\begin{aligned} \mathbf{p} &\propto E_{\text{opt}}^2 \\ &\propto \text{optical intensity,} \end{aligned}$$

and

$$\text{optical intensity} = \frac{\text{optical power}}{\text{optical spot area}}.$$

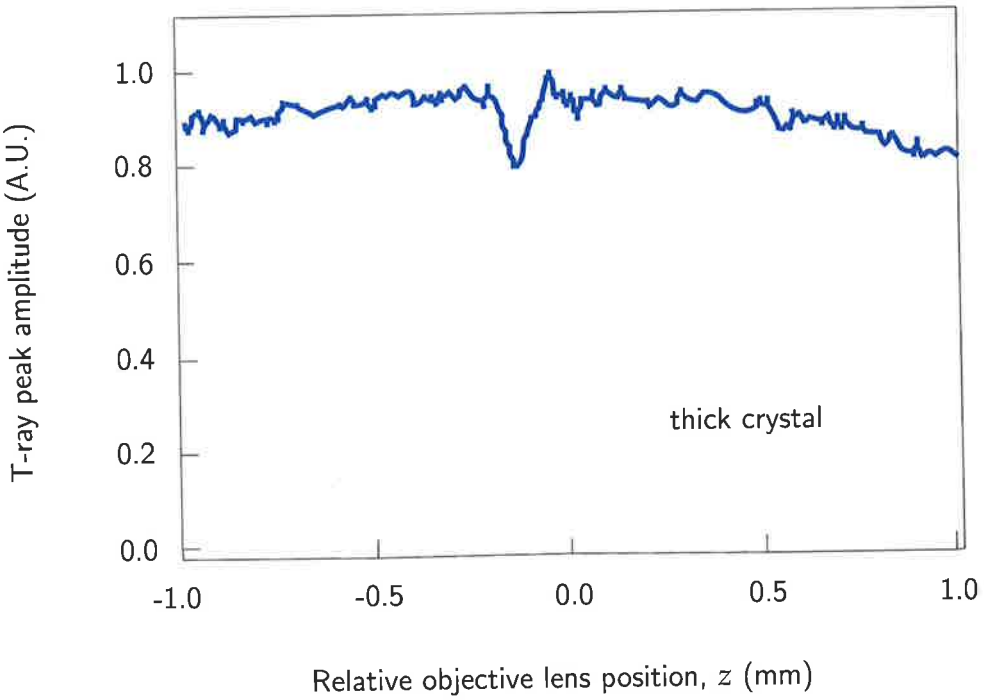

Figure 10.13. Measured peak T-ray electric field for a 250-μm-thick electro-optic emitter (ZnTe). This graph shows the peak amplitude of T-ray pulses generated in a 250-μm-thick crystal of $\langle 110 \rangle$ ZnTe as the Z-axis distance between the lens and the crystal, z sketched in Fig. 10.12, is scanned. The T-ray peak amplitude has been normalised to the maximum observed T-ray signal. The signal remains approximately constant as displacement changes, increasing slightly towards $z = 0$, where the optical beam is tightly focused in the crystal. At the focal point, however, there is a sharp dip in the generated T-ray signal. This sharp dip is due to depletion of the optical beam through competing nonlinear processes in the crystal, specifically two-photon absorption (Yuan et al., 2002).

As the Z-axis distance between the lens and crystal changes, the optical power in the crystal remains constant, so long as the crystal area is larger than the optical spot area, and the optics are correctly aligned. With constant power, the optical intensity increases inversely proportional to the area as the spot size becomes smaller. However, the volume where OR takes place reduces proportionally to the area. The combination of these two effects should result in an approximately constant generated T-ray field, regardless of the Z position of the EO crystal.

The slight change in the measured T-ray along the Z axis in Fig. 10.13 may be due to a number of effects, including changes in the alignment of the T-ray beam in the EO

detection setup (see Fig. 10.9 and Sec. 3.3.2). Such an alignment change may be due to the propagation path of the T-ray beam as it is generated in different volumes.

Two-photon absorption generates a green colour in the crystal, depleting photons from the red pump beam. This is a higher order nonlinear process than OR and occurs only at the focus, where the very high optical electric field intensity enables such higher order nonlinearities to be observable. This competing process potentially places a limit on the T-ray power that will be available from a tightly-focused optical beam in an EO crystal – however, experiments with a ZnTe crystal thinner than 250 μm indicated an interesting and unexpected result.

The second crystal used for T-ray generation was a 16-μm-thick sample of ZnTe. It was scanned in the same manner as the 250-μm thick crystal, and the interesting results are shown in Fig. 10.14.

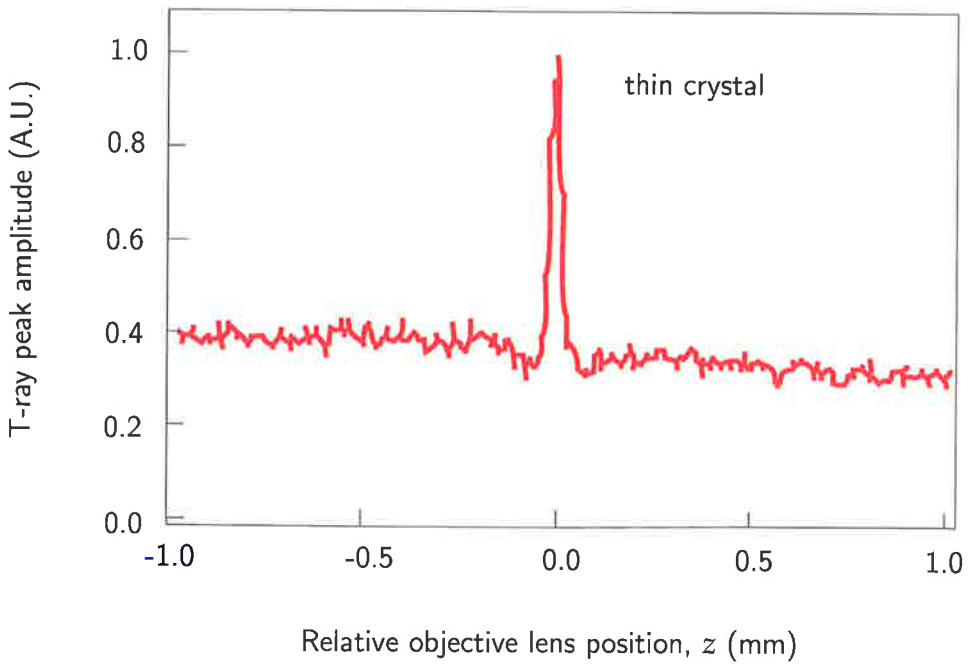

Figure 10.14. Measured peak T-ray electric field for a 16-μm-thick electro-optic emitter (ZnTe). This plot shows the peak amplitude of T-ray pulses generated in a 16-μm-thick crystal of ⟨110⟩ ZnTe as the Z distance between the lens and the crystal, z sketched in Fig. 10.12, was scanned. The T-ray peak amplitude has been normalised to the maximum observed T-ray signal. The signal remains approximately constant as displacement changes, however at the focal point there is a sharp spike in the generated T-ray signal (Yuan et al., 2002).

The enhanced T-ray generation shown in Fig. 10.14 at the optical focus was repeatable and unexpected. The power in the optical beam for the 16 μm crystal was less than that in the 250 μm, but the theory considered above predicts that the generated signal should remain constant or decrease for a tightly-focused pump beam, not increase.

To explore this enhancement, the full T-ray waveforms as generated by the thin crystal for different Z positions were measured, as shown in Fig. 10.15. The entire waveform generated from the focused spot has a larger amplitude, but similar phase and shape.

The origin of the enhancement in T-ray emission from a very tightly focused pump beam was not clear. To investigate whether this effect was related to third-order nonlinear effects, such as a reduction in two-photon absorption, the peak of the T-ray pulse was measured relative on the power in the optical pump beam. From the analysis of optical power and E_{THz} above, the T-ray power was expected to increase linearly with optical pump power while second-order nonlinear effects, such as OR, dominate. Figure 10.16 shows the measured T-ray signal, shown as both the peak and peak-to-peak amplitudes of the waveforms, at the focal point versus optical pump power. Below the range of 15 mW, the T-ray signal seems to be linearly dependent to the pump power. This discounts a large influence from third-order effects, such as a contribution to the signal by a depletion in losses due to two-photon absorption.

A second possible cause of the enhancement in T-ray generation from the thinner crystal was an increase in emitted higher-frequency T-rays from the focal point, which are less likely to be absorbed by the EO crystal itself. To investigate this possibility, a frequency analysis of the waveforms shown in Fig. 10.15 is shown in Fig. 10.17. It seems, however, that the T-ray enhancement is approximately equal across all detected T-ray frequencies.

Although the origin of the T-ray enhancement remained unclear, a measurement of the spatial resolution of the EO emitter was made using a metal pinhole attached directly to the EO crystal, much as a sample would be in the proposed microscope setup (see Fig. 10.7). A lateral scan of the crystal using the XY stage in Fig. 10.9 was able to reveal features with a resolution in the order of tens of microns, well below the average wavelength of the detected T-ray pulses. Figure 10.18 shows an X scan of the sample, demonstrating a measured resolution of 66 μm.

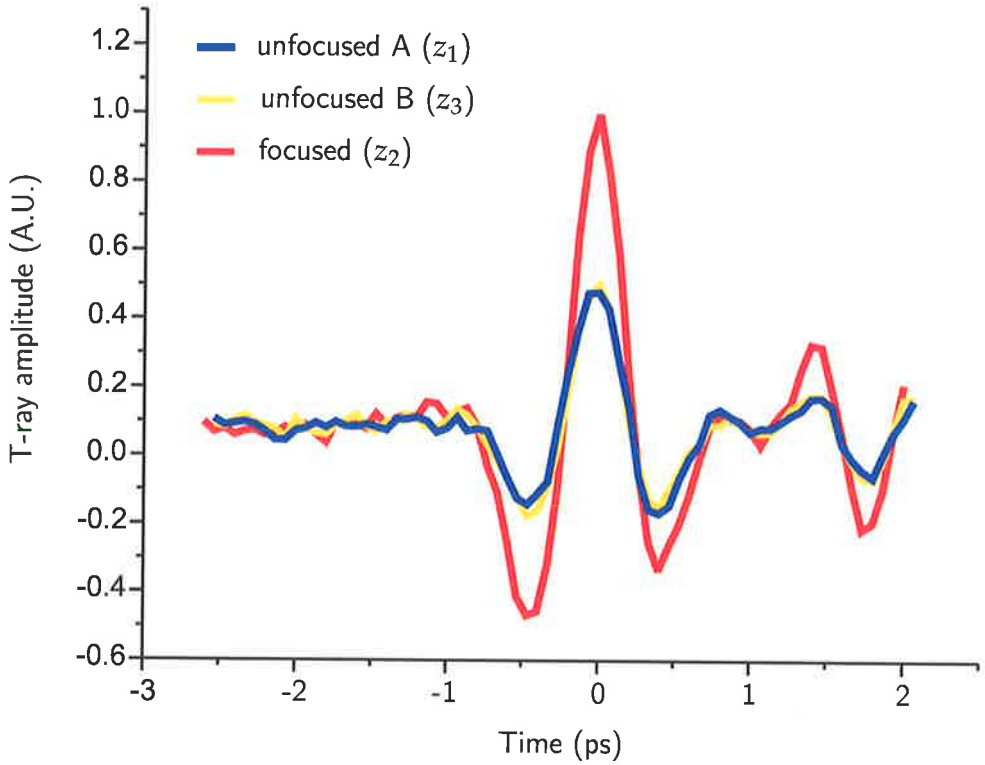

Figure 10.15. Measured T-ray pulses generated from a 16-μm ZnTe emitter. This graph shows three T-ray waveforms generated by OR in a ZnTe crystal and measured with EOS with the setup sketched in Fig. 10.9. The three waveforms were measured at different z-axis displacements of the objective lens relative to the generating crystal. The configuration for measuring these three pulses is sketched in Fig. 10.12. The three waveforms have similar phase and amplitude, the two unfocused waveforms are essentially identical for generation with a converging and diverging optical beam, and the waveform generated by the focused spot has a larger amplitude. This agrees with the enhancement of the T-ray peak found in Fig. 10.14. The optical pump power in this experiment was 10 mW, and the unfocused points were ± 60 μm from the focus (Yuan et al., 2002).

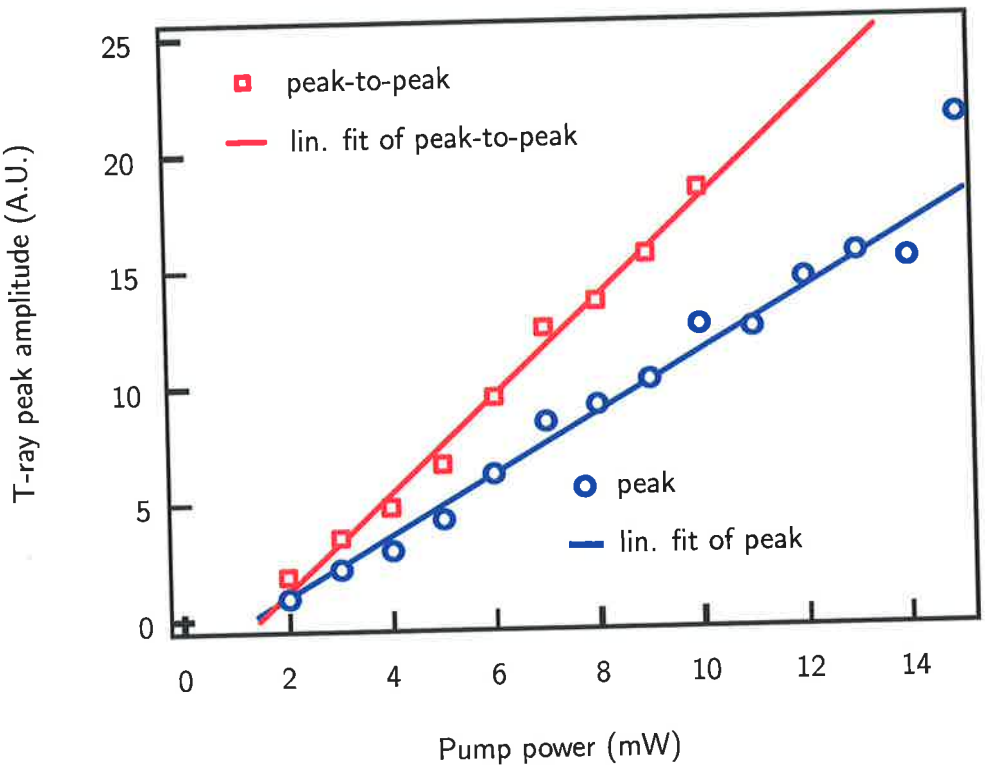

Figure 10.16. Measured peak T-ray electric field from a 16-μm-thick ZnTe emitter as a function of optical pump power. These plots show the amplitude of generated T-ray waveforms as a function of optical pump power, measured as both the peak value (circles) and the peak-to-peak value (squares) for each waveform. The close linear fit to these data indicate a proportionality expected for T-rays generated through a second-order nonlinearity. The measurements were made using the apparatus described above (Yuan et al., 2002).

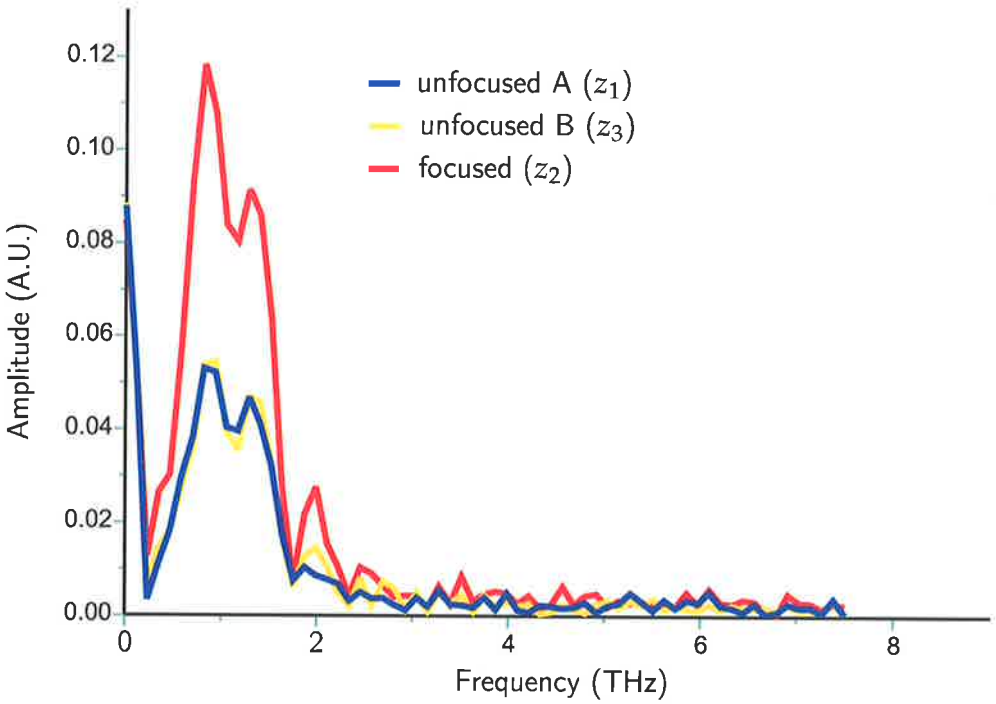

Figure 10.17. Measured T-ray pulse spectra generated in a 16-μm ZnTe emitter. This graph compares the generated T-ray spectral components OR from a small volume versus from a larger volume. The three spectra are obtained by processing the measured waveforms in Fig. 10.15 with a numerical Fourier Transform. The algorithm used a square window and zero padding of the time waveform. As in Fig. 10.15, the optical pump power in this experiment was 10 mW, and the unfocused points were ± 60 μm from the focus. The configuration for measuring these three pulses is sketched in Fig. 10.12. The results in this Figure show that the T-ray generation enhancement at the focus of the pump beam in the thin crystal is not T-ray frequency dependent.

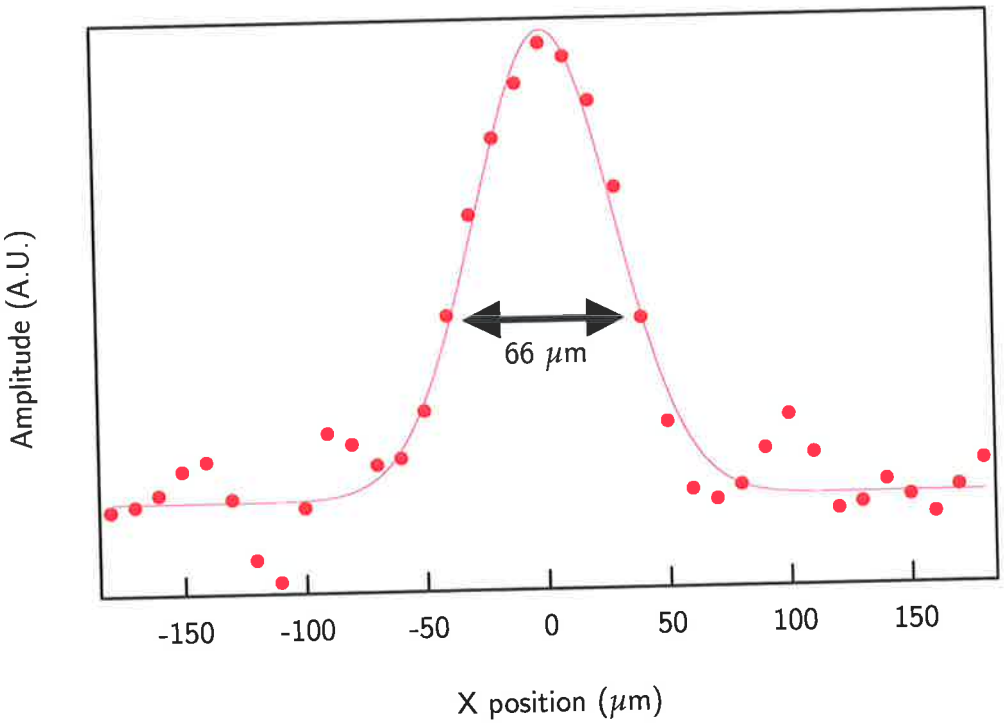

Figure 10.18. Measured spatial resolution of the T-ray radiation generated in a 16-μm-thick ZnTe emitter. This curve shows the measured T-ray pulse peak amplitude for a pinhole translated across the T-ray beam in the X direction. The pinhole was attached directly to the EO crystal, thus both were scanned across the point where OR was occurring, fixed in the XY plane by the location of the optical focal point. The Gaussian curve fitted to the experimental data shows a full-width half-maximum width of about 66 μm, which gives a measure of the spatial resolution of the system. The oscillations in the data at the edges of the pinhole are due to diffraction effects of the T-rays around the metal edge of the pinhole. The experiment was conducted using 10 mW of pump power. The Y position of the scan was chosen to be at the centre of the pinhole by scanning across the X axis at many Y values, and selecting the scan with maximum peak transmission.

10.4 Conclusions

The results in this Chapter demonstrate the fundamentals of a T-ray microscope based on near-field T-ray generation in an EO crystal. A spatial resolution of 66 μm has been demonstrated, and there is an indication that using thinner crystals will enable increased spatial resolution in the future. Thinner EO crystals also ensure that unfocused T-rays are not generated by diverging parts of the optical pump beam before and after the optical focus, but still present inside the crystal.

10.4.1 Future work

The main technical challenge facing this project in the future include preparing and mounting micron-thick crystals without damaging them thermally, mechanically or optically.

The main theoretical challenge is in modelling the enhancement in T-ray generation observed for tightly focused optical beams in very thin EO crystals. This exploration can be carried out using a broader range of crystal thicknesses, different types of EO crystals and accurate models of the OR process. It is possible that this effect is due to an amplification of the pump beam power from Fabry-Pérot reflections in the crystal. Research is continuing into this open question.

10.5 Chapter summary

The experimental investigations in this Chapter demonstrate a form of T-ray microscope that has the potential for applications in T-ray imaging and spectroscopy of thin samples, including medical tissues and thin layers of biomolecules.

Chapter 11

Conclusions and Recommendations

THis Chapter draws together the conclusions from the work described in this Thesis, and proposes directions for further research. So far a number of novel contributions to T-ray science in protein spectroscopy, DTDS, bioaffinity sensing, liquid spectroscopy and near-field T-ray generation have been described. The future for T-ray science and applications is rich, especially in the development of biologically-relevant technologies.

11.1 Introduction

The conclusions presented in this Chapter arise from the review and background Chapters, and from the experiments described in Chs. 5, 6, 7, 8 and 10. The recommendations arise from both the experimental and review Chapters.

Please note that the Figures in this Chapter, except Fig. 11.6, are repeated from other Chapters, where they are described in more detail. These Figures are repeated primarily for clarification and ease of reference.

11.2 Thesis conclusions

The conclusions drawn from the experiments in this Thesis fall into a number of categories: (i) biomolecular spectroscopy with T-rays, (ii) the double-modulated DTDS system, (iii) using DTDS for bioaffinity sensing, (iii) using DTDS for sensitive liquid spectroscopy, and (iv) near-field T-ray sources for high spatial resolution.

11.2.1 Review of T-rays and CW T-rays

Chapter 1 introduced the T-ray band, spanning frequencies from 0.1 to 10 THz, lying between millimetre waves (mm-waves) and the far-infrared (FIR, see Fig. 11.1). In the past this has been referred to as the THz Gap due to the lack of sources and detectors with sufficient power and sensitivity. Chapter 2 addressed the importance of the T-ray band, a theme developed in subsequent Chapters. The gradual development of science and technology in the T-ray region promises to open up new applications, just as other regions of the electromagnetic spectrum are crowded with operating devices and systems.

The importance of the T-ray band to biosensing is due to the following characteristics:

- the diffraction-limited resolution of 0.3 mm at 1 THz, which is much higher than radio and mm-waves,
- the low Rayleigh scattering of T-rays from particles, being much less than the scattering of optical light,
- the high sensitivity T-rays have for water, being useful for exploring hydration in materials, or in controlling the distance travelled by T-rays in the atmosphere,

- the transparent nature of dry non-polar materials to T-rays, thus enabling non-invasive studies of non-polar liquids, and imaging through paper envelopes, clothing and plastic packaging, with the added safety of being non-ionising (unlike X-rays), and

- the specific absorption and refractive index properties of molecules to T-ray frequencies, including for example the rotational and vibrational modes linked to biomolecular conformations, the O-H bonds in DNA strands, relaxation modes in gases, phonons in crystals, and physical properties of semiconductor materials.

Many applications of T-rays have been limited by the technology available to generate and detect T-ray radiation. In the late 1980's however, a new T-ray spectrometer based on ultrafast lasers was developed, which in the 1990's and early 2000's led to a rapid increase in T-ray research.

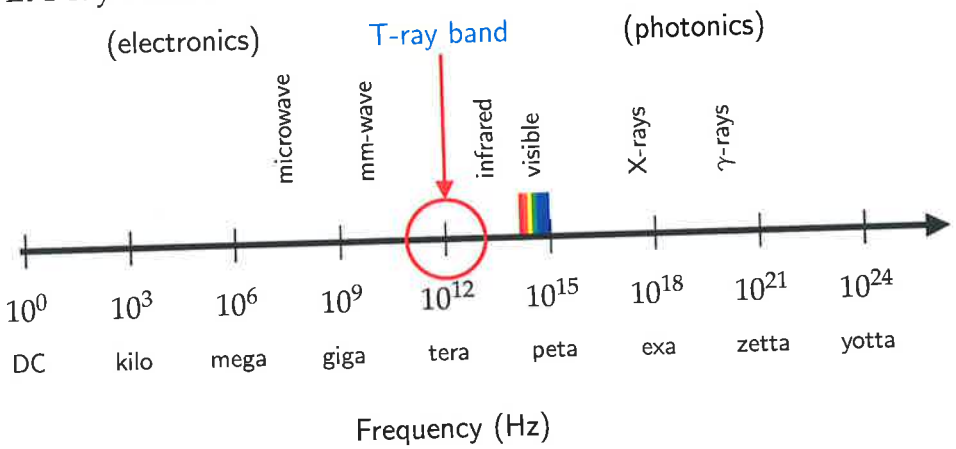

Figure 11.1. Electromagnetic spectrum. A representation of the electromagnetic spectrum, showing the T-ray band between the well-developed fields of mm-waves and the infrared (from Fig. 1.1).

11.2.2 Review of pulsed T-ray systems

The T-ray spectrometer in its various forms is described in detail in Ch. 3, including its history, the sources and detectors available, and the tradeoffs in designing and operating these systems.

The main advantages of the pulsed T-ray systems over other T-ray techniques are (i) their high sensitivity, and therefore signal-to-noise ratio, and (ii) their broad bandwidth, simultaneously generating all T-ray frequencies from 0.1 to 10 THz depending on the system. The T-ray spectrometer essentially takes the ultrafast broadband pulses (femtosecond duration pulses) from an optical laser and converts them to ultrafast broadband pulses in the T-ray frequency band. This down conversion can be accomplished with antennas on photo-active semiconductor substrates (photoconductive antennas) or with nonlinear optical effects in electro-optic (EO) crystals, among other methods. However the real beauty of T-ray spectrometers has been their size and cost – it is possible to have a reliable pulsed T-ray system on a laboratory bench for less than $200,000, and this cost is reducing with the price of ultrafast lasers, which comprise 90% of the expense.

These highly-sensitive T-ray systems have opened the way for a diverse range of sensing and imaging applications.

11.2.3 Review of T-ray sensing

The sensing applications of T-ray spectrometers are reviewed in Ch. 4 in two main sections: (i) the techniques that have been used, and (ii) to which materials these techniques have been applied. The main techniques used have transmission and reflection spectroscopy, applied a range of materials from semiconductor quantum wells to biomedical cancer samples.

Of particular interest in this Thesis are the experimental techniques for biosensing – studying biomolecules with T-rays. The importance of T-rays in: (i) biomolecular spectroscopy is described in more detail in Ch. 5, (ii) biosensing in Ch. 7, and (iii) liquid spectroscopy in Ch. 8.

11.2.4 Protein spectroscopy experiments

Chapter 5 describes how a T-ray spectrometer can be used to clearly observe low concentrations of water bound to biomolecules. T-ray studies of biomolecules promise to provide a non-invasive method for measuring the conformation and activity of important biological molecules, such as proteins. Biomolecules have been studied in the past in dried films or at cryogenic temperatures, but Ch. 5 describes for the first time

experimental measurements of protein hydration, where the protein molecules were suspended in an inorganic solvent at room temperature. These experiments showed that T-rays could measure the level of protein hydration. Furthermore, it was shown that, in the T-ray band, there is a clear difference between the absorption of bound water molecules (closely attached to the protein), and free water, not connected to the biomolecule.

Chapter 5 also showed that the organic solvent, 1,4-dioxane, was an ideal candidate for T-ray biomolecular studies because (i) it has a 100% miscibility with water, allowing a very wide range of hydration control, and (ii) it has low T-ray absorption itself.

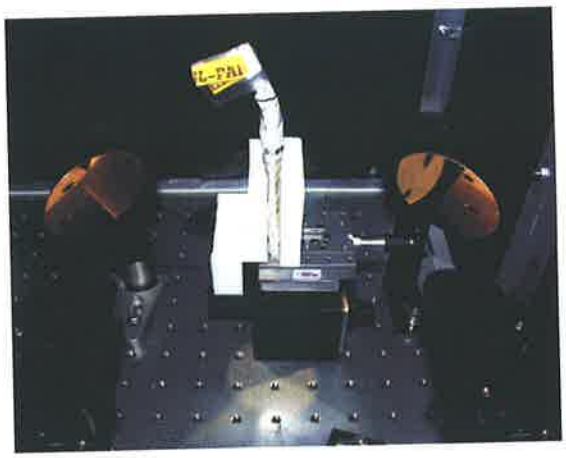

Figure 11.2. Variable-thickness sample holder. This photograph shows the holder used for novel measurements of protein hydration with T-rays (from Fig. 5.6(a)).

11.2.5 Double-modulated DTDS experiments

In T-ray biosensing, as in other T-ray sensing experiments, a primary limiting factor on the accuracy of measurements is the noise in the T-ray signal caused by fluctuations in the ultrafast laser. One method to improve the accuracy of T-ray measurements is to rapidly swap between a sample to be studied and a reference that has unvarying characteristics. If the sample is swapped rapidly, the laser has less time to fluctuate, and the noise is reduced. The magnitude of the laser fluctuations is proportional to the time between measurements; that is, the noise is proportional to $1/f$, where f is the swapping (modulation) frequency. Such a scheme has been dubbed T-ray Differential Time-Domain Spectroscopy (DTDS).

The major problem with DTDS, however, is that T-ray spectrometers already use a modulation of the T-ray beam to reduce background noise. To combine the benefits

of both, Ch. 6 demonstrated for the first time a system of double-modulated DTDS. The noise performance of double-modulated DTDS compared to normal Time Domain Spectroscopy (TDS) and to DTDS is fully described in Ch. 6, both experimentally and theoretically. The capabilities of double-modulated DTDS were used to characterise a very thin film of Silicon Dioxide, which would not normally be possible with standard T-ray TDS.

The sensitivity of double-modulated DTDS enabled the development of a new technique for sensing binding between biomolecules on a thin film, described in Ch. 7. Double-modulated DTDS also offers to improve the accuracy of liquid T-ray measurements by over two orders of magnitude, as discussed in Ch. 8.

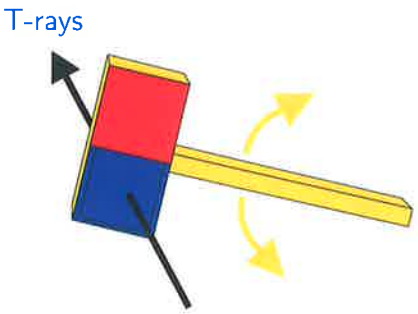

Figure 11.3. DTDS sample. This sketch shows the sample holder used for characterising thin films in novel double-modulation experiments, and in the demonstrations of the T-ray bioaffinity sensor (from Fig. 6.1).

11.2.6 Bioaffinity sensing experiments

Bioaffinity sensing implies the detection of binding events between biomolecules, and is an important technique in the biochip industry. Bioaffinity detection is used to detect the presence of certain target molecules, including drugs and hazardous substances, and to observe binding between nucleotide strands in gene expression chips. Chapter 7 described how T-rays were used for the first time to detection binding between biomolecules. The binding was observed between a layer of detection molecules, laid out on a flat substrate (a quartz slide), and a layer of target molecules that became bound to the detection layer. The detector molecules were chosen because they had a very specific affinity for the target molecules and not for other molecules, so that if binding was detected, that binding could have only been due to the presence of the target. A set of biosensor slides, designed for different targets, would then enable a search for a wide variety of substances.

A number of detector and target molecules were used to demonstrate the sensor: (i) the lipid Biotin binding to the protein Avidin, (ii) Avidin amplified with Agarose beads binding to Biotin, and (iii) the explosive TNT binding to its antibody. The clearest signal came from amplified Avidin – the sensitivity of this system was comparable to commercial biosensing equipment based on well-established technologies.

The mechanism for the T-ray signal in the bioaffinity slide was modelled in Ch. 7 as T-ray reflections from the interface between the biomolecular layers – this model showed a close match to the experimental results. The T-ray bioaffinity sensor shows for the first time that T-rays can be used to detect binding events between T-ray active molecules. Although other techniques exist to detect bioaffinity, the system described in Ch. 7 is the first to rely entirely on the T-ray frequency response of the molecules.

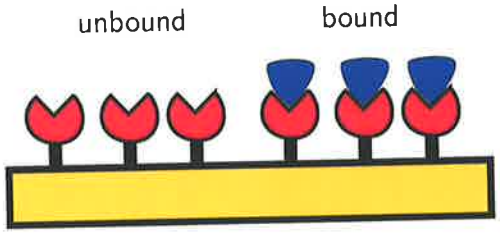

Figure 11.4. Model of ligand-analyte binding. This diagram shows a model of ligand-analyte binding, as detected by the T-ray biosensor (from Fig. 7.1).

11.2.7 Liquid DTDS experiments

Liquid DTDS is a novel system developed for studying liquid samples with the high accuracy of double-modulated DTDS. In Ch. 8, liquid DTDS was proposed for the first time and the noise performance of the system was analysed – it was shown that for a highly absorbing liquid, such as water, the accuracy could be improved by over two orders of magnitude. The idea was prototyped using an audio speaker to modulate the liquid sample, which enabled the idea to be proven experimentally.

The noise reduction was achieved using *amplitude and mean detection*, in which the sample and reference T-ray pulses were measured simultaneously. The reference pulse enabled non-varying properties in the T-ray system to be normalised out of the sample pulse, leaving only information on the sample to be studied. The noise performance of liquid DTDS with amplitude and mean detection, when implemented in a second-generation system, offers to be better than any previous liquid studies at T-ray frequencies.

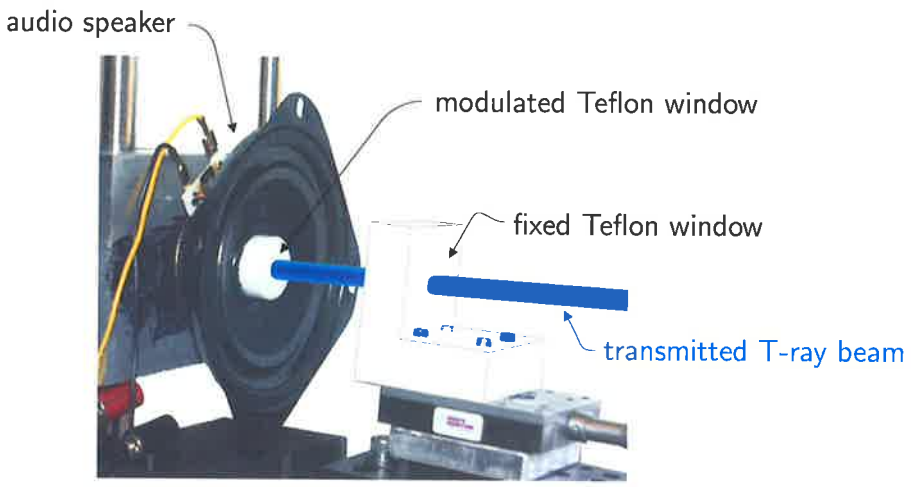

Figure 11.5. Liquid DTDS sample holder. This photograph shows the prototype liquid sample holder used to demonstrate double-modulated DTDS being applied for the time to liquid samples (from Fig. 8.6).

11.2.8 T-ray imaging

Imaging with T-ray spectrometers are reviewed in Ch. 9, covering the properties of T-ray images and some demonstrated applications. Three of the main advantages of T-ray imaging compared to X-ray imaging are: (i) its non-ionising, and therefore safe, nature, (ii) the sensitivity to polar materials and not to non-polar (dry) materials, and (iii) the automatic provision of spectroscopic information, due to the broad bandwidth of each measurement.

One of the main limitations of T-ray imaging is its resolution – in the far-field, the spatial resolution of T-ray images is limited to 0.33 mm at 1 THz. This can only be improved by operating in the optical near-field, that is within a wavelength's distance from the T-ray source (or equivalently, from the detector). For high-density biosensing applications, for example, this higher resolution is necessary.

11.2.9 Near-field generation experiments

Chapter 10 explores and demonstrates a novel near-field source for use in a T-ray microscope – this would enable cell-level study of biomedical sample and high-resolution biochip measurements. Using a tightly-focussed optical beam in an electro-optic (EO) crystal, a T-ray source was created with a spatial resolution of 66-μm.

The experiments in Ch. 10 also uncovered an unexpected enhancement in T-rays generated from a very small source. This enhancement overcame to some extent the reduction in T-ray power due to shrinking the volume of the T-ray source.

11.3 Recommendations for future work

T-ray sensing and imaging has developed and spread widely since the early 1990s. Initially present primarily in physics and electrical and electronic engineering research groups, T-rays are now used by physicists, engineers, chemists and biologists. The T-ray band can play a role in industry, homeland security and medicine.

There are currently over a hundred groups world-wide using T-rays and commercial systems are on the market. There are, however, still numerous hurdles to be overcome before T-ray spectrometers compete with other techniques in spectroscopy, biosensing, medical diagnostics and industrial imaging. These challenges include size, cost, output power, SNR, bandwidth, depth penetration, water sensitivity, spatial resolution, speed of data acquisition and the lack of a large T-ray knowledge base. As indicated in this Chapter, these challenges are being addressed and future development will probably find T-rays implanted in vital biological applications.

A number of recommendations to support future developments have arisen out of the studies in this Thesis. A number of outstanding open questions arising, directions for future work, and recommendations are summarised by topic below.

11.3.1 T-rays and CW T-rays

Although pulsed T-ray systems are extremely sensitive, there is still a push to achieve higher power T-ray systems. One very promising direction for the future is a synchrotron T-ray source – although requiring an electron accelerator, this would provide a very high-power pulsed source of T-ray radiation. This idea is being explored at the Jefferson Lab in the US (Carr et al., 2002) and at the Australian Synchrotron Project in Australia (Chan et al., 2003).

Another very promising source is the T-ray Quantum Cascade Laser (QCL), which continues to be developed by scientists world-wide. Meanwhile, p-Germanium (Ge) lasers, T-ray gas-vapour lasers and backward wave oscillators continue to be used as convenient laboratory T-ray sources.

11.3.2 Pulsed T-ray systems

Pulsed T-ray systems depend intimately on the stability of their ultrafast laser. An open question, being addressed by laser companies and research teams, is to improve the stability of ultrafast pulsed lasers. This can be achieved by using laser-diodes to power the ultrafast laser, instead of another gas laser, or by using a power limiting device. Ultrafast lasers are also reducing in size and cost, therefore reducing the size and cost of T-ray spectrometers. Figure 11.6 shows a model compact T-ray spectrometer, based on a fibre laser, that is about one foot (about 30 cm) in length on all sides.

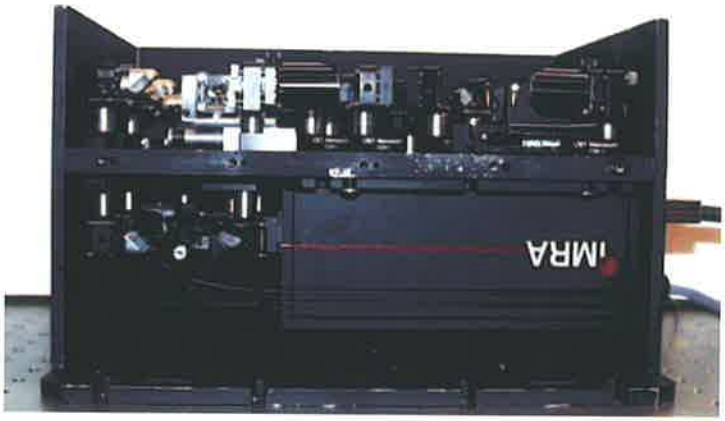

Figure 11.6. Compact T-ray spectrometer. This photograph shows a compact T-ray system, based on a fibre laser (manufacturer: IMRA America Inc., Ann Arbor, Michigan, USA; URL: `http://www.imra.com`), sitting on a table with one-inch spaced holes (after (Li et al., 1999b)).

A number of future system developments of T-ray systems can be envisaged, including: (i) a short path-length system, in which the T-ray travel only a very small distance in the atmosphere, (ii) a reflective system directly in contact with a sample, for example in an endoscope, and (iii) semi-integrated turn-key T-ray systems connected to ultrafast lasers.

11.3.3 Protein spectroscopy experiments

The major problem with all current T-ray biosensing studies is a lack of fundamental physical understanding, especially of the observed T-ray absorption spectra. An important initiative will be highly-detailed modelling of large biomolecules at T-ray frequencies, using numerical modelling techniques. Such models could also be used to explain the solvation of water in charged solvents, such as 1,4-dioxane.

The protein studies in this Thesis could be greatly enhanced by further studies at cryogenic temperatures and in a vacuum – under such conditions, the higher resonances are no longer populated, and the fundamental molecular structure is easier to discern. A related improvement would be a T-ray spectrometer with a bandwidth spanning to 10 THz and above. It would be interesting to integrate a broad-band T-ray system with other spectroscopic techniques, such as mm-wave and far-infrared (FIR) spectroscopy, to measure a continuous spectrum of certain materials.

A long-range project for T-ray spectroscopy is the observation of molecular conformation changing in real-time, for example by probing the T-ray absorption of photo-activated biomolecules, such as bacteriorhodopsin, a molecule linked to photon detection in human vision (Walther et al., 2000a). This experiment would take advantage of a number of unique T-ray properties: (i) non-invasiveness, (ii) conformation-sensitivity, and (iii) ps time response.

11.3.4 Double-modulated DTDS experiments

Double-modulated DTDS, used to study a Silicon Dioxide layer in Ch. 6, has the potential for dielectric measurements for the electronics industry as integrated circuits move from lower to upper GHz speeds. T-ray sensing is a competitive technology for characterising these materials.

A more specific improvement of double-modulated DTDS will be a modulation frequency in the MHz range, rather than at kHz, as used in Ch. 6. This would require a high-frequency modulator, such as an electro-optic modulator, and a high frequency Lock-In Amplifier (LIA).

11.3.5 Bioaffinity sensing experiments

T-ray bioaffinity sensing can be used for a very large range of binding pairs: (i) the Biotin-Avidin system can be extended by attaching other species of interest, or amplified with gold micro-spheres, and (ii) antibodies and antigen pairs have been developed for many interesting substances, for example, proteins, polysaccharides, nucleic acids, including more complex particles such as pollens, infectious agents, viruses and tissue cells.

The quality of the sensor slides used in Ch. 7 was limited by their preparation – surface inhomogeneities made a large contribution to experimental noise. In the future, a more uniform sensor preparation technique can be used to coat the quartz slide, such as spin coating, or the Langmuir-Blodgett (LB) technique (Atkins, 2002). Spin coating uses a rapidly rotating disk to evenly coat a thin layer of biomolecules onto a sensor slide. The LB technique uses a mono-molecular layer of biomolecules floating in a liquid-filled trough float – the sensor slide is pulled through the floating layer on the surface of the liquid, and is coated with a single homogeneous layer of molecules.

For high-volume analysis, sample and reference films can be deposited into a biochip array containing many samples. A large array of samples, all modulated for DTDS, and addressed with near-field T-ray pulses, is sketched in Fig. 11.7.

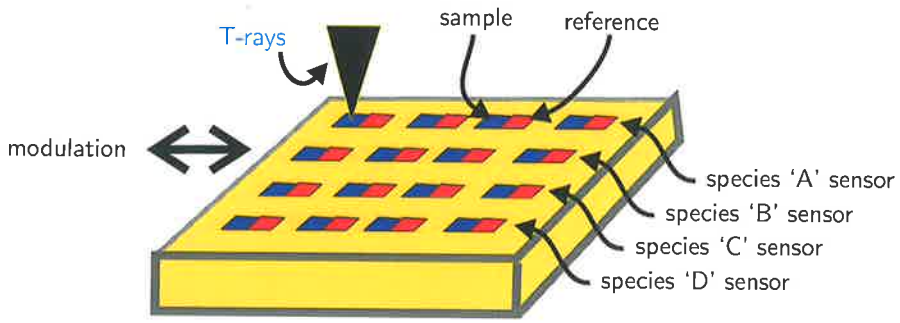

Figure 11.7. Biosensor array implementation. This concept diagram shows an array of sample and reference films being probed by near-field T-ray DTDS (from Fig. 7.15).

11.3.6 Liquid DTDS experiments

The liquid DTDS system demonstrated in this Thesis will be ideal for further studies of enzymes in organic solvents, as was first attempted in Ch. 5 but still had noise limitations. Other important liquids to be studied with high accuracy are: pure water, sugars and salts in water, biomolecules mixed with liquids, and bioliquids, for example sugar levels in blood or drug testing. T-ray liquid spectroscopy could also be of use in the fermentation industry, for non-invasively detecting the progress of the fermentation process.

An initial system improvement would be to use a high-quality modulation driver, such as a piezoelectric actuator, to change the thickness of the liquid sample (see Fig. 11.8).

A separate field of study is trace water in the petrochemical industry, where the base material is transparent to T-rays, and any water impurities are easy to detect.

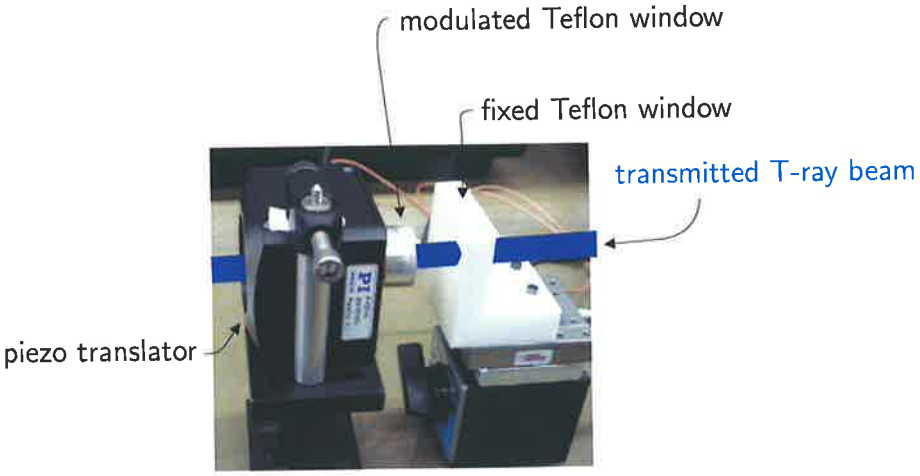

Figure 11.8. Piezoelectric sample modulator concept. This photograph shows how a piezoelectric positioner might be used to implement liquid DTDS with sufficient accuracy to improve the noise performance by over two orders of magnitude (from Fig. 8.17).

11.3.7 Near-field generation experiments

High-resolution bioaffinity sensing is a significant area for the study of living systems and the discovery and development of new drugs. Near-field T-ray sources would enable T-ray biosensing to be integrated in a manner similar to Fig. 7.15.

Cell-level studies of biomedical samples also requires a higher resolution than far-field T-rays can provide. A near-field source or detection system could be investigated for a T-ray microscope in, for example, malignant cancer identification.

11.4 Summary of original contributions

The original contributions in this Thesis were described in Sec. 1.3 in the introductory Chapter. In summary, the key contributions are as follows:

1. T-ray protein spectroscopy. Experimental studies were carried out for the first time to measure the response of protein and water mixtures using T-rays. These experiments revealed that T-rays could non-invasively sense the difference between bound and free water in solution, all at room temperature. The hydration levels that were detected are similar to hydration levels that determine the activity of enzymes, suggesting an application for T-rays in monitoring enzyme activity in real time.

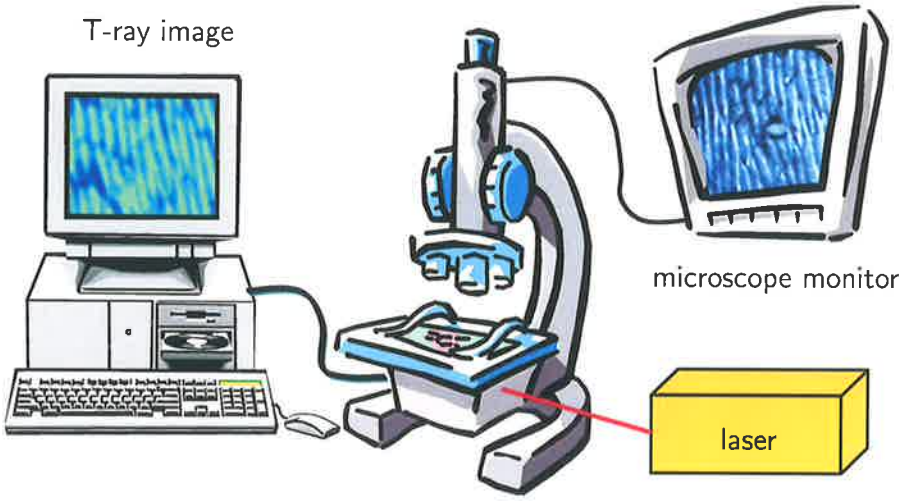

Figure 11.9. A T-ray microscope concept. This concept diagram shows how high-resolution T-ray imaging could be combined with optical microscopy into a system for high resolution biosensing (from Fig. 10.1).

2. Double-modulated DTDS. A method for characterising thin films, DTDS, was implemented practically through the use of double modulation. The noise improvement of double modulation was modelled and tested for the first time.

3. T-ray bioaffinity sensing. T-rays were used for the first time to detect binding between analytes and ligands. This effect was modelled as a series of reflections at the dielectric interfaces.

4. Liquid T-ray spectroscopy. Accurate liquid spectroscopy was demonstrated for the first time, using a prototype liquid DTDS system. The novel implementation of T-ray mean and amplitude detection promises to improve the accuracy of these measurements by two orders of magnitude.

5. T-ray microscopy. High-resolution T-ray imaging was demonstrated using a novel nearfield source, created by a sub-wavelength-sized generating volume in an electro-optic (EO) crystal. Jointly with Tao Yuan, an unexpected enhancement of T-ray generation was observed at the focus for very thin EO crystals (Yuan et al., 2002).

11.5 Chapter summary

This Chapter has given an overview of the major conclusions of this Thesis, and presented a number of recommendations for future work in the field. As summarised in the Chapter, this Thesis has made a number of major contributions to T-ray science and technology. The work herein is unique, original, and provides a direction for further contributions to T-ray science.

Appendix A

The Limit of Spectral Resolution in T-ray TDS

THIS Appendix describes a study conducted into the limit of T-ray spectral resolution due to the signal-to-noise ratio (specifically the *dynamic range*) of T-ray Time-Domain Spectroscopy (TDS). The pulsed nature of T-ray TDS sets a fundamental limit on its spectral resolution; although the spectral resolution of T-ray spectroscopy can be improved by increasing the duration of the temporal measurement, it is fundamentally limited by the signal-to-noise ratio in the time-domain. This Appendix presents calculations and experimental results relating the temporal signal-to-noise ratio of a T-ray spectroscopy system to its spectral resolution. Three typical pulsed T-ray sources are described.

A.1 Introduction

A.1.1 Motivation

T-ray Time-Domain Spectroscopy (TDS) is an innovative sensing and imaging technology for generating electromagnetic radiation at T-ray frequencies. T-ray spectroscopy provides information unavailable through conventional methods, such as microwave and X-ray techniques. To optimise T-ray spectroscopy, efforts have been made to extend the bandwidth (Huber et al., 2000; Kono et al., 2002) and improve the signal-to-noise-ratio (SNR) of T-ray systems (Duvillaret et al., 2000; Mickan et al., 2002c).

A desirable characteristic of any spectroscopy measurement is high spectral resolution, which is critical for observing resonances with narrow line widths, associated with distinct energy transitions at T-ray frequencies (Beard et al., 2002). Molecular absorption resonances have linewidths of approximately 1 to 3 GHz (1 to 3 cm^{-1}) for vapour rotational modes (van Exter and Grischkowsky, 1990b) or vibrational modes in simple biomolecules (Walther et al., 2000a).

This Appendix reviews the fundamental dependencies of spectral resolution in TDS and shows how a typical T-ray system is fundamentally limited by its SNR, or more specifically the *dynamic range* (the ratio of T-ray signal to probe beam noise).

A.1.2 Previous studies

In T-ray TDS, the spectrum is calculated by a numerical Fast Fourier Transformation (FFT) from the measured temporal waveform, $y(t)$. The measured waveform is a series of N discrete values $y(n)$ sampled at time intervals of t_s seconds, that is,

$$y(n) = y(t = nt_s), \quad n = 0 \ldots N.$$

The spectrum is also a discrete set of values,

$$Y(k) = \mathrm{FFT}(y(n)), \quad k = 0 \ldots N.$$

From Fourier theory, a higher spectral resolution Δf is obtained by extending the temporal measurement window $\mathcal{T}$, which corresponds to the scanning distance – that is

$$\Delta f \approx \frac{1}{\mathcal{T}}, \tag{A.1}$$

where $\mathcal{T} = (N-1)t_s$.

The duration of the temporal measurement window is limited by one of three experimental considerations: (i) the repetition rate f_{laser} of the laser source (used to generate and detect T-ray pulses), (ii) the length of the scanning delay stage L that translates into a scanning duration $\mathcal{T}$, and (iii) the amount of noise in the measurement.

The time duration between consecutive pulses, $1/f_{laser}$, can be improved by using a lower repetition rate laser – for example, a regenerative amplified laser.

The length L of the scanning delay can be extended by using an alternative time scanning method – for example, a multi-reflection configuration.

The limitation due to noise in the measurement is the most difficult to overcome, and therefore tends to be the fundamental limitation on frequency resolution in T-ray spectroscopy measurements.

The noise in T-ray TDS arises from two sources: (i) fluctuations in the T-ray radiation $N_T(t)$, and (ii) fluctuations in the laser probe beam $N_B(t)$ (Xu et al., 2003). The contributions of these noise sources, and their dependence on the temporal measurement duration, are described in Sec. A.2. The physical sources of T-ray noise and probe beam noise are discussed in other publications (van Exter and Grischkowsky, 1990b).

A.1.3 Objective summary

In this Appendix, the spectral resolution of time-domain spectroscopy is shown to be limited fundamentally by the temporal *dynamic range*, or signal-to-noise ratio (SNR) caused by the laser probe beam, of the T-ray spectrometer.

The relationship between the dynamic range and the achievable frequency resolution is demonstrated in this Appendix using calculations and experimental data.

A.2 Theory

Any sampled T-ray waveform includes the electric field of T-ray radiation $E_T(t)$, noise due to fluctuations in the T-ray field $N_T(t)$ and background noise from the T-ray detection (probe) beam, $N_B(t)$:

$$y(t) = E_T(t) + N_T(t) + N_B(t). \tag{A.2}$$

In T-ray TDS, the time-domain waveform $y(t)$ is measured at a series of points from $t = 0$ to $t = \mathcal{T}$. The waveform samples are uniformly spaced by a time t_s over the duration $\mathcal{T} = (N-1)t_s$, where N is the total number of samples. The waveform is therefore represented by the discrete series:

$$y(n) = E_T(n) + N_T(n) + N_B(n), \tag{A.3}$$

for $n = 0$ to $N-1$.

The electric field of the T-ray radiation, E_T, occurs as a pulse, with a duration τ of approximately $\tau \approx 1$ to 10 ps. The pulse has a sharp rise time and decay in the first few ps, followed by a low amplitude decay. The exact form of the T-ray pulse depends on the T-ray emitter, the most common of which are Photoconductive Dipole Antennas (PDAs), semiconductor wafers exhibiting Surface Current Generation (SCG), and electro-optic crystals exhibiting Optical Rectification (OR). Equations that model the shape of these generated T-ray waveforms are listed Table A.1, and an example simulated PCA waveform is shown in Fig. A.1. The energy of E_T is concentrated in the initial part of the pulse, $t \approx \tau$, as shown in the example energy waveform in Fig. A.2.

Currently, T-ray radiation for most systems is generated by photo-switching (Auston et al., 1984a) or Optical Rectification (Wu and Zhang, 1995). The temporal waveform of the T-ray pulse generated by photo-switching may be described as either bipolar (with an outer electrical field) or unipolar (with an inner electrical field). The temporal waveform of the T-ray pulse generated by Optical Rectification (OR) is considered as a damped oscillation.

Table A.1. Model equations of waveforms generated by alternate T-ray sources. The temporal waveform of the T-ray pulse depends mainly on the generation and detection mechanism and varies from one T-ray spectrometer to another. The waveforms may be simulated using several simple formulas. This Table lists the temporal waveforms ($E_T(t)$) for T-ray pulses generated by three common sources of pulsed T-ray radiation: (i) a Photoconductive Antenna (PCA), see Sec. 3.2.1, which has a bi-polar waveform; (ii) an unbiased semiconductor and Surface Current Generation (SCG) (SCG), see Sec. 3.2.4, which has a unipolar waveform; and (iii) Optical Rectification (OR), see Sec. 3.2.2, which has a decaying oscillation. In these models, A is the maximum amplitude of the T-ray field (in A.U. or Volts), τ represents the pulse duration (in s), t is time (in s), and ω_0 is the oscillation frequency (in rad/s) and a is the decay constant (a function of τ) of generated beam in OR. (These equations are taken from Xu et al. (2003).)

T-ray source	Model generated waveform
PCA	$2A\frac{t}{\tau^2}\exp(-t^2/\tau^2)$
SCG	$\frac{2A}{\tau^2}\exp(-t^2/\tau^2) - 4A\frac{t^2}{\tau^4}\exp(-t^2/\tau^2)$
OR	$A\sin(\omega_0 t)\exp(-at), \quad t > 0$ $0, \quad t \leq 0$

Table A.2. Model equations of spectra generated by alternate T-ray sources. This Table lists the temporal spectra ($E_T(\omega)$) for T-ray pulses generated by three common sources of pulsed T-ray radiation: (i) Photoconductive Antenna (PCA), (ii) Surface Current Generation (SCG), and (iii) Optical Rectification (OR). These equations are obtained by Fourier theory from the time-domain pulse models in Table A.1. In these models, A is the maximum amplitude of the T-ray field (in A.U. or Volts), τ represents the pulse duration (in s), ω is frequency (in rad/s), and ω_0 is the oscillation frequency (in rad/s) and a is the decay constant (a function of τ) of generated beam in OR. (These equations are taken from Xu et al. (2003).)

T-ray source	Model generated spectra
PCA	$A \frac{\omega\tau}{\sqrt{2}} \exp(-\omega^2\tau^2/4)$
SCG	$A \frac{\omega^2\tau}{\sqrt{2}} \exp(-\omega^2\tau^2/4)$
OR	$A \sqrt{\frac{\omega_0^2}{[a^2+(\omega_0-\omega)^2][a^2+(\omega_0+\omega)^2]}}$

The noise in the T-ray beam, N_T, is caused by fluctuations in T-ray generation, due to pump beam noise. This noise has a zero mean, a $1/f$ spectral distribution and is proportional to the T-ray electric field at each moment in time, $N_T(t) \propto E_T(t)$. As it is proportional to the T-ray electric field, the energy in the T-ray noise is concentrated in the same duration, that is $t \approx \tau$. For short measurement durations, the noise in the T-ray beam dominates the noise in the probe laser beam. However, for large values of $\mathcal{T}$, the noise in the probe beam makes a larger contribution. This Appendix is a study of SNR for large values of $\mathcal{T}$, thus the effect of N_T is neglected in comparison to the effect of N_B.

The noise in the laser probe beam, N_B, is directly due to laser fluctuations and is zero-mean, white, Gaussian noise with a variance of σ_B. Unlike N_T, the noise in the probe beam is not dependent on the T-ray power. For large T, the contribution of probe beam noise dominates the T-ray noise.

The *dynamic range* is the ratio of the T-ray signal to the probe beam noise,

$$\textit{dynamic range} = \frac{E_T}{N_B}. \tag{A.4}$$

The two contributions to the dynamic range, E_T and N_B, are shown in Fig. A.1 as waveforms in the time-domain. The T-ray pulse has a high initial amplitude that quickly dies away. The probe beam noise has a low but constant amplitude and a Gaussian probability distribution.

The contribution of E_T is greater than N_B or N_T at small values of the measurement duration $\mathcal{T}$ (when $\mathcal{T}$ is approximately equal to the signal duration τ). However, at large values of $\mathcal{T}$, the contribution of N_B begins to dominate. The contribution of N_T falls in proportion to E_T, so for low values of E_T at large $\mathcal{T}$, N_B dominates.

The contributions of E_T and N_B can be compared in terms of energy. Figure A.2, the energy waveform, shows that for large values of $\mathcal{T}$, the noise in the probe beam makes a larger contribution to the energy in the measurement than the signal E_T. This result shows that increasing the value of $\mathcal{T}$ will lead to an eventual reduction in overall signal-to-noise ratio. Thus the fundamental limit on spectral resolution in T-ray TDS, $\Delta f \approx 1/\mathcal{T}$, is caused by the probe beam noise.

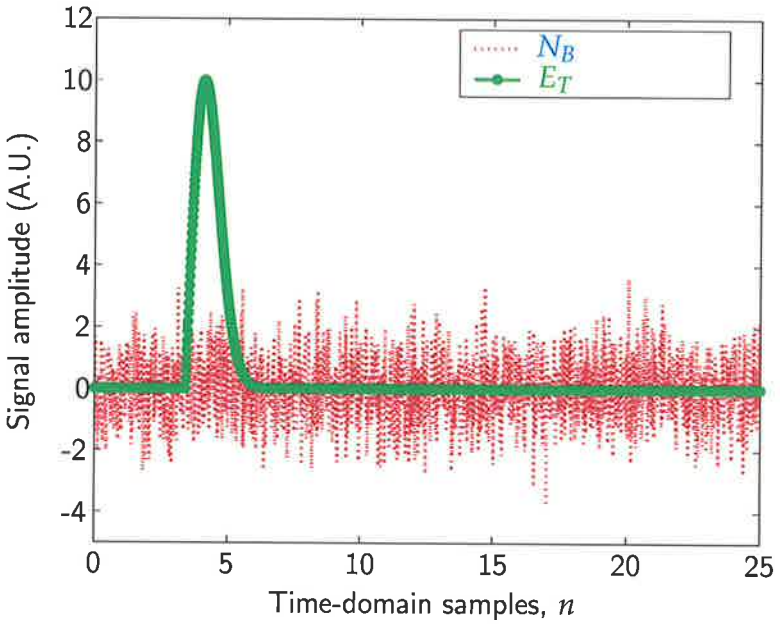

Figure A.1. Simulated time-domain T-ray waveform and probe beam noise. This Figure shows a portion of a simulated T-ray signal E_T and accompanying probe beam noise N_B. The T-ray waveform shows a sharp rise and fall, while the probe beam noise shows a lower but constant amplitude with a Gaussian probability distribution. These waveforms were simulated using the time-domain equation for a PCA pulse in Table A.1 and the `randn` random Gaussian noise generation function in MATLAB. The parameters for this simulation are shown in Table A.3.

Table A.3. Parameter values used to simulate the T-ray pulse in Fig. A.1 in Matlab. The parameters used in the simulation are listed in Col. 1, and the values used in this simulation are in Col. 2. The simulated pulse from a PCA was modelled using the equation in Table A.1. The values listed in this table are similar to those used in T-ray experiments. The dynamic range is the ratio of T-ray pulse amplitude to probe beam noise amplitude. The stage scan length is the distance travelled by the delay state in a T-ray spectrometer L that would create a scan time of $\mathcal{T}$; the $1/2$ factor is caused by the optical delay being double the physical translation of the stage.

Parameter	Symbol	Value
Dynamic range	A/σ_{B-t}	10 V/V
Pulse duration	τ	5 ps
Sample separation	t_s	66.67 fs
No. of samples	N	16,384 (2^{14}) points
Scan time	$\mathcal{T} = t_s(N-1)$	1.09 ns
Stage scan length	$L = \mathcal{T}\ c_0/2$	16.3 cm

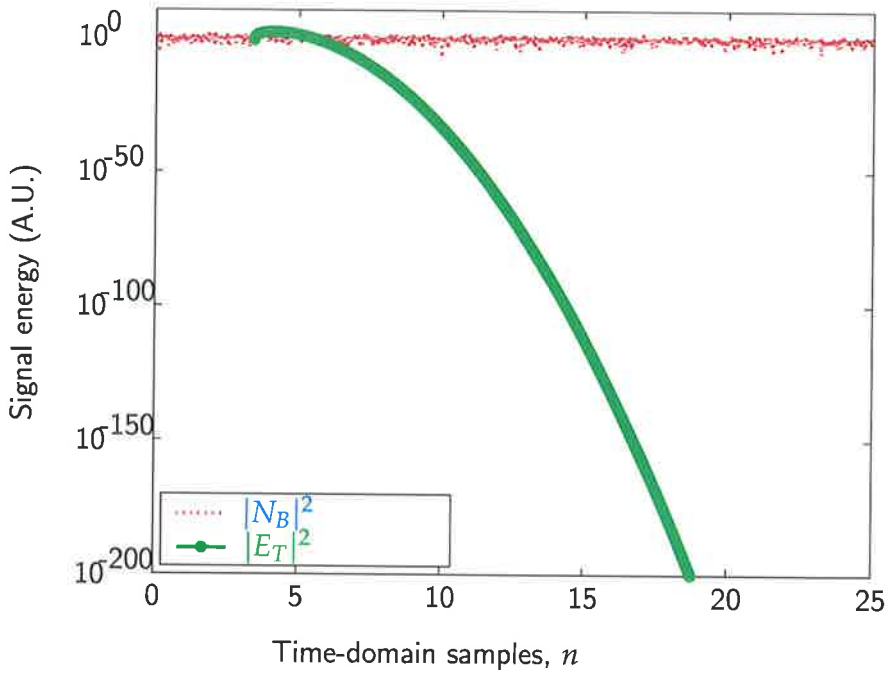

Figure A.2. Simulated T-ray energy and probe beam noise energy as a function of time. The plots of probe beam noise energy $|N_B|^2$ and T-ray signal energy $|E_T|^2$ show the energy in the signal and beam noise as a function of time $n = t/t_s$. The T-ray signal has most of its energy in the initial part of the pulse, with very little energy remaining for larger times. The average energy in the probe beam noise is constant over time. These plots are obtained by taking the amplitude of the waveforms in Fig. A.1.

The limit of acceptable SNR in a particular experiment depends on the specific measurement, but there will always be some limit beyond which the signal of interest is obscured.

The SNR in an experiment can be quantified in the time domain by comparing the total sum of the signal energy $\sum_0^{N-1} |E_T|^2$ to the sum of the noise energy $\sum_0^{N-1} (|N_T|^2 + |N_B|^2)$. As a larger value of $\mathcal{T}$ is chosen, the total contribution due to N_B will rise while the signal power remains approximately constant. At some point the accumulated noise energy (from the probe beam) will be greater than the accumulated T-ray energy, and the average frequency signal will be obscured by noise.

The cumulative contributions of T-ray power and probe beam noise can be compared by summing the energy over each scan; Fig. A.3 shows the total signal and noise energies as a function of increasing $\mathcal{T}$.

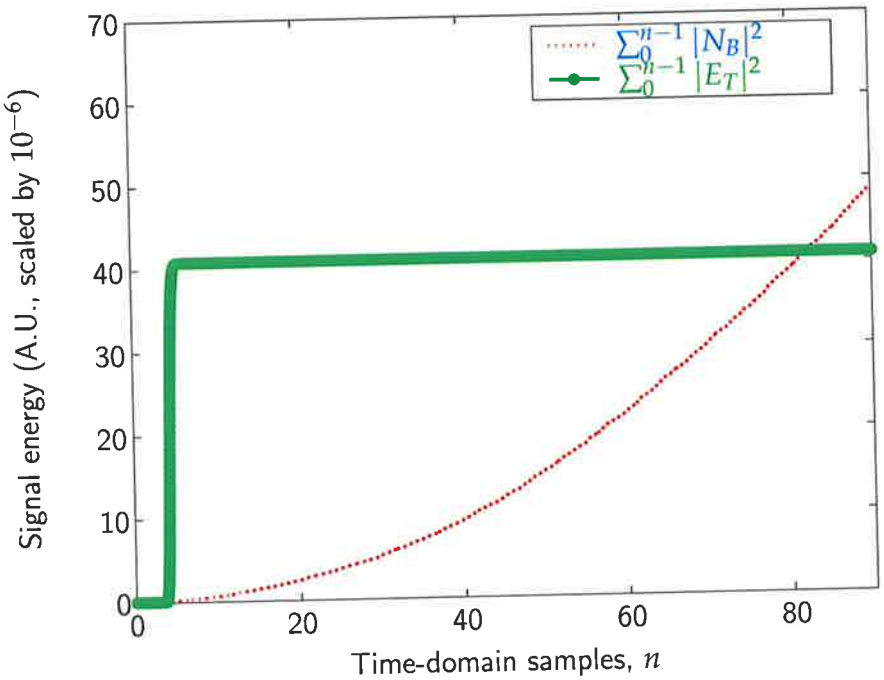

Figure A.3. Simulated T-ray and probe beam noise energy accumulation as a function of time. The plots in this graph show the accumulation of energy over a measurement time $n = t/t_s$: accumulated probe beam noise energy $\sum_0^{n-1} |N_B|^2$, and accumulated T-ray signal energy $\sum_0^{n-1} |E_T|^2$. These simulated graphs are obtained by numerically integrating the graphs in Fig. A.2, but the time scale has been extended to show the point where the accumulated probe beam noise energy equals the accumulated T-ray signal energy: at this point the average signal-to-noise ratio (due to probe beam noise) $= 1$. The vertical axis values have been scaled down by 10^6 from Fig. A.2 for clarity.

The point in Fig. A.3 where the two curves intersect corresponds to the duration at which the total T-ray signal energy equals the total noise energy in the probe beam. Thus, at the intersection point, the average SNR of the T-ray spectrum is unity.

The average SNR of a spectroscopy measurement depends on the temporal measurement duration $\mathcal{T}$. However, T-ray TDS is typically used to study specific frequency ranges, depending on the frequencies of interest – for example, specific absorption modes in gas molecules, or the dielectric constant of a material in a specific frequency range. To show the SNR of a measurement in a specific frequency range, and how it depends on $\mathcal{T}$, the spectra of a T-ray pulse (in this case simulated from a PCA) and the probe beam noise are shown in Fig. A.4. This Figure shows that the SNR of the spectrum is different for different frequencies, thus the average SNR (as calculated in the time domain) is less important than the SNR at a specific frequency of interest.

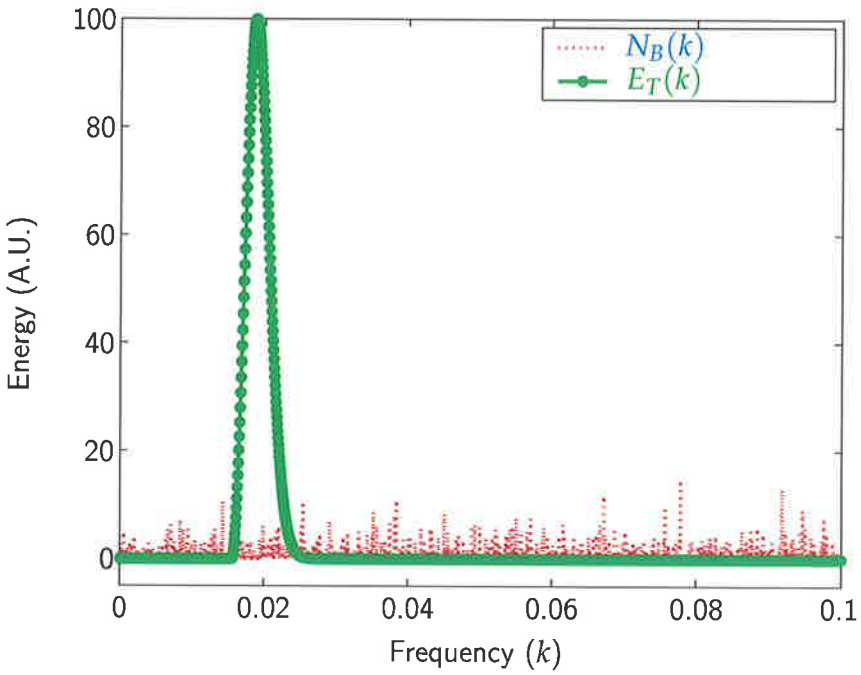

Figure A.4. Simulated T-ray and probe beam noise spectra. This graph shows a portion of the sampled (amplitude) spectra of the T-ray signal $E_T(k)$ and the probe beam noise $N_B(k)$. Most of the T-ray energy lies in a narrow part of the spectrum while the white, Gaussian probe beam noise is distributed equally across all frequencies, thus the SNR of interest depends on the frequency range of interest. The spectra in this graph were obtained using a Fast Fourier Transform (FFT) in MATLAB of the temporal waveforms in Fig. A.1.

In T-ray TDS, the spectrum of T-ray pulse energy, $E_T(\omega)$, is represented by a discrete frequency-domain data series, $E_T(k)$, where $k = 0$ to $N-1$. The frequency spacing of the points, Δf, equals $1/\mathcal{T}$ (from Fourier theory). The T-ray signal power at a given frequency, for example f_1, can be seen through measurement (using the FFT, as in Fig. A.4) or calculation of the T-ray spectrum, E_T, using the expressions in Table A.1 and substituting $\omega = 2\pi f_1$.

From Fourier theory, it can be shown that the mean of the probe beam noise in the frequency domain, and its variance $\sigma^2_{B-\omega}$, depend on the variance in the time domain, σ^2_{B-t}, and the number of points in the FFT, N (Proakis and Manolakis, 1996):

$$\sigma^2_{B-\omega} = N\,\sigma^2_{B-t}. \tag{A.5}$$

From the discussion of an increased contribution from probe beam noise for long scanning times, it is not surprising that the mean level of the noise, and its variance, are proportional to N, as shown in Eq. (A.5).

The maximum frequency resolution of a measurement at a frequency of interest, for example f_1, is determined by the length of $\mathcal{T}$, which is in turn determined by the acceptable SNR at f_1 in the frequency spectrum.

To measure the response at frequency f_1 of a sample with a material absorption of strength $M(\omega)$, an SNR of at least $1/M(f_1)$ is required. For a time-domain probe beam of variance of σ^2_{B-t} (which can be measured), the maximum frequency resolution at f_1 will be given by

$$\Delta f_{\min}(f_1) = 1/\mathcal{T}_{\max},$$

where $\mathcal{T}_{\max}$ is the value of $\mathcal{T}$ such that the T-ray signal energy at f_1 equals $1/M(f_1)$-times the noise energy at f_1, that is,

$$|E_T(f_1)|^2 = \frac{1}{M(f_1)}\,N\,\sigma^2_{B-t}. \tag{A.6}$$

Thus since $N = \mathcal{T}/t_s$,

$$\mathcal{T}_{\max} = \frac{t_s\,|E_T(f_1)|^2\,M(f_1)}{\sigma^2_{B-t}}. \tag{A.7}$$

An example limit on Δf, using Eq. (A.7) with realistic experimental quantities, is given in Sec. A.4.

The dependence of the SNR at a frequency of interest (f_1) can be expressed as a function of $\mathcal{T}$:

$$\begin{aligned} \mathrm{SNR}(f_1) &= \frac{E_T(f_1)}{\sigma_{B-\omega}} \\ &= \frac{\sqrt{t_s}\, E_T(f_1)}{\sqrt{\mathcal{T}}\, \sigma_{B-t}}. \end{aligned} \tag{A.8}$$

For a given time-domain probe beam variance σ^2_{B-t} and sampling interval t_s, the signal-to-noise ratio at a given frequency is inversely proportional to the square root of the scanning range $\mathcal{T}$. This result is confirmed experimentally in the following Section.

A.3 Experiments

To demonstrate experimentally the relationship between the dynamic range in the frequency domain and temporal scanning range, a T-ray waveform was measured using a femtosecond laser and a 2-mm-thick ZnTe crystal (Zhang et al., 1992b). The emitted T-ray wave was collimated and focused by two parabolic mirrors and detected using Electro-Optic Sampling (EOS) by a 5-mm-thick ZnTe crystal (Wu and Zhang, 1995). The entire T-ray beam path was purged by dry air and the humidity was limited to less than 6%; water vapour absorption was not considered to be significant in these experiments. The delay stage resolution in the experiment was 10 μm (t_s = 66.67 fs) and the temporal measurement dynamic range was 1000.

A series of T-ray spectra were extracted by Fourier transform (FFT) of the temporal waveforms in the range of 0 to $2^n\mathcal{T}_0$, where $\mathcal{T}_0$ = 8.53 ps and $n = 0, 1, \cdots 11$. That is, 12 measurements were made, each with a duration ranging from 0 to $2^n\mathcal{T}_0$. The different duration measurements were designed to measure different amounts of background noise.

A.4 Results

The signal-to-noise ratio at the frequency with the maximum amplitude (f_1) is presented as a function of temporal scanning range in Fig. A.5. The solid dots are experimental data and the curve is fitted by Eq. (A.8). The SNR in the frequency domain is inversely proportional to the square root of the temporal scan duration, as predicted by the theory in Sec. A.2.

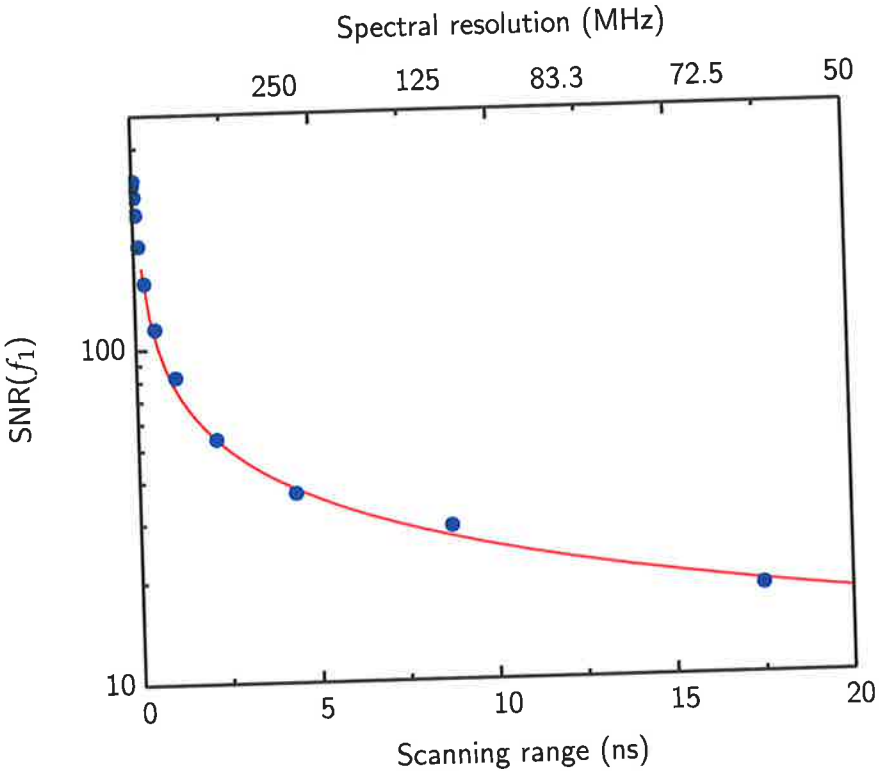

Figure A.5. Measured SNR of T-ray TDS at one frequency (f_1) versus scan duration. This graph shows the variation of the SNR of T-ray TDS at one frequency as a function of the temporal scanning range $\mathcal{T}$. The frequency chosen for these measurements was the frequency that had the highest amplitude. The solid dots are experimental data and the curve is fitted the calculated results from Eq. (A.8), thus confirming its accuracy. The experimental conditions are described in Sec. A.3. The spectral resolution Δf is also shown in this graph, and is inversely proportional to the scanning range $\mathcal{T}$.

For a generated T-ray spectrum from a PCA, such as in Fig. A.4, the spectral shape can be modelled using the equation for a PCA in Table A.2,

$$E_T(\omega) = A\frac{\omega\tau}{\sqrt{2}}\exp -\omega^2\tau^2/4. \tag{A.9}$$

From Eq. (A.9), Eq. (A.7), and $\Delta f = 1/\mathcal{T}_{\max}$, the best frequency resolution for a sample with absorption $M(\omega)$ can be expressed as

$$\begin{aligned}\Delta f_{\min} &= \frac{1}{\mathcal{T}_{\max}} \\ &= \sigma_{B-t}^2 / \left(\sqrt{2t_s M(f_1)}\, A\, \pi\, f_1\, \tau\, \exp[-\pi^2 f_1^2\, \tau^2]\right)^2.\end{aligned} \tag{A.10}$$

For example, for a sample with $M(f_1)$ = 1% at a frequency of interest f_1 = 0.18 THz, probed with a T-ray spectrometer (sampled at t_s = 66.67 fs) using a PCA emitter (pulse duration τ = 5 ps, spectrum from Table A.2) and a measured dynamic range $A/\sigma_{B-t} = 10^6$, the highest spectral resolution of the T-ray spectrometer is approximately 0.8 GHz.

A.5 Conclusion

In summary, this Appendix has demonstrated that the spectral resolution of T-ray spectroscopy depends not only on the duration of the sampled time-domain waveform $y(t)$, but more fundamentally on the *dynamic range* of the T-ray spectrometer. A high-dynamic range system is required for high-resolution spectroscopy.

For a typical spectroscopy system limited by probe beam noise, an achievable resolution of approximately 0.8 GHz is achievable at around 0.5 THz. This compares favourably to molecular linewidths, which are of the order of 1 GHz. For higher frequency measurements, broadband T-ray generation using Surface Current Generation (SCG) or Optical Rectification (OR) is required (Han and Zhang, 1998a; Leitenstorfer et al., 1999).

A.5.1 Future work

For high-resolution T-ray spectroscopy, the ratio of T-ray power to laser probe beam power must be maximised.

Research is ongoing into high-power T-ray sources based on PCAs (Zhao et al., 2002b) and electron beams (Williams, 2002).

Noise in the probe beam can be reduced by using stable solid-state-pumped ultrafast lasers (Moon, 1993), by hard-limiting the output power of the laser (Zhang et al., 2001a) and by using longer integration times (signal averaging).

A.6 Appendix summary

This Appendix has shown that the spectral resolution of T-ray spectrometers is limited not only by the time duration of a scanned measurement, but also on the dynamic range of the spectrometer. This understanding is critical to planning high resolution studies with pulsed T-rays.

Appendix B

Experimental Equipment

THIS Appendix describes some of the experimental equipment used in T-ray measurements in further detail, and summarises part of the experimental procedure used for spectroscopy experiments in this Thesis. Data acquisition is discussed below. Numerical data processing is covered in Appendix D.

B.1 Femtosecond laser

The most important part of a pulsed T-ray spectrometer. The laser used for most of the spectroscopy experiments in this Thesis is shown in Figs. B.1 and B.2. A full description of its operation can be found in the manufacturer's manual.

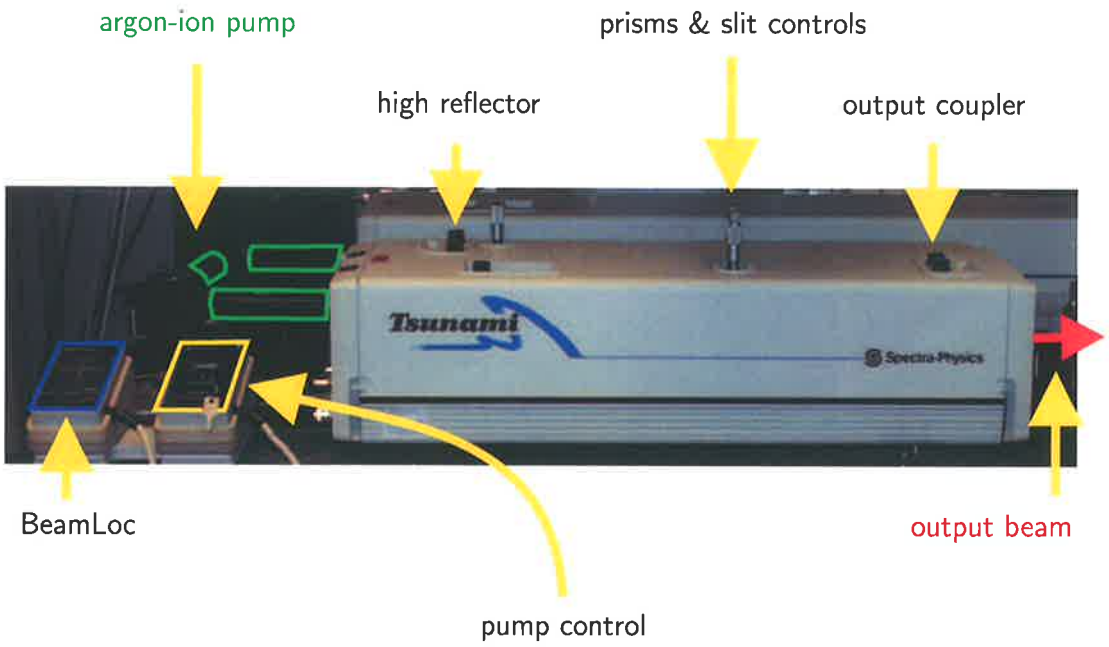

Figure B.1. Photograph of an ultrafast laser – closed. This photograph shows the exterior of the fs laser used in most experiments in this Thesis (model: Tsunami, manufacturer: Spectra Physics, Mountain View, CA, USA; URL: `http://www.spectraphysics.com`). The fs laser is powered by a CW argon-ion laser, running on all wavelengths (blue–green), labelled as the pump in this photograph. The pump control is used to control the power of the argon-ion laser; typically, an optimum level of pump power from the argon-ion laser is selected for maximum pulsed output power from the fs laser, without adding any extra CW from the fs laser. BeamLoc is a control system used to stabilise the alignment of the argon-ion laser, which in turn stabilises the fs laser output. The alignment of the fs laser is optimised on a day-to-day basis using the high reflector and output coupler alignment controls. The prisms & slit controls are used to optimise the power and pulse duration of the output fs pulses.

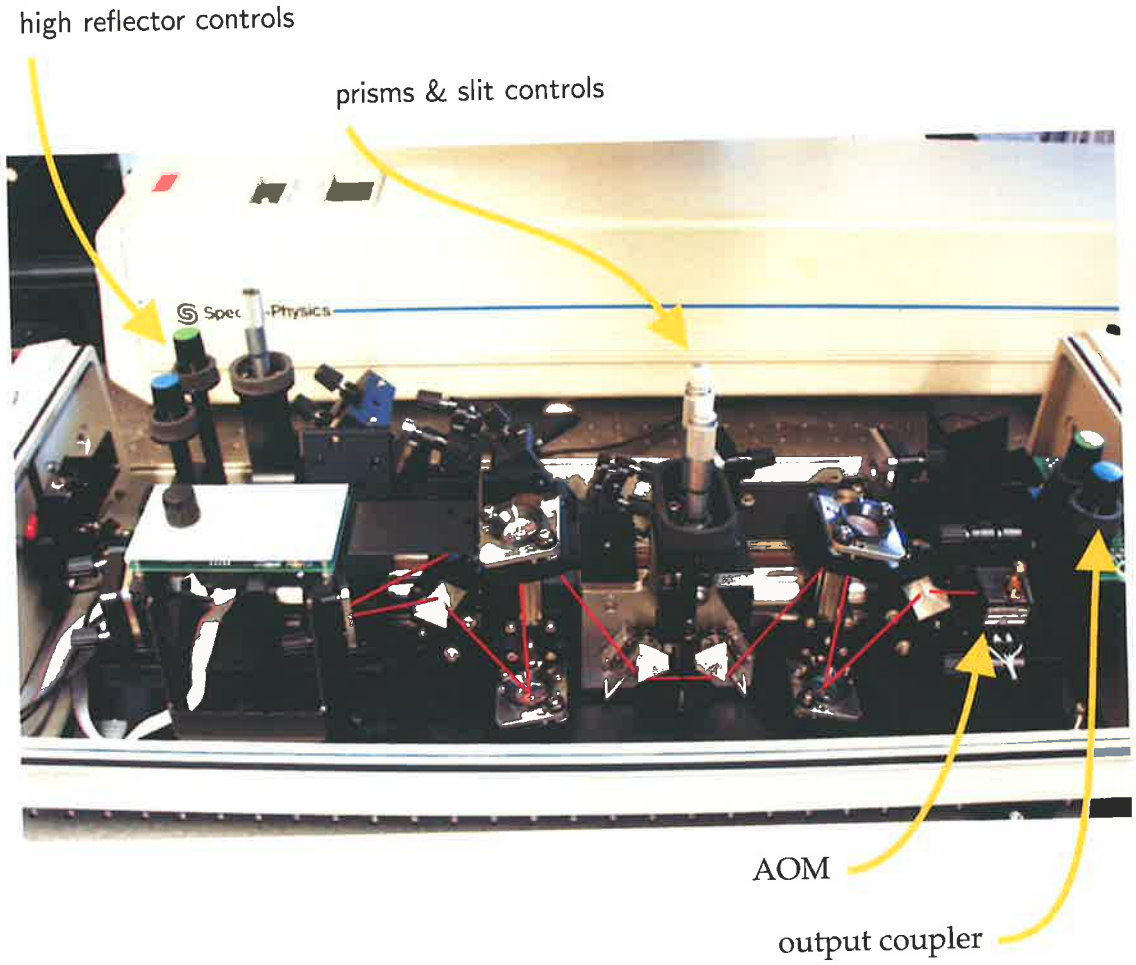

Figure B.2. Photograph of an ultrafast laser – open. This photograph shows the interior of the femtosecond laser used in most experiments in this Thesis (model: Tsunami, manufacturer: Spectra Physics, Mountain View, CA, USA; URL: `http://www.spectraphysics.com`). Visible in this diagram is the Acousto-Optic Modulator (AOM unit, used to sustain mode-locking (pulsed operation) over long periods of time. The path of the laser beam is marked in red, refracting through the four dispersion-control prisms and into the AOM and output coupler (from left to right).

B.2 Example ultrafast T-ray experimental layout

The photograph in Fig. B.3 shows the layout of the experimental T-ray system used for most of the experiments in this Thesis. Visible are the Argon-Ion and Ultrafast Lasers, used to generated femtosecond laser pulses (see Sec. B.1), and the optical components used to generate and detect T-rays (see sneq:optics), all attached to a vibration-isolating optical table.

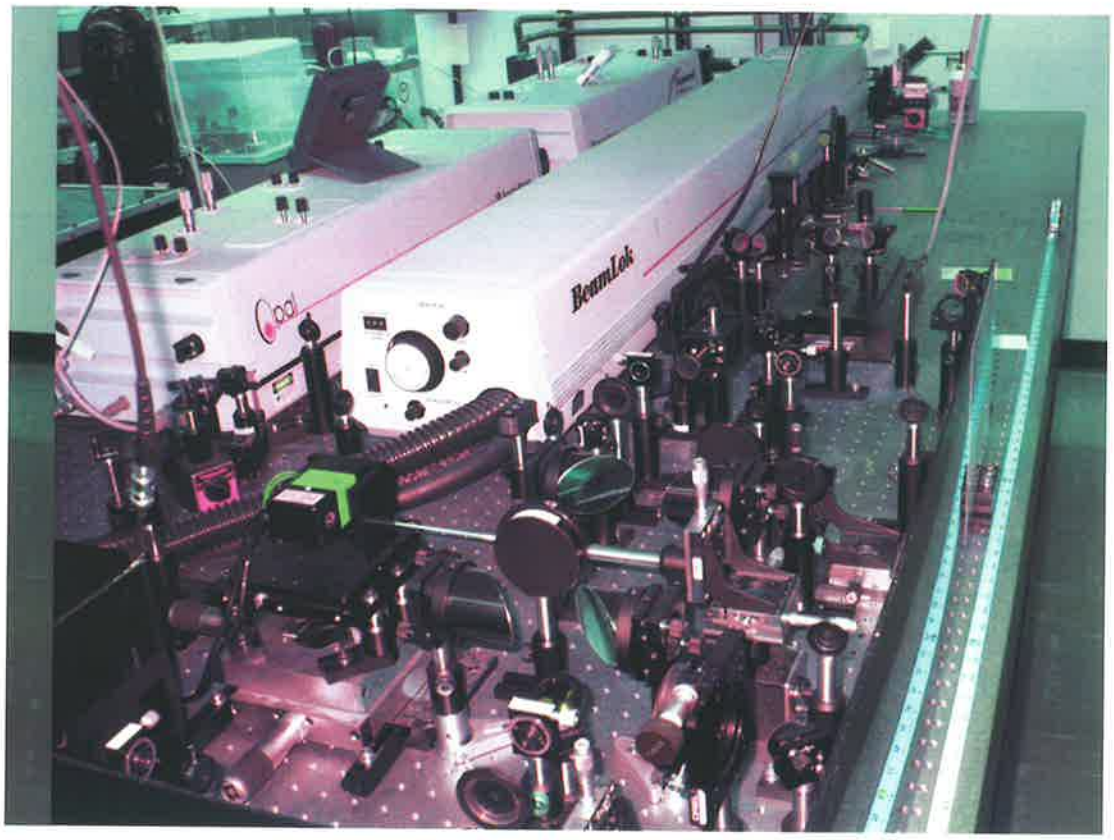

Figure B.3. Example T-ray system photo. The T-ray spectroscopy system shown in this photograph was used for most of the experiments in this Thesis. The ultrafast laser and optics required for T-ray generation and detection were laid out on a vibration-isolating optical table.

B.3 Practical alignment of a T-ray system for DTDS

Careful and repeatable alignment of the T-ray spectrometer is critical to making good measurements. The following list outlines the important steps used in experiments for double-modulated DTDS in Ch. 6 of this Thesis – the list relates to the setup in Fig. B.4. The times indicate the approximate duration of each step.

1. Power up argon-ion laser and allow to warm up. Turn on all electronics (2.5hrs).
2. Set sample in place.
3. Check alignment on laser and all irises, and record laser power (10min).
4. Set sample such that T-rays pass through the substrate, and find the timing on the delay stage with the first Lock-In Amplifier (LIA1). Record the laser position (15min).
5. Check laser alignment with irises (5min).
6. Optimise power at the T-ray pulse peak by tweaking the alignment of the pump and probe mirrors (15min).
7. Balance photodiodes' current by rotating the quarter-wave plate (QWP).
8. Set the LIA1 phase to synchronise with the chopper phase, and record the SNR.
9. Turn on the DTDS galvanometer, widen the time constant on LIA1, and check that timing is still correct. Optimise the galvanometer in its XYZ position, and set the phase on the second LIA (LIA2). Record the SNR (15min).
10. Set LIA2's time constant to 1 s. Scan the delay stage 5120 μm starting at -600 μm from the peak with 20 μm resolution. This gives a maximum frequency of 12 THz and 256 data points. Save the reference pulse y_r (25min).
11. Move the galvanometer so the T-ray spot is on the sample/substrate boundary. Set the delay stage timing to the T-ray pulse peak and optimise the galvanometer's XYZ position. Record the SNR (15min).
12. Set LIA2's time constant to 1 s and scan. Save the differential pulse y_d (25min).
13. Save scanned data into graphing software, and show dy_r/dt. It should be approximately the same as y_d.

14. Repeat step 12 at least twice.

15. Process the saved pulse waveforms numerically using the DTDS algorithm for refractive index and absorption coefficient.

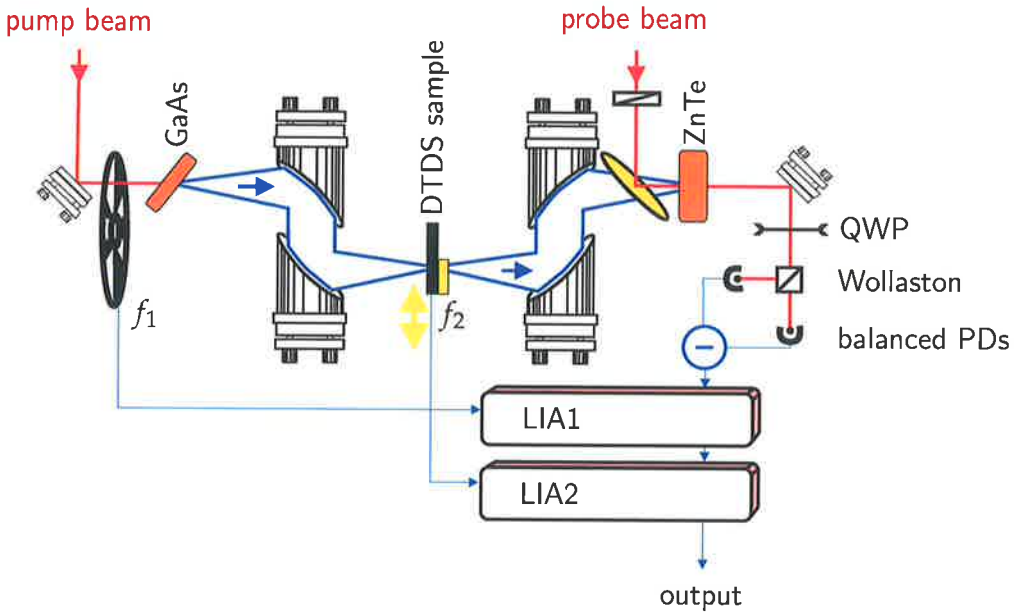

Figure B.4. DTDS spectrometer schematic with dual LIAs. Double-modulated DTDS schematic. The pump and probe beams are split from a femtosecond laser and act to generate and detect the T-rays. The T-rays, shown in blue, are generated in the GaAs wafer, then collimated and focused with gold-plated parabolic mirrors. The T-ray electric field is converted to an electronic signal with the ZnTe EO crystal, a quarter-wave plate (QWP), a Wollaston polariser and balanced photodiodes (PDs). Two Lock-In Amplifiers (LIAs), with the shaker and an optical modulator, implement the double-modulation scheme. The DTDS output signal depends on the differences between the films on opposite ends of the slide (from Fig. 6.4.)

B.4 Data acquisition

The T-ray spectrometer used in this Thesis was controlled from a LABVIEW program (manufacturer: National Instruments, model: Version 9.0). The computer controlled the delay stages and acquired data from the Lock-In Amplifiers (LIAs) via a General Purpose Interface Bus (GPIB, manufacturer: National Instruments) network. A screen shot of the LABVIEW computer interface is shown in Fig. B.5.

Figure B.5. Screen shot of control software for operating T-ray TDS experiments. This is a screen shot of the LabView computer interface used to control the T-ray spectrometer used in this Thesis. The controls for the experiment are shown on the left and the readouts are on the right. In the centre is a large time-domain graph of a sampled T-ray waveform – the X-axis is a readout of the delay stage position and the Y-axis is channel one of the Lock-In Amplifier (LIAs). The smaller graph underneath shows channel two of the LIA, which should be much smaller than channel one if channel one is in phase with the optical modulator (chopper). The large display half-visible on the right-hand side was used for reading the LIA output from across the room when aligning certain optics.

B.5 T-ray microscope layout

The T-ray microscope system described in Ch. 10 had a layout on the optical table as shown in Fig. B.6. To a large extent this layout was typical of T-ray spectrometers (described in Ch. 3), although two main features were unique. The first was the objective lens mounted on a Z-translation stage to enable focussing of the optical pump beam into different positions in the crystal. The second was the EO emitter, with sample attached, being mounted on an X-Y stage to enable two-dimensional imaging of the sample in the near field.

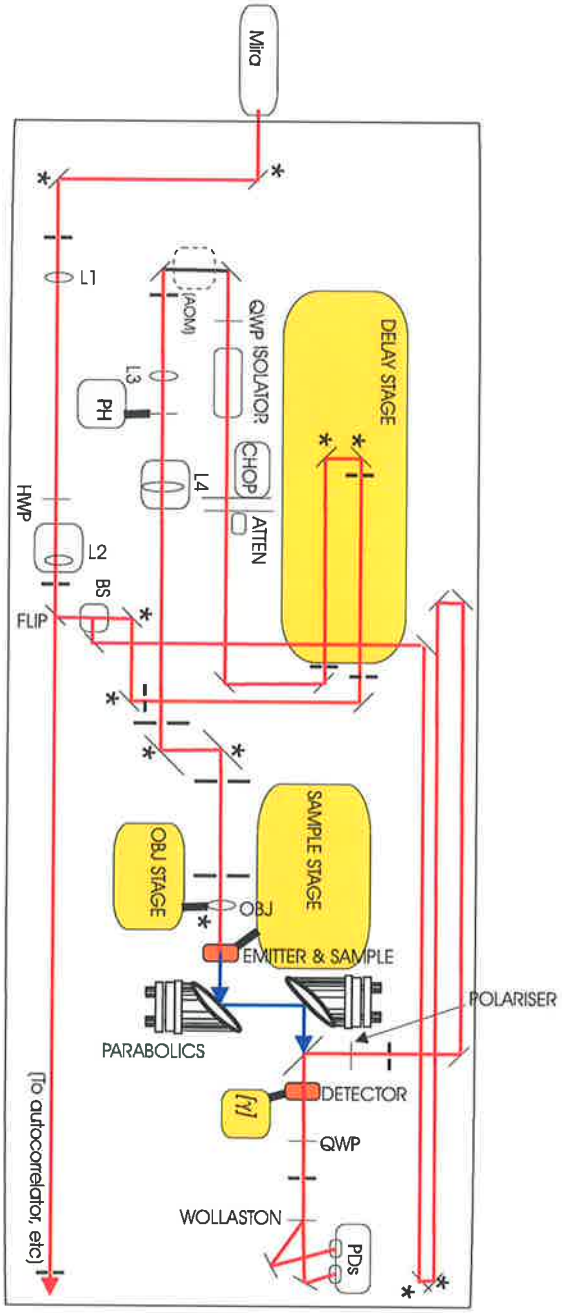

Figure B.6. Full schematic of the T-ray microscope experiment. This is a sketch of the actual layout of the T-ray microscope experiment on the optical table. The sketch is more detailed than the schematics in Ch. 10 because it represents a real experiment. The optics included in this layout are listed in Table B.1. The mirrors marked with an asterisk '*' are critical to the alignment of the laser beam, and the divided thick black lines are metal apertures for exactly aligning the laser beam.

Table B.1. Full microscope layout components. This Table lists the components of the full T-ray microscope experiments shown in Fig. B.6. For a detailed description of the role these components play in the system, see Ch. 3.

Component	Description
Mira	Femtosecond Ti:sapphire laser (Coherent Inc, Mira 9000)
mirrors	Dielectric mirrors for 800-nm light and 45° angle of incidence
apertures	Metal iris apertures
L1	Lens to collimate the beam (to reduce divergence)
HWP	Half-wave plate divide power between pump & probe
L2	Lens focus the probe beam into the detector
FLIP	Removable mirror to send the beam to the autocorrelator
BS	Polarising beam splitter to separate pump and probe beams
DELAY STAGE	To change the delay between pump and probe
ATTEN	Variable attenuator to reduce the pump beam power
CHOP	Mechanical chopper
ISOLATOR	Faraday isolator to block retro-reflected pulses returning to the laser
QWP	Quarter-wave plate to set pump polarisation for maximum generation
(AOM)	Space for an Acousto-Optic Modulator, to potentially replace chopper
L3	Lens to expand the beam into L4
L4	Lens to collimate the expanded beam for the objective lens
OBJ	Objective lens to tightly focus the pump beam into the emitter
OBJ STAGE	Stage to position the objective lens (Z position)
EMITTER & SAMPLE	Electro-optic (EO) T-ray emitter with sample attached to lower side
SAMPLE STAGE	Stage to position the sample (X-Y position)
PARABOLICS	Two gold-coated parabolics to collect and focus T-rays
POLARISER	Polariser to ensure the probe beam is polarised
DETECTOR	Electro-optic (EO) detector for EO sampling (EOS) of the T-rays
QWP	Quarter-wave plate to compensate the EOS signal
WOLLASTON	Wollaston polariser to split the EOS signal into two polarisations
PDs	Balanced photodetectors to read the EOS signal as a current
autocorrelator	Autocorrelator: a device for testing and diagnostics of the laser beam

B.6 Crossed-polariser detection

A fundamental part of Electro-Optic Sampling (EOS, see Sec. 3.3.2) is the photodiode detection circuit. A photograph of the balanced photodiodes used in the experiments in this Thesis is shown in Fig. B.7. The probe beam, entering the Figure from the left, has passed though the EO crystal, and therefore has had its polarisation modulated by the T-ray power. This polarisation modulation is turned into an intensity modulation with a Wollaston polariser – depending on the rotation of the probe polarisation, the optical power shifts between the two output beams of the Wollaston. These beams are directed onto two photodiodes, visible in Fig. B.8(a).

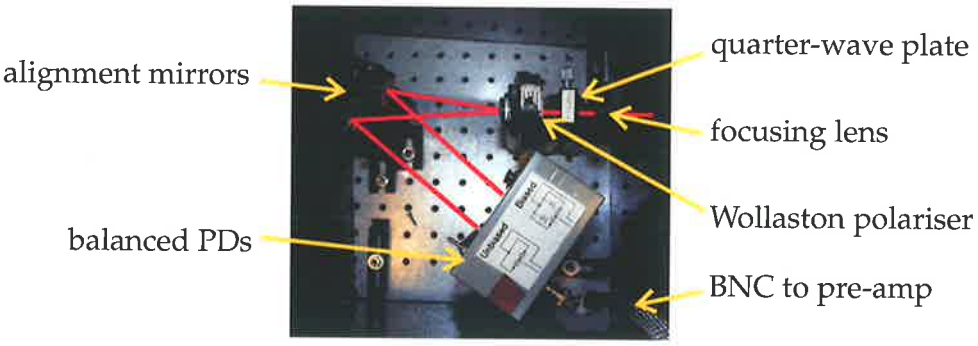

Figure B.7. Photograph of crossed polarisers in Electro-Optic Sampling. The polarisation of the optical probe beam in EOS is detected using crossed polarisers. The probe beam is focused onto the photodiodes using a lens to minimise noise from fluctuations in the alignment of the probe beam. A quarter-wave plate is used to balance the polarisation of the probe beam equally between the s- and p-polarisations when no T-ray field is present. The two polarisations are directed to two photodiodes using a Wollaston polariser. For zero T-ray field, the current in the photodiodes is equalised using the quarter-wave plate, thus minimising the difference current between the two (as measured on a digital ammeter). When the polarisation rotates due to the T-ray field, the change in difference current is measured on a current pre-amplifier.

The two photodiodes are connected to output a *difference current* – common mode fluctuation in the probe power (that is, not due to T-rays being detected) are attenuated, while difference currents produced by polarisation rotation are amplified.

A quarter-wave plate is used to balance the power in the two beams to zero for no T-ray power. The T-ray path is blocked and the quarter-wave plate rotated. A DC ammeter is needed to read the output of the balanced circuit for optimisation. Normally during measurement, the output of the preamplifier was attached directly to the LIA.

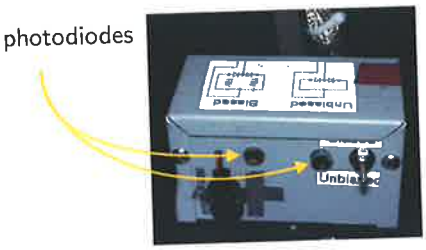

(a) Mounted balanced photodiodes and current difference circuit

(b) Digital ammeter

Figure B.8. Photographs of the detection electronics: photodiodes and current meter. These photographs show the balanced photodiodes and an example ammeter used in this Thesis to detect the current caused by a T-ray pulse in Electro-Optic Sampling. The two balanced photodiodes are mounted at the height of the optical beam and wired to deliver a difference current to the current amplifier. A DC ammeter is used to measure the difference current when balancing the quarter-wave place in the crossed polarisers. When the T-ray signal, chopped with a mechanical chopper, is being measured, the current is directed through a current amplifier into a Lock-In Amplifier (LIAs).

B.7 Lock-in amplifier and preamplifier

B.7.1 SRS 830 lock-in amplifier

The operation of the Stanford Research Systems 830 digital Lock-In Amplifier (LIAs) is described in detail in the manufacturer's manual, which is also available on the SRS web site (URL: `http://www.thinksrs.com`). This was the standard LIA used in the experiments in this Thesis. A photograph of the LIA is shown in Fig. 6.7.

A block diagram of the LIA in Fig. B.9 outlines its operation. The features of note are the frequency multipliers in the Phase Sensitive Detectors (PSDs), which are followed directly by the low pass filters (LPFs). The PSD mixer operates by multiplying the detected current signal y_i, which in a T-ray spectrometer comes from balanced photodiodes, by a sinusoidal wave at the reference frequency f_r, set by the optical chopper frequency:

$$y_{\text{PSD out}} = y_i \times \sin(2\pi f_r). \tag{B.1}$$

The input signal, y_i, has many frequency components. When multiplied by $\sin(2\pi f_r)$, these components are shifted by $\pm f_r$.

The next stage of the LIA has a very narrow-band low pass filter, which attempts to cut out any frequencies that are not at DC – and the only component at DC is that of $y_i(f = f_r)$. The bandwidth of the filter depends on the time constant of the LIA; a long time constant means a narrow-band filter, which is desirable for cutting out unwanted signals (that is, noise at frequencies other than f_r). The trade off is that a narrower bandwidth means longer measurement times. The relationship between filter bandwidth $\mathrm{BW_{LIA}}$ and LIA time constant τ_{LIA} is given by

$$\mathrm{BW_{LIA}} = \frac{1}{S \times \tau_{\mathrm{LIA}}}$$

where S is the slope of the filter, and can be set to 6 db/octave ($S = 4$), 12 db/octave ($S = 8$), 18 db/octave ($S = 32/3$) or 24 db/octave ($S = 64/5$).

The DC output of the mixer is then the amplitude of the frequency component in the input current that was at f_r. After the LPF, it is only this amplitude that is displayed by the LIA. There are two mixers in the PSD to measure phase variation between the detected frequency component and the chopper's input sine wave. The bandwidth of the LPF determines how tightly the LIA filters out anything from the mixer that is above DC – this determines the input noise bandwidth of the LIA and is set by the LIA time constant.

An understanding of LIA operation was critical in the design of the double-modulated DTDS system in Ch. 6.

B.7.2 SRS optical chopper

An optical chopper wheel was used in conjunction with the LIA to modulate the T-ray beam at frequencies up to 2 kHz (see Ch. 6).

A chopper wheel is a black metal disc with equi-spaced gaps. When the disc is spun at a set speed and placed in a laser beam path, the beam is chopped on and off with a duty cycle of 50%. In T-ray spectrometers, the pump beam or the T-ray beam is chopped (see Fig. B.4), so the generated T-ray signal turns rapidly on and off. The LIA is designed to detect the amplitude of this on-off signal, and therefore lock into the T-ray signal. The LIA locks into the AC modulation of the probe beam (caused by the AC T-rays) and ignores the far larger background power of the probe beam, because it is mostly at other frequencies.

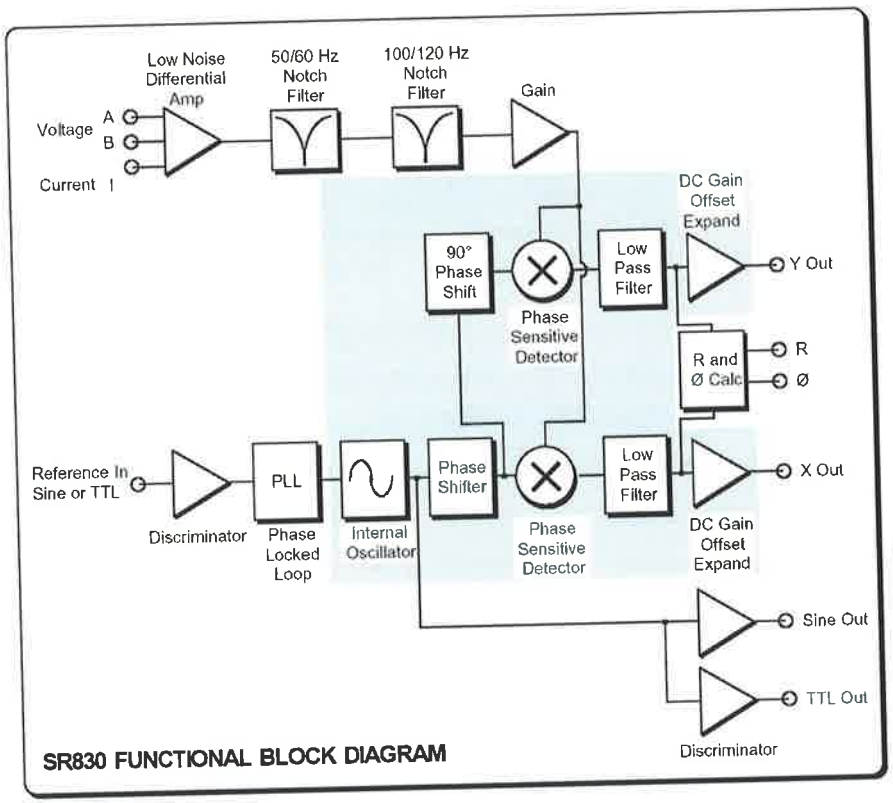

Figure B.9. SRS SR830 LIA functional block diagram. This diagram shows the operation of the LIA. The important features are the dual mixers (Phase Sensitive Detectors), referenced to the chopper frequency (Reference In), and the Low Pass Filters, which have an acceptance bandwidth set by the time constant on the LIA. From the *MODEL SR830 DSP Lock-In Amplifier Manual*, Revision 2.0 (11/2002), Copyright 1993 by SRS, Inc. (1290-D Reamwood Avenue, Sunnyvale, California 94089).

B.7.3 Current preamplifier

In some instances, a low-noise current preamplifier was used to amplify the current signal from the balanced detectors in EOS (see Sec. 3.3.2). This enabled the signal to be amplified sufficiently so electronic noise made no contribution to the noise in the signal – optical noise dominated. The preamplifier was used to scale the output level so that the Lock-In Amplifier (LIA) did not saturate.

Figure B.10. Photograph of the low-noise current amplifier. Stanford Research Systems low-noise current preamplifier. The preamplifier took the current signal from the balanced photodetectors (PDs) and converted it to a voltage signal for the Lock-In Amplifier (LIA, see Sec. B.7.1). The main benefit of using the preamplifier was its adjustable gain-bandwidth product – the gain could be set sufficiently high to avoid any contributions from electronic noise without reducing the bandwidth below the modulation frequency (for example, the chopper frequency).

B.8 Optical and mechanical components

The optical and mechanical components described in this section comprise a typical T-ray system. They are commercially available from both standard optics suppliers and smaller optics companies.

B.8.1 Mirrors: for laser light

The mirrors used in our T-ray system must be broadband and have a high reflectivity for the ultrafast 800-nm pulses. The optical beam size remains less than 5-mm in diameter throughout the system, so 0.5" or 1"-diameter mirrors are appropriate. Larger mirrors are only required when the optical beam is expanded in, for example, an imaging application (see Ch. 3).

To achieve a high reflectivity over a broad bandwidth, special *ultrafast* dielectric coatings are available, although they are quite expensive. A cheaper alternative, with slightly higher loss, is a silver metallic coating on the mirror.

B.8.2 Mirrors: for T-rays

T-ray are reflected by metallic surfaces, so gold- or silver-coated mirrors are typically used for directing T-ray radiation.

Metal-coated parabolic mirrors are used for collimating and focussing T-rays. Although gold-coated parabolic mirrors are more expensive than other common optical components, they provide a broadband and low-loss method of focussing the T-rays. Using plastic lenses to focus the radiation causes wavelength-dependent focal points and reflective losses (no anti-reflection coatings are available for T-ray radiation).

T-ray lenses are not commercially available, although they have been constructed by researchers from plastics such as polyethylene (see Ch. 3 for details).

B.8.3 Polarisers and beam splitters: for laser light

Optical polarisers and beam splitters are required in crossed-polariser detection (in Electro-Optic Sampling, see Sec. 3.3.2). The polarisers and beam splitters should be anti-reflection coated for 800-nm broad bandwidth pulses.

The polariser most commonly used to split the pump and probe beams as a cubic polarising beam splitter. The thickness of the cube beam splitter does introduce some dispersion into the pulse (pulse spreading), but it has a very good extinction ratio (low leakage between polarisations).

A pellicle beam splitter is commonly used to collinearly combine the optical and T-ray beams in Electro-Optic Sampling (see Sec. 3.3.2). A pellicle is a thin membrane that is transparent to T-rays and can be coated to reflect approximately 50% of an incident optical pulse at 45°. A no-loss pellicle coating must be selected because any power absorption will damage the membrane.

In crossed-polariser detection (see Sec. B.6), a *Wollaston* polariser is commonly used to split the s- and p-polarisation and direct the two beams into balanced photodiodes. Whereas a cubic beam splitter divides the two polarisations at 90° to each other, a Wollaston polariser splits the two polarisations at an angle of about 30°, making it easier to built a balanced photodiode circuit (see Fig. B.8(a)).

B.8.4 Quarter- and half-wave plates

Quarter- and half-wave plates are used to alter the polarisation of the optical beam. A half-wave plate is used to rotate the beam from the laser, thus controlling the ratio of the power in the pump and probe beams (the pump-probe beam splitter is fixed, so the fraction of power in each output beam depends on the polarisation state of the incoming beam).

A quarter-wave plate is used in crossed-polariser detection (see Sec. B.6) to balance the power between the two polarisations. When no T-ray signal is present, and thus the probe beam polarisation is unmodulated by Electro-Optic Sampling, the signal detected by the balanced photodiodes is set to zero by balancing the polarisations with a quarter-wave plate (QWP).

B.8.5 Motorised linear delay stage

A motorised delay stage is required for delaying the probe beam in pump-probe detection (or gated detection, see Ch. 3).

The translation distance of the stage will determine the limit on frequency resolution of T-ray spectroscopy (assuming sufficient signal power, see Appendix A), and the

stage resolution will determine the maximum observable T-ray frequency. For a total delay stage distance D, the measured T-ray frequency resolution is $\Delta f = 1/(2D)$. For a delay-stage resolution of Δd, the maximum measurable T-ray frequency is $f_{\max} = 1/(2\Delta d)$. We use $2D$ and $2\Delta d$ because the optical pulse experiences a delay double that of the stage delay, as shown in Fig. B.11.

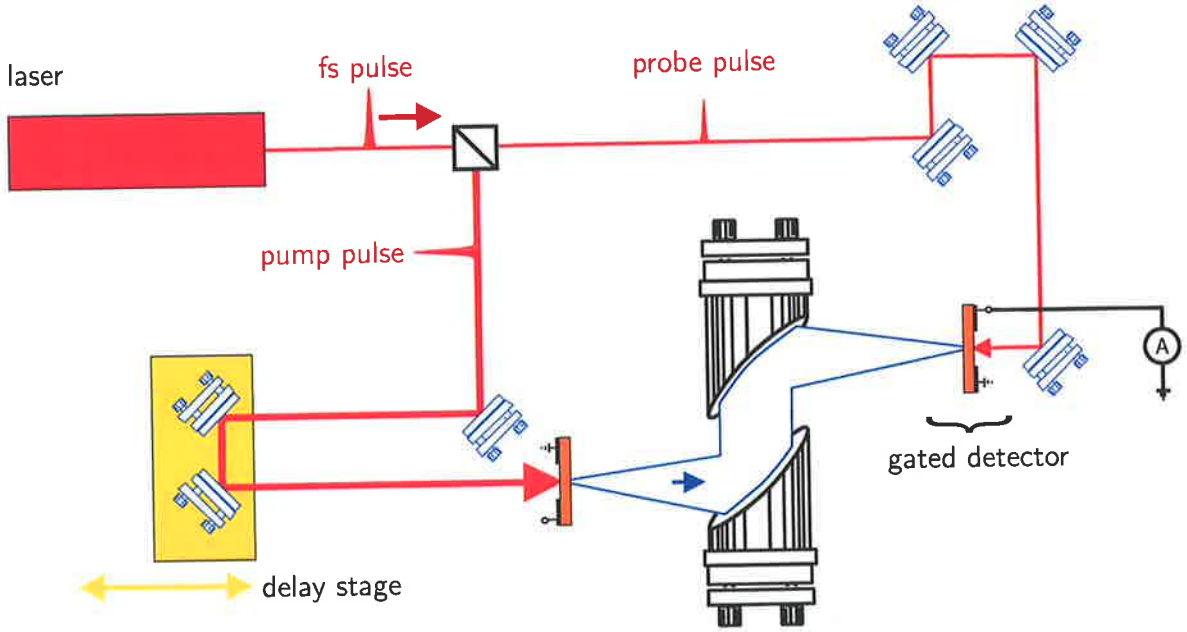

Figure B.11. Gated detection schematic. This T-ray generation and detection schematic is an example of a pump–probe experiment (from Fig. 3.6.)

A total travel distance $D \geq 10$ cm is typically chosen, and stage resolution of $\Delta d \leq 1\mu$m. The stage must be motor controlled to coordinate the delay with signal acquisition, thus measuring the T-ray pulse point-by-point (see Sec. 3.3). The stage with a motor controller is one of the most expensive components in a T-ray system, excluding the ultrafast laser.

B.8.6 Other common components

The common optical components that were used in the T-ray systems used in the experiments in this Thesis were:

- Optical lenses (for collimating the laser beams over long distances, or changing the beam size to match the T-ray beam size in imaging or in electro-optic sampling);

- Optical beam blocks can be any piece of opaque material with a high damage threshold and low T-ray absorption (for example, paper or plastic);
- Linear translation stages (for optimising the alignment and position of components, such as the T-ray emitter and detector);
- Iris diaphragms (for optical beam alignment);
- Mounts (kinematic mounts for mirrors, lenses, beam splitters, irises and crystals);
- Optical tables (for vibration isolation and positioning of the optical components);
- Rods, posts and holders (to secure components to the optical table).

Appendix C

Experimental Materials

THIS Appendix summarises the basic physical properties of the sample materials used in the experiments in this Thesis. This includes the solid-state materials used as T-ray emitters and detectors, and the solvents and proteins used in Ch. 5.

C.1 Wafers and crystals

The semiconductor samples and crystal used for T-ray generation and detection were supplied either by private corporations or other research collaborators.

C.1.1 ZnTe

The $< 110 >$-ZnTe crystals used for T-ray detection were purchased from two suppliers:

- *eV Products* (Saxonburg, PA, USA; URL: `http://www.evproducts.com`), a division of *II-VI Inc.* (Saxonburg, PA, USA; URL: `http://www.iivi.com`), and
- *MaTecK GmbH* (Juelich, Germany; URL: `http://www.mateck.de`).

The ZnTe must be polished on both sides to allow transmission of the 800-nm optical beams in Optical Rectification or Electro-Optic Sampling (see Ch. 3). The orientation of the crystals must be <110> so the transmitted beams interact with the maximum nonlinear coefficient of the crystal (the magnitude nonlinear coefficient depends on the crystallographic orientation).

The thickness of the crystal will influence: (i) the optical-to-T-ray conversion efficiency (a longer crystal has better efficiency), (ii) the generated or detected T-ray bandwidth (a shorter crystal has a higher bandwidth), and (iii) the separation of multi-reflected T-ray and optical pulses pulses, due to Fabry-Pérot reflections at the entry and exit faces of the crystal.

C.1.2 GaAs

The GaAs used for T-ray emission in the experiments in this Thesis was supplied by a collaborator in the US Army Research Laboratory. The T-ray generation efficiency of the sample was higher than for commercial GaAs and was due to a micro-scale roughness in the surface of the GaAs wafer. This roughness produced localised concentrations of the surface field, contributing an enhanced T-ray emission. The details of the emitter are being studied by scientists at Rensselaer Polytechnic Institute.

C.2 Water

Water is an important consideration in T-ray biosamples because: (i) it is vital to living systems, and (ii) water has a very high T-ray absorption coefficient. The published physical properties of water are summarised in Table C.1.

Table C.1. Physical properties of water. This Table lists some of the physical properties of water, according to Burdick & Jackson, a division of Honeywell (URL: `http://www.bandj.com`).

Material property	Value
dielectric constant, ϵ (at 20°C)	80.1
optical refractive index (at 20°C)	1.3330
density (at 20°C)	0.9982 g/mL
density (at 25°C)	0.9971 g/mL
molecular weight	18.02
dipole moment (at 20°C)	1.87
polarity index	10.2
solubility in water	miscible

The complex refractive index of pure water $\tilde{n}_{THz}$ was measured by dual-thickness T-ray TDS using a standard T-ray spectrometer. We obtained an estimate at 1 THz of $\tilde{n}$ = 2.4 - j0.478. This corresponded closely with the published values of Thrane et al. (1995): $\tilde{n}$ = 2.3 - j0.48 (absorption α = 200 cm^{-1}), at 1 THz.

C.3 Non-polar solvents

Non-polar solvents are of interest in T-ray systems because of their very low absorption. The non-polar solvent 1,4-dioxane was used as a medium to study protein hydration in Ch. 5 because it had a high water miscibility but low T-ray absorption. Since having thick samples improves the accuracy of spectroscopy, low-absorption samples can be characterised with a higher accuracy.

C.3.1 1,4-dioxane

The organic solvent 1,4-dioxane was used extensively in protein studies in Ch. 5 for its low T-ray absorption and high water miscibility. A summary of its physical properties is listed in Table C.3.

Table C.2. Non-polar solvents. This Table lists the physical properties of some non-polar solvents, according to Burdick & Jackson, a division of Honeywell (URL: `http://www.bandj.com`) and Sigma-Aldrich Co. (URL: `http://www.sigmaaldrich.com`).

Solvent	Optical refractive index	Microwave dielectric constant
Hexane	1.3749	1.88
Iso-octane	1.3914	1.94
Acetonitrile	1.3441	37.5
Chloroform	1.4458	4.81
Cyclohexane	1.4262	2.02
Tetrahydrofuran	1.4072	7.58
Toluene	1.4969	2.38
Tert-amyl alcohol	1.4050	–

Table C.3. Physical properties of 1,4-dioxane. The data in this Table are according to Burdick & Jackson, a division of Honeywell (URL: `http://www.bandj.com`). Dioxane is a colourless, flammable, toxic liquid.

Material property	Value
ϵ (at 20°C)	2.2189
molecular weight	88.11
refractive index (at 20°C)	1.4224
density (at 20°C)	1.0336 g/mL
density (at 25°C)	1.0280 g/mL
dipole moment (25°C)	0.45
polarity index	4.8
solubility in water	miscible

It is often useful to model the absorption spectrum of a liquid sample using a Debye model, that is a sum of resonators. In the literature, the Debye model for 1,4-dioxane-water mixtures requires either one or two decay constants depending on the molar fractions of the mixture. For a single-decay-constant model, Mashimo et al. (1992) presents Debye model coefficients for a range of water:dioxane molar ratios, and Crossley and Smith (1969) has a limited range but it is good supporting data. Unfortunately, the Debye models for dioxane did not provide sufficiently accurate data to fit the experimental data – this is discussed in the protein hydration studies, in Sec. 5.3.4.

C.4 Protein

C.4.1 Subtilisin Carlsberg (SC)

The protein Subtilisin Carlsberg (SC) was used extensively in the experiments in Ch. 5 to study protein hydration with T-rays. SC was a good choice because it was readily available, had been used in other hydration experiments, and demonstrates a change in catalytic activity for small changes in hydration levels (Pal et al., 2002).

Subtilisin Carlsberg is a commonly-available protease – that is, an enzyme for breaking down other proteins – with an activity that changes greatly for small changes in hydration. The structure and properties of SC can be found in the *Protein Data Bank* (URL: `http://www.rcsb.org`), where there are two suitable compounds: 'Crystal Structure of Subtilisin Carlsberg (serine protease) in Anhydrous Dioxane' (1AF4) and 'Subtilisin Carlsberg in 20% Dioxane' (1BFU). Some of these properties are summarised in Table C.4. One representation of the three dimensional structure is shown in Fig. C.1, where the largely spherical shape of the molecule can be seen.

Table C.4. Physical details of Subtilisin Carlsberg. This Table lists some properties of the protein (for both 1AF4 and 1BFU structures). A Dalton is a unit of mass equal to one-twelfth of the mass of an atom of carbon-12 (1.66033×10^{-27} kg). The Dalton is also called the atomic mass unit (amu). Alpha helix and beta sheet structures are visible in the SC diagram in Fig. C.1: the alpha helices are shown in red and the beta sheets in yellow. The molecular diameter was estimated using the average of six measurements in the protein structure viewing program RasMol (URL: `http://www.rasmol.org`).

Material property	Value	Reference
molecular weight	26698.00 g/Mol	`http://www-structure.llnl.gov/cd/subtilis.htm`
molecular weight	27274 Dalton	*Protein Data Bank*
number of residues	274	
number of alpha helix (content)	10 (29.56%)	
number of beta sheet (content)	9 (16.42%)	
molecular diameter, $2r$	43 ± 5 Å	RasMol
molecular volume, $4\pi r^3/3$	$33,510 \times 10^{-30}$ m^3	
dielectric constant	40 to 50	Russell et al. (1987)
no. of assoc. water molecules	~100	Pal et al. (2002)

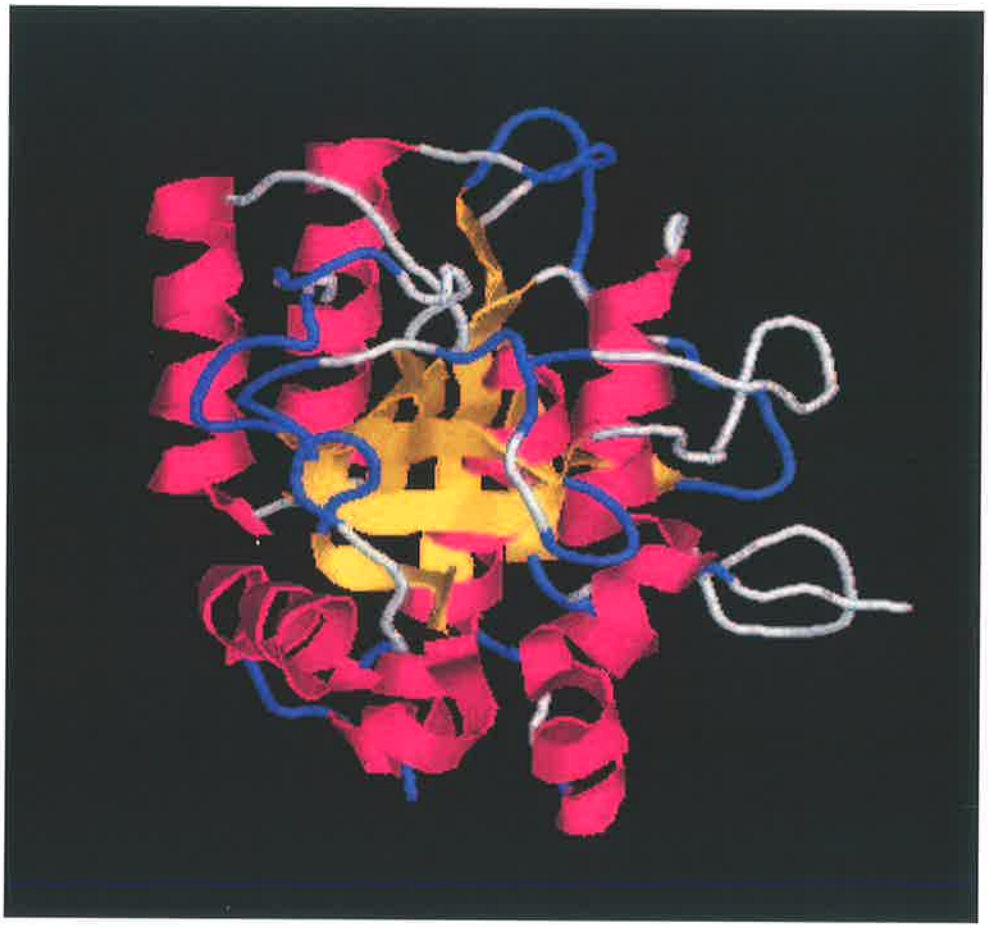

Figure C.1. Diagram of Subtilisin Carlsberg (SC) structure. This diagram outlines the structure of SC. The common formations of alpha helices (red) and beta sheets (yellow) are visible. This diagram was viewed using RASMOL (URL: `http://www.rasmol.org`) from data in the *Protein Data Bank* (URL: `http://www.rcsb.org`).

C.5 Plastics

C.5.1 High-density polyethylene

High-density polyethylene (HDPE) was used to hold the solvents, including dioxane, in experimental alignment in Chs. 5 and 8. HDPE is good because it does not react chemically with most solvents and it has a low T-ray absorption.

The T-ray refractive index of HDPE was measured to be approximately $n = 1.5$. The absorption of HDPE was too low for an accurate measurement, being approximately $\alpha < 10\ \text{cm}^{-1}$, or $\kappa < 0.001$.

C.5.2 Teflon

Teflon is good material for use in T-ray systems because it has low refractive index, so T-rays are not heavily reflected at the interface between free-space (air) and Teflon. The windows in the liquid sample holders in Chs. 5 and 8 were constructed from Teflon.

The T-ray optical parameters for Teflon are similar to those of HDPE. The optical properties are approximately $n \approx 1.5$ and $\kappa < 0.001$.

Appendix D

Data Processing Algorithms

THIS Appendix outlines some of the algorithms used to analyse the raw T-ray waveforms. These algorithms were mostly implemented in MATLAB (manufacturer: The MathWorks, model: 6.1; URL: `http://www.mathworks.com`), and are available on the attached CD-ROM, `SPM_PhD_Thesis/MATLAB_Algorithms`, as MATLAB files. Also included on the CD-ROM is a directory of raw data files, included as examples of typical T-ray experimental output.

D.1 Iterative parameter estimation algorithm

The iterative parameter estimation algorithm described in detail in Sec. 6.3.3 appears as a code outline in Sec. D.3.1. The basic idea of this code is to estimate a parameter, n, generate a model based on that guess, compare the guess to the experiments, then try to improve the guess.

The code is structured as shown in Fig. D.1 – repeated from Ch. 6.

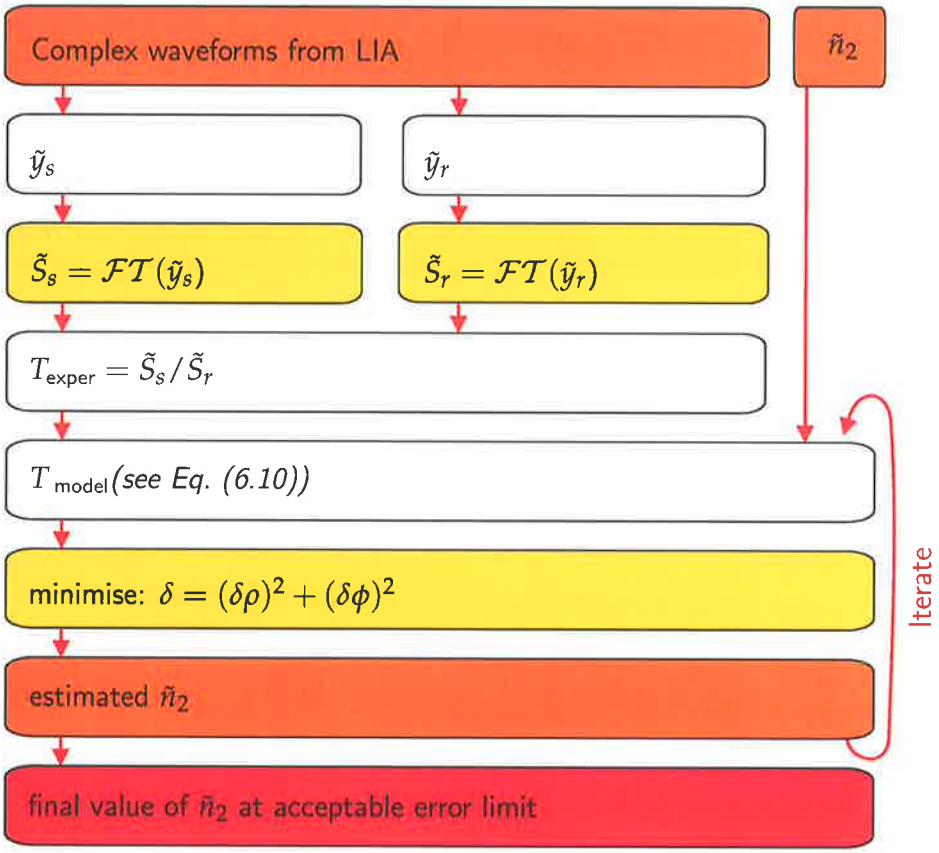

Figure D.1. Iterative parameter estimation algorithm. This flow chart shows the algorithm used to iteratively estimate the material parameters n and κ from Eq. (6.10), as described in Sec. 6.3.3 – this algorithm is based on Duvillaret et al. (1996). The complex waveforms $\tilde{y}_s$ and $\tilde{y}_r$ are obtained from the experiment, where the real and imaginary values are the X and Y outputs of the LIA. An estimate of $\tilde{n}_2$ is provided as seed for the search algorithm, which operates to minimise the error metric δ, where $\delta\rho = \log|T_{\text{model}}| - \log|T_{\text{exper}}|$, and $\delta\phi = \arg(T_{\text{model}}) - \arg(T_{\text{exper}})$. The re-estimation step is performed with MATLAB's fminsearch function, which minimises a function of several variables, using the simplex search algorithm of Lagarias et al. (1998) (from Fig. 6.11).

D.2 Data processing

D.2.1 Data collection

In the experiments in this Thesis, T-ray waveforms were measured using a spectrometer controlled by a computer via a GPIB bus. During measurements, the waveforms were saved as text files with two columns: delay stage position (from the stage controller), and T-ray amplitude from the Lock-In Amplifier (LIAs). This data file could be read into a mathematical analysis program as a waveform vector, y. Part of such a file is reproduced in Fig. D.2, showing the displacements of the delay stage, typically in the first column, and the T-ray amplitude (both positive and negative) in the second column. (Other data measurements that may have the data in the first column are marked as such in the experimental parameter file – see Sec. D.2.2.) The notation `Ex` in the file indicates a number multiplied by 10^x, and is recognised by mathematical packages such as MATLAB. The file name is standardised to be `Xx.txt`, where `X` is a mnemonic, `x` indicates the in-phase channel of the LIA (which is always used for T-ray measurements), and the file extension is for a plain text file.

```
-2.600000E+1   1.735700E-4
-2.599000E+1   1.907360E-4
-2.598000E+1   2.193460E-4
-2.597000E+1   2.117170E-4
-2.596000E+1   3.204360E-4
-2.595000E+1   4.005460E-5
-2.594000E+1  -6.294300E-5
-2.593000E+1   8.392380E-5
```

Figure D.2. Raw data file of a T-ray waveform. This Figure shows a portion of a text file of T-ray data, sampled as two columns: a distance measurement from the delay stage, and an amplitude measurement (in volts) from the LIA.

D.2.2 Experimental parameters

Experimental parameters, such as sample thickness, were recorded in another text file, along with the names of the waveform data files. This enabled a single MATLAB script to read in the experimental parameter file, load the waveforms from that experiment, and perform various analysis tasks. The analysis depended greatly on the type of

experiment being conducted; for example, dual-thickness measurements, or a DTDS experiment. An example parameter file is shown in Fig. D.3 and the meaning of each line is described in Table D.1. Those lines commencing with %%% are ignored, while each line starting with a two-letter code contains a parameter. Blank parameters are not used in this particular experiment.

```
 %%%%NO_SPACES_ON_A_LINE
ID=abc
Di=Data/2002_07_22/
Pa={'twoAC1','negative1DC1','positive1DC1'}
DC=[2]*ones(1,50)
dd=[20]*1e-6*ones(1,50)
CP=[651]*ones(1,50)
CF=ones(50,1)*[0.05,1.1]*1e12
Le={'twoAC1','negative1DC1','positive1DC1'}
Tr=
Dt=
Fi=[]
Ti={'Data/2002_07_18/GenericMultiPlot_SC08'}
FO=1
%%%%In_this_file,_ds(3)_is_the_ERROR_in_d*.
%%%%_And_[ds(1)-ds(2)]=X_mm,_but
%%%%_their_absolute_vals_are_unimportant.
ds=
```

Figure D.3. Experimental parameters file. This Figure shows an example of a text file, containing information on a particular experiment, and formatted so the parameters can be read by the generic MATLAB analysis script described in Sec. D.2.3. This example file contains a number of common features, including the formatting with no spaces, the comments prefixed with %%% and two-letter codes defining the parameters of the experiment (the meanings of these codes are listed in Table D.1). Other experimental parameter files would include different two-letter codes to define parameters that are not used in the file shown here – for example, an amplitude and mean experiment (see Sec. 8.3.1) would include the code Mo.

Table D.1. Codes in the file of experimental parameters. This Table lists the codes used in the experimental parameters file. These codes contain information summarising the experiment, and are used by the MATLAB processing algorithm to calculate information from the raw waveform measurements. For example, in dual-thickness measurements, two waveform measurements and a thickness measurement are required to determine the material parameters (see Sec. 4.2.1). Not all the codes listed here are required information for every experiment – if they are not required, they are either unassigned (for example, `ds=` in Fig. D.3), or omitted entirely from the parameter file. These codes are used to build up the `DataFile` parameter array used by the processing algorithm *Generic.m* in Sec. D.2.3.

Code	Parameter
`ID`	a single ASCII char used to uniquely identify each waveform (required)
`Di`	'Directory' where data files are
`Pa`	'Path(s)' is cells of strings of the data file names, without the suffix 'x.txt' (this uploads each waveform vector y)
`DC`	'Data Column' where the data, as opposed to the stage step, is stored in the data file
`dd`	**actual** path length delay step size (double the stage step), in m
`CP`	'Cutoff Points' is the number of points used from the data waveform, including any desired clipping – for example, to upload only the first pulse in a train
`CF`	'Cutoff Freq(s)' to cut the unwrapped and displayed spectra (in Hz) – these are chosen for the frequency range of highest signal-to-noise ratio
`Le`	'Legend' text(s) to label waveforms on any graphs – each data file has a legend label
`Tr`	which pairs of waveform vectors to use for any spectral ratios, referenced by code `ID` – for example, y_s/y_r, where y_s and y_r are waveforms loaded by code `Pa`
`Dt`	for any DTDS plots (Ch. 6), which waveform vectors to use (format as `Tr`)
`Mo`	for amplitude and mean plots (Sec. 8.3.1), which waveforms to use (format for `Tr`)
`Fi`	the figure number(s) to be exported to a graphics file (Encapsulated Post Script)
`Ti`	the directory and filename to be used when exporting graphics
`FO`	'Figures On', if set to '0' then waveform and spectral plots will not be displayed
`FP`	'Fabry-Pérot' is the number of FP reflections in the sample or substrate
`ds`	the sample thickness, if required by part of the algorithm (Sec. 4.2.1), in m
`n1`	in DTDS simulations (Ch. 6), the complex refractive index $\tilde{n} = n - j\kappa$ of the surrounding medium
`nx`	in DTDS simulations, $\tilde{n}$ of the solid substrate (e.g. glass or quartz)
`ns`	in DTDS simulations, $\tilde{n}$ of the thin film or target layer
`n2`	in DTDS simulations, $\tilde{n}$ of the sensor layer deposited on the substrate.

D.2.3 Loading and analysing raw data

The generic processing algorithm is a script that generates T-ray waveforms and spectra, and performs further analysis depending on the experiment. An outline of this code, written as pseudo code, is shown below. An explanation of numerical processing of T-ray data is found in Sec. 4.2.9.

- Preliminary
  - Clear variable values.
- Start
  - Define constants (for example, $c_0 = 2.99792 \times 10^8$ is the speed of light in a vacuum).
  - Select graphic properties.
- Load up parameters
  - Select the experimental parameters file to be used (`expfile`).
  - Load the parameters from a text file and convert to MATLAB variables.
- Run program
  - Loop for the number of waveforms that are loaded (each with a unique ID)
    * Load the waveform data from a text file, performing any time-domain clipping specified in the parameter file.
    * Define the time-domain T-ray amplitude data as y_a, or `Wave`.
    * Calculate the timing vector from the delay step size parameter, `Time`.
    * Normalise the T-ray amplitude to the laser power if required.
    * Perform a Fast Fourier Transform (FFT) in the un-windowed time-domain data to generate a T-ray spectrum, optionally padding the time-domain waveform with zeros to interpolate in the frequency domain (that is, smooth the spectral curves), creating a T-ray amplitude spectrum S_a, or `Abs`.
    * Use the complex FFT output to calculate the T-ray phase spectrum, but only for the range of high signal-to-noise ratio (SNR), defined by the parameter 'CF' in Table D.1; estimate phase values back to low frequency with a straight line.

    * Generate a band pass filter (BPF) from the frequency range in 'CF', and use only the selected frequency components to return to a smoothed version of the data waveform – this shows how noise can be removed by using only T-ray frequencies with a high SNR.
    * Calculate transmission ratios, $T = S_a / S_b$, for pairs of spectra. The calculation is different for DTDS (Ch. 6) or amplitude & mean (Ch. 8) experiments.

- Plots
    - Waveforms y.
    - Spectra S.
    - Smoothed waveforms.
    - Spectral ratios T.
    - Normalised, smoothed plots.
    - DTDS ratios.
- Export plots
    - Export to graphics files in various formats, including Encapsulated Post Script (EPS) format and Joint Pictures Expert Group (JPEG, JPG) format.
- Options
    - Optional paragraphs appended to the file for specific studies and experiments, for example, including error bars, or studying very long time scanned data.

The raw code for this generic analysis and plotting file is presented in Sec. D.3.3 and stored on the CD-ROM included with this Thesis. More specific data analysis programs, used for specific purposes, are contained in the other MATLAB files on the CD-ROM. These files are listed in Table D.4.

D.3 Code

The first section of MATLAB code below contains the four main files used in iterative parameter estimation, listed in Table D.2.

Table D.2. Matlab files on CD-ROM: iterative parameter estimation. These files carry out the iterative parameter estimation task described in Sec. D.1.

File name	Description
SpecDTDSMain.m	Main file for loading data and running iterations.
SpecDTDSTexperfn.m	To estimate the experimental transmission ratio.
SpecDTDSTmodelfn.m	To estimate the modelled transmission ratio.
SpecDTDSDelfn.m	To determine the error in the modelled ratio.

The LoadFile function is not listed as it is very similar to the LoadFile function for loading and studying raw data, which is already listed in this Section. All these code files are available on the attached CD-ROM in the folder, SPM_PhD_Thesis/MATLAB_Algorithms.

The two following MATLAB code files were the most commonly used for loading and studying raw experimental data, described in Sec. D.2.3. These files are listed in Table D.3.

Table D.3. Matlab files on CD-ROM: loading and analysing raw data. These are the MATLAB files used to load raw data from data files generated during T-ray experiments, as described in Sec. D.2.3. They are generic in that they were used for data from very different experiments.

File name	Description
SPM_GenericMultiPlot.m	Generic data analysis and plotting file, described in Sec. D.2.2.
SPM_GenericMultiPlotLoadFilefn.m	For parsing the text file of experimental parameters.
fnGenericDrawFigure.m	For generating plots and graphs: (sub-function of SPM_GenericMultiPlot.m)
fnLoadFile.m	A function to load text files into MATLAB arrays: (sub-function of SPM_GenericMultiPlotLoadFilefn.m)

The files were used to process the data presented in this Thesis are listed in Table D.4.

D.3.1 Iterative parameter estimation algorithm

Main file

```
%SPECDTDSMAIN is for running Sam's algorithm.
%
%  This script reads in all experimental data from a carefully-
```

Table D.4. Matlab files on CD-ROM: data analysis for this Thesis. This Table lists the MATLAB files used to analyse the data found in this Thesis. These files are stored on the CD-ROM attached to this Thesis, SPM_PhD_Thesis/MATLAB_Algorithms.

File name	Description
Thesis.m	Master file to set global variables and run MATLAB files, listed below, for each Chapter in this Thesis.
Thesis_ChPr.m	Analyse data found in Ch. 5.
Thesis_ChDt.m	Analyse data found in Ch. 6.
Thesis_ChBi.m	Analyse data found in Ch. 7.
Thesis_ChLi.m	Analyse data found in Ch. 8.
Thesis_ChIm.m	Analyse data found in Ch. 9.
Thesis_ChNf.m	Analyse data found in Ch. 10.

```
%  formatted text file, which must in turm hold all experimental
%  parameters and the filenames of the data files.  For a description
%  of the input text file requirements, see the SpecDTDSREADME.txt.
%
% Sam Mickan Aug 2001

% Setup and get to My Documents
fprintf('\n **** SpecDTDSMain **** \n'), cd ../../, clear all

% Load up parameters for this extraction
expfile='/matlab/DTDS_New/SpecDTDSParylene_KSL.txt';
[waveform,param,fr]=SpecDTDSLoadFilefn(expfile);

% Measured transmission coefficient at freqs fr()
[Texper,Spectra] = SpecDTDSTexperfn(fr,waveform,param);

% Loop thru diffnt freqs
for cK=1:length(fr), fprintf('[%d]  ',cK)

    % Scalar error min search (accurate to about 3 sf)
    WhichXtic='Rdex'; Xtic2=-1*imag(param.n2);
    TexpercK=struct('Abs',Texper.Abs(cK),'Arg',Texper.Arg(cK));
    [Rdex,FVAL,EXFLAG,OUTPUT] = fminbnd(@SpecDTDSDelfn,1,10,...
        optimset('TolX',0.000001),...
        WhichXtic,Xtic2,fr(cK),Spectra.F,TexpercK,param);
    WhichXtic='Kappa'; Xtic2=Rdex;
    [Kappa,FVAL,EXFLAG,OUTPUT] = fminbnd(@SpecDTDSDelfn,0,10,...
        optimset('TolX',0.000001),...
        WhichXtic,Xtic2,fr(cK),Spectra.F,TexpercK,param);

    OUTPUT.iterations;

    % Record characteristics
```

```
    RdexOut(cK)=Rdex; KappaOut(cK)=Kappa;
    AlphaOut(cK)=4*pi*fr(cK)*Kappa/param.c0;

end %for cK
```

Experimental transmission: T_{exper}

```
function f = SpecDTDSDelfn(Xtic1,WhichXtic,Xtic2,fr,F,Texper,param)

%SPECDTDSDELFN is the duvill96 error metric for the
%  amplitude error metric squared
%  plus the phase error metric squared.  The error metrics are calculated
%  from the log-amplitude and phase differences between the calculated
%  transmission coef for 'n' and 'k' and the measured transmission
%  coefficient at freq 'omega' .
%
%  ***Input1(1): refractive index of layer 2, n
%  ***Input1(2): kappa of layer 2, k
%  Input2: reference frequency
%  Input3: measured transmission coef at freq. omega
%  Input4: parameters for the T equation
%
%  Sam Mickan Aug 2001

% Calculated complex transmission coefficient
Tmodel = SpecDTDSTmodelfn(Xtic1,WhichXtic,Xtic2,fr,F,param);

% Error metrics
dRho = log(Tmodel.Abs)-log(Texper.Abs);
dPhi = Tmodel.Arg-Texper.Arg;
f = dRho.^2+dPhi.^2;
```

Modelled transmission: T_{model}

```
function [Tmodel] = SpecDTDSTmodelfn(Xtic1,WhichXtic,Xtic2,fr,F,param)

%SpecDTDSModelfn returns the calculated (complex) transmission coefficient of
%  a three-layer system at a given frequency, omega. The function has
%  internal constants describing the sample thickness in meters, and
%  the dielectric constants of layer1, layer3 and the air (or substrate,
%  depending on what the sample displaces).  Note that this models a
%  reference case where layer1 and layer3 are in contact with each other
%  (i.e. when sample is removed).
%
%  Input1: x = (refractive index of medium 2, kappa of medium 2)
%  Input2: reference frequency
%  Input3: parameters
%    - .c0
%    - .L2 length of sample
%    - .n1 complex refractive index of medium 1, pre sample
%    - .n3 complex refractive index of medium 3, post sample
%    - .ns compex refractive index of substrate (displaced by sample)
```

```
%    - .fp boolean - '1' to include the Fabry-Perot correction factor
%    (i.e.  more than one pulses in the sample waveform overlap)
%    - Version of experimental setup
%
%  Sam Mickan Aug 2001

% Constants
omega=2*pi*F;
c0=param.c0;
L2=param.L2;
n1=param.n1;
n3=param.n3;
%ns=param.ns;

% Xtic (required because this fuction works in a scalar bounded minimisation)
if strcmp(WhichXtic,'Rdex'), Rdex=Xtic1; Kappa=Xtic2; elseif ...
    strcmp(WhichXtic,'Kappa'), Kappa=Xtic1; Rdex=Xtic2; else printf('Error\n')
end, n2=Rdex-j*Kappa;

% Fabry-Perot effects
if 1==1 %strcmp(param.FP,'In')
    FP=1./(1-(n2-n1)./(n2+n1).*(n2-n3)./(n2+n3).*exp(-2.*j.*n2.*omega.*L2./c0)); else
    FP=1;  fprintf('NOT modelling for any FP reflections\n'), end %if param.FP==1

% (Complex) transmission coefficient, depending on experimental setup
Tran=1 - 2.*n2.*(n1+n3)./((n1+n2).*(n2+n3)).*exp(-j.*(n2-n3).*omega.*L2./c0).*FP;

% The unwrap step is very important in providing the correct phase value
TranAbs=abs(Tran); TranArg=unwrap(angle(Tran));

% Loop thru diffnt freqs
for cK=1:length(fr)

    % Find discrete frequency values on both sides of fr
    Fr=F(:,1);
    val1=max(find(Fr<=fr(cK))); val2=min(find(Fr>=fr(cK)));

    % Transmission at specific frequency from linear approximation of slope
    %  around point fr
    if val1==val2, TranAbsLoc(cK,:)=TranAbs(val1,:); else
    aAbs=(TranAbs(val2,:)-TranAbs(val1,:))./(Fr(val2)-Fr(val1));
    bAbs=TranAbs(val1,:)-aAbs.*F(val1,:);
    TranAbsLoc(cK,:)=aAbs.*fr(cK)+bAbs;
    aArg=(TranArg(val2,:)-TranArg(val1,:))./(Fr(val2)-Fr(val1));
    bArg=TranArg(val1,:)-aArg.*F(val1,:);
    TranArgLoc(cK,:)=aArg.*fr(cK)+bArg; end %if val1==val2

end %for cK=1:length(fr)

% Prepare the output
Tmodel=struct('Abs',TranAbsLoc',...
    'Arg',TranArgLoc');
```

Error measurement function

This function is the metric for quantifying the differences between the current model and experiment. This metric is used as a decision for continuing the algorithm, or accepting the current approximation.

```
function f = SpecDTDSDelfn(Xtic1,WhichXtic,Xtic2,fr,F,Texper,param)

%SPECDTDSDELFN is the duvill96 error metric for the
%  amplitude error metric squared
%  plus the phase error metric squared.  The error metrics are calculated
%  from the log-amplitude and phase differences between the calculated
%  transmission coef for 'n' and 'k' and the measured transmission
%  coefficient at freq 'omega' .
%
%  ***Input1(1): refractive index of layer 2, n
%  ***Input1(2): kappa of layer 2, k
%  Input2: reference frequency
%  Input3: measured transmission coef at freq. omega
%  Input4: parameters for the T equation
%
%  Sam Mickan Aug 2001

% Calculated complex transmission coefficient
Tmodel = SpecDTDSTmodelfn(Xtic1,WhichXtic,Xtic2,fr,F,param);

% Error metrics
dRho = log(Tmodel.Abs)-log(Texper.Abs);
dPhi = Tmodel.Arg-Texper.Arg;
f = dRho.^2+dPhi.^2;
```

D.3.2 Loading and analysing raw data

```
% GENERIC.M
% For plotting any one or multiple waveforms and their spectra.
%
% Plots are:
%   Waveforms:
%   Spectra:
%   Spectral Ratios:
%   DTDS Spectral Ratios:
%
% Sam Mickan Oct 2001, Jan 2002.



%%%%%%%%%%%%%%%%%%%%%%%%%%%%%%
% PRELIM
%%%%%%%%%%%%%%%%%%%%%%%%%%%%%%
if ~exist('DO_NOT_CLEAR')
```

```
    cd ../
    clear
    fprintf('\n\n --------------------')
end


%%%%%%%%%%%%%%%%%%%%%%%%%%%%%
% Start
%%%%%%%%%%%%%%%%%%%%%%%%%%%%%
fprintf('\n **** Generic Multi Waveform Plotting Script **** ')
c0=2.99792e8;
if ~exist('LineStyle')
    MyFontSize = 14;
    MyLineWidth = 2;
    LineStyle={'k.',':b','-r.','-c.','-m.','-g.','-y.','-k',};
    %LineStyle={'-k',':k','-ko','-k+','-k*','-kp','k.',':k.'};
    %LineStyle={'-b.','-b.','-b.','-b.','-b.','-b.','-r.'};
    %LineColor={[0 0 1],[0 .5 0],[1 0 0],[0 .75 .75],[.75 0 .75],};
    LineColor={[0 0 1],[0 0 1],[0 .5 0],[0 .5 0],[1 0 0],[1 0 0]};
    LineMarker={'none','none','none','.','.','.','o','o','o'};
    LineMarker={'none','.'};
end


%%%%%%%%%%%%%%%%%%%%%%%%%%%%%
% Load up parameters for this extraction
%%%%%%%%%%%%%%%%%%%%%%%%%%%%%
if ~exist('expfile')
    expfile='Data/2002_09_12_Biosensor/GenericMultiPlot.txt';
end

fprintf('\n ----  Expfile:%s',expfile)
[DataFile,Path,Legend,PlotTitle]=GenericMultiPlotLoadFilefn(expfile);
DataFilePath=Path{1};
DataFileLegendText=Legend{1};
PlotTitle=PlotTitle{1};
titl=expfile; titl=titl(1:(length(titl)-4)); titl(find(titl=='_'))='-';


%%%%%%%%%%%%%%%%%%%%%%%%%%%%%
% Run prog.
%%%%%%%%%%%%%%%%%%%%%%%%%%%%%
for cK=(1:length(DataFile.ID))
    % Load waveform
    LoadVar=load('-ascii',[DataFile.Di DataFilePath{cK} 'x.txt']);
    Wave{cK}=LoadVar([1:DataFile.CP(cK)],DataFile.DC(cK));
    Time{cK}=[0:length(Wave{cK})-1]*DataFile.dd(cK)/c0;
    % Normalize to the pump beam power, if recorded
    if ~isempty(DataFile.PP) & ~isempty(find(DataFile.ID(cK)...
        ==DataFile.PP))
        fprintf('\n Normalize to pump power ,cK)
        LoadVar=load('-ascii',[DataFile.Di DataFilePath{cK} 'p.txt']);
        PumpPower{cK}=LoadVar([1:DataFile.CP(cK)],DataFile.DC(cK));
```

```
        Wave{cK} = Wave{cK}./PumpPower{cK};
    end
    % Insert manual windowing fun. here (multiply in the time domain)
    % FFT w/ ZeroPad
    fprintf('\n -- Zero-padding time-domain waveform')
    PadMultiple = 2; fprintf(' (PadMultiple = %d).',PadMultiple)
    FT{cK}=fft(Wave{cK},PadMultiple*length(Wave{cK}));
    Abs{cK}=abs(FT{cK});
    FreqAbs{cK}=[0:(length(Abs{cK})-1)]'/(DataFile.dd(cK)/...
        cO*(length(Abs{cK})-1));
    NCutAbs{cK}=[max(find(FreqAbs{cK}<=DataFile.CF(cK,1))):...
            min(find(FreqAbs{cK}>=DataFile.CF(cK,2)))];
    Wrapped=angle(FT{cK});
    FreqArg{cK}=FreqAbs{cK}(NCutAbs{cK});
    % Minus inserted to give a +ve, incr. phase, as implied by the
    %  refractive index Eq. (10) in [arjava90] (2002.05.09).
    PreArg = -unwrap(Wrapped(NCutAbs{cK}));
    Slope = mean(diff(PreArg)./diff(FreqArg{cK}));
    Arg{cK} = PreArg + Slope*FreqArg{cK}(1) - PreArg(1);
    % Band pass filter
    BPF{cK} = zeros(length(FT{cK}),1); BPF{cK}(NCutAbs{cK}) = 1;
    % Smoothed waveform
    WaveSmooth{cK} = real(ifft(FT{cK}.*BPF{cK},length(Wave{cK})));
end, clear LoadVar Wrapped cK  PreArg Slope
% Transmission (and Normalisation) for traditional TDS data:
for cK=1:(size(DataFile.Tr,2)/2)
    TranAbs{cK}=Abs{find(DataFile.ID==DataFile.Tr(2*cK-1))}./...
        Abs{find(DataFile.ID==DataFile.Tr(2*cK))};
    TranArg{cK}=Arg{find(DataFile.ID==DataFile.Tr(2*cK-1))}-...
        Arg{find(DataFile.ID==DataFile.Tr(2*cK))};
    TransFileLegndText{cK} = ...
        [DataFileLegendText{find(DataFile.ID==DataFile.Tr(2*cK-1))} ...
         '/' DataFileLegendText{find(DataFile.ID==DataFile.Tr(2*cK))}];
    % Normalise 1st file to the AMPD of the 2nd
    WaveNormSmooth{cK} = ...
        real(ifft(FT{find(DataFile.ID==DataFile.Tr(2*cK-1))}./...
        Abs{find(DataFile.ID==DataFile.Tr(2*cK))}.*...
        BPF{find(DataFile.ID==DataFile.Tr(2*cK-1))},...
        length(Wave{find(DataFile.ID==DataFile.Tr(2*cK-1))})));
end, clear cK
% Transmission for DTDS data:
for cK=1:(size(DataFile.Dt,2)/2)
    Ref = Wave{find(DataFile.ID==DataFile.Dt(2*cK))};
    Sam =  Ref - Wave{find(DataFile.ID==DataFile.Dt(2*cK-1))};
    SamFT = fft(Sam);
    SamAbs = abs(SamFT);
    SamWrapped = angle(SamFT);
    SamArg = unwrap(SamWrapped(NCutAbs{find(DataFile.ID...
        ==DataFile.Dt(2*cK))}));
    DTDSAbs{cK}=SamAbs./...
        Abs{find(DataFile.ID==DataFile.Dt(2*cK))};
    DTDSArg{cK}=...
        - Arg{find(DataFile.ID==DataFile.Dt(2*cK))} + ...
```

```
        SamArg;
    DTDSFileLegndText{cK} = ...
        ['1 - ' DataFileLegendText{find(DataFile.ID...
            ==DataFile.Dt(2*cK-1))} ...
            ' / ' DataFileLegendText{find(DataFile.ID...
                ==DataFile.Dt(2*cK))}];
end, clear cK Ref Sam SamFT SamAbs SamWrapped SamArg
% Transmission for Monoscan DTDS data:
for cK=1:(size(DataFile.Mo,2)/2)
    Mean = Wave{find(DataFile.ID==DataFile.Mo(2*cK))};
    Diff =  Wave{find(DataFile.ID==DataFile.Mo(2*cK-1))};
    Ref{cK} = Mean + Diff;
    Sam{cK} = Mean - Diff;
    FT_r{cK}=fft(Ref{cK},PadMultiple*length(Ref{cK}));
    FT_s{cK}=fft(Sam{cK},PadMultiple*length(Sam{cK}));
    Abs_r{cK}=abs(FT_r{cK});
    Abs_s{cK}=abs(FT_s{cK});
    Wrapped_r = angle(FT_r{cK});
    Wrapped_s = angle(FT_s{cK});
    PreArg_r = -unwrap(Wrapped_r(NCutAbs{2*cK}));
    PreArg_s = -unwrap(Wrapped_s(NCutAbs{2*cK}));
    Slope_r = mean(diff(PreArg_r)./diff(FreqArg{2*cK}));
    Slope_s = mean(diff(PreArg_s)./diff(FreqArg{2*cK}));
    Arg_r{cK} = PreArg_r + Slope_r*FreqArg{2*cK}(1) - PreArg_r(1);
    Arg_s{cK} = PreArg_s + Slope_s*FreqArg{2*cK}(1) - PreArg_s(1);
    DTDSTranAbs{cK} = Abs_s{cK}./Abs_r{cK};
    DTDSTranArg{cK} = Arg_s{cK} - Arg_r{cK};
    DTDSTransFileLegndText{cK} = ...
        [DataFileLegendText{find(DataFile.ID...
            ==DataFile.Mo(2*cK-1))} ...
            ' / ' DataFileLegendText{find(DataFile.ID...
                ==DataFile.Mo(2*cK))}];
end, clear cK Mean Diff Wrapped_r Wrapped_s PreArg_r PreArg_s


%%%%%%%%%%%%%%%%%%%%%%%%%%%%
% Plots
%%%%%%%%%%%%%%%%%%%%%%%%%%%%
if eq(DataFile.FO,'O'),  end


%%%%%%%%%%%%%%%%%%%%%%%%%%%%
% Plot waveforms 'H1'
%%%%%%%%%%%%%%%%%%%%%%%%%%%%
if ne(DataFile.FO,'O')
    H1=figure(1); clf, set(H1,'PaperPosition',[0.1 0.2 6 4],...
        'Name','Waveforms'), A1=axes; set(A1,'NextPlot','add')
    for cK=1:length(DataFile.ID)
        P1{cK} = plot(Time{cK}.*1e12,Wave{cK});
        set(P1{cK},'Color',LineColor{mod(cK-1,14)+1},...
            'Marker',LineMarker{mod(cK-1,2)+1})
    end, clear cK
    set(gca,'FontSize',MyFontSize)
```

```
    L1=legend(DataFileLegendText);
    title(titl)
    ylabel('THz Electric Field (a.u.)')
    xlabel('Time (ps)')
    grid on
end

%%%%%%%%%%%%%%%%%%%%%%%%%%%%%%
% Plot spectra 'H2'
%%%%%%%%%%%%%%%%%%%%%%%%%%%%%%
if ne(DataFile.FO,'0')
    % Switch
    SubPlotOn=1;
    % Plots
    H2=figure(2); clf, set(H2,'PaperPosition',[0.1 0.2 6 4],...
        'Name','Spectra','NextPlot','add')
    if SubPlotOn
        A22=subplot(212); set(A22,'NextPlot','add')
        A21=subplot(211); set(A21,'NextPlot','add')
    else
        A21=axes; set(A21,'NextPlot','add')
    end
    for cK=1:length(DataFile.ID)
        if  SubPlotOn
            axes(A22)
            P2=plot(FreqArg{cK}*1e-12,Arg{cK});
            set(P2,'Color',LineColor{mod(cK-1,14)+1},...
                'Marker',LineMarker{mod(cK-1,2)+1})
        end
        axes(A21)
        P1=plot(FreqAbs{cK}(NCutAbs{cK})*1e-12,Abs{cK}(NCutAbs{cK}));
        %P1=semilogy(FreqAbs{cK}(NCutAbs{cK})*1e-12,...
        %   Abs{cK}(NCutAbs{cK}));
        set(P1,'Color',LineColor{mod(cK-1,14)+1},...
            'Marker',LineMarker{mod(cK-1,2)+1})
    end, clear cK P1 P2
    if SubPlotOn
        set(A22,'FontSize',MyFontSize)
        axes(A22)
        ylabel('Phase (rad)')
        grid on
    end
    set(A21,'FontSize',MyFontSize)
    axes(A21)
    L2=legend(DataFileLegendText);
    title(titl)
    ylabel('Magnitude (a.u.)')
    grid on
    xlabel('Frequency (THz)')
end


%%%%%%%%%%%%%%%%%%%%%%%%%%%%%%
```

```
% Plot smoothed plots 'H5'
%%%%%%%%%%%%%%%%%%%%%%%%%%%%%
if ne(DataFile.FO,'0')
    H5=figure(5); clf, set(H5,'PaperPosition',[0.1 0.2 6 4],...
        'Name','SmoothWaveforms')
    A5=axes; set(A5,'NextPlot','add')
    for cK=1:length(DataFile.ID)
        H5A{cK} = plot(Time{cK}.*1e12,WaveSmooth{cK});
        set(H5A{cK},'Color',LineColor{mod(cK-1,14)+1},...
            'Marker',LineMarker{mod(cK-1,2)+1},...
            'LIneWidth',MyLineWidth)
    end, clear cK
    set(gca,'FontSize',MyFontSize)
    L5=legend(DataFileLegendText);
    title(titl)
    ylabel('THz Electric Field (a.u.)')
    xlabel('Time (ps)')
    grid on
end


%%%%%%%%%%%%%%%%%%%%%%%%%%%%%
% Plot spectral ratios 'H3'
%%%%%%%%%%%%%%%%%%%%%%%%%%%%%
if ~isempty(DataFile.Tr) & ne(DataFile.FO,'0')
    % Switch
    SubPlotOn = 0;
    % Plots
    H3=figure(3); clf, set(H3,'PaperPosition',[0.1 0.2 6 4],...
        'Name','Trans')
    if SubPlotOn
        A31=subplot(211); set(A31,'NextPlot','add')
        A32=subplot(212); set(A32,'NextPlot','add')
    else
        A31=axes; set(A31,'NextPlot','add')
    end
    for cK=1:(size(DataFile.Tr,2)/2)
        axes(A31)
        P1 = plot(FreqAbs{cK}(NCutAbs{cK})*1e-12,...
            TranAbs{cK}(NCutAbs{cK})); hold on
        %P1 = semilogy(FreqAbs{cK}(NCutAbs{cK})*1e-12,...
        %   TranAbs{cK}(NCutAbs{cK})), hold on
        set(P1,'Color',LineColor{mod(cK-1,14)+1},'Marker',...
            LineMarker{mod(cK-1,2)+1});
        if SubPlotOn
            axes(A32)
            %P2 = plot(FreqArg{cK}(NCutArg{cK})*1e-12,...
            %   TranArg{cK}(NCutArg{cK})), hold on
            P2 = plot(FreqArg{cK}*1e-12,TranArg{cK}); hold on
            set(P2,'Color',LineColor{mod(cK-1,14)+1},...
                'Marker',LineMarker{mod(cK-1,2)+1})
        end
    end, clear cK
```

```
    axes(A31)
    set(gca,'FontSize',MyFontSize)
    L3=legend(TransFileLegndText);
    title(titl)
    ylabel('Magnitude (a.u.)')
    grid on
    if SubPlotOn
        axes(A32)
        set(gca,'FontSize',MyFontSize)
        ylabel('Phase (rad)')
        xlabel('Frequency (THz)')
        grid on
    end
end %if


%%%%%%%%%%%%%%%%%%%%%%%%%%%%%%%
% Plot normalised smoothed plots 'H6'
%  (these look terrible)
%%%%%%%%%%%%%%%%%%%%%%%%%%%%%%%
if 0 %~isempty(DataFile.Tr) & ne(DataFile.FO,'0')
    H6=figure(6); clf, set(H6,'PaperPosition',[0.1 0.2 6 4],...
        'Name','NormalisedSmoothWaveforms')
    A6=axes; set(A6,'NextPlot','add')
    for cK = 1:(size(DataFile.Tr,2)/2)
        H6A{cK} = plot(Time{cK}.*1e12,WaveNormSmooth{cK});
        set(H6A{cK},'Color',LineColor{mod(cK-1,14)+1},...
            'Marker',LineMarker{mod(cK-1,2)+1},...
            'LineWidth',MyLineWidth)
    end, clear cK
    set(gca,'FontSize',MyFontSize)
    L6=legend(DataFileLegendText);
    title(titl)
    ylabel('THz Electric Field (a.u.)')
    xlabel('Time (ps)')
    grid on
end


%%%%%%%%%%%%%%%%%%%%%%%%%%%%%%%
% Plot DTDS ratios 'H4'
%%%%%%%%%%%%%%%%%%%%%%%%%%%%%%%
if ~isempty(DataFile.Dt) & ne(DataFile.FO,'0')
    H4=figure(4); clf, set(H4,'PaperPosition',[0.1 0.2 6 4],...
        'Name','DTDS')
    for cK=1:(size(DataFile.Dt,2)/2)
        subplot(211)
        % PLOT DTDS TRANSMISSION: (1-S/R) ******
        plot(FreqAbs{cK}(NCutAbs{cK})*1e-12,...
            DTDSAbs{cK}(NCutAbs{cK}),LineStyle{cK}), hold on
        subplot(212)
        %plot(FreqArg{cK}(NCutArg{cK})*1e-12,...
        %   TranArg{cK}(NCutArg{cK}),LineStyle{cK}), hold on
```

```
        plot(FreqArg{cK}*1e-12,DTDSArg{cK},LineStyle{cK}), hold on
    end, clear cK
    subplot(211)
    set(gca,'FontSize',14)
    L4=legend(DTDSFileLegndText);
    set(L4,'FontSize',14)
    title(titl)
    ylabel('Magnitude (a.u.)','FontSize',14)
    grid on
    subplot(212)
    ylabel('Phase (rad)','FontSize',14)
    xlabel('Frequency (THz)','FontSize',14)
    set(gca,'FontSize',14)
    grid on
end %if


%%%%%%%%%%%%%%%%%%%%%%%%%%%%%
% Export selected plots
%%%%%%%%%%%%%%%%%%%%%%%%%%%%%
for cK=1:length(DataFile.Fi)
    figure(DataFile.Fi(cK))
    if DataFile.Fi(cK)==1
        title(''), grid off
        ylabel('mag'), xlabel('tim')
    elseif (DataFile.Fi(cK)==2) | (DataFile.Fi(cK)==3)
        subplot(211)
        title(''), grid off
        ylabel('mag')
        subplot(212)
        ylabel('pha'), xlabel('fre'), grid off
    end
    %print('-depsc2',PlotTitle{cK})
    %print('-dmeta',PlotTitle{cK})
    print('-dtiff',PlotTitle{cK})
    if DataFile.Fi(cK)==1
        title(titl), grid off
        ylabel('THz Electric Field (a.u.)'), xlabel('Time (ps)')
    elseif (DataFile.Fi(cK)==2) | (DataFile.Fi(cK)==3)
        subplot(211)
        title(titl), grid on
        ylabel('Magnitude (a.u.)')
        subplot(212)
        ylabel('Phase (rad)'), xlabel('Frequency (THz)'), grid on
    end
end


%%%%%%%%%%%%%%%%%%%%%%%%%%%%%
% Options
%%%%%%%%%%%%%%%%%%%%%%%%%%%%%
if 0 % Difference Waveform
    Sensitivity=1 %input('What is sensitivity (as fraction of 1.0)?')
```

```
    H5=figure(5); clf, set(H5,'PaperPosition',[0.1 0.2 6 4],...
        'Name','Difference')
    subplot(211)
    plot(Time{3},Wave{3}.*Sensitivity,'-',Time{3},...
        0.5*(Wave{1}-Wave{2}),':.r')
    %plot(Time{3},Wave{3}.*Sensitivity,'-',Time{3},...
    %    (Wave{1}-Wave{2}),':.r',...
    %    Time{4},2*Wave{4},Time{5},Wave{5})
    legend('DTDS','0.5*(Glass-Tape)') %,'Repeat-f1','Repeat-f2')
    title(titl)
    subplot(212)
    Sd=fft(Wave{3}.*Sensitivity); Sdiff=fft(0.5*(Wave{1}-Wave{2}));
    plot(FreqAbs{1}(NCutAbs{1}),abs(Sd(NCutAbs{1})),'-',...
        FreqAbs{1}(NCutAbs{1}),abs(Sdiff(NCutAbs{1})),':.r')
    %subplot(313)
    %Dif=fft(Wave{3}.*Sensitivity,NPhase);
    %RefMinSam=fft((Wave{1}-Wave{2}),NPhase);
    %plot(FreqArg{1}(NCutArg{1}),...
    %   unwrap(angle(Dif(NCutArg{1}))),'-',...
    %    FreqArg{1}(NCutArg{1}),...
    %   unwrap(angle(RefMinSam(NCutArg{1}))),':.r')
    %print('-deps2','MyPictures/Matlab_2002_01_25_DTDS.eps')
end
if 0 % Slow time scans of repeatability
    dt=1 %sec
    H2=figure(2); clf, set(H2,'PaperPosition',[0.1 0.2 6 4],...
        'Name','Spectra')
    for cK=1:length(DataFile.ID)
        subplot(211)
        N=length(Abs{cK});
        NewFreqAbs=[0:(N-1)]/(N-1)/dt;
        plot(NewFreqAbs(3:round(N/4)),Abs{cK}(3:round(N/4)),...
            LineStyle{cK}), hold on
        subplot(212)
        NewFreqArg=[0:(length(Arg{cK})-1)]/(length(Arg{cK})-1)/dt;
        plot(NewFreqArg,Arg{cK},LineStyle{cK}), hold on
    end, clear cK
    subplot(211)
    L2=legend(DataFileLegendText);
    set(L2,'FontSize',14)
    title(mfilename)
    ylabel('MAGNITUDE','FontSize',14)
    set(gca,'FontSize',14)
    subplot(212)
    ylabel('PHASEOORADO','FontSize',14)
    xlabel('FREQUENCYOOHZO','FontSize',14)
    set(gca,'FontSize',14)
end
if 0
    grid on
    ylim=[0,1]; xlim=[0 3.2];
    errorbar(Spectra.F(Ncut)*1e-12,TranAbs(Ncut),TAbsEbar)
end
```

```
if 0 % ERROR BARS
    Error = 0.001; % for today, +/-1mV
    H10=figure(10); clf, set(H10,'PaperPosition',[0.1 0.2 6 4],...
        'Name','Waveforms - Error')
    for cK=1:length(DataFile.ID)
        errorbar(Time{cK}*1e12,Wave{cK},...
            ones(size(Wave{cK})).*Error,LineStyle{cK}), hold on
    end, clear cK
    set(gca,'FontSize',14)
    L10=legend(DataFileLegendText);
    set(L10,'FontSize',14)
    title(titl)
    ylabel('THZOELECTRICOFIELDOOAUO','FontSize',14)
    xlabel('DELAYOTIMEOOPSO','FontSize',14)
    grid on
end
if 0 % Spectral magnitude on seperate plot, plots with no text
    % WAVEFORM
    H1=figure(1); clf, set(H1,'PaperPosition',[0.1 0.2 6 4],...
        'Name','Waveforms')
    for cK=1:length(DataFile.ID)
        plot(Time{cK}*1e12,Wave{cK},LineStyle{cK},'LineWidth',2)
        hold on
    end, clear cK
    set(gca,'FontSize',14,'LineWidth',2)
    ylim([-0.1 0.2]), xlim([0 30])
    print('-depsc2',PlotTitle{1})
    % SPECTRUM
    H6=figure(2); clf, set(H2,'PaperPosition',[0.1 0.2 6 4],...
        'Name','Spectra')
    for cK=1:length(DataFile.ID)
    %plot(FreqAbs{cK}(NCutAbs{cK})*1e-12,Abs{cK}(NCutAbs{cK}),...
    %   LineStyle{cK}), hold on
    semilogy(FreqAbs{cK}(NCutAbs{cK})*1e-12,Abs{cK}(NCutAbs{cK}),...
        LineStyle{cK},'LineWidth',2), hold on
    end, clear cK
    set(gca,'FontSize',14,'LineWidth',2)
    print('-depsc2',PlotTitle{2})
end
```

D.3.3 Matlab load file function for experimental parameters

```
function
    [DataFile,Path,Legend,PlotTitle]=GenericMultiPlotLoadFilefn(expfile)

% Load experimental data from a file
ExpName=textread(expfile,'%s');

% Fill the file data into a structure
Exp=struct('ExpFile',expfile);
for cK=1:length(ExpName)
    Name=ExpName{cK}(1:2); Cont=ExpName{cK}(4:end);
```

```
    switch Name
    case '%%', % DO NOTHING
    otherwise,  if ExpName{cK}(3)=='=', Exp=setfield(Exp,Name,Cont);
        else fprintf('Error in Exp file\n'), end
    end
end

% Construct
DataFile=struct('ID',Exp.ID,...
    'DC',str2num(Exp.DC),...
    'dd',str2num(Exp.dd),...
    'CP',str2num(Exp.CP),...
    'CF',str2num(Exp.CF),...
    'Tr',Exp.Tr,...
    'Fi',str2num(Exp.Fi));
if isfield(Exp,'Dt')
    DataFile.Dt=Exp.Dt; else
    DataFile.Dt=''; end
if isfield(Exp,'Mo')
    DataFile.Mo=Exp.Mo; else
    DataFile.Mo=''; end
if isfield(Exp,'Di')
    DataFile.Di=Exp.Di; else
    DataFile.Di=''; end
[Path{1:length(DataFile.ID)}]=deal(str2num(Exp.Pa));
[Legend{1:length(DataFile.ID)}]=deal(str2num(Exp.Le));
if ~isempty(DataFile.Fi)
    [PlotTitle{1:length(DataFile.Fi)}]=deal(str2num(Exp.Ti)); else
    PlotTitle={''}; end
if isfield(Exp,'FO')
    DataFile.FO=Exp.FO; else
    DataFile.FO='1'; end
if isfield(Exp,'ds')
    DataFile.ds=str2num(Exp.ds); else
    DataFile.ds=[]; end
if isfield(Exp,'PP')
    DataFile.PP=Exp.PP; else
    DataFile.PP=''; end
if isfield(Exp,'FP')
    DataFile.FP=str2num(Exp.FP); else
    DataFile.FP=NaN; end
if isfield(Exp,'Se')
    DataFile.Se=str2num(Exp.Se); else
    DataFile.Se=NaN; end
if isfield(Exp,'n1')
    DataFile.n1=str2num(Exp.n1); else
    DataFile.n1=NaN; end
if isfield(Exp,'nx')
    DataFile.nx=str2num(Exp.nx); else
    DataFile.nx=NaN; end
if isfield(Exp,'ns')
    DataFile.ns=str2num(Exp.ns); else
    DataFile.ns=NaN; end
```

```
if isfield(Exp,'n2')
    DataFile.n2=str2num(Exp.n2); else
    DataFile.n2=NaN; end
if isfield(Exp,'Ph')
    DataFile.Ph=str2num(Exp.Ph); else
    DataFile.Ph=NaN; end
if isfield(Exp,'Bi')
    DataFile.Bi=str2num(Exp.Bi); else
    DataFile.Bi=NaN; end
```

Bibliography

ABBOTT-D. (2000). Directions in terahertz technology, *Proc. 22nd IEEE GaAs IC Symposium*, Seattle, USA, pp. 263–266.

AGGARWAL-R. L., LAX-B., FETTERMAN-H. R., TANNENWALD-P. E. AND CLIFTON-B. J. (1974). CW generation of tunable narrow-band far-infrared radiation, *Journal of Applied Physics*, **45**(9), pp. 3972–3974.

ALEKSEEV-E. AND PAVLIDIS-D. (2000). GaN Gunn diodes for THz signal generation, *2000 IEEE MTT-S International Microwave Symposium Digest*, Vol. 3, IEEE, Boston, MA, pp. 1905–1908.

ALEKSEEV-E., PAVLIDIS-D., SUTTON-W. E., PINER-E. AND REDWING-J. (2001). GaN-based Gunn diodes: their frequency and power performance and experimental considerations, *IEICE Transactions on Electronics*, **E84-C**(10), pp. 1462–1469.

ANDOR-L., LÖRINCZ-A., SIEMION-J., SMITH-D. D. AND RICE-S. A. (1984). Shot-noise-limited detection scheme for two-beam laser spectroscopies, *Review of Scientific Instruments*, **55**(1), pp. 64–67.

ANDREWS-S. R., HUGGARD-P. G. AND ARMITAGE-A. (2001). Optimisation of photoconducting receivers for THz spectroscopy, *in* J. M. Chamberlain and M. A. Smith (eds.), *First International Conference on Biomedical Imaging & Sensing Applications of Terahertz Technology*, Leeds, UK.

ARJAVALINGAM-G., PASTOL-Y., EPP-L. W. AND MITTRA-R. (1992). Characterization of quasi-optical filters with picosecond transient radiation, *IEEE Transactions on Antennas and Propagation*, **40**(1), pp. 63–66.

ARJAVALINGAM-G., PASTOL-Y., HALBOUT-J.-M. AND KOPCSAY-G. V. (1990). Broad-band microwave measurements with transient radiation from optoelectronically pulsed antennas, *IEEE Transactions on Microwave Theory and Techniques*, **38**(5), pp. 615–621.

ARJAVALINGAM-G., PASTOL-Y., HALBOUT-J.-M. AND ROBERTSON-W. M. (1991). Optoelectronically-pulsed antennas: characterization and applications, *IEEE Antennas and Propagation Magazine*, **33**(1), pp. 7–11.

ARJAVALINGHAM-G., PASTOL-Y., HALBOUT-J.-M. AND KOPCSAY-G. V. (1989). Application of picosecond optoelectronics in broadband microwave material measurements, *Microwave Journal*, **32**(11), pp. 133–140.

ASAKI-M. L. T., REDONDO-A., ZAWODZINSKI-T. A. AND TAYLOR-A. J. (2002). Dielectric relaxation of electrolyte solutions using terahertz transmission spectroscopy, *Journal of Chemical Physics*, **116**(19), pp. 8469–8482.

ATKINS-P. W. (2002). *Atkins' Physical Chemistry*, 7th edn, Oxford University Press, Oxford.

AUSTON-D. H. (1983). Subpicosecond electro-optic shock waves, *Applied Physics Letters*, **43**(8), pp. 713–715.

AUSTON-D. H. (1988). Ultrafast optoelectronics, *in* W. Kaiser (ed.), *Ultrashort Laser Pulses and Applications*, Vol. 60 of *Topics in Applied Physics*, Springer-Verlag, Berlin, Germany, chapter 5, pp. 183–233.

AUSTON-D. H. AND CHEUNG-K. P. (1985). Coherent time-domain far-infrared spectroscopy, *Journal of the Optical Society of America B: Optical Physics*, **2**(4), pp. 606–612.

AUSTON-D. H. AND GLASS-A. M. (1972). Optical generation of intense picosecond electrical pulses, *Applied Physics Letters*, **20**(10), pp. 398–399.

AUSTON-D. H. AND NUSS-M. C. (1988). Electrooptic generation and detection of femtosecond electrical transients, *IEEE Journal of Quantum Electronics*, **24**(2), pp. 184–197.

AUSTON-D. H. AND SMITH-P. R. (1983). Generation and detection of millimeter waves by picosecond photoconductivity, *Applied Physics Letters*, **43**(7), pp. 631–633.

AUSTON-D. H., CHEUNG-K. P. AND SMITH-P. R. (1984a). Picosecond photoconducting Hertzian dipoles, *Applied Physics Letters*, **45**(3), pp. 284–286.

AUSTON-D. H., CHEUNG-K. P., VALDMANIS-J. A. AND KLEINMAN-D. A. (1984b). Cherenkov radiation from femtosecond optical pulses in electro-optic media, *Physical Review Letters*, **53**(16), pp. 1555–1558.

AUSTON-D. H., GLASS-A. M. AND BALLMAN-A. A. (1972). Optical rectification by impurities in polar crystals, *Physical Review Letters*, **28**(14), pp. 897–900.

AZZAM-R. M. A. AND BASHARA-N. M. (1977). *Ellipsometry and Polarized Light*, North Holland, Amsterdam, The Netherlands.

BAGASARYAN-D., MAKARYAN-A. AND POGOSYAN-P. (1983). Cherenkov radiation from a propagating nonlinear polarization wave, *JETP Letters*, **37**, p. 595.

BARRY-L. P., DUDLEY-J. M., THOMSEN-B. C. AND HARVEY-J. D. (1998). Measurement of 1.4 THz beat frequencies from a dual wavelength gain-switched laser diode using frequency-resolved optical gating, *in* T. Elsaesser, J. G. Fujumoto, D. A. Wiersma and W. Zinth (eds.), *Ultrafast Phenomena XI*, Vol. 63 of *Springer Series in Chemical Physics*, Springer-Verlag, Berlin, pp. 185–187.

BASS-M., FRANKEN-P. A., WARD-J. F. AND WEINREICH-G. (1962). Optical rectification, *Physical Review Letters*, **9**(11), pp. 446–448.

BEAN-B. L. AND PERKOWITZ-S. (1979). Far infrared submillimeter spectroscopy with an optically pumped laser, *Infrared and Millimeter Waves*, Vol. 2 of *Infrared and Millimeter Waves*, Academic Press, New York, chapter 4, pp. 273–298.

BEARD-M. C. AND SCHMUTTENMAER-C. A. (2001). Using the finite-difference time-domain pulse propagation method to simulate time-resolved THz experiments, *Journal of Chemical Physics*, **114**(7), pp. 2903–2909.

BEARD-M. C., TURNER-G. M. AND SCHMUTTENMAER-C. A. (2000a). Transient photoconductivity in GaAs as measured by time-resolved terahertz spectroscopy, *Physical Review B*, **62**(23), pp. 15764–15777.

BEARD-M. C., TURNER-G. M. AND SCHMUTTENMAER-C. A. (2001). Subpicosecond carrier dynamics in low-temperature grown GaAs as measured by time-resolved terahertz spectroscopy, *Journal of Applied Physics*, **90**(12), pp. 5915–5923.

BEARD-M. C., TURNER-G. M. AND SCHMUTTENMAER-C. A. (2002). THz spectroscopy, *Journal of Physical Chemistry B*, **106**, pp. 7146–7159.

BEARD-M. C., TURNER-G. M., VENABLES-D. S. AND SCHMUTTENMAER-C. A. (2000b). Two-dimensional time-resolved THz spectroscopy of solvent response to photoexcitation, *Trends in Optics and Photonics. Twelfth International Conference on Ultrafast Phenomena*, Vol. 43, OSA, Charleston S.C. USA, pp. 592–594.

BELABAS-N., LIKFORMAN-J.-P., CANIONI-L., BOUSQUET-B. AND JOFFRE-M. (2001). Coherent broadband pulse shaping in the mid infrared, *Optics Letters*, **26**(10), pp. 743–745.

BENICEWICZ-P. K. AND TAYLOR-A. J. (1993). Scaling of terahertz radiation from large-aperture biased InP photoconductors, *Optics Letters*, **18**(16), pp. 1332–1334.

BENICEWICZ-P. K., ROBERTS-J. P. AND TAYLOR-A. J. (1994). Scaling of terahertz radiation from large-aperture biased photoconductors, *Journal of the Optical Society of America B: Optical Physics*, **11**(12), pp. 2533–2546.

BIRCH-J. R., PING-K. F., HUSAIN-S. K., YARWOOD-J. AND CATLOW-B. (1985). Upper bounds for discrete features in the far-infrared spectrum of liquid acetonitrile, *Chemical Physics Letters*, **117**(3), pp. 197–202.

BJORKHOLM-J. E. (1966). Optical second-harmonic generation using a focused Gaussian laser beam, *Physical Review*, **142**(1), pp. 126–136.

BLAKE-G. A., LAUGHLIN-K. B., COHEN-R. C., BUSAROW-K. L., GWO-D.-H., SCHMUTTENMAER-C. A., STEYERT-D. W. AND SAYKALLY-R. J. (1991). Tunable far infrared laser spectrometers, *Review of Scientific Instruments*, **62**(7), pp. 1693–1700.

BLASER-S., ROCHAT-M., BECK-M., FAIST-J. AND OESTERLE-U. (2000). Far-infrared emission and Stark-cyclotron resonances in a quantum-cascade structure based on photon-assisted tunneling transition, *Physical Review B*, **61**(12), pp. 8369–8374.

BONVALET-A. AND JOFFRE-M. (1998). Terahertz femtosecond pulses, *in* C. Rullière (ed.), *Femtosecond Laser Pulses*, Springer-Verlag, Berlin, chapter 10, pp. 285–305.

BONVALET-A., JOFFRE-M., MARTIN-J.-L. AND MIGUS-A. (1995). Generation of ultrabroadband femtosecond pulses in the mid-infrared by optical rectification of 15 fs light pulses at 100 MHz repetition rate, *Applied Physics Letters*, **67**(20), pp. 2907–2909.

BONVALET-A., NAGLE-J., BERGER-V., MIGUS-A., MARTIN-J.-L. AND JOFFRE-M. (1996). Femtosecond infrared emission resulting from coherent charge oscillations in quantum wells, *Physical Review Letters*, **76**(23), pp. 4392–4395.

BORN-M. AND WOLF-E. (1997). *Principles of Optics*, 6th edn, Cambridge University Press.

BOSTAK-J. S., VAN DER WEIDE-D. W., BLOOM-D. M. AND AULD-B. A. (1994). All-electronic terahertz spectroscopy system with terahertz free-space pulses, *Journal of the Optical Society of America B: Optical Physics*, **11**(12), pp. 2561–2565.

BOWEN-J., NOE-L. J., SULLIVAN-B. P., MORRIS-K., MARTIN-V. AND DONNELLY-G. (2003). Gas-phase detection of trinitrotoluene utilizing a solid-phase antibody immobilized on a gold film by means of surface plasmon resonance spectroscopy, *Applied Spectroscopy*, **57**(8), pp. 906–914.

BRENER-I., DYKAAR-D., FROMMER-A., PFEIFFER-L. N., LOPATA-J., WYNN-J., WEST-K. AND NUSS-M. C. (1996). Terahertz emission from electric field singularities in biased semiconductors, *Optics Letters*, **21**(23), pp. 1924–1926.

BRENER-I., HUNSCHE-S., CAI-Y., NUSS-M. C., WYNN-J., LOPATA-J. AND PFEIFFER-L. (1998). Time resolved near field imaging and diffraction with sub-wavelength far-infrared dipole sources, *in* T. Elsaesser, J. G. Fujumoto, D. A. Wiersma and W. Zinth (eds.), *Ultrafast Phenomena XI*, Vol. 63 of *Springer Series in Chemical Physics*, Springer-Verlag, Berlin, pp. 171–176.

BRENER-I., PLANKEN-P. C. M., NUSS-M. C., LUO-M. S. C., CHUANG-S. L., PFEIFFER-L., LEAIRD-D. E. AND WEINER-A. M. (1994). Coherent control of terahertz emission and carrier populations in semiconductor heterostructures, *Journal of the Optical Society of America B: Optical Physics*, **11**(12), pp. 2457–2469.

BROMAGE-J., RADIC-S., AGRAWAL-G. P., STROUD-C. R., FAUCHET-P. M. AND SOBOLEWSKI-R. (1998). Spatiotemporal shaping of half-cycle terahertz pulses by diffraction through conductive apertures of finite thickness, *Journal of the Optical Society of America B: Optical Physics*, **15**(4), pp. 1399–1405.

BROMAGE-J., RADIC-S., AGRAWAL-G. P., STROUD, JR.-C. R., FAUCHET-P. M. AND SOBOLEWSKI-R. (1997). Spatiotemporal shaping of terahertz pulses, *Optics Letters*, **22**(9), pp. 627–629.

BROMAGE-J., WALMSLEY-I. A. AND STROUD JR.-C. R. (1999). Direct measurement of a photoconductive receiver's temporal response by dithered-edge sampling, *Optics Letters*, **24**(23), pp. 1771–1773.

BROMBERG-A. AND MATHIES-R. A. (2003). Homogeneous immunoassay for detection of TNT and its analogues on a microfabricated capillary electrophoresis chip, *Analytical Chemistry*, **75**(5), pp. 1188–1195.

BROWN-E. R., MCINTOSH-K. A., NICHOLS-K. B. AND DENNIS-C. L. (1995). Photomixing up to 3.8 THz in low-temperature-grown GaAs, *Applied Physics Letters*, **66**(3), pp. 285–287.

BROWN-E. R., MCINTOSH-K. A., SMITH-F. W., MANFRA-M. J. AND DENNIS-C. L. (1993a). Measurements of optical-heterodyne conversion in low-temperature-grown GaAs, *Applied Physics Letters*, **62**(11), pp. 1206–1208.

BROWN-E. R., MCINTOSH-K. A., SMITH-F. W., NICHOLS-K. B., MANFRA-M. J., DENNIS-C. L. AND MATTIA-J. P. (1994). Milliwatt output levels and superquadratic bias dependence in a low-temperature-grown GaAs photomixer, *Applied Physics Letters*, **64**(24), pp. 3311–3313.

BROWN-E. R., SMITH-F. W. AND MCINTOSH-K. A. (1993b). Coherent millimeter-wave generation by heterodyne conversion in low-temperature-grown GaAs photoconductors, *Journal of Applied Physics*, **73**(3), pp. 1480–1484.

BRUCHERSEIFER-M., HARING BOLÍVAR-P., KLINGENBERG-H. AND KURZ-H. (2001). Angle-dependent THz tomography – characterization of thin ceramic oxide films for fuel cell applications, *Applied Physics B: Lasers and Optics*, **72**(3), pp. 361–366.

BRUCHERSEIFER-M., NAGEL-M., HARING BOLÍVAR-P., KURZ-H., BOSSERHOFF-A. AND BÜTTNER-R. (2000a). Electrical generation of terahertz electromagnetic pulses by hot-electrons in quantum wells, *Applied Physics Letters*, **77**(24), pp. 4049–4051.

BRUCHERSEIFER-M., PELLEMANS-H. P. M., HARING BOLÍVAR-P. AND KURZ-H. (2000b). THz spectroscopy with ultrahigh sensitivity, *Conference on Lasers and Electro-Optics '00*, Vol. 39 of *TOPS*, Optical Society of America, San Francisco, CA, U.S.A., pp. 553–554.

BRÜNDERMANN-E., CHAMBERLIN-D. R. AND HALLER-E. E. (1998). Thermal effects in widely tunable germanium terahertz lasers, *Applied Physics Letters*, **73**(19), pp. 2757–2759.

BRÜNDERMANN-E., CHAMBERLIN-D. R. AND HALLER-E. E. (1999). Novel design concepts of widely tunable germanium terahertz lasers, *Infrared Physics and Technology*, **40**(3), pp. 141–151.

BRÜNDERMANN-E., CHAMBERLIN-D. R. AND HALLER-E. E. (2000). High duty cycle and continuous terahertz emission from germanium, *Applied Physics Letters*, **76**(21), pp. 2991–2993.

BUDIARTO-E., MARGOLIES-J., JEONG-S., SON-J. AND BOKOR-J. (1996). High-intensity terahertz pulses at 1-kHz repetition rate, *IEEE Journal of Quantum Electronics*, **32**(10), pp. 1839–1846.

CAI-Y., BRENER-I., LOPATA-J., WYNN-J., PFEIFFER-L. AND FEDERICI-J. (1997). Design and performance of singular electric field terahertz photoconducting antennas, *Applied Physics Letters*, **71**(15), pp. 2076–2078.

CAI-Y., BRENER-I., LOPATA-J., WYNN-J., PFEIFFER-L., STARK-J. B., WU-Q., ZHANG-X.-C. AND FEDERICI-J. (1998). Coherent terahertz radiation detection: Direct comparison between free-space electro-optic sampling and antenna detection, *Applied Physics Letters*, **73**(4), pp. 444–446.

CAO-H., HEINZ-T. F. AND NAHATA-A. (2002). Electro-optic detection of femtosecond electromagnetic pulses by use of poled polymers, *Optics Letters*, **27**(9), pp. 775–777.

CARR-G. L., MARTIN-M. C., MCKINNEY-W. R., DN G. R. NEIL-K. J. AND WILLIAMS-G. P. (2002). High-power terahertz radiation from relativistic electrons, *Nature*, **420**, pp. 153–156.

CARRIG-T. J., RODRIGUEZ-G., CLEMENT-T. S., TAYLOR-A. J. AND STEWART-K. R. (1995). Scaling of terahertz radiation via optical rectification in electro-optic crystals, *Applied Physics Letters*, **66**(2), pp. 121–123.

CHAN-C. A., MICKAN-S. P., WILLIAMS-G. AND ABBOTT-D. (2003). Terahertz calculations for the Australian synchrotron, *in* C. Jagadish (ed.), *Proceedings of SPIE - Photonics: Design, Technology, and Packaging*, Vol. 5277, SPIE, p. Submitted.

CHANSUNGSAN-C., TSANG-L. AND CHUANG-S. L. (1994). Coherent terahertz emission from coupled quantum wells with exciton effects, *Journal of the Optical Society of America B: Optical Physics*, **11**(12), pp. 2508–2518.

CHANTRY-G. W. (1971). *Submillimeter Spectroscopy*, Academic Press, New York.

CHATTOPADHYAY-T. AND BHATTACHARYA-M. (2002). Submillimeter wave generation through optical four-wave mixing using injection-locked semiconductor lasers, *Journal of Lightwave Technology*, **20**(3), pp. 502–506.

CHEN-P., BLAKE-G. A., GAIDIS-M. C., BROWN-E. R., MCINTOSH-K. A., CHOU-S. Y., NATHAN-M. I. AND WILLIAMSON-F. (1997). Spectroscopic applications and frequency locking of THz photomixing with distributed-Bragg-reflector diode lasers in low-temperature-grown GaAs, *Applied Physics Letters*, **71**(12), pp. 1601–1603.

CHEN-Q. AND ZHANG-X.-C. (1999). Polarization modulation in optoelectronic generation and detection of terahertz beams, *Applied Physics Letters*, **74**(23), pp. 3435–3437.

CHEN-Q. AND ZHANG-X.-C. (2000). Terahertz transceiver, *Optics and Photonics News*, **11**(12), pp. 46–47.

CHEN-Q. AND ZHANG-X.-C. (2001). Semiconductor dynamic aperture for near-field terahertz wave imaging, *IEEE Journal of Selected Topics in Quantum Electronics*, **7**(4), pp. 608–614.

CHEN-Q., JIANG-Z., TANI-M. AND ZHANG-X.-C. (2000a). Electro-optic terahertz transceiver, *Electronics Letters*, **36**(15), pp. 1298–1299.

CHEN-Q., JIANG-Z., XU-G. AND ZHANG-X.-C. (1998). Applications of terahertz time-domain measurement on paper currencies, *Conference on Lasers and Electro-Optics Pacific Rim '99*, Vol. 2, Optical Society of America, pp. 457–458.

CHEN-Q., JIANG-Z., XU-G. X. AND ZHANG-X.-C. (2000b). Near-field terahertz imaging with a dynamic aperture, *Optics Letters*, **25**(15), pp. 1122–1124.

CHEN-Q., TANI-M., JIANG-Z. AND ZHANG-X.-C. (2001). Electro-optic transceivers for terahertz-wave applications, *Journal of the Optical Society of America B: Optical Physics*, **18**(6), pp. 823–831.

CHEUNG-K. P. AND AUSTON-D. H. (1986). A novel technique for measuring far-infrared absorption and dispersion, *Infrared Physics*, **26**(1), pp. 23–27.

CHEVILLE-R. A. AND GRISCHKOWSKY-D. (1995a). Far-infrared terahertz time-domain spectroscopy of flames, *Optics Letters*, **20**(16), pp. 1646–1648.

CHEVILLE-R. A. AND GRISCHKOWSKY-D. (1995b). Time domain terahertz impulse ranging studies, *Applied Physics Letters*, **67**(14), pp. 1960–1962.

CHEVILLE-R. A. AND GRISCHKOWSKY-D. (1998). Observation of pure rotational absorption spectra in the μ_2 band of hot H_2O in flames, *Optics Letters*, **23**(7), pp. 531–533.

CHEVILLE-R. A., MCGOWAN-R. W. AND GRISCHKOWSKY-D. (1988). Time resolved measurements which isolate the mechanisms responsible for terahertz glory scattering from dielectric spheres, *Physical Review Letters*, **80**(2), pp. 269–272.

CHEVILLE-R. A., MCGOWAN-R. W. AND GRISCHKOWSKY-D. (1997). Late-time target response measured with terahertz impulse ranging, *IEEE Transactions on Antennas and Propagation*, **45**(10), pp. 1518–1524.

CHO-G. C., BAKKER-H. J. AND KURZ-H. (1998). THz pulse distortion in electro-optic detection by phonon-polariton propagation, *Conference on Lasers and Electro-Optics '98*, Optical Society of America, San Francisco, CA, U.S.A., pp. 60–61.

CHO-G. C., HAN-P. Y., ZHANG-X.-C. AND BAKKER-H. J. (2000). Optical phonon dynamics of GaAs studied with time-resolved terahertz spectroscopy, *Optics Letters*, **25**(21), pp. 1609–1611.

CHUANG-S. L., SCHMITT-RINK-S., GREENE-B. I., SAETA-P. N. AND LEVI-A. F. J. (1992). Optical rectification at semiconductor surfaces, *Physical Review Letters*, **68**(1), pp. 102–105.

CHUNG-Y.-S., CHEON-C., SON-J.-H. AND HAHN-S.-Y. (2000). FDTD analysis of propagation characteristics of terahertz electromagnetic pulses, *IEEE Transactions on Magnetics*, **36**(4), pp. 951–955.

CHWALEK-J. M. AND DYKAAR-D. R. (1990). A mixer based electro-optic sampling system for submillivolt signal detection, *Review of Scientific Instruments*, **61**(4), pp. 1273–1276.

CITRIN-D. S. (1997). Generation of 10-THz transients from a subpicosecond optical pulse and a 1-THz field in quantum wells, *Applied Physics Letters*, **70**(10), pp. 1189–1191.

CITRIN-D. S. (1999). Terahertz sideband generation and coherent control in semiconductor microcavities, *Physical Review Letters*, **82**(15), pp. 3172–3175.

CLEMETT-C. J., FOREST-E. AND SMYTH-C. P. (1964). Microwave absorption and molecular structure in liquids. LVI. dielectric behavior of water and heavy water in dioxane, *Journal of Chemical Physics*, **40**(8), pp. 2123–2128.

COLE-B. E., WILLIAMS-J. B., KING-B. T., SHERWIN-M. S. AND STANLEY-C. R. (2001). Coherent manipulation of semiconductor quantum bits with terahertz radiation, *Nature*, **410**(6824), pp. 60–63.

COLEMAN-P. D. (2000). Reminiscences on selected millennium highlights in the quest for tunable terahertz-submillimeter wave oscillators, *IEEE Journal of Selected Topics in Quantum Electronics*, **6**(6), pp. 1000–1007.

COLLINS-C. E., MILES-R. E., DIGBY-J. W., PARKHURST-G. M., POLLARD-R. D., CHAMBERLAIN-J. M., STEENSON-D. P., CRONIN-N. J., DAVIES-S. R. AND BOWEN-J. W. (1999). New micro-machined millimeter-wave and terahertz snap-together rectangular waveguide technology, *IEEE Microwave and Guided Wave Letters*, **9**(2), pp. 63–65.

COLLINS-C. E., MILES-R. E., POLLARD-R. D., STEENSON-D. P., DIGBY-J. W., PARKHURST-G. M., CHAMBERLAIN-J. M., CRONIN-N. J., DAVIES-S. R. AND BOWEN-J. W. (1998). Millimeter-wave measurements of the complex dielectric constant of an advanced thick film UV photoresist, *Journal of Electronic Materials*, **27**(6), pp. L40–L42.

COOK-D. J. AND HOCHSTRASSER-R. M. (2000). Intense terahertz pulses by four-wave rectif ication in air, *Optics Letters*, **25**(16), pp. 1210–1212.

CORCHIA-A., MCLAUGHLIN-R., JOHNSTON-M. B., WHITTAKER-D. M., ARNONE-D. D., LINFIELD-E. H., DAVIES-A. G. AND PEPPER-M. (2001). Effects of magnetic field and optical fluence on terahertz emission in gallium arsenide, *Physical Review B*, **64**(20), pp. 205204/1–5.

CÔTÉ-D., FRASER-J. M., DECAMP-M., BUCKSBAUM-P. H. AND VAN DRIEL-H. M. (1999). THz emission from coherently controlled photocurrents in GaAs, *Applied Physics Letters*, **75**(25), pp. 3959–3961.

CRITCHFIELD-F. E., GIBSON, JR.-J. A. AND HALL-J. L. (1953). Dielectric constant for the dioxane-water system from 20 to 35°, *Journal of the American Chemical Society*, **75**, pp. 1991–1992.

CROSSLEY-J. AND SMITH-C. P. (1969). Dielectric behavior of dilute solutions of water in *p*-dioxane, *Journal of Chemical Physics*, **50**(5), pp. 2259–2260.

CUATRECASAS-P. AND WILCHEK-M. (1968). Single-step purification of avidin from egg white by affinity chromatography on biocytin-Sepharose columns, *Biochemical and Biophysical Research Communications*, **33**(2), pp. 235–239.

CUMMING-D. R. S. AND BLAIKIE-R. J. (1999). A variable polarisation compensator using artificial dielectrics, *Optics Communications*, **163**(4-6), pp. 164–168.

DARMO-J., MÜLLER-T., STRASSER-G. AND UNTERRAINER-K. (2002). Voltage-controlled intracavity THz generator for self-starting Ti:Sapphire lasers, *Conference on Lasers and Electro-Optics '02*, IEEE LEOS & OSA, Long Beach C.A, USA. PostDeadline Digest.

DECKERT-V., ZEISEL-D., ZENOBI-R. AND VO-DINH-T. (1998). Near-field surface-enhanced raman imaging of dye-labeled DNA with 100-nm resolution, *Analytical Chemistry*, **70**(13), pp. 2646–2650.

DEFONZO-A. P. AND LUTZ-C. R. (1987). Optoelectronic transmission and reception of ultrashort electrical pulses, *Applied Physics Letters*, **51**(4), pp. 212–214.

DEFONZO-A. P., JARWALA-M. AND LUTZ-C. R. (1987). Transient respose of planar integrated optoelectronic antennas, *Applied Physics Letters*, **50**(17), pp. 1155–1157.

DEKORSKY-T., AUER-H., WASCHKE-C., BAKKER-H. J., ROSKOS-H. G., KURZ-H., WAGNER-V. AND GROSSE-P. (1995). Emission of submillimeter electromagnetic waves by coherent phonons, *Physical Review Letters*, **74**(5), pp. 738–741.

DEKORSKY-T., LEISCHING-P., KÖHLER-K. AND KURZ-H. (1994). Electro-optic detection of Bloch oscillations, *Physical Review B*, **50**(11), pp. 8106–8109.

DERENIAK-E. L. AND BOREMAN-G. D. (1996). *Infrared Detectors and Systems*, Wiley series in pure and applied optics, John Wiley & Sons, Inc., New York, NY, U.S.A.

DHILLON-S. S., DAVIES-A. G., HARRELL-R., LINFIELD-E. H., RITCHIE-D. A., PEPPER-M. AND ARNONE-D. D. (2001). Terahertz (THz) electro-luminescence from AlGaAs-GaAs quantum cascade heterostructures, *Conference on Lasers and Electro-Optics '01*, Optical Society of America, Baltimore, MD, U.S.A., pp. 483–484.

DIGBY-J., MCINTOSH-C. E., PARKHURST-G. M., TOWLSON-B. M., HADJILOUCAS-S., BOWEN-J. W., CHAMBERLAIN-J. M., POLLARD-R. D., MILES-R. E., STEENSON-D. P., CRONIN-N. J. AND DAVIES-S. R. (2000). Fabrication and characterization of micromachined rectangular waveguide components for use at millimeter-wave and terahertz frequencies, *IEEE Transactions on Microwave Theory and Techniques*, **48**(8), pp. 1293–1302.

DIMITRAKOPOULOS-C. D., PURUSHOTHAMAN-S., KYMISSIS-J., CALLEGARI-A. AND SHAW-J. (1999). Low-voltage organic transistors on plastic comprising high-dielectric constant gate insulators, *Science*, **283**(5403), pp. 822–824.

DORNEY-T. D., BARANIUK-R. G. AND MITTLEMAN-D. M. (2001a). Material parameter estimation with terahertz time-domain spectroscopy, *Journal of the Optical Society of America A: (Optics & Vision)*, **18**(7), pp. 1562–1571.

DORNEY-T. D., JOHNSON-J. L., RUDD-J. V., BARANIUK-R. G., SYMES-W. W. AND MITTLEMAN-D. M. (2001b). Terahertz reflection imaging using Kirchhoff migration, *Optics Letters*, **26**(19), pp. 1513–1515.

DRESSEL-M. (2001). Microspectroscopy in the millimeter and far-infrared spectral range using coherent CW radiation, *in* J. M. Chamberlain and M. A. Smith (eds.), *First International Conference on Biomedical Imaging & Sensing Applications of Terahertz Technology*, Leeds, UK.

DUFFY-S. M., VERGHESE-S., MCINTOSH-A., JACKSON-A., GOSSARD-A. C. AND MATSUURA-S. (2001). Accurate modeling of dual dipole and slot elements used with photomixers for coherent terahertz output power, *IEEE Transactions on Microwave Theory and Techniques*, **49**(6), pp. 1032–1038.

DUPONT-E., BYLOOS-M., GAO-M., BUCHANAN-M., SONG-C.-Y., WASILEWSKI-Z. R. AND LIU-H. C. (2002). Pixelless thermal imaging with integrated quantum-well infrared photodetector and light-emitting diode, *IEEE Photonics Technology Letters*, **14**(2), pp. 182–184.

DUVILLARET-L., GARET-F. AND COUTAZ-J.-L. (1996). A reliable method for extraction of material parameters in terahertz time-domain spectroscopy, *IEEE Journal of Selected Topics in Quantum Electronics*, **2**(3), pp. 739–746.

DUVILLARET-L., GARET-F. AND COUTAZ-J.-L. (1999). Highly precise determination of optical constants and sample thickness in terahertz time-domain spectroscopy, *Applied Optics*, **38**(2), pp. 409–415.

DUVILLARET-L., GARET-F. AND COUTAZ-J. L. (2000). Influence of noise on the characterization of materials by terahertz time-domain spectroscopy, *Journal of the Optical Society of America B: Optical Physics*, **17**(3), pp. 452–461.

DUVILLARET-L., GARET-F., ROUX-J.-F. AND COUTAZ-J.-L. (2001). Analytical modeling and optimization of terahertz time-domain spectroscopy experiments, using photoswitches as antennas, *IEEE Journal of Selected Topics in Quantum Electronics*, **7**(4), pp. 615–623.

DYAKONOV-M. I. AND SHUR-M. S. (1997). Plasma wave electronics: Terahertz detectors and sources using two dimensional electronic fluid in high electronic mobility transistors, *1997 Advanced Workshop on Frontiers in Electronics, WOFE*, IEEE, Piscataway, NJ, USA, pp. 105–108.

DYKAAR-D. R., GREENE-B. I., FEDERICI-J. F., LEVI-A. F., PFEIFFER-L. N. AND KOPF-R. F. (1991). Log-periodic antennas for pulsed terahertz radiation, *Applied Physics Letters*, **59**(3), pp. 262–264.

EICKEMEYER-F., KAINDL-R. A., WOERNER-M., ELSAESSER-T. AND WEINER-A. M. (2000). Controlled shaping of ultrafast electric field transients in the mid-infrared spectral range, *Optics Letters*, **25**(19), pp. 1472–1474.

EISELE-H., RYDBERG-A. AND HADDAD-G. I. (2000). Recent advances in the performance of InP Gunn devices and GaAs TUNNETT diodes for the 100–300-GHz frequency range and above, *IEEE Transactions on Microwave Theory and Techniques*, **48**(4), pp. 626–631.

FAIST-J., CAPASSO-F., SIVCO-D. L., SIRTORI-C., HUTCHINSON-A. L. AND CHO-A. Y. (1994). Quantum cascade laser, *Science*, **264**, pp. 553–556.

FATTINGER-C. AND GRISCHKOWSKY-D. (1988). Point source terahertz optics, *Applied Physics Letters*, **53**(16), pp. 1480–1482.

FATTINGER-C. AND GRISCHKOWSKY-D. (1989). Terahertz beams, *Applied Physics Letters*, **54**(6), pp. 490–492.

FENG-S. AND WINFUL-H. G. (1998). Fields of single-cycle terahertz pulses generated by loop antenna, *Conference on Lasers and Electro-Optics '98*, Optical Society of America, San Francisco, CA, U.S.A., pp. 59–60.

FERGUSON-B. AND ABBOTT-D. (2000). Signal processing for T-ray bio-sensor systems, *Proceedings of SPIE - Symposium on Smart Materials and MEMS*, Vol. 4236, Melbourne, Australia, pp. 157–169.

FERGUSON-B. AND ABBOTT-D. (2001a). De-noising techniques for terahertz responses of biological samples, *Microelectronics Journal* (Elsevier), **32**(12), pp. 943–953.

FERGUSON-B. AND ABBOTT-D. (2001b). Wavelet de-noising of optical terahertz pulse imaging data, *Fluctuation and Noise Letters*, **1**(2), pp. 65–69.

FERGUSON-B., WANG-S. AND ZHANG-X.-C. (2001a). T-ray computed tomography, *2001 IEEE/LEOS Annual Meeting Conference Proceedings*, Vol. 1, IEEE, San Diego, CA, U.S.A., pp. PD1.7–PD1.8.

FERGUSON-B., WANG-S., GRAY-D., ABBOTT-D. AND ZHANG-X.-C. (2001b). Terahertz imaging of biological tissue using a chirped probe pulse, *in* N. W. Bergmann (ed.), *Proceedings of SPIE - Electronics and Structures for MEMS II*, Vol. 4591, Adelaide, Australia, pp. 172–184.

FERGUSON-B., WANG-S., GRAY-D., ABBOTT-D. AND ZHANG-X.-C. (2002a). T-ray computed tomography, *Optics Letters*, **27**(15), pp. 1312–1314.

FERGUSON-B., WANG-S., GRAY-D., ABBOTT-D. AND ZHANG-X.-C. (2002b). T-ray diffraction tomography, *OSA TOPS, The Thirteenth International Conference on Ultrafast Phenomena*, Vol. 72, Washington, DC, U.S.A., pp. 450–451.

FERGUSON-B., WANG-S., GRAY-D., ABBOTT-D. AND ZHANG-X.-C. (2002c). Three dimensional imaging using T-ray computed tomography, *Conference on Lasers and Electro-Optics '02*, IEEE LEOS & OSA, Long Beach, CA, U.S.A., p. 132.

FILIN-A., STOWE-M. AND KERSTING-R. (2001). Time-domain differentiation of terahertz pulses, *Optics Letters*, **26**(24), pp. 2008–2010.

FILLARD-J. P. (1996). *Near Field Optics and Nanoscopy*, World Scientific, Singapore.

FITZGERALD-A. J., BERRY-E., MILES-R. E., ZINOV'EV-N. N., SMITH-M. A. AND CHAMBERLAIN-J. M. (2002a). Evaluation of image quality in terahertz pulsed imaging using test objects, *Physics in Medicine and Biology*, **47**(21), pp. 3865–3873.

FITZGERALD-A. J., BERRY-E., ZINOV'EV-N. N., WALKER-G. C., SMITH-M. A. AND CHAMBERLAIN-J. M. (2002b). An introduction to medical imaging with coherent terahertz frequency radiation, *Physics in Medicine and Biology*, **47**(7), pp. 67–84.

FRANKEL-M. Y., WHITAKER-J. F. AND MOUROU-G. A. (1992). Optoelectronic transient characterization of ultrafast devices, *IEEE Journal of Quantum Electronics*, **28**(10), pp. 2313–2324.

FRANKEN-P. A., HILL-A. E., PETERS-C. W. AND WEINREICH-G. (1961). Generation of optical harmonics, *Physical Review Letters*, **7**(4), pp. 118–119.

FROLOV-S. V. AND VARDENY-Z. V. (1998). Double-modulation electro-optic sampling for pump-and-probe ultrafast correlation measurements, *Review of Scientific Instruments*, **69**(3), pp. 1257–1260.

GADIR-M. A., HARRISON-P. AND SOREF-R. A. (2002). Responsivity of quantum well infrared photodetectors at terahertz detection wavelengths, *Applied Physics Letters*, **91**(9), pp. 5820–5825.

GAGLIARDI-G., VICIANI-S., INGUSCIO-M., DE NATALE-P., GMACHL-C., CAPASSO-F., SIVCO-D. L., BAILLARGEON-J. N., HUTCHINSON-A. L. AND CHO-A. Y. (2002). Generation of tunable far-infrared radiation with a quantum cascade laser, *Optics Letters*, **27**(7), pp. 521–523.

GALLERANO-G. P., DORIA-A., GIOVENALE-E. AND RENIERI-A. (1999). Compact free electron lasers: from Cerenkov to waveguide free electron lasers, *Infrared Physics and Technology*, **40**(3), pp. 161–174.

GALLOT-G. AND GRISCHKOWSKY-D. (1999). THz time-domain spectroscopy (THz-TDS) with electro-optic sampling, *Conference on Lasers and Electro-Optics '99*, Optical Society of America, Baltimore, MD, U.S.A., pp. 492–493.

GALLOT-G., JAMISON-S. P., MCGOWAN-R. W. AND GRISCHKOWSKY-D. (2000). Terahertz waveguides, *Journal of the Optical Society of America B: Optical Physics*, **17**(5), pp. 851–863.

GALLOT-G., JIANGQUAN-Z., MCGOWAN-R. W., JEON-T.-I. AND GRISCHKOWSKY-D. (1999). Measurements of the THz absorption and dispersion of ZnTe and their relevance to the electro-optic detection of THz radiation, *Applied Physics Letters*, **74**(23), pp. 3450–3452.

GARRETT-G. A., ALBRECHT-T. F., WHITAKER-J. F. AND MERLIN-R. (1996). Coherent THz phonons driven by light pulses and the Sb problem: What is the mechanism?, *Physical Review Letters*, **77**(17), pp. 3661–3664.

GAUTHIER-LAFAYE-O., JULIEN-F. H., CABARET-S., LOURTIOZ-J.-M., STRASSER-G., GORNIK-E., HELM-M. AND BOIS-P. (1999). High-power GaAs/AlGaAs quantum fountain unipolar laser emitting at 14.5 μm with 2.5% tunability, *Applied Physics Letters*, **74**(11), pp. 1537–1539.

GELTNER-I., HASHIMSHONY-D. AND ZIGLER-A. (2002). Detection and electrical characterization of hidden layers using time-domain analysis of terahertz reflections, *Journal of Applied Physics*, **92**(1), pp. 203–206.

GENZEL-L., SANTO-L. AND SHEN-S. C. (1998). Far-infrared Fourier transform spectroscopy, *in* G. Grüner (ed.), *Millimeter and submillimeter wave spectroscopy of solids*, Vol. 74 of *Topics in Applied Physics*, Springer-Verlag, Berlin, Germany, chapter 5, pp. 169–220.

GHORANNEVISS-M., KASHANI-M. A. M., HOGABRI-A., KOHIYAN-A. AND ANVARI-A. (1998). Design and modification of the FIR HCN laser, *in* M. N. Afsar (ed.), *Proceedings of SPIE - Millimeter and Submillimeter Waves IV*, Vol. 3465, San Diego, CA, U.S.A., pp. 85–87.

GITIN-M. M., WISE-F. W., ARJAVALINGAM-G., PASTOL-Y. AND COMPTON-R. C. (1994). Broad-band characterization of millimeter-wave log-periodic antennas by photoconductive sampling, *IEEE Transactions on Antennas and Propagation*, **42**(3), pp. 335–339.

GLOBUS-T. R., WOOLARD-D. L., SAMUELS-A. C., GELMONT-B. L., HESLER-J., CROWE-T. W. AND BYKHOVSKAIA-M. (2002). Submillimeter-wave fourier transform spectroscopy of biological macromolecules, *Applied Physics Letters*, **91**(9), pp. 6105–6113.

GORNIK-E. AND KERSTING-R. (2001). Coherent THz emission in semiconductors, *in* K. T. Tsen (ed.), *Ultrafast Physical Processes in Semiconductors*, Vol. 67 of *Semiconductors and Semimetals*, Academic Press, New York, chapter 8, pp. 389–440.

GORNIK-E., UNTERRAINER-K. AND KREMSER-C. (1991). Tunable far-infrared solid-state lasers based on hot holes in germanium, *Optical and Quantum Electronics*, **23**(2), pp. 267–286.

GOYETTE-T. M., GUO-W., LUCIA-F. C. D., SWARTZ-J. C., EVERITT-H. O., GUENTHER-B. D. AND BROWN-E. R. (1995). Femtosecond demodulation source for high-resolution submillimeter spectroscopy, *Applied Physics Letters*, **67**(25), pp. 3810–3812.

GREBENEV-V., KNOESEL-E. AND BARTELS-L. (2001). Destructive interference of freely propagating terahertz pulses and its potential for high-resolution spectroscopy and optical computing, *Applied Physics Letters*, **79**(2), pp. 145–147.

GREENE-B. I., FEDERICI-J., DYKAAR-D. R., LEVI-A. F. J. AND PFEIFFER-L. N. (1991). Picosecond pump and probe spectroscopy utilizing freely propagating terahertz radiation, *Optics Letters*, **16**(1), pp. 48–49.

GREEN-M. L., GUSEV-E. P., DEGRAEVE-R. AND GARFUNKEL-E. L. (2001). Ultrathin (<4 nm) SiO_2 and Si-O-N gate dielectric layers for silicon microelectronics: Understanding the processing, structure, and physical and electrical limits, *Journal of Applied Physics*, **90**(5), pp. 2057–2121.

GREEN-N. M. (1975). Avidin, *Advances in Protein Chemistry*, **29**, pp. 85–133.

GRIFFITHS-P. R. (1975). *Chemical infrared Fourier transform spectroscopy*, Vol. 43 of *Chemical Analysis*, John Wiley & Sons, Inc., New York.

GRISCHKOWSKY-D. AND KEIDING-S. R. (1990). THz time-domain spectroscopy of high t_c substrates, *Applied Physics Letters*, **57**(10), pp. 1055–1057.

GRISCHKOWSKY-D., KEIDING-S., VAN EXTER-M. AND FATTINGER-C. (1990). Far-infrared time-domain spectroscopy with terahertz beams of dielectrics and semiconductors, *Journal of the Optical Society of America B: Optical Physics*, **7**(10), pp. 2006–2015.

GRISCHKOWSKY-D. R. (2000). Optoelectronic characterization of transmission lines and waveguides by terahertz time-domain spectroscopy, *IEEE Journal of Selected Topics in Quantum Electronics*, **6**(6), pp. 1122–1135.

GROENEVELD-R. H. M. AND GRISCHKOWSKY-D. (1994). Picosecond time-resolved far-infrared experiments on carriers and excitons in GaAs-AlGaAs multiple quantum wells, *Journal of the Optical Society of America B: Optical Physics*, **11**(12), pp. 2502–2506.

GROUP-T. F. (2002). Chemical sensors to 2006: Liquid gas & biosensors, *Industry Study 1542*, 767 Beta Drive, Cleveland, OH 44143, USA. http://www.freedoniagroup.com/.

GU-P., TANI-M., HYOHO-M., SAKAI-K. AND HIDAKA-T. (1998). Generation of cw-terahertz radiation using a two-longitudinal-mode laser diode, *Japanese Journal of Applied Physics*, **37**(8B), pp. L976–L978.

GU-P., TANI-M., KONO-S., SAKAI-K. AND ZHANG-X.-C. (2002). Study of terahertz radiation from InAs and InSb, *Applied Physics Letters*, **91**(9), pp. 5533–5537.

GÜRTLER-A., WINNEWISSER-C., HELM-H. AND JEPSEN-P. U. (2000). Terahertz pulse propagation in the near field and the far field, *Journal of the Optical Society of America A: (Optics & Vision)*, **17**(1), pp. 74–83.

HADJILOUCAS-S., GALVAO-R. K. H., BOWEN-J. W., MARTINI-R., BRUCHERSEIFER-M., PELLEMANS-H. P., BOLÍVAR-P. H., KURZ-H., DIGBY-J., PARKHURST-G. M. AND CHAMBERLAIN-J. M. (2003). Measurement of propagation constant in waveguides with wideband coherent terahertz spectroscopy, *Journal of the Optical Society of America B: Optical Physics*, **20**(2), pp. 391–401.

HADJILOUCAS-S., HARATZAS-L. S. AND BOWEN-J. W. (1999). Measurements of leaf water content using terahertz radiation, *IEEE Transactions on Microwave Theory and Techniques*, **47**(2), pp. 142–149.

HAN-P. Y. AND ZHANG-X.-C. (1998a). Coherent, broadband midinfrared terahertz beam sensors, *Applied Physics Letters*, **73**(21), pp. 3049–3051.

HAN-P. Y. AND ZHANG-X.-C. (1998b). Mid-infrared THz pulse, *Nonlinear Optics '98: Materials, Fundamentals and Applications Topical Meeting*, IEEE, Princeville, HI, U.S.A., pp. 401–402.

HAN-P. Y. AND ZHANG-X.-C. (2001). Free-space coherent broadband terahertz time-domain spectroscopy, *Measurement Science and Technology*, **12**(11), pp. 1747–1756.

HAN-P. Y., CHO-G. C. AND ZHANG-X.-C. (1999). Mid-infrared THz beam sensors: Exploration and application for phonon spectroscopy, *Proceedings of SPIE - Ultrafast Phenomena in Semiconductors III*, Vol. 3624, pp. 224–33.

HAN-P. Y., CHO-G. C. AND ZHANG-X.-C. (2000a). Time-domain transillumination of biological tissues with terahertz pulses, *Optics Letters*, **25**(4), pp. 242–244.

HAN-P. Y., HUANG-X. G. AND ZHANG-X.-C. (2000b). Direct characterization of terahertz radiation from the dynamics of the semiconductor surface field, *Applied Physics Letters*, **77**(18), pp. 2864–2866.

HAN-P. Y., TANI-M., PAN-F. AND ZHANG-X.-C. (2000c). Characterization and application of DAST at THz frequency, *Conference on Lasers and Electro-Optics '00*, Vol. 39 of *TOPS*, Optical Society of America, San Francisco, CA, U.S.A., pp. 556–557.

HAN-P. Y., TANI-M., PAN-F. AND ZHANG-X.-C. (2000d). Use of the organic crystal DAST for terahertz beam applications, *Optics Letters*, **75**(9), pp. 675–677.

HAN-P. Y., TANI-M., USAMI-M., KONO-S., KERSTING-R. AND ZHANG-X.-C. (2001). A direct comparison between terahertz time-domain spectroscopy and far-infrared Fourier transform spectroscopy, *Journal of Applied Physics*, **89**(4), pp. 2357–2359.

HARDE-H. AND GRISCHLOWSKY-D. (1991). Coherent transients exicted by subpicosecond pulses of terahertz radiation, *Journal of the Optical Society of America B: Optical Physics*, **8**(8), p. 1642.

HARDE-H., CHEVILLE-R. A. AND GRISCHKOWSKY-D. (1997a). Collision-induced tunneling in methyl halides, *Journal of the Optical Society of America B: Optical Physics*, **14**(12), pp. 3282–3293.

HARDE-H., CHEVILLE-R. A. AND GRISCHKOWSKY-D. (1997b). Terahertz studies of collision-broadened rotational lines, *Journal of Physical Chemistry A*, **101**(20), pp. 3646–3660.

HARDE-H., KATZENELLENBOGEN-N. AND GRISCHKOWSKY-D. R. (1994). Terahertz coherent transients from methyl chloride vapor, *Journal of the Optical Society of America B: Optical Physics*, **11**(6), p. 1018.

HARDE-H., ZHAO-J., WOLFF-M., CHEVILLE-R. A. AND GRISCHKOWSKY-D. (2001). THz time-domain spectroscopy on ammonia, *Journal of Physical Chemistry A*, **105**(25), pp. 6038–6047.

HAREL-R., BRENER-I., PFEIFFER-L. N., WEST-K., VANDENBERG-J. M. AND CHU-S. N. G. (1999). Coherent terahertz emission from cavity polaritons in semiconductor microcavities, *Conference on Lasers and Electro-Optics '99*, Optical Society of America, Baltimore, MD, U.S.A., pp. 461–462.

HARRISON-P. AND KELSALL-R. W. (1997). Population inversion in optically pumped asymmetric quantum well terahertz lasers, *Journal of Applied Physics*, **81**(11), pp. 7135–7140.

HASHIMSHONY-D., GELTNER-I., COHEN-G., AVITZOUR-Y., ZIGLER-A. AND SMITH-C. (2001a). Characterization of the electrical properties and thickness of thin epitaxial semiconductor layers by THz reflection spectroscopy, *Journal of Applied Physics*, **90**(11), pp. 5778–5781.

HASHIMSHONY-D., ZIGLER-A. AND PAPADOPOULOS-K. (2001b). Conversion of electrostatic to electromagnetic waves by superluminous ionization fronts, *Physical Review Letters*, **86**(13), pp. 2806–2809.

HAUS-H. A. (2000). Mode-locking of lasers, *IEEE Journal of Selected Topics in Quantum Electronics*, **6**(6), pp. 1173–1185.

HAUS-H. A. AND MECOZZI-A. (1993). Noise of mode-locked lasers, *IEEE Journal of Quantum Electronics*, **29**(3), pp. 983–996.

HAYWARD-S. AND GO-N. (1995). Collective variable description of native protein dynamics, *Annual Review of Physical Chemistry*, **46**, pp. 223–50.

HEMENWAY-B. R., HEINRICN-H. K., GOLL-J. H., XU-Z. AND BLOOM-D. M. (1987). Optical detection of charge modulation in silicon integrated circuits using a multimode laser-diode probe, *IEEE Electron Device Letters*, **8**(8), pp. 344–346.

HERRMANN-M., TANI-M., SAKAI-K. AND FUKASAWA-R. (2002). Terahertz imaging of silicon wafers, *Journal of Applied Physics*, **91**(3), pp. 1247–1250.

HIDAKA-T., MATSUURA-S., TANI-M. AND SAKAI-K. (1997). CW terahertz wave generation by photomixing using a two-longitudinal-mode laser diode, *Electronics Letters*, **33**(24), pp. 2039–2040.

HILLENBRAND-R., TAUBNER-T. AND KEILMANN-F. (2002). Phonon-enhanced light-matter interaction at the nanometre scale, *Nature*, **418**, pp. 159–162.

HOUGHTON-J. T. AND SMITH-S. D. (1966). *Infra-red Physics*, Oxford University Press, Oxford.

HU-B. B. AND NUSS-M. C. (1995). Imaging with terahertz waves, *Optics Letters*, **20**(16), pp. 1716–1718.

HU-B. B., ZHANG-X.-C. AND AUSTON-D. H. (1990). Free-space radiation from electro-optic crystals, *Applied Physics Letters*, **56**(6), pp. 506–508.

HUBER-R., BRODSCHELM-A., TAUSER-F. AND LEITENSTORFER-A. (2000). Generation and field-resolved detection of femtosecond electromagnetic pulses tunable up to 41 THz, *Applied Physics Letters*, **76**, pp. 3191–3193.

HUBER-R., TAUSER-F., BRODSCHELM-A., BICHLER-M., ABSTREITER-G. AND LEITENSTORFER-A. (2001). How many-particle interactions develop after ultrafast excitation of an electron-hole plasma, *Nature*, **414**(6861), pp. 286–289.

HUGGARD-P. G., SHAW-C. J., CLUFF-J. A. AND ANDREWS-S. R. (1998). Polarization-dependent efficiency of photoconducting THz transmitters and receivers, *Applied Physics Letters*, **72**(17), pp. 2069–2071.

HUNSCHE-S., FENG-S., WINFUL-H. G., LEITENSTORFER-A., NUSS-M. C. AND IPPEN-E. P. (1999). Spatiotemporal focusing of single-cycle light pulses, *Journal of the Optical Society of America A: (Optics & Vision)*, **16**(8), pp. 2025–2028.

HUNSCHE-S., KOCH-M., BRENER-I. AND NUSS-M. C. (1998a). THz near-field imaging, *Optics Communications*, **150**(1–6), pp. 22–26.

HUNSCHE-S., MITTLEMAN-D. M., KOCH-M. AND NUSS-M. C. (1998b). New dimensions in T-ray imaging, *IEICE Transactions on Electronics*, **E81-C**(2), pp. 269–276.

HYODO-M., TANI-M., MATSUURA-S., ONODERA-N. AND SAKAI-K. (1996). Generation of millimetre-wave radiation using a dual-longitudinal-mode microchip laser, *Electronics Letters*, **32**(17), pp. 1589–1591.

IMAI-K. AND KAWASE-K. (2001). A frequency-agile terahertz-wave parametric oscillator, *Optics Express*, **8**(13), pp. 699–704.

IZUMIDA-S., ONO-S., LIU-Z., OHTAKE-H. AND SARUKURA-N. (1999). Spectrum control of THz radiation from InAs in a magnetic field by duration and frequency chirp of the excitation pulses, *Applied Physics Letters*, **75**(4), pp. 451–453.

JACKSON-J. D. (1998). *Classical Electrodynamics*, 3rd edn, John Wiley & Sons, Inc.

JACKSON-M., TELLES-E. M., ALLEN-M. D. AND EVENSON-K. M. (2001). Short-wavelength far-infrared laser cavity yielding new laser emissions in CD_3OH, *Applied Physics B: Lasers and Optics*, **72**(7), pp. 815–818.

JACOBSEN-R. H., MITTLEMAN-D. M. AND NUSS-M. C. (1996). Chemical recognition of gases and gas mixtures with terahertz waves, *Optics Letters*, **21**(24), pp. 2011–2013.

JAMISON-S. P., MCGOWAN-R. W. AND GRISCHKOWSKY-D. (2000). Single-mode waveguide propagation and reshaping of sub-ps terahertz pulses in sapphire fibers, *Applied Physics Letters*, **76**(15), pp. 1987–1989.

JEON-T.-I. AND GRISCHKOWSKY-D. (1998). Characterization of optically dense, doped semiconductors by reflection THz time domain spectroscopy, *Applied Physics Letters*, **72**(23), pp. 3032–3034.

JEON-T. I., GRISCHKOWSKY-D., MUKHERJEE-A. K. AND MENON-R. (2000). Electrical characterization of conducting polypyrrole by THz time-domain spectroscopy, *Applied Physics Letters*, **77**(16), pp. 2452–2454.

JEON-T.-I., GRISCHKOWSKY-D., MUKHERJEE-A. K. AND MENON-R. (2001). Electrical and optical characterization of conducting poly-3-methylthiophene film by THz time-domain spectroscopy, *Applied Physics Letters*, **79**(25), pp. 4142–4144.

JEON-T.-I., KIM-K.-J., KANG-C., OH-S.-J., SON-J.-H., AN-K. H., BAE-D. J. AND LEE-Y. H. (2002). Terahertz conductivity of anisotropic single walled carbon nanotube films, *Applied Physics Letters*, **80**(18), pp. 3403–3405.

JEPSEN-P. U. AND KEIDING-S. R. (1995). Radiation patterns from lens-coupled terahertz antennas, *Optics Letters*, **20**(8), pp. 807–809.

JEPSEN-P. U., SCHAIRER-W., LIBON-I. H., LEMMER-U., HECKER-N. E., BIRKHOLZ-M., LIPS-K. AND SCHALL-M. (2001). Ultrafast carrier trapping in microcrystalline silicon observed in optical pump-terahertz probe measurements, *Applied Physics Letters*, **79**(9), pp. 1291–1293.

JIANG-Z. AND ZHANG-X.-C. (1998a). Electro-optic measurement of THz field pulses with a chirped optical beam, *Applied Physics Letters*, **72**(16), pp. 1945–1947.

JIANG-Z. AND ZHANG-X.-C. (1998b). Free-space electro-optic sampling of THz radiation with chirped optical beam, *in* T. Elsaesser, J. G. Fujumoto, D. A. Wiersma and W. Zinth (eds.), *Ultrafast Phenomena XI*, Vol. 63 of *Springer Series in Chemical Physics*, Springer-Verlag, Berlin, pp. 197–201.

JIANG-Z. AND ZHANG-X.-C. (1998c). Single-shot spatiotemporal terahertz field imaging, *Optics Letters*, **23**(14), pp. 1114–1116.

JIANG-Z. AND ZHANG-X.-C. (1999a). 2D measurement and spatio-temporal coupling of few-cycle THz pulses, *Optics Express*, **5**(11), pp. 243–248.

JIANG-Z. AND ZHANG-X.-C. (1999b). Terahertz imaging via electrooptic effect, *IEEE Transactions on Microwave Theory and Techniques*, **47**(12), pp. 2644–2650.

JIANG-Z. AND ZHANG-X.-C. (2000). Measurement of spatio-temporal terahertz field distribution by using chirped pulse technology, *IEEE Journal of Quantum Electronics*, **36**(10), pp. 1214–1222.

JIANG-Z., LI-M. AND ZHANG-X.-C. (2000). Dielectric constant measurement of thin films by differential time-domain spectroscopy, *Applied Physics Letters*, **76**(22), pp. 3221–3223.

JIANG-Z., SUN-G. F. AND ZHANG-X.-C. (1999). Terahertz pulse measurement with an optical streak camera, *Optics Letters*, **24**(17), pp. 1245–1247.

JOFFRE-M., BONVALET-A., MIGUS-A. AND MARTIN-J.-L. (1996). Femtosecond diffracting fourier-transform infrared interferometer, *Optics Letters*, **21**(13), pp. 964–966.

JOHNSON-B. C., PUTHOFF-H. E., SOOHOO-J. AND SUSSMAN-S. S. (1971). Power and linewidth of tunable stimulated far-infrared emission in $LiNbO_3$, *Applied Physics Letters*, **18**(5), pp. 181–183.

JOHNSON-J. L., DORNEY-T. D. AND MITTLEMAN-D. M. (2001a). Enhanced depth resolution in terahertz imaging using phase-shift interferometry, *Applied Physics Letters*, **78**(6), pp. 835–837.

JOHNSON-J. L., DORNEY-T. D. AND MITTLEMAN-D. M. (2001b). Interferometric imaging with terahertz pulses, *IEEE Journal of Selected Topics in Quantum Electronics*, **7**(4), pp. 592–599.

JOHNSTON-M. B., WHITTAKER-D. M., CORCHIA-A., DAVIES-A. G. AND LINFIELD-E. H. (2002). Theory of magnetic-field enhancement of surface-field terahertz emission, *Journal of Applied Physics*, **91**(4), pp. 2104–2106.

JONES-R. R. (1996). Creating and probing electronic wave packets using half-cycle pulses, *Physical Review Letters*, **76**(21), pp. 3927–3930.

JONES-R. R., YOU-D. AND BUCKSBAUM-R. H. (1993). Ionization of Rydberg wave atoms by subpicosecond half-cycle electromagetic pulses, *Physical Review Letters*, **70**(9), pp. 1236–1239.

KAGAN-C. R., MITZI-D. B. AND DIMITRAKOPOULOS-C. D. (1999). Organic-inorganic hybrid materials as semiconducting channels in thin-film field-effect transistors, *Science*, **286**(5441), pp. 945–947.

KALSSON-R. AND STAHLBERG-R. (1995). *Analytical Chemistry*, **228**, p. 274.

KAMBA-S., PETZELT-J., BUIXADERAS-E., HAUBRICH-D., VANK-P., KUEL-P., JAWAHAR-I. N., SEBASTIAN-M. T. AND MOHANAN-P. (2001). High frequency dielectric properties of $A_5B_4O_{15}$ microwave ceramics, *Journal of Applied Physics*, **88**(7), pp. 3900–3906.

KAPLAN-A. E. (1998). Diffraction-induced transformation of near-cycle and subcycle pulses, *Journal of the Optical Society of America B: Optical Physics*, **15**(3), pp. 951–956.

KATTERLOHER-R., JAKOB-G., BAUSER-E., ZEHENDER-S., HALLER-E. E., BEEMAN-J., HENNING-T. AND PILBRATT-G. (1995). Recent results from the development of a far infra-red n-type GaAs detector array for FIRST, *in* M. S. Scholl and B. F. Andresen (eds.), *Proceedings of SPIE - Infrared Spaceborne Remote Sensing III*, Vol. 2553, Washington, DC, U.S.A., pp. 524–535.

KATZENELLENBOGEN-N. AND GRISCHKOWSKY-D. (1991). Efficient generation of 380 fs pulses of THz radiation by ultrafast laser pulse excitation of a biased metal-semiconductor interface, *Applied Physics Letters*, **58**(3), pp. 222–224.

KATZENELLENBOGEN-N. AND GRISCHKOWSKY-D. (1992). Electrical characterization to 4 THz of *N*- and *P*-type GaAs using THz time-domain spectroscopy, *Applied Physics Letters*, **61**(7), pp. 840–842.

KAWASE-K. AND HIROMOTO-N. (1998). Terahertz wave antireflection coating on Ge and GaAs with fused quartz., *Applied Optics*, **37**(10), pp. 1862–1866.

KAWASE-K., HATANAKA-T., TAKAHASHI-H., NAKAMURA-K., TANIUCHI-T. AND ITO-H. (2000). Tunable terahertz-wave generation from DAST crystal by dual signal-wave parametric oscillation of periodically poled lithium niobate, *Optics Letters*, **25**(23), pp. 1714–1716.

KAWASE-K., MIZUNO-M., SOHMA-S., TAKAHASHI-H., TANIUCHI-T., URATA-Y., WADA-S., TASHIRO-H. AND ITO-H. (1999). Difference-frequency terahertz-wave generation from 4-dimethylamino-*n*-methyl-4-stilbazoliu-tosylate by use of an electrically tuned Ti:sapphire laser, *Optics Letters*, **24**(15), pp. 1065–1067.

KAWASE-K., SATO-M., NAKAMURA-K., TANIUCHI-T. AND ITO-H. (1997). Uni-directional radiation of widely tunable THz-wave using a prism coupler under noncollinear phase matching condition, *Applied Physics Letters*, **71**(6), pp. 753–755.

KAWASE-K., SHIKATA-J., IMAI-K. AND ITO-H. (2001). Transform-limited, narrow-linewidth, terahertz-wave parametric generator, *Applied Physics Letters*, **78**(19), pp. 2819–2821.

KAZEMI-H., WOOTTON-S. T. J., CRONIN-N. J., DAVIES-S. R., MILES-R. E., POLLARD-R. D., CHAMBERLAIN-J. M. AND BOWEN-D. P. S. W. (1999). Active micromachined integrated terahertz circuits, *International Journal of Infrared and Millimeter Waves*, **20**(5), pp. 967–974.

KEILMANN-F. (1995). FIR microscopy, *Infrared Physics and Technology*, **36**(1), pp. 217–224.

KERSTING-R., HEYMAN-J. N., STRASSER-G. AND UNTERRAINER-K. (1998a). Coherent plasmons in *n*-doped GaAs, *Physical Review B*, **58**(8), pp. 4553–4559.

KERSTING-R., HEYMAN-J. N., STRASSER-G. AND UNTERRAINER-K. (1998b). Driving intersubband transitions with THz pulses, *in* T. Elsaesser, J. G. Fujumoto, D. A. Wiersma and W. Zinth (eds.), *Ultrafast Phenomena XI*, Vol. 63 of *Springer Series in Chemical Physics*, Springer-Verlag, Berlin, pp. 208–210.

KERSTING-R., UNTERRAINER-K., STRASSER-G., KAUFFMANN-H. F. AND GORNIK-E. (1997). Few-cycle THz emission from cold plasma oscillations, *Physical Review Letters*, **79**(16), pp. 3038–3041.

KHAZAN-M., MEISSNER-R. AND WILKE-I. (2001). Convertible transmission-reflection time-domain terahertz spectrometer, *Review of Scientific Instruments*, **72**(8), pp. 3427–3430.

KHURGIN-J. B. (1994). Optical rectification and terahertz emission in semiconductors excited above the band gap, *Journal of the Optical Society of America B: Optical Physics*, **11**(12), pp. 2492–2501.

KINDT-J. T. AND SCHMUTTENMAER-C. A. (1996). Far-infrared dielectric properties of polar liquids probed by femtosecond terahertz pulse spectroscopy, *Journal of Physical Chemistry*, **100**(24), pp. 10373–10379.

KINGON-A. I., MARIA-J.-P. AND STREIFFER-S. K. (2000). Alternative dielectrics to silicon dioxide for memory and logic devices, *Nature*, **406**(6779), pp. 1032–1038.

KINSLER-P., HARRISON-P. AND KELSALL-R. W. (1999). Intersubband terahertz lasers using four-level asymmetric quantum wells, *Journal of Applied Physics*, **85**(1), pp. 23–28.

KIWA-T. AND TONOUCHI-M. (2001). High frequency properties of YBCO thin films diagnosed by time-domain terahertz spectroscopy, *Physica C*, **362**, pp. 314–318.

KLAPPENBERGER-F., IGNATOV-A. A., WINNERL-S., SCHOMBURG-E., WEGSCHEIDER-W., RENK-K. F. AND BICHLER-M. (2001). Broadband semiconductor superlattice detector for THz radiation, *Applied Physics Letters*, **78**(12), pp. 1673–1675.

KLAUS-T., TAKANO-S. AND WINNEWISSER-G. (1997). Laboratory measurement of the $N = 1 \leftarrow 0$ rotational transition of NH at 1 THz, *Astronomy and Astrophysics*, **322**, pp. L1–L4.

KLEINE-OSTMANN-T., KNOBLOCH-P., KOCH-M., HOFFMANN-S., BREEDE-M., HOFMANN-M., HEIN-G., PIERZ-K., SPERLING-M. AND DONHUIJSEN-K. (2001). Continuous-wave THz imaging, *Electronics Letters*, **37**(24), pp. 1461–1463.

KLEINMAN-D. A. AND AUSTON-D. H. (1984). Theory of electro-optic shock radiation in nonlinear media, *IEEE Journal of Quantum Electronics*, **20**(8), pp. 964–970.

KNOLL-B. AND KEILMANN-F. (1999). Near-field probing of vibrational absorption for chemical microscopy, *Nature*, **399**, pp. 134–137.

KOCH-M., LIBON-I. H., HEMPEL-M., SEITZ-S., HECKER-N. E., FELDMANN-J., MITTLEMEN-D., BARTL-F., HAYD-A. AND ZUNDEL-G. (1999). THz spectroscopy on polar liquids, *in* V. J. Corcoran and T. A. Goldman (eds.), *International Conference on Lasers 1998*, The Society for Optical & Quantum Electronics, Tucson, AZ, USA, pp. 225–231.

KONO-S., TANI-M. AND SAKAI-K. (2001). Ultrabroadband photoconductive detection: Comparison with free-space electro-optic sampling, *Applied Physics Letters*, **79**(7), pp. 898–900.

KONO-S., TANI-M. AND SAKAI-K. (2002). Coherent detection of mid-infrared radiation up to 60 THz with an LT-GaAs photoconductive antenna, *IEE Proceedings Optoelectronics*, **149**, pp. 105–109.

KONO-S., TANI-M., GU-P. AND SAKAI-K. (2000). Detection of up to 20 THz with a low-temperature-grown GaAs photoconductive antenna gated with 15 fs light pulses, *Applied Physics Letters*, **77**(25), pp. 4104–4106.

KOZLOV-G. AND VOLKOV-V. (1998). Coherent source submillimeter wave spectroscopy, *in* G. Grüner (ed.), *Millimeter and submillimeter wave spectroscopy of solids*, Vol. 74 of *Topics in Applied Physics*, Springer-Verlag, Berlin, chapter 3, pp. 51–109.

KRAUSE-J. L., SCHAFER-K. J., BEN-NUN-M. AND WILSON-K. R. (1997). Creating and detecting shaped Rydberg wave packets, *Physical Review Letters*, **79**(25), pp. 4978–4981.

KRISHNAMURTHY-S., REITEN-M. T., HARMON-S. A. AND CHEVILLE-R. A. (2001). Characterization of thin polymer films using terahertz time-domain interferometry, *Applied Physics Letters*, **79**(6), pp. 875–7.

KWON-Y. AND PAVLIDIS-D. (1995). Phasor diagram analysis of millimeter-wave HEMT mixers, *IEEE Transactions on Microwave Theory and Techniques*, **43**(9), pp. 2166–2167.

KYUSHIK-H., MARSH-P. F., NG-G. I., PAVLIDIS-D. AND CHANG-H. H. (1994). Optimization of MOVPE grown $In_xAl_{1-x}AsIn_{0.53}Ga_{0.47}As$ planar heteroepitaxial Schottky diodes for terahertz applications, *IEEE Transactions on Electron Devices*, **41**(9), pp. 1489–1497.

LAGARIAS-J. C., REEDS-J. A., WRIGHT-M. H. AND WRIGHT-P. E. (1998). Convergence properties of the Nelder-Mead simplex method in low dimensions, *SIAM Journal of Optimization*, **9**(1), pp. 112–147.

LAI-R. K., HWANG-J.-R., NORRIS-T. B. AND WHITAKER-J. F. (1998). A photoconductive, miniature terahertz source, *Applied Physics Letters*, **72**(24), pp. 3100–3102.

LAVRIK-N. V. AND DATSKOS-P. G. (2003). Femtogram mass detection using photothermally actuated nanomechanical resonators, *Applied Physics Letters*, **82**(16), pp. 2697–2699. pgd@ornl.gov, 865-574-6205, www.ornl.mnl.gov.

LAX-B. (1976). Applications of far infrared lasers, *in* A. Mooradian, T. Jaeger and P. Stokseth (eds.), *Tunable Lasers and Applications*, Vol. 3 of *Springer Series in Optical Sciences*, Springer-Verlag, Berlin, pp. 340–347.

LEE-H., LEE-J. AND KIM-J. (2001a). Picosecond-domain radiation pattern measurement using fiber-coupled photoconductive antenna, *IEEE Journal of Selected Topics in Quantum Electronics*, **7**(4), pp. 667–673.

LEE-K.-S., KIM-J. Y., FORTIN-J., JIANG-Z., LI-M., LU-T.-M. AND ZHANG-X.-C. (2000a). Dielectric property measurement of sub-micron thin films by differential time-domain spectroscopy, *in* T. Elsaesser, S. Mukamel, M. M. Murnane and N. F. Scherer (eds.), *Ultrafast Phenomena XII*, Vol. 66 of *Springer Series in Chemical Physics*, Springer-Verlag, Berlin, pp. 232–234.

LEE-Y. S., MEADE-T., DECAMP-M., NORRIS-T. B. AND GALVANAUSKAS-A. (2000b). Temperature dependence of narrow-band terahertz generation from periodically poled lithium niobate, *Applied Physics Letters*, **77**(9), pp. 1244–1246.

LEE-Y. S., MEADE-T., NORRIS-T. B. AND GALVANAUSKAS-A. (2001b). Tunable narrow-band terahertz generation from periodically poled lithium niobate, *Applied Physics Letters*, **78**(23), pp. 3583–3585.

LEE-Y. S., MEADE-T., PERLIN-V., WINFUL-H., NORRIS-T. B. AND GALVANAUSKAS-A. (2000c). Generation of narrow-band terahertz radiation via optical rectification of femtosecond pulses in periodically poled lithium niobate, *Applied Physics Letters*, **76**(18), pp. 2505–2507.

LEITENSTORFER-A., HUNSCHE-S., SHAH-J., NUSS-M. C. AND KNOX-W. H. (1999). Detectors and sources for ultrabroadband electro-optic sampling: Experiment and theory, *Applied Physics Letters*, **74**(11), pp. 1516–1518.

LEITENSTORTER-A. (2001). Ultrabroadband THz experiments in femtosecond solid-state physics, *Quantum Electronics and Laser Science Conference '01*, IEEE LEOS & OSA, Baltimore, MD, U.S.A., pp. 163–164.

LIBON-I. H., HEMPEL-M., SEITZ-S., HECKER-N. E., FELDMANN-J., HAYD-A., ZUNDELA-G., MITTLEMAN-D. AND KOCH-M. (1999). THz spectroscopy of polar liquids, *Proceedings of SPIE - Terahertz Spectroscopy and Applications*, Vol. 3617, San Jose, CA, U.S.A., pp. 24–29.

LI-M., CHO-G. C., LU-T.-M., ZHANG-X.-C., WANG-S.-Q. AND KENNEDY-J. T. (1999a). Time-domain dielectric constant measurement of thin film in GHz-THz frequency range near Brewster angle, *Applied Physics Letters*, **74**(15), pp. 2113–2115.

LI-M., SUCHA-G., HAN-P.-Y., GALVANAOSKAS-A., HARTER-D. AND ZHANG-X.-C. (2000). THz generation and detection using 1550-nm pulses from a fiber laser, *Conference on Lasers and Electro-Optics '00*, Vol. 39 of *TOPS*, Optical Society of America, San Francisco, CA, U.S.A., pp. 559–60.

LI-M., ZHANG-X.-C., SUCHA-G. D. AND HARTER-D. J. (1999b). Portable terahertz system and its applications, *in* J. Neev and M. K. Reed (eds.), *Proceedings of SPIE - Commercial and Biomedical Applications of Ultrafast Lasers*, Vol. 3616, San Jose, CA, U.S.A., pp. 126–135.

LIU-D., CARETTE-D., BERGERON-M., KARWACKI-H., ADAMS-S., LANNING-B. AND KUSTAS-F. (1998). Structurally embedded photoconductive silicon bowtie antenna, *IEEE Photonics Technology Letters*, **10**(5), pp. 716–718.

LIU-Y., PARK-S.-G. AND WEINER-A. M. (1996). Terahertz waveform synthesis via optical pulse shaping, *IEEE Journal of Selected Topics in Quantum Electronics*, **2**(3), pp. 709–719.

LÖFFLER-T., JACOB-F. AND ROSKOS-H. G. (2000). THz generation by photo-ionization of electrically biased air, *Conference on Lasers and Electro-Optics '00*, Vol. 39 of *TOPS*, Optical Society of America, San Francisco, CA, U.S.A., pp. 356–357.

LOHSE-D. (2003). Bubble puzzles, *Physics Today*, **56**(2), pp. 36–41.

LUO-M. S. C., CHUANG-S. L., PLANKEN-P. C. M., BRENER-I. AND NUSS-M. C. (1993). Coherent double-pulse control of quantum beats in a coupled quantum well, *Physical Review B*, **48**(15), pp. 11043–11050.

LURYI-S. (1991). Polarization oscillations in coupled quantum wells - a scheme for generation of submillimeter electromagnetic waves, *IEEE Journal of Quantum Electronics*, **27**(1), pp. 54–60.

LU-Z. G., CAMPBELL-P. AND ZHANG-X.-C. (1997). Free-space electro-optic sampling with a high-repetition-rate regenerative amplified laser, *Applied Physics Letters*, **71**(5), pp. 593–595.

MACDONALD-M. E., ALEXANIAN-A., YORK-R. A., POPOVIC-Z. AND GROSSMAN-E. N. (2000). Spectral transmittance of lossy printed resonant-grid terahertz bandpass filters, *IEEE Transactions on Microwave Theory and Techniques*, **48**(4), pp. 712–718.

MARKELZ-A. G., ROITBERG-A. AND HEILWEIL-E. J. (2000). Pulsed terahertz spectroscopy of DNA, bovine serum albumin and collagen between 0.1 and 2.0 THz, *Chemical Physics Letters*, **320**(1-2), pp. 42–48.

MARSHALL-A. G. AND VERDUN-F. R. (1990). *Fourier Transforms in NMR, Optical, and Mass Spectroscopy*, Elsevier, Amsterdam, The Netherlands.

MASHIMO-S., MIURA-N., UMEHARA-T., YAGIHARA-S. AND HIGASI-K. (1992). The structure of water and methanol in p-dioxane as determined by microwave dielectric spectroscopy, *Journal of Chemical Physics*, **96**(9), pp. 6358–66361.

MATEI-A. AND DRESSEL-M. (2002). Far infrared spectroscopy of biological material, *in* G. P. Gallerano and M. R. Scarfi (eds.), *THz-BRIDGE Workshop*, ENEA, Capri, Italy, pp. Mo–3.

MATSUURA-S., TANI-M. AND SAKAI-K. (1997). Generation of coherent terahertz radiation by photomixing in dipole photoconductive antennas, *Applied Physics Letters*, **70**(5), pp. 559–561.

MA-X. F. AND ZHANG-X.-C. (1993). Determination of ratios between nonlinear-optical coefficients by using subpicosecond optical rectification, *Journal of the Optical Society of America B: Optical Physics*, **10**(7), pp. 1175–1179.

McCLATCHEY-K., REITEN-M. T. AND CHEVILLE-R. A. (2001). Time resolved synthetic aperture terahertz impulse imaging, *Applied Physics Letters*, **79**(27), pp. 4485–4487.

McGOWAN-R. W., CHEVILLE-R. A. AND GRISCHKOWSKY-D. (2000). Experimental study of the surface waves on a dielectric cylinder via terahertz impulse radar ranging, *IEEE Transactions on Microwave Theory and Techniques*, **48**(3), pp. 417–422.

McINTOSH-K. A., BROWN-E. R., NICHOLS-K. B., McMAHON-O. B., DiNATALE-W. F. AND LYSZCZARZ-T. M. (1995). Terahertz photomixing with diode lasers in low-temperature-grown GaAs, *Applied Physics Letters*, **67**(26), pp. 3844–3846.

McLAUGHLIN-R., CHEN-Q., CORCHIA-A., CIESLA-C. M., ARNONE-D. D., ZHANG-X.-C., JONES-G. A. C., LINFIELD-E. H. AND PEPPER-M. (2000). Enhanced coherent terahertz emission from indium arsenide, *Journal of Modern Optics*, **47**(11), pp. 1847–1856.

MENDIS-R. AND GRISCHKOWSKY-D. (2000). Plastic ribbon THz waveguides, *Journal of Applied Physics*, **88**(7), pp. 4449–4451.

MENDIS-R. AND GRISCHKOWSKY-D. (2001). THz interconnect with low-loss and low-group velocity dispersion, *IEEE Microwave and Wireless Components Letters*, **11**(11), pp. 444–446.

MENIKH-A., MACCOLL-R., MANNELLA-C. A. AND ZHANG-X.-C. (2002). Terahertz biosensing technology: Frontiers and progress, *ChemPhysChem*, **3**(8), pp. 655–658.

MERLIN-R. (1997). Generating coherent THz phonons with light pulses, *Solid State Communications*, **102**(2–3), pp. 207–220.

MEYER ZU HERINGDORF-F.-J., REUTER-M. C. AND TROMP-R. M. (2001). Growth dynamics of pentacene thin films, *Nature*, **412**(6846), pp. 517–520.

MICKAN-S. P., ABBOTT-D., MUNCH-J. AND ZHANG-X. C. (2000a). Chemical sensing in the submillimeter wave regime, *Proceedings of SPIE - Smart Structures and Devices 2000*, Vol. 4235, Melbourne, Australia, pp. 434–442.

MICKAN-S. P., ABBOTT-D., MUNCH-J., ZHANG-X.-C. AND VAN DOORN-T. (2000b). Analysis of system trade-offs for terahertz imaging, *Microelectronics Journal* (Elsevier), **31**(7), pp. 503–514.

MICKAN-S. P., DORDICK-J. S., MUNCH-J., ABBOTT-D. AND ZHANG-X.-C. (2002a). Pulsed THz protein spectroscopy in organic solvents, *Conference on Lasers and Electro-Optics '02*, IEEE LEOS & OSA, Long Beach, CA, U.S.A., p. 640.

MICKAN-S. P., DORDICK-J. S., MUNCH-J., ABBOTT-D. AND ZHANG-X.-C. (2002b). Terahertz spectroscopy of bound water in nano suspensions, *in* D. Nicolau (ed.), *Proceedings of SPIE - Biomedical Applications of Micro- and Nanoengineering*, Vol. 4937, Melbourne, Australia, pp. 49–61.

MICKAN-S. P., LEE-K. S., LU-T.-M., MUNCH-J., ABBOTT-D. AND ZHANG-X.-C. (2002c). Double modulated differential THz-TDS for thin film dielectric characterization, *Microelectronics Journal* (Elsevier), **33**(12), pp. 1033–1042.

MICKAN-S. P., MENIKH-A., LIU-H., MANNELLA-C. A., MACCOLL-R., ABBOTT-D., MUNCH-J. AND ZHANG-X.-C. (2002d). Label-free bioaffinity detection using terahertz technology, *Physics in Medicine and Biology*, **47**(21), pp. 3789–3796.

MINAMIDE-H., KAWASE-K., IMAI-K., SATO-A. AND ITO-H. (2001). A continuously tunable ring-cavity THz-wave parametric oscillator, *Review of Laser Engineering*, **29**(11), pp. 744–748.

MING-L., FORTIN-J., KIM-J. Y., FOX-G., CHU-F., DAVENPORT-T., LU-T.-M. AND ZHANG-X.-C. (2001). Dielectric constant measurement of thin films using goniometric terahertz time-domain spectroscopy, *IEEE Journal of Selected Topics in Quantum Electronics*, **7**(4), pp. 624–629.

MITROFANOV-O., BRENER-I., HAREL-R., WYNN-J. D., PFEIFFER-L. N., WEST-K. W. AND FEDERICI-J. (2000a). Terahertz near-field microscopy based on a collection mode detector, *Applied Physics Letters*, **77**(22), pp. 3496–8.

MITROFANOV-O., BRENER-I., WANKE-M. C., RUEL-R. R., WYNN-J. D., BRUCE-A. J. AND FEDERICI-J. (2000b). Near-field microscope probe for far infrared time domain measurements, *Applied Physics Letters*, **77**(4), pp. 591–3.

MITROFANOV-O., HAREL-R., LEE-M., PFEIFFER-L. N., WEST-K., WYNN-J. D. AND FEDERICI-J. (2001a). Study of single-cycle pulse propagation inside a terahertz near-field probe, *Applied Physics Letters*, **78**(2), pp. 252–4.

MITROFANOV-O., LEE-M., HSU-J. W. P., BRENER-I., HAREL-R., FEDERICI-J., WYNN-J. D., PFEIFFER-L. N. AND WEST-K. W. (2001b). Collection mode near-field imaging with 0.5-THz pulses, *IEEE Journal of Selected Topics in Quantum Electronics*, **7**(4), pp. 600–607.

MITROFANOV-O., LEE-M., HSU-J. W. P., PFEIFFER-L. N., WEST-K. W., WYNN-J. D. AND FEDERICI-J. F. (2001c). Terahertz pulse propagation through small apertures, *Applied Physics Letters*, **79**(7), pp. 907–909.

MITTLEMAN-D. M., CUNNINGHAM-J., NUSS-M. C. AND GEVA-M. (1997a). Noncontact semiconductor wafer characterization with the terahertz Hall effect, *Applied Physics Letters*, **71**(1), pp. 16–18.

MITTLEMAN-D. M., GUPTA-M., NEELAMANI-R., BARANIUK-R. G., RUDD-J. V. AND KOCH-M. (1999). Recent advances in terahertz imaging, *Applied Physics B: Lasers and Optics*, **68**(6), pp. 1085–1094.

MITTLEMAN-D. M., HUNSCHE-S., BOIVIN-L. AND NUSS-M. C. (1997b). T-ray tomography, *Optics Letters*, **22**(12), pp. 904–906.

MITTLEMAN-D. M., JACOBSEN-R. H., NEELAMANI-R., BARANIUK-R. G. AND NUSS-M. C. (1998). Gas sensing using terahertz time-domain spectroscopy, *Applied Physics B: Lasers and Optics*, **67**(3), pp. 379–390.

MITTLEMAN-D. M., JACOBSON-R. H. AND NUSS-M. C. (1996). T-ray imaging, *IEEE Journal of Selected Topics in Quantum Electronics*, **2**(3), pp. 679–692.

MOHAMMADI-S., PAVLIDIS-D. AND BAYRAKTAROGLU-B. (2000). Relation between low-frequency noise and long-term reliability of single AlGaAs/GaAs power HBTs, *IEEE Transactions on Electron Devices*, **47**(4), pp. 677–686.

MÖLLER-K. D. AND ROSCHILD-W. G. (1971). *Far-Infrared Spectroscopy*, Wiley series in pure and applied optics, Wiley-Interscience, New York.

MOON-J. A. (1993). Optimization of signal-to-noise ratios in pump-probe spectroscopy, *Review of Scientific Instruments*, **64**(7), pp. 1775–1778.

MORINO-J., YAMADA-K. M. T., KLEIN-H., BELOV-S. P., WINNEWISSER-G., BOCQUET-R., WLODARCZAK-G. AND KREGLEWSKI-W. L. M. (2000). Terahertz rotational spectra of NH_2OH in the ground and some low excited vibrational states, *Journal of Molecular Structure*, **517-518**, pp. 367–373.

MORRIS-J. AND SHEN-Y. R. (1971). Far-infrared generation by picosecond pulses in electro-optic materials, *Optics Communications*, **3**(2), pp. 81–84.

MORRIS-J. R. AND SHEN-Y. R. (1977). Theory of far-infrared generation by optical mixing, *Physical Review A*, **15**(3), pp. 1143–1156.

MOURET-G., CHEN-W., BOUCHER-D., BOCQUET-R., MOUNAIX-P. AND LIPPENS-D. (1999). Gas filter correlation instrument for air monitoring at submillimeter wavelengths, *Optics Letters*, **24**(5), pp. 351–353.

MOUROU-G., STANCAMPIANO-C. V. AND BLUMENTHAL-D. (1981). Picosecond microwave pulse generation, *Applied Physics Letters*, **38**(6), pp. 470–472.

NAGASHIMA-T. AND HANGYO-M. (2001). Measurement of complex optical constants of a highly doped Si wafer using terahertz ellipsometry, *Applied Physics Letters*, **79**(24), pp. 3917–3919.

NAGEL-M., HARING BOLÍVAR-P., BRUCHERSEIFER-M., KURZ-H., BOSSERHOFF-A. AND BÜTTNER-R. (2002a). Integrated planar terahertz resonators for femtomolar sensitivity label-free detection of DNA hybridization, *Applied Optics*, **41**(10), pp. 2074–2078.

NAGEL-M., HARING BOLÍVAR-P., BRUCHERSEIFER-M., KURZ-H., BOSSERHOFF-A. AND BÜTTNER-R. (2002b). Integrated THz technology for label-free genetic diagnostics, *Applied Physics Letters*, **80**(1), pp. 154–156.

NAHATA-A. AND HEINZ-T. F. (1996). Reshaping of freely propagating terahertz pulses by diffraction, *IEEE Journal of Selected Topics in Quantum Electronics*, **2**(3), pp. 701–708.

NAHATA-A., AUSTON-D. H. AND HEINZ-T. F. (1996a). Coherent detection of freely propagating terahertz radiation by electo-optic sampling, *Applied Physics Letters*, **68**(2), pp. 150–152.

NAHATA-A., AUSTON-D. H., WU-C. AND YARDLEY-J. T. (1995). Generation of terahertz radiation from a poled polymer, *Applied Physics Letters*, **67**(10), pp. 1358–1360.

NAHATA-A., WELING-A. S. AND HEINZ-T. F. (1996b). A wideband coherent terahertz spectroscopy system using optical rectification and electro-optic sampling, *Applied Physics Letters*, **69**(16), pp. 2321–2323.

NAHATA-A., YARDLEY-J. T. AND HEINZ-T. F. (1999). Free-space electro-optic detection of continuous-wave terahertz radiation, *Applied Physics Letters*, **75**(17), pp. 2524–2526.

NAKANISHI-H. (1990). Organic material for nonlinear optics, *Japanese Patent*. 1,716,929 (March 23).

NANDI-N. AND BAGCHI-B. (1997). Dielectric relaxation of biological water, *Journal of Physical Chemistry B*, **101**(50), pp. 10954–10961. DOI 10.1021/jp971879g.

NICHOLSON-J. W., RUDOLPH-W. AND HAGER-G. (1998). Generation of 14 GHz radiation using a two frequency iodine laser, *Applied Physics Letters*, **72**(26), pp. 3402–3404.

NIKON CORP. (2002). *Tochigi Nikon Corporation*, Tochigi, Japan, *URL: http://www.tochigi-nikon.co.jp/technologies/terahertz/*.

NUSS-M. C. (1996). Chemistry is right for T-rays, *IEEE Circuits and Devices*, **12**(2), pp. 25–30.

NUSS-M. C. AND ORENSTEIN-J. (1998). Terahertz time-domain spectroscopy, *in* G. Grüner (ed.), *Millimeter and submillimeter wave spectroscopy of solids*, Vol. 74 of *Topics in Applied Physics*, Springer-Verlag, Berlin, Germany, chapter 2, pp. 7–50.

O'HARA-J. AND GRISCHKOWSKY-D. (2001). Quasi-optic terahertz imaging, *Optics Letters*, **26**(23), pp. 1918–1920.

O'HARA-J. AND GRISCHKOWSKY-D. (2002). Synthetic phased-array terahertz imaging, *Optics Letters*, **27**(12), pp. 1070–1072.

OHTAKE-H., LIU-Z., IZUMIDA-S., ONO-S. AND SARUKURA-N. (1998). Spectrum control of intense THz-radiation from InAs under magnetic field irradiated with stretched femtosecond laser pulses, *in* T. Elsaesser, J. G. Fujumoto, D. A. Wiersma and W. Zinth (eds.), *Ultrafast Phenomena XI*, Vol. 63 of *Springer Series in Chemical Physics*, Springer-Verlag, Berlin, pp. 202–204. Proceedings of the 11th International Conference, Garmisch-Partenkirchen, Germany, July 12-17, 1998.

ONO-S., TSUKAMOTO-T., KAWAHATA-E., YANO-T., OHTAKE-H. AND SARUKURA-N. (2001). Terahertz radiation from a shallow incidence-angle InAs emitter in a magnetic field irradiated with femtosecond laser pulses, *Applied Optics*, **40**(9), pp. 1369–1371.

ONO-S., TSUKAMOTO-T., SAKAI-M., LIU-Z., OHTAKE-H., SARUKURA-N., NISHIZAWA-S., A.NAKANISHI AND YOSHIDA-M. (2000). Compact THz-radiation source consisting of a bulk semiconductor, a mode-locked fiber laser, and a 2-T permanent magnet, *Review of Scientific Instruments*, **71**(2), pp. 554–556.

ORELLANA-P. AND CLARO-F. (1999). A mesoscopic terahertz pulse detector, *Applied Physics Letters*, **75**(11), pp. 1643–1645.

PALIK-E. D. (1985). *Handbook of Optical Constants of Solids*, Academic Press, New York.

PAL-S. K., PEON-J. AND ZEWAIL-A. H. (2002). Biological water at the protein surface: Dynamical solvation probed directly with femtosecond resolution, *Proceedings of the National Academy of Sciences*, **99**(4), pp. 1763–1768. doi/10.1073/pnas.042697899.

PARK-S.-G., MELLOCH-M. R. AND WEINER-A. M. (1998). Comparison of terahertz waveforms measured by electro-optic and photoconductive sampling, *Applied Physics Letters*, **73**(22), pp. 3184–3186.

PARK-S.-G., MELLOCH-M. R. AND WEINER-A. M. (1999a). Analysis of terahertz waveforms measured by photoconductive and electrooptic sampling, *IEEE Journal of Quantum Electronics*, **35**(5), pp. 810–819.

PARK-S.-G., WEINER-A. M., MELLOCH-M. R., SIDERS-C. W., SIDERS-J. L. W. AND TAYLOR-A. J. (1999b). High-power narrow-band terahertz generation using large-aperture photoconductors, *IEEE Journal of Quantum Electronics*, **35**(8), pp. 1257–1268.

PARTRIDGE-J., DENNISON-P. R., MOORE-B. D. AND HALLING-P. J. (1998). Activity and mobility of subtilisin in low water organic media: hydration is more important than solvent dielectric, *Biochimica et Biophysica Acta*, **1386**, pp. 79–89.

PASTOL-Y., ARJAVALINGAM-G., KOPCSAY-G. V. AND HALBOUT-J.-M. (1989a). Dielectric properties of uniaxial crystals measured with optoelectronically generated microwave transient radiation, *Applied Physics Letters*, **55**(22), pp. 2277–2279.

PASTOL-Y., ARJAVALINGHAM-G., HALBOUT-J.-M. AND KOPSCAY-G. V. (1989b). Absorption and dispersion of low-loss dielectrics measured with microwave transient radiation, *Electronics Letters*, **25**(8), pp. 523–524.

PASTOL-Y., ARJAVALINGHAM-G., HALBOUT-J.-M. AND KOPSCAY-G. V. (1989c). Coherent broadband microwave spectroscopy using picosecond optoelectronic antennas, *Applied Physics Letters*, **54**(4), pp. 307–309.

PAVLIDIS-D. (1999). HBT vs. PHEMT vs. MESFET: what's best and why, *Compound Semiconductor*, **55**(5), pp. 56–59.

PAVLIDIS-D., ALEKSEEV-E., KYUSHIK-H. AND DELONG-C. (1997). InP-based millimeter-wave PIN diodes for switching and phase-shifting applications, *Solid State Electronics*, **41**(10), pp. 1635–1639.

PAVLOV-S. G., HÜBERS-H.-W., RÜMMELI-M. H., ZHUKAVIN-R. K., ORLOVA-E. E., SHASTIN-V. N. AND RIEMANN-H. (2002). Far-infrared stimulated emission from optically excited bismuth donors in silicon, *Applied Physics Letters*, **80**(25), pp. 4717–4719.

PEALE-R. E., MURAVJOV-A. V., NELSON-E. W., FREDRICKSEN-C., PAVLOV-S. G. AND SHASTIN-V. N. (2002). The far-infrared p-Ge laser: cavity and modulation advances, *Conference on Lasers and Electro-Optics '02*, IEEE LEOS & OSA, Long Beach, CA, U.S.A., pp. 181–182.

PEARCE-J. AND MITTLEMAN-D. M. (2001). The propagation of single-cycle THz pulses in random media, *Optics Letters*, **26**(24), pp. 2002–2004.

PEDERSEN-J. E. AND KEIDING-S. R. (1992). THz time-domain spectroscopy of nonpolar liquids, *IEEE Journal of Quantum Electronics*, **28**(10), pp. 2518–2522.

PELLEMANS-H. P. M., BOLÍVAR-P. H., BRUCHERSEIFER-M., KURZ-H., MANN-C. M., BOWEN-J. W. AND HADJILOUCAS-S. (2000). Characterization techniques for passive devices from 150 GHz to 3 THz using THz-transient spectroscopy, *Conference on Lasers and Electro-Optics '00*, Vol. 39 of *TOPS*, Optical Society of America, San Francisco, CA, U.S.A., pp. 557–558.

PETHIG-R. AND KELL-D. B. (1987). The passive electrical properties of biological systems: Their significance in physiology, biophysics and biotechnology, *Physics in Medicine and Biology*, **32**(8), pp. 933–970.

PFEIDER-T., HEILIGER-H.-M., VON KAMIENSKI-E. S., ROSKOS-H. G. AND KURZ-H. (1994). Fabrication and characterization of freely positionable silicon-on-sapphire photoconductive probes, *Journal of the Optical Society of America B: Optical Physics*, **11**(12), pp. 2547–2552.

PIESTRUP-M. A., FLEMING-R. N. AND PANTELL-R. H. (1975). Continuously tunable submillimeter wave source, *Applied Physics Letters*, **26**(8), pp. 418–421.

PIMENOV-A., PRONIN-A. V., LOIDL-A., KAMPF-A. P., KRASNOSVOBODTSEV-S. I. AND NOZDRIN-V. S. (2000). Submillimeter spectroscopy of tilted $Nd_{1.85}Ce_{0.15}CuO_{4-\delta}$ films: Observation of a mixed ac-plane excitation, *Applied Physics Letters*, **77**(3), pp. 429–431.

PINE-A. S., SUENRAM-R. D., BROWN-E. R. AND MCINTOSH-K. A. (1996). A terahertz photomixing spectrometer: application to SO_2 self broadening, *Journal of Molecular Spectroscopy*, **175**(1), pp. 37–47.

PLANKEN-P. C. M., NIENHUYS-H.-K., BAKKER-H. J. AND WENCKEBACH-T. (2001). Measurement and calculation of the orientation dependence of terahertz pulse detection in ZnTe, *Journal of the Optical Society of America B: Optical Physics*, **18**(3), pp. 313–317.

POPPE-A., XU-L., KRAUSZ-F. AND SPIELMANN-C. (1998). Noise characterization of sub-10-fs Ti:sapphire oscillators, *IEEE Journal of Selected Topics in Quantum Electronics*, **4**(2), pp. 179–184.

PÖTZ-W. (1996). Infrared light emission from semiconductor double wells, *Applied Physics Letters*, **68**(18), pp. 2553–2555.

PROAKIS-J. G. AND MANOLAKIS-D. G. (1996). *Digital Signal Processing: Principles, Algorithms, and Applications*, 3rd edn, Prentice-Hall, Upper Saddle River, NJ, U.S.A.

RALPH-S. E. AND GRISCHKOWSKY-D. (1992). THz spectroscopy and source characterization by optoelectronic interferometry, *Applied Physics Letters*, **60**(9), pp. 1070–1072.

RAMAN-C., CONOVER-C. W. S., SUKENIK-C. I. AND BUCKSBAUM-P. H. (1996). Ionization of Rydberg wave packets by subpicosecond, half-cycle electromagetic pulses, *Physical Review Letters*, **76**(14), pp. 2436–2439.

REEDIJK-J. A., MARTENS-H. C. F., SMITS-B. J. G. AND BROM-H. B. (2000). Measurement of the complex dielectric constant down to helium temperatures. II. Quasioptical technique from 0.03 to 1 THz, *Review of Scientific Instruments*, **71**(2), pp. 478–481.

REE-M., CHEN-K.-J., KIRBY-D. P., KATZENELLENBOGEN-N. AND GRISCHKOWSKY-D. (1992). Anisotropic properties of high-temperature polyimide thin films: Dielectric and thermal-expansion behaviors, *Journal of Applied Physics*, **72**(5), pp. 2014–2021.

REGAN-F., MEANEY-M., VOS-J. G., MACCRAITH-B. D. AND WALSH-J. E. (1996). Determination of pesticides in water using ATR-FTIR spectroscopy on PVC/chloroparaffin coatings, *Analytica Chimica Acta*, **334**(1–2), pp. 85–92.

REITEN-M. T., GRISCHKOWSKY-D. AND CHEVILLE-R. A. (2001a). Optical tunneling of single-cycle terahertz bandwidth pulses, *Physical Review E*, **64**(03), pp. 036604/1–5.

REITEN-M. T., GRISCHKOWSKY-D. AND CHEVILLE-R. A. (2001b). Properties of surface waves determined via bistatic terahertz impulse ranging, *Applied Physics Letters*, **78**(8), pp. 1146–1148.

REITEN-M. T., MCCLATCHEY-K., GRISCHKOWSKY-D. AND CHEVILLE-R. A. (2001c). Incidence-angle selection and spatial reshaping of terahertz pulses in optical tunneling, *Optics Letters*, **26**(23), pp. 1900–1902.

RICE-A., JIN-Y., MA-X. F., ZHANG-X.-C., BLISS-D., LARKIN-J. AND ALEXANDER-M. (1994). Terahertz optical rectification from $\langle 110 \rangle$ zinc-blende crystals, *Applied Physics Letters*, **64**(11), pp. 1324–1326.

RIORDAN-J. A., SUN-F. G., LU-Z. G. AND ZHANG-X.-C. (1997). Free-space transient magneto-optic sampling, *Applied Physics Letters*, **71**(11), pp. 1452–1454.

ROCHAT-M., FAIST-J., BECK-M., OESTERLE-U. AND ILEGEMS-M. (1998). Far-infrared ($\lambda = 88\ \mu$m) electroluminescence in a quantum cascade structure, *Applied Physics Letters*, **73**(25), pp. 3724–3726.

ROITBERG-A., GERBER-R. B., ELBER-R. AND RATNER-M. A. (1995). Anharmonic wave functions of proteins: Quantum self-consistent field calculations of BPTI, *Science*, **268**(5215), pp. 1319—1322.

RØNNE-C. AND KEIDING-S. R. (1998). THz reflection spectroscopy of H_2O(l) and D_2O(l), *in* T. Elsaesser, J. G. Fujumoto, D. A. Wiersma and W. Zinth (eds.), *Ultrafast Phenomena XI*, Vol. 63 of *Springer Series in Chemical Physics*, Springer-Verlag, Berlin, pp. 568–570.

RØNNE-C., JENSBY-K., LOUGHNANE-B. J., FOURKAS-J., NIELSEN-O. F. AND KEIDING-S. R. (2000). Temperature dependence of the dielectric function of C_6H_6(l) and $C_6H_5CH_3$(l) measured with THz spectroscopy, *Journal of Chemical Physics*, **113**(9), pp. 3749–3756.

RØNNE-C., THRANE-L., ÅSTRAND-P.-O., WALLQVIST-A., MIKKELSEN-K. V. AND KEIDING-S. R. (1997). Investigation of the temperature dependence of dielectric relaxation in liquid water by THz reflection spectroscopy and molecular dynamics simulation, *Journal of Chemical Physics*, **107**(14), pp. 5319–5331.

ROSKOS-H. G., NUSS-M. C., SHAH-J., LEO-K., MILLER-D. A. B., FOX-A. M., SCHMITT-RINK-A. AND KÖHLER-K. (1992). Coherent submillimeter-wave emission from charge oscillations in a double-well potential, *Physical Review Letters*, **68**(14), pp. 2216–2219.

ROSNER-B. T. AND VAN DER WEIDE-D. W. (2002). High-frequency near-field microscopy, *Review of Scientific Instruments*, **73**(7), pp. 2505–2525.

RUDD-J. V. AND MITTLEMAN-D. M. (2002). Influence of substrate-lens design in terahertz time-domain spectroscopy, *Journal of the Optical Society of America B: Optical Physics*, **19**(2), pp. 319–329.

RUDD-J. V., JOHNSON-J. L. AND MITTLEMAN-D. M. (2000a). Quadrupole radiation from terahertz dipole antennas, *Optics Letters*, **25**(20), pp. 1556–1558.

RUDD-J. V., JOHNSON-J. L. AND MITTLEMAN-D. M. (2001). Cross-polarized angular emission patterns from lens-coupled terahertz antennas, *Journal of the Optical Society of America B: Optical Physics*, **18**(10), pp. 1524–1533.

RUDD-J. V., ZIMDARS-D. AND WARMUTH-M. (2000b). Compact fiber-pigtailed terahertz imaging system, *in* J. Neev and M. K. Reed (eds.), *Proceedings of SPIE - Commercial and Biomedical Applications of Ultrafast Lasers II*, Vol. 3934, San Jose, CA, U.S.A., pp. 27–35.

RUFFIN-A. B., DECKER-J., SANCHEZ-PALENCIA-L., LE HORS-L., WHITAKER-J. F., NORRIS-T. B. AND RUDD-J. V. (2001). Time reversal and object reconstruction with single-cycle pulses, *Optics Letters*, **26**(10), pp. 681–683.

RUFFIN-A. B., RUDD-J. V., FENG-S., WINFUL-H. G. AND WHITAKER-J. F. (1999). Phase manipulation of free-space THz pulses using transmissive optics, *Ultrafast Electronics and Optoelectronics*, Vol. 28 of *OSA TOPS*, Optical Society of America, pp. 98–102.

RU-M. T., WU-K. C., LINDSAY-J. P., DORDICK-J. S., REIMER-J. A. AND CLARK-D. S. (2001). Towards more active biocatalysts in organic media: Increasing the activity of salt-activated enzymes, *Biotechnology and Bioengineering*, **75**(2), pp. 187–196.

RUSSELL-A. J., THOMAS-P. G. AND FERSHT-A. R. (1987). Electrostatic effects on modification of charged groups in the active site cleft of subtilisin by protein engineering, *Journal of Molecular Biology*, **193**, pp. 803–813.

RYZHII-V., KHMYROVA-I. AND SHUR-M. (2002). Terahertz photomixing in quantum well structures using resonant excitation of plasma oscillations, *Journal of Applied Physics*, **91**(4), pp. 1875–1881.

SAETA-P. N., GREENE-B. I. AND CHUANG-S. L. (1993). Short terahertz pulses from semiconductor surfaces: The importance of bulk difference-frequency mixing, *Applied Physics Letters*, **63**(25), pp. 3482–3484.

SALDIN-E. L., SCHNEIDMILLER-E. A. AND YURKOV-M. V. (2000). *The Physics of Free Electron Lasers*, Advanced Texts in Physics, Springer-Verlag, Berlin.

SALEH-B. E. A. AND TEICH-M. C. (1991). *Fundamentals of Photonics*, John Wiley & Sons, Inc., New York.

SARUKURA-N., OHTAKE-H., IZUMIDA-S. AND LIU-Z. (1998a). High average-power THz radiated from femtosecond laser-irradiated InAs in a magnetic field and its ellipical polarization characteristics, *Journal of Applied Physics*, **84**(1), pp. 654–656.

SARUKURA-N., OHTAKE-H., IZUMIDA-S., LIU-Z., ONO-S. AND YAMANAKA-T. (1998b). Submilliwatt, short-pulse, terahertz radiation from femtosecond-laser irradiated InAs in a magnetic field, *Conference on Lasers and Electro-Optics '98*, Optical Society of America, San Francisco, CA, U.S.A., p. 63.

SATO-A., KAWASE-K., MINAMIDE-H., WADA AND ITO-H. (2001). Tabletop terahertz-wave parametric generator using a compact, diode-pumped Nd:YAG laser, *Review of Scientific Instruments*, **72**(9), pp. 3501–3504.

SATO-S., HAYAKAWA-S., MATSUMOTO-T., MATSUO-H., MURAKAMI-H., SAKAI-K., LANGE-A. E. AND RICHARDS-P. L. (1989). Submillimeter wave low pass filters made of glass beads, *Applied Optics*, **28**(20), p. 4478.

SCHAFER-K. AND KRAUSE-J. (1997). Tunable terahertz radiation from Stark wave packets, *Optics Express*, **1**(7), pp. 210–215.

SCHALL-M. AND JEPSEN-P. U. (2000). Photoexcited GaAs surfaces studied by transient terahertz time-domain spectroscopy, *Optics Letters*, **25**(1), pp. 13–15.

SCHALL-M., WALTHER-M., HELM-H. AND JEPSEN-P. U. (2000). Two-phonon processes in II-VI semiconductors investigated with terahertz time-domain spectroscopy, *Conference on Lasers and Electro-Optics '00*, Vol. 39 of *TOPS*, Optical Society of America, San Francisco, CA, U.S.A., pp. 465–466.

SCHOLZ-E. (1984). *Karl Fischer Titration: Determination of Water. Chemical Laboratory Practice*, Springer, New York.

SCHRODER-D. K. (1990). *Semiconductor material and device characterization*, John Wiley & Sons, Inc., New York.

SCHWETTMAN,-H. A. (ED.) (1993). *Free-electron laser spectroscopy in biology, medicine, and materials science*, Vol. 1854, SPIE, SPIE, Washington, DC, U.S.A., Los Angeles, CA.

SHAN-J., WEISS-C., WALLENSTEIN-R., BEIGANG-R. AND HEINZ-T. F. (2001). Origin of magnetic field enhancement in the generation of terahertz radiation from semiconductor surfaces, *Optics Letters*, **26**(11), pp. 849–851.

SHAN-J., WELING-A. S., KNOESE-E., BARTELS-L., BONN-M., NAHATA-A., REIDER-G. A. AND HEINZ-T. F. (2000). Single-shot measurement of terahertz electromagnetic pulses by use of electro-optic sampling, *Optics Letters*, **25**(6), pp. 426–428.

SHASTIN-V. N., ZHUKAVIN-R. K., ORLOVA-E. E., PAVLOV-S. G., RÜMMELI-M. H., HÜBERS-H.-W., HOVENIER-J. N., KLAASSEN-T. O., RIEMANN-H., BRADLEY-I. V. AND VAN DER MEER-A. F. G. (2002). Stimulated terahertz emission from group-V donors in silicon under intracenter photoexcitation, *Applied Physics Letters*, **80**(19), pp. 3512–3514.

SHEN-Y.-R. (1976). Far-infrared generation by optical mixing, *Progress in Quantum Electronics*, **4**(3), pp. 207–232.

SHEN-Y. R. (1984). *The Principles of Nonlinear Optics*, Wiley, New York.

SHERWOOD-P. M. A. (1972). *Vibrational Spectroscopy Of Solids*, Vol. 1 of *Cambridge monographs in physical chemistry*, Cambridge University Press, London.

SHIKATA-J., KAWASE-K., SATO-M., TANIUCHI-T. AND ITO-H. (1999). Enhancement of THz-wave output from $LiNbO_3$ optical parametric oscillators by cryogenic cooling, *Optics Letters*, **24**(4), pp. 202–204.

SHUR-M. S., LÜ-J.-Q. AND DYAKONOV-M. I. (1999). Terahertz applications of plasma wave electronics, *in* M. Matloubian and E. Ponti (eds.), *IEEE MTT-S International Microwave Symposium Digest*, Vol. 3, IEEE, IEEE, Anaheim, CA, pp. 937–940.

SIDERS-J. L. W., TRUGMAN-S. A., GARZON-F. H., HOULTON-R. J. AND TAYLOR-A. J. (2000). Terahertz emission from $YBa_2Cu_3O_{7-\delta}$ thin films via bulk electric-quadrupole-magnetic-dipole optical rectification, *Physical Review B*, **61**(20), pp. 13633–13638.

SIEBE-F., SIEBERT-K., LEONHARDT-R. AND ROSKOS-H. G. (1999). A fully tunable dual-color CW Ti:Al_2O_3 laser, *IEEE Journal of Quantum Electronics*, **35**(11), pp. 1731–1736.

SIEBERT-K. J., QUAST-H., LEONHARDT-R., LÖFFLER-T., THOMSON-M., BAUER-T., ROSKOS-H. G. AND CZASCH-S. (2002). Continuous-wave all-optoelectronic terahertz imaging, *Applied Physics Letters*, **80**(16), pp. 3003–3005.

SIEGEL-P. H. (2002). Terahertz technology, *IEEE Transactions on Microwave Theory and Techniques*, **50**(3), pp. 910–928.

SINYUKOV-A. M. AND HAYDEN-L. M. (2002). Generation and detection of terahertz radiation with multilayered electro-optic polymer films, *Optics Letters*, **27**(1), pp. 55–57.

SMITH-P. R., AUSTON-D. H. AND NUSS-M. C. (1988). Subpicosecond photoconducting dipole antennas, *IEEE Journal of Quantum Electronics*, **24**(2), pp. 255–260.

SMYE-S. W., CHAMBERLAIN-J. M., FITZGERALD-A. J. AND BERRY-E. (2001). The interaction between terahertz radiation and biological tissue, *Physics in Medicine and Biology*, **46**(9), pp. 101–112.

SOHN-J. Y., AHN-Y. H., PARK-D. J., OH-E. AND KIM-D. S. (2002). Tunable terahertz generation using femtosecond pulse shaping, *Applied Physics Letters*, **81**(1), pp. 13–15.

SONG-X. AND SWANSON-B. I. (1999). Direct, ultrasensitive, and selective optical detection of protein toxins using multivalent interactions, *Analytical Chemistry*, **71**(11), pp. 2097–2107.

SON-J., RUDD-J. V. AND WHITAKER-J. F. (1992). Noise characterization of a self-mode-locked Ti:sapphire laser, *Optics Letters*, **17**(10), pp. 733–735.

SRIDHAR-S., REAGOR-D. AND GRUNER-G. (1985). Complex conductivity measurements between 26 and 110 GHz using complex impedance bridges, *Review of Scientific Instruments*, **56**(10), pp. 1946–1952.

SUN-F. G., JI-W. AND ZHANG-X.-C. (2000). Two-photon absorption induced saturation of THz radiation in ZnTe, *Conference on Lasers and Electro-Optics '00*, Vol. 39 of *TOPS*, Optical Society of America, San Francisco, CA, U.S.A., pp. 479–80.

SVANBERG-S. (1991). *Atomic and molecular spectroscopy: Basic aspects and practical applications*, Vol. 6 of *Springer series on atoms and plasmas*, Springer-Verlag, Berlin.

TAKANO-S., KLAUS-T. AND WINNEWISSER-G. (1998). The ND radical: Laboratory measurement of the N=2–1 rotational transition at 1 THz, *Journal of Molecular Spectroscopy*, **192**(2), pp. 309–319.

TANI-M., JIANG-Z. AND ZHANG-X.-C. (2000a). Photoconductive terahertz transceiver, *Electronics Letters*, **36**(9), pp. 804–805.

TANI-M., LEE-K.-S. AND ZHANG-X.-C. (2000b). Detection of terahertz radiation with low-temperature-grown GaAs-based photoconductive antenna using 1.55 μm probe, *Applied Physics Letters*, **77**(9), pp. 1396–1398.

TANI-M., MATSUURA-S., SAKAI-K. AND NAKASHIMA-S. (1997). Emission characteristics of photoconductive antennas based on low-temperature-grown GaAs and semi-insulating GaAs, *Applied Optics*, **36**(30), pp. 7853–7859.

TELLES-E. M., VISCOVINI-R. C., SCALABRIN-A. AND PEREIRA-D. (1998). Far-infrared laser lines from CH_3-rocking of $^{13}CD_3OD$, *in* M. N. Afsar (ed.), *Proceedings of SPIE - Millimeter and Submillimeter Waves IV*, Vol. 3465, San Diego, CA, U.S.A., pp. 60–63.

TERAVIEW LTD. (2002). *TeraView Limited*, Cambridge, UK, URL: `http://www.teraview.co.uk`.

THRANE-L., JACOBSEN-R. H., JEPSEN-P. U. AND KEIDING-S. R. (1995). THz reflection spectroscopy of liquid water, *Chemical Physics Letters*, **240**, pp. 330–333.

TOMINARI-Y., KIWA-T., MURAKAMI-H., TONOUCHI-M., WALD-H., SEIDEL-P. AND SCHNEIDEWIND-H. (2002). Resonant terahertz radiation from $Tl_2Ba_2CaCu_2O_{8+\delta}$ thin films by ultrafast optical pulse excitation, *Applied Physics Letters*, **80**(17), pp. 3147–3149.

TONOUCHI-M., YAMASHITA-M. AND HANGYO-M. (2000). Vortex penetration in YBCO thin film strips observed by THz radiation imaging, *Physica B*, **284–288**, pp. 853–854.

TREDICUCCI-A., GMACHL-C., CAPASSO-F., WANKE-M. C., HUTCHINSON-A. L., SIVCO-D. L., CHU-S.-N. G. AND CHO-A. Y. (2001). Novel quantum cascade devices for long wavelength IR emission, *Optics Materials*, **17**(1–2), pp. 211–217.

UEHARA-K., MIYASHITA-K., NATSUME-K.-I., HATAKEYAMA-K. AND MIZUNO-K. (1992). Lens-coupled imaging arrays for the millimeter and sub-millimeter wave regions, *IEEE Transactions on Microwave Theory and Techniques*, **40**(5), pp. 806–811.

UHD JEPSEN-P., WINNEWISSER-C., SCHALL-M., SCHYA-V., KEIDING-S. R. AND HELM-H. (1996). Detection of THz pulses by phase retardation in lithium tantalate, *Physical Review E*, **53**(4), pp. R3052–R3054.

ULMAN,-A. (ED.) (1995). *Characterization of organic thin films*, Butterworth-Heinemann, Stoneham, MA USA.

VALDMANIS-J. A. AND MOUROU-G. A. (1986). Subpicosecond electrooptic sampling: Principles and applications, *IEEE Journal of Quantum Electronics*, **22**(1), pp. 69–78.

VALDMANIS-J. A., MOUROU-G. A. AND GABEL-C. W. (1983). Subpicosecond electrical sampling, *IEEE Journal of Quantum Electronics*, **19**(4), pp. 664–667.

VALDMANIS-J. A., MOUROU-G. AND GABEL-C. W. (1982). Picosecond electro-optic sampling system, *Applied Physics Letters*, **41**(3), pp. 211–212.

VAN DER VALK-N. C. J. AND PLANKEN-P. C. M. (2002). Electro-optic detection of subwavelength terahertz spot sizes in the near field of a metal tip, *Applied Physics Letters*, **80**(9), pp. 1558–1560.

VAN DER WEIDE-D. W. (1994). Planar antennas for all-electronic terahertz systems, *Journal of the Optical Society of America B: Optical Physics*, **11**(12), pp. 2553–2560.

VAN DER WEIDE-D. W. AND KEILMANN-F. (1998). Coherent periodically pulsed radiation spectrometer, *US Patent & Trademark Office*. No. **5,748,309** (May 5).

VAN DER WEIDE-D. W., BOSTAK-J. S., AULD-B. A. AND BLOOM-D. M. (1991). All-electronic free-space picosecond pulse generation and detection, *Electronics Letters*, **27**(16), pp. 1412–1413.

VAN DER WEIDE-D. W., MURAKOWSKI-J. AND KEILMANN-F. (2000). Gas-absorption spectroscopy with electronic terahertz techniques, *IEEE Transactions on Microwave Theory and Techniques*, **48**(4), pp. 740–743.

VAN EXTER-M. AND GRISCHKOWSKY-D. (1990a). Carrier dynamics of electrons and holes in moderately doped silicon, *Physical Review B*, **41**(17), pp. 12140–12149.

VAN EXTER-M. AND GRISCHKOWSKY-D. (1990b). Characterization of an optoelectronic terahertz beam system, *IEEE Transactions on Microwave Theory and Techniques*, **38**(11), pp. 1684–1691.

VAN EXTER-M., FATTINGER-C. AND GRISCHKOWSKY-D. (1989a). High-brightness terahertz beams characterized with an ultrafast detector, *Applied Physics Letters*, **55**(4), pp. 337–339.

VAN EXTER-M., FATTINGER-C. AND GRISCHKOWSKY-D. (1989b). Terahertz time-domain spectroscopy of water vapor, *Optics Letters*, **14**(20), pp. 1128–1130.

VEITAS-G. AND DANIELIUS-R. (1999). Generation of narrow-bandwidth tunable picosecond pulses by difference-frequency mixing of stretched pulses, *Journal of the Optical Society of America B: Optical Physics*, **16**(9), pp. 1561–1565.

VENABLES-D. S. AND SCHMUTTENMAER-C. A. (1998). Time-resolved THz studies of liquid dynamics, *in* T. Elsaesser, J. G. Fujumoto, D. A. Wiersma and W. Zinth (eds.), *Ultrafast Phenomena XI*, Vol. 63 of *Springer Series in Chemical Physics*, Springer-Verlag, Berlin, pp. 565–567.

VENABLES-D. S. AND SCHMUTTENMAER-C. A. (2000a). Spectroscopy and dynamics of mixtures of water with acetone, acetonitrile, and methanol, *Journal of Chemical Physics*, **113**(24), pp. 11222–11236.

VENABLES-D. S. AND SCHMUTTENMAER-C. A. (2000b). Structure and dynamics of nonaqueous mixtures of dipolar liquids. II. Molecular dynamics simulations, *Journal of Chemical Physics*, **113**(8), pp. 3249–3260.

VENABLES-D. S., CHIU-A. AND SCHMUTTENMAER-C. A. (2000). Structure and dynamics of nonaqueous mixtures of dipolar liquids. I. Infrared and far-infrared spectroscopy, *Journal of Chemical Physics*, **113**(8), pp. 3243–3248.

VERGHESE-S., MCINTOSH-K. A. AND BROWN-E. R. (1997). Highly tunable fiber-coupled photomixers with coherent terahertz output power, *IEEE Transactions on Microwave Theory and Techniques*, **45**(8), pp. 1301–1309.

VERGHESE-S., MCINTOSH-K. A., CALAWA-S., DINATALE-W. F., DUERR-E. K. AND MOLVAR-K. A. (1998). Generation and detection of coherent terahertz waves using two photomixers, *Applied Physics Letters*, **73**(26), pp. 3824–3826.

VERYRET-B. (2002). Biological effects in the microwave, THz and infrared regions, *in* G. P. Gallerano and M. R. Scarfi (eds.), *THz-BRIDGE Workshop*, ENEA, Capri, Italy, pp. Mo–11.

VICTOR-K., ROSKOS-H. G. AND WASCHKE-C. (1994). Efficiency of submillimeter-wave generation and amplification by coherent wave-packet oscillations in semiconductor structures, *Journal of the Optical Society of America B: Optical Physics*, **11**(12), pp. 2470–2479.

VON DER LINDE-D. (1986). Characterization of the noise in continuously operating mode-locked lasers, *Applied Physics B: Photophysics and Laser Chemistry*, **39**(4), pp. 201–217.

VOSSEBRGER-M., BRUCHERSEIFER-M., CHO-G. C., ROSKOS-H. G. AND KURZ-H. (1998). Propagation effects in electro-optic sampling of terahertz pulses in GaAs, *Applied Optics*, **37**(15), pp. 3368–3371.

WALKER-G. C., BERRY-E., ZINOV'EV-N. N., FITZGERALD-A. J., MILES-R. E., CHAMBERLAIN-J. M. AND SMITH-M. A. (2002). Terahertz imaging and international safety guidelines, *Proceedings of the SPIE*, **4682**, pp. 683–690.

WALTHER-M., FISCHER-B., SCHALL-M., HELM-H. AND JEPSEN-P. U. (2000a). Far-infrared vibrational spectra of all-trans, 9-cis and 13-cis retinal measured by THz time-domain spectroscopy, *Chemical Physics Letters*, **332**(3–4), pp. 389–395.

WALTHER-M., JEVSKY-K., KEIDIG-S. R., TAKAHIRO-H. AND ITO-H. (2000b). Far infrared properties of DAST, *Optics Letters*, **25**(12), pp. 911–913.

WALTHER-M., PLOCHOCKA-P., FISCHER-B., HELM-H. AND JEPSEN-P. U. (2002). Collective vibrational modes in biological molecules investigated by terahertz time-domain spectroscopy, *Biopolymers*, **67**(4–5), pp. 310–313.

WANG-C.-L. AND PAN-C.-L. (1995). Tunable multiterahertz beat signal generation from a two-wavelength laser-diode array, *Optics Letters*, **20**(11), pp. 1292–1294.

WANG-S., YUAN-T., WALSBY-E. D., BLAIKIE-R. J., DURBIN-S. M., CUMMING-D. R. S., XU-J. AND ZHANG-X.-C. (2002). Characterization of t-ray binary lenses, *Optics Letters*, **27**(13), pp. 1183–1185.

WARREN-A. C., KATZENELLENBOGEN-N., GRISCHKOWSKY-D., WOODALL-J. M., MELLOCH-M. R. AND OTSUKA-N. (1991). Subpicosecond, freely propagating electromagnetic pulse generation and detection using GaAs:As epilayers, *Applied Physics Letters*, **58**(14), pp. 1512–1514.

WASCHKE-C., ROSKOS-H. G., SCHWEDLER-R., LEO-K., KURZ-H. AND KÖHLER-K. (1993). Coherent submillimeter-wave emission from Bloch oscillations in a semiconductor superlattice, *Physical Review Letters*, **70**(21), pp. 3319–3322.

WEISS-C., TOROSYAN-G., AVETISYAN-Y. AND BEIGANG-R. (2001). Generation of tunable narrow-band surface-emitted terahertz radiation in periodically poled lithium niobate, *Optics Letters*, **26**(8), pp. 563–565.

WELING-A. S. AND AUSTON-D. H. (1996). Novel sources and detectors for coherent tunable narrow-band terahertz radiation in free space, *Journal of the Optical Society of America B: Optical Physics*, **13**(12), pp. 2783–2791.

WELING-A. S. AND HEINZ-T. F. (1999). Enhancement in the spectral irradiance of photoconducting terahertz emitters by chirped-pulse mixing, *Journal of the Optical Society of America B: Optical Physics*, **16**(9), pp. 1455–1467.

WELING-A. S., BONN-M., SHAN-J., REIDER-G. A., NAHATA-A. AND HEINZ-T. F. (1999). Simultaneous recording of THz waveforms by multi-channel electro-optic detection, *Ultrafast Electronics and Optoelectronics*, Vol. 28 of *OSA TOPS*, OSA, Snowmass, Col. U.S.A., pp. 95–97.

WELING-A. S., HU-B. B., FROBERG-N. M. AND AUSTON-D. H. (1994). Generation of tunable narrow-band THz radiation from large aperture photoconducting antennas, *Applied Physics Letters*, **64**(2), pp. 137–139.

WHITE-J. O., LUDWIG-C. AND KUHL-J. (1995). Response of grating pairs to single-cycle electromagnetic pulses, *Journal of the Optical Society of America B: Optical Physics*, **12**(9), pp. 1687–1694.

WIESENFELD-J. M. (1990). Electro-optic sampling of high-speed devices and integrated circuits, *IBM Journal of Research and Development*, **34**(2/3), pp. 141–161.

WILCHEK-M. AND BAYER-E. A. (1988). The avidin-biotin complex and bioanalytical applications, *Analytical Biochemistry*, **171**(1), pp. 1–32.

WILKE-I., MACLEOD-A. M., GILLESPIE-W. A., BERDEN-G., KNIPPELS-G. M. H. AND VAN DER MEER-A. F. G. (2002). Single-shot electron-beam bunch length measurements, *Physical Review Letters*, **88**(12), pp. 124801–1–124801–4.

WILLIAMS-G. P. (2002). Far-IR/THz radiation from the Jefferson Laboratory, energy recovered linac, free electron laser, *Review of Scientific Instruments*, **73**(3), pp. 1461–1463.

WILTSE-J. C. (1984). History of millimeter and submillimeter waves, *IEEE Transactions on Microwave Theory and Techniques*, **32**(9), pp. 1118–1127.

WINNEWISSER-C., LEWEN-F. AND HELM-H. (1998). Transmission characteristics of dichroic filters measured by THz time-domain spectroscopy, *Applied Physics A: Materials Science & Processing*, **66**(6), pp. 593–598.

WINNEWISSER-C., LEWEN-F. T., SCHALL-M., WALTHER-M. AND HELM-H. (2000). Characterization and application of dichroic filters in the 0.1–3-THz region, *IEEE Transactions on Microwave Theory and Techniques*, **48**(4), pp. 744–749.

WINNEWISSER-C., LEWEN-F., WEINZIERL-J. AND HELM-H. (1999). Transmission features of frequency-selective components in the far infrared determined by terahertz time-domain spectroscopy, *Applied Optics*, **38**(18), pp. 3961–3967.

WOODWARD-R. M., COLE-B., WALLACE-V. P., ARNONE-D. D., PYE-R., LINFIELD-E. H., PEPPER-M. AND DAVIES-A. G. (2001). Terahertz pulse imaging of in-vitro basal cell carcinoma samples, *Conference on Lasers and Electro-Optics '01*, Optical Society of America, Baltimore, MD, U.S.A., pp. 329–330.

WOOLARD-D., KAUL-R., SUENRAM-R., WALKER-A. H., GLOBUS-T. AND SAMUELS-A. (1999). Terahertz electronics for chemical and biological warfare agent detection, *in* M. Matloubian and E. Ponti (eds.), *IEEE MTT-S International Microwave Symposium Digest*, Vol. 3, IEEE, IEEE, Anaheim, CA, pp. 925–928.

WU-Q. AND ZHANG-X.-C. (1995). Free-space electro-optic sampling of terahertz beams, *Applied Physics Letters*, **67**(24), pp. 3523–3525.

WU-Q. AND ZHANG-X.-C. (1996a). Design and characterization of travelling-wave electrooptic terahertz sensors, *IEEE Journal of Selected Topics in Quantum Electronics*, **2**(3), pp. 693–700.

WU-Q. AND ZHANG-X.-C. (1996b). Ultrafast electro-optic field sensor, *Applied Physics Letters*, **68**(12), pp. 1604–1606.

WU-Q. AND ZHANG-X.-C. (1997a). 7 terahertz broadband GaP electo-optic sensor, *Applied Physics Letters*, **70**(14), pp. 1784–1786.

WU-Q. AND ZHANG-X.-C. (1997b). Free-space electro-optic sampling of mid-infrared pulses, *Applied Physics Letters*, **71**(10), pp. 1285–1286.

WU-Q., HEWITT-T. D. AND ZHANG-X.-C. (1996a). Two-dimensional electro-optic imaging of terahertz beams, *Applied Physics Letters*, **69**(8), pp. 1026–1028.

WU-Q., LITZ-M. AND ZHANG-X.-C. (1996b). Broadband detection capability of ZnTe electo-optic field detectors, *Applied Physics Letters*, **68**(21), pp. 2924–2926.

WU-Q., SUN-F. G., CAMPBELL-P. AND ZHANG-X.-C. (1996c). Dynamic range of an electro-optic field sensor and its imaging applications, *Applied Physics Letters*, **68**(23), pp. 3224–3226.

WYNNE-K. AND JAROSZYNSKI-D. A. (1999). Superluminal terahertz pulses, *Optics Letters*, **24**(1), pp. 25–27.

WYNNE-K., CAREY-J. J., ZAWADZKA-J. AND JAROSZYNSKI-D. A. (2000). Tunneling of single-cycle terahertz pulses through waveguides, *Optics Communications*, **176**(4–6), pp. 429–435.

XU-B., HU-Q. AND MELLOCH-M. R. (1997). Electrically pumped tunable terahertz emitter based on intersubband transition, *Applied Physics Letters*, **71**(4), pp. 440–442.

XU-J., YUAN-T., MICKAN-S. P. AND ZHANG-X.-C. (2003). Limits of spectral resolution in terahertz time-domain spectroscopy, *Chinese Physics Letters*, **20**(8), pp. 1266–1268.

XU-L., ZHANG-X.-C. AND AUSTON-D. H. (1992). Terahertz beam generation by femtosecond optical pulses in electo-optic materials, *Applied Physics Letters*, **61**(15), pp. 1784–1786.

YAJIMA-T. AND TAKEUCHI-N. (1971). Spectral properties and tunability of far-infrared difference-frequency radiation produced by picosecond laser pulses, *Japanese Journal of Applied Physics*, **10**(7), pp. 907–915.

YAKYMYSHYN-C. P., STEWART-K. R., BODEN-E. P., MARDER-S. R., PERRY-J. W. AND SCHAEFER-W. P. (1991). Second-order non-linear optical properties of 4*n*-methylstilbazolium tosylate salts, *in* R. A. Hann and D. Bloor (eds.), *Organic Materials for Non-linear Optics II*, Royal Society of Chemistry, London, pp. 108–114.

YANG-K. H., RICHARDS-P. L. AND SHEN-Y. R. (1971). Generation of far-infrared radiation by picosecond light pulses in $LiNbO_3$, *Applied Physics Letters*, **19**(9), pp. 320–323.

YARBOROUGH-M., SUSSMAN-S. S., PUTHOFF-H. E., PANTELL-R. H. AND JOHNSON-B. C. (1969). Efficient, tunable emission from $LiNbO_3$ without a resonator, *Applied Physics Letters*, **15**(3), pp. 102–105.

YARIV-A. (1989). *Quantum Electronics*, 3rd edn, Wiley, New York.

YARIV-A. (1991). *Optical Electronics*, 4th edn, Oxford University Press, Oxford.

YNGVESSON-K. S. (2000). Ultrafast two-dimensional electron gas detector and mixer for terahertz radiation, *Applied Physics Letters*, **76**(6), pp. 777–779.

YONEDA-H., TOKUYAMA-K., UEDA-K., YAMAMOTO-H. AND BABA-K. (2001). High-power terahertz radiation emitter with a diamond photoconductive switch array, *Applied Optics*, **40**(36), pp. 6733–6736.

YOU-D. AND BUCKSBAUM-P. H. (1997). Propagation of half-cycle far infrared pulses, *Journal of the Optical Society of America B: Optical Physics*, **14**(7), pp. 1651–1655.

YOU-D., JONES-R. R., BUCKSBAUM-P. H. AND DYKAAR-D. R. (1994). Coherent generation of far-infrared radiation from InP, *Journal of the Optical Society of America B: Optical Physics*, **11**(3), p. 486.

YUAN-T., MICKAN-S. P., XU-J.-Z., ABBOTT-D. AND ZHANG-X.-C. (2002). Towards an apertureless electro-optic T-ray microscope, *Conference on Lasers and Electro-Optics '02*, IEEE LEOS & OSA, Long Beach, CA, U.S.A., pp. 637–638.

ZERNIKE-F. (1969). Temperature-dependent phase matching for far-infrared difference-frequency generation in InSb, *Physical Review Letters*, **22**(18), pp. 931–933.

ZERNIKE, JR.-F. AND BERMAN-P. R. (1965). Generation of far infrared as a difference frequency, *Physical Review Letters*, **15**(26), pp. 999–1001.

ZHANG-C., LEE-K.-S., ZHANG-X.-C., WEI-X. AND SHEN-Y. R. (2001a). Optical constant of ice Ih crystal at terahertz frequencies, *Applied Physics Letters*, **79**(4), pp. 491–493.

ZHANG-J. AND GRISCHKOWSKY-D. (2002). Whispering-gallery mode terahertz pulses, *Optics Letters*, **27**(8), pp. 661–662.

ZHANG-J. M., RUO-R. L. AND JACKSON-M. K. (1999). Noise suppression in Ti:sapphire laser-based electro-optic sampling, *Applied Physics Letters*, **75**(22), pp. 3446–3448.

ZHANG-W., ZHANG-J. AND GRISCHKOWSKY-D. (2001b). Quasioptic dielectric tetrahertz cavity: Coupled through optical tunneling, *Applied Physics Letters*, **78**(17), pp. 2425–2427.

ZHANG-X.-C., DARROW-J. T., HU-B. B., AUSTON-D. H., SCHMIDT-M. T., THAM-P. AND YANG-E. S. (1990a). Optically induced electromagnetic radiation from semiconductor surfaces, *Applied Physics Letters*, **56**(22), pp. 2228–2230.

ZHANG-X.-C., HU-B. B., DARROW-J. T. AND AUSTON-D. H. (1990b). Generation of femtosecond electromagnetic pulses from semiconductor surfaces, *Applied Physics Letters*, **56**(11), pp. 1011–1013.

ZHANG-X.-C., JIN-Y. AND MA-X. F. (1992a). Coherent measurement of THz optical rectification from electro-optic crystals, *Applied Physics Letters*, **61**(23), pp. 2764–2766.

ZHANG-X.-C., JIN-Y., HEWITT-T. D., SANGSIRI-T., KINGSLEY-L. E. AND WEINER-M. (1993a). Magnetic switching of THz beams, *Applied Physics Letters*, **62**(17), pp. 2003–2005.

ZHANG-X.-C., JIN-Y., KINGSLEY-L. E. AND WEINER-M. (1993b). Influence of electric and magnetic fields on THz radiation, *Applied Physics Letters*, **62**(20), pp. 2477–2479.

ZHANG-X.-C., JIN-Y., YANG-K. AND SCHOWALTER-L. J. (1992b). Resonsant nonlinear susceptibility near the GaAs band gap, *Physical Review Letters*, **69**(15), pp. 2303–2306.

ZHANG-X.-C., MA-X. F., JIN-Y., LU-T.-M., BODEN-E. P., PHELPS-P. D., STEWART-K. R. AND YAKYMYSHYN-C. P. (1992c). Terahertz optical rectification from a nonlinear organic crystal, *Applied Physics Letters*, **61**(26), pp. 3080–3082.

ZHAO-G., SCHOUTEN-R. N., VAN DER VALK-N., WENCKEBACH-W. T. AND PLANKEN-P. C. M. (2002a). Design and performance of a THz emission and detection setup based on a semi-insulating GaAs emitter, *Review of Scientific Instruments*, **73**(4), pp. 1715–1719.

ZHAO-G., SCHOUTEN-R. N., VAN DER VALK-N., WENCKEBACH-W. T. AND PLANKEN-P. C. M. (2002b). A terahertz system using semi-large emitters: Noise and performance characteristics, *Physics in Medicine and Biology*, **47**(21), pp. 3699–3704.

ZOIDIS-E., BESNARD-M. AND YARWOOD-J. (1996). Far infrared spectroscopic studies of the molecular dynamics and interactions of pyridine in organic solvents, *Chemical Physics Letters,* **203**, pp. 233–243.

Glossary & Symbols

This is a list of commonly used symbols and acronyms used in this Thesis and the T-ray literature. The page numbers for each entry refer to the first use of the symbol or acronym in the text; the page numbers for all other uses are listed in the Index.

λ	Wavelength (m), 58
$\tilde{\epsilon} = \epsilon' - j\epsilon''$	Complex dielectric constant, 46
$\tilde{n} = n - j\kappa$	Complex index of refraction, 47
c_0	Speed of light in a vacuum (m/s), 46
T_c	Superconducting transition temperature (K), 29
AC	'Alternating Current' (oscillating with time), 39
AF	Audio Frequency, 111
AFM	Atomic Force Microscope, 140
AlGaAs	Aluminium Gallium Arsenide, 69
AOM	Acousto-Optic Modulator, 261
ATR-FTIR	Attenuated Total Internal Reflection Fourier Transform Infrared spectroscopy, 133
BSA	Bovine Serum Albumin, 145
BWO	Backward Wave Oscillator, 16
CAS No.	Chemical Abstracts Service Registry Number, 78
CCD	Charge Coupled Device, 36
CT	Computed Tomography, 194
CW	Continuous-Wave, 11
D_2O	Deuterated Water, 66
DAST	4-dimethylamino-*N*-methyl-4-stilbazolium-tosylate, 13
DBR	Distributed Bragg Reflector, 15
DC	'Direct Current' (constant over time), 20
DFG	Difference Frequency Generation, 13
DGDG	Digalactosyldiacyl Glycerol, 148
DNA	Deoxyribonucleic Acid, 64
DSP chip	Digital Signal Processing chip, 190
DTDS	Differential Time-Domain Spectroscopy, xv

EO	Electro-Optic, 20
EOS	Electro-Optic Sampling, 2
FEL	Free-Electron Laser, 10
FFT	Fast Fourier Transform, 10
FIR	Far-InfraRed, 8
FP	Fabry-Pérot (or FP factor in equations), 49
FTIR	Fourier Transform InfraRed, 3
GaP	Gallium Phosphide, 36
Ge	Germanium, 12
GFC	Gas Filter Correlation, 65
GPIB	General Purpose Interface Bus, 33
HBT	Heterojunction Bipolar Transistor, 16
HCN	Hydrogen Cyanide, 11
HDPE	High-Density PolyEthylene, 80
HEMT	High-Electron-Mobility Transistor, 16
HF	Hydrogen Fluoride, 118
HPLC	High-Performance Liquid Chromatography, 145
HWP	Half-Wave Plate, 42
LIA	Lock-In Amplifier, 31
$LiNbO_3$	Lithium Niobate, 14
$LiTaO_3$	Lithium Tantalate, 14
LT-GaAs	Low-Temperature-grown Gallium Arsenide, 15
MOEMS	Micro-Opto-Electro-Mechanical Systems, 103
NA	Numerical Aperture, 212
Nd:YAG	Neodymium:Yttrium Aluminum Garnet, 13
NLTL	Nonlinear Transmission Line, 16
NMR	Nuclear Magnetic Resonance, 3
OPG	Optical Parametric Generation, 14
OPO	Optical Parametric Oscillator, 13
OR	Optical Rectification, 2
PCA	PhotoConductive Antenna, 2
PD	PhotoDiode, 38
PPLN	Periodically-Poled Lithium Niobate, 26
PSD	Phase Sensitive Detector, 271
QCL	Quantum Cascade Laser, 10

QW	Quantum Well, 26
QWIP	Quantum Well Infrared Photodetector, 17
QWP	Quarter-Wave Plate, 35
RF LIA	Radio Frequency Lock-In Amplifier, 111
SC	Subtilisin Carlsberg, 6
SCG	Surface Current Generation, 245
Si	Silicon, 68
SI-GaAs	Semi-Insulating Gallium Arsenide, 23
SiO_2	Silicon Dioxide, 118
SNR	Signal-to-Noise Ratio, 3
SOS	Silicon-On-Sapphire, 23
SPR	Surface Plasmon Resonance, 132
TDS	Time-Domain Spectroscopy, 46
THz-TDS	Terahertz Time-Domain Spectroscopy, 20
TiO_x	Titanium Oxide, 68
TIR	Total Internal Reflection, 43
TNT	TriNitroToluene, 135
TPG	T-ray Parametric Generation, 14
ZnTe	Zinc Telluride, 26

Index

Résumé

Sam Mickan graduated from a Bachelor of Engineering (Electrical and Electronic) at the University of Adelaide in 1997 and from a Bachelor of Arts (German & History) in 2002.

He commenced his Ph.D. in 1999 under the supervision of A/Prof. Derek Abbott (Electrical and Electronic Engineering) and Prof. Jesper Munch (Experimental Physics) at the University of Adelaide.

During 2001 and 2002, he worked with Prof. Xi-Cheng Zhang (Center for Terahertz Technology) as a Fulbright Scholar at Rensselaer Polytechnic Institute in New York, USA.

Sam has received a number of other university awards and scholarships, including a George Murray Scholarship from the University of Adelaide, competitive travel grants from the IEEE (LEOS), New Focus and the SPIE, a AFUW Barbara Crase Bursary, and a University of Adelaide Research Abroad Scholarship. His professional activities have included establishing a Student Branch of the IEEE at the University of Adelaide.

He has authored and co-authored over 20 publications, including a book chapter, and has given more than 10 presentations at conferences, including an invited talk at the First International Conference on T-rays in Biology (BISAT 2001).

In 2003 he began lecturing in the School of Electrical and Electronic Engineering at his Alma Mater.